

Wanchun Chen
Hao Zhou
Wenbin Yu
Liang Yang

Steady Glide Dynamics and Guidance of Hypersonic Vehicle



Science Press
Beijing



Springer

Steady Glide Dynamics and Guidance of Hypersonic Vehicle

Wanchun Chen · Hao Zhou ·
Wenbin Yu · Liang Yang

Steady Glide Dynamics and Guidance of Hypersonic Vehicle



Science Press
Beijing



Springer

Wanchun Chen
School of Astronautics
Beihang University
Beijing, China

Wenbin Yu
School of Astronautics
Beihang University
Beijing, China

Hao Zhou
School of Astronautics
Beihang University
Beijing, China

Liang Yang
School of Astronautics
Beihang University
Beijing, China

ISBN 978-981-15-8900-3 ISBN 978-981-15-8901-0 (eBook)
<https://doi.org/10.1007/978-981-15-8901-0>

Jointly published with Science Press, Beijing
The print edition is not for sale in China Mainland. Customers from China Mainland please order the print book from Science Press, Beijing

© Science Press 2021

This work is subject to copyright. All rights are reserved by the Publishers, whether the whole or part of the material is concerned, specifically the rights of translation, reprinting, reuse of illustrations, recitation, broadcasting, reproduction on microfilms or in any other physical way, and transmission or information storage and retrieval, electronic adaptation, computer software, or by similar or dissimilar methodology now known or hereafter developed.

The use of general descriptive names, registered names, trademarks, service marks, etc. in this publication does not imply, even in the absence of a specific statement, that such names are exempt from the relevant protective laws and regulations and therefore free for general use.

The publishers, the authors, and the editors are safe to assume that the advice and information in this book are believed to be true and accurate at the date of publication. Neither the publishers nor the authors or the editors give a warranty, express or implied, with respect to the material contained herein or for any errors or omissions that may have been made. The publishers remain neutral with regard to jurisdictional claims in published maps and institutional affiliations.

This Springer imprint is published by the registered company Springer Nature Singapore Pte Ltd.
The registered company address is: 152 Beach Road, #21-01/04 Gateway East, Singapore 189721,
Singapore

Preface

With the development of aerospace technology, space transportation application is getting conventional. In particular, the research on reentry flight dynamics and guidance has received considerable attention, and a lot of valuable work has been accomplished by scholars all over the world. In order to better satisfy the constraints of heating rate and obtain better control qualities during the reentry flight, the concept of steady glide trajectory and a series of guidance methods based on it are proposed in this book.

Involving many branches of disciplines, such as the reentry flight dynamics, aerodynamics, preliminary design of aircraft, optimal control theory, and optimization theory, steady glide dynamics and guidance are developed systematically based on the flight dynamics and classic guidance theory. Currently, it has been widely applied.

With the experience of working in the field of flight dynamics and guidance for more than 20 years, the author Prof. Wanchun Chen and his team have completed a number of studies on reentry trajectory optimization, reentry performance analysis, reentry guidance algorithm, reentry penetration trajectory planning and guidance, etc., and put forward a series of theoretical methods adapted to reentry missions. This book makes a summary of the existing methods and extract general dynamics and guidance theory.

This book consists of 17 chapters, mainly focusing on the steady glide reentry dynamics and guidance as well as their applications. Chapter 1 describes the state of the art of reentry guidance and the problems encountered during the reentry of hypersonic vehicles. Chapter 2 introduces the relevant mathematical fundamentals. Chapter 3 introduces the dynamics model of the reentry glide vehicle. Chapter 4 presents the optimal control problem for reentry glide. Chapters 5 and 6 introduce the indirect and direct methods to solve the optimal glide trajectory, respectively. Chapter 7 proposes the concept of the steady glide reentry trajectory and the stability of its regular perturbation solutions. Chapter 8 introduces the analytical solutions of steady glide reentry trajectory and their application to trajectory planning. Chapter 9 introduces the trajectory damping control technique for hypersonic glide reentry. Chapter 10 introduces the steady glide dynamic modeling

and trajectory optimization for high lift-to-drag ratio reentry vehicle. Chapter 11 introduces the singular perturbation guidance of hypersonic glide reentry. Chapter 12 introduces the 3-D reentry guidance with real-time planning based on spectral decomposition analysis method. Chapter 13 introduces the omnidirectional autonomous reentry guidance based on the 3-D analytical glide formulas with consideration of the effect of the Earth's rotation. Chapter 14 introduces the analytical entry guidance based on steady glide. Chapter 15 introduces the linear pseudospectral general normal effort miss distance guidance method. Chapter 16 introduces the linear pseudospectral adaptive flight phase segmentation general nominal effort miss distance reentry guidance. Chapter 17 introduces the trajectory-shaping guidance with final speed and load constraints.

The outline of this book was drawn up by Prof. Wanchun Chen. All Chapters are written by Wanchun Chen, Hao Zhou, Wenbin Yu, and Liang Yang. Special thanks to Jiafeng Li, Jinchuan Hu, Qingqing Qiao, Jinglin Li, Penglei Zhao, and Wanqing Zhang for their contributions. The authors are also indebted to Wenhao Du, Heng Li, Shilei Zhao, Yang Li, Xingcai He, Liming Huang, Qi Yu, Jin Yang, and Yuzheng Yao for participating in translations, sorting, and revision work during writing the book.

Due to the authors' limited knowledge, there might be some mistakes and flaws in this book. Please do not hesitate to correct us.

Beijing, China

July 2020

Wanchun Chen

Hao Zhou

Wenbin Yu

Liang Yang

Acknowledgments Thanks for the support of the Chinese national science and technology academic works publishing fund.

Contents

1	Introduction	1
1.1	Problem Description	1
1.2	Research Significance	2
1.3	Research Progress	4
References		8
2	Mathematical Fundamentals	11
2.1	Regular Perturbation Method	11
2.2	Singular Perturbation Method	13
2.3	Spectral Decomposition Method	16
2.3.1	Idempotent Matrix	16
2.3.2	Spectral Decomposition Theorem	16
2.3.3	Inference	17
2.3.4	Example	19
2.4	Pseudospectral Method	19
2.4.1	Introduction of Method	19
2.4.2	Pseudospectral Discrete Process	23
2.5	Linear Gauss Pseudospectral Model Predictive Control	33
References		38
3	Mathematical Modeling for Hypersonic Glide Problem	41
3.1	The Coordinate System Adopted in This Book	41
3.1.1	Geocentric Inertial Coordinate System (I)	41
3.1.2	Geographic Coordinate System (T)	41
3.1.3	Orientation Coordinate System (O)	42
3.1.4	Velocity Coordinate System (V)	42
3.1.5	Half-Velocity Coordinate System (H)	42
3.1.6	Body Coordinate System (B)	43
3.2	Transformation Between Coordinate Systems	43

3.2.1	Transformation Between the Orientation Coordinate System and the Half-Velocity Coordinate System	43
3.2.2	Transformation Between the Velocity Coordinate System and the Half-Velocity Coordinate System	43
3.2.3	Transformation Between the Velocity Coordinate System and the Body Coordinate System	44
3.2.4	Transformation Between the Body Coordinate System and the Half-Velocity Coordinate System	45
3.3	Dynamic Equations of Hypersonic Vehicle in Half-Velocity Coordinate System	45
3.3.1	Dynamics Equations of the Center of Mass in Half-Velocity Coordinate System	45
3.3.2	The Dynamic Equations of the Center of Mass of the Vehicle	48
3.3.3	Dynamic Equations of Hypersonic Gliding Vehicle Based on BTT Control	48
3.3.4	Dynamic Equations of Hypersonic Vehicle in Vertical Plane	49
3.3.5	Atmospheric Model	50
3.3.6	Aerodynamic Model	50
3.3.7	The Stagnation Point Heat Flow, Overload and Dynamic Pressure	50
4	Mathematical Description of Glide-Trajectory Optimization Problem	53
4.1	Mathematical Description for Optimal Control Problem	53
4.1.1	Performance Index of Optimal Control Problem	53
4.1.2	Description of Optimal Control Problem	54
4.1.3	The Minimum Principle	55
4.1.4	Final Value Performance Index of Time-Invariant Systems	56
4.1.5	Integral Performance Index of Time-Invariant Systems	57
4.1.6	Optimal Control Problem with Inequality Constraints	58
4.1.7	Methods for Solving Optimal Control Problems	58
4.2	Mathematical Description of Optimal Control Problem for Hypersonic Vehicle Entry Glide	61
4.2.1	Maximum Final Speed Problem	61
4.2.2	Maximum Range Problem	62
4.2.3	Shortest Time Problem	62
4.2.4	Optimal Trajectory Problem with Heating Rate Constraint	63
4.2.5	Optimal Trajectory Problem with Heating Rate and Load Factor Constraints	64

5 Indirect Approach to the Optimal Glide Trajectory Problem	65
5.1 Combined Optimization Strategy for Solving the Optimal Gliding Trajectory of Hypersonic Aircraft	67
5.1.1 Mathematical Model of Hypersonic Gliding	67
5.1.2 Necessary Conditions for Optimal Gliding Trajectory	68
5.1.3 Solving Two-Point Boundary Value Problem by Combination Optimization Strategy	69
5.1.4 Numerical Calculation Results	70
5.1.5 Conclusion	73
5.2 Trajectory Optimization of Transition Section of Gliding Hypersonic Flight Vehicle	74
5.2.1 Aerodynamic Data for the Transition Section	74
5.2.2 Unconstrained Trajectory of Maximum Terminal Velocity	75
5.2.3 Heat Flow Constrained Trajectory of Maximum Terminal Velocity	76
5.2.4 Solving the Two-Point Boundary Value Problem for the Transition Section	77
5.2.5 Optimizing the Transition Trajectory with Direct Method	77
5.2.6 Steps for Solving the Optimal Transition Trajectory	78
5.2.7 Transitional Trajectory Obtained by Indirect Method	81
5.3 The Maximum Range Gliding Trajectory of the Hypersonic Aircraft	84
5.3.1 Guess Initial Values for Optimal Control Problem by Direct Method	84
5.3.2 Indirect Method for Solving Optimal Control Problems	89
5.3.3 The Maximum Range Gliding Trajectory of the Hypersonic Aircraft	94
References	101
6 Direct Method for Gliding Trajectory Optimization Problem	103
6.1 Direct Method for Solving Optimal Control Problems	103
6.2 Direct Shooting Method	104
6.2.1 Direct Multiple Shooting Method	104
6.2.2 Direct Method of Discrete Control	105
6.2.3 Gradual Subdividing Optimization Strategy	106
6.3 Direct Collocation Method	107
6.3.1 General Form of Direct Collocation Method	107
6.3.2 Direct Transcription	108

6.3.3	Implicit Integral Method	109
6.3.4	Solving Optimal Trajectory Problems with NLP	110
6.4	Direct Collocating Method for Trajectory with Maximum Gliding Cross Range of Hypersonic Aircraft	111
6.4.1	Mathematical Model	111
6.4.2	Re-entry Flight Control Law with Given Angle of Attack Profile	113
6.4.3	Solution of Maximum Cross Range Problem by Direct Collocation Method	113
6.4.4	Optimization Example	116
6.4.5	Summary	118
6.5	Pseudo-spectral Method for the Optimal Trajectory of the Hypersonic Vehicle with the Longest Cross-Range	119
6.5.1	Introduction of Pseudo-spectral Method	119
6.5.2	Optimization Examples and Results	122
7	Concept of Steady Glide Reentry Trajectory and Stability of Its Regular Perturbation Solutions	125
7.1	Introduction	125
7.2	Kinetic Equations	126
7.3	Definition of the Steady Glide Trajectory	127
7.4	Effects of Control Variable on SGT	128
7.5	Effects of Initial Value on SGT	129
7.6	Analytical Solution of SGT	129
7.6.1	Altitude Dynamic Differential Equation	129
7.6.2	Analytical Steady Glide Altitude	131
7.6.3	Second-Order Item	133
7.6.4	Analytical Solutions of Flight Path Angle and Vertical Acceleration	134
7.7	Dynamic Characteristics of SGT	135
7.7.1	Stability Analysis	135
7.7.2	Natural Frequency and Damping	137
7.8	Feedback Control of SGT	140
7.8.1	Feedback Design	140
7.8.2	Fixed-Damping Differential Feedback Method	144
7.9	Conclusions	147
	References	147
8	Analytical Solutions of Steady Glide Reentry Trajectory in Three Dimensions and Their Application to Trajectory Planning	149
8.1	Introduction	149
8.2	Mathematical Model	150

8.2.1	Definition of Coordinate Frame	150
8.2.2	Kinematic Equations	150
8.2.3	Decoupling of Equations	152
8.3	Analytical Solution of Glide Trajectory	153
8.3.1	Analytical Solution of Altitude	153
8.3.2	Analytical Solution of Range	154
8.3.3	Analytical Solution of Heading Angle	154
8.3.4	Analytical Solution of Longitude and Latitude	155
8.3.5	Analytical Solution of Velocity	156
8.3.6	Optimal Initial Glide Angle	157
8.4	Simulation	157
8.4.1	Comparison Between Analytical Solution and Numerical Integral	157
8.4.2	Comparison with Bell Analytical Solution	157
8.4.3	Application of Analytic Solutions in Trajectory Planning	160
8.5	Summary	164
	References	164
9	Trajectory Damping Control Technique for Hypersonic Glide Reentry	167
9.1	Introduction	167
9.2	Guidance Scheme	168
9.2.1	Mathematical Proof	168
9.2.2	Command Flight-Path Angle for L/D_{\max}	170
9.2.3	Guidance Scheme for Range Maximization and Trajectory Damping Control	172
9.2.4	Extended Guidance Scheme for Glide Range Control	173
9.3	Hypersonic Vehicle Model	174
9.4	Results and Discussion	176
9.4.1	Performance of Guidance Scheme	176
9.4.2	Application of the Extended Guidance Scheme	183
9.5	Conclusions	189
	References	189
10	Steady Glide Dynamic Modeling and Trajectory Optimization for High Lift-To-Drag Ratio Reentry Vehicle	191
10.1	Introduction	191
10.2	Dynamics and Vehicle Description	193
10.2.1	Entry Dynamics	193
10.2.2	Entry Trajectory Constraints	194
10.2.3	Vehicle Description and Model Assumption	194
10.3	Trajectory-Oscillation Suppressing Scheme	195

10.3.1	Generic Theory for the Oscillation Suppressing Scheme	195
10.3.2	Performance of the Trajectory-Oscillation Suppressing Scheme	197
10.4	Steady Glide Dynamic Modeling and Trajectory Optimization	198
10.4.1	Steady Glide Dynamic Modeling	199
10.4.2	H _p -Adaptive Gaussian Quadrature Collocation Method	200
10.4.3	Numerical Example of Trajectory Optimization Without Bank Reversal	201
10.4.4	Numerical Example of Trajectory Optimization with Bank Reversal	205
10.4.5	Verification of Feasibility for the Pseudospectral Solution	206
10.5	Conclusion	209
	References	210
11	Singular Perturbation Guidance of Hypersonic Glide Reentry	213
11.1	Singular Perturbation Guidance for Range Maximization of a Hypersonic Glider	213
11.1.1	Problem Formulation (Dimensionless Model)	213
11.1.2	Reduced-Order System Solutions	215
11.1.3	Slow-Boundary Layer Solutions	216
11.1.4	Fast-Boundary Layer Solutions	218
11.1.5	Simulation Results	220
11.1.6	Comparison and Analysis	221
11.2	Improved Singular Perturbation Guidance for Maximum Glide Range	225
11.2.1	Dynamic Model and Solutions to the Reduced-Order System	226
11.2.2	Boundary Layer Correction	227
11.2.3	Slow Boundary-Layer Correction	227
11.2.4	Fast Boundary-Layer Correction	228
11.2.5	Guidance Law Derivation	228
11.2.6	Simulation Results and Analyses	229
11.3	Summary	232
	References	232
12	3-D Reentry Guidance with Real-Time Planning of Reference using New Analytical Solutions Based on Spectral Decomposition Method	233
12.1	Introduction	233
12.2	Equations of Motion	235

12.3	Entry Trajectory Constraints	237
12.3.1	Path Constraints	237
12.3.2	Terminal Conditions	237
12.4	Analytical Solutions to Hypersonic Gliding Problem	237
12.4.1	Auxiliary Geocentric Inertial (AGI) Frame	237
12.4.2	Linearization of the Equations of Motion	239
12.4.3	Analytical Solutions	241
12.4.4	Example for Accuracy Verification	245
12.5	Entry Guidance	248
12.5.1	Descent Phase	248
12.5.2	Quasi-Equilibrium Glide Phase	249
12.5.3	Altitude Adjustment Phase	260
12.5.4	Results and Discussion	262
12.5.5	Nominal Cases	262
12.6	Conclusions	273
Appendix	273
References	275
13	Omnidirectional Autonomous Reentry Guidance Based on 3-D Analytical Glide Formulae Considering Influence of Earth's Rotation	277
13.1	Introduction	277
13.2	Entry Guidance Problem	280
13.2.1	Equations of Motion	280
13.2.2	Path Constraints	281
13.2.3	Terminal Conditions	282
13.3	Omnidirectional Autonomous Entry Guidance	282
13.3.1	Overview	282
13.3.2	Descent Phase	285
13.3.3	Steady Glide Phase	286
13.4	Altitude Adjustment Phase	300
13.4.1	Correction of Baseline AOA Profile and Second Bank Reversal	300
13.4.2	Baseline Bank Angle in AAP	304
13.4.3	AOA and Bank Angle Commands in AAP	305
13.5	Results and Discussion	306
13.5.1	Nominal Cases	306
13.5.2	Monte Carlo Simulations	309
13.6	Conclusions	314
Appendix 1: Generalized States of Motion	315
Appendix 2: Generalized Aerodynamic Forces	318
References	319

14 Analytical Steady-Gliding Guidance Employing Pseudo-Aerodynamic Profiles	323
14.1 Introduction	323
14.2 Entry Guidance Problem	325
14.2.1 Equations of Motion	325
14.2.2 Path Constraints	326
14.2.3 Terminal Conditions	327
14.3 Analytical Entry Guidance Design	327
14.3.1 Descent Phase	328
14.3.2 Steady Glide Phase	328
14.3.3 Altitude Adjustment Phase	344
14.4 Results and Discussion	349
14.4.1 Nominal Cases	349
14.4.2 Monte Carlo Simulations	354
14.5 Conclusions	361
References	364
15 Linear Pseudospectral Guidance Method for Eliminating General Nominal Effort Miss Distance	365
15.1 Introduction	365
15.2 Generic Theory of LGPMPC	366
15.2.1 Linearization of Nonlinear Dynamic System and Formulation of Linear Optimal Control Problem	367
15.2.2 Linear Gauss Pseudospectral Method	369
15.2.3 Singularity of Differential Approximation Matrices for Different Pseudospectral Methods	374
15.2.4 Boundary Control of Linear Gauss Pseudospectral Method	374
15.2.5 Implementation of LGPMPC	375
15.3 Application to Terminal Guidance	377
15.3.1 Terminal Guidance Problem and Three-Dimensional Mode	377
15.3.2 Initial Guess and Target Model	379
15.3.3 Cases for Target with Straight-Line Movements	380
15.3.4 Comparison with Adaptive Terminal Guidance	384
15.4 Conclusion	386
Appendix	387
References	388

16 Linear Pseudospectral Reentry Guidance with Adaptive Flight Phase Segmentation and Eliminating General Nominal Effort Miss Distance	389
16.1 Introduction	389
16.2 Entry Dynamics, Entry Trajectory Constraints and Vehicle Description	391
16.2.1 Entry Dynamics	391
16.2.2 Entry Trajectory Constraints	392
16.2.3 Vehicle Description and Model Assumption	393
16.2.4 Auxiliary Geocentric Inertial Frame and Emotion Dynamics	393
16.3 Linear Pseudospectral Model Predictive Entry Guidance	394
16.3.1 Descent Phase Guidance	395
16.3.2 Glide Phase Entry Guidance	395
16.3.3 Terminal Adjustment Phase	411
16.3.4 Implementation of the Proposed Method	416
16.4 Numeric Results and Discussion	417
16.4.1 Normal Cases for Various Destinations	417
16.4.2 Monte Carlo Simulations	423
16.5 Conclusion	430
References	431
17 Trajectory-shaping Guidance with Final Speed and Load Factor Constraints	433
17.1 Introduction	433
17.2 Equations of Motion	435
17.3 Guidance Law Overview	437
17.4 Trajectory Shaping Guidance	437
17.4.1 Guidance Form	437
17.4.2 Generalized Closed Form Solutions for TSG	438
17.4.3 Stability Domain of Guidance Coefficients	448
17.5 Final Speed Control Scheme	452
17.6 Model of CAV-H	453
17.7 Results and Discussion	454
17.8 Conclusions	460
References	460

Abbreviations

x	State vector
u	Control vector
t_I	Initial time
t_F	Final time
\mathbf{g}_L	Lower bound
\mathbf{g}_U	Upper bound
Δ	Error
L	Lift
D	Drag
M	Mass
g	Acceleration of gravity
v	Velocity
γ	Flight path angle
ψ	Azimuth angle
σ	Bank angle
R_0	Earth radius
h	Altitude
θ	Longitude
ϕ	Latitude
C_L	Lift coefficients
C_D	Drag coefficients
q	Dynamic pressure
S_{ref}	Reference area
ρ	Atmospheric density
Ma	Mach number
α	Angle of attack
\mathbf{K}_{cl}	Lift coefficient matrices
\mathbf{K}_{cd}	Drag coefficient matrices
Q	Stagnation heat flux
n_N	Normal overload

l_{t_F}	Cross range
t_{span}	Time step
PM	Pseudospectral method
CPM	Chebyshev Pseudospectral method
LPM	Legendre Pseudospectral method
GPM	Gauss Pseudospectral method
RPM	Radau Pseudospectral method
KKT	Karush-Kuhn-Tucher
HBVP	Hamilton Boundary Value Problem
LGR	Lagrange-Gauss-Radau
NPSAT1	Naval Postgraduate School Satellite 1
LGL	Legendre-Gauss-Labatto
LG	Legendre-Gauss
NLP	Nonlinear Programming Problem
LGPMPC	Linear Gauss Pseudospectral Model Predictive Control
TPBVP	Two Point Boundary Value Problem
SQP	Sequential quadratic programming
CAV	Common Aero Vehicle
LQR	Linear-Quadratic Regulator
FCS	Flight control system
GER	Geocentric equatorial rotating
NED	North-east-down
TAEM	Terminal area energy management
RLV	Reusable launch vehicle
AGI	Auxiliary geocentric inertial
AOA	Angle of attack
YCGF	Yu-Chen's glide formulas
BGF	Bell's glide formulas
DP	Descent phase
QEGP	Quasi-equilibrium glide phase
AAP	Altitude adjustment phase
PN	Proportional navigation
QEGC	Quasi-equilibrium glide condition
DOF	Degrees of freedom
CAV-H	High-lift Common Aero Vehicle
SPG	Singular perturbation guidance
MLDRM	Maximum lift-drag ratio method
CM	Collocation method
SPM	Singular perturbed method
ISPG	Improved singular perturbed guidance
MPC	Model predictive control
MPSP	Model predictive static programming
LQR	Linear quadratic regulator
MLPMPC	Multi-segment linear pseudospectral model predictive control

TAEM	Terminal area energy management
AGI	Auxiliary geocentric inertial
FPA	Flight path angle
IMU	Inertial measurement unit
LOS	Line of sight
E Guidance	Explicit guidance
TSG	Trajectory-shaping guidance
FSCS	Final-speed-control scheme
FCS	Flight control system
INS	Inertial navigation system

List of Figures

Fig. 1.1	Trajectory of maximum lift-to-drag ratio flight	2
Fig. 1.2	Heating rate of maximum lift-to-drag ratio flight	2
Fig. 1.3	Profiles of maximum heating rate, initial altitude and initial Mach number corresponding to the maximum lift-to-drag ratio flight	3
Fig. 2.1	The comparison of regular perturbation solutions and exact solutions	13
Fig. 2.2	The comparison of regular perturbation solutions and exact solutions	15
Fig. 2.3	Comparison of LGR nodes and LG nodes	30
Fig. 2.4	The connections of LG and LGR	33
Fig. 5.1	Combination algorithm diagram	66
Fig. 5.2	Gliding schematic	67
Fig. 5.3	Trajectory of maximum lift-to-drag ratio	71
Fig. 5.4	Trajectory of maximum range	71
Fig. 5.5	Angle of attack over range	72
Fig. 5.6	Genetic algorithm convergence curve	72
Fig. 5.7	Simplex convergence curve	73
Fig. 5.8	Neighboring extremum convergence curve	73
Fig. 5.9	Angle of attack of the transition section over time	78
Fig. 5.10	Transition angle of attack curve obtained by direct method	78
Fig. 5.11	Transition trajectory obtained by direct method	79
Fig. 5.12	Transition Mach number obtained by direct method	79
Fig. 5.13	Transition flight path angle obtained by direct method	80
Fig. 5.14	Transition heat flow obtained by direct method	80
Fig. 5.15	λ_{γ_0} over initial angle of attack	81
Fig. 5.16	Transition angle of attack over time by indirect method	81
Fig. 5.17	Transition trajectory by indirect method	82
Fig. 5.18	Transition Mach number over time by indirect method	82

Fig. 5.19	Transition flight path angle over time by indirect method	83
Fig. 5.20	Transition heat flow over time by indirect method	83
Fig. 5.21	λ_γ over time	84
Fig. 5.22	λ_h over time	84
Fig. 5.23	Terminal Mach number and maximum heat flow over λ_{γ_0}	85
Fig. 5.24	The sensitivity of the terminal Mach number and maximum heat flow to λ_{γ_0} over λ_{γ_0}	85
Fig. 5.25	Angle of attack over λ_{γ_0} near the optimal value	86
Fig. 5.26	Gradually subdivision optimization strategy	88
Fig. 5.27	Constraint trajectory of the sub-optimal solution obtained by the direct method	91
Fig. 5.28	Step-by-step optimization process	96
Fig. 5.29	The height history of different precision in the optimization process	97
Fig. 5.30	Optimal control and optimal state variables	97
Fig. 5.31	Costate variables for the optimal solution of the equivalent system	98
Fig. 5.32	Sensitivity of glide range over costate	98
Fig. 5.33	Optimal glide trajectory under different heat flow constraints	99
Fig. 5.34	Maximum glide range over heat flow constraint	99
Fig. 5.35	Optimal control and states under heat flow constraints	100
Fig. 5.36	The heat flow of the optimal trajectory	100
Fig. 5.37	Heat flow over range with or without constraints	101
Fig. 6.1	Multiple shooting method schematic diagram	105
Fig. 6.2	Gradual subdividing optimization strategy schematic diagram	107
Fig. 6.3	General rule of angle of attack against velocity	113
Fig. 6.4	Change law of bank angle	117
Fig. 6.5	Bank angle changing with time	117
Fig. 6.6	Speed changing with time	117
Fig. 6.7	Attitude changing with time	118
Fig. 6.8	Latitude and longitude curve	118
Fig. 6.9	Bank angle history	123
Fig. 6.10	Velocity history	123
Fig. 6.11	Altitude history	123
Fig. 6.12	Longitude and latitude history	124
Fig. 7.1	Glide trajectories with different initial states	127
Fig. 7.2	Glide trajectories under different cost functions	128
Fig. 7.3	Effect of angle of attack curve continuity on steady glide trajectories	129
Fig. 7.4	Altitude deviation and flight path angle deviation	130
Fig. 7.5	Difference between the equilibrium glide altitude and the steady glide altitude	131

Fig. 7.6	Accuracy of steady glide altitude analytical solutions in different orders	133
Fig. 7.7	Analytical solutions of steady glide flight path angle	134
Fig. 7.8	Analytical solutions of steady glide longitudinal acceleration	135
Fig. 7.9	Comparison of the accuracy for different analytical solutions	136
Fig. 7.10	Dynamic system structure of altitude error	137
Fig. 7.11	Root loci of parameters V	137
Fig. 7.12	The impact of the initial altitude on the natural frequency (fixed angle of attack)	138
Fig. 7.13	The impact of the initial flight path angles on the natural frequency (fixed angle of attack)	138
Fig. 7.14	The impact of angle of attack change on the natural frequency	139
Fig. 7.15	The natural frequencies obtained by different methods	140
Fig. 7.16	Damping curves	140
Fig. 7.17	The impact of k_1 and k_2 on the parameter root locus	141
Fig. 7.18	Comparison of the control increments	142
Fig. 7.19	The impact of the feedback coefficients on glide trajectories (small perturbation)	142
Fig. 7.20	The impact of the feedback coefficients on delta altitude (small perturbation)	143
Fig. 7.21	The impact of the feedback coefficients on bank angles (small perturbation)	143
Fig. 7.22	The impact of the k_1 (large perturbation)	143
Fig. 7.23	Steady glide trajectories with initial errors	144
Fig. 7.24	Angle of attack histories of the initial descent phase	145
Fig. 7.25	Trajectories of the initial descent phase	145
Fig. 7.26	Heating rate histories of the initial descent phase	146
Fig. 7.27	Comparison of the maximum heating rates	146
Fig. 7.28	Bank angle histories and angle of attack histories	146
Fig. 7.29	Reentry trajectories and heating rate histories	147
Fig. 8.1	Generalized equator and coordinate definition	151
Fig. 8.2	Velocity solution contrast	158
Fig. 8.3	Longitudinal trajectory solution contrast	158
Fig. 8.4	Lateral trajectory solution contrast	158
Fig. 8.5	Precision comparison for 1 phase	159
Fig. 8.6	Precision comparison for 2 phases	159
Fig. 8.7	Precision comparison for 5 phases	159
Fig. 8.8	Flowchart of the gliding maneuvering trajectory planning algorithm	161
Fig. 8.9	Angle of attack histories	161
Fig. 8.10	Bank angle histories	162

Fig. 8.11	Longitudinal trajectories	162
Fig. 8.12	Velocity histories	162
Fig. 8.13	Lateral trajectories.	163
Fig. 8.14	H-V corridor	163
Fig. 9.1	H has little effect on the value of $f(E, H)$ since $\mathbf{H} \ll \mathbf{R}_0$	170
Fig. 9.2	C_{l0} as a function of Ma	174
Fig. 9.3	C_l^x as a function of Ma	175
Fig. 9.4	C_{d0} as a function of Ma	175
Fig. 9.5	K as a function of Ma	175
Fig. 9.6	Trajectories with different values of k_γ	176
Fig. 9.7	Glide range as a function of k_γ	177
Fig. 9.8	Maximum heating rate as a function of k_γ	177
Fig. 9.9	Maximum dynamic pressure as a function of k_γ	178
Fig. 9.10	Maximum load factor as a function of k_γ	178
Fig. 9.11	Trajectories without path constraint	179
Fig. 9.12	Angle of attack histories without path constraint	180
Fig. 9.13	Speed history for the scheme when $k_\gamma = 0.15$	180
Fig. 9.14	Flight-path angle history for the scheme when $k_\gamma = 0.15$	180
Fig. 9.15	L/D history for the scheme when $k_\gamma = 0.15$	181
Fig. 9.16	Load factor history for the scheme when $k_\gamma = 0.15$	181
Fig. 9.17	Trajectories with $\dot{Q}_{\max} \leq 500 \text{ W/cm}^2$	182
Fig. 9.18	Angle of attack histories with $\dot{Q}_{\max} \leq 500 \text{ W/cm}^2$	182
Fig. 9.19	Speed histories with $\dot{Q}_{\max} \leq 500 \text{ W/cm}^2$	183
Fig. 9.20	Flight-path angle histories with $\dot{Q}_{\max} \leq 500 \text{ W/cm}^2$	183
Fig. 9.21	L/D histories with $\dot{Q}_{\max} \leq 500 \text{ W/cm}^2$	184
Fig. 9.22	Load factor histories with $\dot{Q}_{\max} \leq 500 \text{ W/cm}^2$	184
Fig. 9.23	Heating rate histories with $\dot{Q}_{\max} \leq 500 \text{ W/cm}^2$	185
Fig. 9.24	Dynamic pressure histories with $\dot{Q}_{\max} \leq 500 \text{ W/cm}^2$	185
Fig. 9.25	Glide range as a function of $k_{L/D}$	186
Fig. 9.26	Maximum heating rate as a function of $k_{L/D}$	186
Fig. 9.27	Trajectories when $k_\gamma = 3$	187
Fig. 9.28	Special energy histories when $k_\gamma = 3$	187
Fig. 9.29	Angle of attack histories when $k_\gamma = 3$	187
Fig. 9.30	Speed histories when $k_\gamma = 3$	188
Fig. 9.31	Flight-path angle histories when $k_\gamma = 3$	188
Fig. 9.32	L/D histories when $k_\gamma = 3$	188
Fig. 10.1	Three-dimensional view of trajectory	198
Fig. 10.2	Histories of angle of attack and bank angle	198
Fig. 10.3	Numeric results of steady glide trajectory optimization without bank reversal	203
Fig. 10.4	Distribution of mesh nodes (Blue: new method, Red: traditional method)	204

Fig. 10.5	Numeric results of steady glide trajectory optimization with bank reversal.....	207
Fig. 10.6	Comparison between Numerical Optimal Trajectories and Integral Trajectories	209
Fig. 11.1	The relationship between the optimal altitude and specific energy.....	216
Fig. 11.2	The maximum glide range trajectory for SPG.....	221
Fig. 11.3	The velocity histories for SPG	221
Fig. 11.4	The flight-path angle histories for SPG.....	222
Fig. 11.5	The command load histories for SPG.....	222
Fig. 11.6	The angle of attack histories for SPG.....	222
Fig. 11.7	The trajectories	223
Fig. 11.8	The velocity histories	223
Fig. 11.9	The angle of attack histories.....	224
Fig. 11.10	The heating rate histories with respect to the downrange	224
Fig. 11.11	The maximum glide-range trajectory for ISPG	229
Fig. 11.12	The actual and optimal altitude histories.....	229
Fig. 11.13	Velocity histories	230
Fig. 11.14	The flight-path angle histories.....	230
Fig. 11.15	The command overload histories.....	230
Fig. 11.16	The heating rate histories	231
Fig. 12.1	Geocentric Equatorial Rotating (GER) frame: $E-x_e y_e z_e$ and local North-East-Down (NED) frame: $o-xyz$	235
Fig. 12.2	The AGI frame $E-\tilde{x}\tilde{y}\tilde{z}$ is static during each guidance cycle.....	238
Fig. 12.3	Downrange results	246
Fig. 12.4	Crossrange results	247
Fig. 12.5	Generalized heading angle results	247
Fig. 12.6	Entry guidance timeline in descent phase	249
Fig. 12.7	Entry guidance timeline during the QEGP and AAP	250
Fig. 12.8	Altitude corridor	251
Fig. 12.9	Planned L/D profile with respect to E	252
Fig. 12.10	Weakly-damped phugoid oscillation	257
Fig. 12.11	3-D oscillation suppressing scheme	257
Fig. 12.12	Altitude versus speed histories	263
Fig. 12.13	Ground tracks	263
Fig. 12.14	Flight-path angle histories.....	263
Fig. 12.15	\tilde{E} versus E profiles look like straight lines	263
Fig. 12.16	Angle of attack histories	264
Fig. 12.17	Bank angle histories	264
Fig. 12.18	Heating rate histories	264
Fig. 12.19	Dynamic pressure histories	264
Fig. 12.20	Percentage deviations of the L/D over time	266
Fig. 12.21	Altitude versus speed profiles	266

Fig. 12.22	Ground tracks	266
Fig. 12.23	Angle of attack histories	267
Fig. 12.24	Bank angle histories	267
Fig. 12.25	Heating rate histories	267
Fig. 12.26	Dynamic pressure histories	267
Fig. 12.27	Altitude versus speed for the EGAS	269
Fig. 12.28	Altitude versus speed for the PCGG	269
Fig. 12.29	Ground tracks for the EGAS	270
Fig. 12.30	Ground tracks for the PCGG	270
Fig. 12.31	AOA for the EGAS	270
Fig. 12.32	AOA for the PCGG	270
Fig. 12.33	Bank angle for the EGAS	271
Fig. 12.34	Bank angle for the PCGG	271
Fig. 12.35	Heating rate for the EGAS	271
Fig. 12.36	Heating rate for the PCGG	271
Fig. 12.37	Dynamic pressure for the EGAS	272
Fig. 12.38	Dynamic pressure for the PCGG	272
Fig. 12.39	Final states for the EGAS	272
Fig. 12.40	Final states for the PCGG	272
Fig. 12.41	Assuming that \tilde{V}_f is parallel to \mathbf{x}_1	275
Fig. 13.1	Entry trajectory of CAV guided by OAEG	282
Fig. 13.2	Altitude corridor	286
Fig. 13.3	Baseline L/D profile with respect to E	287
Fig. 13.4	Auxiliary geocentric inertial frame: $E - \tilde{x}\tilde{y}\tilde{z}$	287
Fig. 13.5	The \tilde{E} -vs- E profile looks like a straight line	289
Fig. 13.6	The natural trajectory of CAV has weakly-damped phugoid oscillations	297
Fig. 13.7	γ_{SG} is a perfect approximation of the flight-path angle corresponding to steady glide trajectory	297
Fig. 13.8	Process of calling the three iterative algorithms	301
Fig. 13.9	Ground tracks of the entry trajectories	307
Fig. 13.10	Altitude-vs-speed profiles	307
Fig. 13.11	Histories of the AOA	307
Fig. 13.12	Histories of the bank angle	307
Fig. 13.13	Histories of the heating rate	308
Fig. 13.14	Histories of the dynamic pressure	308
Fig. 13.15	Ground tracks of the trajectories	309
Fig. 13.16	Histories of the bank angle	310
Fig. 13.17	Profile of the maximum possible wind speed	310
Fig. 13.18	Profile of maximum possible percent deviation of the atmospheric density	310
Fig. 13.19	Ground tracks for OAEG	312
Fig. 13.20	Ground tracks for PCGG	312
Fig. 13.21	Altitude versus speed histories for OAEG	312

Fig. 13.22	Altitude versus speed histories for PCGG	312
Fig. 13.23	AOA histories for OAEG	313
Fig. 13.24	AOA histories for PCGG	313
Fig. 13.25	Bank angle histories for OAEG	313
Fig. 13.26	Bank angle histories for PCGG	314
Fig. 13.27	Distribution of final speeds and heading errors for OAEG	314
Fig. 13.28	Distribution of final speeds and heading errors for PCGG	314
Fig. 13.29	\hat{V}_{TAEM} is assumed to be tangent to the generalized equator	317
Fig. 13.30	Relationship between the conventional and generalized aerodynamic forces	318
Fig. 14.1	Entry trajectory of CAV corresponding to the proposed guidance	327
Fig. 14.2	Definitions of downrange and crossrange	329
Fig. 14.3	Baseline L/D profile corresponding to α_{bsl}	331
Fig. 14.4	Aerodynamic and inertial forces are merged as pseudo-aerodynamic forces	333
Fig. 14.5	Calculation of range to go s_{go}	339
Fig. 14.6	Nominal ground tracks	350
Fig. 14.7	Nominal altitude versus speed histories	351
Fig. 14.8	Nominal AOA histories	351
Fig. 14.9	Nominal bank angle histories	352
Fig. 14.10	Nominal heating rate histories	352
Fig. 14.11	Nominal dynamic pressure histories	353
Fig. 14.12	Nominal load factor histories	353
Fig. 14.13	Profile of $V_{wind(max)}$	355
Fig. 14.14	Profile of $\delta_{\rho(max)}$	355
Fig. 14.15	Ground tracks of AEG, PCGG, and SEG for Cases T2, T3, T4, and T6	357
Fig. 14.16	Altitude versus speed histories for Case T6	358
Fig. 14.17	AOA histories for Case T6	359
Fig. 14.18	Bank angle histories for Case T6	360
Fig. 14.19	Distribution of final speeds and heading errors for Case T6	361
Fig. 14.20	Distribution of final bank angles and altitudes for Case T6	362
Fig. 14.21	Distribution of computing time per one simulation for Case T6	363
Fig. 15.1	Flowchart for implementing the LGPMPC	376
Fig. 15.2	Three-dimensional motion of flight vehicle over a flat earth	378
Fig. 15.3	Three-dimensional view of various trajectories	380
Fig. 15.4	Time histories of lateral and longitudinal accelerations for various cases	381

Fig. 15.5	Time histories of flight-path angle and heading angle for various cases	382
Fig. 15.6	Convergence rate histories for various cases	383
Fig. 15.7	Comparison of the proposed method and adaptive terminal guidance	385
Fig. 15.8	Comparison of the proposed method and adaptive terminal guidance	386
Fig. 16.1	State variation at the normal bank reversal point	404
Fig. 16.2	Ground tracks	406
Fig. 16.3	Azimuth histories	407
Fig. 16.4	Longitudinal L/D updating histories	407
Fig. 16.5	Bank reversal updating histories	408
Fig. 16.6	Latitude error in each iteration	408
Fig. 16.7	Longitude error in each iteration	408
Fig. 16.8	Predictive time in each iteration	409
Fig. 16.9	Calculation time in each iteration	409
Fig. 16.10	Definition of the frames and sight-line angle	412
Fig. 16.11	Flowchart of implementation	416
Fig. 16.12	Nominal altitude histories	418
Fig. 16.13	Nominal ground tracking	418
Fig. 16.14	Nominal velocity histories	419
Fig. 16.15	Nominal FPA histories	419
Fig. 16.16	Nominal AOA histories	420
Fig. 16.17	Nominal bank angle histories	420
Fig. 16.18	Nominal heading error histories	420
Fig. 16.19	Nominal L/D histories	421
Fig. 16.20	Nominal heating rate histories	421
Fig. 16.21	Nominal dynamic pressure histories	421
Fig. 16.22	Nominal load factor histories	422
Fig. 16.23	Nominal total CPU time	422
Fig. 16.24	Ground tracks	424
Fig. 16.25	Altitude histories	424
Fig. 16.26	AOA histories	425
Fig. 16.27	Bank angle histories	425
Fig. 16.28	Heating rate histories	426
Fig. 16.29	Dynamic pressure histories	426
Fig. 16.30	Load factor histories	427
Fig. 16.31	Heading error histories	427
Fig. 16.32	FPA histories	428
Fig. 16.33	Final altitude and bank angle	428
Fig. 16.34	Final heading error and velocity	429
Fig. 16.35	Final FPA	429
Fig. 16.36	Comparison of total CPU time	430

Fig. 17.1	Inertial reference frame $o\text{-}xyH$ and the corresponding state variables	435
Fig. 17.2	Engagement geometry in vertical plane.	438
Fig. 17.3	Trajectory obtained by the nonlinear engagement simulation when $\lambda_1 = -2$ and $\lambda_2 = -2.5$	443
Fig. 17.4	Acceleration command goes to zero finally when $\lambda_1 = -2$ and $\lambda_2 = -2.5$	443
Fig. 17.5	Trajectory obtained by the engagement simulation when $\lambda_1 = -2 + 2i$ and $\lambda_2 = -2 - 2i$	445
Fig. 17.6	Acceleration command goes to zero finally when $\lambda_1 = -2 + 2i$ and $\lambda_2 = -2 - 2i$	445
Fig. 17.7	Trajectory obtained by the nonlinear engagement simulation when $\lambda_1 = \lambda_2 = -2$	448
Fig. 17.8	Acceleration command also goes to zero finally when $\lambda_1 = \lambda_2 = -2$	448
Fig. 17.9	The stability domain of the trajectory-shaping guidance coefficients	451
Fig. 17.10	C_{L0} and C_L^x as functions of Ma	453
Fig. 17.11	C_{D0} and K as functions of Ma	453
Fig. 17.12	The final speed V_f is a decreasing function of k_{Vf}	454
Fig. 17.13	The iteration algorithm converges quickly	455
Fig. 17.14	Trajectories and ground tracks	455
Fig. 17.15	Speed histories	455
Fig. 17.16	Flight-path angle histories	455
Fig. 17.17	Load factor histories	456
Fig. 17.18	Bank angle histories	456
Fig. 17.19	Dynamic pressure histories	456
Fig. 17.20	Trajectory for the proposed guidance	458
Fig. 17.21	Trajectory for the reference-tracking guidance	458
Fig. 17.22	Load factor histories for the proposed guidance	459
Fig. 17.23	Load factor histories for the reference-tracking guidance	459
Fig. 17.24	Bank angle histories for the proposed guidance	459
Fig. 17.25	Bank angle histories for the reference tracking guidance	460

List of Tables

Table 2.1	Interpolation polynomials and node types of various Pseudospectral methods	20
Table 5.1	Comparison between SQP algorithm and genetic algorithm	97
Table 6.1	Differences of pseudo-spectral methods	119
Table 7.1	Cost functions.	128
Table 7.2	Curves of angle of attack and bank angle.	135
Table 8.1	Simulation parameters.	157
Table 8.2	Accuracy of Analytical Solutions	160
Table 8.3	Trajectory planning parameters.	161
Table 8.4	No-fly zone parameters.	161
Table 9.1	Values of k_j and Downrange	177
Table 10.1	Initial and final conditions for different methods	201
Table 10.2	Optimal results by SNOPT	205
Table 10.3	Different terminal states for various cases.	206
Table 10.4	Optimal results by SNOPT	208
Table 10.5	Final errors for various integral trajectories	209
Table 11.1	The flight time, downrange, terminal velocity, and maximal heating rate	225
Table 11.2	The comparison of the terminal states before and after improvement	231
Table 12.1	Comparison of the analytical solutions and trajectory simulation	248
Table 12.2	Simulation results for nominal cases.	265
Table 12.3	Simulation results for aerodynamic dispersion cases.	268
Table 12.4	Numerical characteristics of the normally distributed random variables	268
Table 13.1	The initial and terminal conditions of the four cases	306
Table 13.2	The simulation results of the four cases	306
Table 13.3	Simulation results for the guidance developed in [16]	308

Table 13.4	Statistical characteristics of the normally distributed random parameters	311
Table 14.1	Simulation conditions for nominal cases.....	349
Table 14.2	Nominal terminal results of AEG.....	349
Table 14.3	Nominal terminal results of EGAS.....	350
Table 14.4	Statistical characteristics of the normally distributed random parameters	356
Table 15.1	Simulation parameters.....	378
Table 15.2	Initial and final state condition for different cases.....	380
Table 15.3	Miss distances for different cases	381
Table 15.4	Comparison of CPU time for terminal impact example	383
Table 16.1	Initial states for various cases.....	406
Table 16.2	Terminal conditions for various cases.....	418
Table 16.3	Statistics on the final deviations	422
Table 16.4	Initial and final conditions	423
Table 16.5	Dispersion parameters.....	423
Table 16.6	Statistics on the terminal constraints.....	430
Table 17.1	Comparison of the simulation results	458

Chapter 1

Introduction



1.1 Problem Description

Hypersonic Glide Vehicle (HGV) is generally a near-space vehicle that can fly at a velocity of more than Mach number 5. It is characterized by high velocity, long flight distance and high heating rate. Therefore, through traditional methods, it is difficult to obtain the optimal trajectory satisfying various constraints for HGV. Reference [1] drew the conclusion that the maximum range flight scheme can be approximated by the maximum lift-to-drag ratio gliding flight. Hence, simulations of the maximum lift-to-drag ratio flight are carried out and the trajectory and heating rate profiles are shown in Figs. 1.1 and 1.2 respectively, where the initial altitude is 94 km, initial Mach number is 20.4 and initial flight-path angle is 0.

As shown in Figs. 1.1 and 1.2, the maximum lift-to-drag ratio flight trajectory is a skipping gliding trajectory with a large range. Due to the severe oscillations of trajectory, the heating rate at the stagnation point cannot be controlled and the maximum heating rate may far exceed the endurance of the vehicle, thus leading to destructive damage to the vehicle structure. It can be seen from Fig. 1.2 that the maximum heating rate reaches 1400 W/cm^2 , which is far beyond the allowable peak heating rate of 650 W/cm^2 . The influences of the initial altitude and the initial Mach number on the maximum heating rate for the maximum lift-to-drag ratio flight are presented in Fig. 1.3.

Figure 1.3 shows the possibility that the maximum heating rate can be controlled below 650 W/cm^2 at a certain initial height and Mach number. However, due to the constraints of each phase and the requirement of the maximum range, the initial altitude and the initial Mach number of the entry flight may not satisfy the heating rate constraint. This means that the constrained maximum range problem cannot be addressed by adopting the maximum lift-to-drag ratio gliding flight scheme directly. As a result, it is necessary to further study the optimal control problem under various constraints and propose a fast on-line guidance algorithm.

Fig. 1.1 Trajectory of maximum lift-to-drag ratio flight

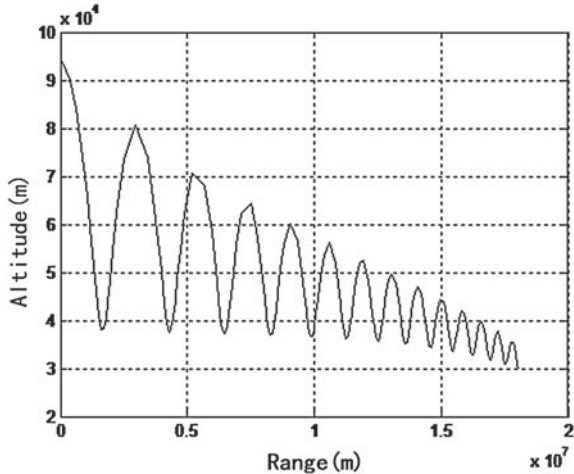
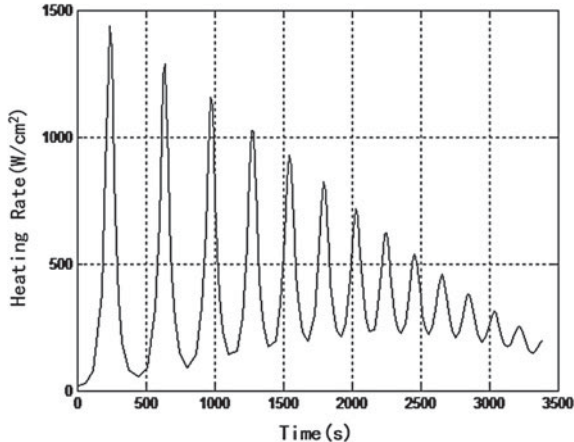


Fig. 1.2 Heating rate of maximum lift-to-drag ratio flight



1.2 Research Significance

Owing to advance in long-range, high velocity, near-space flight, low detectability and strong maneuverability, HGV has been developed vigorously by many countries.

With characteristics of high speed, wide range of speed variation and long range in entry phase, HGV shows strong maneuverability and wide maneuvering range. Because of its advantages in fast arrival and maneuverability, hypersonic glider is considered to be a re-entry vehicle with wide application prospect, which can achieve long-distance, fast and precise strike and force delivery.

This book introduces the entry dynamic characteristics and various entry guidance methods for unpowered hypersonic gliding vehicle. The trajectory of hypersonic

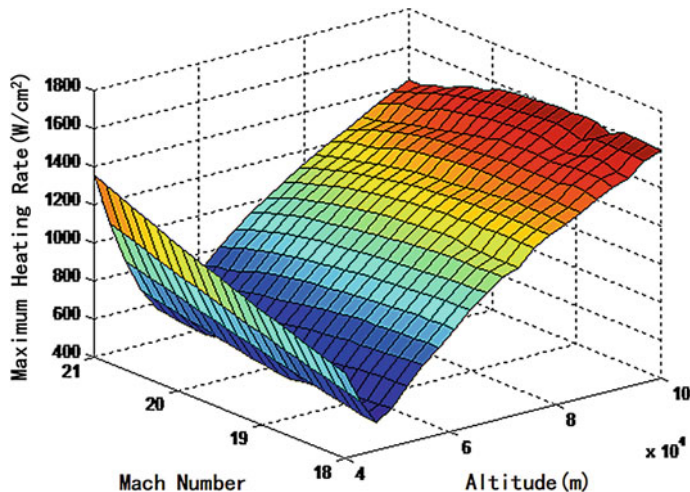


Fig. 1.3 Profiles of maximum heating rate, initial altitude and initial Mach number corresponding to the maximum lift-to-drag ratio flight

gliding vehicle can be generally divided into the ascending phase, transition phase, gliding phase and descending phase.

The ascending phase is similar to that of ballistic flight vehicle and carrier rocket, where rocket is used as the booster and has a comparatively mature technology. The transition phase has characteristics of high altitude and weak control ability, thus large Angle of Attack (AOA) and small bank angle control method are adopted here to guide the vehicle to the starting point of the gliding phase. And the flight mission of hypersonic gliding vehicle is mainly realized by the flight control in gliding phase and descending phase.

During entry flight of hypersonic vehicle, the flight distance is long, the airspace is large, and the flight Mach number varies widely. Due to the continuous increase of heat during the long-range flight, the structure of the vehicle will be under great pressure. Therefore, the peak and accumulation value of heating rate should be fully considered in trajectory design and entry guidance, thus it is important to find a reasonable guidance method which can reduce the peak heating rate and total heat flux during the research. At the same time, the control of dynamic pressure is also very imperative. When the vehicle mainly flies in near space with small air density, if the dynamic pressure is too small, the rudder will not have the capacity to provide enough moment to stabilize the attitude of the vehicle. Moreover, in order to accomplish some specific missions, the gliding vehicle needs to drop down rapidly at the end of the descending phase, which may lead to large dynamic pressure and load factor. Large dynamic pressure will produce too much hinge moment for rudder structure to sustain, and large load factor will cause damage to some weak parts of the vehicle structure. Therefore, the path constraints of heating rate, total heat

flux, dynamic pressure, load factor and control variables should be fully considered in entry gliding flight. Aiming at the problem of accurate attack, not only the target must be hit accurately, but also the desired impact angle, attitude angle and required velocity for specific missions should be achieved. In addition, the impact time constraint also needs to be considered in the study of salvo attack. Therefore, the constraints of the terminal impact angle, flight vehicle attitude angle, velocity and impact time as well as the path constraints of seeker field of view angle need to be imposed to the terminal descent guidance method. Because of the long entry flight time and drastic environmental changes, there are uncertainties in environmental parameters such as atmospheric density, atmospheric temperature and wind field, which make it impossible to obtain accurate values of those parameters. Meanwhile, the aerodynamic model of the vehicle is uncertain, and the mass of the vehicle also has some deviations due to the ablation in the entry process. In addition, the deviation of the parameters measured by the navigation system also exists. In conclusion, there are too many uncertainties in the entry flight, so the guidance system demands strong robustness. And all the constraints and deviations are addressed onboard, as the result of which the command generation must satisfy the real-time requirements.

To sum up the requirements of entry flight for hypersonic vehicle, the design of guidance method should satisfy the following conditions:

1. Strong path constraints such as heating rate, dynamic pressure, load factor and control variables can be handled.
2. Accurate terminal constraints such as velocity, flight-path angle, heading angle, position and attitude angle can be satisfied.
3. Severe model uncertainties and measurement deviations caused in the vehicle flight can be considered.
4. Strong external disturbance and uncertainty of environmental parameters can be resisted.
5. The calculation speed of guidance loop meets the real-time requirement.

As there are many new requirements for hypersonic vehicle in entry gliding flight, higher requirements for guidance methods are put forward. The traditional reference trajectory guidance method has some defects, such as low guidance accuracy, large off-line workload and poor adaptability. And the guidance method based on online trajectory planning cannot be applied on-line because of its large amount of calculation and insufficient convergence. In this book, some guidance methods are introduced to overcome the above problems.

1.3 Research Progress

Due to the strong application prospects of hypersonic vehicles, the exploration and development of hypersonic technology has been regarded as an important goal in the aeronautics and astronautics field for all countries of the world, which has set off a wave of research and development for hypersonic vehicles [2, 3]. Accuracy

guidance technology is one of the key technologies for hypersonic vehicle. The guidance problem for hypersonic vehicle in the gliding phase involves trajectory dynamic quality, robustness, real-time performance, terminal accuracy, constraint satisfaction and trajectory implementability, etc. Scholars have carried out in-depth research on these problems and obtained rich results.

1. Research on entry glide trajectory characteristics for hypersonic vehicle

The gliding phase is the main part of the whole trajectory for hypersonic vehicle. It is of great significance to analyze the characteristics of gliding trajectory and provide theoretical basis for the trajectory planning and entry guidance. Sänger [4] first proposed the concept of equilibrium glide, which has the advantages of gentle change in altitude, small heating rate and dynamic pressure peak, smooth AOA and bank angle profiles, etc. However, entry trajectory is highly sensitive to control variables, so it is often difficult to obtain the whole equilibrium glide trajectory via trajectory optimization. Besides, various disturbances in entry process can easily cause the trajectory to deviate from the equilibrium glide state, resulting in trajectory oscillation. Therefore, in entry flight, not only the reference trajectory of equilibrium glide should be obtained, but also the oscillation should be suppressed.

Bell [5] obtained the closed form solutions of the entry trajectory by using the Equilibrium Glide Condition (EGC), but the error of the analytical crossrange solution is large. Chapman [6] analyzed the dynamic characteristics of entry trajectory based on EGC, and put forward the method to suppress the trajectory oscillation by adding an negative feedback of altitude difference and altitude first derivative difference. Yu [7] analyzed the law of the flight-path angle of the equilibrium glide trajectory with a given AOA and bank angle profiles, and gave the feedback control form that can suppress the oscillation. Although many achievements have been made in the analysis of characteristics of equilibrium glide trajectory, the reference trajectory cannot be directly integrated based on EGC, which is due to the fact that the actual entry trajectory flight-path angle is not constant. Zhang [8] added the influence of slope rate to improve EGC, which was used to obtain the equilibrium glide trajectory, but the corresponding AOA profile changed too much. Hu [9] put forward the concept of steady glide on the basis of equilibrium glide and pointed out that the steady glide trajectory corresponding to the given AOA and bank angle profiles maintain steady state in the gliding phase. Using the steady glide condition, Yu [10] obtained the semi-analytical reference trajectory based on spectral-decomposition method, which can be generated online.

In conclusion, EGC is a dynamic condition, while the concept of steady glide is proposed for the index of the smooth longitudinal trajectory in the whole phases. The steady glide entry flight is conducive to satisfying the longitudinal constraints and realizing the control, and helps to obtain the analytical solutions by reducing the order of the dynamic equation. Therefore, entry guidance based on steady glide has great potential.

2. Research on entry guidance with multiple constraints for hypersonic vehicle

Entry guidance for hypersonic vehicle in gliding phase is mainly divided into three kinds of methods: One is the profile-following guidance, which consists of reference trajectory design and tracking. Both Apollo entry [11] and American space shuttle return [12] adopted this method. Sanjay [13] and Sudhir [14] used a feedback linearization method and LQR method respectively to realize entry reference trajectory tracking. The advantage of these methods is fast command generation, which is suitable for online applications. The reliability of these methods has been verified by Apollo and space shuttle entry guidance. However, the reference trajectory cannot be updated in real-time and the bank reversal is controlled by the heading error corridor, which will lead to a large terminal error in gliding phase. Although the space shuttle and Apollo entry can compensate for the error through the terminal energy management phase, this method is not conducive to improving the terminal guidance accuracy for hypersonic gliding vehicle due to its fast landing speed and short terminal reaction time.

The second kind of guidance method is the on-line trajectory planning guidance, which generates commands through real-time trajectory planning. Shen [15] used on-line programming to generate three-dimensional entry trajectory by transforming the constraints into control boundaries, and then obtained the corresponding guidance commands. This method needs multiple on-line iterations for each guidance command, which is solved iteratively with a large amount of calculation. Bollino [16] obtained the optimal trajectory directly through online trajectory optimization by using DIDO software based on Legendre pseudospectral technology, and then used open-loop control as the guidance command to achieve the precise landing of RLV with only a single disturbance of wind considered. The commands of each guidance loop are obtained by solving the optimal control problem from the current state to the terminal state based on the direct method. This kind of method needs to install a non-linear programming solution tool on the flight vehicle, which takes up a large amount of resources for the onboard computer. And it requires several iterations to obtain the corresponding accurate feasible solutions since the result of each iteration is not necessarily feasible solution. Therefore, the calculation of this method is too large to be suitable for online application.

But the development of high-precision analytical solution of gliding trajectory provides the possibility for on-line trajectory planning. Yu [10] obtained the semi-analytical solutions of trajectory using spectral-decomposition method based on steady glide condition and realized fast generation of reference trajectory. Compared with traditional methods, this method has much faster computation speed and higher accuracy of semi-analytical crossrange solution.

The third kind of guidance method is model predictive guidance, also known as predictor-corrector guidance. It corrects commands according to the deviation of predictive landing state value. Predictor-corrector guidance can be divided into analytical predictor-corrector guidance and numerical predictor-corrector guidance. Analytical predictor-corrector guidance simplifies the model and the analytical solution of the trajectory can be obtained under some assumptions. The terminal state

is predicted analytically in each guidance loop and the control variable is corrected according to the predictive terminal state deviation. Tigges [17] proposed a Mars equilibrium glide predictive guidance scheme based on the assumption that the altitude change rate is constant. Levesque [18] used the ratio of flight path angle to atmospheric density to propose a predictive guidance scheme for precise landing on Mars. The analytical predictor-corrector guidance method has the advantages of insensitivity to initial values, strong anti-jamming ability, less on-line calculation, and is suitable for engineering applications. However, the accuracy of analytical prediction is not high enough, especially for the case of maneuvering entry flight and long-range flight, and the ability to deal with path constraints is lacking.

The numerical predictor-corrector guidance is a method that integrates the prediction of entry trajectory by numerical method, and then corrects the guidance command according to the deviation between the predicted value and the expected value. There are two key research points in this method. One is the on-line trajectory prediction. The usage of the complex dynamic model prediction and integration method will directly affect guidance accuracy and command generation time. The other is the correction algorithm. Different correction algorithms have different effects. Generally, the control law is parameterized first, and the whole control can be described by several parameters. Then, according to the deviation between predicted trajectory and expected trajectory, these parameters can be corrected by iterative algorithm, so that the corrected control variables can be obtained and the deviation can be eliminated. Hu [19] used the fourth-and fifth-order Runge-Kutta-Fehlberg adaptive step-size integration algorithm for trajectory prediction. Ashok [20] and Songbai [21] successfully guided the entry vehicle to the target with reference path constraints, where the bank reversals were determined passively by the constraint boundary. Fuhr [22] designed an adaptive predictor-corrector entry guidance law by using the magnitude of bank angle and bank reversals as control variables. But the accuracy and optimality cannot be guaranteed since the corrected Jacobian matrix is obtained from a simplified model. Youssef [23] calculated and stored the sensitivity matrix of the guidance parameters caused by the downrange error and the heading error offline. And then iterative correction method were adopted to determine the required bank angle and bank reversal online without considering the optimal performance index. Christopher [24] compared the numerical predictor-corrector algorithm with the Apollo guidance algorithm. The results show that the numerical predictor-corrector guidance method has higher accuracy than the traditional Apollo entry guidance algorithm.

Halbe [25] proposed a model predictive static programming technique, which also predicted trajectory by numerical integration. In order to eliminate the deviation between the terminal state and the expected state, the trajectory is linearized based on the predicted trajectory, and then the corresponding new control variable is obtained. Yang [26] proposed a prediction control method based on Gauss pseudospectral model for air-to-surface flight vehicle guidance. It obtains the terminal state deviation first by integrating the predicted trajectory, and linearizes the model according to the trajectory prediction. And then the linear optimal control problem is solved by using Gauss pseudospectral method. In this way, this algorithm does not need optimization

and can improve the convergence speed. The methods proposed by O. Halbe and L. Yang to solve the optimal control problem belong to quasilinear method with fast convergence speed, and the results are close to optimal energy trajectory.

In summary, the entry guidance based on steady glide analytical solution and linear pseudospectral guidance can not only guarantee high guidance accuracy and fast calculation speed, but also deal with various path constraints and terminal constraints. Due to these characteristics, the two methods are both advanced and well applicable for entry problem.

References

1. Sheu, D.L., Chen, Y.M., Chernf, J.S.: Optimal three-dimensional glide for maximum reachable domain. In: AIAA Atmospheric Flight Mechanics Conference and Exhibit, p. 4245. AIAA, Portland, OR (1999)
2. Chen, X.: Research on maneuvering technology of hypersonic gliding vehicle. Ph.D. Dissertation of National Defense University of Science and Technology (2011) [in Chinese]
3. Li, W., Niu, W., Zhang, H., et al.: Summary of world hypersonic vehicle development in 2013. *Aerial Missile* (2), 3–10 (2014) (in Chinese)
4. Jorris, T.R., Cobb, R.G.: Three-dimensional trajectory optimization satisfying waypoint and no-fly zone constraints. *J. Guidance Control Dyn.* **32**(2), 551–571 (2009)
5. Bell, B.N.: A Closed-Form Solution to Lifting Reentry, AFFDL-TR-65-65. AFFDL (1965)
6. Chapman, D.R.: An Approximate Analytical Method for Studying Entry into Planetary Atmospheres, TR-R-11. NASA (1959)
7. Yu, W., Chen, W.: Guidance scheme for glide range maximization of a hypersonic vehicle. In: AIAA Guidance, Navigation, and Control Conference, p. 6714. AIAA (2011)
8. Zhang, K., Chen, W.: Reentry vehicle constrained trajectory optimization. In: AIAA International Space Planes and Hypersonic Systems and Technologies Conference, p. 2231. AIAA (2011)
9. Hu, J., Chen, W.: Research on steady gliding trajectory design of hypersonic vehicle. *J. Beijing Univ. Aeronaut. Astronaut.* **41**(8), 1464–1474 (2015) (in Chinese)
10. Yu, W., Chen, W.: Entry guidance with real-time planning of reference based on analytical solution. *Adv. Space Res.* **55**(9), 2325–2345 (2015)
11. Moseley, P.E.: The Apollo entry guidance: a review of the mathematical development and its operational characteristics. Task MSC/TRW A-220 (1969)
12. Harpold, J.C., Graves, C.A.: Shuttle entry guidance. *J. Astronaut. Sci.* **37**(3), 239–268 (1979)
13. Saraf, J.A., Leavitt, J.A., Chen, D.T., et al.: Design of evaluation of an acceleration guidance algorithm for entry. In: AIAA Guidance, Navigation, and Control Conference and Exhibit, p. 5737. AIAA (2003)
14. Sudhir, M., Tewari, A.: Autonomous maneuvering entry guidance with ground-track control. In: 45th AIAA Aerospace Sciences Meeting and Exhibit, p. 856. AIAA, Reno, Nevada (2007)
15. Shen, Z.: On-board generation of three-dimensional constrained entry trajectories. *J. Guidance Control Dyn.* **26**(1), 111–121 (2003)
16. Bollino, K.P., Ross, I.M.: Optimal nonlinear feedback guidance for reentry vehicle. In: AIAA Guidance, Navigation, and Control Conference and Exhibit, pp. 1–19. Keystone, Colorado (2006)
17. Tigges, M.: Predictive guidance algorithm for mars entry. In: 27th Aerospace Sciences Meeting, p. 632. AIAA (1989)
18. Levesque, J., Lafontaine, J.D.: Optimal guidance using density-proportional flight path angle profile for precision landing on mars. In: AIAA Guidance, Navigation, and Control Conference and Exhibit, pp. 21–24. Keystone, Colorado (2006)

19. Hu, J.: Research on Reentry Guidance Technology for Reusable Transatmospheric Vehicles. University of Defense Science and Technology (2007) (in Chinese)
20. Joshi, A., Sivan, K., Amma, S.S.: Predictor-corrector reentry guidance algorithm with path constraints for atmospheric entry vehicles. *J. Guidance Control Dyn.* **30**(5), 1307–1318 (2007)
21. Xue, S., Lu, P.: Constrained predictor-corrector entry guidance. *J. Guidance Control Dyn.* **33**(4), 1273–1281 (2010)
22. Fuhr, D.: Adaptive atmospheric reentry guidance for the Kistler K-1 orbital vehicle. In: Guidance, Navigation, and Control Conference and Exhibit, p. 4211. AIAA (1999)
23. Youssef, H., Chowdhry, R., Lee, H.: Predictor-corrector entry guidance for reusable launch vehicles. In: AIAA Guidance, Navigation, and Control Conference and Exhibit, p. 4043. AIAA (2001)
24. Brunner, C.W., Lu, P.: Comparison of numerical predictor-corrector and Apollo skip entry guidance algorithms. In: AIAA Guidance, Navigation, and Control Conference, p. 8307. AIAA (2010)
25. Halbe, O., Raja, R., Padhi, R.: Robust reentry guidance of a reusable launch vehicle using model predictive static programming. *J. Guidance Control Dyn.* **37**(1), 134–148 (2014)
26. Yang, L., Zhou, H., Chen, W.: Application of linear gauss pseudospectral method in model predictive control. *Acta Astronaut.* **96**, 175–187 (2014)

Chapter 2

Mathematical Fundamentals



2.1 Regular Perturbation Method

Such a Taylor expansion Equation in this chapter Sect. 2.1.

$$e^{-\varepsilon \lambda} - 1 = -(\varepsilon t) + \frac{1}{2}(-\varepsilon t)^2 + \frac{1}{3!}(-\varepsilon t)^3 + \cdots + \frac{1}{n!}(-\varepsilon t)^n + \cdots \quad (2.1)$$

is a regular expansion or asymptotic expansion if $O((\varepsilon t)^2) < O(\varepsilon t)$. Similarly, perturbation expansion can be defined as:

Definition 1: Consider a sequence $\phi_1(\varepsilon), \phi_2(\varepsilon), \phi_3(\varepsilon), \dots$ as functions of ε . $\phi_1(\varepsilon), \phi_2(\varepsilon), \phi_3(\varepsilon), \dots$ is sequential asymptotic if for every $m < n$. There is $\phi_n = O(\phi_m)$ when $\varepsilon \rightarrow \varepsilon_0$; If $\phi_1(\varepsilon), \phi_2(\varepsilon), \phi_3(\varepsilon), \dots$ is sequential asymptotic and $f = \sum_{k=1}^m a_k \phi_k(\varepsilon) + O(\phi_m)$ $m = 1, 2, \dots, n$, ($a_k, k = 1, 2, \dots, n$ is related to ε) when $\varepsilon \rightarrow \varepsilon_0$, then $f(\varepsilon)$ has n -order asymptotic expansions, where $\{\phi_k\} k = 1, 2, \dots$ is called the scale function or basis function. The common basis function used for perturbation expansion are: $1, \varepsilon, \varepsilon^2, \varepsilon^3, \dots, \varepsilon^n, \dots$.

Regular perturbation method (i.e. direct expansion method) is a technique used for solving the asymptotic power series of solutions to regular perturbation problems. By assuming that the solutions are in the form of power series with respect to the basis function and substituting the power series into the regular perturbation equation, we can obtain the regular equation of the problem. Then collect coefficients of like powers of ε . Since the system is an identity for ε , each coefficient of ε vanishes independently. Thus by setting these coefficients to zero, we can get a set of equations about the coefficients. After solving the coefficients, we can obtain the asymptotic power series of the solutions [1, 2].

Example 1:

$$\frac{d^2y}{dt^2} + 2\varepsilon \frac{dy}{dt} + y = 0 \quad (2.2)$$

where $y(0) = 0$, $dy(0)/dt = 1$. $\varepsilon = 0.001$ is a small parameter.

Solution: we expand y in powers of ε as follows

$$y = y_0 + \varepsilon y_1 + \varepsilon^2 y_2 + \dots \quad (2.3)$$

Substitute Eq. (2.3) into Eq. (2.2) and collect coefficients of like powers of ε yield

$$\left(\frac{d^2 y_0}{dt^2} + y_0\right) + \varepsilon \left(\frac{d^2 y_1}{dt^2} + 2\frac{dy_0}{dt} + y_1\right) + \varepsilon^2 \left(\frac{d^2 y_2}{dt^2} + 2\frac{dy_1}{dt} + y_2\right) + \dots = 0 \quad (2.4)$$

By repeatedly applying the limit process $\varepsilon \rightarrow 0$, we obtain the following sequence of linear problems.

$$\frac{d^2 y_0}{dt^2} + y_0 = 0; \quad y_0(0) = 0, \quad \frac{dy_0(0)}{dt} = 1 \quad (2.5)$$

$$\frac{d^2 y_1}{dt^2} + y_1 = -2\frac{dy_0}{dt}; \quad y_1(0) = \frac{dy_1(0)}{dt} = 0 \quad (2.6)$$

$$\frac{d^2 y_i}{dt^2} + y_i = -2\frac{dy_{i-1}}{dt}; \quad y_i(0) = \frac{dy_i(0)}{dt} = 0, \quad i = 1, 2, \dots \quad (2.7)$$

The solutions are

$$y_0 = \sin t \quad (2.8)$$

$$y_1 = -t \sin t \quad (2.9)$$

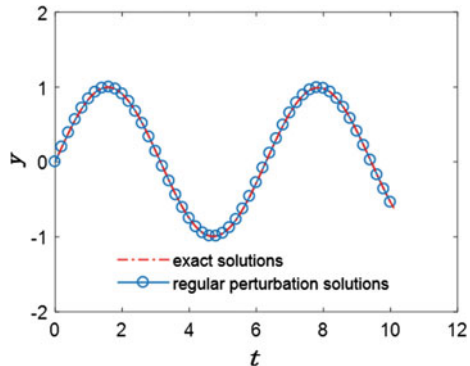
etc. Thus, as far as the solution has been solved the result is

$$y = \sin t - \varepsilon t \sin t + O(\varepsilon^2 t^2) \quad (2.10)$$

As shown in Fig. 2.1. We can see that the solutions obtained by regular perturbation method is consistent with the exact solutions which are

$$y = \frac{e^{-\varepsilon t}}{\sqrt{1 - \varepsilon^2}} \sin\left(\sqrt{1 - \varepsilon^2}t\right) \quad (2.11)$$

Fig. 2.1 The comparison of regular perturbation solutions and exact solutions



2.2 Singular Perturbation Method

Consider the following system described by a linear, second-order, initial value problem

$$\varepsilon \ddot{x}(t, \varepsilon) + \dot{x}(t, \varepsilon) + x(t, \varepsilon) = 0; \quad x(t=0) = x(0), \quad \dot{x}(t=0) = \dot{x}(0) \quad (2.12)$$

where the small parameter ε multiplies the highest derivative. The degenerate problem is obtained by suppressing the small parameter ε in Eq. (2.12) as

$$\dot{x}^{(0)}(t) + x^{(0)}(t) = 0; \quad x^{(0)}(t=0) = x(0) \quad (2.13)$$

with the solution as

$$x^{(0)}(t) = x^{(0)} e^{-t} = x(0) e^{-t} \quad (2.14)$$

It should be noted that the degenerate problem in Eq. (2.13) is only of first order where the initial conditions $\dot{x}(0)$ have been sacrificed in the process of degeneration. As a result, the whole solutions cannot be expected to satisfy all the initial conditions given in Eq. (2.12). The problem like this is called a singular perturbation problem [3]. The origin of the problem is that singular perturbation problem possesses a two-time scale property. In order to obtain an effective approximate solution at each scale, it is necessary to normalize the equations at different scales so as to obtain some new equations that can be solved by conventional perturbation method. If the solution of a perturbed problem can be approximated by an asymptotic expansion over the whole domain of the problem, whether in space or time, such a case is called conventional perturbation.

Singular perturbation method is a technique for solving asymptotic solutions of differential equations. The zero-order approximate solution of a conventional perturbation problem is usually obtained by setting the small parameter ε to zero. This is equivalent to taking only the first term of the asymptotic expansion to obtain the

corresponding approximate solution. Therefore, this method cannot be directly used to solve a singular perturbation problem. In singular perturbation method, the small parameter ε multiplies the highest-order derivative. Thus, the essence of the problem will be changed if the small parameter is set to zero. For differential equations, some boundary conditions will not be satisfied; for algebraic equations, the total number of solutions will be reduced.

Singular perturbation method can decompose the high-order system into two or more low-order systems. Firstly, the simplified solution (outer solution or steady state solution) of the problem can be obtained by ignoring the fast phenomena. The steady state solution represents slow phenomena that maintains a dominant role in the system, and reflects the essence of the problem. Then, in order to recover the lost initial conditions, it is required to stretch the boundary layer using a stretching transformations such as $\tau = t/\varepsilon$. By solving the full-order problem, the boundary layer correction can be obtained, which is an approximate solution between the outer solution and complete solution. The accuracy of the approximate solution can be improved by adding the correction term to the outer solution. In this way, not only the order of the problem can be reduced, but also the rigidity of the problem can be eliminated due to the separation of fast and slow variables, which greatly reduces the amount of calculation required.

The basis of singular perturbation method is not the linear characteristic of the system, but the time scale characteristic of the system. It is not only applicable to linear time-invariant systems, but also to linear time-varying system. Hence, singular perturbation method has a wide range of applications.

Example 2:

$$\begin{cases} \frac{dx}{dt} = z \\ \varepsilon \frac{dz}{dt} = -x - z \end{cases} \quad (2.15)$$

where $x(0) = 1$, $z(0) = 0$. $\varepsilon = 0.001$ is a small parameter.

Solution: The outer solutions are obtained from Eq. (2.13)

$$x^{(0)} = e^{-t}, \quad z^{(0)} = -e^{-t} \quad (2.16)$$

Stretching the boundary layer by $\tau = t/\varepsilon$ yields

$$\begin{cases} \frac{dx}{d\tau} = \varepsilon z \\ \frac{dz}{d\tau} = -x - z \end{cases} \quad (2.17)$$

Let $\varepsilon = 0$. Then the inner solutions are obtained by solving

$$\begin{cases} \frac{d\bar{x}^{(0)}}{d\tau} = 0, \quad \bar{x}^{(0)}(\tau = 0) = x^{(0)}(0) = x(0) = 1 \\ \frac{d\bar{z}^{(0)}}{d\tau} = -\bar{x}^{(0)} - \bar{z}^{(0)}, \quad \bar{z}^{(0)}(\tau = 0) = z(0) = 0 \end{cases} \quad (2.18)$$

and we have

$$\bar{x}^{(0)} = 1, \bar{z}^{(0)} = e^{-\tau} - 1 \quad (2.19)$$

The intermediate solutions are obtained by solving

$$\begin{cases} \frac{dx^{(0)}}{dt} = 0, \underline{x}^{(0)}(\tau = 0) = x^{(0)}(0) = x(0) = 1 \\ \frac{dz^{(0)}}{dt} = -\underline{x}^{(0)} - \underline{z}^{(0)}, \underline{z}^{(0)}(\tau = 0) = z^{(0)}(0) = -1 \end{cases} \quad (2.20)$$

and we have

$$\underline{x}^{(0)} = 1, \underline{z}^{(0)} = -1 \quad (2.21)$$

The boundary layer corrections are

$$\begin{cases} x_c = \bar{x}^{(0)} - \underline{x}^{(0)} = 0 \\ z_c = \bar{z}^{(0)} - \underline{z}^{(0)} = e^{-\tau} \end{cases} \quad (2.22)$$

Thus, the solutions are

$$\begin{cases} x = x^{(0)} + x_c = e^{-t} \\ z = z^{(0)} + z_c = -e^{-t} + e^{-\tau} \end{cases} \quad (2.23)$$

As shown in Fig. 2.2, the results are in good agreements with the exact solutions which are

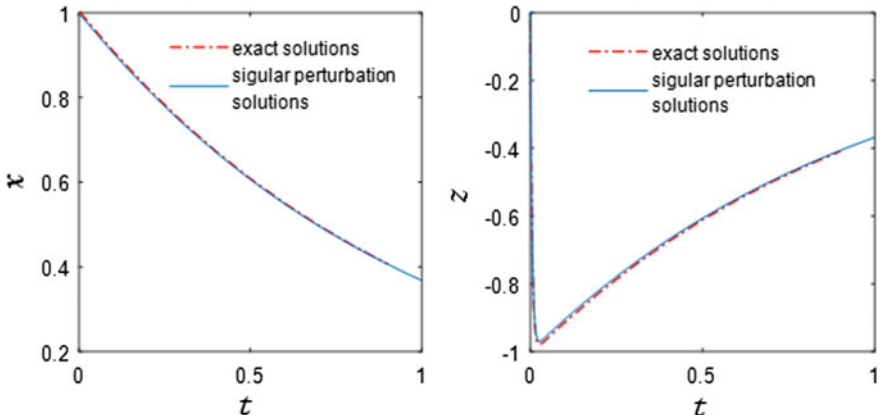


Fig. 2.2 The comparison of regular perturbation solutions and exact solutions

$$\begin{cases} x = c_1 e^{mt} + c_2 e^{nt} \\ z_c = mc_1 e^{mt} + nc_2 e^{nt} \end{cases} \quad (2.24)$$

where $c_1 = \frac{1}{2} - \frac{1}{2\sqrt{1-4\varepsilon}}$, $c_2 = \frac{1}{2} + \frac{1}{2\sqrt{1-4\varepsilon}}$,

$$m = \frac{-1 - \sqrt{1-4\varepsilon}}{2\varepsilon}, n = \frac{-1 + \sqrt{1-4\varepsilon}}{2\varepsilon}$$

2.3 Spectral Decomposition Method

2.3.1 Idempotent Matrix

Definition 2: Let $\mathbf{A} \in \mathbb{C}^{n \times n}$ be given. If $\mathbf{A}^2 = \mathbf{A}$, then \mathbf{A} is said to be an idempotent matrix.

2.3.2 Spectral Decomposition Theorem

Theorem 1: If $\mathbf{A} \in \mathbb{C}^{n \times n}$ is a simplex matrix (i.e., diagonalizable matrix) that has k distinct eigenvalues $\lambda_1, \lambda_2, \dots, \lambda_k (k \leq n)$, then there exists k idempotent matrixes, such that:

- (1) $\mathbf{G}_i^m = \mathbf{G}_i (1 \leq i \leq k)$;
- (2) $\mathbf{G}_i \mathbf{G}_j = 0 (i \neq j)$;
- (3) $\sum_{i=1}^k \mathbf{G}_i = \mathbf{I}_n$;
- (4) $\mathbf{A} = \sum_{i=1}^k \lambda_i \mathbf{G}_i$, and $\mathbf{G}_i (1 \leq i \leq k)$ is unique. Here, λ_i is spectral values of \mathbf{A} , \mathbf{G}_i is the spectral array of \mathbf{A} , and $\mathbf{A} = \sum_{i=1}^k \lambda_i \mathbf{G}_i$ is the spectral decomposition of \mathbf{A} .

Proof: Each simplex matrix \mathbf{A} can be written as

$$\mathbf{A} = \mathbf{Q} \begin{bmatrix} \lambda_1 & 0 & \cdots & 0 \\ 0 & \lambda_2 & \cdots & 0 \\ \vdots & \vdots & \ddots & \vdots \\ 0 & 0 & \cdots & \lambda_n \end{bmatrix} \mathbf{Q}^H = \mathbf{Q} \mathbf{D} \mathbf{Q}^H \quad (2.25)$$

where \mathbf{Q} is a orthogonal matrix and \mathbf{D} is the diagonal matrix whose entries are the eigenvalues of \mathbf{A} . Let us express the multiple eigenvalues together such as

$$\mathbf{D} = \begin{bmatrix} 2 & & \\ & 2 & \\ & & 3 \\ & & & 3 \end{bmatrix} = \begin{bmatrix} 2\begin{pmatrix} 1 & 0 \\ 0 & 1 \end{pmatrix} & & \\ & 3\begin{pmatrix} 1 & 0 \\ 0 & 1 \end{pmatrix} & \\ & & \end{bmatrix} = \begin{bmatrix} 2\mathbf{I}_1 & 0 \\ 0 & 2\mathbf{I}_2 \end{bmatrix} \quad (2.26)$$

where \mathbf{I}_1 and \mathbf{I}_2 are unit matrix. Then the diagonal matrix \mathbf{D} can be rewritten as

$$\mathbf{D} = \begin{bmatrix} \lambda_1 \mathbf{I}_1 & & & \\ & \lambda_2 \mathbf{I}_2 & & \\ & & \ddots & \\ & & & \lambda_k \mathbf{I}_k \end{bmatrix} = \lambda_1 \begin{bmatrix} \mathbf{I}_1 & & & \\ & 0 & & \\ & & \ddots & \\ & & & 0 \end{bmatrix} + \cdots + \lambda_k \begin{bmatrix} 0 & & & \\ & 0 & & \\ & & \ddots & \\ & & & \mathbf{I}_k \end{bmatrix} \quad (2.27)$$

where $\lambda_1, \dots, \lambda_k$ are all non-repetitive eigenvalues of \mathbf{A} .

Let $\mathbf{D}_1 = \begin{bmatrix} \mathbf{I}_1 & & & \\ & 0 & & \\ & & \ddots & \\ & & & 0 \end{bmatrix}, \dots, \mathbf{D}_k = \begin{bmatrix} 0 & & & \\ & 0 & & \\ & & \ddots & \\ & & & \mathbf{I}_k \end{bmatrix}$. Then Eq. (2.27) can be simplified as

$$\mathbf{D} = \lambda_1 \mathbf{D}_1 + \lambda_2 \mathbf{D}_2 + \cdots + \lambda_k \mathbf{D}_k \quad (2.28)$$

and there must be $\mathbf{D}_1 + \mathbf{D}_2 + \cdots + \mathbf{D}_k = \mathbf{I}_n, \mathbf{D}_i^m = \mathbf{D}_i (1 \leq i \leq k), \mathbf{D}_i \mathbf{D}_j = \mathbf{0}^{n \times n} (i \neq j)$.

Substituting Eq. (2.28) into Eq. (2.25) yields

$$\begin{aligned} \mathbf{A} &= \lambda_1 \mathbf{Q} \mathbf{D}_1 \mathbf{Q}^H + \lambda_2 \mathbf{Q} \mathbf{D}_2 \mathbf{Q}^H + \cdots + \lambda_k \mathbf{Q} \mathbf{D}_k \mathbf{Q}^H \\ &= \lambda_1 \mathbf{G}_1 + \lambda_2 \mathbf{G}_2 + \cdots + \lambda_k \mathbf{G}_k \\ &= \sum_{i=1}^k \lambda_i \mathbf{G}_i \end{aligned} \quad (2.29)$$

In addition, it is easy to obtain that $\sum_{i=1}^k \mathbf{G}_i = \mathbf{G}_1 + \mathbf{G}_2 + \cdots + \mathbf{G}_k = \mathbf{I}_n, \mathbf{G}_i^m = \mathbf{G}_i (1 \leq i \leq k), \mathbf{G}_i \mathbf{G}_j = \mathbf{0}^{n \times n} (i \neq j)$.

2.3.3 Inference

(1) $\mathbf{G}_i = \frac{\varphi_i(\mathbf{A})}{\varphi_i(\lambda_i)}$, where $\varphi_i(\mathbf{A}) = \prod_{\substack{j=1 \\ j \neq i}}^k (\mathbf{A} - \lambda_j \mathbf{I}_n)$ and $\varphi_i(\lambda) = \prod_{\substack{j=1 \\ j \neq i}}^k (\lambda - \lambda_j)$;

Proof: Let $\mathbf{F}_i = \frac{\varphi_i(\mathbf{A})}{\varphi_i(\lambda_i)}$. For each \mathbf{G}_i , there must be

$$\begin{aligned}
\mathbf{F}_i \mathbf{G}_l &= \frac{1}{\varphi_i(\lambda_i)} \left(\prod_{\substack{j=1 \\ j \neq i}}^k (\mathbf{A} - \lambda_j \mathbf{I}_n) \right) \mathbf{G}_l = \frac{1}{\varphi_i(\lambda_i)} \left(\prod_{\substack{j=1 \\ j \neq i}}^k (\mathbf{A} - \lambda_j \mathbf{I}_n) \mathbf{G}_l \right) \\
&= \frac{1}{\varphi_i(\lambda_i)} \left(\prod_{\substack{j=1 \\ j \neq i}}^k (\mathbf{A}\mathbf{G}_l - \lambda_j \mathbf{G}_l) \right) = \frac{1}{\varphi_i(\lambda_i)} \left(\prod_{\substack{j=1 \\ j \neq i}}^k (\lambda_l - \lambda_j) \mathbf{G}_l \right) \\
&= \frac{\varphi_i(\lambda_j)}{\varphi_i(\lambda_i)} \mathbf{G}_l = \delta_{il} \mathbf{G}_l
\end{aligned} \tag{2.30}$$

where

$$\delta_{il} = \begin{cases} 1, & i = l \\ 0, & i \neq l \end{cases} \tag{2.31}$$

It should be noted that the property (1) of **Theorem 1** and $\mathbf{A}\mathbf{G}_l = \lambda_l \mathbf{G}_l$ have been used during the derivation in Eq. (2.30). Thus, we can obtain that

$$\mathbf{F}_i = \mathbf{F}_i \sum_{j=1}^k \mathbf{G}_j = \sum_{j=1}^k \mathbf{F}_i \mathbf{G}_j = \sum_{j=1}^k \delta_{ij} \mathbf{G}_j = \mathbf{G}_i, \quad i = 1, \dots, k \tag{2.32}$$

(2) Suppose $f(\lambda)$ is a polynomial. Then,

$$f(\mathbf{A}) = f(\lambda_1) \mathbf{G}_1 + f(\lambda_2) \mathbf{G}_2 + \dots + f(\lambda_k) \mathbf{G}_k \tag{2.33}$$

In particular, there is

$$\mathbf{A}^m = \lambda_1^m \mathbf{G}_1 + \lambda_2^m \mathbf{G}_2 + \dots + \lambda_k^m \mathbf{G}_k \tag{2.34}$$

Because the proof is very simple, the proof is omitted here.

2.3.4 Example

Example 3:

Suppose that $\mathbf{A} = \begin{bmatrix} 1 & 4 & 2 \\ 0 & -3 & 4 \\ 0 & 4 & 3 \end{bmatrix}$. Please find the spectral decomposition of \mathbf{A} and calculate \mathbf{A}^{100} .

Solution: The eigenvalues of \mathbf{A} are $\lambda_1 = 1, \lambda_2 = 5, \lambda_3 = -5$. Obviously, the eigenvalues are different. So \mathbf{A} is a simplex matrix. Then, we can obtain the spectral array of \mathbf{A} by

$$\mathbf{G}_1 = \frac{(\mathbf{A} - \lambda_2 \mathbf{I}^{3 \times 3})(\mathbf{A} - \lambda_3 \mathbf{I}^{3 \times 3})}{(\lambda_1 - \lambda_2)(\lambda_1 - \lambda_3)} = \begin{bmatrix} 1 & 0 & -1 \\ 0 & 0 & 0 \\ 0 & 0 & 0 \end{bmatrix} \quad (2.35)$$

Similarly,

$$\mathbf{G}_2 = \begin{bmatrix} 0 & \frac{2}{5} & \frac{4}{5} \\ 0 & \frac{1}{5} & \frac{2}{5} \\ 0 & \frac{2}{5} & \frac{4}{5} \end{bmatrix}, \quad \mathbf{G}_3 = \begin{bmatrix} 0 & -\frac{2}{5} & \frac{1}{5} \\ 0 & \frac{4}{5} & -\frac{2}{5} \\ 0 & -\frac{2}{5} & \frac{1}{5} \end{bmatrix} \quad (2.36)$$

Thus, the spectral decomposition of \mathbf{A} is

$$\mathbf{A} = \lambda_1 \mathbf{G}_1 + \lambda_2 \mathbf{G}_2 + \lambda_3 \mathbf{G}_3 = \mathbf{G}_1 + 5\mathbf{G}_2 - 5\mathbf{G}_3 \quad (2.37)$$

and,

$$\mathbf{A}^{100} = \mathbf{G}_1 + 5^{100}\mathbf{G}_2 + (-5)^{100}\mathbf{G}_3 \quad (2.38)$$

2.4 Pseudospectral Method

2.4.1 Introduction of Method

As a direct transcription method, Pseudospectral method (PM) has drawn special attentions from researchers because of its fast convergence and perfect theoretical system. The state and control variables are approximated by using linear combinations of global interpolation polynomials at a set of discrete points. Therefore, the derivative of the state variables can be directly expressed as the explicit function of the

Table 2.1 Interpolation polynomials and node types of various Pseudospectral methods

Methods	Interpolation polynomial basis function	Collocation points	Node value range
CPM	Chebyshev	Chebyshev-Gauss-Lobatto	$[-1, 1]$
LPM	Legendre	Legendre-Gauss-Lobatto	$[-1, 1]$
GPM	Legendre	Legendre-Gauss-Lobatto	$(-1, 1)$
RPM	Legendre	Legendre-Gauss-Radau	$(-1, 1]$

global states by taking the derivative of the polynomials. And the differential equation constraints are transferred into algebraic constraints. The roots of orthogonal polynomials generally are chosen as the collocation points. The orthogonal polynomials are orthogonal to each other in the defined function space. Due to different treatments of terminal constraints, the collocation points may include one or two of the boundary points.

For smooth problems, the Pseudospectral method is of the exponential convergence rate. For non-smooth problems, it can be segmented at appropriate locations. Then we can discretize the segments and set up appropriate connection conditions. The commonly used Pseudospectral methods can be classified into the following three categories: Chebyshev Pseudospectral method (CPM), Legendre Pseudospectral method (LPM), Gauss Pseudospectral method (GPM), and Radau Pseudospectral method (RPM). The difference of different Pseudospectral methods lies in the different interpolation basis functions, collocation points and node types, which can be seen in Table 2.1.

In addition, some literatures name the collocation point method (i.e., the piecewise discretization of state and control variables) as local method, while the Pseudospectral method is called as global method. Compared with the traditional method, Pseudospectral method is of high accuracy though there are fewer discrete points. Therefore, Pseudospectral method is considered to be of the potential to realize real-time optimization.

The theoretical source of Pseudospectral method is the spectral method for solving fluid mechanics problems early. Reddien's research work in 1979 promoted the development of solving optimal control problems based on the orthogonal collocation method [4]. In the 1990s, Elnagar et al. proposed the Legendre Pseudospectral method and applied it directly to discretize the nonlinear optimal control problem [5]. Ross et al. studied the equivalence of the Karush-Kuhn-Tucher (KKT) conditions of nonlinear programming problem and the first-order necessary condition of optimal control problem, and established costate mapping theory [6], which greatly promoted the theoretical research on optimal control problem discretized by Pseudospectral method. Since then, Pseudospectral method has been widely applied in solving optimal control problems in robot, solar panel, ascending stage of carrier rocket, formation flight, orbit transfer and etc. Meanwhile, the Pseudospectral method is further used to solve the system described by differential inclusion equations, differential algebraic equations and differential flat equations. This comes with drawbacks

of costate state mapping due to the problems of discrete method and collocation points of Legendre Pseudospectral method. A new Gauss Pseudospectral method that is proposed by Benson overcame the drawbacks [7]. It proves that the KKT condition of nonlinear programming problem is completely consistent with the first-order optimality condition of discrete Hamilton Boundary Value Problem (HBVP).

In recent years, with the further study of Pseudospectral method, the researchers found that the single method of global configuration of orthogonal points could not meet the needs of solving multiple optimal controls. Because global collocation points are relatively fixed, the generated interpolation polynomials cannot well represent the solution of optimal control problem with discontinuous state and fast change of state quantity. Therefore, the focus of the Pseudospectral method will be transferred to the piecewise Pseudospectral method with mesh refinement. Such pioneering work can be seen in Divya Garg's research paper [8, 9]. Since all nodes configured by Gauss Pseudospectral method do not include boundary points. Therefore, the solution obtained by solving the nonlinear programming problem does not include the control at two boundary points. And the control must be obtained by solving the additional optimal problem. So, this class of collocation nodes is not suitable for segmented collocation nodes. In order to overcome such problems, Divya Garg studied Radau Pseudospectral method including one boundary point based on Lagrange-Gauss-Radau (LGR) points and obtained the costate mapping principle of Radau Pseudospectral method. In addition, by studying the integral form and differential form of polynomial fitting function, the general framework of numerical solution for optimal control problem is put forward by Divya Garg. Divya Garg also gave the conditions of complete performance of Pseudospectral differential approximation matrix and compared Legendre, Gauss and Radau Pseudospectral methods. The analysis results show that the differential approximation matrix of the Legendre Pseudospectral method is of the form $N \times N$, which leads to singular phenomena. Therefore, the nonlinear programming problem discretized by Legendre Pseudospectral method is inconsistent with the original optimal control problem. The differential approximation matrix of Radau Pseudospectral method and Gauss Pseudospectral method are of the form $N \times (N + 1)$, which can well establish a bridge between the discrete nonlinear programming problem and the original optimal control problem. In addition, Divya Garg applied the Pseudospectral method to solve the optimal control problem in infinite domain [10]. Several conversion functions were proposed to transfer the time interval from $[0, \inf]$ to $[-1, 1]$. Gauss Pseudospectral method and Radau Pseudospectral method which can deal with optimal control problems in infinite domain are obtained. The principle of costate mapping is derived and the costate variables of the optimal control problem in infinite domain are estimated by Divya Garg. When Radau Pseudospectral method provides a naturally appropriate discrete form for piecewise Pseudospectral method, Christopher Darby studied the segmented Radau Pseudospectral method and proposed two adaptive mesh updating methods [11]. The first method uses the proportional term of arithmetic mean to determine the grid position of the main deviation. Later, combining with the research achievements of Zhao [12], the second set of segmentation strategy is proposed. The number and size of configuration meshes are determined by curvature density

function. According to the obtained optimization results, the density function characterized by curvature distribution is established. And then the number of mesh nodes that need to be increased and the configuration position are obtained through curvature probability distribution. In addition, Chinese scholar Li Hongfu [13] also proposed a set of mesh refinement strategy with multiple criteria (prior knowledge, intermediate error and curvature), which can well adapt to multiple complex optimal control problems. Mesh refinement points are also assigned according to the density function of curvature.

It should be noted that although Legendre Pseudospectral method is of drawbacks. As an early researcher, Elnagar [5] made indelible contribution to solving the optimal control problem by Pseudospectral method. He proposed the idea of using Legendre Pseudospectral method to solve the optimal control problem and pioneered the approach of global orthogonal polynomials based on Legendre polynomials to the optimal control problem. It is generally regarded as a landmark work to solve the optimal control problem by using Pseudospectral method. In addition, Gong Qi has made great contributions to the theoretical discussion of Pseudospectral method [14]. He mainly studied the convergence of the Pseudospectral method for solving the optimal control problem of systems with feedback linearization. One of the advantages of Pseudospectral method is pointed out: Pseudospectral method is of exponential convergence property in providing simple discrete form for analytic functions. Gong [15] also introduced the comprehensive application of Pseudospectral method in five parts. Firstly, based on the basic principle of Pseudospectral method, the general form of Pseudospectral method for solving constrained nonlinear optimal control problems is introduced. And an inner and outer loop algorithm is proposed to solve the optimal feedback control in real time. In the second part, taking maneuvering of space station as an example, the effect of optimal control obtained by Pseudospectral method is introduced. The third part is about the real-time optimization of NPSAT1, which illustrates the control effect obtained by using the real-time optimization framework. Through the comparison of experiment and theory, it is of a good application prospect. In the fourth part, the Pseudospectral method is applied to path optimization with obstacle avoidance function. The ability of real-time calculation of Pseudospectral method is illustrated again by this method. In the last part, the Pseudospectral method is applied to the reentry on-line guidance of spacecraft. The Pseudospectral method is used to quickly obtain the optimal trajectory under the current state, thus eliminate the influence of interference.

Now, the Flight Mechanics and Optimization Laboratory of Florida University is the authoritative organization for the development of Pseudospectral software. They have made a lot of achievements in terms of derivative algorithm, mesh updating and practical aviation application. With the further development of Pseudospectral method, Pseudospectral method is becoming more and more perfect in solving optimal control problems.

2.4.2 Pseudospectral Discrete Process

2.4.2.1 Continuous Optimal Control Problem

Considering the continuous optimal control problem in Sect. 2.2.1, minimize the following performance index

$$J = \Phi(\mathbf{x}(t_0), t_0, \mathbf{x}(t_f), t_f) + \int_{t_0}^{t_f} g(\mathbf{x}(t), \mathbf{u}(t), t) dt \quad (2.39)$$

subject to the dynamic constraint

$$\dot{\mathbf{x}} = f(\mathbf{x}(t), \mathbf{u}(t), t) \quad (2.40)$$

The boundary constraint is

$$\phi(\mathbf{x}(t_0), t_0, \mathbf{x}(t_f), t_f) = 0 \quad (2.41)$$

And the inequality constraint is

$$C(\mathbf{x}(t), \mathbf{u}(t), t) \leq 0 \quad (2.42)$$

where, all vector functions are row vectors, and the Hamiltonian function is defined as

$$\begin{aligned} H(\mathbf{x}(t), \mathbf{u}(t), \boldsymbol{\lambda}(t), \gamma(t), t) &= g(\mathbf{x}(t), \mathbf{u}(t), t) + \boldsymbol{\lambda}^T f(\mathbf{x}(t), \mathbf{u}(t), t) \\ &\quad - \gamma^T C(\mathbf{x}(t), \mathbf{u}(t), t) \end{aligned} \quad (2.43)$$

Now, we define $p : \mathbf{R}^n \rightarrow \mathbf{R}^m$. And ∇_p is a $m \times n$ Jacobian matrix. Hence, the gradient of a scalar function is going to be a row vector. The first order necessary condition of the optimal control problem is expressed as

$$\left\{ \begin{array}{l} \dot{\mathbf{x}}(t) = \nabla_{\lambda} H \\ \dot{\boldsymbol{\lambda}}(t) = \nabla_x H \\ \nabla_u H = 0 \\ \boldsymbol{\lambda}(t_0) = -\nabla_{x_0}(\Phi - \psi^T \phi) \\ \boldsymbol{\lambda}(t_f) = \nabla_{x_f}(\Phi - \psi^T \phi) \\ H|_{t=t_0} = \nabla_{t_0}(\Phi - \psi^T \phi) \\ H|_{t=t_f} = -\nabla_{t_f}(\Phi - \psi^T \phi) \\ \gamma_i(t) = 0, C_i(\mathbf{x}(t), \mathbf{u}(t)) < 0 \\ \gamma_i(t) < 0, C_i(\mathbf{x}(t), \mathbf{u}(t)) = 0 \\ \phi = 0 \end{array} \right. \quad (2.44)$$

The initial value of the Hamiltonian function can be expressed as

$$H|_{t=t_0} = \frac{1}{t_f - t_0} \left(\int_{t_0}^{t_f} H dt - \int_{t_0}^{t_f} \frac{dH}{dt} (t_f - t) dt \right) \quad (2.45)$$

Similarly, the terminal value of the Hamiltonian function can be expressed as

$$H|_{t=t_f} = \frac{1}{t_f - t_0} \left(\int_{t_0}^{t_f} H dt - \int_{t_0}^{t_f} \frac{dH}{dt} (t - t_0) dt \right) \quad (2.46)$$

The total derivative of the Hamiltonian function with respect to time is defined as

$$\frac{dH}{dt} = \frac{\partial H}{\partial t} + \frac{\partial H}{\partial \dot{\mathbf{x}}} \dot{\mathbf{x}} + \frac{\partial H}{\partial \dot{\lambda}} \dot{\lambda} + \frac{\partial H}{\partial \dot{\mathbf{u}}} \dot{\mathbf{u}} + \frac{\partial H}{\partial \dot{\gamma}} \dot{\gamma} \quad (2.47)$$

By adding the first order necessary condition into Eq. (2.47), we can obtain an equation as

$$\frac{dH}{dt} = \frac{\partial H}{\partial t} \quad (2.48)$$

Hence, the initial and terminal value of the Hamilton function can be expressed as

$$\begin{cases} H|_{t=t_0} = \frac{1}{t_f - t_0} \left(\int_{t_0}^{t_f} H dt - \int_{t_0}^{t_f} \frac{\partial H}{\partial t} (t_f - t) dt \right) \\ H|_{t=t_f} = \frac{1}{t_f - t_0} \left(\int_{t_0}^{t_f} H dt - \int_{t_0}^{t_f} \frac{\partial H}{\partial t} (t - t_0) dt \right) \end{cases} \quad (2.49)$$

The collocation points of the interpolation polynomial that used in the Pseudospectral method are all the null points of Legendre polynomial or that of the linear combination of the derivative of Legendre polynomial. Hence, the first step of discretization is to transfer the time domain from the time interval $[t_0, t_f]$ to the time interval $[-1, 1]$ via the following equation.

$$t = \frac{t_f - t_0}{2} \tau + \frac{t_f + t_0}{2} \quad (2.50)$$

Thus,

$$\frac{dt}{d\tau} = \frac{t_f - t_0}{2} \quad (2.51)$$

The original performance index is transferred into

$$J = \Phi(x(-1), t_0, x(1), t_f) + \frac{t_f - t_0}{2} \int_{-1}^1 g(\mathbf{x}(\tau), \mathbf{u}(\tau), \tau) d\tau \quad (2.52)$$

Subject to the dynamic constraint

$$\frac{d\mathbf{x}}{d\tau} = \frac{t_f - t_0}{2} f(\mathbf{x}(\tau), \mathbf{u}(\tau), \tau) \quad (2.53)$$

The boundary constraint is

$$\phi(x(-1), t_0, x(1), t_f) = 0 \quad (2.54)$$

The inequality constraint is

$$\frac{t_f - t_0}{2} C(\mathbf{x}(\tau), \mathbf{u}(\tau), \tau) \leq 0 \quad (2.55)$$

The Hamiltonian function of the above problem can be defined as

$$\begin{aligned} H(\mathbf{x}(\tau), \mathbf{u}(\tau), \boldsymbol{\lambda}(\tau), \boldsymbol{\gamma}(\tau), \tau) &= g(\mathbf{x}(\tau), \mathbf{u}(\tau), \tau) \\ &+ \boldsymbol{\lambda}^T f(\mathbf{x}(\tau), \mathbf{u}(\tau), \tau) - \boldsymbol{\gamma}^T C(\mathbf{x}(\tau), \mathbf{u}(\tau), \tau) \end{aligned} \quad (2.56)$$

The initial and terminal value of the Hamilton function can be expressed as

$$\left\{ \begin{array}{l} H|_{t=t_0} = \frac{1}{2} \int_{-1}^1 H d\tau - \frac{t_f - t_0}{2} \int_{-1}^1 \frac{dH}{dt_0} d\tau \\ H|_{t=t_f} = \frac{1}{2} \int_{-1}^1 H d\tau - \frac{t_f - t_0}{2} \int_{-1}^1 \frac{dH}{dt_f} d\tau \end{array} \right. \quad (2.57)$$

Hence, the first order necessary condition of the continuous optimal control problem is transferred into

$$\left\{ \begin{array}{l} \dot{\mathbf{x}}(t) = \frac{t_f - t_0}{2} \nabla_{\boldsymbol{\lambda}} H \\ \dot{\boldsymbol{\lambda}}(t) = -\frac{t_f - t_0}{2} \nabla_{\mathbf{x}} H \\ \nabla_{\mathbf{u}} H = 0 \\ \boldsymbol{\lambda}(t_0) = -\nabla_{\mathbf{x}_0} (\boldsymbol{\Phi} - \boldsymbol{\psi}^T \boldsymbol{\phi}) \\ \boldsymbol{\lambda}(t_f) = \nabla_{\mathbf{x}_f} (\boldsymbol{\Phi} - \boldsymbol{\psi}^T \boldsymbol{\phi}) \\ \nabla_{t_0} (\boldsymbol{\Phi} - \boldsymbol{\psi}^T \boldsymbol{\phi}) = \frac{1}{2} \int_{-1}^1 H d\tau - \frac{t_f - t_0}{2} \int_{-1}^1 \frac{dH}{dt_0} d\tau \\ -\nabla_{t_f} (\boldsymbol{\Phi} - \boldsymbol{\psi}^T \boldsymbol{\phi}) = \frac{1}{2} \int_{-1}^1 H d\tau - \frac{t_f - t_0}{2} \int_{-1}^1 \frac{dH}{dt_f} d\tau \\ \boldsymbol{\gamma}_i(\tau) = 0, C_i(\mathbf{x}(\tau), \mathbf{u}(\tau)) < 0 \\ \boldsymbol{\gamma}_i(\tau) < 0, C_i(\mathbf{x}(\tau), \mathbf{u}(\tau)) = 0 \\ \boldsymbol{\phi} = 0 \end{array} \right. \quad (2.58)$$

2.4.2.2 Legendre Pseudospectral Method

Legendre Pseudospectral method is a direct conversion method that transform the continuous optimal control problem into a discrete nonlinear programming problem. The method adopts Legendre-Gauss-Labatto (LGL) points as the collocation points of polynomial to approximate state variables and control variables. The discrete derivation of Legendre Pseudospectral is given as follows.

We consider N LGL collocation points, $(\tau_1 \ \tau_2 \ \dots \ \tau_N)$, where, $\tau_1 = -1, \tau_N = 1$. Then, the Lagrange polynomial of degree $(N-1)$ is defined as

$$L_i(\tau) = \prod_{\substack{j=1 \\ j \neq i}}^N \frac{\tau - \tau_j}{\tau_i - \tau_j} \quad (2.59)$$

The state, $\mathbf{x}(\tau)$, can be expressed as a linear combination of Lagrange interpolation polynomials of degree $(N-1)$.

$$\mathbf{x}(\tau) \approx X(\tau) = \sum_{i=1}^N X_i L_i(\tau) \quad (2.60)$$

where, $X_i = X(\tau_i)$. The derivative of state can be obtained by taking the derivative of Lagrange interpolation polynomials as

$$\dot{\mathbf{x}}(\tau) \approx \dot{X}(\tau) = \sum_{i=1}^N X_i \dot{L}_i(\tau) \quad (2.61)$$

Hence, the differential constraint can be expressed as the following algebraic constraint.

$$\sum_{i=1}^N \mathbf{D}_{ki} Y_i = \frac{t_f - t_0}{2} f(Y_k, \mathbf{U}_k, \tau_k : t_0, t_f) \quad (2.62)$$

where, $\mathbf{U}_k = \mathbf{U}(\tau_k)$, \mathbf{D} is a $N \times N$ square matrix, and is called Lobatto Pseudospectral Differentiation Matrix. The reason why \mathbf{D} is a square matrix is that the number of collocation points of Lagrange polynomials is equal to the number of derivatives of the configuration state. The state is defined as

$$\mathbf{Y}^{LGL} = \begin{bmatrix} Y_1 \\ \vdots \\ Y_N \end{bmatrix} \quad (2.63)$$

Using the above definition, the dynamic equation constraints can be expressed as

$$\mathbf{D}_k \mathbf{Y}^{LGL} = \frac{t_f - t_0}{2} f(\mathbf{Y}_k, \mathbf{U}_k, \tau_k : t_0, t_f) \quad (2.64)$$

where, \mathbf{D}_k is the k-th row vector of matrix \mathbf{D} . The path constraint on N LGL nodes can be expressed as

$$\frac{t_f - t_0}{2} C(\mathbf{X}_k, \mathbf{U}_k) \leq 0 \quad (2.65)$$

Finally, the performance index is discretized at LGL nodes by Gauss quadrature.

$$J = \Phi(\mathbf{X}(\tau_1), \tau_1, \mathbf{X}(\tau_N), \tau_N) + \frac{t_f - t_0}{2} \sum_{k=1}^N \omega_k g(\mathbf{x}_k, \mathbf{u}_k, \tau_k; t_0, t_f) \quad (2.66)$$

where, ω_k is the weight of Gauss quadrature.

Hence, the performance index of the obtained nonlinear programming problem is described as Eq. (2.66), which is subject to equality constraints and inequality constraints as Eq. (2.67).

$$\begin{aligned} \mathbf{D}_k \mathbf{Y}^{LGL} &= \frac{t_f - t_0}{2} f(\mathbf{Y}_k, \mathbf{U}_k, \tau_k : t_0, t_f) \\ \phi(\mathbf{X}(\tau_1), \tau_1, \mathbf{X}(\tau_N), \tau_N) &= 0 \\ \frac{t_f - t_0}{2} C(\mathbf{X}_k, \mathbf{U}_k, \tau_k : t_0, t_f) &\leq 0 \end{aligned} \quad (2.67)$$

2.4.2.3 Gauss Pseudospectral Method

In order to improve the computational accuracy and efficiency, David Benson developed Gauss Pseudospectral method based on the work of Reddien, Cuthrell and Biegler. Similar to Legendre Pseudospectral method, the method adopts the null points of Legendre polynomial as the collocation points of Lagrange interpolating polynomial. And the states of two boundary points are calculated via Gauss quadrature. The concrete discrete steps of Gauss Pseudospectral method are given as follows.

In general, considering the continuous optimal control problem, we approximate state variables and control variables using Lagrange interpolation polynomial of degree $N + 1$ and N respectively.

$$\begin{aligned} \mathbf{x}(\tau) &\approx \mathbf{X}(\tau) = \sum_{i=0}^N \mathbf{X}(\tau_i) L_i(\tau) \\ \mathbf{u}(\tau) &\approx \mathbf{U}(\tau) = \sum_{i=0}^N \mathbf{U}(\tau_i) L_i^*(\tau) \end{aligned} \quad (2.68)$$

where, $L_i(\tau_k)$ and $L_i^*(\tau)$ are Lagrange interpolation polynomials.

So, the state differential equation can be expressed as

$$\dot{\mathbf{x}}(\tau) \approx \dot{\mathbf{X}}(\tau) = \sum_{i=0}^N X(\tau_i) \dot{L}_i(\tau) \quad (2.69)$$

The differential equation of each Lagrange polynomial at LG points can be approximated by a differential matrix, $\mathbf{D} \in \mathbf{R}^{N \times N+1}$. The elements of the differential matrix can be calculated by the following algebraic relation.

$$D_{kl} = \dot{L}_i(\tau_k) = \sum_{l=0}^N \frac{\prod_{j=0, j \neq i, l}^N (\tau_k - \tau_j)}{\prod_{j=0, j \neq i}^N (\tau_k - \tau_j)} \quad (2.70)$$

Hence, the state equations can be converted into the following algebraic constraints by the differential matrices.

$$\sum_{l=0}^N D_{kl} X_l - \frac{(t_f - t_0)}{2} f(X_k, \mathbf{U}_k, \tau; t_0, t_f) = 0 \quad (2.71)$$

where, $X_k = X(\tau_k)$, and τ_k is Legendre-Gauss (LG) point. LG points are the roots of Legendre polynomial of degree $N + 1$. Note that the dynamic constraint is collocated only at the LG points and not at the boundary points. The state vectors at the boundary points are defined as X_0 and X_f . The constraint relationship between X_0 , X_f and state and control vectors at LG points can be obtained as follows via Gauss quadrature.

$$X_f = X_0 + \frac{(t_f - t_0)}{2} \sum_{k=1}^N \omega_k f(X_k, \mathbf{U}_k, \tau; t_0, t_f) \quad (2.72)$$

where, ω_k is the weight of Gauss quadrature. The objective function with Lagrange terms can be expressed algebraically as

$$J = \Phi(x(-1), x(1), t_0, t_f) + \frac{(t_f - t_0)}{2} \sum_{k=1}^N \omega_k g(X_k, \mathbf{U}_k, \tau; t_0, t_f) \quad (2.73)$$

The boundary constraint is

$$\phi(X_0, X_f, t_0, t_f) = 0 \quad (2.74)$$

The control constraint can also be expressed as

$$C(\mathbf{X}_k, \mathbf{U}_k, \tau; t_0, t_f) \leq 0 \quad (2.75)$$

By this way, continuous optimal control problem can be transcribed into a nonlinear programming problem (NLP). The optimal solution in discrete form can be obtained via well-developed nonlinear programming algorithms.

2.4.2.4 Radau Pseudospectral Method

In order to overcome the problem that the solution of the nonlinear programming problem does not include the boundary control, a Pseudospectral method based on LGR points is developed. Since the selected LGR points include the initial boundary point, the solution of the discrete nonlinear programming problem also naturally includes the initial boundary control. Different from Legendre Pseudospectral method, since LGR points only include the initial boundary point, the differential approximation matrix obtained via LGR points is of the characteristics of non-square and full rank. Therefore, the optimal control problem discretized by Radau Pseudospectral method is consistent with the original optimal control problem. And accurate estimation of costate variables of the original optimal control problem can be obtained by Radau Pseudospectral method.

In the implementation process, Radau Pseudospectral method has the following characteristics:

- (1) The method is simple and easy to implement, and it can deal with various constraints well.
- (2) The method can use the mature sparse nonlinear solver to obtain the solution with good precision, and it is not sensitive to initial values.
- (3) The method can accurately estimate the costate state of optimal control problem by KKT multiplier of nonlinear programming problem. This property indicates that the method is of the exponential convergence property of spectral method, which means that the solution with higher precision can be obtained by using fewer nodes and less computing time.

Figure 2.3 compares LGR nodes and LG nodes. It can be seen that LG nodes do not include boundary points -1 and 1 , while LGR nodes include an boundary point -1 . The concrete discrete progress of Radau Pseudospectral method is given as following.

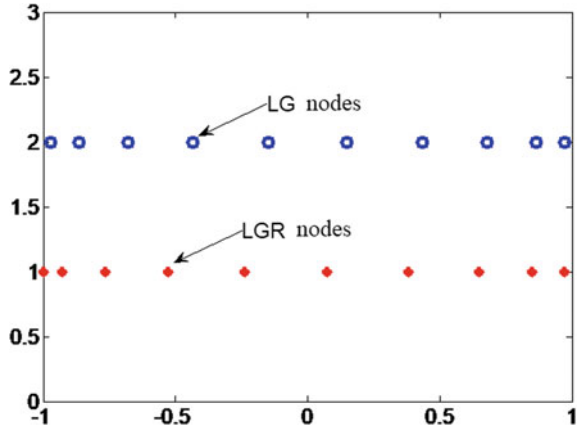
Consider the general optimal control problem with the objective function as

$$J = \Phi(\mathbf{x}(-1), t_0, \mathbf{x}(1), t_f) + \frac{t_f - t_0}{2} \int_{-1}^1 g(\mathbf{x}(\tau), \mathbf{u}(\tau), \tau; t_0, t_f) d\tau \quad (2.76)$$

And the state variables satisfy the following dynamic equation.

$$\frac{d\mathbf{x}}{d\tau} = \dot{\mathbf{x}}(\tau) = \frac{t_f - t_0}{2} f(\mathbf{x}(\tau), \mathbf{u}(\tau), \tau; t_0, t_f) \quad (2.77)$$

Fig. 2.3 Comparison of LGR nodes and LG nodes



The boundary constraint is

$$\phi(\mathbf{x}(-1), t_0, \mathbf{x}(1), t_f) = 0 \quad (2.78)$$

And the inequality constraint is

$$C(\mathbf{x}(\tau), \mathbf{u}(\tau), \tau; t_0, t_f) \leq 0 \quad (2.79)$$

We consider NLGR collocation points, $(\tau_1, \tau_2, \dots, \tau_N)$, where, $\tau_1 = -1, \tau_N < 1$. And define the new collocation point $\tau_{N+1} = 1$. Then, the Lagrange polynomial of degree N is defined as

$$L_i(\tau) = \prod_{\substack{i=1 \\ j \neq i}}^{N+1} \frac{\tau - \tau_j}{\tau_i - \tau_j} \quad (2.80)$$

State variables are approximated by using Lagrange interpolation polynomials as

$$\mathbf{x}(\tau) \approx X(\tau) = \sum_{i=1}^{N+1} X_i L_i(\tau) \quad (2.81)$$

Then, the dynamical equations of state are also approximated by using Lagrange interpolation polynomials as

$$\dot{\mathbf{x}}(\tau) \approx \dot{X}(\tau) = \sum_{i=1}^{N+1} X_i \dot{L}_i(\tau) \quad (2.82)$$

and

$$\sum_{i=1}^{N+1} \mathbf{X}_i \dot{\mathbf{L}}_i(\tau) = \sum_{i=1}^{N+1} \mathbf{D}_{ki} \mathbf{X}_i = \frac{t_f - t_0}{2} f(\mathbf{x}(\tau), \mathbf{u}(\tau), \tau; t_0, t_f) \quad (2.83)$$

where, differential matrix \mathbf{D} is a $N \times (N + 1)$ non-square matrix, and it is called Radau Pseudospectral approximation matrix. It should be noted that present $\mathbf{U}(\tau_i)$ does not include the control at $N + 1$ point.

The performance index is discretized at LGR points by Gauss quadrature.

$$J = \Phi(\mathbf{X}(\tau_1), \tau_1, \mathbf{X}(\tau_{N+1}), \tau_{N+1}) + \frac{t_f - t_0}{2} \sum_{k=1}^N \omega_k g(\mathbf{X}_k, \mathbf{U}_k, \tau; t_0, t_f) \quad (2.84)$$

where, ω_k is the weight of Gauss quadrature associated with LGR points.

Hence, the finite-dimensional nonlinear programming problem discretized by Radau Pseudospectral method can be expressed as the following form

$$\begin{aligned} J &= \Phi(\mathbf{X}(\tau_1), \tau_1, \mathbf{X}(\tau_{N+1}), \tau_{N+1}) + \frac{t_f - t_0}{2} \sum_{k=1}^N \omega_k g(\mathbf{X}_k, \mathbf{U}_k, \tau; t_0, t_f) \\ \sum_{i=1}^{N+1} D_{ki} \mathbf{X}_i &= \frac{t_f - t_0}{2} f(\mathbf{x}(\tau), \mathbf{u}(\tau), \tau; t_0, t_f) \\ \phi(\mathbf{X}(\tau_1), \tau_1, \mathbf{X}(\tau_{N+1}), \tau_{N+1}) &= 0 \\ \frac{t_f - t_0}{2} C(\mathbf{X}(\tau_k), \mathbf{U}(\tau_k), \tau; t_0, t_f) &\leq 0 \end{aligned} \quad (2.85)$$

where, $(\mathbf{X}_1, \mathbf{X}_2, \dots, \mathbf{X}_{N+1})$, $(\mathbf{U}_1, \mathbf{U}_2, \dots, \mathbf{U}_N)$, t_0 and t_f are the independent variables of the nonlinear programming problem. This problem can be solved by using advanced NLP solver tools.

In order to better reflect the structure of the solution of the optimal control problem and deal with the optimal control problem that the optimal solution changes rapidly or discontinuously in some intervals, it is necessary to develop the segmented Radau Pseudospectral method. This method can allocate the collocation points to the intervals where the optimal solution changes rapidly or discontinuously. And it can overcome the defects of the global orthogonal strategy.

Next, the time domain of the optimal control problem above is divided into K segments, and the starting point of the k -th interval is defined as t_{k-1} , and the end point of the k -th interval is defined as t_k . So, there are $t_0 < t_1 < t_2 < \dots < t_k$ and $t_k = t_f$. Then, the time domain of each interval is transferred into the time interval $[-1, 1]$ via the following equation.

$$\tau = \frac{2t - (t_{k-1} + t_k)}{t_k - t_{k-1}} \quad (2.86)$$

Hence, time can be expressed as

$$t = \frac{t_k - t_{k-1}}{2} \tau + \frac{t_k + t_{k-1}}{2}; \frac{dt}{d\tau} = \frac{t_k - t_{k-1}}{2} \quad (2.87)$$

The end point of each interval can be represented by the boundary points of the optimal control problem as

$$t_k = t_0 + a_k(t_f - t_0), (k = 0, 1, \dots, K) \quad (2.88)$$

Therefore, the original optimal control problem can be expressed as the optimal control problem of K intervals.

$$J = \Phi(\mathbf{x}^1(-1), t_0, \mathbf{x}^K(1), t_K) + \sum_{k=1}^N \frac{t_k - t_{k-1}}{2} \int_{-1}^1 g(\mathbf{x}^k(\tau), \mathbf{u}^k(\tau)) d\tau \quad (2.89)$$

Subject to the dynamic constraint

$$\frac{d\mathbf{x}^k(\tau)}{d\tau} = \frac{t_k - t_{k-1}}{2} f(\mathbf{x}^k(\tau), \mathbf{u}^k(\tau), \tau; t_0, t_f), (k = 1, 2, \dots, K) \quad (2.90)$$

And the inequality constraint is

$$\frac{t_k - t_{k-1}}{2} C(\mathbf{x}^k(\tau), \mathbf{u}^k(\tau), \tau; t_0, t_f) \leq 0, (k = 1, 2, \dots, K) \quad (2.91)$$

The boundary constraint is

$$\phi(\mathbf{x}^1(-1), t_0, \mathbf{x}^K(1), t_K) = 0 \quad (2.92)$$

And the inner-point restriction is

$$\mathbf{x}^k(-1) - \mathbf{x}^{k-1}(-1) = 0, (k = 1, 2, \dots, K - 1) \quad (2.93)$$

Therefore, the piecewise optimal control problem is established. Next, we will discuss why Radau Pseudospectral method is used to discretize the piecewise optimal control problem.

When the piecewise optimal control problem is discretized by Gauss Pseudospectral method, an additional Gauss quadrature is needed to estimate the state of the end point of each interval, and the control variables are only at the LG points between discontinuities. If Legendre Pseudospectral method is used for discretizing the piecewise optimal control problem, then the improved variables include the state and control variables at every collocation point (including two boundary points) between discontinuities, which will cause redundancy control. Moreover, the incompleteness of differential approximation matrix will lead to the inconsistency of adjacent intervals.

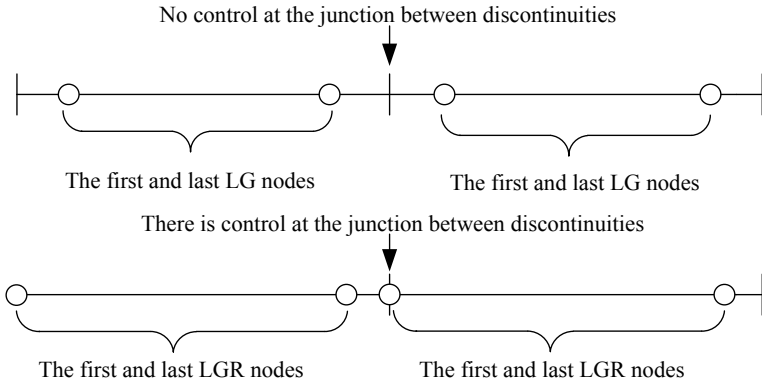


Fig. 2.4 The connections of LG and LGR

However, when the multi-segment optimal control problem is discretized by Radau Pseudospectral method, there will be no redundant control between each interval. And perfect overlap can be achieved between intervals with complete consistency and convenient implementation. The comparison between the collocation points of Gauss Pseudospectral method and Radau Pseudospectral method for multi-segment optimal control problem are given as follows.

Figure 2.4 shows the advantages of LGR points in discretizing multi-segment optimal control problems.

2.5 Linear Gauss Pseudospectral Model Predictive Control

In general, the Pseudospectral methods can only obtain the off-line optimal control command and standard trajectory, and they are of poor real-time performance. Linear Gauss Pseudospectral Model Predictive Control (LGPMP) is an on-line optimal control method. The nonlinear dynamical system is linearized around the nominal trajectory which is needed to be predicted in advance.

For general linear time-varying system, the system differential equations can be expressed with system matrix $\mathbf{A}(t)$ and input matrix $\mathbf{B}(t)$ as

$$\dot{\mathbf{x}}(t) = \mathbf{A}(t)\mathbf{x}(t) + \mathbf{B}(t)\mathbf{u}(t) \quad (2.94)$$

The adjoint system is expressed as

$$\dot{\lambda}(t) = -\mathbf{A}^T \lambda(t) - \mathbf{Q}(t)\mathbf{x}(t) \quad (2.95)$$

where, λ is the costate vector, and \mathbf{Q} is a symmetric matrix.

The relationship between control and costate vectors is given as

$$\mathbf{u}(t) = -\mathbf{R}^{-1}(t)\mathbf{B}^T(t)\boldsymbol{\lambda}(t) \quad (2.96)$$

where, \mathbf{R} is a symmetric matrix.

LGPMPC obtains the control deviations via the corresponding state deviations. Hence, it is needed to obtain the relationship between control deviations and state deviations. According to the above linear time-varying system, the relationship between control deviations and state deviations is obtained as

$$\begin{aligned}\delta\dot{\mathbf{x}}(t) &= \mathbf{A}(t)\delta\mathbf{x}(t) + \mathbf{B}(t)\mathbf{u}(t) + \mathbf{B}(t)\mathbf{u}_p(t) \\ &= \mathbf{A}(t)\delta\mathbf{x}(t) - \mathbf{B}(t)\mathbf{R}(t)^{-1}\mathbf{B}^T(t)\boldsymbol{\lambda}(t) + \mathbf{B}(t)\mathbf{u}_p(t)\end{aligned} \quad (2.97)$$

$$\dot{\boldsymbol{\lambda}}(t) = -\mathbf{Q}(t)\delta\mathbf{x} - \mathbf{A}^T(t)\boldsymbol{\lambda}(t) - \mathbf{Q}(t)\mathbf{x}_p(t) \quad (2.98)$$

$$\delta\mathbf{u} = \mathbf{u}_p - \mathbf{R}^{-1}\mathbf{B}^T\boldsymbol{\lambda} \quad (2.99)$$

The matrix expression of Eqs. (2.97) and (2.98) can be represented as follows

$$\begin{bmatrix} \delta\dot{\mathbf{x}} \\ \dot{\boldsymbol{\lambda}} \end{bmatrix} = \begin{bmatrix} \mathbf{A} & -\mathbf{B}\mathbf{R}^{-1}\mathbf{B}^T \\ -\mathbf{Q} & -\mathbf{A}^T \end{bmatrix} \begin{bmatrix} \delta\mathbf{x} \\ \boldsymbol{\lambda} \end{bmatrix} + \begin{bmatrix} \mathbf{B}\mathbf{u}_p \\ \mathbf{Q}\mathbf{x}_p \end{bmatrix} \quad (2.100)$$

where, $\delta\mathbf{x}$ is the deviation vector of state, \mathbf{x}_p and \mathbf{u}_p are the nominal state and control vectors respectively (the state and control vectors of the predictive trajectory).

The performance index is expressed as following Eq. (2.101) by the deviation vectors of state and control.

$$\begin{aligned}J &= \delta\mathbf{x}^T(1)\mathbf{P}_f\delta\mathbf{x}(1) + \nu^T\left(\frac{\partial\Psi}{\partial x_f}\delta\mathbf{x}(1) - d\Psi\right) \\ &\quad + \frac{1}{2} \int_{-1}^1 \left[(\mathbf{x}_p - \delta\mathbf{x})^T \mathbf{Q} (\mathbf{x}_p - \delta\mathbf{x}) + (\mathbf{u}_p - \delta\mathbf{u})^T \mathbf{R} (\mathbf{u}_p - \delta\mathbf{u}) \right] d\tau\end{aligned} \quad (2.101)$$

where, $\mathbf{P}_f \in \mathbf{R}^{s \times s}$ is the positive semidefinite weighting matrix of terminal state; $\mathbf{Q} \in \mathbf{R}^{s \times s}$ is the positive semidefinite weighting matrix of state in performance index; $\mathbf{R} \in \mathbf{R}^{c \times c}$ is the positive semidefinite weighting matrix of control in performance index. s is the number of state variables and c is the number of control variables.

Equations (2.99) and (2.100) are discretized at the LG points which are the roots of Legendre Polynomial of degree N. And the time domain is transferred from the time interval $[t_0, t_f]$ to the time interval $[-1, 1]$. The derivative of the deviation vector of state $\delta\dot{\mathbf{x}}$ can be expressed by the differential approximation matrix \mathbf{D} , and the derivative of $\boldsymbol{\lambda}$ can be expressed by the differential approximation matrix \mathbf{D}^* similarly. The relationship between \mathbf{D} and \mathbf{D}^* is represented as

$$D_{lk}^* = -\frac{w_k}{w_l} D_{kl}, \quad k = 1, 2, \dots, N; l = 1, 2, \dots, N \quad (2.102)$$

where, w_i is the weight of Gauss quadrature at the i -th node. The $(N+1)$ column of differential approximation matrix \mathbf{D}^* can be expressed as

$$D_{l(N+1)}^* = - \sum_{k=1}^N D_{lk}^*, \quad l = 1, 2, \dots, N \quad (2.103)$$

In summary, by discretizing Eq. (2.99) and Eq. (2.100), we can obtain the linear algebraic equations as

$$\begin{cases} \sum_{l=0}^N D_{kl} \delta x_l - \frac{t_f - t_0}{2} (\mathbf{A}_k \delta x_k - \mathbf{B}_k \mathbf{R}^{-1} \mathbf{B}_k^T \lambda_k) = \frac{t_f - t_0}{2} \mathbf{B}_k u_{pk} \\ \sum_{l=1}^{N+1} D_{kl}^* \lambda_l + \frac{t_f - t_0}{2} (\mathbf{Q}_k \delta x_k + \mathbf{A}_k^T \lambda_k) = \frac{t_f - t_0}{2} \mathbf{Q}_k x_{pk} \end{cases}, \quad k = 1, 2, \dots, N \quad (2.104)$$

$$u_k = u_{pk} - \delta u_k = \mathbf{R}_k^{-1} \mathbf{B}_k^T \lambda_k, \quad k = 1, 2, \dots, N \quad (2.105)$$

Because LG points do not include the boundary points, two additional boundary constraint equation should be formulated to obtain the boundary control. The relationship between the initial deviations of state and the terminal deviations of state is represented as

$$\delta x_{N+1} = \delta x_0 + \frac{t_f - t_0}{2} \sum_{k=1}^N \omega_k (\mathbf{A}_k \delta x_k - \mathbf{B}_k \mathbf{R}^{-1} \mathbf{B}_k^T \lambda_k + \mathbf{B}_k u_{pk}) \quad (2.106)$$

The relationship between the initial costate variables and the terminal costate variables is represented as

$$\lambda_0 = \lambda_{N+1} + \frac{t_f - t_0}{2} \sum_{k=1}^N \omega_k (\mathbf{Q}_k \delta x_k + \mathbf{A}_k^T \lambda_k - \mathbf{Q}_k x_{pk}) \quad (2.107)$$

Equations (2.104), (2.106) and (2.107) can be rearranged as

$$\mathbf{S}\mathbf{Z} = \mathbf{K} \quad (2.108)$$

where, \mathbf{Z} is a column vector including the unknown state and costate variables. Generally, the initial deviations of state δx_0 are known, and the initial costate variables are unknown. Hence, the unknown column vector \mathbf{Z} can be expressed as

$$\mathbf{Z} = [\delta \mathbf{x} \ \lambda]^T = [\delta x_1 \ \dots \ \delta x_{N+1} \ \lambda_0 \ \dots \ \lambda_{N+1}]^T_{(2N+3)s \times 1} \quad (2.109)$$

where,

$$\delta \mathbf{x}_k = \begin{bmatrix} \delta \mathbf{x}_{k1} \\ \delta \mathbf{x}_{k2} \\ \vdots \\ \delta \mathbf{x}_{ks} \end{bmatrix}, k = 1, 2, \dots, N+1; \boldsymbol{\lambda}_k = \begin{bmatrix} \lambda_{k1} \\ \lambda_{k2} \\ \vdots \\ \lambda_{ks} \end{bmatrix}, k = 0, 1, \dots, N+1 \quad (2.110)$$

The elements of coefficient matrix \mathbf{S} of the linear algebraic equations are defined as

$$\mathbf{S} = \begin{bmatrix} \mathbf{S}^{xx} & \mathbf{S}^{x\lambda} \\ \mathbf{S}^{\lambda x} & \mathbf{S}^{\lambda\lambda} \end{bmatrix} \quad (2.111)$$

where, \mathbf{S}^{xx} denotes the coefficient matrix of state variables with respect to state variables, and there are s state variables with each state variable discretized at N LG nodes. In addition, there is the relationship between the initial deviations of state and the terminal deviations of state in Eq. (2.106). Hence, \mathbf{S}^{xx} is a $(N+1)s$ square matrix. $\mathbf{S}^{x\lambda}$ is a $(N+1)s \times (N+2)s$ matrix which denotes the coefficient matrix of state variables with respect to costate variables. $\mathbf{S}^{\lambda x}$ is a $(N+1)s \times (N+1)s$ matrix which denotes the coefficient matrix of costate variables with respect to state variables. $\mathbf{S}^{\lambda\lambda}$ is a $(N+1)s \times (N+1)s$ matrix which denotes the coefficient matrix of costate variables with respect to costate variables.

$$\mathbf{S}^{xx} = \begin{bmatrix} D_{11} - \frac{t_f - t_0}{2} \mathbf{A}_1 & D_{12} & \cdots & D_{1N} & \mathbf{0} \\ D_{21} & D_{22} - \frac{t_f - t_0}{2} \mathbf{A}_2 & \cdots & D_{2N} & \mathbf{0} \\ \vdots & \vdots & \ddots & \vdots & \vdots \\ D_{N1} & D_{N2} & \cdots & D_{NN} - \frac{t_f - t_0}{2} \mathbf{A}_N & \mathbf{0} \\ -\frac{t_f - t_0}{2} w_1 \mathbf{A}_1 & -\frac{t_f - t_0}{2} w_2 \mathbf{A}_2 & \cdots & -\frac{t_f - t_0}{2} w_N \mathbf{A}_N & \mathbf{I} \end{bmatrix}_{(N+1)s \times (N+1)s} \quad (2.112)$$

$$\mathbf{S}^{x\lambda} = \begin{bmatrix} \mathbf{0} & \frac{t_f - t_0}{2} \mathbf{B}_1 \mathbf{R}^{-1} \mathbf{B}_1^T & \mathbf{0} & \cdots & \mathbf{0} & \mathbf{0} \\ \mathbf{0} & \mathbf{0} & \frac{t_f - t_0}{2} \mathbf{B}_2 \mathbf{R}^{-1} \mathbf{B}_2^T & \cdots & \mathbf{0} & \mathbf{0} \\ \vdots & \vdots & \vdots & \ddots & \vdots & \vdots \\ \mathbf{0} & \mathbf{0} & \mathbf{0} & \cdots & \frac{t_f - t_0}{2} \mathbf{B}_N \mathbf{R}^{-1} \mathbf{B}_N^T & \mathbf{0} \\ \mathbf{0} & \frac{t_f - t_0}{2} w_1 \mathbf{B}_1 \mathbf{R}^{-1} \mathbf{B}_1^T & \frac{t_f - t_0}{2} w_2 \mathbf{B}_2 \mathbf{R}^{-1} \mathbf{B}_2^T & \cdots & \frac{t_f - t_0}{2} w_N \mathbf{B}_N \mathbf{R}^{-1} \mathbf{B}_N^T & \mathbf{0} \end{bmatrix}_{(N+1)s \times (N+2)s} \quad (2.113)$$

$$\mathbf{S}^{\lambda x} = \begin{bmatrix} -\frac{t_f-t_0}{2} w_1 \mathbf{Q}_1 & -\frac{t_f-t_0}{2} w_2 \mathbf{Q}_2 & \cdots & -\frac{t_f-t_0}{2} w_N \mathbf{Q}_N & \mathbf{0} \\ \frac{t_f-t_0}{2} \mathbf{Q}_1 & \mathbf{0} & \cdots & \mathbf{0} & \mathbf{0} \\ \mathbf{0} & \frac{t_f-t_0}{2} \mathbf{Q}_2 & \ddots & \mathbf{0} & \mathbf{0} \\ \vdots & \vdots & \ddots & \vdots & \vdots \\ \mathbf{0} & \mathbf{0} & \cdots & \frac{t_f-t_0}{2} \mathbf{Q}_N & \mathbf{0} \end{bmatrix}_{(N+1)s \times (N+1)s} \quad (2.114)$$

$$\mathbf{S}^{\lambda\lambda} = \begin{bmatrix} \mathbf{I} & -\frac{t_f-t_0}{2} w_1 \mathbf{A}_1^T & -\frac{t_f-t_0}{2} w_2 \mathbf{A}_2^T & \cdots & -\frac{t_f-t_0}{2} w_N \mathbf{A}_N^T & -\mathbf{I} \\ \mathbf{0} D_{11}^* + \frac{t_f-t_0}{2} \mathbf{A}_1^T & D_{12}^* & \cdots & D_{1N}^* & D_{1(N+1)}^* & \\ \mathbf{0} & D_{21}^* & D_{22}^* + \frac{t_f-t_0}{2} \mathbf{A}_2^T & \cdots & D_{2N}^* & D_{2(N+1)}^* \\ \vdots & \vdots & \vdots & \ddots & \vdots & \vdots \\ \mathbf{0} & D_{N1}^* & D_{N2}^* & \cdots D_{NN}^* + \frac{t_f-t_0}{2} \mathbf{A}_N^T & D_{N(N+1)}^* & \end{bmatrix}_{(N+1)s \times (N+2)s} \quad (2.115)$$

The expressions of \mathbf{S}^{xx} , $\mathbf{S}^{x\lambda}$, $\mathbf{S}^{\lambda x}$ and $\mathbf{S}^{\lambda\lambda}$ are defined as Eq. (2.112)~(2.115). Where, \mathbf{A}_k is a s square matrix which denotes the value of system matrix \mathbf{A} at τ_k . $A_k(i, j)$ denotes the partial derivatives of the i-th state variable differential equation with respect to the j-th state variable, and the expression of $A_k(i, j)$ is given as

$$A_{k(ij)} = \frac{\partial f_i}{\partial x_j}(\tau_k), \quad k = 1, 2, \dots, N; \quad i, j = 1, 2, \dots, s \quad (2.116)$$

\mathbf{B}_k is a $s \times c$ matrix which denotes the value of output matrix \mathbf{B} at τ_k . $B_k(i, j)$ denotes the partial derivatives of the i-th state variable differential equation with respect to the j-th control variable, and the expression of $B_k(i, j)$ is given as

$$B_{k(ij)} = \frac{\partial f_i}{\partial u_j}(\tau_k), \quad k = 1, 2, \dots, N; \quad i = 1, 2, \dots, s; \quad j = 1, 2, \dots, c \quad (2.117)$$

The expression of matrix \mathbf{K} is given as Eq. (2.118). The right side of the equal sign is a $(2N+2)s$ column vector. Corresponding to coefficient matrix \mathbf{S} , \mathbf{K} is divided into two parts.

$$\mathbf{K} = \begin{bmatrix} \mathbf{K}^x \\ \mathbf{K}^\lambda \end{bmatrix} \quad (2.118)$$

where,

$$\mathbf{K}^x = \begin{bmatrix} \frac{t_f - t_0}{2} \mathbf{B}_1 \mathbf{u}_{p1} \\ \frac{t_f - t_0}{2} \mathbf{B}_2 \mathbf{u}_{p2} \\ \vdots \\ \frac{t_f - t_0}{2} \mathbf{B}_N \mathbf{u}_{pN} \\ \frac{t_f - t_0}{2} \sum_{k=1}^N w_k \mathbf{B}_k \mathbf{u}_{pk} + \delta \mathbf{x}_0 \end{bmatrix}, \mathbf{K}^\lambda = \begin{bmatrix} -\frac{t_f - t_0}{2} \sum_{k=1}^N w_k \mathbf{Q}_k \mathbf{x}_{pk} \\ \frac{t_f - t_0}{2} \mathbf{Q}_1 \mathbf{x}_{p1} \\ \vdots \\ \frac{t_f - t_0}{2} \mathbf{Q}_N \mathbf{x}_{pN} \end{bmatrix} \quad (2.119)$$

Through the above process, the linear algebraic equations composed of Eqs. (2.104), (2.106) and (2.107) are transferred into matrix form. It can be seen that there are $(2N + 3)s$ unknown numbers and only $(2N + 2)s$ equations in the linear algebraic equations. According to the terminal constraints and the transversality conditions, s unknown numbers can be deleted.

Assuming that the number of state variables that are related to the terminal constraints is nf . The value of corresponding $\delta \mathbf{x}_{N+1}$ can be determined by $\delta \mathbf{x}_{N+1} = \mathbf{x}(t_f) - \mathbf{x}_f$.

So, the number of state variables that are independent of the terminal constraints is $(s - nf)$. According to the transversality conditions, the corresponding costate variables can be obtained as $\lambda_{N+1} = 0$.

Hence, nf terminal deviations of state and $(s - nf)$ terminal costate variables can be deleted. The corresponding s columns of coefficient matrix \mathbf{S} can be deleted. The expression of \mathbf{K} is represented in the following form

$$\mathbf{K} = \begin{bmatrix} \mathbf{K}^x \\ \mathbf{K}^\lambda \end{bmatrix}_{(2N+3)s \times 1} - \mathbf{S}_d \mathbf{Z}_d \quad (2.120)$$

where, \mathbf{S}_d is a matrix composed of the deleted columns of coefficient matrix \mathbf{S} , \mathbf{Z}_d is a column vector composed of the deleted elements of \mathbf{Z} .

Hence, $\mathbf{S}\mathbf{Z} = \mathbf{K}$ is transferred into a set of linear algebraic equations of $(2N + 2)s$ variables with a unique solution exiting. $\delta \mathbf{x}_k$ and λ_k can be obtained by solving the linear algebraic equations, and the current control can be obtained via Eq. (2.105).

References

1. Nayfeh, A.H.: Perturbation Methods. Wiley, New York (1973)
2. Kevorkian, J., Cole, J.D.: Perturbation Methods in Applied Mathematics. Springer-Verlag, New York (1981)
3. Naidu, D.S., Calise, A.J.: Singular perturbations and time scales in guidance and control of aerospace systems: a survey. *J. Guid. Control Dyn.* **24**(6), 1057–1078 (2001)
4. Reddien, W.: Collocation at gauss points as a discretization in optimal contro. *SIAM J. Control Opt.* **17**(2), 518–525 (1979)
5. Elnagar, G., Kazemi, M.A., Razzaghi, M.: The Pseudospectral Legendre method for discretizing optimal control problems. *IEEE Trans. Auto. Control* **40**(10), 1793–1796 (1995)
6. Ross, I.M., Fahroo, F.: Pseudospectral knotting methods for solving optimal con problems. *J. Guid. Control Dyn.* **27**, 397–405 (2004)

7. Benson, D.: A Gauss pseudospectral transcription for optimal control. Massachusetts Institute of Technology, Cambridge, Massachusetts (2005)
8. Garg, D., Patterson, M.A., Francolin, C., et al.: Direct trajectory optimization and costate estimation of finite-horizon and infinite-horizon optimal control problems using a Radau Pseudospectral method. *Comput. Opt. Appl.* **49**(2), 335–358 (2011)
9. Garg, D., Patterson, M., Hager, W.W., et al.: A unified framework for the numerical solution of optimal control problems using pseudospectral methods. *Automatica* **46**(11), 1843–1851 (2010)
10. Garg, D., Hager, W.W., Rao, A.V.: Pseudospectral methods for solving infinite-horizon optimal control problems. *Automatica* **47**(4), 829–837 (2011)
11. Darby, C.: HP-Pseudospectral method for solving continuous-time nonlinear optimal control problems. University of Florida
12. Zhao, Y., Tsotras, P. A.: Density-function based mesh refinement algorithm for optimal control problems. In: Infotech and Aerospace Conference, AIAA Paper 2009–2019, Washington, April 2009
13. Liu, H., Chen, S., Shen, L., et al.: An integrated multicriterion hp-adaptive Pseudospectral method for direct optimal control problems solving. *Math. Prob. Eng.* (pt.10), 760890.1–760890.22 (2012)
14. Gong, Q., Kang, W., Ross, I.M.: A Pseudospectral method for the optimal control of constrained feedback linearizable systems. *IEEE Trans. Autom. Control* **51**(7), 1115–1129 (2006)
15. Gong, Q., Kang, W., Bedrossian, N. S.: Pseudospectral optimal control for military and industrial applications. In: IEEE Conference on Decision & Control, New Orleans, LA, USA, 12–14 December 2007

Chapter 3

Mathematical Modeling for Hypersonic Glide Problem



In order to solve the optimization problem of multi-phase trajectory and obtain the optimal trajectory, dynamic equations for hypersonic vehicle are established first. On this basis, further analysis and solution are carried out later.

3.1 The Coordinate System Adopted in This Book

This book adopts American coordinate system. To establish the dynamic equations for hypersonic vehicle, we need to introduce the following coordinate systems first.

3.1.1 Geocentric Inertial Coordinate System (I)

Geocentric Inertial Coordinate System $O_E-x_Iy_Iz_I$ (abbreviated as I): The origin O_E is at the Earth's core; the O_Ex_I axis points to the equinox or a fixed point in the Earth equatorial plane; the O_Ez_I axis is perpendicular to the equatorial plane and coincides with the Earth's rotational axis, pointing to the North Pole; the direction of the O_Ey_I axis is determined by the right hand rule.

3.1.2 Geographic Coordinate System (T)

Geographic Coordinate System $o_I-x_Ty_Tz_T$ (abbreviated as T): The origin o_I is at the center of mass of the vehicle; o_Iz_T points to the Earth's center O_E ; o_Ix_T is perpendicular to the o_Iz_T in the meridian plane of o_I and points to the North Pole; o_Iy_T is determined by the right hand rule. In practical application, the origin of coordinate is often defined as the intersection of the standard elliptical Earth surface

with the line specified by the Earth's core O_E and the center of mass o_I , and the coordinate system is usually named $o\text{-}x_Ty_Tz_T$.

3.1.3 Orientation Coordinate System (O)

Orientation Coordinate System $o_o\text{-}x_ox_oz_o$ (abbreviated as O): This is a dynamic coordinate system fixed with the Earth. Define the point o_I as the center of mass of the aircraft at the moment when the aircraft enters the transition phase from the ascending phase. Since this book only studies the transition phase, gliding phase and descending phase, the origin of this coordinate system is chosen as the intersection point o of the standard elliptical Earth surface with the line specified by the point o_I and the Earth's center. o_oz_o points to the Earth's center from the origin o ; o_ox_o is perpendicular to o_oz_o , pointing to the direction of the vehicle's initial velocity of the transition phase in the trajectory plane; o_oy_o is determined by the right hand rule. Using this coordinate system, the relative dynamic equations of hypersonic vehicle can be established.

3.1.4 Velocity Coordinate System (V)

Velocity Coordinate System $o_I\text{-}x_vy_vz_v$ (abbreviated as V): The origin o_I is the center of mass of the vehicle; o_Ix_v points to the direction of the vehicle's velocity; o_Iz_v is perpendicular to the o_Ix_v downward in the longitudinal symmetry plane of the vehicle; o_Iy_v is determined by the right hand rule and points to right side of the $x_vo_Iz_v$ plane looking in the direction of the motion. The relationship between this coordinate system and other coordinate systems reflects the state of velocity vector of vehicle.

3.1.5 Half-Velocity Coordinate System (H)

Half-velocity Coordinate System $o_I\text{-}x_hy_hz_h$ (abbreviated as H): The origin o_I is the center of mass of the vehicle; o_Ix_h points to the direction of the vehicle's velocity; o_Iz_h is perpendicular to o_Ix_h downward in local vertical plane; o_Iy_h is determined by the right hand rule. This coordinate system is also called the trajectory coordinate system or flightpath coordinate system.

3.1.6 Body Coordinate System (B)

Body Coordinate System $o_1x_1y_1z_1$ (abbreviated as B): The originate o_1 is the center of mass of the vehicle; o_1x_1 is along the longitudinal axis of the vehicle, pointing to the head; o_1z_1 is perpendicular to the o_1x_v downward in the longitudinal symmetry plane of the vehicle; o_1y_1 is determined by the right hand rule and points to right side of the $x_1o_1z_1$ plane looking in the direction of the motion. The position of this coordinate system can reflect the attitude of the vehicle.

3.2 Transformation Between Coordinate Systems

3.2.1 Transformation Between the Orientation Coordinate System and the Half-Velocity Coordinate System

Since the o_1y_h axis of the half-velocity coordinate system is in the vertical plane of o_1z_T axis, there are only two Euler angles σ_T and θ_T between the two coordinate systems, and it is stipulated to rotate in the order of ‘3–2–1’. In other words, the orientation coordinate system first rotates σ_T on the o_oz_T axis, and then rotates θ_T on the oy_h axis. In this way, the orientation coordinate system coincides with the half-velocity coordinate system. The transformation between the two coordinate systems is as follows:

$$\begin{bmatrix} x_h^0 \\ y_h^0 \\ z_h^0 \end{bmatrix} = \mathbf{H}_T \begin{bmatrix} x_T^0 \\ y_T^0 \\ z_T^0 \end{bmatrix} \quad (3.1)$$

where,

$$\mathbf{H}_T = \begin{bmatrix} \cos \theta_T \cos \sigma_T & \cos \theta_T \sin \sigma_T & -\sin \theta_T \\ -\sin \sigma_T & \cos \sigma_T & 0 \\ \sin \theta_T \cos \sigma_T & \sin \sigma_T \sin \theta_T & \cos \theta_T \end{bmatrix} \quad (3.2)$$

3.2.2 Transformation Between the Velocity Coordinate System and the Half-Velocity Coordinate System

According to the definition, the velocity coordinate system $o_1x_vy_vz_v$ can be obtained by making the half-velocity coordinate system $o_1x_hy_hz_h$ rotate a bank angle ν on the o_1x_v axis. The transformation is as follows:

$$\begin{bmatrix} x_v^0 \\ y_v^0 \\ z_v^0 \end{bmatrix} = \mathbf{H}_T \begin{bmatrix} x_h^0 \\ y_h^0 \\ z_h^0 \end{bmatrix} \quad (3.3)$$

and

$$\mathbf{V}_H = \begin{bmatrix} 1 & 0 & 0 \\ 0 & \cos \nu & \sin \nu \\ 0 & -\sin \nu & \cos \nu \end{bmatrix} \quad (3.4)$$

From the properties of directional cosine matrix, we have

$$\mathbf{H}_V = (\mathbf{V}_H)^T = \begin{bmatrix} 1 & 0 & 0 \\ 0 & \cos \nu & -\sin \nu \\ 0 & \sin \nu & \cos \nu \end{bmatrix} \quad (3.5)$$

3.2.3 Transformation Between the Velocity Coordinate System and the Body Coordinate System

The o_1z_v axis of the velocity coordinate system is in the longitudinal symmetry plane of the vehicle ($o_1x_1z_1$), namely, there are only two Euler angles and one order of rotation between the two coordinate systems. The velocity coordinate system first rotates the Angle of Sideslip (AOS) β on the o_1z_v axis, and then rotates the AOA α on the new axis o_1y_1 . In this way, the velocity coordinate system coincides with the body coordinate system. The transformation between the two coordinate systems is as follows:

$$\begin{bmatrix} x_1^0 \\ y_1^0 \\ z_1^0 \end{bmatrix} = \mathbf{B}_V \begin{bmatrix} x_v^0 \\ y_v^0 \\ z_v^0 \end{bmatrix} \quad (3.6)$$

where,

$$\mathbf{B}_V = \begin{bmatrix} \cos \alpha \cos \beta & -\cos \alpha \sin \beta & -\sin \alpha \\ \sin \beta & \cos \beta & 0 \\ \sin \alpha \cos \beta & -\sin \alpha \sin \beta & \cos \alpha \end{bmatrix} \quad (3.7)$$

From the properties of directional cosine matrix, we have

$$\mathbf{V}_B = \begin{bmatrix} \cos \alpha \cos \beta & \sin \beta & \sin \alpha \cos \beta \\ -\cos \alpha \sin \beta & \cos \beta & -\sin \alpha \sin \beta \\ -\sin \alpha & 0 & \cos \alpha \end{bmatrix} \quad (3.8)$$

3.2.4 Transformation Between the Body Coordinate System and the Half-Velocity Coordinate System

From above, we can obtain the transformation between the body coordinate system and the half-velocity coordinate system as follows:

$$\mathbf{H}_B = \mathbf{H}_V \mathbf{V}_B = \begin{bmatrix} 1 & 0 & 0 \\ 0 \cos \nu & -\sin \nu & 0 \\ 0 \sin \nu & \cos \nu & 0 \end{bmatrix} \begin{bmatrix} \cos \alpha \cos \beta & \sin \beta & \sin \alpha \cos \beta \\ -\cos \alpha \sin \beta & \cos \beta & -\sin \alpha \sin \beta \\ -\sin \alpha & 0 & \cos \alpha \end{bmatrix} \quad (3.9)$$

3.3 Dynamic Equations of Hypersonic Vehicle in Half-Velocity Coordinate System

3.3.1 Dynamics Equations of the Center of Mass in Half-Velocity Coordinate System

The vector form of the dynamic equation of the center of mass is

$$\frac{d\mathbf{v}}{dt} = \mathbf{P} + \mathbf{R} + m\mathbf{g} + \mathbf{F}_c \quad (3.10)$$

The geographic coordinate system is taken as the reference system here. Since it rotates at the angular velocity of the Earth's rotation ω_e relative to the inertial coordinate system, there is

$$m \frac{\delta^2 \mathbf{r}}{\delta t^2} = \mathbf{P} + \mathbf{R} + m\mathbf{g} + \mathbf{F}_c - m\mathbf{a}_e - m\mathbf{a}_k \quad (3.11)$$

The relative acceleration $\frac{\delta^2 \mathbf{r}}{\delta t^2}$: $\frac{\delta \mathbf{r}}{\delta t}$ is the relative velocity of the center of mass of the vehicle relative to the geographic coordinate system and is along the o_1x_h axis of the half-velocity coordinate system. It can be obtained according to the vector differential law because the half-velocity coordinate system has angular velocity Ω relative to the geographic coordinate system.

$$\frac{\delta^2 \mathbf{r}}{\delta t^2} = \dot{\mathbf{v}}_{ox_h^o} + \boldsymbol{\Omega} \times \mathbf{v} \quad (3.12)$$

Expanding this equation gives

$$\frac{\delta^2 \mathbf{r}}{\delta t^2} = \begin{bmatrix} \dot{v} \\ -v(\dot{\sigma}_T \cos \theta_T - \frac{vtg\phi \cos^2 \theta_T \sin \sigma_T}{r}) \\ -v(\dot{\theta}_T - \frac{v \cos \dot{\theta}_T}{r}) \end{bmatrix} \quad (3.13)$$

The aerodynamic force \mathbf{R} : If \mathbf{R} is decomposed into X , Y and Z along the velocity coordinate system, and then the projection on the half-velocity coordinate system is as follows

$$\begin{bmatrix} R_{xh} \\ R_{yh} \\ R_{zh} \end{bmatrix} = \mathbf{H}_V \begin{bmatrix} -X \\ Y \\ Z \end{bmatrix} = \begin{bmatrix} -X \\ Y \cos \nu - Z \sin \nu \\ Z \cos \nu + Y \sin \nu \end{bmatrix} \quad (3.14)$$

The thrust \mathbf{P} : Assuming that \mathbf{P} is decomposed into P_{x1} , P_{x2} and P_{x3} in the body coordinate system, it becomes

$$\begin{bmatrix} P_{xh} \\ P_{yh} \\ P_{zh} \end{bmatrix} = \mathbf{H}_B \begin{bmatrix} P_{x1} \\ P_{y1} \\ P_{z1} \end{bmatrix} \quad (3.15)$$

The gravity $m\mathbf{g}$: The projection of the component of the gravity in the \mathbf{r} direction on the half-velocity coordinate system is as follows:

$$\begin{bmatrix} g'_{rxh} \\ g'_{ryh} \\ g'_{rzh} \end{bmatrix} = \mathbf{H}_T \begin{bmatrix} 0 \\ 0 \\ -g'_r \end{bmatrix} = \begin{bmatrix} g'_r \sin \theta_T \\ 0 \\ -g'_r \cos \theta_T \end{bmatrix} \quad (3.16)$$

where, $g'_r = -\frac{fM}{r^2}[1 + J(\frac{a_e}{r})^2(1 - 5 \sin^2 \phi)]$, the projection of gravity acceleration components along ω_e in half-velocity coordinate system is

$$\begin{bmatrix} g_{\omega_e xh} \\ g_{\omega_e yh} \\ g_{\omega_e zh} \end{bmatrix} = \mathbf{H}_T \begin{bmatrix} g_{\omega_e} \cos \phi \\ 0 \\ -g_{\omega_e} \sin \phi \end{bmatrix} \quad (3.17)$$

where, $g_{\omega_e} = -\frac{2fM}{r^2} J(\frac{a_e}{r})^2 \sin \phi$.

The control force \mathbf{F}_c : Assuming that the control force is decomposed in the o_I - $x_I y_I z_I$, it becomes

$$\begin{bmatrix} F_{cxh} \\ F_{cyh} \\ F_{czh} \end{bmatrix} = \mathbf{H}_V \mathbf{V}_B \begin{bmatrix} F_{cx1} \\ F_{cy1} \\ F_{cz1} \end{bmatrix} \quad (3.18)$$

The centrifugal inertial force \mathbf{F}_e : The projection of $-\mathbf{a}_e$ in the o_I - $XYTzT$ is

$$-\mathbf{a}_e = \begin{bmatrix} -\omega_e^2 r \cos \phi \sin \phi \\ 0 \\ -\omega_e^2 r \cos^2 \phi \end{bmatrix} \quad (3.19)$$

Thus its projection in the half-velocity coordinate system is as follows:

$$\begin{bmatrix} F_{exh} \\ F_{eyh} \\ F_{ezh} \end{bmatrix} = \mathbf{H}_T \begin{bmatrix} -m\omega_e^2 r \cos \phi \sin \phi \\ 0 \\ -m\omega_e^2 r \cos^2 \phi \end{bmatrix} \quad (3.20)$$

The Coriolis inertial force \mathbf{F}_k : The projection of it in the half-velocity coordinate system is:

$$\begin{bmatrix} F_{kxh} \\ F_{kyh} \\ F_{kzh} \end{bmatrix} = \begin{bmatrix} 0 \\ 2mv\omega_e(\cos \sigma_T \sin \theta_T \cos \phi - \cos \theta_T \sin \phi) \\ 2mv\omega_e \sin \sigma_T \cos \phi \end{bmatrix} \quad (3.21)$$

And then the dynamic equation of the center of the mass of the vehicle in the half-velocity coordinate system is as follows:

$$\left. \begin{aligned} & \begin{bmatrix} \dot{v} \\ -v(\dot{\sigma}_T \cos \theta_T - \frac{vtg\phi \cos^2 \theta_T \sin \sigma_T}{r}) \\ -v(\dot{\theta}_T - \frac{v \cos \dot{\theta}_T}{r}) \end{bmatrix} = \mathbf{H}_B \begin{bmatrix} P_{x1} \\ P_{y1} \\ P_{z1} \end{bmatrix} + \mathbf{H}_V \begin{bmatrix} -X \\ Y \\ Z \end{bmatrix} \\ & + \mathbf{H}_B \begin{bmatrix} F_{cx1} \\ F_{cy1} \\ F_{cz1} \end{bmatrix} + mg_r' \begin{bmatrix} \sin \theta_T \\ 0 \\ -\cos \theta_T \end{bmatrix} + mg\omega_e \mathbf{H}_T \begin{bmatrix} \cos \phi \\ 0 \\ -\sin \phi \end{bmatrix} + \mathbf{H}_T \begin{bmatrix} -m\omega_e^2 r \cos \phi \sin \phi \\ 0 \\ -m\omega_e^2 r \cos^2 \phi \end{bmatrix} \\ & + \begin{bmatrix} 0 \\ 2mv\omega_e(\cos \sigma_T \sin \theta_T \cos \phi - \cos \theta_T \sin \phi) \\ 2mv\omega_e \sin \sigma_T \cos \phi \end{bmatrix} \end{aligned} \right\} \quad (3.22)$$

Substituting \mathbf{H}_B , \mathbf{H}_V and \mathbf{H}_T into Eq. (3.22) gives

$$\left. \begin{aligned} \frac{dv}{dt} &= g'_r \sin \theta_T + g_{\omega_e} (\cos \sigma_T \cos \theta_T \cos \phi + \sin \theta_T \sin \phi) \\ &\quad + \frac{P_{xh} - X}{m} + \frac{F_{cxh}}{m} \\ &\quad - \omega_e^2 r \cos \phi (\sin \phi \cos \sigma_T \cos \theta_T - \cos \phi \sin \theta_T) \\ \frac{d\theta_T}{dt} &= g'_r \frac{\cos \theta_T}{v} + g_{\omega_e} \frac{-\cos \phi \cos \sigma_T \sin \theta_T + \sin \phi \cos \theta_T}{v} + \frac{v \cos \theta_T}{r} \\ &\quad + \frac{-P_{zh} + Y \cos v - Z \sin v}{mv} - \frac{F_{czh}}{mv} \\ &\quad - 2\omega_e \cos \phi \sin \sigma_T + \frac{\omega_e^2 r \cos \phi}{mv} (\sin \phi \cos \sigma_T \sin \theta_T + \cos \phi \cos \theta_T) \\ \frac{d\sigma_T}{dt} &= -g_{\omega_e} \frac{\cos \phi \sin \sigma_T}{v \cos \theta_T} + \frac{v \tan \phi \cos^2 \theta_T \sin \sigma_T}{r \cos \theta_T} \\ &\quad - \frac{P_{yh} - Z \cos v - Y \sin v}{mv \cos \theta_T} - \frac{F_{cyh}}{mv \cos \theta_T} \\ &\quad + \frac{2\omega_e}{\cos \theta_T} (\cos \phi \cos \sigma_T \sin \theta_T - \sin \phi \cos \theta_T) + \omega_e^2 r \frac{\cos \phi \sin \phi \sin \sigma_T}{v \cos \theta_T} \end{aligned} \right\} \quad (3.23)$$

In these equations, the first line of each differential equation represents the gravity and centrifugal force, which is generated by the motion of the vehicle; the second line represents the control force, and the third line represents the Coriolis force and centrifugal force, which is generated by the rotation of the Earth.

3.3.2 The Dynamic Equations of the Center of Mass of the Vehicle

The dynamic equations of the center of mass of the vehicle are:

$$\left. \begin{aligned} \dot{\phi} &= \frac{v \cos \theta_T \cos \sigma_T}{r \cos \phi} \\ \dot{\lambda} &= \frac{-v \cos \theta_T \sin \sigma_T}{r \cos \phi} \\ \dot{r} &= v \sin \theta_T \end{aligned} \right\} \quad (3.24)$$

3.3.3 Dynamic Equations of Hypersonic Gliding Vehicle Based on BTT Control

In the study of this book, the unpowered phase of the flight is mainly concerned. Therefore, the thrust P_{xh} , P_{yh} and P_{zh} in Eq. (3.23) are all zero, and the control forces F_{cxh} , F_{cyh} and F_{czh} are also zero. The total AOA and bank angle are used as control variables. Thus the total lift force L is:

$$L = \sqrt{Y^2 + Z^2} = C_L^\alpha \alpha_t q A_\omega \quad (3.25)$$

The dynamic equations of hypersonic gliding vehicle based on BTT control are as follows:

$$\left. \begin{aligned} \frac{dv}{dt} &= g'_r \sin \theta_T + g_{\omega_e} (\cos \sigma_T \cos \theta_T \cos \phi + \sin \theta_T \sin \phi) \\ -\frac{D}{m} &- \omega_e^2 r \cos \phi (\sin \phi \cos \sigma_T \cos \theta_T - \cos \phi \sin \theta_T) \\ \frac{d\theta_T}{dt} &= g'_r \frac{\cos \theta_T}{v} + g_{\omega_e} \frac{-\cos \phi \cos \sigma_T \sin \theta_T + \sin \phi \cos \theta_T}{v} \\ &+ \frac{v \cos \theta_T}{r} + \frac{L \cos \mu_t}{mv} - 2\omega_e \cos \phi \sin \sigma_T \\ &+ \frac{\omega_e^2 r \cos \phi}{v} (\sin \phi \cos \sigma_T \sin \theta_T + \cos \phi \cos \theta_T) \\ \frac{d\sigma_T}{dt} &= -g_{\omega_e} \frac{\cos \phi \sin \sigma_T}{v \cos \theta_T} + \frac{v \tan \phi \cos^2 \theta_T \sin \sigma_T}{r \cos \theta_T} \\ -\frac{L \sin \mu_t}{mv \cos \theta_T} &+ \frac{2\omega_e}{\cos \theta_T} (\cos \phi \cos \sigma_T \sin \theta_T - \sin \phi \cos \theta_T) \\ &+ \omega_e^2 r \frac{\cos \phi \sin \phi \sin \sigma_T}{v \cos \theta_T} \end{aligned} \right\} \quad (3.26)$$

3.3.4 Dynamic Equations of Hypersonic Vehicle in Vertical Plane

In order to solve the problem conveniently, the dynamic equation is further simplified without considering the Earth's rotation and assuming that the earth is a sphere. So the dynamic equations of the hypersonic vehicle in the vertical plane can be simplified as

$$\frac{dM}{dt} = \frac{-D - mg \sin \theta_T}{am} \quad (3.27)$$

$$\frac{d\theta_T}{dt} = \frac{L - mg \cos \theta_T}{Mam} + \frac{Ma \cos \theta_T}{R_0 + h} \quad (3.28)$$

$$\frac{dh}{dt} = Ma \sin \theta_T \quad (3.29)$$

$$\frac{dr}{dt} = \frac{R_0 Ma \cos \theta_T}{R_0 + h} \quad (3.30)$$

where $v = Ma$.

3.3.5 Atmospheric Model

The present atmospheric model is based on the 1976 American Standard Atmospheric COESA Model, the input of which is altitude, and the output is density and sound speed.

3.3.6 Aerodynamic Model

The formulae for calculating lift force and drag force are as follows:

$$L = q C_L A_\omega \quad (3.31)$$

$$D = q C_D A_\omega \quad (3.32)$$

where, $q = \frac{1}{2} \rho (Ma)^2$, C_D and C_L can be fitted into empirical formulae from the original aerodynamic data in the appendix, which are data tables of C_A and C_N . In order to facilitate calculation, the data tables of C_A and C_N are converted into data tables of C_D and C_L by the following formulae firstly, and then the data fitting can be carried out.

$$C_D = C_N \sin \alpha + C_A \cos \alpha \quad (3.33)$$

$$C_L = C_N \cos \alpha - C_A \sin \alpha \quad (3.34)$$

The fitting formulae of C_D and C_L can be expressed in the following forms:

$$\left. \begin{aligned} C_D &= f_D(h, h^2, \dots, M, M^2, \dots, \alpha, \alpha^2, \dots) \\ C_L &= f_L(h, h^2, \dots, M, M^2, \dots, \alpha, \alpha^2, \dots) \end{aligned} \right\} \quad (3.35)$$

3.3.7 The Stagnation Point Heat Flow, Overload and Dynamic Pressure

3.3.7.1 The Stagnation Point Heat Flow

The formula for calculating the heating rate at the stagnation point is as follows:

$$\dot{Q} = 5.21 \times 10^{-9} \sqrt{\rho/r_n} (Ma)^{3.15} \quad (3.36)$$

where, r_n is the head radius at stagnation point. The constraint of heating rate at stagnation point is $c_Q = \dot{Q} - \dot{Q}_{\max} \leq 0$.

3.3.7.2 Overload

The overload n can be expressed as:

$$n = \sqrt{L^2 + D^2}/mg \quad (3.37)$$

The constraint of overload is $c_n = n - n_{\max} \leq 0$.

3.3.7.3 Dynamic Pressure

The dynamic pressure q can be defined as

$$q = 0.5 \cdot \rho \cdot V^2 \quad (3.38)$$

And the constraint is $c_q = q - q_{\max} \leq 0$.

Chapter 4

Mathematical Description of Glide-Trajectory Optimization Problem



The entry process of hypersonic gliding vehicle is constrained by path constraints such as heating rate, load factor, dynamic pressure, control variables and terminal constraints such as position, velocity, flight path angle and heading angle. Therefore, it is necessary to establish an optimal control problem considering multiple path constraints and terminal constraints for entry flight. Then the optimal entry glide trajectory can be obtained by solving this optimal control problem.

4.1 Mathematical Description for Optimal Control Problem

The essence of optimal control problem is to determine the control of a specific system under specific conditions, so that the system performance index (objective function) can be optimal. In other words, solving the optimal control problem is to find the admissible control to transfer the dynamic system from the initial state to a desired terminal state, and to ensure that the specified performance index reaching the maximum (minimum) value.

4.1.1 Performance Index of Optimal Control Problem

In the state space, different control can be used to transfer the system state from initial state $\mathbf{x}(t_0)$ to terminal state $\mathbf{x}(t_f)$. A performance index is needed to evaluate the performance of the system under various control commands. The form of performance index mainly depends on the task of the optimal control problem. Therefore, different optimal control problems have different performance indexes, which mainly varies with the different control commands. That is to say, the performance index is a function of the control $\mathbf{u}(t)$, recording as $J(\mathbf{u})$.

Generally, there are three types of performance indexes for optimal control problems:

Integral performance index

$$J(\mathbf{u}) = \int_{t_0}^{t_f} L(\mathbf{x}(t), \mathbf{u}(t), t) dt \quad (4.1)$$

Final value performance index

$$J(\mathbf{u}) = \Phi(\mathbf{x}(t_f), t_f) \quad (4.2)$$

Comprehensive performance index

$$J(\mathbf{u}) = \Phi(\mathbf{x}(t_f), t_f) + \int_{t_0}^{t_f} L(\mathbf{x}(t), \mathbf{u}(t), t) dt \quad (4.3)$$

For optimal trajectory problem, the maximum range is integral performance index, the maximum terminal speed is final performance index, and the weighted sum of the above two indexes are comprehensive performance index.

4.1.2 Description of Optimal Control Problem

Optimal control problems are generally described as:

The state equation of the system:

$$\dot{\mathbf{x}}(t) = f(\mathbf{x}(t), \mathbf{u}(t), t) \quad (4.4)$$

where $\mathbf{x}(t) \in \mathbf{R}^n$ is state variable, $\mathbf{u}(t) \in \mathbf{R}^m (m \leq n)$ is control variable, $f(\mathbf{x}(t), \mathbf{u}(t), t)$ is a n -dimensional vector function, which is continuously differentiable for $\mathbf{x}(t)$, $\mathbf{u}(t)$ and t . In the optimal trajectory problem, the state equations of the system are the dynamic differential equations of the vehicle.

Admissible control $\mathbf{u}(t)$ takes value in bounded closed set \mathbf{U} of m -dimensional vector space \mathbf{R}^m , $\mathbf{u}(t) \in \mathbf{U} \subseteq \mathbf{R}^m$. Here $t \in [t_0, t_f]$.

Initial conditions: $\zeta(\mathbf{x}(t_0), t_0) = 0$, where $\zeta = [\zeta_1, \zeta_2, \dots, \zeta_s]^T$ are s -dimension initial constraint functions.

Terminal conditions: $\xi(\mathbf{x}(t_f), t_f) = 0$, where $\xi = [\xi_1, \xi_2, \dots, \xi_r]^T$ are r -dimensional terminal constraint functions.

Performance index:

$$J(\mathbf{u}) = \Phi(\mathbf{x}(t_f), t_f) + \int_{t_0}^{t_f} L(\mathbf{x}(t), \mathbf{u}(t), t) dt \quad (4.5)$$

where Φ and L are both scalar functions.

Then, optimal control $\mathbf{u}^*(t)$ is determined to transfer the system from the initial state $\mathbf{x}(t_0)$ to the final state $\mathbf{x}(t_f)$, and to ensure the performance index $J(\mathbf{u})$ maximum (minimum).

4.1.3 The Minimum Principle

The maximum principle is proposed by Pontryagin, a Soviet mathematician, in the 1950s, which is also called the minimum principle. In this book, the minimum principle is adopted, which is used to solve optimal control problems.

The Hamiltonian function is defined as

$$H(\mathbf{x}(t), \mathbf{u}(t), \boldsymbol{\lambda}(t), t) = L(\mathbf{x}(t), \mathbf{u}(t), t) + \boldsymbol{\lambda}^T(t) f(\mathbf{x}(t), \mathbf{u}(t), t) \quad (4.6)$$

where $\boldsymbol{\lambda}(t) = [\lambda_1(t), \lambda_2(t), \dots, \lambda_n(t)]^T$ is an undetermined n -dimensional Lagrange multiplier vector.

The necessary conditions to minimize the system performance index are as follows

1. Regular equations

State equations

$$\dot{\mathbf{x}}^*(t) = \frac{\partial H}{\partial \boldsymbol{\lambda}}(\mathbf{x}^*(t), \mathbf{u}^*(t), \boldsymbol{\lambda}(t), t) = f(\mathbf{x}^*(t), \mathbf{u}^*(t), t) \quad (4.7)$$

Costate equations

$$\dot{\boldsymbol{\lambda}}(t) = -\frac{\partial H}{\partial \mathbf{x}}(\mathbf{x}^*(t), \mathbf{u}^*(t), \boldsymbol{\lambda}(t), t) \quad (4.8)$$

where $\mathbf{u}^*(t)$ is the optimal control, $\mathbf{x}^*(t)$ is the optimal trajectory.

2. Extremum Conditions

$$H(\mathbf{x}^*(t), \mathbf{u}^*(t), \boldsymbol{\lambda}(t), t) = \min_{\mathbf{u}(t) \in U} H(\mathbf{x}^*(t), \mathbf{u}(t), \boldsymbol{\lambda}(t), t) \quad (4.9)$$

If $\frac{\partial H}{\partial \mathbf{u}}$ and $\frac{\partial^2 H}{\partial \mathbf{u}^2}$ exist, the extremum condition can be given as:

$$\frac{\partial H}{\partial \mathbf{u}} = 0 \quad (4.10)$$

and

$$\frac{\partial^2 H}{\partial \mathbf{u}^2} \geq 0 \quad (4.11)$$

3. Boundary constraints

$$\boldsymbol{\zeta}(\mathbf{x}^*(t_0^*), t_0^*) = 0 \quad (4.12)$$

$$\boldsymbol{\xi}(\mathbf{x}^*(t_f^*), t_f^*) = 0 \quad (4.13)$$

where t_0^* and t_f^* are the optimal initial time and the optimal terminal time, respectively.

4. Transversality conditions

$$\boldsymbol{\lambda}(t_0^*) = \frac{\partial \boldsymbol{\xi}^T}{\partial \mathbf{x}(t_0)}(\mathbf{x}^*(t_0^*), t_0^*) \boldsymbol{\gamma} \quad (4.14)$$

$$\boldsymbol{\lambda}(t_f^*) = \frac{\partial \Phi}{\partial \mathbf{x}(t_f)}(\mathbf{x}^*(t_f^*), t_f^*) + \frac{\partial \boldsymbol{\xi}^T}{\partial \mathbf{x}(t_f)}(\mathbf{x}^*(t_f^*), t_f^*) \boldsymbol{\nu} \quad (4.15)$$

$$H(\mathbf{x}^*(t_0^*), \mathbf{u}^*(t_0^*), \boldsymbol{\lambda}(t_0^*), t_0^*) + \boldsymbol{\gamma}^T \frac{\partial \boldsymbol{\xi}}{\partial t_0}(\mathbf{x}^*(t_0^*), t_0^*) = 0 \quad (4.16)$$

$$H(\mathbf{x}^*(t_f^*), \mathbf{u}^*(t_f^*), \boldsymbol{\lambda}(t_f^*), t_f^*) + \frac{\partial \Phi}{\partial t_f}(\mathbf{x}^*(t_f^*), t_f^*) + \boldsymbol{\nu}^T \frac{\partial \boldsymbol{\xi}}{\partial t_f}(\mathbf{x}^*(t_f^*), t_f^*) = 0 \quad (4.17)$$

where $\boldsymbol{\gamma} = (\gamma_1, \gamma_2, \dots, \gamma_s)^T$ is an undetermined s -dimensional multiplier vector, $\boldsymbol{\nu} = (\nu_1, \nu_2, \dots, \nu_r)^T$ is an undetermined r -dimensional multiplier vector.

4.1.4 Final Value Performance Index of Time-Invariant Systems

The time-invariant optimal control problem with free final state and final-value performance index can be described as follows.

State equation:

$$\dot{\mathbf{x}}(t) = f(\mathbf{x}(t), \mathbf{u}(t)) \quad (4.18)$$

Performance index:

$$J(\mathbf{u}(t)) = \Phi(\mathbf{x}(t_f)) \quad (4.19)$$

Hamiltonian function:

$$H(\mathbf{x}(t), \mathbf{u}(t), \boldsymbol{\lambda}(t)) = \boldsymbol{\lambda}^T(t) f(\mathbf{x}(t), \mathbf{u}(t)) \quad (4.20)$$

The regular equations, extremum conditions and boundary constraints are consistent with the general form.

Transversality conditions:

$$\boldsymbol{\lambda}(t_f) = \frac{\partial \Phi(\mathbf{x}^*(t_f^*))}{\partial \mathbf{x}(t_f)} \quad (4.21)$$

$$H(\mathbf{x}^*(t), \mathbf{u}^*(t), \boldsymbol{\lambda}(t)) = H(\mathbf{x}^*(t_f^*), \mathbf{u}^*(t_f^*), \boldsymbol{\lambda}(t_f^*)) = 0 \quad (t_f \text{ is free}) \quad (4.22)$$

$$H(\mathbf{x}^*(t), \mathbf{u}^*(t), \boldsymbol{\lambda}(t)) = H(\mathbf{x}^*(t_f), \mathbf{u}^*(t_f), \boldsymbol{\lambda}(t_f)) = \text{const} \quad (t_f \text{ is fixed}) \quad (4.23)$$

Maximum final speed is a final-value performance index.

4.1.5 Integral Performance Index of Time-Invariant Systems

The time-invariant optimal control problem with integral performance index and free final state can be described as follows.

For time-invariant state Eq. (4.18), the terminal time t_f is unknown. The integral performance index is:

$$J(\mathbf{u}(t)) = \int_{t_0}^{t_f} L(\mathbf{x}(t), \mathbf{u}(t)) dt \quad (4.24)$$

Hamiltonian function:

$$H(\mathbf{x}(t), \mathbf{u}(t), \boldsymbol{\lambda}(t)) = L(\mathbf{x}(t), \mathbf{u}(t)) + \boldsymbol{\lambda}^T(t) f(\mathbf{x}(t), \mathbf{u}(t)) \quad (4.25)$$

The regular equations, extremum conditions and boundary constraints are consistent with the general form.

Transversality conditions:

$$\boldsymbol{\lambda}(t_f) = 0 \quad (4.26)$$

$$H(\mathbf{x}^*(t), \mathbf{u}^*(t), \boldsymbol{\lambda}(t)) = H(\mathbf{x}^*(t_f^*), \mathbf{u}^*(t_f^*), \boldsymbol{\lambda}(t_f^*)) = 0 \quad (t_f \text{ is free}) \quad (4.27)$$

$$H(\mathbf{x}^*(t), \mathbf{u}^*(t), \boldsymbol{\lambda}(t)) = H(\mathbf{x}^*(t_f), \mathbf{u}^*(t_f), \boldsymbol{\lambda}(t_f)) = \text{const} \quad (t_f \text{ is fixed}) \quad (4.28)$$

Maximum range is an integral performance index.

4.1.6 Optimal Control Problem with Inequality Constraints

All the problems introduced above are optimal control problems without constraints. In this section, optimal control problems with inequality constraints are considered.

The inequality constraints are:

$$C(\mathbf{x}(t), \mathbf{u}(t), t) \leq 0 \quad (4.29)$$

The augmented Hamiltonian function is:

$$\bar{H} = L + \lambda^T F + \mu C \quad (4.30)$$

where $\mu > 0$, if $C = 0$, and $\mu = 0$, if $C < 0$.

The conjugate equation can be expressed as

$$\dot{\lambda} = -\frac{\partial \bar{H}}{\partial x} \quad (4.31)$$

The necessary condition for the optimal control is

$$\bar{H}(\mathbf{x}^*(t), \mathbf{u}^*(t), \lambda(t), t) = \min_{\mathbf{u}(t) \in U} \bar{H}(\mathbf{x}^*(t), \mathbf{u}(t), \lambda(t), t) \quad (4.32)$$

If $\frac{\partial \bar{H}}{\partial u}$ exists, the extremum condition is

$$\frac{\partial \bar{H}}{\partial u} = 0 \quad (4.33)$$

4.1.7 Methods for Solving Optimal Control Problems

Optimal control problem can be solved by transforming it into a two-point boundary value problem. Given the initial conditions, terminal conditions, transversal conditions and constraints of the optimal control problem, we only need to find the appropriate initial values of the adjoint variables to satisfy the above conditions, then the problem can be solved.

The methods for solving two-point boundary value problems consist of gradient method, boundary value shooting method, adjacent extremum method, genetic algorithm and so on. Both the boundary value shooting method and the adjacent extremum method iteratively change the initial value to satisfy the specified terminal conditions.

4.1.7.1 Boundary Value Shooting Method

Since $\dot{\lambda} = -\partial H / \partial x$ is a linear system for the variable λ , the value of the control variable and the solution of the equation of state will not be affected if λ_0 is increased by the same multiple. Arbitrary values can be taken as λ_{i0} , and remaining λ_i can be estimated according to experience. Given a t_f , we can find an optimal trajectory that meets the requirements through iterations, satisfying $H(t_f) = 0$ and initial constraints. Boundary value shooting method obtains different trajectories by changing the value of λ_0 through several iterations, then finding the optimal trajectory satisfying constraints and $H = 0$ from the obtained trajectories.

4.1.7.2 Adjacent Extremum Method and Improved Adjacent Extremum Method

The adjacent extremum method can obtain the optimal trajectory satisfying the terminal constraints from the optimal trajectory cluster. Since $H(t) = 0$, we have

$$H(t_0) = L_0 + \sum_{i=1}^n \lambda_i f_i = 0 \quad (4.34)$$

Assuming one λ_{i0} , another λ_{j0} can be determined by formula (4.34), and the rest of $n - 2$ λ_{i0} need to be estimated. Because $H(t) = 0$ and the necessary conditions are satisfied, the obtained trajectories are all optimal trajectories. The optimal trajectory satisfying terminal constraints can be found from the optimal trajectory cluster by iterations.

The proximal extremum method ascertains an optimal trajectory satisfying terminal constraints from the optimal trajectory cluster, hence t_f is not fixed and determined by the trajectory satisfying terminal constraints. The numerical integration simulation of the improved adjacent extremum method does not apply $t = t_f$ as the stopping condition, but stops when the terminal conditions are satisfied. Consequently, the problem of t_f selection is solved.

For the initial value of n -dimensional conjugate vector of the improved adjacent extremum method, one can be selected by using the linear property of conjugate equation, and one can be calculated by using $H(t_0) = 0$, then only $n - 2$ components need to be estimated. t_f can be determined by terminal constraints. Then the difficulty of estimating the initial value will be greatly reduced.

The steps of the adjacent extremum method are as follows.

1. Use the linear property of conjugate equation to choose λ_0 , assuming as λ_{10} , then choose $\lambda_{i0}(3 \leq i \leq n)$ by experience;
2. One λ_0 is calculated by $H(t_0) = 0$, assuming as λ_{20} .
3. Determine “transfer matrix” and $\lambda_{i0}(3 \leq i \leq n)$.

According to the given $\lambda_{i0}(1 \leq i \leq n)$, the state equations and adjoint equations are integrated until the terminal conditions are satisfied. It should be noted that $\mathbf{x}(t_f) \neq \mathbf{x}_f$.

$$x_i(t_f) = f_i \quad (4.35)$$

then

$$\Delta \mathbf{x}_f = \left[\frac{\partial f}{\partial \lambda} \right] \Delta \lambda_0 = \mathbf{B} \Delta \lambda_0 \quad (4.36)$$

where \mathbf{B} is a partial differential matrix, also known as a transfer matrix.

$$\Delta \lambda_0 = \mathbf{B}^{-1} \Delta \mathbf{x}_f = \mathbf{B}^{-1} (\mathbf{x}_f - \mathbf{x}(t_f)) \quad (4.37)$$

Then λ_f can be solved iteratively. The iterative formula is as follows

$$\lambda_0^{(k+1)} = \lambda_0^k + \Delta \lambda_0 \cdot \varepsilon \quad (4.38)$$

ε should be small enough and can be obtained by optimization.

4.1.7.3 Nonlinear Programming Method

The two-point boundary value problem can be transferred into a non-linear programming problem by taking the error values of boundary conditions and transversality conditions as objective functions, the initial values of adjoint variables λ_0 as optimization variables and remaining the constraints unchanged. A more appropriate initial value of λ_0 is required. If the objective function is not close to 0, the initial value of λ_0 should be re-selected until the objective function is close to or equal to 0. Then the appropriate λ_0 can be acquired, while the optimal control and optimal state can be obtained. The difficulty of this method is that the initial value λ_0 is difficult to predetermined. When the initial value λ_0 deviates greatly, the solution may not be found.

4.1.7.4 Genetic Algorithm

Genetic algorithm is a global search algorithm, which does not require accuracy initial value and only needs to know the approximate range of the initial value.

Nonlinear programming methods are easy to produce local optimal solutions. In addition, the optimization may not be carried out because of the unreasonable initial value selection of optimization variables. Since λ_0 has no physical meaning, it is difficult to estimate accurately, and a rough range can only be obtained by sensitivity analysis. Genetic algorithm is a global optimization algorithm, which only needs to know the approximate interval of λ_0 . Thus the difficulty of estimating initial value λ_0 and solving two-point boundary value problem is reduced. The constraints in the non-linear programming method are solved by penalty function in genetic algorithm. It is proved that this method is very effective in solving the optimal trajectory.

4.2 Mathematical Description of Optimal Control Problem for Hypersonic Vehicle Entry Glide

The trajectory optimization problems for hypersonic vehicle mainly consists of maximum range problem, maximum final velocity problem and shortest flight time problem. Hamilton function is usually constructed to solve these problems. The initial value λ_0 of the costate variable can be obtained by solving the two-point boundary value problem, thus the optimal control and the optimal trajectory can be obtained. Angle of attack is often used as the control variable when solving the optimal trajectory of a hypersonic vehicle in the plumb plane.

4.2.1 Maximum Final Speed Problem

The performance index for the maximum terminal velocity problem is

$$J = M_f \quad (4.39)$$

According to the dynamic equations of a hypersonic vehicle in the vertical plane (3.27)–(3.29), the Hamiltonian function can be written as

$$H = \lambda_M \frac{dM}{dt} + \lambda_h \frac{dh}{dt} + \lambda_\gamma \frac{d\gamma}{dt} \quad (4.40)$$

The costate equations are

$$\frac{d\lambda_h}{dt} = -\frac{\partial H}{\partial h}; \frac{d\lambda_M}{dt} = -\frac{\partial H}{\partial M}; \frac{d\lambda_\gamma}{dt} = -\frac{\partial H}{\partial \gamma} \quad (4.41)$$

The expression of optimal control law can be obtained from state Eqs. (3.27)–(3.29), costate Eqs. (4.41) and the following equation.

$$\frac{\partial H}{\partial \alpha} = 0 \quad (4.42)$$

According to the initial conditions $h(t_0) = h_{t0}$, $M(t_0) = M_{t0}$, $\gamma(t_0) = \gamma_{t0}$, boundary conditions $h(t_f) = h_{tf}$, $\gamma(t_f) = \gamma_{tf}$, and transversal condition $H \equiv 0$, the initial costate state variables λ_{M0} , λ_{h0} , $\lambda_{\gamma0}$ can be obtained by solving the two-point boundary value problem. Then, the maximum terminal velocity trajectory and the corresponding optimal angle of attack control law can be solved.

4.2.2 Maximum Range Problem

The performance index for the maximum range problem is

$$J = r_f = \int_{t_0}^{t_f} \frac{dr}{dt} dt \quad (4.43)$$

According to the dynamic equations of a hypersonic vehicle in the vertical plane (3.27)–(3.29), The Hamiltonian function is

$$H = \frac{dr}{dt} + \lambda_M \frac{dM}{dt} + \lambda_h \frac{dh}{dt} + \lambda_\gamma \frac{d\gamma}{dt} \quad (4.44)$$

The costate equations are

$$\frac{d\lambda_h}{dt} = -\frac{\partial H}{\partial h}; \frac{d\lambda_M}{dt} = -\frac{\partial H}{\partial M}; \frac{d\lambda_\gamma}{dt} = -\frac{\partial H}{\partial \gamma} \quad (4.45)$$

The expression of optimal control law can be obtained from state Eqs. (3.27)–(3.29), costate Eq. (4.45) and the following equation.

$$\frac{\partial H}{\partial \alpha} = 0 \quad (4.46)$$

Then, according to the initial conditions $h(t_0) = h_{g0}$, $M(t_0) = M_{g0}$, $\gamma(t_0) = \gamma_{g0}$, boundary conditions $h(t_f) = h_{gf}$, $M(t_f) = M_{gf}$, and transversal condition $\lambda_{\gamma f} = 0$, $H \equiv 0$, the two-point boundary value problem can be solved, obtaining the initial costate state variables λ_{M0} , λ_{h0} , $\lambda_{\gamma0}$, as well as the maximum range trajectory and the corresponding optimal angle of attack control law.

4.2.3 Shortest Time Problem

The performance index for the shortest time problem is

$$J = t_f - t_0 = \int_{t_0}^{t_f} 1 dt \quad (4.47)$$

According to the dynamic equations of hypersonic vehicle in the vertical plane (3.27)–(3.30), we have

$$H = 1 + \lambda_M \frac{dM}{dt} + \lambda_h \frac{dh}{dt} + \lambda_\gamma \frac{d\gamma}{dt} \quad (4.48)$$

The costate equations are

$$\frac{d\lambda_h}{dt} = -\frac{\partial H}{\partial h}; \frac{d\lambda_M}{dt} = -\frac{\partial H}{\partial M}; \frac{d\lambda_\gamma}{dt} = -\frac{\partial H}{\partial \gamma} \quad (4.49)$$

The expression of optimal control law can be obtained from state Eqs. (3.27)–(3.29), costate Eq. (4.49) and the following equation.

$$\frac{\partial H}{\partial \alpha} = 0 \quad (4.50)$$

Then, according to the initial conditions $h(t_0) = h_{d0}$, $M(t_0) = M_{d0}$, $\gamma(t_0) = \gamma_{d0}$, boundary conditions $h(t_f) = h_{df}$, $M(t_f) = M_{df}$, $\gamma_f \leq \gamma_{df}$ and transversal condition $H \equiv 0$, we can get the initial costate state variables λ_{M0} , λ_{h0} , $\lambda_{\gamma0}$, so as to obtain the shortest time trajectory and the corresponding optimal angle of attack control law.

4.2.4 Optimal Trajectory Problem with Heating Rate Constraint

In the trajectory optimization of hypersonic vehicle, the heating rate constraint should be considered in the transition and glide phases. The integral penalty function with switching functions is applied to solve the problem.

Heating rate constraint: $c(M, h) = \dot{Q} - \dot{Q}_{\max} \leq 0$

New objective function: $\bar{J} = J + \mu \int_{t_0}^{t_f} [c(M, h)]^2 1(c) dt$, where $1(c) = \begin{cases} 0 & c < 0 \\ 1 & c > 0 \end{cases}$

Then we have $\bar{H} = H + \mu [c(M, h)]^2 1(c)$

$$\frac{d\lambda_h^T}{dt} = -\frac{\partial \bar{H}}{\partial h}; \frac{d\lambda_M^T}{dt} = -\frac{\partial \bar{H}}{\partial M}; \frac{d\lambda_\gamma^T}{dt} = -\frac{\partial \bar{H}}{\partial \gamma} \quad (4.51)$$

The control law of α is obtained by solving $\frac{\partial \bar{H}}{\partial \alpha} = \frac{\partial H}{\partial \alpha} = 0$.

Combination optimization strategy is used to solve the two-point boundary value problem. Then a set of suitable λ_{h0} , λ_{M0} , $\lambda_{\gamma0}$ can be found, and the optimal control problem can be solved.

4.2.5 Optimal Trajectory Problem with Heating Rate and Load Factor Constraints

In the trajectory optimization of hypersonic vehicle, the heating rate and load factor constraints should be considered in the dive phases. The integral penalty function with switching function is used to solve the problem.

Heating rate constraint: $c(M, h) = \dot{Q} - \dot{Q}_{\max} \leq 0$

Load factor constraints: $d(M, h) = n - n_{\max} \leq 0$

New objective function: $\bar{J} = J + \mu \int_{t_0}^{t_f} [c(M, h)]^2 1(c) dt + \eta \int_{t_0}^{t_f} [d(M, h)]^2 1(d) dt$, where $1(c) = \begin{cases} 0 & c < 0 \\ 1 & c > 0 \end{cases}$, $1(d) = \begin{cases} 0 & d < 0 \\ 1 & d > 0 \end{cases}$.

Then we have $\bar{H} = H + \mu[c(M, h)]^2 1(c) + \eta[d(M, h)]^2 1(d)$

$$\frac{d\lambda_h^T}{dt} = -\frac{\partial \bar{H}}{\partial h}; \frac{d\lambda_M^T}{dt} = -\frac{\partial \bar{H}}{\partial M}; \frac{d\lambda_\gamma^T}{dt} = -\frac{\partial \bar{H}}{\partial \gamma} \quad (4.52)$$

$$\frac{\partial \bar{H}}{\partial \alpha} = \frac{\partial H}{\partial \alpha} = 0 \quad (4.53)$$

Combination optimization strategy is used to solve the two-point boundary value problem. Thus a set of appropriate λ_{h0} , λ_{M0} , $\lambda_{\gamma0}$ can be found to solve this optimal control problem.

Chapter 5

Indirect Approach to the Optimal Glide Trajectory Problem



Gliding problem of hypersonic aircrafts is a high-sensitivity two-point boundary value problem, it is difficult to solve with a single method. The initial value of the common state variable has no actual meaning, which is difficult to predict. Therefore, an optimization algorithm is proposed to solve two-point boundary value problem in this chapter, combining genetic algorithm, local optimization algorithm and neighboring extremum method. The key to solve optimal ballistic problem is to solve the two-point boundary value problem, that is, to find the initial value of a suitable set of common state variables to satisfy the terminal constraints. The initial value of the common state variable is very sensitive to results, and it is not necessarily continuous. Therefore, traditional search algorithms can only find local optimal solution, and are related to the selection of initial value. Solving the problem directly with a gradient algorithm sometimes gives no solution. Therefore, the selection of initial value of general optimization algorithm is a difficult problem. Genetic algorithm is an adaptive global optimization probability search algorithm, which simulates the genetic and evolutionary processes of living things in natural environment. It only needs to estimate the range of optimization variables, and it seeks global approximate optimal solution. However, genetic algorithm is computationally intensive, and often simply converge to a rough global optimal solution. Therefore, based on genetic algorithm, the global optimal solution is further obtained by algorithms with strong local search ability. That is to say, the global approximate optimal solution is obtained by genetic algorithm, and then the optimal solution is further obtained by other algorithms with strong local search ability. Then based on strict constraints, the neighboring extremum method is used to solve two-point boundary value problem, and the optimal solution satisfying all constraints is obtained. Feasibility of this method has been proved in practice.

Optimization problem can be generally described as following mathematical programming model.

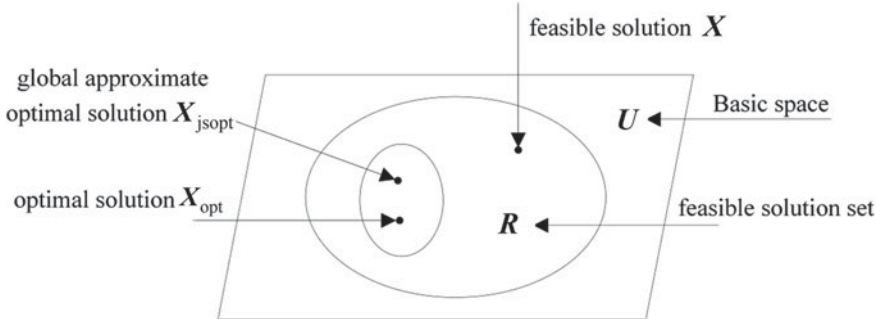


Fig. 5.1 Combination algorithm diagram

$$\begin{cases} \max f(X) \\ s.t. X \in R \\ R \subseteq U \end{cases} \quad (5.1)$$

where $X = [x_1, x_2, \dots, x_n]^T$, $f(X)$ is objective function, U is basic space, R is a subset of U . The solution X satisfying constraint is called a feasible solution, and the set R , which is called feasible solution set, represents a set consisting of all solutions satisfying constraint. Their relationship is shown in Fig. 5.1. Using genetic algorithm, one global approximate optimal solution $X_{j\text{sopt}}$ can be found in feasible solution set. Then $X_{j\text{sopt}}$ is adopted as the initial value and it is further optimized with local optimization algorithm (such as quadratic sequence programming algorithm) to obtain the optimal solution X_{opt} , and then, neighboring extremum method is adopted to find a solution that satisfies all constraints near the optimal solution.

The steps to solve the two-point boundary value problems are

Step 1: Select an λ_0 using linear properties of conjugate equation.

Step 2: Calculate λ_0 with $H(t_0) = 0$.

Step 3: Estimate the remaining $n - 2$ λ_0 , use sensitivity analysis to estimate approximate interval, and use genetic algorithm to find the optimal trajectory that satisfies constraints and terminal boundary conditions in estimated interval.

Step 4: The local optimization algorithm is used to further optimize the initial value λ_0 obtained by genetic algorithm.

Step 5: Strictly satisfy all terminal boundary conditions and constraints with improved neighboring extremum method.

5.1 Combined Optimization Strategy for Solving the Optimal Gliding Trajectory of Hypersonic Aircraft

5.1.1 Mathematical Model of Hypersonic Gliding

The gliding defined in Sect. 5.1 is a type of flight in which the aircraft starts at zero flight path angle with a certain Mach number when the engine is turned off, as is shown in Fig. 5.2.

The problem is described as follows: given initial parameter and terminal parameter, initial gliding height h_0 , initial gliding Mach number Ma_0 , initial flight path angle γ_0 , terminal height h_f , terminal Mach number Ma_f , terminal track angle γ_f , find a control (angle of attack α) history that maximizes the range of the gliding. Since the mass doesn't change during gliding, the engine model is not considered. The mathematical models include density model, dynamic model, and aerodynamic model.

Density model uses a simplified density model, ρ is the air density, h is the height.

$$\rho = 1.225e^{-0.15h} \quad (5.2)$$

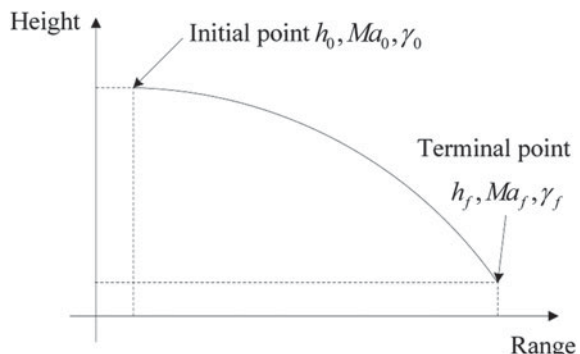
Dynamics model: The dynamic equation of the aircraft without considering the Earth's rotation in the vertical plane is given as follows

$$\frac{dh}{dt} = Ma c \sin \gamma \quad (5.3)$$

$$\frac{dMa}{dt} = \frac{-D - mg \sin \gamma}{cm} \quad (5.4)$$

$$\frac{d\gamma}{dt} = \frac{L - mg \cos \gamma}{Ma cm} + \frac{Ma c \cos \gamma}{R_0 + h} \quad (5.5)$$

Fig. 5.2 Gliding schematic



$$\frac{dr}{dt} = \frac{R_0 Ma c \cos \gamma}{R_0 + h} \quad (5.6)$$

Aerodynamic model: The formula for calculating drag D and lift L is as follows. Where q is the dynamic pressure, C_D is the drag coefficient, C_L is the lift coefficient, and A_w is the reference area.

$$D = q C_D A_w \quad (5.7)$$

$$L = q C_L A_w \quad (5.8)$$

$$C_D = C_{D0} + K C_L^2 \quad (5.9)$$

$$C_L = C_{L0} + C_{L\alpha} \alpha \quad (5.10)$$

where, the dynamic pressure $q = 0.5 \rho (Ma c)^2$, the aerodynamic coefficient C_{D0} , K , C_{L0} , $C_{L\alpha}$ are available in the Sect. 5.1. The optimized objective function is a functional of the range $R = \int_{t_0}^{t_f} \frac{R_0 Ma c \cos \gamma}{R_0 + h} dt$, $t_0 = 0$, t_f is to be determined. Ma , γ and h can be represented by α . Therefore, the functional R can be expressed as a function of the angle of attack α and time t , and the optimal angle of attack α can be solved to maximize the range R .

5.1.2 Necessary Conditions for Optimal Gliding Trajectory

This problem is an optimal control problem, and its Hamiltonian function is shown in Eq. (5.11).

$$H = \frac{dr}{dt} + \lambda_h \frac{dh}{dt} + \lambda_{Ma} \frac{dM}{dt} + \lambda_\gamma \frac{d\gamma}{dt} \quad (5.11)$$

where λ_h , λ_{Ma} , and λ_γ are adjoint variable.

The adjoint differential equations

$$\frac{d\lambda_h}{dt} = -\frac{\partial H}{\partial h}, \frac{d\lambda_{Ma}}{dt} = -\frac{\partial H}{\partial Ma}, \frac{d\lambda_\gamma}{dt} = -\frac{\partial H}{\partial \gamma} \quad (5.12)$$

It can be obtained from Eq. (5.6)

$$H_\alpha = -\lambda_{Ma} \frac{1}{cm} 2 K C_L C_{L\alpha} q A_w + \lambda_\gamma \frac{1}{Ma cm} C_{L\alpha} q A_w \quad (5.13)$$

Let $H_\alpha = 0$, we can get the optimal control α

$$\alpha = \frac{\lambda_\gamma}{2\lambda_{Ma} Ma KC_{L\alpha}} - \frac{C_{L0}}{C_{L\alpha}} \quad (5.14)$$

The boundary conditions are $h(t_0) = h_0$, $Ma(t_0) = Ma_0$, $\gamma(t_0) = 0$, $h(t_f) = h_f$, $Ma(t_f) = Ma_f$, $\lambda_r(t_f) = 0$. The transversality condition $H \equiv 0$.

Solving this problem of optimal control is equivalent to finding the maximum range trajectory under the above boundary conditions.

5.1.3 Solving Two-Point Boundary Value Problem by Combination Optimization Strategy

The key to solving the optimal ballistic problem is to solve the two-point boundary value problem, that is, to find the initial value of a suitable set of common state variables to satisfy the terminal constraints. For this problem, the value of the co-state variable at the initial moment is mainly explored, and the flight range of the aircraft is the farthest under certain initial conditions. In Sects. 5.1 and 5.2, the sub-optimal trajectory is used to obtain the initial value of the optimal trajectory. The method used in the literature has strict requirements on the initial value. However, the genetic algorithm does not require strict initial values, and it is sufficient to know the approximate range. However, in this case, the lift-to-drag ratio is used to estimate the range of the initial value, and then the genetic algorithm is used to find the value of the co-state variable at the initial moment of the approximate optimal trajectory. Based on this, other local optimization algorithms are used to further obtain the value of the co-state variable at the initial moment of the optimal range. The steps to solve the optimal sliding trajectory are summarized as follows:

Step 1: The optimized parameters are λ_{h0} , λ_{M0} and $\lambda_{\gamma0}$, which can be obtained by the value of the cross-section condition at time t_0 .

$$\lambda_{\gamma0} = - \left(\frac{dr}{dt} \Big|_{t_0} + \lambda_{h0} \frac{dh}{dt} \Big|_{t_0} + \lambda_{Ma0} \frac{dMa}{dt} \Big|_{t_0} \right) \Bigg/ \left(\frac{d\gamma}{dt} \Big|_{t_0} \right) \quad (5.15)$$

where $\frac{dr}{dt} \Big|_{t_0}$, $\frac{dh}{dt} \Big|_{t_0}$, $\frac{dMa}{dt} \Big|_{t_0}$ and $\frac{d\gamma}{dt} \Big|_{t_0}$ are chosen to be the value when the lift-to-drag ratio is maximum.

Step 2: From the trajectory of the maximum lift-to-drag ratio, $\lambda_n(t_0)$ is estimated by Eq. (5.16), and $\lambda_n(t_0)/\lambda_{1/a}(t_0)$ is estimated by comparing the initial angle of attack derived from the trajectory of the maximum lift-to-drag ratio to Eqs. (5.14) and (5.15), then we can get $\lambda_{Ma}(t_0)$. It provides an initial estimate in the next step for selecting the optimal range of the genetic algorithm optimization.

$$\lambda_h(t_0) = \frac{\partial r_f}{\partial h(t_0)} \quad (5.16)$$

Step 3: The range R can be obtained from integrating the system dynamic equation from the initial value $\lambda_n(t_0)$, $\lambda_{Ma}(t_0)$, $\lambda_\gamma(t_0)$. Optimize $\lambda_n(t_0)$ and $\lambda_{Ma}(t_0)$ with genetic algorithm in circles with $\lambda_h(t_0)$ and $\lambda_{Ma}(t_0)$ as the centers and $|\lambda_h(t_0)|$ and $|\lambda_{Ma}(t_0)|$ as the radius. After obtaining a new set of $\lambda_h(t_0)$, λ_{Ma0} , we Optimize $\lambda_n(t_0)$ and $\lambda_{Ma}(t_0)$ with genetic algorithm again. After narrowing the genetic algorithm range several times to obtain a more accurate global approximate optimal solution, a more accurate initial value for the optimization of the local optimization algorithm is acquired. Then the values of $\lambda_h(t_0)$ and λ_{Ma0} obtained by genetic algorithm with no constraints are taken as the initial values of the nonlinear simplex method. Then the maximum range is optimized

Step 4: Solving two-point boundary value problem using the neighboring extremum method with initial value obtained from Step 3. $\lambda_r(t_f) = 0$ is used as the termination condition. $\Delta\lambda_{h0}$ and $\Delta\lambda_{Ma0}$ is obtained by the transfer matrix of Eq. (5.18). Then the simplex optimization algorithm is used to find the appropriate step size ε . Then after multiple iterations of Eq. (5.19), λ_{h0} and λ_{Ma0} is obtained satisfying the boundary conditions.

Since

$$\begin{bmatrix} \Delta h_f \\ \Delta Ma_f \end{bmatrix} = \begin{bmatrix} \frac{\partial h}{\partial \lambda_{h0}} & \frac{\partial h}{\partial \lambda_{Ma0}} \\ \frac{\partial Ma_f}{\partial \lambda_{h0}} & \frac{\partial Ma_f}{\partial \lambda_{Ma0}} \end{bmatrix} \begin{bmatrix} \Delta \lambda_{h0} \\ \Delta \lambda_{Ma0} \end{bmatrix} = B \begin{bmatrix} \Delta \lambda_{h0} \\ \Delta \lambda_{Ma0} \end{bmatrix} \quad (5.17)$$

We have

$$\begin{bmatrix} \Delta \lambda_{h0} \\ \Delta \lambda_{Ma0} \end{bmatrix} = B^{-1} \begin{bmatrix} \Delta h_f \\ \Delta Ma_f \end{bmatrix} \quad (5.18)$$

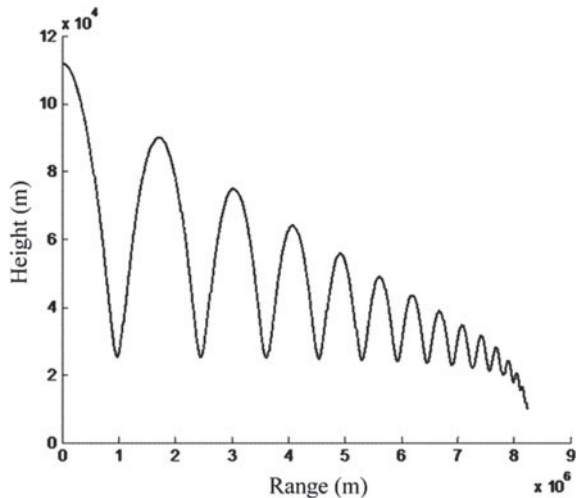
$$\begin{cases} \lambda_{h0}^{(k+1)} = \lambda_{h0}^k + \Delta \lambda_{h0} \varepsilon \\ \lambda_{Ma0}^{(k+1)} = \lambda_{Ma0}^k + \Delta \lambda_{Ma0} \varepsilon \end{cases} \quad (5.19)$$

5.1.4 Numerical Calculation Results

The initial gliding height $h_0 = 111.9838$ km, initial gliding Mach number $Ma_0 = 15.1896$, initial flight path angle $\gamma_0 = 0$. The terminal condition is $h_f = 10.0$ km where h_f is the terminal height. The result of simulation to the maximum lift-to-drag ratio flight is: the terminal Mach number $Ma_f = 1.2$ the range $r_f = 8226$ km, the trajectory is shown in Fig. 5.3.

Calculating by the method based on optimal control with terminal condition of $h_f = 10.0$ km, $Ma_f = 1.2$ and $\lambda_{\gamma f} = 0$, the result is $r_f = 8334$ km, $\lambda_{\gamma f} = 0$,

Fig. 5.3 Trajectory of maximum lift-to-drag ratio



$M_{af} = 1.207$, $h_f = 9.97$ km, the initial value of the common state variables are $\lambda_{h0} = -6.5131$ and $\lambda_{Ma0} = -1.3376e6$. The trajectory is shown in Fig. 5.4, the figure of angle of attack over range is shown in Fig. 5.5. The terminal conditions are satisfied, and the range is 1.3% farther than that of the maximum flight. The optimization calculation begins with the genetic algorithm, then the nonlinear simplex method is applied, finally the nearest extremum method is adopted to solve the problem.

Sensitivity analysis are performed for λ_{h0} and λ_{Ma0} . If λ_{h0} changes by 1%, let $\lambda_{h,0} = -6.4479$, λ_{Ma0} remains unchanged, then the range $r = 7750$ km, r_f is shortened by 7%, $h_f = 3.67$ km, the error is 63.3%, $M_{af} = 3.91$, the error is 225.8%; If λ_{Ma0} changes by 1%, let $\lambda_{Ma0} = -1.3242e6$, λ_{h0} remains unchanged, then the range

Fig. 5.4 Trajectory of maximum range

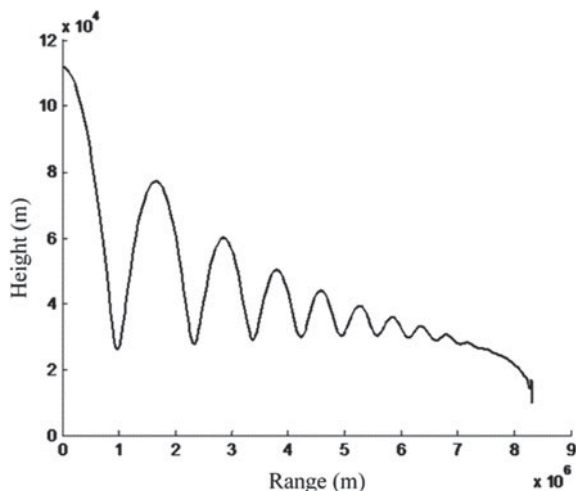
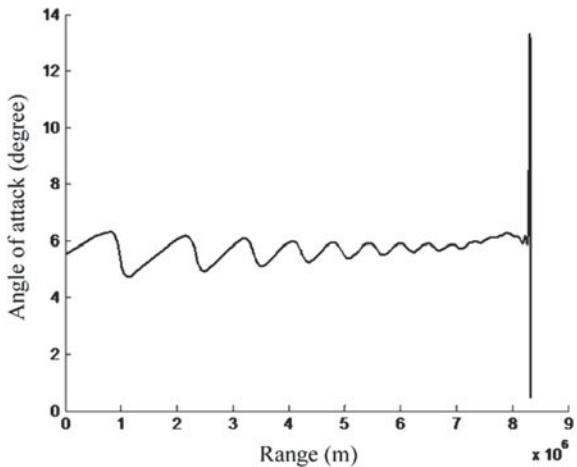


Fig. 5.5 Angle of attack over range



$r = 7696$ km, r_f is shortened by 7.66%, $h_f = 6.2$ km, the error is 38%, $Maf = 2.6$, the error is 116.7%. It can be seen that the results are very sensitive to the initial values λ_{h0} and λ_{Ma0} . The convergence curve of the last relative inter-cell genetic algorithm is shown in Fig. 5.6. After 200 generations, it basically tends to a stable value. The simplex method convergence curve is shown in Fig. 5.7. The convergence curve of the neighboring extremum method is shown in Fig. 5.8. The longitudinal coordinate of this convergence curve is the comprehensive error value of each constraint at the final time. It is difficult to find the optimal solution directly by using the gradient algorithm or the direct optimization algorithm. The local maximum value is obtained instead of the global maximum value. Therefore, the genetic algorithm is used to optimize a good initial value, and then the simplex method and the neighboring extremum method are used, by which a better result can be obtained.

From the results above, it can be seen that the trajectories obtained by the optimal control method is better than the flight trajectory of the maximum lift-to-drag ratio.

Fig. 5.6 Genetic algorithm convergence curve

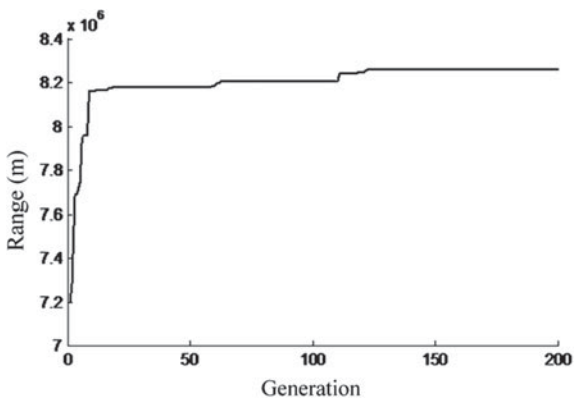


Fig. 5.7 Simplex convergence curve

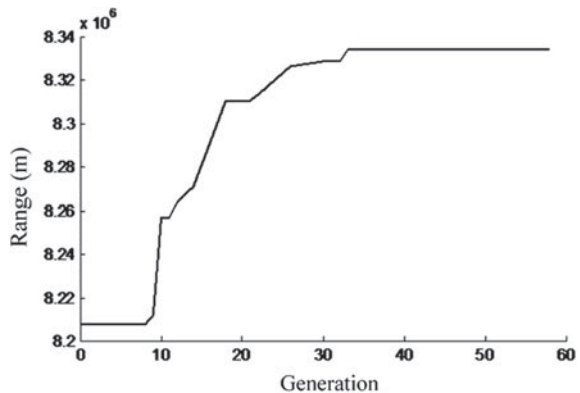
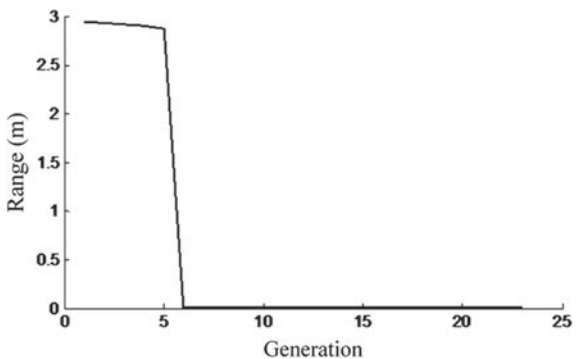


Fig. 5.8 Neighboring extremum convergence curve



However, when the optimal control method is used to solve the ballistic problem, the initial value of the common state variable has a great influence on the result, that is, the sensitivity of the result to the initial value of the accompanying variable is very large. Combination optimization method which is consisted of multiple variable interval genetic algorithm, nonlinear simplex method and neighboring extremum method is a better solution for this kind of problem, and the global optimal solution can be obtained.

5.1.5 Conclusion

In this section the optimal control theory and the method for solving the optimal control is studied. According to the optimal control theory, a mathematical model is established for solving optimal angle of attack of maximum terminal velocity trajectory, maximum gliding range trajectory and minimum compression time trajectory of hypersonic vehicle, and the optimal angle of attack control is solved considering the heat flow constraint and the overload constraint. A combined optimization strategy

using genetic algorithm, local optimization algorithm and adjacent extremum method is proposed to solve the two-point boundary value problem of high sensitivity. And this combination optimization strategy is used to solve the maximum trajectory of the hypersonic aircraft taxiing range. The resulting range is 1.3% higher than the lift of the maximum flight. The example shows that the combination algorithm of genetic algorithm, simplex optimization algorithm and neighboring extremum method is an effective approach to solve the two-point boundary value problem of high sensitivity.

5.2 Trajectory Optimization of Transition Section of Gliding Hypersonic Flight Vehicle

The task of the transition section is to let flight vehicle to make a transition from the end of boost segment to the starting point of gliding segment. The problem is described as follows: set initial parameters and end parameters firstly, such as initial glide height h_0 , initial glide Mach number M_0 , initial flight path angle γ_0 , terminal flight path angle $\gamma_f = 0$, and then find a control (angle of attack) law that can maximize the terminal Mach number, and satisfy the constraint on heat flow $\dot{Q} < \dot{Q}_{\max}$. In this simulation, we use $\gamma_f = 0$ as the stop criterion. In this segment, C_D and C_L is a function of angle of attack α and the height h , the aerodynamic formulas are fitted from the given aerodynamic data, an indirect method is adopted to solve the optimal transition trajectory.

5.2.1 Aerodynamic Data for the Transition Section

The aerodynamic data of the transition section is fitted to the formula as shown in Eqs. (5.20) and (5.21).

$$C_D = \begin{cases} [h^3, h^2, h, 1] \text{coef_Cd1}'[\alpha^3, \alpha^2, \alpha, 1]^T & 40 \text{ km} \leq h \leq 80 \text{ km} \\ [h^3, h^2, h, 1] \text{coef_Cd2}'[\alpha^3, \alpha^2, \alpha, 1]^T & 80 \text{ km} < h \leq 120 \text{ km} \end{cases} \quad (5.20)$$

$$C_L = \begin{cases} [h^3, h^2, h, 1] \text{coef_Cl1}'[\alpha^3, \alpha^2, \alpha, 1]^T & 40 \text{ km} \leq h \leq 80 \text{ km} \\ [h^3, h^2, h, 1] \text{coef_Cl2}'[\alpha^3, \alpha^2, \alpha, 1]^T & 80 \text{ km} < h \leq 120 \text{ km} \end{cases} \quad (5.21)$$

`coef_Cd1'`, `coef_Cd2'`, `coef_Cl1'`, `coef_Cl2'` are all coefficient matrix of 4×4 .

5.2.2 Unconstrained Trajectory of Maximum Terminal Velocity

This problem can be solved based on optimal control theory, and the objective function is $J = M_f$.

The Hamiltonian function is shown in Eq. (5.22).

$$H = \lambda_M \frac{dM}{dt} + \lambda_h \frac{dh}{dt} + \lambda_\gamma \frac{d\gamma}{dt} \quad (5.22)$$

then we can get the adjoint equation

$$\frac{d\lambda_x^T}{dt} = -\frac{\partial H}{\partial x} \quad (5.23)$$

in detail,

$$\frac{d\lambda_h^T}{dt} = -\frac{\partial H}{\partial h} = \lambda_\gamma \left[\frac{Ma \cos \gamma}{(R_0 + h)^2} - \frac{1}{Ma m} \frac{\partial L}{\partial h} \right] + \lambda_M \frac{1}{am} \frac{\partial D}{\partial h} \quad (5.24)$$

$$\begin{aligned} \frac{d\lambda_M^T}{dt} &= -\frac{\partial H}{\partial M} = -\lambda_h a \sin \gamma + \lambda_M \frac{1}{am} \frac{\partial D}{\partial M} \\ &\quad - \lambda_\gamma \left(\frac{mg \cos \gamma}{M^2 am} + \frac{a \cos \gamma}{R_0 + h} + \frac{1}{am} \left[-\frac{L}{M^2} + \frac{1}{M} \frac{\partial L}{\partial M} \right] \right) \end{aligned} \quad (5.25)$$

$$\frac{d\lambda_\gamma^T}{dt} = -\frac{\partial H}{\partial \gamma} = -\lambda_h Ma \cos \gamma + \lambda_M \frac{g \cos \gamma}{a} - \lambda_\gamma \left(\frac{g \sin \gamma}{Ma} - \frac{Ma \sin \gamma}{R_0 + h} \right) \quad (5.26)$$

where

$$\frac{\partial D}{\partial h} = \frac{1}{2} M^2 a^2 A_\omega \left(\frac{\partial \rho}{\partial h} C_D + \rho \frac{\partial C_D}{\partial h} \right) \quad (5.27)$$

$$\frac{\partial D}{\partial M} = \rho Ma^2 A_\omega C_D \quad (5.28)$$

$$\frac{\partial L}{\partial h} = \frac{1}{2} M^2 a^2 A_\omega \left(\frac{\partial \rho}{\partial h} C_L + \rho \frac{\partial C_L}{\partial h} \right) \quad (5.29)$$

$$\frac{\partial L}{\partial M} = \rho Ma^2 A_\omega C_L \quad (5.30)$$

$$\frac{\partial C_D}{\partial h} = \begin{cases} [3h^2, 2h, 1, 0] \text{coef_Cd1}'[\alpha^3, \alpha^2, \alpha, 1]^T & 40 \text{ km} \leq h \leq 80 \text{ km} \\ [3h^2, 2h, 1, 0] \text{coef_Cd2}'[\alpha^3, \alpha^2, \alpha, 1]^T & 80 \text{ km} < h \leq 120 \text{ km} \end{cases} \quad (5.31)$$

$$\frac{\partial C_L}{\partial h} = \begin{cases} [3h^2, 2h, 1, 0] \text{coef_Cl1}'[\alpha^3, \alpha^2, \alpha, 1]^T & 40 \text{ km} \leq h \leq 80 \text{ km} \\ [3h^2, 2h, 1, 0] \text{coef_Cl2}'[\alpha^3, \alpha^2, \alpha, 1]^T & 80 \text{ km} < h \leq 120 \text{ km} \end{cases} \quad (5.32)$$

where $\frac{\partial \rho}{\partial h}$ is obtained by numerical difference method.

From the equation above

$$\frac{\partial H}{\partial \alpha} = \lambda_M \left(-\frac{1}{am} q A_\omega \frac{\partial C_D}{\partial \alpha} \right) + \lambda_\gamma \left(\frac{1}{Ma m} q A_\omega \frac{\partial C_L}{\partial \alpha} \right) \quad (5.33)$$

and

$$\frac{\partial C_D}{\partial \alpha} = \begin{cases} [h^3, h^2, h, 1] \text{coef_Cd1}'[3\alpha^2, 2\alpha, 1, 0]^T & 40 \text{ km} \leq h \leq 80 \text{ km} \\ [h^3, h^2, h, 1] \text{coef_Cd2}'[3\alpha^2, 2\alpha, 1, 0]^T & 80 \text{ km} < h \leq 120 \text{ km} \end{cases} \quad (5.34)$$

$$\frac{\partial C_L}{\partial \alpha} = \begin{cases} [h^3, h^2, h, 1] \text{coef_Cl1}'[3\alpha^2, 2\alpha, 1, 0]^T & 40 \text{ km} \leq h \leq 80 \text{ km} \\ [h^3, h^2, h, 1] \text{coef_Cl2}'[3\alpha^2, 2\alpha, 1, 0]^T & 80 \text{ km} < h \leq 120 \text{ km} \end{cases} \quad (5.35)$$

From $\frac{\partial H}{\partial \alpha} = 0$ we can get $-\lambda_M \frac{\partial C_D}{\partial \alpha} + \frac{\lambda_\gamma}{M} \frac{\partial C_L}{\partial \alpha} = 0$, from which α can be obtained. The boundary conditions are

$$h(t_0) = h_{g0}$$

$$M(t_0) = M_{g0}$$

$$\gamma(t_0) = \gamma_{g0}$$

$$h(t_f) = h_{gf}$$

$$\gamma(t_f) = \gamma_{gf}.$$

5.2.3 Heat Flow Constrained Trajectory of Maximum Terminal Velocity

This problem is solved by the method of integral penalty function with switching function.

The heat flow constraints are $c(M, h) = \dot{Q} - \dot{Q}_{max} \leq 0$

Then the new objective function is $\bar{J} = J + \mu \int_{t_0}^{t_f} [c(M, h)]^2 l(c), dt$

$$\text{where } l(c) = \begin{cases} 0 & c < 0 \\ 1 & c > 0 \end{cases}$$

Hence $\bar{H} = H + \mu[c(M, h)]^2 l(c)$, the adjoint equations are

$$\frac{d\lambda_h^T}{dt} = -\frac{\partial \bar{H}}{\partial h}, \frac{d\lambda_M^T}{dt} = -\frac{\partial \bar{H}}{\partial M}, \frac{d\lambda_\gamma^T}{dt} = -\frac{\partial \bar{H}}{\partial \gamma} \quad (5.36)$$

the control law of α can be solved from $\frac{\partial \bar{H}}{\partial \alpha} = \frac{\partial H}{\partial \alpha} = 0$.

Using the genetic algorithm to solve the two-point boundary value problem, we can find a suitable set of λ_{h0} , λ_{M0} and $\lambda_{\gamma0}$, then the optimal control problem can be solved.

5.2.4 Solving the Two-Point Boundary Value Problem for the Transition Section

The key to solve the two-point boundary value problem of the transition segment is to find a suitable set of λ_{h0} , λ_{M0} and $\lambda_{\gamma0}$. Using the nature of the conjugate equation we can assume that $\lambda_{h0} = 1$, then it can be concluded from $H(t_0) = 0$ that λ_{M0} can be represented by $\lambda_{\gamma0}$. Thus, the problem can be solved once we find a suitable $\lambda_{\gamma0}$. Firstly, direct parameter optimization method is used to optimize the trajectory, and then the range of the angle of attack is estimated from the trajectory obtained by the parameter optimization method, so that the genetic algorithm can be used in next step.

5.2.5 Optimizing the Transition Trajectory with Direct Method

The maximum allowable angle of attack is chosen to be 30° , the terminal height is greater than 50 km, and zero flight path angle is chosen to be simulation stop condition. Assume that the angle of attack changes with time as shown in Fig. 5.9. The flight time t_f is divided into n segments, the angle of attack α at time t_i is α_i , now we only need to optimize the parameters $\alpha_0, \alpha_1, \dots, \alpha_f$ and the flight time t_f to get the optimal trajectory of the corresponding performance index. Here, we set $n = 8$, the performance index is the terminal Mach number, and the heat flow constraint is considered. The initial height is 94 km, the initial Mach number is 20.46, and the maximum heat flow density is no more than 600 W/cm^2 . As for genetic algorithm,

Fig. 5.9 Angle of attack of the transition section over time

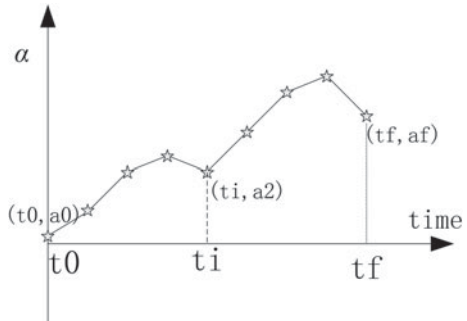
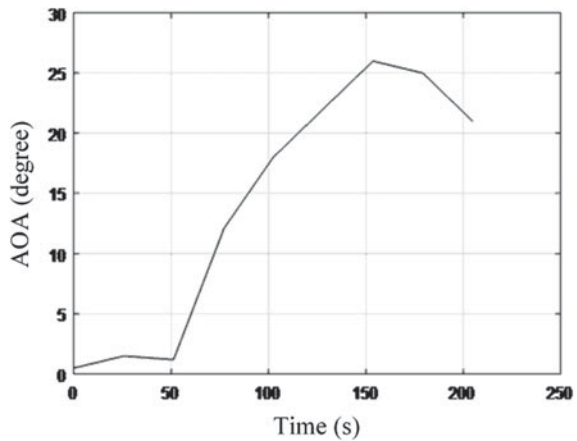


Fig. 5.10 Transition angle of attack curve obtained by direct method



the initial population is 200, and the evolution is 200 generations. The maximum terminal Mach number is 19.81 and the height is 62,900 m. The curve of the angle of attack over time, the trajectory, the curve of the Mach number over time, the curve of the flight path angle over time, and the curve of the heat flow over time are shown in Figs. 5.10, 5.11, 5.12, 5.13, and 5.14, respectively.

5.2.6 Steps for Solving the Optimal Transition Trajectory

Step 1: From the formula (5.22) and $H = 0$, at the initial point, we have

$$H_0 = \lambda_{M0} \frac{dM}{dt} \Big|_{t_0} + \lambda_{h0} \frac{dh}{dt} \Big|_{t_0} + \lambda_{\gamma0} \frac{d\gamma}{dt} \Big|_{t_0} = 0 \quad (5.37)$$

let $\lambda_{M0} = 1$, we have

Fig. 5.11 Transition trajectory obtained by direct method

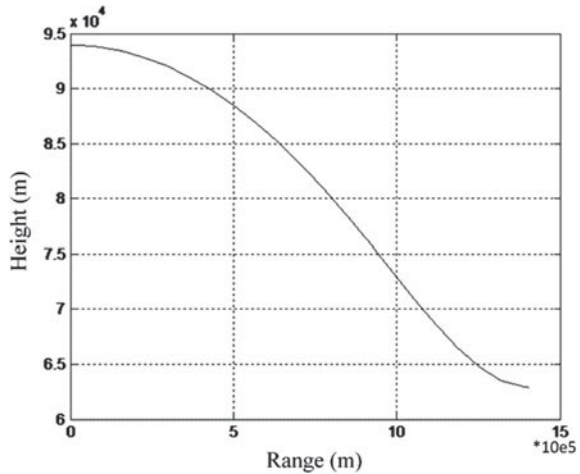
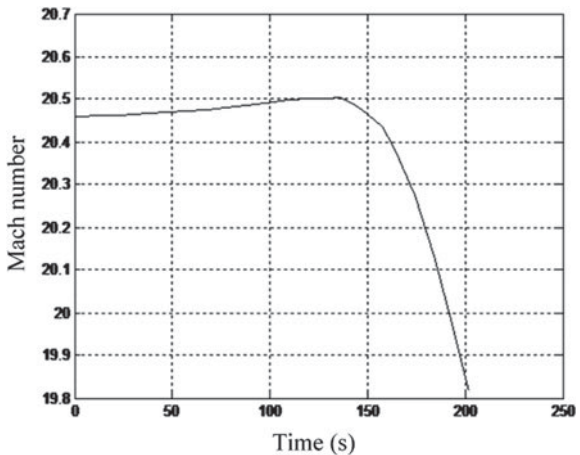


Fig. 5.12 Transition Mach number obtained by direct method



$$\lambda_{h0} = \left(-\frac{dM}{dt} \Big|_{t_0} - \lambda_{\gamma 0} \frac{d\gamma}{dt} \Big|_{t_0} \right) \Bigg/ \frac{dh}{dt} \Big|_{t_0} \quad (5.38)$$

Hence, all we have to do is to find the right $\lambda_{\gamma 0}$, and we will get λ_{h0} , then the optimal trajectory is obtained.

Step 2: Estimate the range of $\lambda_{\gamma 0}$. From the formula (5.33) and $\frac{\partial H}{\partial \alpha} = 0$, $\lambda_{M0} = 1$, we can get (at initial point)

$$-\frac{\partial C_D}{\partial \alpha} + \frac{\lambda_{\gamma 0}}{M} \frac{\partial C_L}{\partial \alpha} = 0 \quad (5.39)$$

Fig. 5.13 Transition flight path angle obtained by direct method

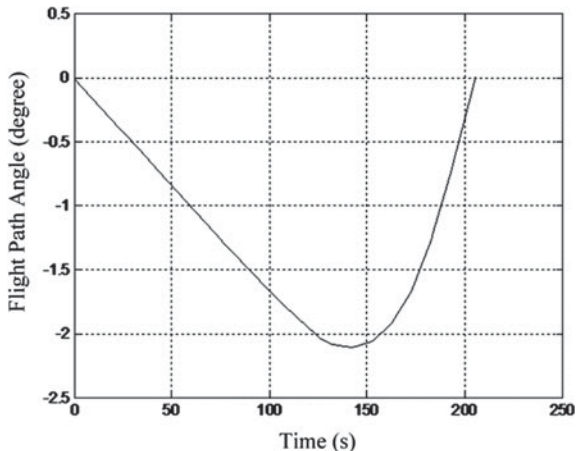
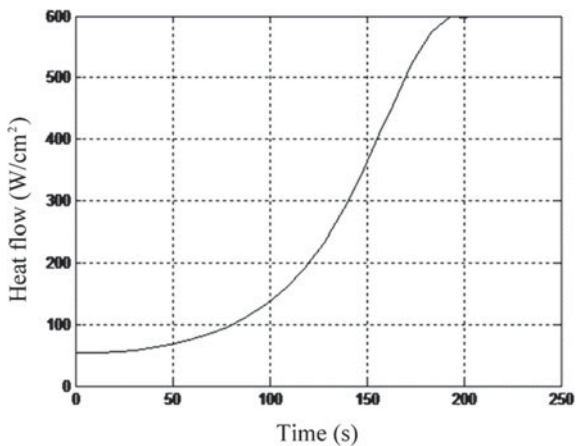


Fig. 5.14 Transition heat flow obtained by direct method



According to the trajectory optimization algorithm of the direct method in 5.2.5, it can be known that it is reasonable for the angle of attack α to change between 0 and 30° , so that the vehicle has the ability of flattening the trajectory with heat flow constraint. Therefore, substituting (5.34) and (5.35) into Eq. (5.39), and set $h = h_0$, $M = M_0$, the given range of α_0 is $0\text{--}30^\circ$, and the range of $\lambda_{\gamma 0}$ can be solved.

Step 3: $\lambda_{\gamma 0}$ is optimized in a certain interval using genetic algorithm. The initial population of the genetic algorithm is 200, and the evolution is 300 generations. Then the desired result is obtained.

5.2.7 Transitional Trajectory Obtained by Indirect Method

The optimal initial value of the common state variable $\lambda_{\gamma 0} = 0.16205$ and $\lambda_{h0} = -1.8988e-005$ are obtained by the steps above. Thereby, the optimal angle of attack and the maximum terminal velocity trajectory of the transition section are obtained. The curve of the $\lambda_{\gamma 0}$ over the angle of attack at initial time is shown in Fig. 5.15. Thus, the range of $\lambda_{\gamma 0}$ is estimated by the range of the angle of attack. The obtained maximum terminal Mach number is 19.83, the maximum heat flow is less than 600 W/cm^2 . The velocity is 0.1% greater than that obtained by direct method. The curve of the angle of attack over time, the trajectory, the curve of the Mach number over time, the curve of the flight path angle over time, and the curve of the heat flow over time are shown in Fig. 5.16, 5.17, 5.18, 5.19 and 5.20, respectively.

Fig. 5.15 $\lambda_{\gamma 0}$ over initial angle of attack

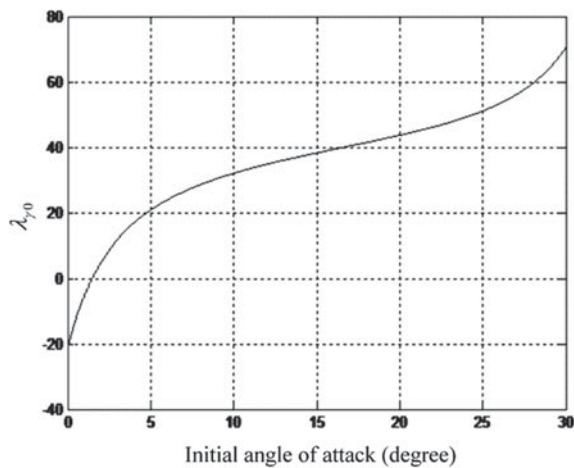


Fig. 5.16 Transition angle of attack over time by indirect method

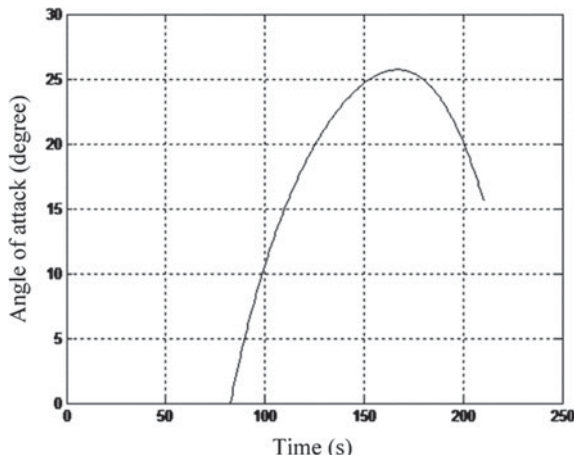


Fig. 5.17 Transition trajectory by indirect method

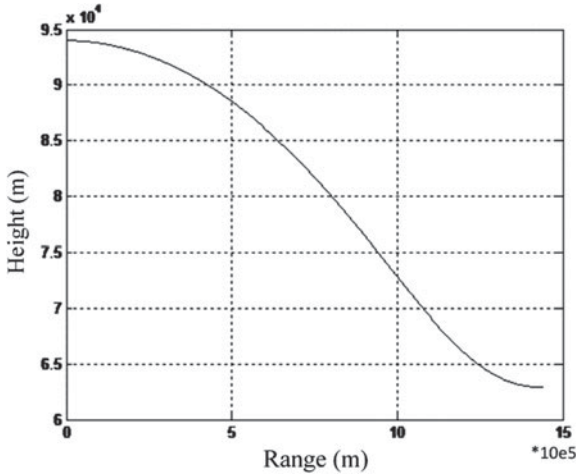
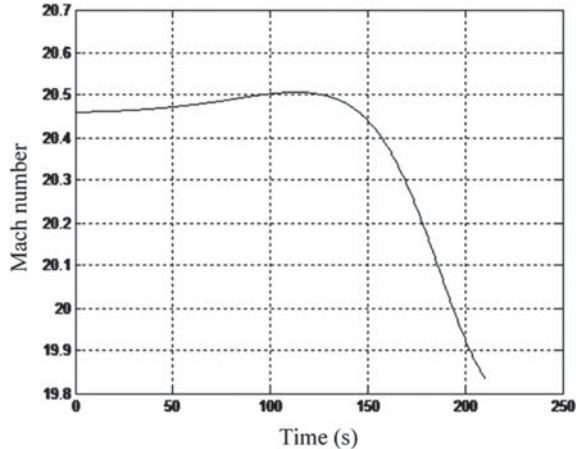


Fig. 5.18 Transition Mach number over time by indirect method



The curve of λ_γ and λ_h over time in the maximum terminal velocity trajectory is shown in Figs. 5.21 and 5.22.

$\lambda_{\gamma 0}$ is the optimization variable when we find the maximum terminal velocity trajectory using the indirect method. The curve of the terminal velocity and maximum heat flow over the design variable $\lambda_{\gamma 0}$ is shown in Fig. 5.23. The sensitivity of the terminal velocity near the optimal solution to the design variable $\lambda_{\gamma 0}$ is -3.6828 , as we calculate. The sensitivity of the terminal Mach number and the maximum heat flow to the design variable $\lambda_{\gamma 0}$ over the value of $\lambda_{\gamma 0}$ near the optimal $\lambda_{\gamma 0}$ is shown in Fig. 5.24. $\lambda_{\gamma 0}$ varies within 10% of the optimal value, the angle of attack over $\lambda_{\gamma 0}$ is shown in Fig. 5.25. It can be seen from the figure that the greater the maximum angle of attack is, the greater the $\lambda_{\gamma 0}$ is, thus the greater the velocity loss is, so the terminal velocity is smaller, which is opposite to the optimal direction. The smaller

Fig. 5.19 Transition flight path angle over time by indirect method

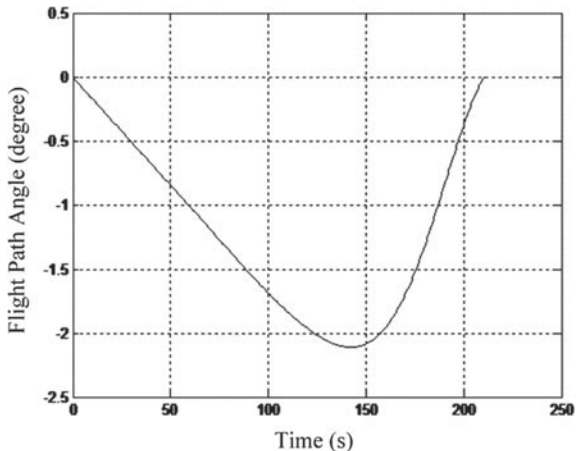
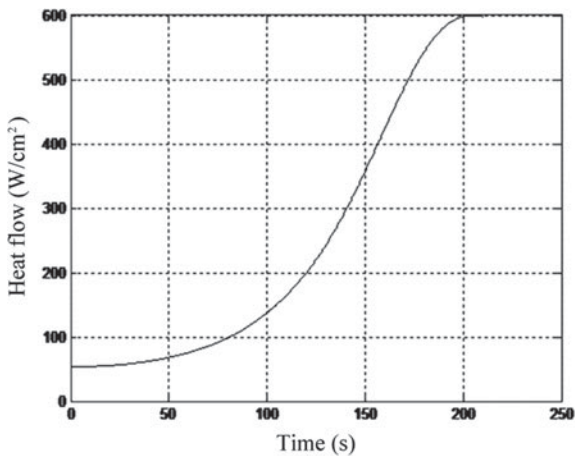
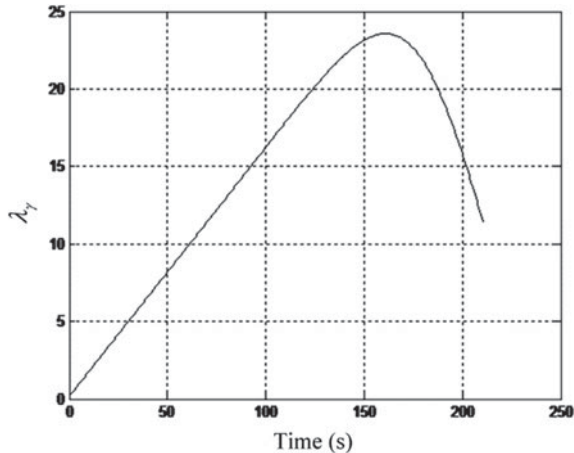
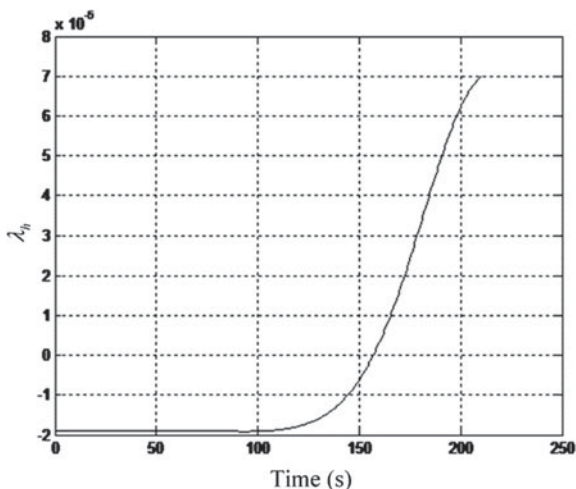


Fig. 5.20 Transition heat flow over time by indirect method



λ_{γ_0} is, the smaller the maximum angle of attack is, which is essential to maintain the maximum terminal velocity, but the smaller angle of attack will lead to smaller lift, and the height where the trajectory is flattened will be lower, thus the heat flow constraint cannot be satisfied.

Fig. 5.21 λ_γ over time**Fig. 5.22** λ_h over time

5.3 The Maximum Range Gliding Trajectory of the Hypersonic Aircraft

5.3.1 Guess Initial Values for Optimal Control Problem by Direct Method

The general optimal control problem can be described as follows

$$\min J(\mathbf{u}) = \Phi[\mathbf{x}(t_f), t_f] + \int_{t_0}^{t_f} L(\mathbf{x}, \mathbf{u}, t) dt \quad (5.40)$$

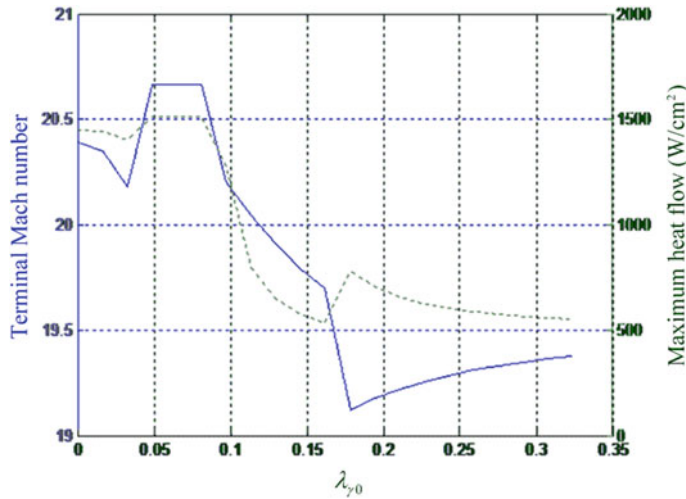


Fig. 5.23 Terminal Mach number and maximum heat flow over λ_{γ_0}

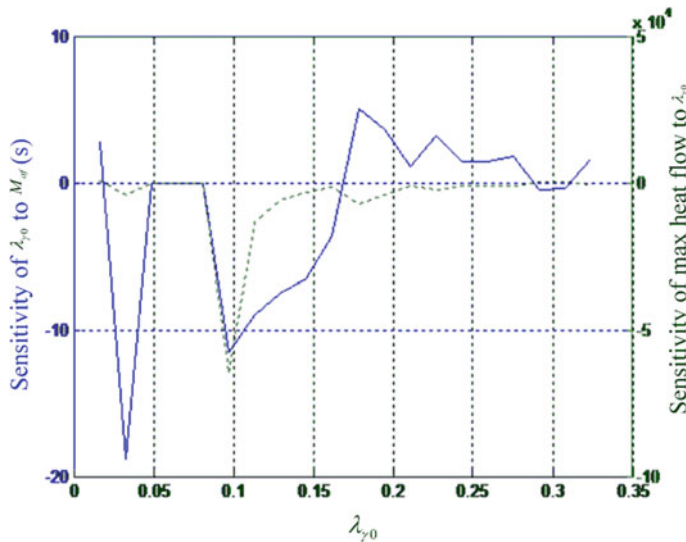


Fig. 5.24 The sensitivity of the terminal Mach number and maximum heat flow to λ_{γ_0} over λ_{γ_0}

where $J(\mathbf{u})$ is a scalar function called the performance function. It has a corresponding value for each control law. It is an indicator for measuring the quality of system control. Φ is a scalar function, which is only related to terminal time and terminal states; L is a function of vector \mathbf{x} , \mathbf{u} and time t ; \mathbf{u} is an m -dimensional piecewise continuous control variable; \mathbf{x} is an n -dimensional state vector satisfying

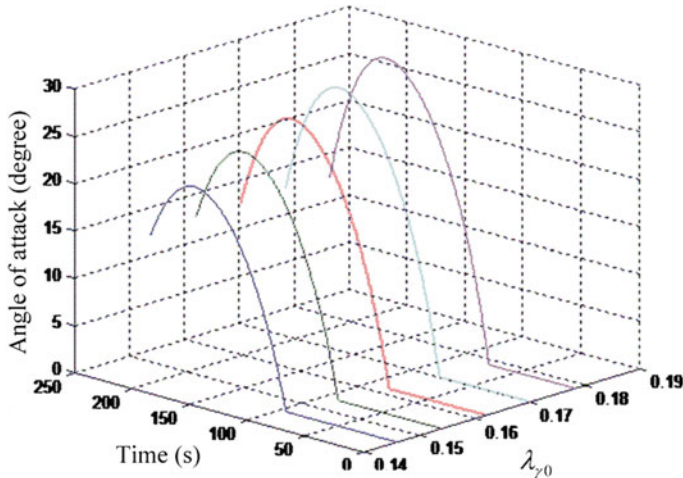


Fig. 5.25 Angle of attack over λ_{y_0} near the optimal value

$$\dot{\mathbf{x}}(t) = \mathbf{f}(\mathbf{x}, \mathbf{u}, t), \quad t \in [t_0, t_f] \quad (5.41)$$

The direct method is to convert the original problem into an NLP problem. It can be divided into two categories according to the conversion method.

1. Parameterize the control variable $\mathbf{u}(t)$ and solve Eq. (5.41) directly by numerical integration to obtain state variables and constraints.
2. An NLP problem is obtained by parameterizing the state variable $\mathbf{x}(t)$ and the control variable $\mathbf{u}(t)$ simultaneously. Then Eq. (5.41) is transformed into an equality constraint by appropriate mathematical rule (such as numerical integration algorithm, Lagrangian interpolation algorithm, etc.) according to system constraints.

The first method requires constant integration in the optimization process, and the amount of calculation is relatively large. Since only the control variables are parameterized, the number of optimization variables are smaller, which can accelerate the convergence speed of the optimization algorithm to some extent. On the contrary, the second method transforms the integration process into an equality constraint in the optimization model, which avoids the integration process, so the amount of calculation is relatively small. However, since the state variables and the control variables are simultaneously parameterized, there are more optimization variables in the optimization model. The optimization algorithm converges more slowly. In application, it is needed to choose appropriate algorithm for specific problem.

5.3.1.1 The First Direct Method

The basic principle of the first direct method is to divide the time interval into N parts, and the corresponding moments are t_0, t_1, \dots, t_N respectively, satisfying $0 = t_0 < t_1 < \dots < t_N = t_f$. The intervals between these moments can be equal or not. One should choose the most suitable partitioning way according to the specific situation. The corresponding control variables are set to be $\mathbf{u}_0, \mathbf{u}_1, \dots, \mathbf{u}_N$. It should be noted that if the terminal time of the system t_f is not fixed, then t_f will become a one-dimensional optimization variable and will be constantly changed during the optimization process. To better adapt to this change, t_1, t_2, \dots, t_{N-1} are expected to change during the optimization process. The general approach is to determine a rule that represents them as a function of terminal time. For example, if the principle of average division is chosen, then

$$t_i = \frac{i}{N} t_f, \quad i = 0, 1, 2, \dots, N \quad (5.42)$$

Then the control variables are written in the form of a function of $\mathbf{u}_0, \mathbf{u}_1, \dots, \mathbf{u}_N$ and t_0, t_1, \dots, t_N according to certain interpolation method. For example, using stepwise interpolation, we have

$$\mathbf{u}(t) = \mathbf{u}_i, \quad |t - t_i| < |t - t_j| \quad (j = 0, 1, \dots, i-1, i+1, \dots, N) \quad (5.43)$$

Using a method of straight-line connection yields

$$\mathbf{u}(t) = \mathbf{u}_i + \frac{t - t_i}{t_{i+1} - t_i} (\mathbf{u}_{i+1} - \mathbf{u}_i) \quad t_i \leq t \leq t_{i+1} \quad (5.44)$$

Using Lagrangian interpolation yields

$$\mathbf{u}(t) = \sum_{j=0}^N \left(\prod_{\substack{i=0 \\ i \neq j}}^N \frac{t - t_i}{t_j - t_i} \right) \mathbf{u}_j \quad (5.45)$$

There are also a variety of numerical algorithms available, such as cubic spline interpolation, Hermite interpolation, triangular interpolation, etc.

After obtaining the curve of the control variable over time, the state variables can be calculated by integrating, (5.41) thus obtaining the performance function, terminal constraints and path constraints.

In summary, the resulting NLP problem can be described as: search for variables $\mathbf{u}_0, \mathbf{u}_1, \dots, \mathbf{u}_N$ so that

$$\min J = J(\mathbf{u}_0, \mathbf{u}_1, \dots, \mathbf{u}_N) \quad (5.46)$$

Satisfying the constraints

$$\begin{cases} N_f[\mathbf{x}(t_f), t_f] = 0 \\ \mathbf{g}(\mathbf{x}, \mathbf{u}, t) \leq 0 \end{cases} \quad (5.47)$$

where \mathbf{x} can be expressed as

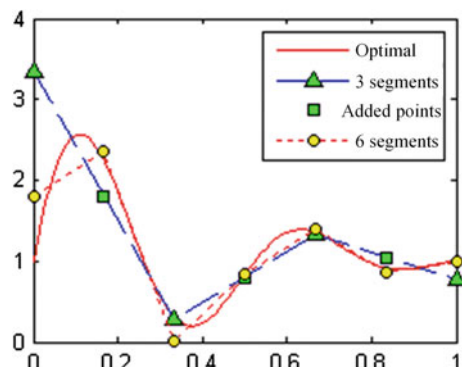
$$\mathbf{x} = \mathbf{x}(\mathbf{u}_0, \mathbf{u}_1, \dots, \mathbf{u}_N) \quad (5.48)$$

5.3.1.2 Gradually Subdivision Optimization Strategy

In the first direct conversion method, on one hand, the calculation amount of the optimization algorithm increases as the number of divisions N increases, and the convergence speed also becomes slower. On the other hand, the most efficient optimization algorithms are sensitive to initial values, and for problems with higher nonlinearity, in order to obtain a more accurate sub-optimal solution, the number of segments N must be increased. In this way, determination of initial value is of great importance. If the initial value is set properly, the algorithm converges quickly. Conversely, the algorithm converges slowly or even fails. In response to this problem, a gradually subdivision optimization strategy is proposed. The steps are as follows

1. The integration time interval is divided into N segments equally, and the feasible initial value of the control quantity is selected. After optimization, $N + 1$ points of control variable are obtained, so that the system is optimal under this control.
2. Insert N new points at the midpoint of each segment, the value is equal to the average value of the control variables on both sides, as shown in Fig. 5.26, where N is 3.
- (3) The $2N + 1$ points obtained are used as the initial point to optimize again and we get $2N + 1$ control points to make the system optimal. If the accuracy requirement is reached, the optimization will stop. Otherwise, let $N = 2N$ and return to step (2).

Fig. 5.26 Gradually subdivision optimization strategy



In essence, this strategy is the process of searching for the initial value closer to the optimal solution. The initial value which constantly approaches the optimal solution will greatly accelerate the convergence speed of this algorithm.

5.3.2 *Indirect Method for Solving Optimal Control Problems*

Compared to direct method, the result obtained by the indirect method satisfies the necessary conditions of the optimal solution. For a physical system with an optimal solution, the solution can be regarded global, and the result is continuous, which is not described by a series of discrete points as in the direct method, so the result is accurate. However, the indirect method has its own shortcomings, that is, the obtained model is very sensitive to initial value, leading to slow convergence speed, and in many cases the algorithm may not converge. Therefore, how to quickly get the solution that satisfies the necessary conditions of the optimal control problem, has become the most concerned problem.

Based on the maximum principle, a costate curve estimation algorithm is proposed in this section, a multi-segment targeting algorithm based on sub-optimal trajectory, and a TPBVP problem conversion method with time as the unknown variable. Based on the costate estimation algorithm, a new algorithm named the costate intermediate variable method is proposed, which is an algorithm between the direct method and the indirect method. The result can approximately satisfy the necessary conditions of optimal control.

5.3.2.1 Costate Curve Estimating Method

In order to get the optimal solution, we need to solve the TPBVP of the system. In references [1, 2], simplex method and gradient method are combined to optimize the most fuel-efficient trajectory. In references [3, 4], the penalty function is applied to transform TPBVP into an unconstrained problem, and uses genetic algorithm to solve the problem of the maximum gliding range and minimum time. It can be seen from the above literature that in order to solve the problem that the indirect method is sensitive to the initial value, tedious steps need to be taken. However, it is found that if the estimated initial value of the costate is very close to the optimal value, direct optimization by sequential quadratic programming (SQP) algorithm can quickly converge to the optimal solution. For the estimation of the costate, Ref. [5] making use of the property that the Hamiltonian function is constant when it does not contain time explicitly. Approximate equations in some neighborhood of the initial costate is obtained by Taylor expansion, and they are solved to guess the initial value. However, the premise of this method is that the Hamiltonian function is fixed, which limits its range of application. Ref. [6], proposes a method for estimating the costate curve based on Legendre quasi-spectral transformation, but it only aims at the segmentation mode of Legendre-Gauss-Lobatto (LGL) point, and

is difficult to deal with general situation. In addition, the key problem in limiting the above-mentioned costate estimation methods is that they are only for the case where there is no inner point constraint in the system. However, most practical problems contain such constraints where the covariate variables may be discontinuous at some points, and the jump variables must also be used as optimization variables for solving TPBVP. It is not only necessary to consider the influence of the jump variables on the initial value of the costate, but also to estimate the jump variables accurately. For this reason, a method to estimate the costate variable throughout the process is proposed, which can not only accurately estimate the initial value of the costate, but also estimate the jump variable in the case of the discontinuous costate.

The optimal control problem with fixed terminal time can be rewritten as follows

$$\min J(\mathbf{u}) = \Phi[\mathbf{x}(t_f), t_f] + \int_{t_0}^{t_f} L(\mathbf{x}, \mathbf{u}, t) dt \quad (5.49)$$

$$st. \quad \dot{\mathbf{x}}(t) = \mathbf{f}(\mathbf{x}, \mathbf{u}, t), \quad \mathbf{x} \in \mathbf{R}^n \quad \mathbf{u} \in \mathbf{R}^m \quad (5.50)$$

The initial and terminal constraints are

$$\mathbf{x}(t_0) = \mathbf{x}_0 \quad (5.51)$$

$$\mathbf{N}_f[\mathbf{x}(t_f), t_f] = 0 \quad N \in \mathbf{R}^p \quad (5.52)$$

There is a first-order path constraint of the state variables in the system

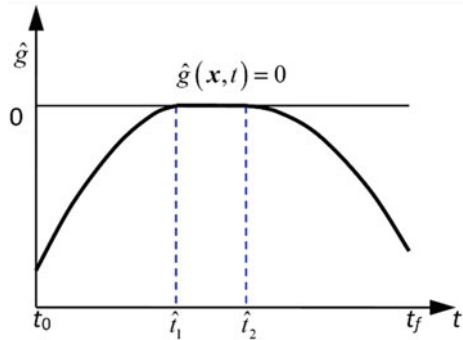
$$\mathbf{g}[\mathbf{x}(t), t] \leq 0 \quad (5.53)$$

The following statements aim at the problem above, while other problem can be formulated by analogy and will not be repeated.

Estimating the initial value of the covariate variable and its jump variable is based on the sub-optimal solution. The more accurate the sub-optimal solution is, the more accurate the estimation is. Therefore, the first step of the estimation algorithm is to obtain the sub-optimal solution of the system, which is generally solved by the direct algorithm with fast convergence rate. Let $\hat{\mathbf{u}}(t)$ denote the control variable corresponding to the suboptimal solution, let $\hat{\mathbf{x}}(t)$ denote the corresponding state variable, and let $\hat{\mathbf{g}}(\mathbf{x}, t)$ denote the path constraint. It is assumed that the path constraints begin at \hat{t}_1 and end at \hat{t}_2 , as is shown in Fig. 5.27.

Now, the integration interval is divided into three segments, $[t_0, \hat{t}_1]$, $[\hat{t}_1, \hat{t}_2]$ and $[\hat{t}_2, t_f]$, which are denoted respectively as S_1 , S_2 and S_3 . Then these three segments are divided up again into N_1 , N_2 and N_3 segments, so that $(N_1 + 1) + (N_2 + 1) + (N_3 + 1)$ nodes are obtained. The sub-optimal state variables and control variables at these points are represented as

Fig. 5.27 Constraint trajectory of the sub-optimal solution obtained by the direct method



$$\begin{cases} \hat{\mathbf{x}} = [\hat{x}_{10}, \hat{x}_{11}, \dots, \hat{x}_{1N_1}, \hat{x}_{20}, \hat{x}_{21}, \dots, \hat{x}_{2N_2}, \hat{x}_{30}, \hat{x}_{31}, \dots, \hat{x}_{3N_3}]^T \\ \hat{\mathbf{u}} = [\hat{u}_{10}, \hat{u}_{11}, \dots, \hat{u}_{1N_1}, \hat{u}_{20}, \hat{u}_{21}, \dots, \hat{u}_{2N_2}, \hat{u}_{30}, \hat{u}_{31}, \dots, \hat{u}_{3N_3}]^T \end{cases} \quad (5.54)$$

These variables are known variables, and the corresponding costate variables on these nodes are

$$\begin{cases} \hat{\boldsymbol{\lambda}} = [\hat{\lambda}_{10}, \hat{\lambda}_{11}, \dots, \hat{\lambda}_{1N_1}, \hat{\lambda}_{20}, \hat{\lambda}_{21}, \dots, \hat{\lambda}_{2N_2}, \hat{\lambda}_{30}, \hat{\lambda}_{31}, \dots, \hat{\lambda}_{3N_3}]^T \\ \hat{\boldsymbol{\mu}} = [\hat{\mu}_{10}, \hat{\mu}_{11}, \dots, \hat{\mu}_{1N_1}, \hat{\mu}_{20}, \hat{\mu}_{21}, \dots, \hat{\mu}_{2N_2}, \hat{\mu}_{30}, \hat{\mu}_{31}, \dots, \hat{\mu}_{3N_3}]^T \end{cases} \quad (5.55)$$

where $\hat{\boldsymbol{\mu}}$ is the Lagrangian multiplier corresponding to the path constraint, according to the necessary conditions of the optimal control

$$\begin{cases} \hat{\boldsymbol{\lambda}}_{1N_1} = \hat{\boldsymbol{\lambda}}_{20} \\ \hat{\mu}_{10} = 0, \hat{\mu}_{11} = 0, \dots, \hat{\mu}_{1N_1} = 0, \hat{\mu}_{30} = 0, \hat{\mu}_{31} = 0, \dots, \hat{\mu}_{3N_3} = 0 \end{cases} \quad (5.56)$$

The adjoint equations of the optimal solution are

$$\dot{\hat{\boldsymbol{\lambda}}} \approx -\frac{\partial \hat{H}}{\partial \hat{\mathbf{x}}} \quad (5.57)$$

At this point, according to the method introduced in literature [7], three differential matrices \mathbf{D}_1 , \mathbf{D}_2 and \mathbf{D}_3 can be obtained according to the partitioned nodes. We have

$$\mathbf{D}\hat{\boldsymbol{\lambda}} \approx -\frac{\partial \hat{H}}{\partial \hat{\mathbf{x}}} \quad (5.58)$$

where \mathbf{D} is the differential matrix over the entire integration process,

$$\mathbf{D} = \begin{bmatrix} \mathbf{D}_1 & \mathbf{0} & \mathbf{0} \\ \mathbf{0} & \mathbf{D}_2 & \mathbf{0} \\ \mathbf{0} & \mathbf{0} & \mathbf{D}_3 \end{bmatrix} \quad (5.59)$$

And because

$$\frac{\partial \hat{H}}{\partial \hat{x}} = \frac{\partial \hat{H}}{\partial \hat{x}} + \hat{\mu} \frac{\partial \hat{g}}{\partial \hat{x}} \quad (5.60)$$

then

$$\mathbf{D} \hat{\lambda} + \hat{\mu} \frac{\partial \hat{g}}{\partial \hat{x}} \approx - \frac{\partial \hat{H}}{\partial \hat{x}} \quad (5.61)$$

Equation (5.61) can be rewritten as

$$\begin{bmatrix} \mathbf{D} & \frac{\partial \hat{g}}{\partial \hat{x}} \end{bmatrix} \begin{bmatrix} \hat{\lambda} \\ \hat{\mu} \end{bmatrix} \approx - \frac{\partial \hat{H}}{\partial \hat{x}} \quad (5.62)$$

There are $n(N_1 + N_2 + N_3 + 3)$ equations in formula (5.62), including $n(N_1 + N_2 + N_3 + 3)$ unknowns $\hat{\lambda}$ and $N_2 + 1$ unknowns $\hat{\mu}$, so the solution cannot be obtained. It should be noted that, even if there is no path constraint in the system, that is, there is no unknown quantity in Eq. (5.62), although the number of equations is equal to the number of unknowns, the estimated value of the costate cannot be obtained through Eq. (5.62), because matrix \mathbf{D} is ill-conditioned at this time. Equation (5.62) contains more unknowns than equations? To obtain a stable solution, new equations are needed.

$$\frac{\partial \hat{H}}{\partial \hat{u}} = \frac{\partial (\hat{\lambda} f + L + \hat{\mu} g)}{\partial \hat{u}} = 0 \quad (5.63)$$

It can be obtained from the equation above that

$$\begin{bmatrix} \frac{\partial f}{\partial \hat{u}} & \frac{\partial g}{\partial \hat{u}} \end{bmatrix} \begin{bmatrix} \hat{\lambda} \\ \hat{\mu} \end{bmatrix} = - \frac{\partial L}{\partial \hat{u}} \quad (5.64)$$

In addition, the boundary condition is

$$\hat{\lambda}_{3N_3} = \frac{\partial \Phi}{\partial \hat{x}_{3N_3}} + \left(\frac{\partial N_f^T}{\partial \hat{x}_{3N_3}} \right) \hat{v} \quad (5.65)$$

where

$$\hat{\mathbf{v}} = [\hat{v}_1, \hat{v}_2, \dots, \hat{v}_q]^T \quad (5.66)$$

The costate connection equation is

$$\hat{\lambda}_{1N_1} = \hat{\lambda}_{20} \quad (5.67)$$

The costate jump equation is

$$\hat{\lambda}_{2N_2} = \hat{\lambda}_{30} + \hat{\pi} \frac{\partial g}{\partial \mathbf{x}_{2N_2}} \quad (5.68)$$

Combine Eqs. (5.62), (5.64), (5.65), (5.67) and (5.68), we have

$$\Psi \begin{bmatrix} \hat{\lambda} & \hat{\mu} & \hat{\mathbf{v}} & \hat{\pi} \end{bmatrix}^T = \begin{bmatrix} -\frac{\partial \hat{H}}{\partial \hat{\mathbf{x}}} & -\frac{\partial L}{\partial \hat{\mathbf{u}}} & \frac{\partial \Phi}{\partial \hat{\mathbf{x}}_{3N_3}} & \mathbf{0} & \mathbf{0} \end{bmatrix}^T \quad (5.69)$$

where Ψ is a combination of the five equations above. There are $n(N_1 + N_2 + N_3 + 3)$ unknowns $\hat{\lambda}$, $N_2 + 1$ unknowns $\hat{\mu}$, q unknowns $\hat{\mathbf{v}}$, 1 unknown $\hat{\pi}$, $n(N_1 + N_2 + N_3 + 3)$ adjoint equations, $m(N_2 + 1)$ control equations, q boundary conditions, m costate jump equations and m connection equations.

It can be seen that the number of equations is more than the number of unknowns. Matrix Ψ is not a square matrix. To solve the costate variables, the generalized inverse of matrix Ψ is needed, so we have

$$\begin{bmatrix} \hat{\lambda} & \hat{\mu} & \hat{\mathbf{v}} & \hat{\pi} \end{bmatrix}^T = \Psi^+ \begin{bmatrix} -\frac{\partial \hat{H}}{\partial \hat{\mathbf{x}}} & -\frac{\partial L}{\partial \hat{\mathbf{u}}} & \frac{\partial \Phi}{\partial \hat{\mathbf{x}}_{3N_3}} & \mathbf{0} & \mathbf{0} \end{bmatrix}^T \quad (5.70)$$

According to the equation above, the value of costate variables and jump variables at the designated time can be estimated.

5.3.2.2 Equivalent System and Its Relationship with the Original System

For practical problems, since the dimensional variables of each dimension and the control variables are quite different, large errors will occur if the covariation variables are directly estimated from the original equations. The normalization processing can effectively improve the calculation accuracy.

The optimal control model is

$$\left. \begin{array}{l} \min J = \Phi(\mathbf{x}(t_f), t_f) + \int_{t_0}^{t_f} L(\mathbf{x}, \mathbf{u}, t) dt \\ \dot{\mathbf{x}} = f(\mathbf{x}, \mathbf{u}, t) \\ \mathbf{x}(t_0) = \mathbf{x}_0 \\ \mathbf{g}(\mathbf{x}, \mathbf{u}, t) \leq 0 \\ \mathbf{N}_f(\mathbf{x}(t_f), t_f) = 0 \end{array} \right\} \quad (5.71)$$

After amplifying state variables, control variables, objective functions, path constraints and boundary conditions by K_x , K_u , K_L , K_g and K_N respectively, the equivalent system is obtained

$$\left. \begin{array}{l} \min \bar{J} = K_L \Phi\left(\frac{\bar{\mathbf{x}}(t_f)}{K_x}, t_f\right) + K_L \int_{t_0}^{t_f} L\left(\frac{\bar{\mathbf{x}}}{K_x}, \frac{\bar{\mathbf{u}}}{K_u}, t\right) dt \\ \dot{\bar{\mathbf{x}}} = K_x f\left(\frac{\bar{\mathbf{x}}}{K_x}, \frac{\bar{\mathbf{u}}}{K_u}, t\right) \\ \bar{\mathbf{x}}(t_0) = K_x \mathbf{x}_0 \\ K_g \mathbf{g}\left(\frac{\bar{\mathbf{x}}}{K_x}, \frac{\bar{\mathbf{u}}}{K_u}, t\right) \leq 0 \\ K_N \mathbf{N}_f\left(\frac{\bar{\mathbf{x}}(t_f)}{K_x}, t_f\right) = 0 \end{array} \right\} \quad (5.72)$$

If the solution of the original system is \mathbf{x}^* , obviously, the solution of the equivalent system is $K_x \mathbf{x}^*$. If the costate variable of the original system is λ^* , it can be concluded according to the necessary conditions of the optimal solution that the costate variable of the equivalent system is $K_L \lambda^*/K_x$.

5.3.3 The Maximum Range Gliding Trajectory of the Hypersonic Aircraft

The reentry section of the single-stage orbital carrier includes a thrust cruise section and a thrust-less gliding section. When the engine fuel is exhausted, the vehicle enters the no-thrust gliding phase. In order to save fuel consumed in the cruise section, the gliding range is required to be long enough. In this section, the maximum range of the gliding section is taken as the optimal objective to study the optimal trajectories under unconstrained heat flow and maximum heat flow constraints respectively.

5.3.3.1 Optimal Control Model

After the boosting section, the aircraft reaches a certain speed and altitude into the gliding phase. At this time, the engine stops working, and the attitude control is realized by changing the angle of attack. The height and speed are gradually reduced. When the state variable meets certain requirements, the gliding phase ends. Ignoring the influence of the Earth's rotation, in the vertical plane, its dynamic equation can be described as

$$\left. \begin{aligned} \frac{dh}{dt} &= Ma \sin \gamma \\ \frac{dM}{dt} &= \frac{-D - mg \sin \gamma}{am} \\ \frac{d\gamma}{dt} &= \frac{L - mg \cos \gamma}{Mam} + \frac{Ma \cos \gamma}{R_0 + h} \\ \frac{dr}{dt} &= \frac{R_0 Ma \cos \gamma}{(R_0 + h)} \end{aligned} \right\} \quad (5.73)$$

where h , M , γ and r are height, Mach number, flight path angle and range, a is the fixed sonic speed, R_0 is the radius of the Earth, t is the time, D and L are drag and lift respectively, which can be expressed as

$$D = qC_D A_w \quad (5.74)$$

$$L = qC_L A_w \quad (5.75)$$

$$C_D = C_{D0}(M) + K(M)C_L^2 \quad (5.76)$$

$$C_L = C_{L0}(M) + C_{L\alpha}(M)\alpha \quad (5.77)$$

where q is the dynamic pressure, A_w is the reference area, C_D and C_L are drag coefficient and lift coefficient respectively, α is the angle of attack. The objective function is

$$\min J = -r(t_f) \quad (5.78)$$

The boundary conditions are

$$\left. \begin{aligned} h(t_0) &= h_0 & M(t_0) &= M_0 & \gamma(t_0) &= \gamma_0 & r(t_0) &= r_0 \\ h(t_f) &= h_f & M(t_f) &= M_f \end{aligned} \right\} \quad (5.79)$$

5.3.3.2 Unconstrained Optimal Trajectory

The initial condition of the gliding section is $h_0 = 111983.3$ m, $M_0 = 15.1896$, $\gamma_0 = 0$, the terminal constraint is $h_f = 10000$ m, $M_f = 2$, mass $m = 89930$ kg, reference area $A_W = 250$ m², sonic speed $a = 340$ m/s, Earth radius $R_0 = 6378$ km, gravitational acceleration $g = 9.80665$ m/s². According to the process of obtaining the equivalent system, the amplification coefficients of the four state variables are respectively set as $K_h = 0.001$, $K_M = 10$, $K_\gamma = 57.296$ and $K_r = 0.001$, the amplification coefficients of objective function and control quantity are set as $K_L = 0.0001$ and $K_\alpha = 57.296$ to establish the equivalent system.

The model was established in Simulink of Matlab 2007a, ode4 was selected as the integral algorithm, the step size was 0.5 s, and SQP algorithm was adopted as the optimization algorithm.

In the process of searching for sub-optimal solution with the gradually subdivision optimization strategy, the whole process is firstly divided into 4 segments. In order to test the sensitivity of the algorithm to the initial value, reasonable initial value $\alpha = 0.10, 0.12, 0.14, 0.16, 0.18$ and 0.20 were respectively taken for optimization, and the algorithm stopped when $N = 64$. The value of the objective function in the process is shown in Fig. 5.28. Different initial value converges to the same point in the first optimization, and it gradually approaches the optimal value as the number of segments increases. Figure 5.29 shows the different optimal height history when the number of segments is 4, 16 and 64 respectively. The oscillation in height decreases as N increases. To verify the rapidity of the algorithm, for the case of $N = 4$, the results obtained by genetic algorithm in Matlab are shown in Table 5.1, it can be seen that this problem is more suitable for SQP algorithm.

After obtaining the sub-optimal solution, the initial value of the costate of the equivalent system can be estimated, then the segmented shooting method can be used for optimization. The process is divided into 6 sections, and the time separation points are 500 s, 1000 s, 1500 s, 2000 s and 2500 s, respectively. The state variables of the sub-optimal solution at each separation point are calculated to construct TPBVP. The final optimal solution is shown in Fig. 5.30.

Fig. 5.28 Step-by-step optimization process

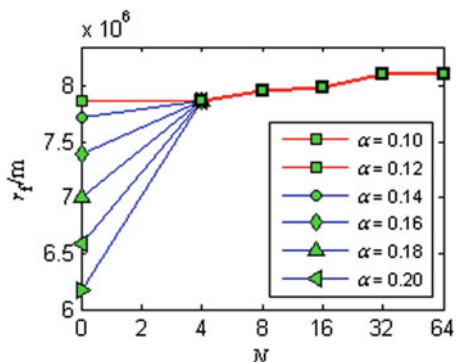


Fig. 5.29 The height history of different precision in the optimization process

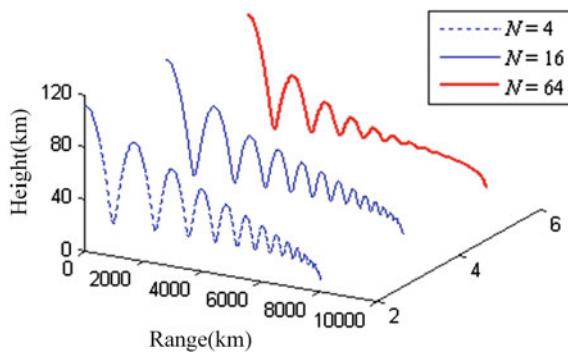


Table 5.1 Comparison between SQP algorithm and genetic algorithm

	Time consuming (s)	Objective function	Constraint 1	Constraint 2
SQP	159.9	7.864e6	-5.564e-6	-6.839e-10
Genetic algorithm	286.3	6.575e6	-0.0210	-1.7117

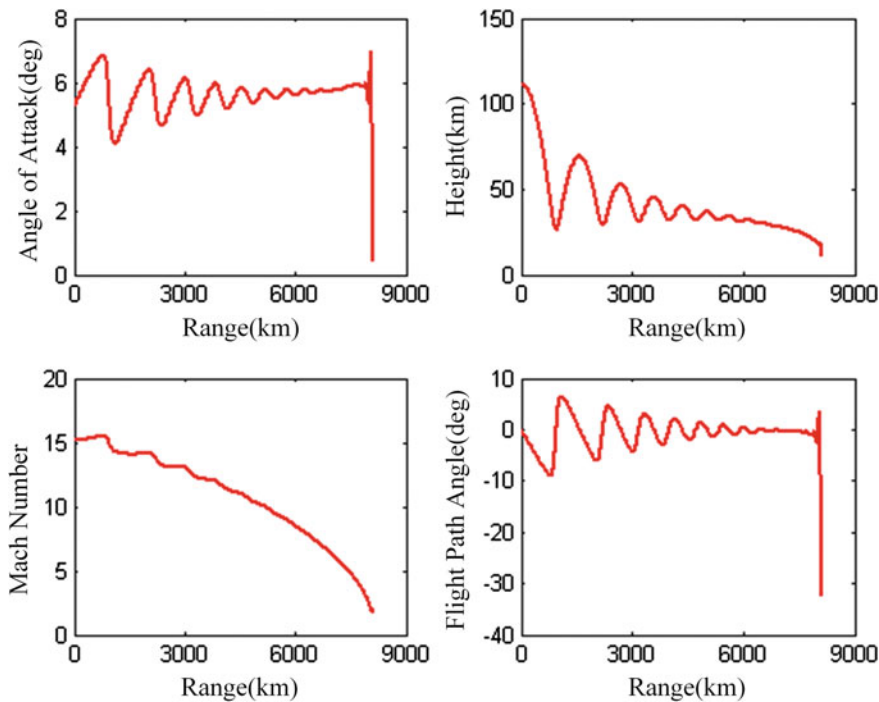


Fig. 5.30 Optimal control and optimal state variables

Fig. 5.31 Costate variables for the optimal solution of the equivalent system

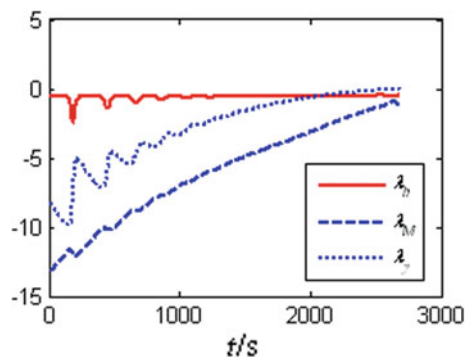
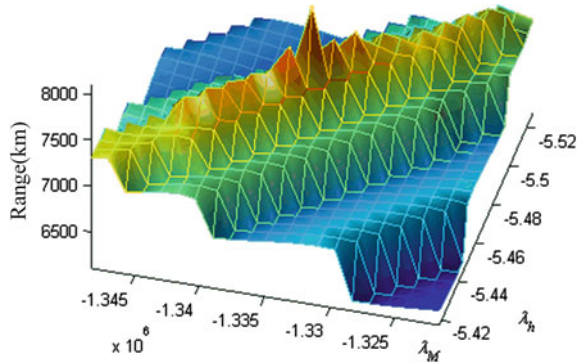


Fig. 5.32 Sensitivity of glide range over costate



It can be seen that although the initial value estimated is quite different from the final solution, the system is not sensitive to the costate at the first target shooting with the help of piecewise shooting method, and the corresponding optimal solution can be quickly obtained at this time. The costate variables of equivalent systems are shown in Fig. 5.31. In the original system, state variables and costate variables differ greatly, while in equivalent systems, they are basically on the same order of magnitude, which is helpful for optimization.

To analyze the sensitivity of the problem to the initial value of the costate, the effective range in the region $\lambda_h \in [-5.527, -5.417]$ and $\lambda_M \in [1.348e6, -1.322e6]$ is calculated, as is shown in Fig. 5.32. It can be seen that a slight change in the initial value of the costate will cause a large drop in the range near the optimal point.

5.3.3.3 Optimal Trajectory Under Heat Flow Constraint

Consider a model with heat flow constraints, where the constraints need to be added is

$$\dot{Q} \leq \dot{Q}_{\max}$$

where the heat flow is expressed as

$$\dot{Q} = 5.188 \times 10^{-8} \rho^{0.5} (Ma)^3$$

where ρ is the density of the atmosphere.

After obtaining the optimal trajectory without constraint, the heat flow constraint is added, and the heat flow constraint is gradually increased to study the influence of heat flow constraint on the optimal range. The maximum limits are set to be 800 W/cm^2 , 700 W/cm^2 , 600 W/cm^2 , 500 W/cm^2 , 400 W/cm^2 , and 300 W/cm^2 , respectively. The optimal trajectories are shown in Fig. 5.33, and the curve of optimal range over heat flow constraint is shown in Fig. 5.34.

For the case of 400 W/cm^2 heat flow constraint, the optimal control law and state variables are given in detail, as shown in Fig. 5.35. Figure 5.36 shows the heat flow curve and its local enlargement. The trajectory enters and leaves the constraint in tangential way, the control variables at these two moments are still continuous, as illustrated in Fig. 5.37. It shows the comparison of unconstrained heat flow with 400 W/cm^2 maximum heat flow.

Fig. 5.33 Optimal glide trajectory under different heat flow constraints

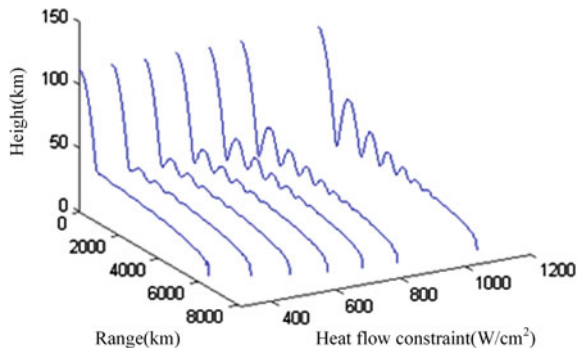
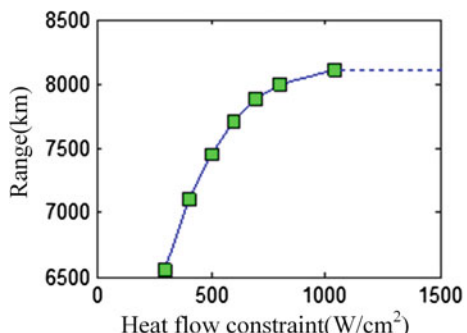


Fig. 5.34 Maximum glide range over heat flow constraint



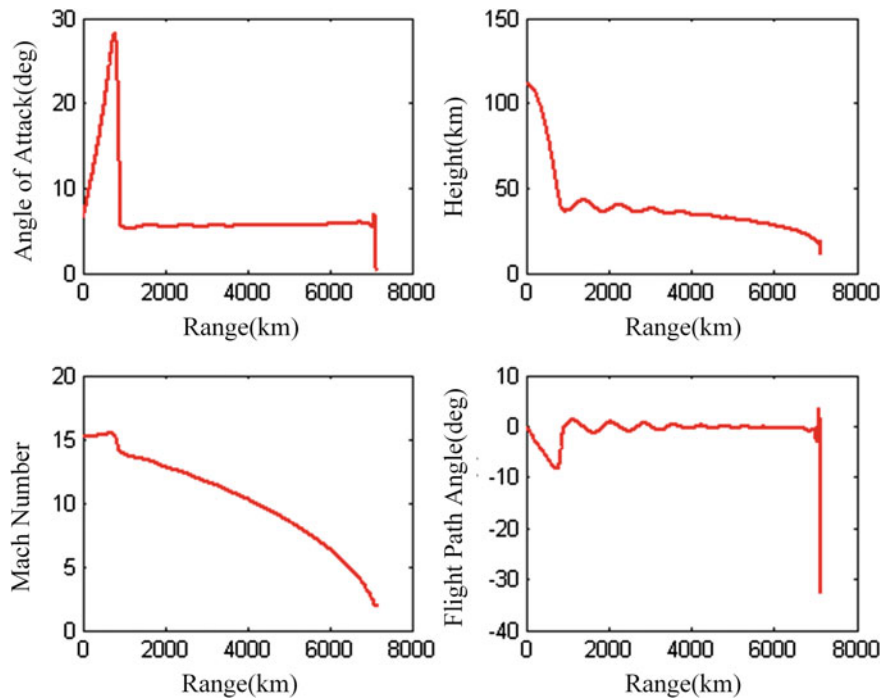


Fig. 5.35 Optimal control and states under heat flow constraints

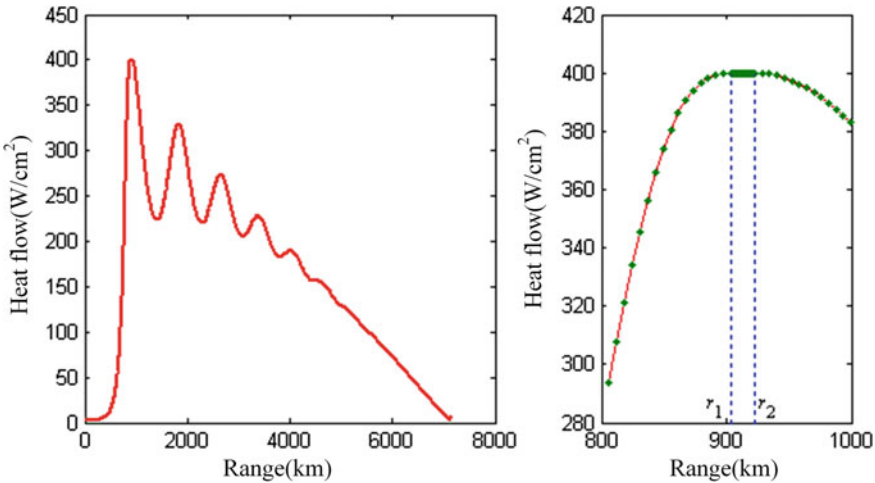
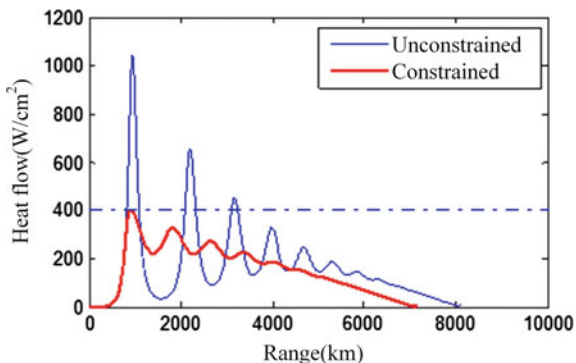


Fig. 5.36 The heat flow of the optimal trajectory

Fig. 5.37 Heat flow over range with or without constraints



References

1. Morimoto, H., Chuang, C.H.: Minimum-fuel trajectory along entire flight profile for a hypersonic vehicle with constraint. AIAA-98-4122 (1998)
2. Chuang, C.H., Morimoto, H.: Periodic optimal cruise for a hypersonic vehicle with constraints. *J. Spacecraft Rockets* **34**(2), 165–171 (1997)
3. Zhou, H., Chen, W., Yin, X.: Optimization of glide trajectory for a hypersonic vehicle. *J. Beijing Univ. Aeronaut. Astronaut.* **32**(5), 513–517 (2006)
4. Zhou, H., Zhou, T., Chen, W., Yin, X.: Trajectory optimization in injection phase for hypersonic gliding vehicle. *J. Astronaut.* **27**(5), 970–973 (2006)
5. Bryson, Jr., E., Ho, Y.-C.: *Applied Optimal Control*. Blaisdell Publishing Co. (1969)
6. Benson, D.A.: *A Gauss Pseudospectral Transcription for Optimal Control*. Ph.D. Thesis, Department of Aeronautics and Astronautics, MIT, Massachusetts, USA (2004)
7. Yang, L., Zhou, H., Chen, W.: Application of linear gauss pseudo-spectral method in model predictive control. *Acta Astronaut.* (2014)

Chapter 6

Direct Method for Gliding Trajectory Optimization Problem



Direct method has been widely applied in trajectory optimization. Direct trajectory optimization software—SOCS, CAMTOS and GPOPS—adopts direct collocation method, direct multiple shooting algorithm and Gauss Pseudo-spectral Method in solving process respectively. Direct method is less complex than indirect method. It is unnecessary to derive adjoint equations, and the number of differential equations is less than half of that in indirect method. However, the scale of discrete optimization variables is very large. As a result, higher requirements of the calculation efficiency for these optimization algorithms are imposed.

6.1 Direct Method for Solving Optimal Control Problems

Typically, the dynamics of aircraft are defined by a set of ordinary differential equations, which is referred to as the state equation

$$\dot{\mathbf{x}}(t) = f(\mathbf{x}(t), \mathbf{u}(t)) \quad (6.1)$$

Initial condition at time t_I is defined by

$$\Psi(\mathbf{x}(t_I), \mathbf{u}(t_I), t_I) = 0 \quad (6.2)$$

And terminal condition at the final time t_F is defined by

$$\Psi(\mathbf{x}(t_F), \mathbf{u}(t_F), t_F) = 0 \quad (6.3)$$

In addition, the solution must satisfy inequality constraints, which is

$$\mathbf{g}_L \leq \mathbf{g}(\mathbf{x}(t), \mathbf{u}(t), t) \leq \mathbf{g}_U \quad (6.4)$$

Finally, the objective function is

$$J(\mathbf{u}) = \Phi(\mathbf{x}(t_F), t_F) + \int_{t_I}^{t_F} L(\mathbf{x}(t), \mathbf{u}(t), t) dt \quad (6.5)$$

The basic optimal control problem is to determine the control vector $\mathbf{u}(t)$ to optimize the objective function under the premise of satisfying initial conditions, terminal conditions and inequality constraints.

Direct method is to convert the original problem into a NLP problem at first. There are two kinds of conversion methods:

- (a) Parameterize control variable $\mathbf{u}(t)$, and Eq. (6.1) can be directly solved by numerical integration. Therefore, state variables and constraints are obtained.
- (b) Parameterize state variable $\mathbf{x}(t)$ and control variable $\mathbf{u}(t)$ simultaneously, and Eq. (6.1) can be transformed into an equality constraint by mathematical principles (such as numerical integration algorithm, Lagrange interpolation algorithm, etc.). Then, coupled with the constraints of the system itself, an NLP problem is obtained.

In comparation, method (a) requires constant integrating during optimization process, leading to enormous amount of calculation. Since only control variables are parameterized, the optimization variables are less, which accelerates the convergence speed of optimization algorithm to some extent. On the contrary, method (b) transforms the integration process into an equality constraint in the optimization model, avoiding integration, so computing load is low. However, the number of optimization variables is large due to simultaneously parameterizing state variables and control variables, which makes optimization algorithm converge slowly. In practical, it is necessary to select a suitable algorithm for specific problem.

6.2 Direct Shooting Method

6.2.1 Direct Multiple Shooting Method

A schematic diagram of direct multiple shooting method with only one state variable in the dynamic differential equation is shown in Fig. 6.1. Direct multiple shooting method approximates the control law with piecewise constant representation law, piecewise linear representation law, continuous polynomial representation law or other laws. If initial condition is settled, the continuous condition and terminal condition are satisfied by changing the parameters in the control representation law. The continuous condition can be described as

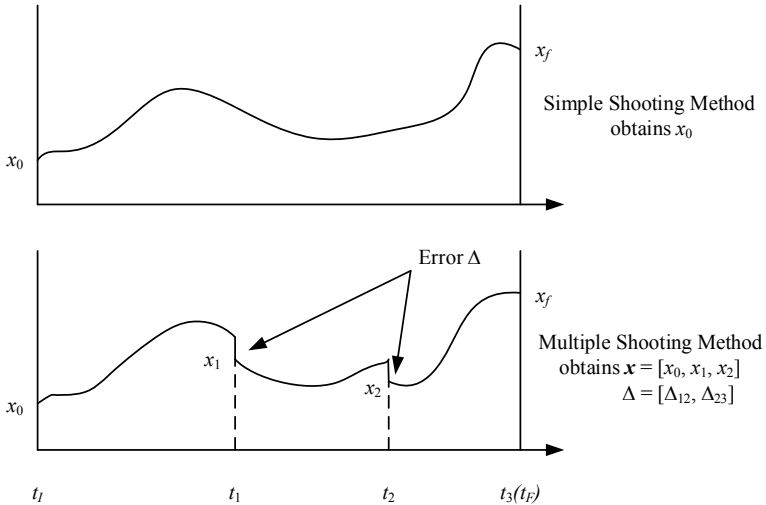


Fig. 6.1 Multiple shooting method schematic diagram

$$\Delta_{ab} = \int_{t_b}^{t_a} f(\mathbf{x}, \mathbf{u}, t) dt + \mathbf{x}_a - \mathbf{x}_b \quad (6.6)$$

where t_a is initial time in the current target range of multiple shooting method, and t_b is terminal time in current target range. In order to keep each segment being continuous, the error must be equal to zero $\Delta_{ab} = 0$.

6.2.2 Direct Method of Discrete Control

The main idea of direct shooting method is to divide time into N parts, and the corresponding moments are respectively t_0, t_1, \dots, t_N , satisfying $0 = t_0 < t_1 < t_2 < \dots < t_N = t_f$. The intervals between these moments may be equal or unequal. The most suitable meshing scheme must be selected according to specific situation. Similarly, the control variable $\mathbf{u}(t)$ is set to $\mathbf{u}_0, \mathbf{u}_1, \dots, \mathbf{u}_N$.

It should be noted that if terminal time t_F is not fixed, then t_F will be a one-dimensional optimization variable, which is constantly changing during the optimization process. In order to better adapt to this change, expected moments t_1, t_2, \dots, t_{N-1} also keep changing. A general approach is to identify a rule that represents the moments as a function of terminal time. For example, if we divide time evenly, then there is

$$t_i = \frac{i}{N} t_F, \quad i = 0, 2, \dots, N \quad (6.7)$$

Under this circumstance, according to some interpolation method, the control variable is written in the form of a function of $\mathbf{u}_0, \mathbf{u}_1, \dots, \mathbf{u}_N$ and t_0, t_1, \dots, t_N . For instance, using stepped interpolation method, we have

$$\mathbf{u}(t) = \mathbf{u}_i, \quad |t - t_i| < |t - t_j| \quad (j = 0, 1, \dots, i-1, i+1, \dots, N) \quad (6.8)$$

Using straight line connection method, we have

$$\mathbf{u}(t) = \mathbf{u}_i + \frac{t - t_i}{t_{i+1} - t_i} (\mathbf{u}_{i+1} - \mathbf{u}_i) \quad t_i \leq t \leq t_{i+1} \quad (6.9)$$

Using Lagrange interpolation method, we have

$$\mathbf{u}(t) = \sum_{j=0}^N \left(\prod_{\substack{i=0 \\ i \neq j}}^N \frac{t - t_i}{t_j - t_i} \right) \mathbf{u}_j \quad (6.10)$$

Of course, there are many other kinds of available numerical algorithms, such as cubic spline interpolation, Hermite interpolation, triangular interpolation, etc.

After obtaining the curve of control variable over time, the state variable curve can be calculated by integrating Eq. (6.1) in order to get the objective, terminal constraint and the curve of path constraint. In summary, NLP problem can be described as follow:

Search for control variables $\mathbf{u}_0, \mathbf{u}_1, \dots, \mathbf{u}_N$, making

$$\min J = J(\mathbf{u}_0, \mathbf{u}_1, \dots, \mathbf{u}_N) \quad (6.11)$$

meeting the constraints

$$\begin{cases} N_f[\mathbf{x}(t_f), t_f] = 0 \\ \mathbf{g}(\mathbf{x}, \mathbf{u}, t) \leq 0 \end{cases} \quad (6.12)$$

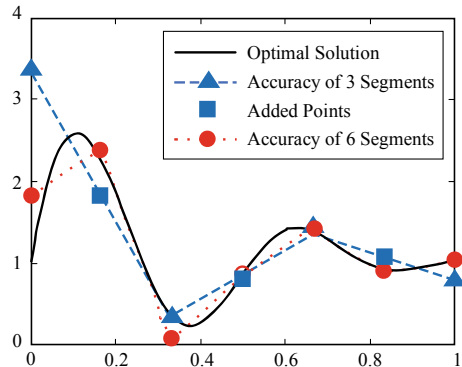
where \mathbf{x} can be expressed as

$$\mathbf{x} = \mathbf{x}(\mathbf{u}_0, \mathbf{u}_1, \dots, \mathbf{u}_N) \quad (6.13)$$

6.2.3 Gradual Subdividing Optimization Strategy

For the first kind of direct conversion method, determining initial values of optimization algorithm is a critical issue. On one hand, computational complexity of the

Fig. 6.2 Gradual subdividing optimization strategy schematic diagram



algorithm increases with increasing phase number N , and convergence rate is also slower. On the other hand, most efficient optimization algorithms are sensitive to initial values. But for the highly nonlinear problems, in order to obtain a more accurate suboptimal solution, it is necessary to increase phase number N . Thus, if initial values are set properly, the algorithm would converge fast. Otherwise, the algorithm would converge slowly, and even would fail to converge. In response to this problem, an optimization strategy of gradual subdivision is proposed. The specific steps are:

1. Divide integration time into N phases evenly, and select feasible initial values of control variables. After optimization, $N + 1$ control points are obtained, and the system is optimal under this group of control variables;
2. Insert N new control points at the midpoint of each segment, the value of which is the mean value of control variables at both ends, as shown in Fig. 6.2, where N is 3;
3. Set the calculated $2N + 1$ points as initial points and optimize the system again. Thereby $2N + 1$ control points that make the system achieve optimal are obtained. If the accuracy requirement is satisfied, the optimization stops, otherwise, set $N = 2N$ and return to step 1.

In essence, this strategy is a process of constantly searching for initial values that are closer to optimal solution. The initial values, which continuously approach the optimal solution, would greatly accelerate the convergence rate of the algorithm.

6.3 Direct Collocation Method

6.3.1 General Form of Direct Collocation Method

An optimal control problem can be formulated as a collection of n phases. In general, the independent variable time t for phase k is defined in the region $t_I^{(k)} \leq t \leq t_F^{(k)}$ where $1 \leq k \leq n$, and the phases are sequential, that is $t_I^{(k+1)} = t_F^{(k)}$. Within phase

k , the dynamics of the system are described by a set of dynamic variables

$$\mathbf{z} = \begin{bmatrix} \mathbf{x}^{(k)}(t) \\ \mathbf{u}^{(k)}(t) \end{bmatrix} \quad (6.14)$$

State equations are

$$\dot{\mathbf{x}}^{(k)} = f^{(k)}(\mathbf{x}^{(k)}(t), \mathbf{u}^{(k)}(t), \mathbf{p}^{(k)}, t) \quad (6.15)$$

where parameters $\mathbf{p}^{(k)}$ are not dependent on time t . The solution must satisfy algebraic path constraints in the form

$$\mathbf{g}_L^{(k)} \leq \mathbf{g}^{(k)}(\mathbf{x}^{(k)}(t), \mathbf{u}^{(k)}(t), \mathbf{p}^{(k)}, t) \leq \mathbf{g}_U^{(k)} \quad (6.16)$$

as well as bounds on the state variables and control variables, those are

$$\mathbf{x}_L^{(k)} \leq \mathbf{x}^{(k)}(t) \leq \mathbf{x}_U^{(k)} \quad (6.17)$$

$$\mathbf{u}_L^{(k)} \leq \mathbf{u}^{(k)}(t) \leq \mathbf{u}_U^{(k)} \quad (6.18)$$

Finally, the objective function is

$$\begin{aligned} J = & \Phi\left(\mathbf{x}^{(1)}(t_I^{(1)}), \mathbf{u}^{(1)}(t_I^{(1)}), \mathbf{p}^{(1)}, t_I^1, \mathbf{x}^{(1)}(t_F^{(1)}), \mathbf{u}^{(1)}(t_F^{(1)}), \mathbf{p}^{(1)}, t_F^1, \dots, \right. \\ & \left. \mathbf{x}^{(N)}(t_I^{(N)}), \mathbf{u}^{(N)}(t_I^{(N)}), \mathbf{p}^{(N)}, t_I^N, \mathbf{x}^{(N)}(t_F^{(N)}), \mathbf{u}^{(N)}(t_F^{(N)}), \mathbf{p}^{(N)}, t_F^N\right) \\ & + \sum_{j=1}^N \left\{ \int_{t_I^j}^{t_F^j} w^{(j)}(\mathbf{x}^{(j)}(t), \mathbf{u}^{(j)}(t), \mathbf{p}^{(j)}, t) dt \right\} \end{aligned} \quad (6.19)$$

The terminal objective function can be expressed as

$$J = \Phi(\mathbf{x}(t_F)) = \mathbf{x}_{n+1}(t_F) \quad (6.20)$$

6.3.2 Direct Transcription

In order to solve optimal control problem in direct method, time domain need to be divided into n_S intervals of the form

$$t_I = t_1 < t_2 < \dots < t_M = t_F \quad (6.21)$$

Define $M \equiv n_s + 1$, $\mathbf{y}_k \equiv \mathbf{y}(t_k)$, $\mathbf{u}_k \equiv \mathbf{u}(t_k)$, $\bar{\mathbf{u}}_k \equiv \mathbf{u}(\bar{t})$, $\bar{t} = \frac{1}{2}(t_k + t_{k-1})$ and $\mathbf{f}_k \equiv \mathbf{f}(\mathbf{x}(t_k), \mathbf{u}(t_k), \mathbf{p}, t_k)$, where k is a mesh point in a phase. The state and control are considered as NLP variables, and the difference equations are replaced by a series of error constraint equations. Also, the boundary conditions and constraints of the optimal control problem are replaced by NLP constraints as follow,

$$\mathbf{c}_L \leq \mathbf{c}(\mathbf{x}) \leq \mathbf{c}_U \quad (6.22)$$

where

$$\mathbf{c}(\mathbf{x}) = [\xi_1, \xi_2, \dots, \xi_{M-1}, \Psi_I, \Psi_F, \mathbf{g}_1, \mathbf{g}_2, \dots, \mathbf{g}_M]^T \quad (6.23)$$

$$\mathbf{c}_L = [0, \dots, 0, \mathbf{g}_L, \dots, \mathbf{g}_L]^T \quad (6.24)$$

Correspondingly, \mathbf{c}_U can also be defined. To satisfy continuous condition of differential Eq. (6.1), $\xi_i = 0 (1 \leq i \leq M-1)$. And boundary constraint and nonlinear path constraint are satisfied by Eqs. (6.2), (6.3) and (6.4). When it comes to equality constraint, $\mathbf{c}_U = \mathbf{c}_L$.

6.3.3 Implicit Integral Method

The implicit Euler scheme is given as follows.

Variable:

$$\mathbf{z}^T = (\mathbf{x}_1, \mathbf{u}_1, \dots, \mathbf{x}_M, \mathbf{u}_M) \quad (6.25)$$

Error:

$$\xi_k = \mathbf{x}_{k+1} - \mathbf{x}_k - h_k \mathbf{f}_k \quad (6.26)$$

The implicit trapezoidal scheme is given as follows.

Variable:

$$\mathbf{z}^T = (\mathbf{x}_1, \mathbf{u}_1, \dots, \mathbf{x}_M, \mathbf{u}_M) \quad (6.27)$$

Error:

$$\xi_k = \mathbf{x}_{k+1} - \mathbf{x}_k - \frac{h_k}{2} (\mathbf{f}_k + \mathbf{f}_{k+1}) \quad (6.28)$$

The implicit Runge-Kutta scheme is given as follows.

Variable:

$$\mathbf{z}^T = (\mathbf{x}_1, \mathbf{u}_1, \bar{\mathbf{u}}_2, \dots, \bar{\mathbf{u}}_M, \mathbf{x}_M, \mathbf{u}_M) \quad (6.29)$$

Error:

$$\boldsymbol{\zeta}_k = \mathbf{x}_{k+1} - \mathbf{x}_k - \frac{1}{6}(\mathbf{k}_1 + 2\mathbf{k}_2 + 2\mathbf{k}_3 + \mathbf{k}_4) \quad (6.30)$$

where

$$\mathbf{k}_1 = h_k \mathbf{f}_k, \quad (6.31)$$

$$\mathbf{k}_2 = h_k \mathbf{f}\left(\mathbf{y}_k + \frac{1}{2}\mathbf{k}_1, \bar{\mathbf{u}}_{k+1}, t_k + \frac{h_k}{2}\right), \quad (6.32)$$

$$\mathbf{k}_3 = h_k \mathbf{f}\left(\mathbf{y}_k + \frac{1}{2}\mathbf{k}_2, \bar{\mathbf{u}}_{k+1}, t_k + \frac{h_k}{2}\right), \quad (6.33)$$

$$\mathbf{k}_4 = h_k \mathbf{f}(\mathbf{y}_k + \mathbf{k}_3, \mathbf{u}_{k+1}, t_{k+1}). \quad (6.34)$$

For the sake of simplicity, the time span of each phase is fixed in these three integration schemes provided above. In the next step of solving NLP problem, the time t_I or t_F must be used as a nonlinearly regulated variable. The step size of the discrete time in Eq. (6.21) is defined as follow,

$$h_k = \tau_k(t_F - t_I) = \tau_k \Delta t \quad (6.35)$$

where $\Delta t \equiv t_F - t_I$, and $0 < \tau_k < 1$. In general, $t_I = 0$ and τ_k is constant, so we can directly use t_F as a NLP variable.

6.3.4 Solving Optimal Trajectory Problems with NLP

We have known that there are many integration methods. Here we choose gradient method to introduce how to solve optimal control problem by NLP method. The optimal design variables for NLP can be described as follow

$$\mathbf{y} = (t_F, \mathbf{x}_1, \mathbf{u}_1, \dots, \mathbf{x}_M, \mathbf{u}_M) \quad (6.36)$$

The system dynamics are described by

$$\dot{\mathbf{x}} = f(\mathbf{x}, \mathbf{u}, t) \quad (6.37)$$

The equality constraint is

$$0 = \mathbf{x}_{k+1} - \mathbf{x}_k - \frac{h_k}{2} (\mathbf{f}_k + \mathbf{f}_{k+1}) = \boldsymbol{\zeta}_k \quad (6.38)$$

Inequality constraint is shown as Eq. (6.4). This problem can be solved by SQP algorithm.

6.4 Direct Collocating Method for Trajectory with Maximum Gliding Cross Range of Hypersonic Aircraft

The solution to the maximum cross range problem at the end of the re-entry gliding section is mainly to solve the maximum lateral maneuverability. According to the properties of the re-entry vehicles, this section gives the relationship between the angle of attack and the velocity, and optimizes the law of the bank angle to maximize the gliding cross range. This problem is described by the collocation method with implicit fourth-order Runge-Kutta integral, which transforms the optimal control problem into a nonlinear programming problem. Finally, the nonlinear programming problem is solved by SQP algorithm.

6.4.1 Mathematical Model

(a) Equation of motion

Consider the earth as a sphere, regardless of its rotation, and the three-degree-of-freedom kinetic equations of motion for the hypersonic re-entry vehicle are expressed as follows

$$\dot{v} = -\frac{D}{m} - g \sin \gamma \quad (6.39)$$

$$\dot{\gamma} = \frac{1}{mv} \left(L \cos \sigma - mg \cos \gamma + \frac{mv^2 \cos \gamma}{R_0 + h} \right) \quad (6.40)$$

$$\dot{\Psi} = \frac{v \cos \gamma \sin \Psi \tan \phi}{R_0 + h} - \frac{L \sin \sigma}{mv \cos \gamma} \quad (6.41)$$

$$\dot{h} = v \sin \gamma \quad (6.42)$$

$$\dot{\theta} = \frac{v \cos \gamma \sin \Psi}{(R_0 + h) \cos \phi} \quad (6.43)$$

$$\dot{\phi} = \frac{v \cos \gamma \cos \Psi}{R_0 + h} \quad (6.44)$$

where $L = C_L q S_{ref}$, $D = C_D q S_{ref}$, and $q = 0.5 q v^2$. S_{ref} is given according to aerodynamic shape. C_L and C_D are fitted by aerodynamic data and can be described as Eqs. (6.45) and (6.46),

$$C_L = [\text{Ma}^2 \text{ Ma } 1] \mathbf{K}_{cl} [\alpha^2 \alpha 1]^T \quad (6.45)$$

$$C_D = [\text{Ma}^2 \text{ Ma } 1] \mathbf{K}_{cd} [\alpha^2 \alpha 1]^T \quad (6.46)$$

where \mathbf{K}_{cl} and \mathbf{K}_{cd} are 3×3 constant coefficient matrices. In order to facilitate the subsequent derivation, let

$$[k_{m1} k_{m2} k_{m3}] = [\text{Ma}^2 \text{ Ma } 1] \mathbf{K}_{cl} \quad (6.47)$$

From the above kinetic equations of motion, it can be known that under certain initial conditions, only the law of the angle of attack and bank angle should be given, and this kinematic problem can be solved. However, different laws of angle of attack and bank angle have a great influence on performance. Therefore, the key to optimizing a certain performance index is to find the optimal law of angle of attack and bank angle.

(b) Maximum cross range problem

The key to solving the maximum re-entry cross range problem is to get the optimal law of angle of attack and bank angle. Meanwhile, it is also necessary to consider the maximum stagnation heat flux, maximum normal overload, maximum dynamic pressure, quasi-balanced gliding constraint and the terminal constraint. These constraints are described as follows.

The maximum stagnation heat flux

$$\dot{Q} = k_1 \sqrt{\rho} V^{k_2} \leq \bar{Q}_{\max} \quad (6.48)$$

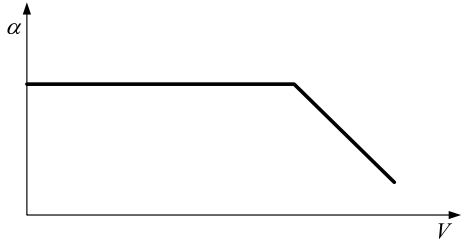
The maximum normal overload

$$n_N = (L \cos \alpha + D \sin \alpha) / G \leq n_{N \max} \quad (6.49)$$

The maximum dynamic pressure

$$q = 0.5 \rho V^2 \leq q_{\max} \quad (6.50)$$

Fig. 6.3 General rule of angle of attack against velocity



If the trajectory needs to be relatively smooth, it also needs to satisfy the quasi-balanced glide constraint

$$\dot{y} \leq 0 \quad (6.51)$$

The longitudinal range, terminal height, velocity and flight path angle are constrained as

$$r_{t_f} = r_f, h_{t_f} = h_F, V_{t_f} = V_F, \gamma_{t_f} = \gamma_F \quad (6.52)$$

The objective function is given as follow

$$J = -l_{t_f} \quad (6.53)$$

where l_{t_f} is the cross range. This optimal trajectory problem is an optimal control problem, and the control variables are the angle of attack and bank angle.

6.4.2 Re-entry Flight Control Law with Given Angle of Attack Profile

The commonly used scheme for law of re-entry gliding angle of attack is that the angle of attack changes with the Mach number. This scheme ensures that the rudders and other actuators can balance the angle of attack at corresponding velocity, in order to ensure stable flight. The general scheme of angle of attack changing with velocity is shown as follow (Fig. 6.3),

6.4.3 Solution of Maximum Cross Range Problem by Direct Collocation Method

- (a) The differential equations of motion can be described as follow

$$\dot{\mathbf{x}}(t) = f(\mathbf{x}(t), \mathbf{u}(t)) \quad (6.54)$$

The initial condition

$$\Psi(\mathbf{x}(t_I), \mathbf{u}(t_I), t_I) = 0 \quad (6.55)$$

The terminal condition

$$\Psi(\mathbf{x}(t_F), \mathbf{u}(t_F), t_F) = 0 \quad (6.56)$$

The inequality constraint

$$\mathbf{g}_L \leq \mathbf{g}(\mathbf{x}(t), \mathbf{u}(t), t) \leq \mathbf{g}_U \quad (6.57)$$

The objective function

$$J(\mathbf{u}) = \Phi(\mathbf{x}(t_F), t_F) + \int_{t_I}^{t_F} L(\mathbf{x}(t), \mathbf{u}(t), t) dt \quad (6.58)$$

The optimal control $u(t)$ is to optimize objective function under the premise of satisfying initial conditions, terminal conditions and inequality constraints.

(b) Direct collocation method based on fourth-order Runge-Kutta integral

To solve the optimal control problem with direct method, first divide the problem into n_s segments.

$$t_I = t_1 < t_2 < \dots < t_M = t_F \quad (6.59)$$

Define $M \equiv n_s + 1$, $\mathbf{y}_i \equiv \mathbf{y}(t_i)$, $\mathbf{u} \equiv \mathbf{u}(t_i)$, $\bar{\mathbf{u}}_i = \mathbf{u}(\bar{t})$, $\bar{t} = \frac{1}{2}(t_i - t_{i-1})$, and $t_{span} \equiv (t_F - t_I)/n_s$, where k is a mesh point of a phase. We set state variables and control variables as nonlinear programming variables. The difference equations are replaced by a series of error constraint equations. The boundary conditions and constraints of optimal control are replaced by constraints of nonlinear programming.

$$\mathbf{c}_L \leq \mathbf{c}(x) \leq \mathbf{c}_U \quad (6.60)$$

where,

$$\mathbf{c}(\mathbf{x}) = [\xi_1, \xi_2, \dots, \xi_{M-1}, \Psi_I, \Psi_F, \mathbf{g}_1, \mathbf{g}_2, \dots, \mathbf{g}_M]^T \quad (6.61)$$

$$\mathbf{c}_L = [0, \dots, 0, \mathbf{g}_L, \dots, \mathbf{g}_L]^T \quad (6.62)$$

$$\mathbf{c}_U = [0, \dots, 0, \mathbf{g}_U, \dots, \mathbf{g}_U]^T \quad (6.63)$$

The ζ_i ($i = 1, \dots, M - 1$) in Eq. (6.61) is implicitly integrated, corresponding to Δ_{ab} in Eq. (6.6). Numerical integration method used to describe $\int_{t_a}^{t_b} f(\mathbf{x}, \mathbf{u}, t) dt$ determines the order of collocation method. To satisfy the continuous condition of the differential Eq. (6.54), $\zeta_i = 0$ ($1 \leq i \leq M - 1$) is required. The boundary constraints and the nonlinear path constraints are satisfied by $\Delta_{ab} = 0$, and equality constraints can be obtained by $\mathbf{c}_U = \mathbf{c}_L$.

The collocation method based on fourth-order classic Runge-Kutta integral method can be described as follow

$$\zeta_i = \mathbf{x}_{i+1} - \mathbf{x}_i - \frac{t_{span}}{6}(\mathbf{k}_1 + 2\mathbf{k}_2 + 2\mathbf{k}_3 + \mathbf{k}_4) \quad (6.64)$$

where, $\mathbf{k}_1 = f(\mathbf{u}_i, \mathbf{x}_i)$, $\mathbf{k}_2 = f(\bar{\mathbf{u}}_i, \mathbf{x}_i + \frac{t_{span}}{2}\mathbf{k}_1)$, $\mathbf{k}_3 = f(\bar{\mathbf{u}}_i, \mathbf{x}_i + \frac{t_{span}}{2}\mathbf{k}_2)$ and $\mathbf{k}_4 = f(\mathbf{u}_{i+1}, \mathbf{x}_i + t_{span}\mathbf{k}_3)$.

(c) Maximum cross range problem based on direct collocation method

The maximum cross range problem is described by implicit fourth-order Runge-Kutta collocation method. The state variables are $[V, \gamma, \Psi, h, \theta, \phi]$, control variable is σ and the state differential equations are Eq. (6.39)–(6.44). Assuming that the flight time is t_F , the trajectory is divided into $M - 1$ phases according to time, then there are M nodes. So, the time step of each phases is $t_{span} = t_F / (M - 1)$, where $t_I = t_1 < t_2 < \dots < t_M = t_F$.

Use Runge-Kutta method to describe the problem. The Eq. (6.39)–(6.44) can be expressed as $\dot{V} = f_V$, $\dot{\gamma} = f_\gamma$, $\dot{\Psi} = f_\Psi$, $\dot{h} = f_h$, $\dot{\theta} = f_\theta$ and $\dot{\phi} = f_\phi$. Then, there is

$$\begin{bmatrix} \zeta_{V_k} \\ \zeta_{\gamma_k} \\ \zeta_{\Psi_k} \\ \zeta_{h_k} \\ \zeta_{\theta_k} \\ \zeta_{\phi_k} \end{bmatrix} = \begin{bmatrix} V_{k+1} - V_k \\ \gamma_{k+1} - \gamma_k \\ \Psi_{k+1} - \Psi_k \\ h_{k+1} - h_k \\ \theta_{k+1} - \theta_k \\ \phi_{k+1} - \phi_k \end{bmatrix} - \frac{t_{span}}{6}(\mathbf{k}_1 + 2\mathbf{k}_2 + 2\mathbf{k}_3 + \mathbf{k}_4) \quad (6.65)$$

where $k = 1, 2, \dots, M - 1$, $\mathbf{k}_1 = [k_{1v}, k_{1\gamma}, k_{1\Psi}, k_{1h}, k_{1\theta}, k_{1\phi}]^T$, $\mathbf{k}_2 = [k_{2v}, k_{2\gamma}, k_{2\Psi}, k_{2h}, k_{2\theta}, k_{2\phi}]^T$ and $\mathbf{k}_3 = [k_{3v}, k_{3\gamma}, k_{3\Psi}, k_{3h}, k_{3\theta}, k_{3\phi}]^T$. Thus, the maximum cross range problem is transformed into a nonlinear programming problem.

The objective function is

$$J = -l_{t_f} \quad (6.66)$$

The optimization state variable is

$$\mathbf{z} = [v_1, \gamma_1, \Psi_1, h_1, \theta_1, \phi_1, \sigma_1, \bar{\sigma}_1, t_1, v_2, \gamma_2, \Psi_2, h_2, \theta_2, \phi_2, \sigma_2, \bar{\sigma}_2, t_2 \dots, v_M, \gamma_M, \Psi_M, h_M, \theta_M, \phi_M, \sigma_M, \bar{\sigma}_M, t_F] \quad (6.67)$$

The inequality constraint is

$$\mathbf{c} = [\dot{Q}_k - \bar{Q}_{\max}, n_{N_k} - n_{N_{\max}}, q_k - q_{\max}]^T \quad (6.68)$$

The equality constraint is

$$\begin{aligned} \mathbf{c}_{eq} = & [\zeta_{v_1}; \dots; \zeta_{v_{M-1}}; \zeta_{\gamma_1}; \dots; \zeta_{\gamma_{M-1}}; \zeta_{\Psi_1}; \dots; \zeta_{\Psi_{M-1}}; \zeta_{h_1}; \dots; \zeta_{h_{M-1}}; \zeta_{\theta_1}; \dots; \zeta_{\theta_{M-1}}; \\ & \zeta_{\phi_1}; \dots; \zeta_{\phi_{M-1}}; v_{t_0} - v_0; \gamma_{t_0} - \gamma_0; \Psi_{t_0} - \Psi_0; h_{t_0} - h_0; \theta_{t_0} - \theta_0; \phi_{t_0} - \phi_0; v_{t_f} - v_f; \\ & \gamma_{t_f} - \gamma_f; \Psi_{t_f} - \Psi_f; h_{t_f} - h_f; \theta_{t_f} - \theta_f; \phi_{t_f} - \phi_f; r_{t_f} - r_f] \end{aligned} \quad (6.69)$$

Through above description, the maximum cross range problem is transformed into a nonlinear programming problem, which is solved by SQP algorithm, thereby obtaining the trajectory with maximum cross range.

6.4.4 Optimization Example

Suppose that there is a re-entry gliding vehicle flying along the equator with an initial height of 100 km, an initial velocity of 7900 m/s, an initial flight path angle of -1° , an initial deflection angle of 90° , and an initial latitude and longitude of $(0^\circ, 0^\circ)$. The optimization result needs to maximize cross range. The terminal height is required to be 24.38 km, and terminal velocity is 734 m/s. The terminal flight path angle is less than -5° and greater than -6° .

In this example, the angle of attack is set to a constant value of 17° . The bank angle follows the initial value of initial condition and linearly decreases to 0° . The specific form is shown as follows (Fig. 6.4),

Taking the number of nodes $M = 33$, the trajectory is divided into 32 phases, with 201 optimization variables. We use fourth-order Runge-Kutta method to formulate this maximum cross range problem as a nonlinear programming problem, and then solve this problem by SQP algorithm. The maximum latitude obtained is 35.5° with the terminal longitude as -94.36° , the terminal height as 24.38 km, the terminal velocity as 734 m/s, and the terminal flight path angle as -5.68° . The terminal states and constraints meet the requirements. Moreover, the corresponding curves of bank angle, velocity and height as functions of time and the latitude and longitude curve are shown as Figs. 6.5, 6.6, 6.7 and 6.8.

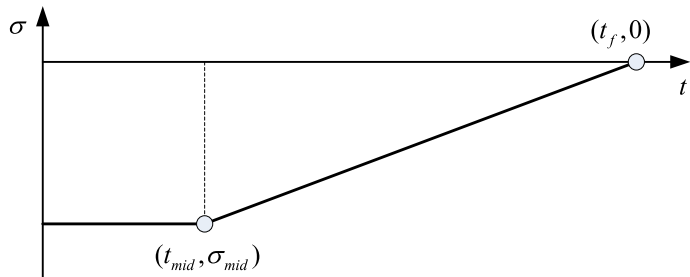


Fig. 6.4 Change law of bank angle

Fig. 6.5 Bank angle changing with time

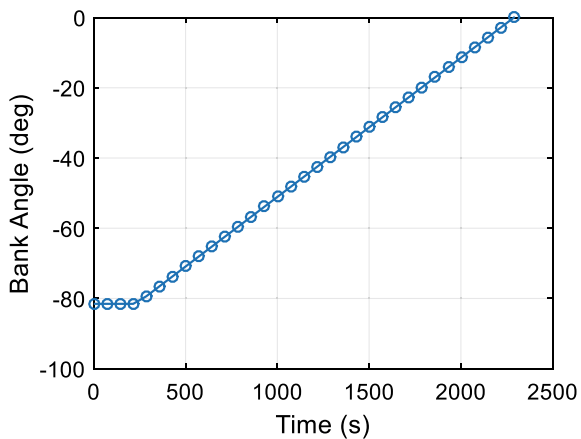


Fig. 6.6 Speed changing with time

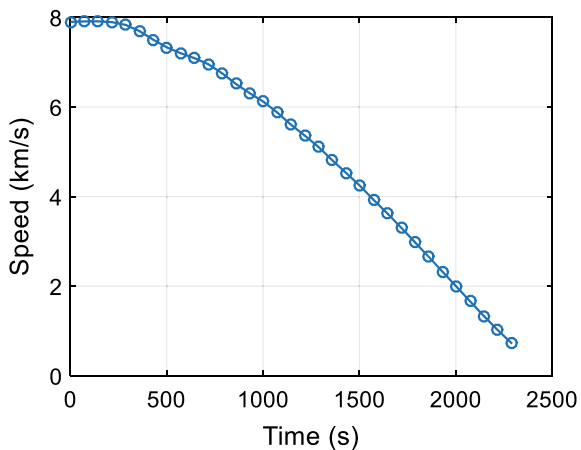


Fig. 6.7 Attitude changing with time

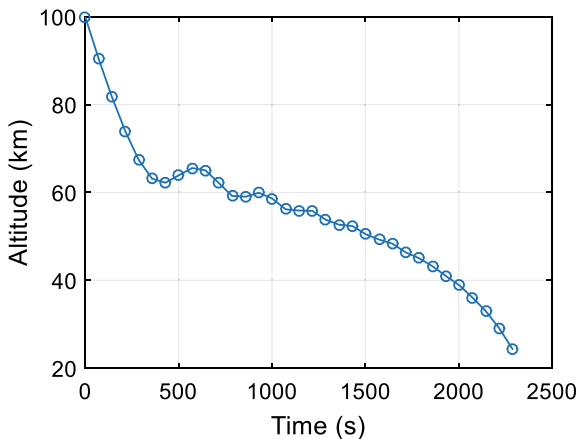
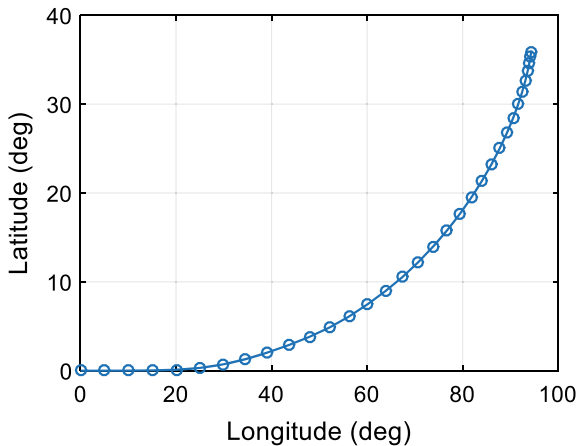


Fig. 6.8 Latitude and longitude curve



Considering control constraints, the maximum cross range obtained by direct collocation method is 35.4° , which is basically consistent with Gaussian pseudo-spectral method in Sect. 6.5.2, indicating that this method is effective.

6.4.5 Summary

In this section, the re-entry maneuvering trajectory with maximum cross range and its corresponding control law are obtained by direct collocation method and SQP algorithm. The results are consistent with Gaussian pseudo-spectral method in Sect. 6.5.2.

It also shows that direct collocation method is an effective method to solve maneuvering trajectory problem with maximum cross range. However, this method still has problems such as convergence rate is slow and it is too sensitive to initial values, etc.

6.5 Pseudo-spectral Method for the Optimal Trajectory of the Hypersonic Vehicle with the Longest Cross-Range

6.5.1 *Introduction of Pseudo-spectral Method*

Pseudo-spectral method is a kind of direct method. Because of its fast convergence property and perfect theoretical system, it has received special attention from researchers. The method uses linear combinations of finite basis of global interpolation polynomials to approximate state variable and control variable on a series of discrete points. Therefore, the derivative of state variable can be expressed as distinctive functions of global state by directly deriving the polynomials. Thereby, differential equation constraint is transformed into algebraic constraint. The zeros of the orthogonal polynomials are generally selected as collocation nodes. These nodes are mutually orthogonal in the correspondingly defined function space. Due to different treatment of terminal constraint, the discrete nodes may also include two endpoints or one of them. For smooth problems, the pseudo-spectral method has exponential convergence property. For non-smooth problems, divide them at appropriate locations, then discrete each phase separately. At the same time, set proper connection condition. Currently, the widely used pseudo-spectral methods can be classified as the following four types: Chebyshev pseudo-spectral method (CPM), Legendre pseudo-spectral method (LPM), Gauss pseudo-spectral method (GPM) and Radau pseudo-spectral method (RPM). The differences between these pseudo-spectral methods lies in the selection of interpolation basis functions, collocation nodes and node types, as shown in Table 6.1.

In addition, some literature refers to collocation method as local method, that is, the method of piecewise discretizing state variable and control variable, and the pseudo-spectral method as global method. Compared with traditional methods, pseudo-spectral method can discretize global states with fewer nodes and obtain

Table 6.1 Differences of pseudo-spectral methods

Method	Interpolation basis function	Collocation nodes	Value range of the nodes
CPM	Chebyshev	Chebyshev-Gauss-Lobatto	$[-1,1]$
LPM	Legendre	Legendre-Gauss-Lobatto	$[-1,1]$
GPM	Legendre	Legendre-Gauss-Lobatto	$(-1,1)$
RPM	Legendre	Legendre-Gauss-Radau	$(-1,1]$

a sufficiently high accuracy. Therefore, it is considered to have the potential for real-time optimization.

The theoretical source of pseudo-spectral method is the early spectral method for solving fluid mechanics problems. The research of Reddien in 1979 promoted the development of solving optimal control problems based on orthogonal collocation method. In the 1990s, after Elnager et al. proposed Legendre pseudo-spectral method and applied it directly to the discrete nonlinear optimal control problems, Ross et al. studied the equivalence of the KKT conditioning nonlinear programming problem and the optimal first-order necessary condition. And they established the theory of costate mapping, which greatly promoted the theoretical study of pseudo-spectral method for discrete optimal control problems. Since then, pseudo-spectral method has been widely used in the aerospace field. It also solves the optimal control problems of robots, solar paddles, ascending phase of launch vehicles, formation flying, and orbital transfer etc. At the same time, the pseudo-spectral method is further used to solve systems described by differential inclusion functions, differential algebraic functions and differential flat functions. Due to the node selection and discrete method of Legendre pseudo-spectral, there are certain defects in co-state mapping. Beason overcame these defects and proposed a new Gauss pseudo-spectral method, which proves that the KKT condition of nonlinear programming problem and the first-order optimality condition of the discrete HBVP problem are completely consistent.

In recent years, with the in-depth research of pseudo-spectral method, researchers have found that the method of global orthogonal collocation nodes alone cannot meet the requirements of solving many kinds of optimal control problem. Because global collocation nodes are relatively fixed, and the generated interpolation polynomials cannot well represent the solution of the optimal control problem with discrete state variable and rapidly changing state variable. Therefore, the research focus on pseudo-spectral method has been transferred to the piecewise pseudo-spectral method with mesh refinement. Such pioneering work can refer to Divya Garg's papers. Since the collocated nodes of pseudo-spectral method are all orthogonal nodes, that do not include endpoints, the nonlinear programming problems solved by them are not controlled at the two endpoints. The control variables must be obtained by solving additional optimal problems. Thus, this type of nodes is not suitable to be piecewise type. In order to overcome this problem, Divya Garg has studied Radau pseudo-spectral method based on the LGR points, and obtained costate mapping principle of RPM. Furthermore, by studying the integral form and the differential form of polynomial fitting functions, a general framework for numerically solving the optimal control problem has been proposed. And the condition for the completeness of the pseudo-spectral differential approximation matrix is given. Also, he has compared three pseudo-spectral methods, that are LPM, GPM and RPM. The analysis result shows that the differential approximation matrix of LPM is in the form of $N \times N$, and has singularity phenomenon. Therefore, the nonlinear programming problem discretized by it and the original optimal control problem are inconsistent. Besides, the differential approximation matrixes of RPM and GPM are in the form of $N \times (N + 1)$, which can well connect the discrete nonlinear programming problem and the original optimal control problem. Moreover, Divya Garg has applied the

pseudo-spectral method to solve the optimal control problem in the infinite domain. Several kinds of transfer functions have been proposed to convert time interval from $[0, \infty)$ to $[-1, 1]$. Also, GPM and RPM have been used to discretize system respectively, then GPM and RPM that can handle the optimal control problem in infinite domain have been obtained. The corresponding principle of costate mapping has been derived, and the costate variables of the optimal control problem in infinite domain have been estimated. After RPM provided a naturally suitable discrete form for the piecewise pseudo-spectral method, Christopher Darby has studied the piecewise RPM and proposed two updating methods of adaptive network. The first method determines the node positions that account for main deviation by mathematic average for proportional term. Then combined with the research results of Zhao Y, the second set of segmentation strategies has been proposed, which uses the method of curvature density function to determine the number and size of the collocation mesh. This method obtains the density function characterized by curvature distribution based on optimization result. And through the curvature probability distribution, it calculates the number of mesh nodes that need to be increased and the collocation locations. Beyond that, Chinese scholar Li Hongfu has also proposed a multi-criteria (prior knowledge, probable error and curvature) hp mesh refinement strategy, which can be well adapted to a variety of complex optimal control problems. The refinement mesh nodes are still collocated according to the density function of curvature.

It is worth mentioning that although LPM has some defects, as an early researcher, Elnager has made an indelible contribution to solving optimal control problem by pseudo-spectral method. He figures out the thoughts of solving the optimal control problems by LPM, that is, approximate the optimal control problem by global orthogonal polynomial based on Legendre polynomial. His work is generally regarded as a milestone work in introducing pseudo-spectral method to solve the optimal control problem. Besides, Gong Qi has made a great contribution to the theoretical study of pseudo-spectral method. He has mainly studied the convergence of the pseudo-spectral method to solve the optimal problem in feedback linear system. The pseudo-spectral method provides a simple discrete form, meanwhile it is also with exponential convergence property for analytic functions. Two examples are used to illustrate the exponential convergence property of the pseudo-spectral method (Euler method is with linear convergence, and Hermite-Simpson is with $N - 1.97$ convergence). The previous articles mainly focus on the algorithm and engineering applications of the pseudo-spectral method, but strict convergence proof and error estimation have not made much progress. The convergence theory on the numerical analysis of differential equations is not suitable for the discrete optimal control problem. The research of Hager and Betts is very interesting. That is, discretizing the optimal control problem by convergent Runge-Kutta method likely leads to non-convergence, while discretizing the problem by non-convergent Runge-Kutta method likely leads to convergence. Gong Qi has also introduced comprehensive applications of pseudo-spectrum method from five parts. Starting from the basic principles of the pseudo-spectral method, the general form of solving limited nonlinear optimal control problem by pseudo-spectral method is firstly introduced. And the algorithm structure for solving optimal feedback control problem in real time is proposed, that

is calculating the optimal control through the inner and external loop structures. The second part takes the maneuver of the space station as an example to show the effect of using pseudo-spectral method in obtaining optimal control. Thirdly, the real-time optimization with NPSAT1 demonstrates the control effect of using real-time optimization framework. Through the comparison of experiment and theory, it has a promising prospect. In the fourth part, the pseudo-spectral method is applied to path optimization with barrier-avoiding capability, and the real-time calculation property of pseudo-spectral method is explained again in this example. Last, the pseudo-spectral method is used in the real-time online guidance of re-entry spacecraft. The optimal trajectory at the current state is calculated quickly by pseudo-spectral method, thereby eliminating the effects of interferences.

At present, the Flight Mechanics and Optimization Laboratory of the University of Florida is an authoritative organization for pseudo-spectral software development. They have yielded many results in derivation algorithms, mesh updates, and practical aviation applications. With further development of pseudo-spectral theory, it will be more and more complete for solving optimal control problem.

6.5.2 Optimization Examples and Results

Gauss Pseudo-spectral method is used to solve the same optimal problem of hypersonic vehicle with the largest cross-range in Sect. 6.4.4.

The angle of attack is constant 17° in numerical example. The initial altitude of reentry gliding vehicle is 100 km, the initial velocity is 7900 m/s, the initial flight path angle is -1° , the initial azimuth angle is 90° , and initial longitude and latitude are $(0^\circ, 0^\circ)$. The desired terminal altitude and velocity are 24.38 km and 762 m/s respectively. And desired terminal flight path angle is between -5° and -6° . The objective to find the maximum cross-range.

This nonlinear programming problem is solved by Radau Pseudo-spectral method. The obtained maximum cross-range is 35.5° . The terminal longitude at this time is -94.36° . The terminal altitude, velocity and flight path angle are 24.38 km, 734 m/s and -5.68° respectively. Each terminal state meets constraint requirements. The obtained largest cross-range consists with that obtained by direct collocation method. Figures 6.9, 6.10 and 6.11 show the corresponding bank angle history, velocity history, altitude history. And Fig. 6.12 shows the curve of latitude and longitude.

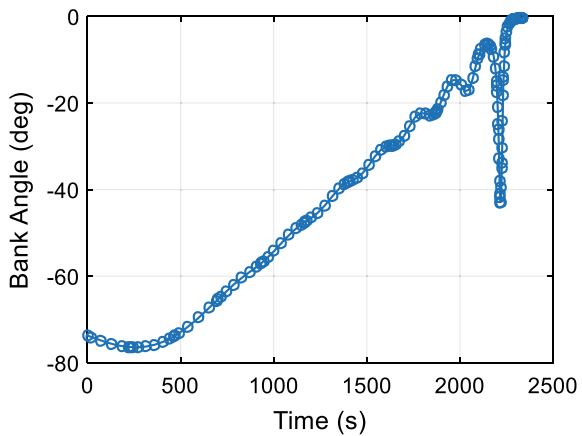
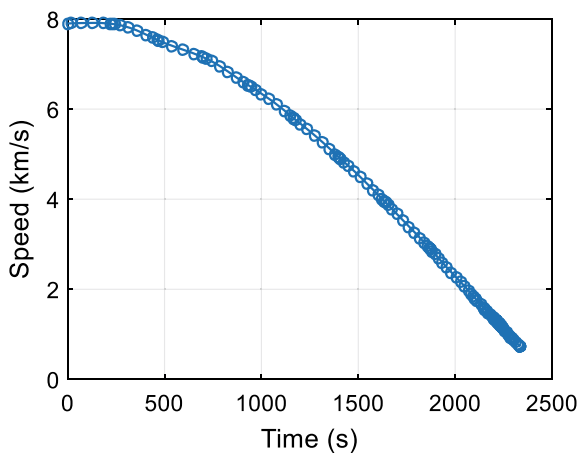
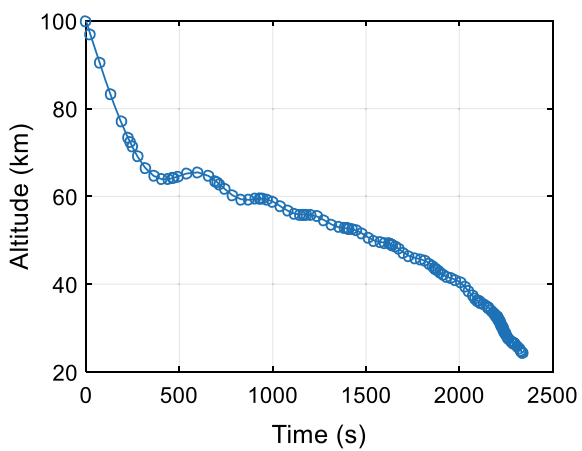
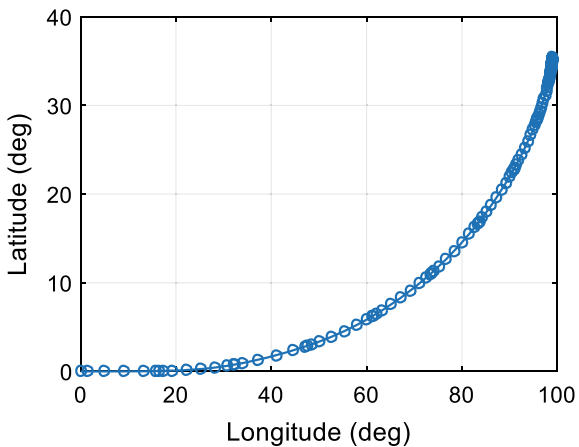
Fig. 6.9 Bank angle history**Fig. 6.10** Velocity history**Fig. 6.11** Altitude history

Fig. 6.12 Longitude and latitude history



Chapter 7

Concept of Steady Glide Reentry Trajectory and Stability of Its Regular Perturbation Solutions



7.1 Introduction

The equilibrium glide [1] proposed by Sänger, is an important reentry flight model. As its vertical forces, including the gravity, centrifugal force and vertical component of the lift, are approximately balanced, the corresponding trajectory has small altitude variation, low peaks of heating rate and dynamic pressure. The equilibrium glide condition is widely used in reentry guidance laws [2, 3, 4].

However, it is difficult to obtain the equilibrium glide state in reentry trajectory optimization due to the sensitivity of altitude variation [5, 6]. In addition, the interferences can easily result in a violent variation. As a result, both equilibrium glide reference trajectory and control law for suppressing trajectory oscillation are needed during the reentry.

The equilibrium glide condition (EGC), which assumes the derivative of flight path angle is zero and transfers the vertical dynamics into algebraic equations, is widely used to obtain the equilibrium glide trajectory. Harbold and Graves [2] planned the reference drag acceleration profile using EGC, and tracked the reference drag profile by configuring the frequency and damping of the drag dynamic system, which used in reentry guidance of Space Shuttle. Chapman [7], Wingrove [8], Etkin [9] analyzed the dynamic characteristics of the reentry trajectory based on EGC, and proposed the negative feedback of the altitude and its first derivative to restrain the trajectory oscillation. Bell [10] and Yu and Chen [11] obtained two different kinds of three-dimensional analytical solutions to hypersonic gliding problem respectively, and Yu's solutions have higher precision because they consider the effect of the Earth's curvature on the heading angle. Shen and Lu [12] transferred the entry flight corridor from the velocity–altitude space to the velocity–bank angle space by EGC. Yu and Chen [13] analyzed the flight path angle of the equilibrium glide trajectory with

© [2020] IEEE. Reprinted, with permission, from [Jinchuan Hu, Jinglin Li, and Wanchun Chen. "Longitudinal characteristics of steady glide trajectory for hypersonic vehicle." International Conference on Control IEEE 2015].

given AOA and bank angle. Although EGC has many successful applications, there is no exact definition of equilibrium glide trajectory. That is because the velocity decreases during the reentry while the EGC is the transient balance of the vertical forces. In Zhang and Chen [14], assumed that the vertical acceleration was a small negative constant to obtain the equilibrium glide trajectory, which results in a large variation of AOA.

In this chapter, based on EGC, the steady glide trajectory (SGT) is proposed for arbitrary given continuously differentiable AOA and bank angle profiles. Then the analytical solutions of the SGT are obtained and dynamic characteristics of the SGT are analyzed. Finally, the fixed-damping differential feedback method (FDDFM) is proposed for damping the trajectory oscillation of the reentry glide trajectory.

7.2 Kinetic Equations

The point-mass vertical dynamics of the reentry vehicle over a non-rotating spherical Earth are described by the following equations of motion:

$$\dot{h} = V \sin \gamma \quad (7.1)$$

$$\dot{V} = -D - g \sin \gamma \quad (7.2)$$

$$\dot{\gamma} = \frac{1}{V} [L_1 + (V^2/r - g) \cos \gamma] \quad (7.3)$$

$$\dot{s} = r V \cos \gamma / R_0 \quad (7.4)$$

where h is the altitude; V is the Earth-relative velocity; γ is the flight-path angle; s is the downrange. r is radial distance from Earth center to vehicle. $r = R_0 + h$, where R_0 is Earth radius. g is the gravitational acceleration as a function of the altitude h . D and L_1 are the aerodynamic drag acceleration and vertical lift acceleration, respectively. They are given by,

$$L_1 = \frac{\rho V^2 S C_{L1}}{2m}, D = \frac{\rho V^2 S C_D}{2m} \quad (7.5)$$

where S is the reference area; m is the vehicle mass. C_{L1} is the vertical component of the lift coefficient, $C_{L1} = C_L \cos \sigma$; σ is the bank angle; C_L and C_D are the lift coefficient and drag coefficient, which depend on the AOA and Mach number; ρ is the atmospheric density and the index atmospheric model described as follows.

$$\rho = \rho_0 e^{-\beta_r h} \quad (7.6)$$

where ρ_0 is the sea-level atmospheric density. β_r is a constant and its value is $1.389 \times 10^{-4} \text{ m}^{-1}$.

The Common Aero Vehicle (CAV) [13, 14] of Lockheed-Martin is used for simulation. The maximum L/D of the vehicle is up to 3.5, the mass is 907 kg, and the reference area is 0.4839 m^2 . The lift and drag coefficients are fitted to be a linear function and parabolic function, respectively.

$$C_L = 0.04675\alpha - 0.10568 \quad (7.7)$$

$$C_D = 0.000508\alpha^2 + 0.004228\alpha + 0.0161 \quad (7.8)$$

where α is the angle of attack.

7.3 Definition of the Steady Glide Trajectory

The reentry trajectories are usually planned by finding suitable angles of attack and bank angles, which is corresponding to vertical component of the lift coefficient and drag coefficient. For the given continuous differentiable vertical component of the lift coefficient C_{L1}^* and drag coefficient C_D^* , the amplitude of the reentry trajectory only depends on the initial altitude and flight path angle. If their values are appropriate, a smooth reentry trajectory without oscillation can be obtained, as shown by the solid line in Fig. 7.1.

In order to obtain the smoothest reentry trajectory, the cost functions in Table 7.1 are selected respectively, in which a_e is the vertical acceleration and it meets the relationship: $a_e = V\dot{\gamma}$; \dot{a}_e is derivative of vertical acceleration; T is a time constant. SQP method was used to search the initial altitude and flight-path angle, and the results were shown in Fig. 7.2. It can be seen from the figure that the altitude

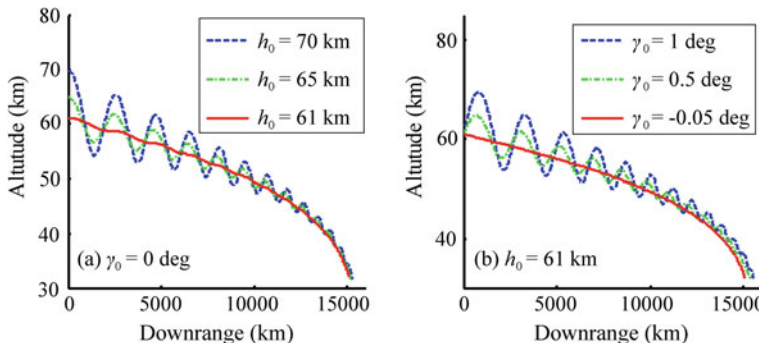
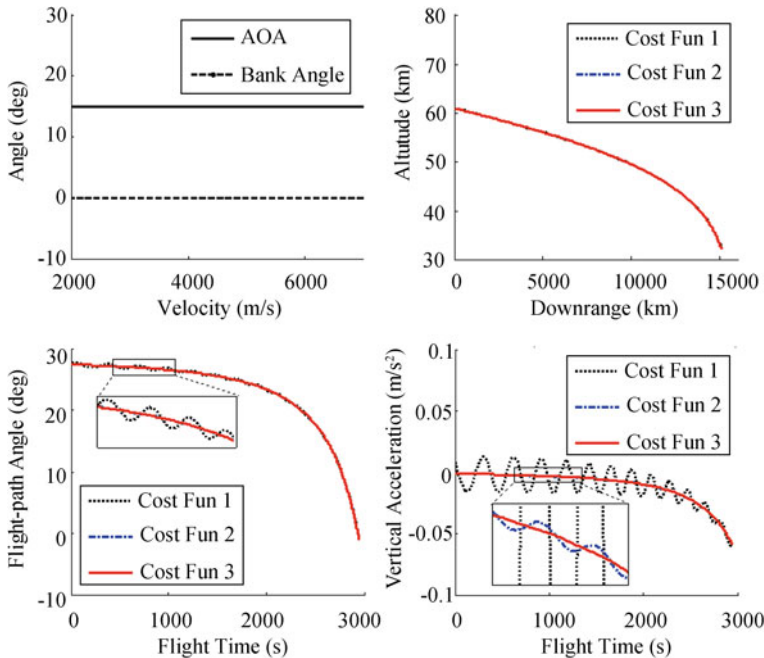


Fig. 7.1 Glide trajectories with different initial states

Table 7.1 Cost functions

Num	Cost function 1	Cost function 2	Cost function 3
Expression	$J = \int_0^T \gamma^2 dt$	$J = \int_0^T \dot{\gamma}^2 dt$	$J = \int_0^T \dot{a}_e^2 dt$

**Fig. 7.2** Glide trajectories under different cost functions

curve obtained by using the cost function 1 is relatively smooth, but there is a small oscillation in the flight-path angle curve. By using cost function 2, the altitude curve and flight-path angle curve are relatively smooth, but the vertical acceleration curve has a small oscillation. The cost function 3 can make all the above three curves smooth. Hence, the reentry trajectory obtained by cost function 3 can be defined as a steady glide trajectory.

7.4 Effects of Control Variable on SGT

The SGT can be obtained only if the reference AOA and bank angle are continuously differentiable. Discontinuous or non-derivable AOA curves (or bank angle curves) can only obtain oscillating reentry trajectories, which is shown in Fig. 7.3.

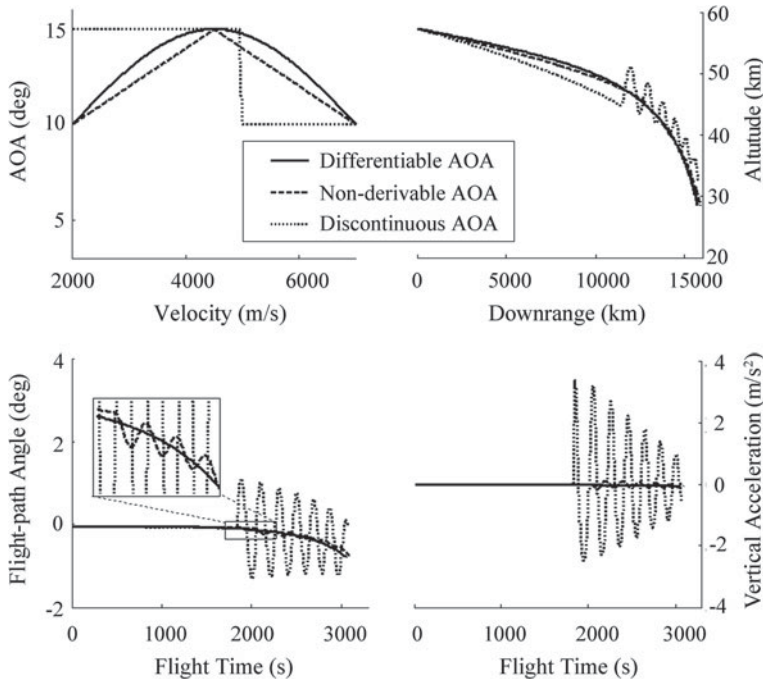


Fig. 7.3 Effect of angle of attack curve continuity on steady glide trajectories

7.5 Effects of Initial Value on SGT

SGT requires specific initial altitude and flight-path angle. If the initial altitude or flight-path angle cannot meet the requirements, the obtained trajectory will oscillate around the SGT.

Figure 7.4 shows the differences between the SGT and the trajectories with different initial altitudes in which $\alpha = 15^\circ$ and $\sigma = 0^\circ$. Both of them oscillate around zero, which means the SGT is the steady state of all reentry trajectories with same the AOA and bank angle profiles.

7.6 Analytical Solution of SGT

7.6.1 Altitude Dynamic Differential Equation

Equation (7.1) shows the time derivative of the altitude. Differentiating (7.1) with respect to time, and substituting (7.2) and (7.3) into it, we obtain:

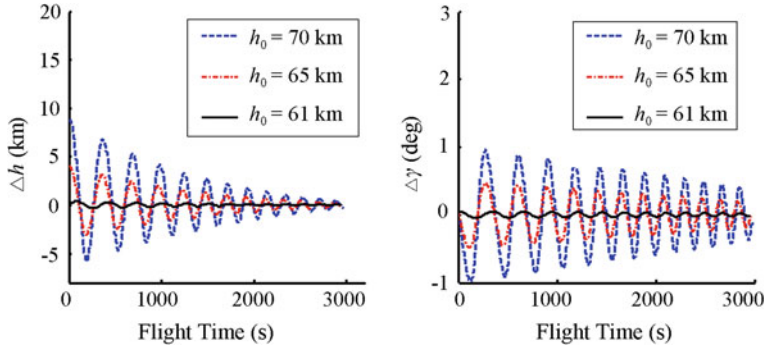


Fig. 7.4 Altitude deviation and flight path angle deviation

$$\ddot{h} = (-D - g \sin \gamma) \sin \gamma + \left[L_1 + \left(\frac{V^2}{r} - g \right) \cos \gamma \right] \cos \gamma \quad (7.9)$$

As the flight path angle is very small in SGT, the following approximations can be made: $\cos \gamma \approx 1$ and $g(\sin \gamma)^2 \approx 0$. Substituting $\sin \gamma = \dot{h}/V$ into (7.9), we obtain:

$$\ddot{h} + (D/V)\dot{h} - L_1 + g - V^2/r = 0 \quad (7.10)$$

In Eq. (7.10), V is long period term which can be regarded as time-varying coefficient, and Eq. (7.10) is a second-order differential equation of altitude. Then the vertical acceleration can be expressed as follow:

$$a_\varepsilon = \ddot{h} + (D/V)\dot{h} \quad (7.11)$$

We define $f_K = C_D^*/C_{L1}^*$, which is the reciprocal of the vertical component of the lift to drag ratio. The drag acceleration can be expressed as follow:

$$D = f_K(g + a_\varepsilon - V^2/r) \quad (7.12)$$

Substituting (7.5) and (7.12) into (7.10) gives,

$$k_c C_{L1}^* V^2 e^{-\beta_r h} - g + \frac{V^2}{r} = \ddot{h} + \frac{f_K(g + a_\varepsilon - V^2/r)}{V} \dot{h} \quad (7.13)$$

where $k_c = \rho_0 S / (2m)$.

7.6.2 Analytical Steady Glide Altitude

In order to realize the fast planning of the SGT, we need the analytical solution of the altitude, flight-path angle and vertical acceleration. Figures 7.2 and 7.3 show that the vertical acceleration of SGT is small, so the altitude of the SGT can be estimated by using the equilibrium glide condition (EGC).

$$k_c C_{L1}^* V^2 e^{-\beta_r h_{eq}} - g + V^2/r = 0 \quad (7.14)$$

where h_{eq} is the altitude of equilibrium glide trajectory.

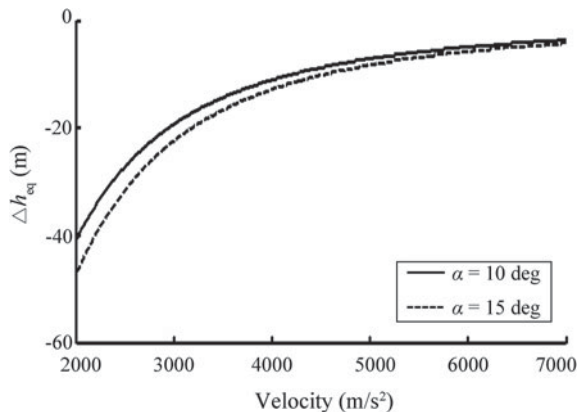
$$h_{eq} = -\ln[(g/V^2 - 1/r)/(k_c C_{L1}^*)]/\beta_r \quad (7.15)$$

However, since the influence of the vertical acceleration is neglected, there is a certain deviation between the altitude of equilibrium glide and steady glide. Figure 7.5 shows the altitude errors $\Delta h_{eq} = h_{eq} - h_{sg}$ (where h_{sg} is the altitude of the SGT), and it is up to 50 m. It can be seen that when the velocity is large, the difference is small, and formula (7.15) is used to estimate the smooth glide height with high accuracy. When the velocity is large, the difference is large, and the accuracy of stable glide height estimated by Eq. (7.15) is poor. In addition, the vertical L/D of hypersonic vehicle also affects the estimation accuracy of Eq. (7.13). The smaller the vertical L/D is, the lower the estimation accuracy is.

In order to obtain a more accurate analytical altitude, the effects of the vertical acceleration should be considered, and the regular perturbation method is used to approximate the actual steady glide altitude. Introducing a small parameter ε , we obtain

$$k_c C_{L1}^* V^2 e^{-\beta_r h} - g + \frac{V^2}{r} = \varepsilon(A_1 \ddot{h} + A_2 \dot{h}) \quad (7.16)$$

Fig. 7.5 Difference between the equilibrium glide altitude and the steady glide altitude



where A_1 and A_2 are given as follows:

$$A_1 = 1/\varepsilon$$

$$A_2 = A_1 f_K (g + a_e - V^2/r)/V$$

According to regular perturbation method, h_{sg} can be formulated as follows:

$$h_{sg}(t, \varepsilon) = h_{e0} + \varepsilon h_{e1} + \varepsilon^2 h_{e2} + \dots \quad (7.17)$$

where h_{e0} , h_{e1} and h_{e2} are the 0th, 1st and 2nd order items, respectively. Substituting the (7.17) into (7.16), we obtain

$$\begin{aligned} & k_c C_{L1}^* V^2 e^{-\beta_r h_{e0}} \left\{ 1 - \beta_r [\varepsilon h_{e1} + \varepsilon^2 h_{e2} + \dots] \right. \\ & \left. + \beta_r^2 [\varepsilon h_{e1} + \varepsilon^2 h_{e2} + \dots]^2 / 2 + \dots \right\} - g + V^2/r \\ & = A_1 \varepsilon [\ddot{h}_{e0} + \varepsilon \ddot{h}_{e1} + \varepsilon^2 \ddot{h}_{e2} + \dots] + A_2 \varepsilon [\dot{h}_{e0} + \varepsilon \dot{h}_{e1} + \varepsilon^2 \dot{h}_{e2} + \dots] \end{aligned} \quad (7.18)$$

Hence, the 0th-order item is the altitude obtained by EGC, that is $h_{e0} = h_{eq}$, and the 1st and 2nd order items satisfy the following expressions,

$$-k_c C_{L1}^* V^2 e^{-\beta_r h_{e0}} \beta_r h_{e1} = A_1 \ddot{h}_{e0} + A_2 \dot{h}_{e0} \quad (7.19)$$

$$k_c C_{L1}^* V^2 e^{-\beta_r h_{e0}} (\beta_r^2 h_{e1}^2 / 2 - \beta_r h_{e2}) = A_1 \ddot{h}_{e1} + A_2 \dot{h}_{e1} \quad (7.20)$$

7.6.2.1 First-Order Item

Differentiating h_{e0} with respect to time, we obtain

$$\dot{h}_{e0} = \frac{1}{\beta_r} [f_a + f_V] \dot{V} \quad (7.21)$$

where f_a and f_V are the coefficients related to velocity,

$$f_a = (\partial C_{L1}^* / \partial V) / C_{L1}^*, f_V = 2g / (gV - V^3/r)$$

Further, the derivative of Eq. (7.21) with respect to time can be obtained,

$$\ddot{h}_{e0} = \frac{1}{\beta_r} [f_a + f_V] \ddot{V} + \frac{1}{\beta_r} \left[\frac{\partial f_a}{\partial V} + \frac{\partial f_V}{\partial V} \right] \dot{V}^2 \quad (7.22)$$

where $\partial f_a / \partial V$ and $\partial f_V / \partial V$ are the partial derivatives of f_a and f_V respectively. The first and second order derivatives of velocity are shown as follows:

$$\dot{V} = -f_K(g + a_e - V^2/r) - \frac{g}{V} \dot{h}_{e0} \quad (7.23)$$

$$\ddot{V} = \frac{2f_K V \dot{V}}{r} + (g + a_{e1} - V^2/r) \frac{\partial f_K}{\partial V} \dot{V} + (g/V^2) \dot{h}_{e0} \dot{V} - (g/V) \ddot{h}_{e0} \quad (7.24)$$

where, $\partial f_K / \partial V$ is the partial derivative of f_K . Substituting (7.21), (7.22) and (7.23) into (7.24), the 1st-order item is expressed as

$$h_{e1} = -\frac{A_1 \ddot{h}_{e0} + A_2 \dot{h}_{e0}}{(g - V^2/r) \beta_r} \quad (7.25)$$

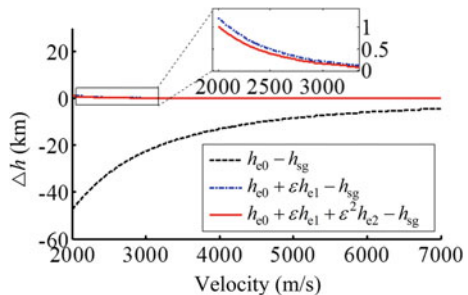
7.6.3 Second-Order Item

Differentiating h_{e1} with respect to time and substituting the results into (7.20), the 2nd-order item is obtained as follows:

$$h_{e2} = \frac{\beta_r h_{e1}^2}{2} - \frac{A_1 \ddot{h}_{e1} + A_2 \dot{h}_{e1}}{\beta_r (g - V^2/r)} \quad (7.26)$$

Figure 7.6 shows the altitude errors between the analytical and numerical steady glide altitudes. The maximum altitude error is up to 40 m only if the 0th-order item is taken into consideration, and it drops to 1 m if the 1st-order item is considered, while the 2nd-order item just decreases 0.2 m of the maximum altitude error. Therefore, only 0th-order and 1st-order item are needed in application.

Fig. 7.6 Accuracy of steady glide altitude analytical solutions in different orders



7.6.4 Analytical Solutions of Flight Path Angle and Vertical Acceleration

The analytical solutions of the steady glide flight path angle and vertical acceleration are expressed as follows:

$$\gamma_{sg} = \dot{h}_{sg}/V \quad (7.27)$$

$$a_{\varepsilon sg} = \frac{\ddot{h}_{sg} + (g - V^2/r)f_K\gamma_{sg}}{1 - f_K\gamma_{sg}} \quad (7.28)$$

where \dot{h}_{sg} and \ddot{h}_{sg} are the first and second order derivatives of steady glide altitude, respectively.

$$\dot{h}_{sg} = \dot{h}_{e0} + \varepsilon \dot{h}_{el} \quad \ddot{h}_{sg} = \ddot{h}_{e0} + \varepsilon \ddot{h}_{el} \quad (7.29)$$

If C_{L1}^* and f_K are constants and the effect of $g \sin \gamma$ is ignored, the (7.27) and (7.28) are simplified to

$$\gamma_{sg} = \frac{-2gf_K}{V^2\beta} \quad (7.30)$$

$$a_{\varepsilon sg} = \frac{4gf_K^2(g - V^2/r)}{V^2\beta_r} \quad (7.31)$$

Figures 7.7 and 7.8 show the analytical solutions of the steady glide flight path angle and vertical acceleration respectively. The AOA and bank angle profiles used in the simulation are shown in Table 7.2. ‘X’ represents the analytical solutions and the line represents the numerical solutions. We can see from the figure that the

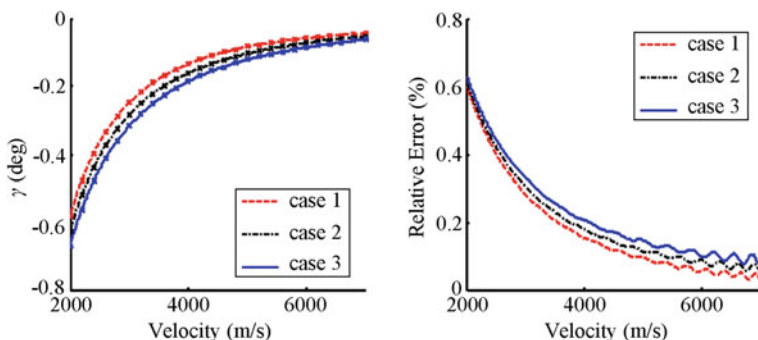


Fig. 7.7 Analytical solutions of steady glide flight path angle

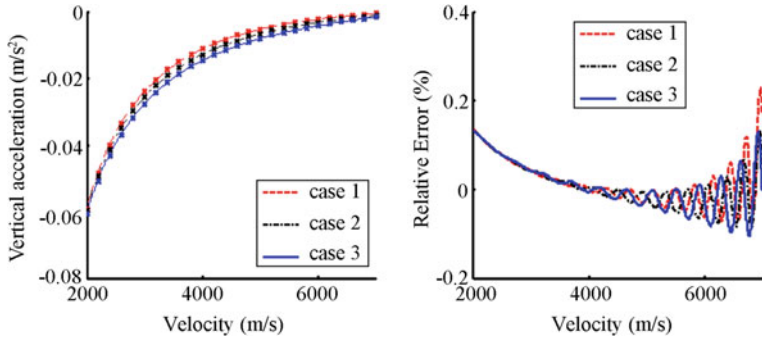


Fig. 7.8 Analytical solutions of steady glide longitudinal acceleration

Table 7.2 Curves of angle of attack and bank angle

Number	AOA ($^{\circ}$)	Bank angle ($^{\circ}$)
Case 1	$\alpha = 17 - 0.001V$	$\sigma = 0$
Case 2	$\alpha = 15$	$\sigma = 0$
Case 3	$\alpha = 8 + 0.001V$	$\sigma = 0$
Case 4	$\alpha = 15 + 5 \sin[0.0008\pi(V - 2000)]$	$\sigma = 0$

analytical and numerical solutions are quite approximate, and both of them increase with increasing velocity. The relative errors of the flight path angle are less than 1%, and the relative errors of the vertical acceleration are less than 2%.

Figure 7.9 compares the analytical solutions of steady glide flight path angle obtained by (7.30) with the solutions proposed by Ferreira [1] and Yu and Chen [13], in which $\Delta\gamma$ is the difference between the analytical solution and the flight-path angle of the steady glide trajectory obtained by the numerical method. The solutions of Ferreira deviate much from the numerical solutions, especially when the AOA is not a constant. This is because Ferreira ignores the effects of aerodynamic coefficients variation. The solutions of Yu are much closer to the numerical solution, while the solutions of this chapter are the most accurate. The reason is that Yu just obtained the 0th-order solution.

7.7 Dynamic Characteristics of SGT

7.7.1 Stability Analysis

In order to obtain SGT, the altitude and flight-path angle must meet Eqs. (7.17) and (7.30) respectively. All the initial state disturbances and interferences during the reentry lead to trajectory oscillations, as shown in Fig. 7.1. The altitude differences between the SGT and the other trajectories with the same AOA and bank angle is

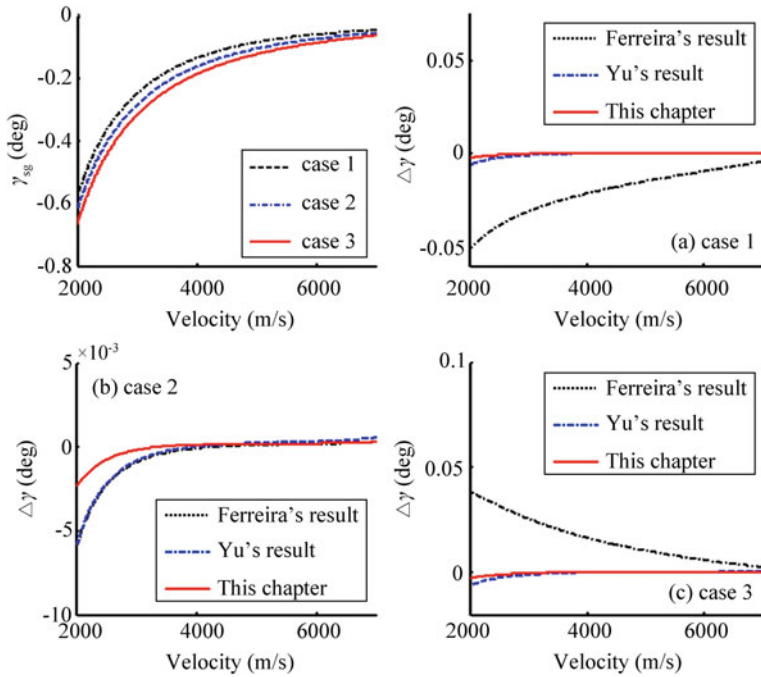


Fig. 7.9 Comparison of the accuracy for different analytical solutions

defined as follows:

$$\Delta h = h - h_{sg} \quad (7.32)$$

The dynamic characteristics of the SGT will be obtained by analyzing Δh . Substituting (7.32) into (7.10), we obtain

$$(\ddot{h}_{sg} + \Delta \ddot{h}) + \frac{f_K L_1^* e^{-\beta_r \Delta h}}{V} (\dot{h}_{sg} + \Delta \dot{h}) - L_1^* e^{-\beta_r \Delta h} + g - V^2/r = 0 \quad (7.33)$$

where L_1^* is the vertical lift acceleration of SGT and it can be expressed as

$$L_1^* = g + a_{esg} - V^2/r \quad (7.34)$$

Expanding $e^{-\beta_r \Delta h}$ by Taylor series in first order and ignoring the term of $\Delta h \Delta \dot{h}$, Eq. (7.33) is simplified to

$$\Delta \ddot{h} + \frac{f_K L_1^*}{V} \Delta \dot{h} - L_1^* \beta_r (1 - f_K \gamma_{sg}) \Delta h = 0 \quad (7.35)$$

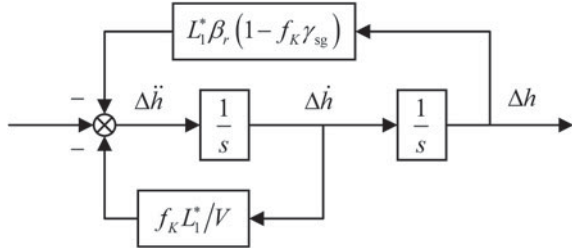


Fig. 7.10 Dynamic system structure of altitude error

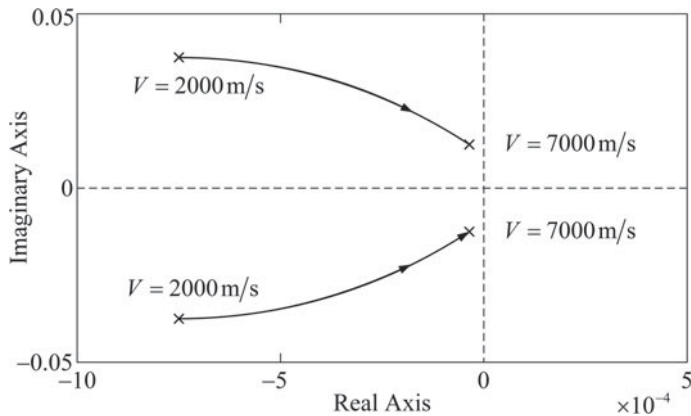


Fig. 7.11 Root loci of parameters V

Equation (7.35) is the second order linear differential equation of the altitude difference, where $L_1^* \beta_r (1 - f_K \gamma_{sg})$ and $f_K L_1^*/V$ are only velocity-dependent. Figures 7.10 and 7.11 gives the root loci of the parameter V , which shows that the root loci are on the left of the imaginary axis during the whole reentry process ($2000 \text{ m/s} < V < 7000 \text{ m/s}$), indicating that the system is stable. With the increase of velocity, the root locus gradually approach to the imaginary axis, and the stability of system decreases. That is to say, the higher the velocity, the easier the trajectory is to oscillate.

7.7.2 Natural Frequency and Damping

From (7.35), the natural frequency and damping of the open loop system are obtained by:

$$\omega_n = \sqrt{L_1^* \beta_r (1 - f_K \gamma_{sg})} \quad (7.36)$$

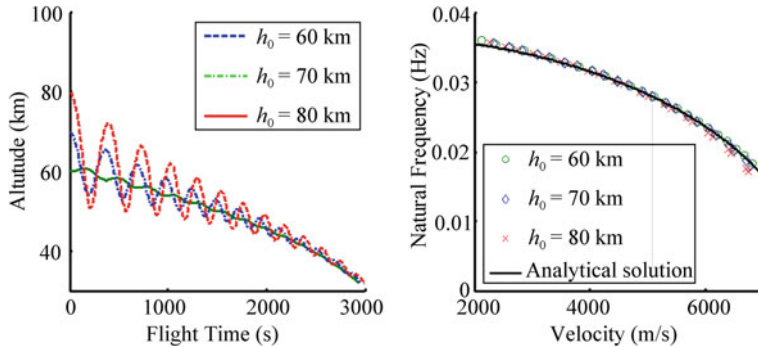


Fig. 7.12 The impact of the initial altitude on the natural frequency (fixed angle of attack)

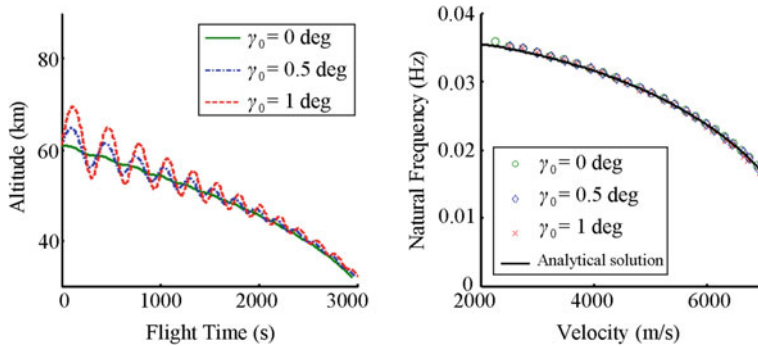


Fig. 7.13 The impact of the initial flight path angles on the natural frequency (fixed angle of attack)

$$\zeta = \frac{f_K L_1^*}{2V \sqrt{L_1^* \beta_r (1 - f_K \gamma_{sg})}} \quad (7.37)$$

Substituting (7.34) into (7.36) and (7.37), and ignoring a_{esg} and γ_{sg} , we obtain,

$$\omega_n = \sqrt{\beta_r (g - V^2/r)} \quad (7.38)$$

$$\zeta = \frac{f_K}{2} \sqrt{\frac{g/V^2 - 1/r}{\beta_r}} \quad (7.39)$$

As shown in (7.38) and (7.39), the natural frequency is only a function of velocity, while the damping depends on the velocity and vertical component of the lift to drag ratio.

Figures 7.12 and 7.13 show the natural frequency under different initial altitude and initial flight-path angle respectively, which was obtained in case 2. It can be seen

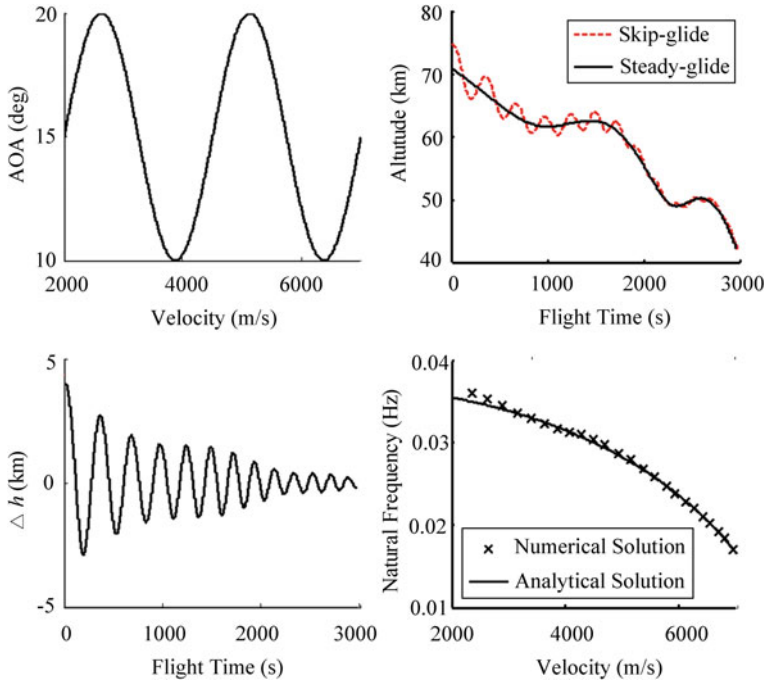


Fig. 7.14 The impact of angle of attack change on the natural frequency

that both of them have very little influence on the natural frequency, and the natural frequency obtained by the actual trajectory simulation almost exactly coincides with the analytical results given by Eq. (7.38). Figure 7.14 shows the impact of the AOA change on the natural frequency, and it can be seen that it has little influence on the natural frequency.

In Sect. 7.2, Harpold obtained the natural frequency of the reentry trajectory in the space shuttle reentry guidance law, which is rewritten as follows:

$$\begin{aligned} \omega_{n, \text{Harpold}}^2 = & 3\dot{D}_{ref} \left(\frac{\dot{D}_{ref}}{D_{ref}^2} - \frac{1}{V} \right) + \frac{4D_{ref}^2}{V^2} - \beta \left(\frac{V^2}{r} - g \right) \\ & - \frac{\ddot{D}_{ref}}{D_{ref}} - \frac{\dot{C}_{Dref}^2}{C_{Dref}^2} + \frac{\ddot{C}_{Dref}}{C_{Dref}} \end{aligned} \quad (7.40)$$

where D_{ref} is reference drag. Figure 7.15 compares the analytical solution of the natural frequency in this chapter with the result obtained by Harpold. They are almost the same, and coincide with the actual situation, but the result given in this chapter is more concise.

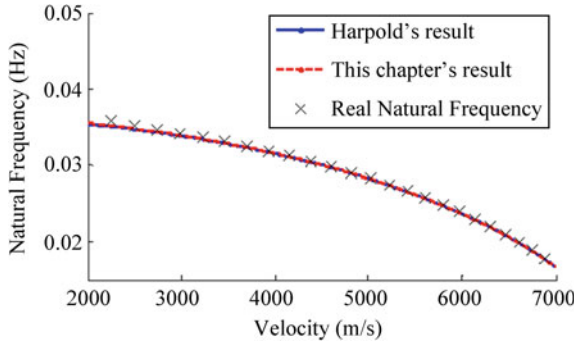


Fig. 7.15 The natural frequencies obtained by different methods

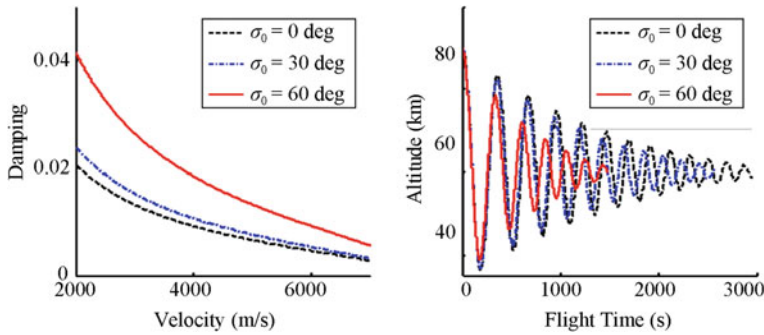


Fig. 7.16 Damping curves

Figure 7.16 shows the damping curves obtained by (7.39). The damping for $\sigma = 60^\circ$ is twice as large as the damping for $\sigma = 0^\circ$, and the corresponding altitude error also converges twice as fast, which verifies (7.39).

7.8 Feedback Control of SGT

7.8.1 Feedback Design

Because the damping of the reentry trajectory is very small, trajectory oscillations deviating from the SGT are difficult to converge. In order to improve the convergence rates of the trajectory oscillation, the pole assignment is required for the dynamic system given by (7.35).

The differential feedback and proportion feedback are the commonly used method in traditional reentry guidance. Substituting the above feedbacks into (7.35), we obtain,

$$\Delta \ddot{h} + \frac{f_K L_1^*}{V} \Delta \dot{h} + L_1^* \beta_r \left(\frac{\cos \sigma}{\cos \sigma_c} - f_K \gamma_{sg} \right) \Delta h = -k_1 \Delta h - k_2 \Delta \dot{h} \quad (7.41)$$

where k_1 and k_2 are the proportional and differential feedback coefficients respectively; σ_c is the desired bank angle; σ is the real bank angle and is given by,

$$\cos \sigma = [1 - (k_1 \Delta h + k_2 \Delta \dot{h}) / L_1^*] \cos \sigma_c \quad (7.42)$$

Figure 7.17 shows the impact of k_1 and k_2 on the parameter root locus. k_1 makes the root locus move up or down, and mainly impacts the natural frequency. k_2 makes them move left or right, and mainly impact the damping. Besides, when $k_1 = 0$, changing k_2 can also make the root locus significantly away from the imaginary axis and significantly change the damping of the system; the increasing of k_1 will reduce the damping growth with k_2 ; changing k_1 will not change the relative position of the root locus and the imaginary axis, but will reduce the damping of the system.

Figure 7.18 compares the additional vertical acceleration of the proportional feedback and differential feedback. The additional vertical acceleration of the differential feedback is much less than that of the proportional feedback when $k_1 = k_2$. Figures 7.19, 7.20 and 7.21 compare the different feedback schemes. It can be seen from Fig. 7.19 that, under tilting inversion (small disturbance), the trajectory will

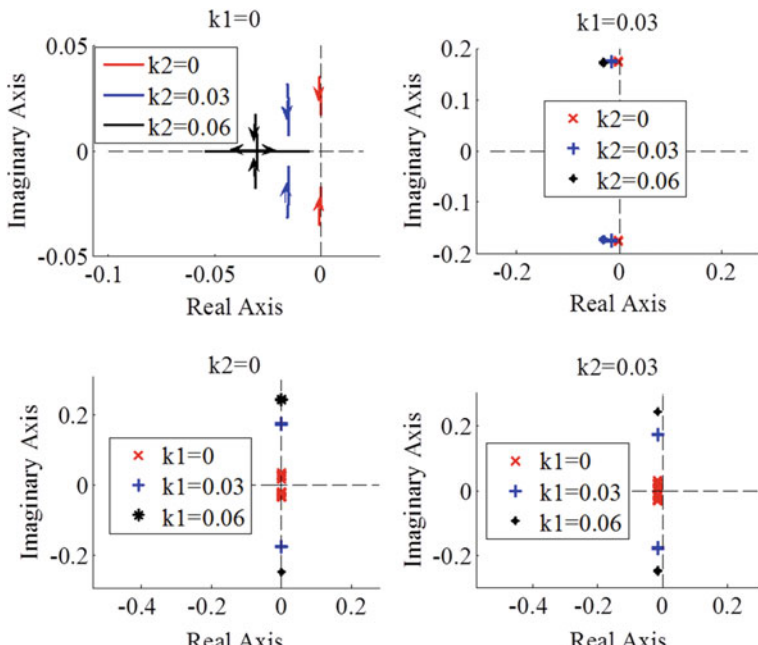


Fig. 7.17 The impact of k_1 and k_2 on the parameter root locus

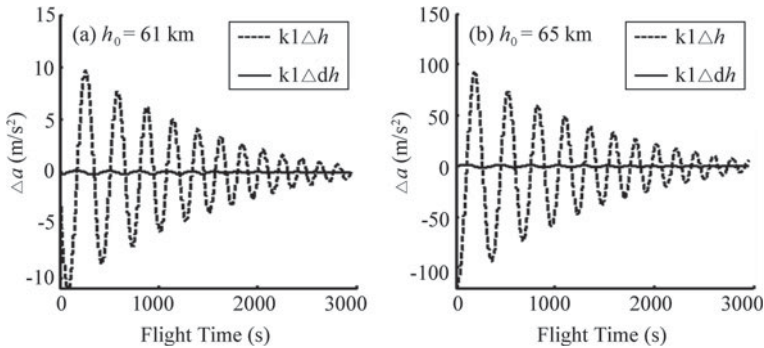
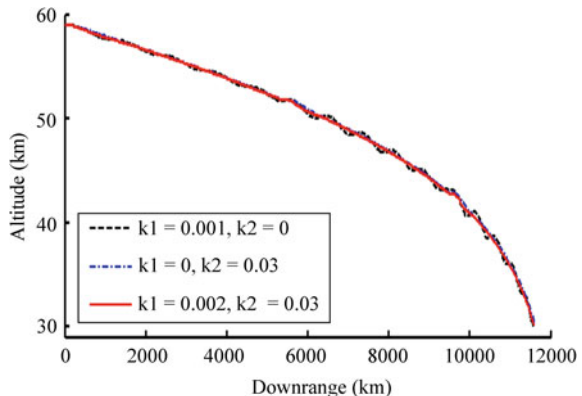


Fig. 7.18 Comparison of the control increments

Fig. 7.19 The impact of the feedback coefficients on glide trajectories (small perturbation)



oscillate near the SGT altitude. According to Figs. 7.20 and 7.21, when $k_2 = 0$, the altitude difference hardly converges, and the bank angle oscillates violently. When $k_2 = 0.03$, the altitude difference quickly converges to zero, and the bank angle also quickly converges to the expected value. Figure 7.22 further analyzes the influence of k_1 . It can be seen that the convergence speed of the trajectory is almost the same when $k_1 = 0$ and 0.001, but the bank angle changes more gently if $k_1 = 0$.

In general, the proportional feedback cannot accelerate the convergence speed of trajectory oscillation while large additional vertical acceleration is required. Hence, the pure differential feedback is the best feedback control scheme of STG. This scheme is called trajectory damping control (TDC), which was proposed by Phillips [3] first and used in the guidance algorithm of guided cartridge for range maximization. Yu and Chen [13] proposed the TDC for hypersonic gliding problem and gave the flight-path angle of the steady glide trajectory corresponding to the maximum L/D. Xu et al. [15] applied it to the reentry predictive guidance law of high L/D aircraft. In this chapter, the theoretical basis of trajectory damping control is further analyzed.

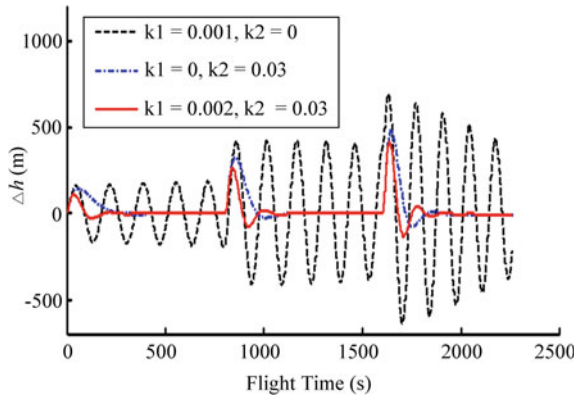


Fig. 7.20 The impact of the feedback coefficients on delta altitude (small perturbation)

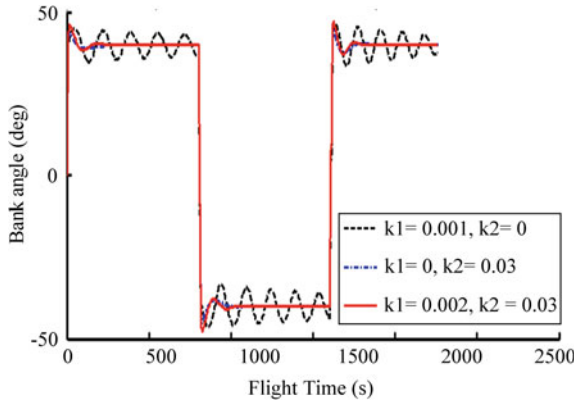


Fig. 7.21 The impact of the feedback coefficients on bank angles (small perturbation)

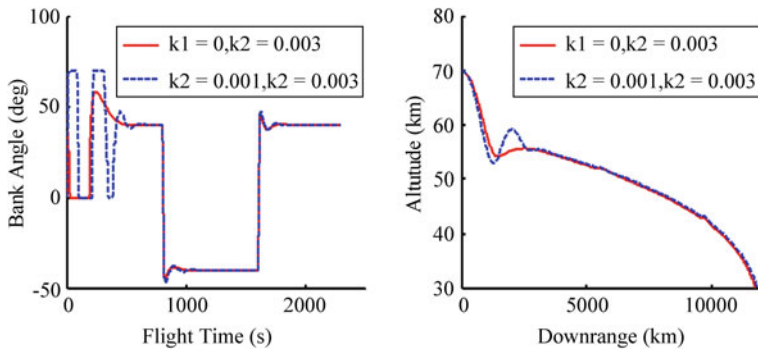


Fig. 7.22 The impact of the k_1 (large perturbation)

7.8.2 Fixed-Damping Differential Feedback Method

If the damping is between 0.4 and 0.8, the regulating time is short and the overshoot is low. But the damping of the dynamic system given by (7.41) changes a lot if k_2 is a constant. In order to obtain a fixed damping, k_2 is expressed as follows,

$$k_2 = -\left(f_K L_1^*/V + 2\zeta_c^2 \beta_r V \Delta\gamma \right) \\ + \sqrt{4\zeta_c^2 \beta_r [\zeta_c^2 \beta_r V^2 \Delta\gamma^2 + L_1^* + f_K L_1^*(\Delta\gamma - \gamma_{sg})]} \quad (7.43)$$

where ζ_c is the desired damping and its value usually is 0.707. Substituting (7.43) into (7.42), then we can obtained the desired bank angle to suppress the trajectory oscillation. If the bank angle exceeds the feasible range, the desired control increment is obtained by adjusting the AOA.

Figure 7.23 shows the trajectory of glide segment obtained by using fixed-damped differential feedback with initial state deviation, and the residual range is shown in the figure. It can be seen that, no matter what the initial state is, the trajectory rapidly converges to steady glide under the action of fixed-damping differential feedback.

Further, the fixed-damping differential feedback method (FDDFM) is applied to the guidance of the initial descent phase. In the simulation, the velocity, altitude and flight-path angle of the initial descent phase's starting and ending points are all given and the cost function of the pseudospectral method is to maximum range. As can be seen from Fig. 7.24, the AOA curve obtained by the fixed-damping differential feedback method is relatively smooth, and the maximum AOA is maintained at the stage of rapid height descent of the initial descent phase, so as to greatly reduce the maximum heating rate of the initial descent phase, which is shown in Fig. 7.26. It can be seen form Fig. 7.25 that the trajectory of the initial descent phase obtained by the fixed-damping differential feedback method is smoother, but the range is slightly smaller than that obtained by the pseudospectral method. Figure 7.27 compares the maximum heating rates obtained by fixed-damping derivative feedback method with

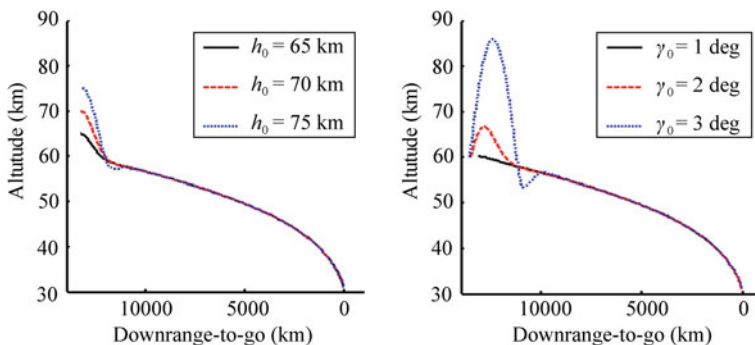
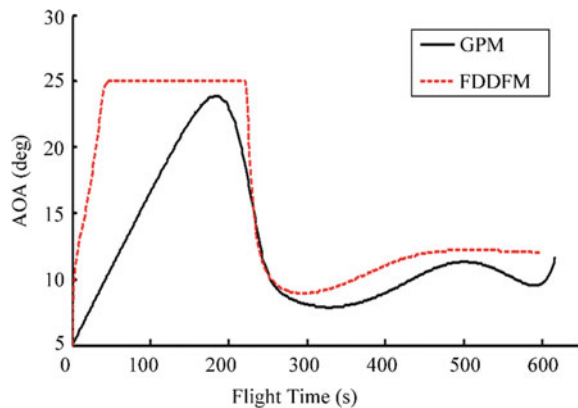


Fig. 7.23 Steady glide trajectories with initial errors

Fig. 7.24 Angle of attack histories of the initial descent phase



that obtained by maximum Angle of attack. It can be seen that they are highly coincident when the maximum heating rates is large. Therefore, fixed-damping derivative feedback method can satisfy the constraints of the maximum heating rates. Moreover, the unification of the guidance control method of the initial descent phase and glide phase is realized.

Figures 7.28 and 7.29 show the simulation results of the induced section and the gliding section based on the fixed-damping differential feedback method. It can be seen from Fig. 7.28 that after the adjustment of the initial descent phase, both the Angle of attack and the bank angle quickly converge to the desired value. Besides, the reentry trajectory only has a “valley” due to insufficient aerodynamics of the aircraft in the initial descent phase, and the subsequent glide phase trajectory is very smooth. The heat rate is decreasing after the “valley” peaks, which can meet the constraints.

Fig. 7.25 Trajectories of the initial descent phase

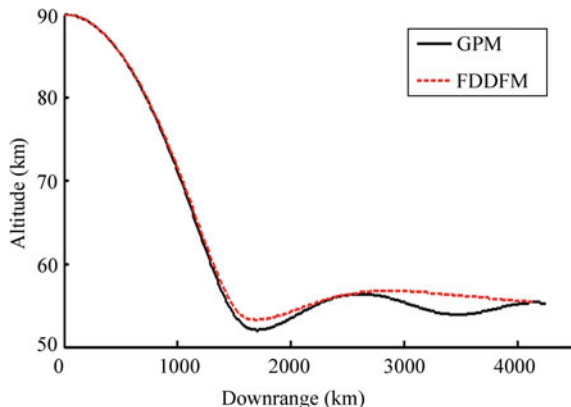


Fig. 7.26 Heating rate histories of the initial descent phase

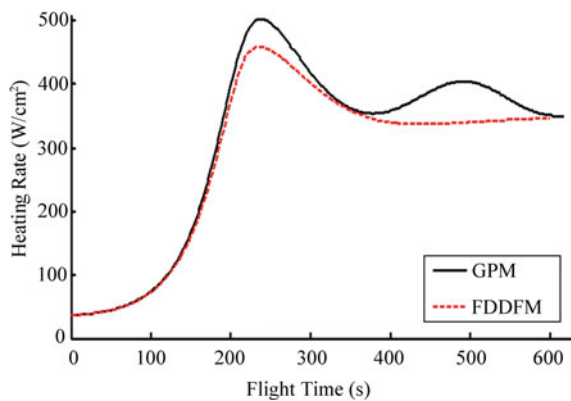


Fig. 7.27 Comparison of the maximum heating rates

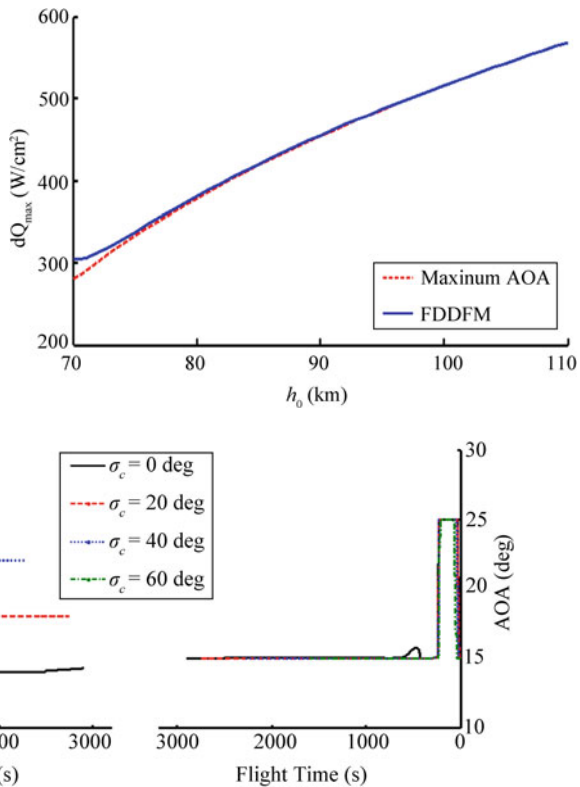


Fig. 7.28 Bank angle histories and angle of attack histories

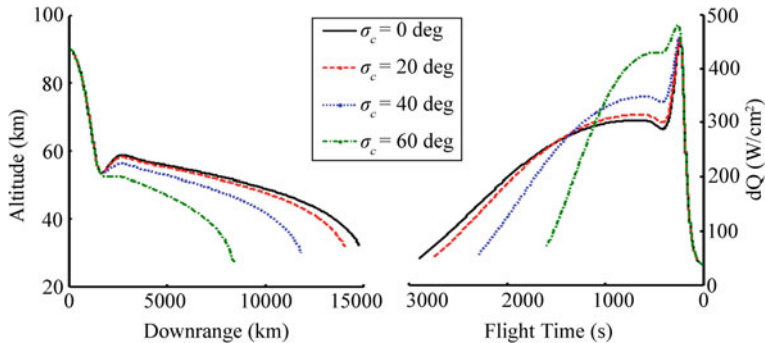


Fig. 7.29 Reentry trajectories and heating rate histories

7.9 Conclusions

In this chapter, the steady glide reentry trajectory is analyzed, and the major contributions are summarized as follows:

1. For a given continuously differentiable AOA and bank angle profiles, the SGT is objective existence, and all the trajectories of the vehicles with different initial conditions will converge to the SGT if the vehicles follow the same baseline AOA and bank angle profiles and are under the control of the FDDFM.
2. Using regular perturbation scheme, the analytical solutions of the SGT are obtained for altitude, flight path angle and vertical acceleration. Thus, it is feasible to obtain the SGT directly.
3. The SGT has natural stability, where the natural frequency is only the function of velocity, and the damping is affected by the vertical component of the lift to drag ratio.
4. As the natural frequency of the SGT is very small, the proportional feedback cannot damp the trajectory oscillation obviously, while large feedback acceleration is required. However, the differential feedback can make it converge quickly with little feedback acceleration. As a result, the pure proportional feedback is the best scheme to restrain the reentry glide trajectory oscillation.
5. The FDDFM is a simple and efficient method for the vertical control of the initial descent phase and glide phase.

References

1. Ferreira, L.O.: Nonlinear dynamics and stability of hypersonic reentry vehicles. University of Michigan, Michigan (1995)
2. Harpold, J.C., Graves, C.A.: Shuttle entry guidance. *J. Astronaut. Sci.* **37**(3), 239–268 (1979)
3. Phillips, C.A.: Guidance algorithm for range maximization and time-of-flight control of a guided projectile. *J. Guidance Control Dyn.* **31**(5), 1447–1455 (2008)

4. Mease, K.D., Chen, D.T., Schönenberger, H.: Reduced-order entry trajectory planning for acceleration guidance. *J. Guidance, Control Dyn.* **25**(2), 257–266 (2002)
5. Hao, Z., Wanchun, C., Xingliang, Y.: Optimization of glide trajectory for a hypersonic vehicle. *J. Beijing Univ. Aeronautics Astronaut.* **32**(5), 513–517 (2006) (in Chinese)
6. Jorris, T.R., Cobb, R.G.: Three-dimensional trajectory optimization satisfying waypoint and no-fly zone constraints. *J. Guidance, Control Dyn.* **32**(2), 551–572 (2009)
7. Chapman, D.R.: An approximate analytical method for studying entry into planetary atmospheres. *NASA TR-R-11* (1959)
8. Wingrove, R.C.: A study of guidance to reference trajectories for lifting re-entry at supercircular velocity. *NASA TR-151* (1963)
9. Etkin, B.: Longitudinal dynamics of a lifting vehicle in orbital flight. *J. Aerospace Sci.* **28**(2), 779–788 (1961)
10. Bell, B.N.: A closed-form solution to lifting reentry. *AFFDL-TR-65-65*
11. Yu, W., Chen, W.: Entry guidance with real-time planning of reference based on analytical solutions. *Adv. Space Res.* **55**, 2325–2345 (2015)
12. Shen, Z., Lu, P.: Onboard generation of three-dimensional constrained entry trajectories. *J. Guidance, Control Dyn.* **26**(1), 111–121 (2003)
13. Yu, W., Chen, W.: Guidance scheme for glide range maximization of a hypersonic vehicle. In: *AIAA Paper*, pp. 2011–6714 (2011)
14. Zhang, K., Chen, W.: Constrained trajectory optimization. In: *AIAA*, pp. 2011–2231 (2011)
15. Mingliang, Xu., Kejun, C., Luhua, L., et al.: Quasi-equilibrium glide adaptive guidance for hypersonic vehicles. *Sci. China Tech. Sci.* **42**(4), 378–387 (2012) (in Chinese)

Chapter 8

Analytical Solutions of Steady Glide Reentry Trajectory in Three Dimensions and Their Application to Trajectory Planning



8.1 Introduction

Hypersonic vehicle ($Ma \geq 5$) has the advantages of long range, strong survivability and great destruction, and it has become a worldwide research hotspot. Glide trajectory programming technology is one of the key techniques in hypersonic vehicles research. Analytical solution of glide trajectory can not only help planning steady glide trajectory rapidly, but also be used for online predictive guidance, which is of great significance.

As far as 1950s, there has been research on analytical solution of glide trajectory. Chapman [1] firstly gave the approximate analytical solution of the reentry trajectory under the assuming of fixed lift-to-drag ratio (L/D). Further, Loh [2] analyzed the approximate analytical solution of the reentry trajectory when the lift-to-drag ratio is not a constant. Shi [3] and Naidu [4] solved the longitudinal and three-dimensional glide trajectory analytically by matching progressive progress, but their accuracy is low in the case of large range. Vinh [5] proposed the analytical solution of equilibrium glide longitudinal trajectory analysis under fixed lift-to-drag ratio (L/D) assumption, which has higher accuracy. Bell [6] further gave the equilibrium glide three-dimensional trajectory under the assumption of fixed lift-to-drag ratio (L/D) and fixed bank angle, but it has a non-negligible error when the lateral maneuver range is large.

Since 1970s, with the advancing of the lateral maneuver strategy of tilting and flipping, the high-accuracy analytical solution of longitudinal trajectory has become the focus of development. Harplod [7] proposed to program longitudinal reentry trajectory with D-V profile, and gave analytical solutions of altitude, first derivative of altitude and range. Zhang [8] proposed the analytical solution of the altitude, flight-path angle and bank angle with the fixed heating rate, aerodynamic load, or dynamic pressure constraints, respectively. Yu [9] gave the analytical solution of the flight-path angle of the fixed lift-to-drag ratio (L/D) trajectory under equilibrium gliding conditions. Li [10] gave the analytical solution of altitude, flight-path angle,

flight time and range of the maximum lift-to-drag ratio (L/D) trajectory under equilibrium gliding conditions; Guo [11] and Xu [12] proposed the longitudinal ballistic analytical solution under the condition of constant flight-path angle.

In the twenty-first century, with the improvement of the lateral maneuverability of the reentry vehicle and the maneuvering penetration, the rapid solution of the three-dimensional (3D) glide trajectory has become a research hotspot. Mease et al. [13] derived the reduced-order reentry equation, and proposed two fast trajectory programming algorithms by the combination of drag acceleration and lateral acceleration, which extended the two-dimensional reentry trajectory of the space shuttle to three-dimensional. Shen [14] programmed glide trajectory rapidly by the dip angle corridor. Rahman and Zhou [15, 16] directly program the geometric trajectory through the Bezier curve and meet the constraints by adjusting the control parameters of the curve. However, all the above methods require ballistic integration, and the calculated quantity is large.

In response to this shortcoming, a kind of analytical solving method for the three-dimensional (3D) steady glide trajectory was proposed. Firstly, kinematic equations of glide phase is decoupled by separating lift coefficient. After that, the altitude, range, head angle, longitude, latitude and velocity are obtained by analytical integral, regular perturbation, Gaussian integral and Runge-Kutta method. Finally, the proposed analytical solution is applied to rapid steady glide trajectory programming.

8.2 Mathematical Model

8.2.1 *Definition of Coordinate Frame*

In this chapter, it is assumed that Earth does not rotate, and a general equator is introduced as shown in Fig. 8.1 for theoretical analysis. The vehicle moves near the general equator. In addition, we need to define two coordinate systems, as shown in Fig. 8.1.

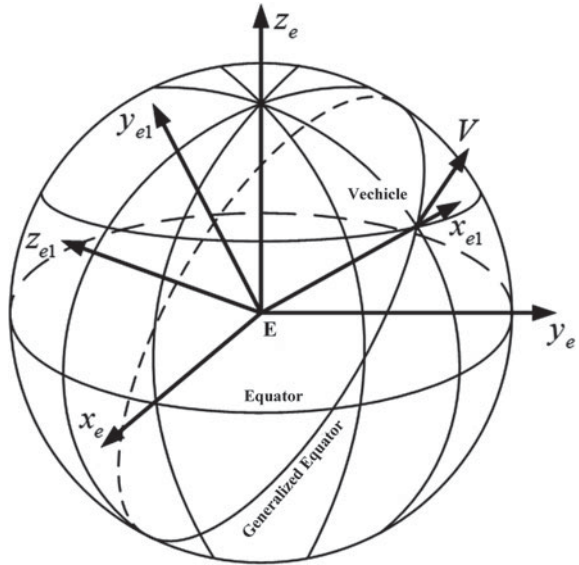
Local Geocentric frame: the origin is at Earth center, x_{e1} axis point from the Earth's center to the vehicle; y_{e1} axis is in the plane formed by x_{e1} and V ; and z_{e1} axis which conforms to the right hand rule is perpendicular to x_{e1} and y_{e1} .

Geocentric Equatorial Rotating (GER) frame: the origin is also at Earth center; z_e axis is along the north polar axis; x_e axis and y_e axis are perpendicular to each other in the equatorial plane.

8.2.2 *Kinematic Equations*

A dynamic model of the hypersonic vehicle in the local geocentric coordinate frame which is simple for analytical calculating is established. The equations over the

Fig. 8.1 Generalized equator and coordinate definition



non-rotating spherical Earth are expressed as

$$\dot{h} = V \sin \gamma \quad (8.1)$$

$$\dot{s} = R_0 V \cos \gamma / r \quad (8.2)$$

$$\dot{\theta} = V \cos \gamma \sin \psi / (r \cos \phi) \quad (8.3)$$

$$\dot{\phi} = V \cos \gamma \cos \psi / r \quad (8.4)$$

$$\dot{V} = -D/m - g \sin \gamma \quad (8.5)$$

$$\dot{\gamma} = \frac{1}{V} \left[\frac{L \cos \sigma}{m} + \left(\frac{V^2}{r} - g \right) \cos \gamma \right] \quad (8.6)$$

$$\dot{\psi} = \frac{1}{V} \left[\frac{L \sin \sigma}{m \cos \gamma} + \frac{V^2}{r} \cos \gamma \sin \psi \tan \phi \right] \quad (8.7)$$

where h is the altitude, S is the range, θ and ϕ are longitude and latitude respectively, V is the velocity relative to the non-rotating Earth, γ , ψ and σ are flight-path angle, heading angle and bank angle respectively; r is the radial distance from Earth center to the vehicle, $r = R_0 + h$, where R_0 is Earth radius; m is the mass; g is the local

gravitational acceleration, which can be expressed as $g = \mu/r^2$; L and D are the lift and drag respectively, given by

$$L = \frac{1}{2}\rho V^2 S C_L \quad D = \frac{1}{2}\rho V^2 S C_D \quad (8.8)$$

where ρ is the atmospheric density, S is reference area, C_L is lift coefficient and C_D is the drag coefficient.

8.2.3 Decoupling of Equations

In order to simplify the solution of the glide trajectory, the lift coefficient is separated into

$$C_L \cos \sigma = C_{N0} + C_{N1} \quad C_L \sin \sigma = C_Y \quad (8.9)$$

where C_Y is the lateral component of lift coefficient, C_{N1} is the vertical maneuver component of lift coefficient, C_{N0} is the vertical equilibrium glide component of lift coefficient, which satisfy

$$C_{N0} = \frac{2m(\mu/r^2 - V/r^2) \cos \gamma}{\rho V^2 S} \quad (8.10)$$

In the local geocentric coordinate frame, flight path angle and latitude approximately satisfy the following relationship

$$\gamma \approx 0 \quad \phi \approx 0 \quad (8.11)$$

Further, assuming a monotonous γ during the reentry, Eqs. (8.1)–(8.7) can be rewritten as

$$\frac{dh}{d\gamma} = \frac{2m \sin \gamma}{\rho S C_{N1}} \quad (8.12)$$

$$\frac{ds}{d\gamma} = \frac{2m R_0}{\rho S C_{N1} r} \quad (8.13)$$

$$\frac{d\psi}{d\gamma} \approx \frac{C_Y}{C_{N1}} + \frac{2m}{\rho S C_{N1} r} \phi \quad (8.14)$$

$$\frac{d\phi}{d\gamma} = \frac{2m}{\rho S C_{N1} r} \cos \psi \quad (8.15)$$

$$\frac{d\theta}{d\gamma} = \frac{2m}{\rho SC_{N1}r} \sin \psi \quad (8.16)$$

$$\frac{dV}{d\gamma} = -V \frac{C_D}{C_{N1}} - \frac{2mg \sin \gamma}{\rho V S C_{N1}} \quad (8.17)$$

It can be seen from Eqs. (8.12) to (8.17) that after separating the vertical lift coefficient, the vertical motion equation is completely decoupled from the lateral motion equation and velocity and the lateral motion is also decoupled from the velocity, which is beneficial to obtain analytical solutions.

8.3 Analytical Solution of Glide Trajectory

In local geocentric coordinate frame, the initial altitude, velocity, heading angle and range of the i -th phase glide trajectory are h_{i0} , V_{i0} , $\pi/2$ and 0 respectively. The initial and final flight-path angle are γ_{i0} and γ_{if} . Then the analytical solutions of this phase can be expressed as following sections.

8.3.1 Analytical Solution of Altitude

Supposing C_{N1} is a constant and integrating the high-order differential equation which was shown in (8.12), the following equation can be obtained

$$\cos \gamma_{if} - \cos \gamma_{i0} = \frac{SC_{N1}}{2m\beta_r} (\rho_{if} - \rho_{i0}) \quad (8.18)$$

where ρ_{i0} and ρ_{if} are the initial and final density of the i th phase, respectively, which can be expressed as

$$\rho_{i0} = \rho_0 e^{-\beta_r h_{i0}} \quad \rho_{if} = \rho_0 e^{-\beta_r h_{if}} \quad (8.19)$$

where ρ_0 is the sea-level atmospheric density; β_r is a constant and with value $1.389 \times 10^{-4} \text{ m}^{-1}$. Substituting (8.19) into (8.18) gives

$$h_{if} = -\frac{1}{\beta_r} \ln \left[\frac{2m\beta_r}{SC_{N1}\rho_0} (K^* + \cos \gamma_{if}) \right] \quad (8.20)$$

where $K^* = SC_{N1}\rho_{i0}/2m\beta_r - \cos \gamma_{i0}$ is the longitudinal maneuver constant, and its absolute value is usually greater than 1 in gliding case.

8.3.2 Analytical Solution of Range

Substituting (8.20) into (8.12), we obtain:

$$\beta_r r ds = \frac{R_0}{\cos \gamma + K^*} d\gamma \quad (8.21)$$

Introducing the average radial distance from Earth center to the vehicle which is defined as $\bar{r} = (2R_0 + h_0 + h)/2$. Integrating the above equation gives

$$\beta_r \bar{r} s_{if} = \frac{2R_0}{1 + K^*} \sqrt{\frac{K^* + 1}{K^* - 1}} (A_1 - A_2) \quad (8.22)$$

where

$$A_1 = \arctan\left(\sqrt{\frac{K^*-1}{K^*+1}} \tan \frac{\gamma_{i0}}{2}\right) \quad A_2 = \arctan\left(\sqrt{\frac{K^*-1}{K^*+1}} \tan \frac{\gamma_{i0}}{2}\right) \quad (8.23)$$

and s_{if} is the range of the i th phase glide trajectory.

8.3.3 Analytical Solution of Heading Angle

Substituting (8.20) into (8.14), we obtain:

$$\frac{d\psi}{d\gamma} = \frac{C_Y}{C_{N1}} + \frac{\phi}{\bar{r}\beta_r(\cos \gamma + K^*)} \quad (8.24)$$

There is also a coupling between ψ and ϕ in Eq. (8.24), which makes it difficult to integrate directly. Considering $C_Y/C_{N1} \gg \phi/[\bar{r}\beta_r(\cos \gamma + K^*)]$, the regular perturbation method can be used. Ignoring the effect of ϕ , then the zero-order estimate of ψ is,

$$\psi^{(0)} = \pi/2 + (C_Y/C_{N1})(\gamma - \gamma_{i0}) \quad (8.25)$$

Substituting (8.20) into the first equation in (8.15), assuming $K^* + 1 \approx 0$ and $\cos \psi \approx \pi/2 - \psi$, we obtain

$$\frac{d\phi}{d\gamma} = \frac{K_1(\gamma - \gamma_{i0})}{\gamma^2} \quad (8.26)$$

where $K_1 = 2C_Y/(\bar{r}\beta_r C_{N1})$. Integrating above equations, the zero-order estimate of ϕ is obtained as follows:

$$\phi^{(0)} = K_1 \ln \frac{\gamma}{\gamma_{i0}} + K_1 \left(\frac{\gamma_{i0}}{\gamma} - 1 \right) \quad (8.27)$$

The differential equation of the 1st-order item obtained by Eqs. (8.27) and (8.24) is given as follows:

$$\frac{d\psi^{(1)}}{d\gamma} = -\frac{K_2}{\gamma^2} \ln \frac{\gamma}{\gamma_{i0}} - K_2 \left(\frac{\gamma_{i0}}{\gamma^3} - \frac{1}{\gamma^2} \right) \quad (8.28)$$

where $K_2 = 2K_1 / (\bar{r}\beta_r)$. Integrating the above equation, we obtain

$$\psi^{(1)} = -K_2 \left(\frac{1}{2\gamma_{i0}} + \frac{1}{\gamma} \ln \frac{\gamma_{i0}}{\gamma} - \frac{\gamma_{i0}}{2\gamma^2} \right) \quad (8.29)$$

Thus the estimated value of the final heading angle is obtained as follows:

$$\psi_{if} = \pi/2 + (C_Y/C_{N1})(\gamma_{if} - \gamma_{i0}) - K_2 \left(\frac{1}{2\gamma_{i0}} + \frac{1}{\gamma_{if}} \ln \frac{\gamma_{i0}}{\gamma_{if}} - \frac{\gamma_{i0}}{2\gamma_{if}^2} \right) \quad (8.30)$$

8.3.4 Analytical Solution of Longitude and Latitude

Substituting (8.20) into (8.15) and (8.16), we obtain

$$\frac{d\phi}{d\gamma} = \frac{1}{\bar{r}\beta_r(\cos\gamma + K^*)} \cos\psi \quad (8.33)$$

$$\frac{d\theta}{d\gamma} = \frac{1}{\bar{r}\beta_r(\cos\gamma + K^*)} \sin\psi \quad (8.34)$$

For hypersonic vehicles with strong lateral maneuverability, ψ may change significantly in the gliding phase. If only the first-order expansion of $\cos\psi$ and $\sin\psi$ are considered, there will be a large error. Therefore, the Gaussian integral formula will be used to estimate the final longitude and latitude, as follows:

$$\phi_{if} = \frac{\gamma_{if} - \gamma_{i0}}{2} \sum_{j=1}^n A_j \dot{\phi}(\gamma_j) \quad (8.35)$$

$$\theta_{if} = \frac{\gamma_{if} - \gamma_{i0}}{2} \sum_{j=1}^n A_j \dot{\theta}(\gamma_j) \quad (8.36)$$

where, $\dot{\phi} = d\phi/d\gamma$; $\dot{\theta} = d\theta/d\gamma$ and γ_j is the j th Gaussian node in $[\gamma_{i0}, \gamma_{if}]$; A_j is the Gaussian quadrature coefficient.

8.3.5 Analytical Solution of Velocity

Substituting (8.20) into (8.17), we obtain

$$\frac{dw}{d\gamma} = -\frac{C_D}{C_{N1}} - \frac{g \sin \gamma}{e^{2w} \beta_r (K^* + \cos \gamma)} \quad (8.37)$$

where e is natural constant, and $w = \ln V$. In the above equation, γ is a small amount, and the change of C_D is small, so Runge-Kutta method can be used to solve the final velocity. We define

$$f_K(w, s) = -\frac{C_D}{C_{N1}} - \frac{g \sin \gamma}{e^{2w} \beta_r (K^* + \cos \gamma)} \quad (8.38)$$

where C_D can be obtained by interpolation of C_L and w , and the expression of C_L is

$$C_L = \sqrt{\left[C_{N1} + \frac{C_{N1}(\mu e^{-2w}/r - 1)}{r \beta_r (K^* + \cos \gamma)} \right]^2 + C_Y^2} \quad (8.39)$$

So we can obtain

$$w_{if} - w_{i0} = \frac{\Delta \gamma}{6} (k_1 + 2k_2 + 2k_3 + k_4) \quad (8.40)$$

where

$$\begin{aligned} k_1 &= f_K(w_{i0}, \gamma_{i0}) \\ k_2 &= f_K(w_{i0} + k_1 \Delta \gamma / 2, \gamma_{i0} / 2 + \gamma_{if} / 2) \\ k_3 &= f_K(w_{i0} + k_2 \Delta \gamma / 2, \gamma_{i0} / 2 + \gamma_{if} / 2) \\ k_4 &= f_K(w_{i0} + k_2 \Delta \gamma, \gamma_{if}) \end{aligned}$$

and $\Delta \gamma = \gamma_{if} - \gamma_{i0}$. Then, the estimated value of the final velocity is obtained as follows:

$$V_{if} = e^{w_{if}} \quad (8.41)$$

Table 8.1 Simulation parameters

Parameter	h_0 (km)	s_0 (km)	θ_0 (deg)	ϕ_0 (deg)	ψ_0 (deg)
Value	60	0	0	0	$\pi/2$
Parameter	V_0 (m/s)	γ_0 (deg)	h_f (km)	C_{N1}	C_Y
Value	7000	-0.0684	30	-0.0011	0.4

8.3.6 Optimal Initial Glide Angle

Known from the theory of steady glide trajectory programming [17], a suitable initial flight-path angle will make the control law of the entire glide phase more stable. Therefore, the initial angle of attack takes a steady glide flight-path angle

$$\gamma_0 = \frac{2g}{V_0 \beta_h K_{N0}} \quad (8.42)$$

where V_0 is the initial velocity of glide phase; K_{N0} is the initial vertical lift-drag ratio (L/D) of glide phase.

8.4 Simulation

8.4.1 Comparison Between Analytical Solution and Numerical Integral

In order to test the accuracy of the analytical solution, CAV-H [18] is used for simulation. The simulation parameters are shown in Table 8.1. Figures 8.2, 8.3 and 8.4 compares the analytical solution and the numerical solution of velocity, longitudinal trajectory and lateral trajectory. It can be seen that the proposed analytical solution has high accuracy. The analytical solution of the longitudinal trajectory is almost completely coincident with the numerical solution, while the analytical solutions of the lateral trajectory and velocity have a small deviation from the numerical solution, and the errors increase with the range.

8.4.2 Comparison with Bell Analytical Solution

Furthermore, the proposed analytical solution is compared with Bell analytical solution. The initial conditions are the same as those in Table 8.1, and the final velocity is set to 2000 m/s, the lateral lift coefficient is gradually increased from 0 to 0.7, and the stepwise method is used to predict the final states. The results are shown in Figs. 8.5,

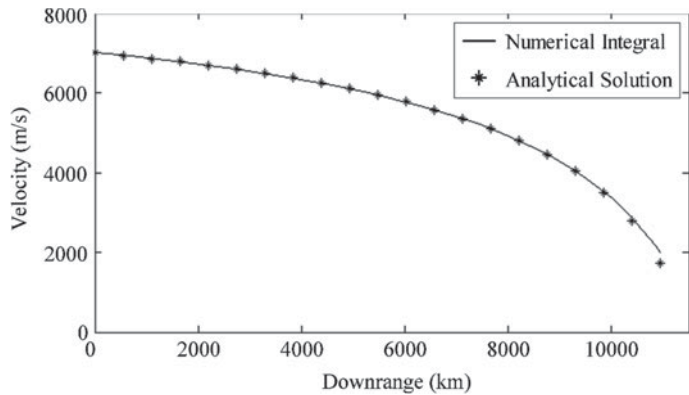


Fig. 8.2 Velocity solution contrast

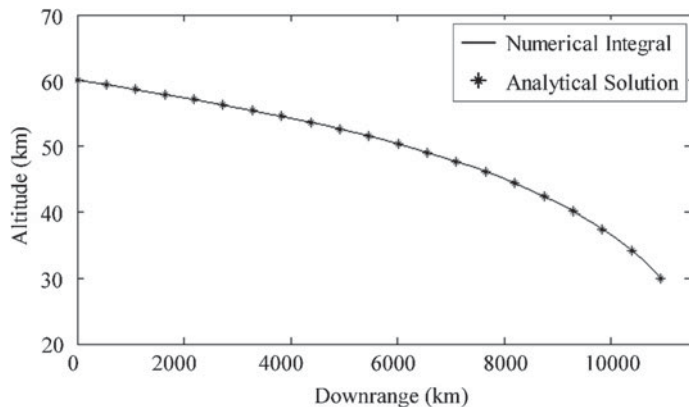


Fig. 8.3 Longitudinal trajectory solution contrast

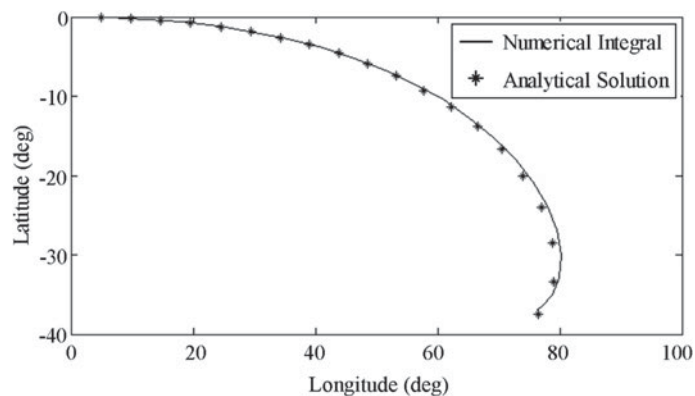


Fig. 8.4 Lateral trajectory solution contrast

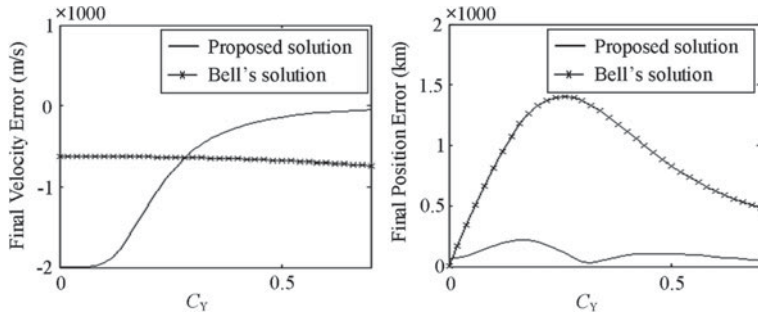


Fig. 8.5 Precision comparison for 1 phase

8.6 and 8.7. It can be seen from Fig. 8.5 that when the final states is directly predicted by one phase, the final position error of the proposed analytical solution is far less than that of the Bell analytical solution and the final speed error is increased with the range. The accuracy of the proposed analytical solution is higher when the range is small, and lower when the range is large than the Bell analytical solution. This

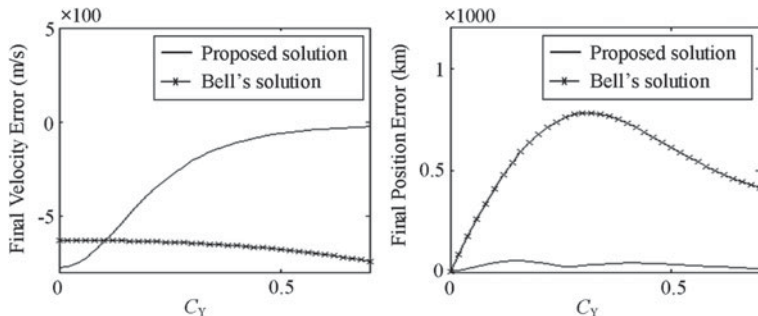


Fig. 8.6 Precision comparison for 2 phases

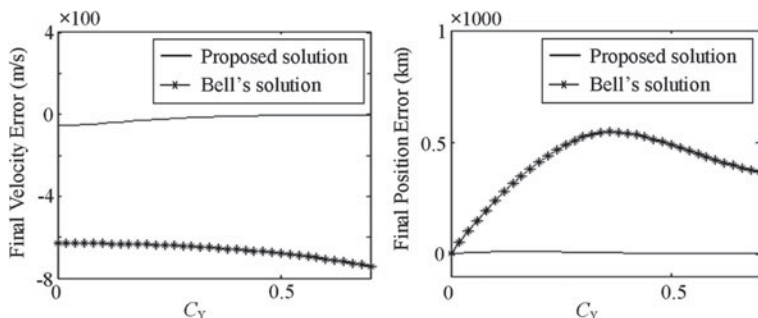


Fig. 8.7 Precision comparison for 5 phases

Table 8.2 Accuracy of Analytical Solutions

Number of phases	C_Y	Position error of proposed solution (km)	Position error of Bell solution(km)	Velocity error of proposed solution (m/s)	Velocity error of Bell solution (m/s)
1	0.1	171.11	811.56	-1940.12	-631.06
2	0.1	47.01	410.28	-642.10	-631.06
5	0.1	9.70	237.18	-44.41	-631.06
1	0.6	85.83	656.80	-90.72	-700.74
2	0.6	29.34	519.40	-41.89	-700.74
5	0.6	1.79	432.99	-3.89	-700.74

is because under the given C_{N1} , there will be subtle changes in the glide trajectory, and the smaller C_Y is, the more C_D changes, which results in integral error. The Bell analytical solution is obtained under invariable longitudinal lift-to-drag ratio K_{N0} , hence the final velocity error due to the neglected change of r is almost constant. It can be seen from Figs. 8.6 to 8.7 that using the stepwise solution method, the accuracy of the proposed analytical solution increases rapidly with the increase of phases, while the final velocity error of the Bell analytical solution has no significant change, and the final position error is slowly reduced.

Table 8.2 compares the error of analytic solutions. It can be seen that the more phases there are, the higher accuracy of proposed analytic solutions than Bell analytical solution. When using 2-phases solution, the final position error of the proposed analytical solution is about one order of magnitude lower than that of the Bell analytical solution, and the final velocity error is also smaller than that of the Bell analytical solution. When using 5-phases solution, the final position error of the proposed analytical solution is about two orders of magnitude lower than that of Bell analytic solution, and the final velocity error is about one order of magnitude lower. In general, the final states' accuracy of the proposed analytical solution is higher than Bell analytical solution.

8.4.3 Application of Analytic Solutions in Trajectory Planning

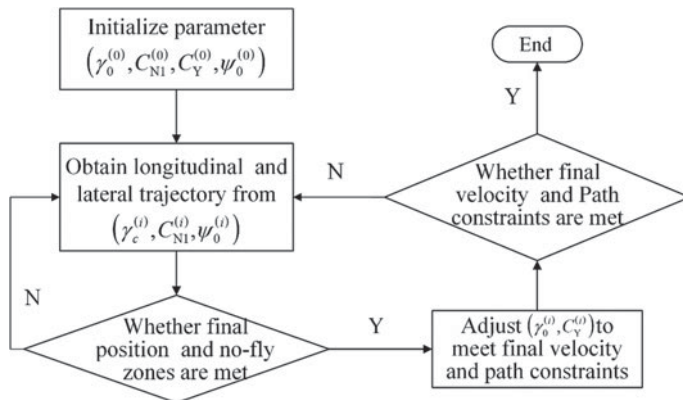
The proposed analytical solution can be applied to the glide maneuver trajectory programming. The initial states of the glide phase are the same as those in Table 8.1, the final states and path constraints are shown in Table 8.3, and no-fly zones are shown in Table 8.4. The process of glide maneuver trajectory planning based on the proposed analytical solution is shown in Fig. 8.8. Longitudinal trajectory and lateral trajectory are obtained by Eqs. (8.35) and (8.36). Final velocity constraint and path constraint are determined by Eqs. (8.20) and (8.41).

Table 8.3 Trajectory planning parameters

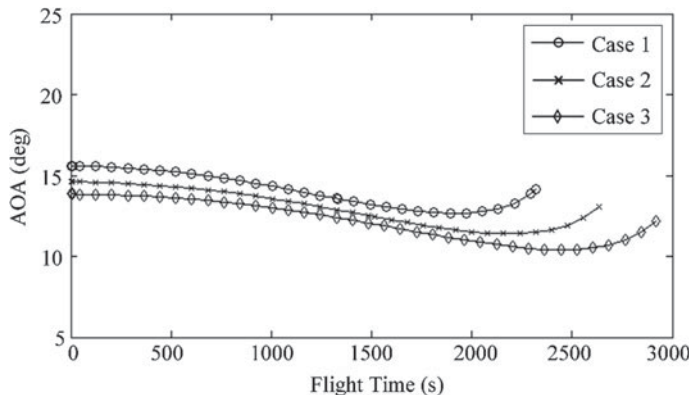
Parameter	h_f (km)	V_f (m/s)	ϕ_f (deg)	θ_f (deg)	\dot{Q}_{\max} (W/cm ²)	q_{\max} (pa)	n_{\max}
Value	30	2000	0	100/115/130	500	60,000	2.5

Table 8.4 No-fly zone parameters

No-fly zone	lon and lat of Centre	Range (km)
1	(40, -6)	891
2	(90, 6)	1002

**Fig. 8.8** Flowchart of the gliding maneuvering trajectory planning algorithm

Figures 8.9, 8.10, 8.11, 8.12, 8.13 and 8.14 show the results of glide maneuver trajectory planning and case 1 to 3 represent the terminal longitude is 100, 115 and

**Fig. 8.9** Angle of attack histories

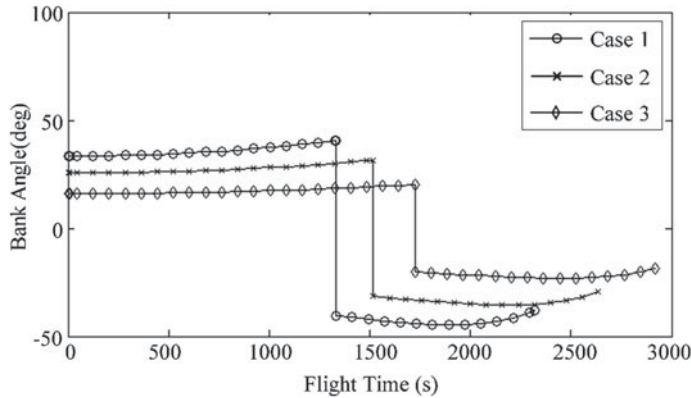


Fig. 8.10 Bank angle histories

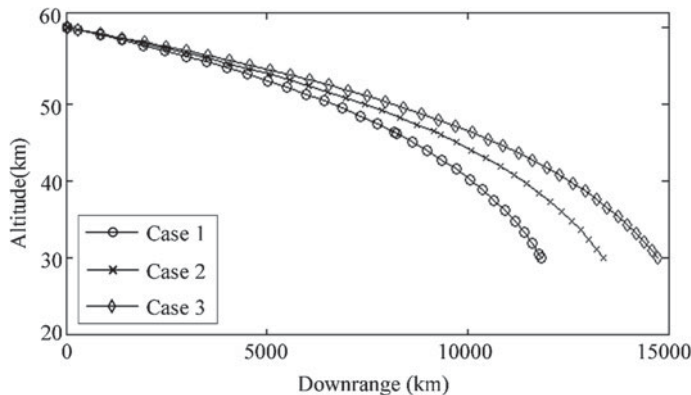


Fig. 8.11 Longitudinal trajectories

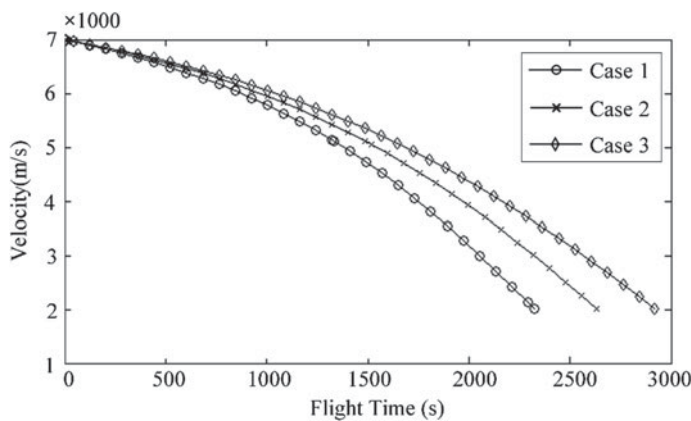


Fig. 8.12 Velocity histories

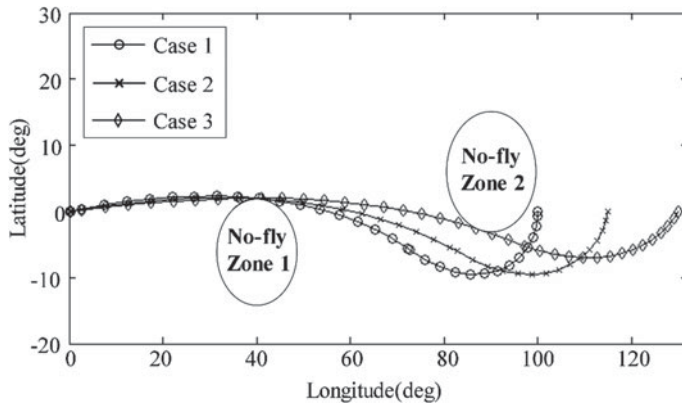


Fig. 8.13 Lateral trajectories

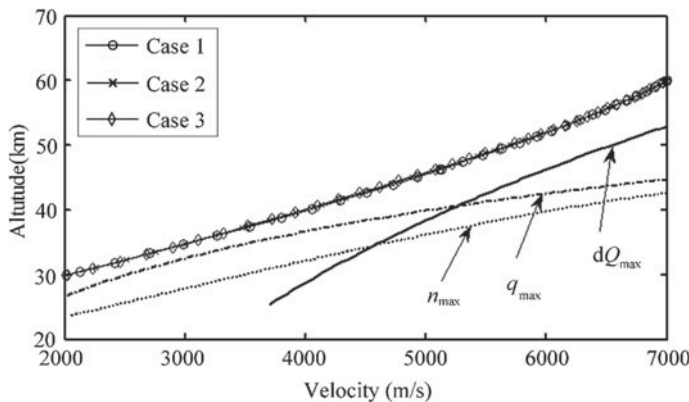


Fig. 8.14 H-V corridor

130 respectively. It can be seen from Figs. 8.9 to 8.10 that the angle of attack curve and bank angle curve obtained based on analytic solution planning are very smooth, and the bank angle reversal can be achieved by segments. It can be seen from Figs. 8.11 to 8.12 that the final height and velocity of the glide trajectory meet the requirements. As can be seen from 8.13, the planned glide maneuver trajectory conforms to the requirements of no-fly zone constraint and final longitude and latitude. The glide trajectory meets the path constraints of maximum heating rate, maximum dynamic pressure and maximum overload, and the trajectories of different missions almost completely coincide in the H-V corridor, which is shown in 8.14.

In general, the glide trajectory that meets the constraints can be obtained using the proposed analytical solution. Under the condition of no specific initial value, the time of programming one glide trajectory on a personal desktop is less than 0.3 s.

8.5 Summary

In this chapter, an analytical solution of three-dimensional (3D) steady glide trajectory is proposed. The major contributions are summarized as follows:

- (1) A separated method of lift coefficient is proposed, which realizes the decoupling of longitudinal motion equation, lateral motion equation and velocity equation of glide trajectory.
- (2) Using the decoupled equation of motion, the exact analytical solution of altitude and range is obtained. Then, the relatively exact analytic solution of bank angle is obtained by regular perturbation method. On this basis, using Gaussian integral, the analytical solutions of longitude and latitude are acquired. Finally, the analytical solution of velocity is obtained by the Runge-Kutta method.
- (3) A stepwise solving method is proposed to improve the accuracy of the analytical solution. It is shown by the simulations that the accuracy of the proposed analytical solution which adopts stepwise method is much higher than the accuracy of the Bell analytical solution.
- (4) Using the proposed analytical solution, ballistic integration is not required for glide trajectory programming. And the computational efficiency can be greatly improved by programming the trajectory that meets the requirements of penetration firstly, and then performing speed correction. The time of programming one glide trajectory on a personal desktop is less than 0.3 s.

References

1. Chapman, D.R.: An approximate analytical method for studying entry into planetary atmospheres. NACA TN-4276 (1958)
2. Loh, W.H.T.: Some exact analytical solutions of planetary entry. AIAA J. **1**(4), 836–842 (1962)
3. Shi, Y.Y., Pottsepp, L.: Asymptotic expansion of a hypervelocity atmospheric entry problem. Tech. Notes, 353–355 (1969)
4. Naidu, D.S.: Three-dimensional atmospheric entry problem using method of matched asymptotic expansion. IEEE Trans. Aerospace Electron. Syst. **25**(5), 660–667 (1989)
5. Vinh, N.X., Busemann, A., Culp, R.D.: Planetary entry flight mechanics, pp. 100–138. The University of Michigan Press, USA (1980)
6. Bell, B.N.: A closed-form solution to lifting reentry. AFFDL-TR-65-65 (1965)
7. Harbold, J.C., Graves, C.A.: Shuttle entry guidance. NASA Lyndon B. Johnson Space Center, Houston, TX. Rep. JSC-14694 (1979)
8. Li, H., Zhang, R., Li, Z., et al.: New method to enforce inequality constraints of entry trajectories. J. Guidance Control Dyn. **35**(5), 1662–1667 (2012)
9. Yu, W., Chen, W.: Guidance scheme for glide range maximization of a hypersonic vehicle. AIAA 2011-6714
10. Li, B.J., Wang, M.H.: Research on glide trajectory of long range glide missile. J. Astronaut. **30**(6), 2122–2126 (2009). (in Chinese)
11. Guo, X.L., Zhang, H.: The approximate solution for long -time and long-range longitudinal gliding flight based on segment constant gliding angle. J. Astronaut. **30**(6), 712–716 (2009). (in Chinese)

12. Xu, M.L., Chen, K.J., Liu, L.H., et al.: Quasi-equilibrium glide adaptive guidance for hypersonic vehicles. *Sci. China Tech. Sci.* **42**(4), 378–387 (2012). (in Chinese)
13. Mease, K.D., Chen, D.T., Teufel, R., et al.: Reduced-order entry trajectory planning for acceleration guidance. *J. Guidance Control Dyn.* **25**(2), 257–266
14. Shen, Z., Lu, P.: Onboard generation of three dimensional constrained entry trajectory. *J. Guidance Control Dyn.* **26**(1), 111–121
15. Zhou, H., Rahman, T., Chen, W.: Neural network assisted inverse dynamic guidance for terminally constrained entry flight. *The Sci. World J.* (in Press)
16. Rahman, T., Zhou, H., Chen, W.: Bezier approximation based inverse dynamic guidance for entry glide trajectory. *ASCC-2013-6606111* (2013)
17. Hu, J.C., Chen, W.C.: Steady glide trajectory planning method for hypersonic reentry vehicle. *J. Beijing Univ. Aeronaut. Astronaut.* <https://doi.org/10.13700/j.bh.1001-5965. 0023> (2015). (in Chinese)
18. Zhang, K., Chen, W.: Reentry vehicle constrained trajectory optimization. *AIAA 2011-2231* (2011)

Chapter 9

Trajectory Damping Control Technique for Hypersonic Glide Reentry



Reprinted by permission of the American Institute of Aeronautics and Astronautics, Inc., from [1]. Copyright © AIAA.

9.1 Introduction

With the development of the computer technology, the optimal control methodology usually is the first choice in designing a glide trajectory of a hypersonic vehicle [2, 3]. This approach is able to obtain the optimal solution that satisfies various constraints, but it usually takes a long computing time. So it's not suitable for real-time control of a vehicle in most cases.

Previous work proved that the L/D_{\max} operation is approximately glide-range-optimal over a flat Earth [4]. Kelley provided a scheme that was based on the theory and used it to control the short-range gliding vehicles, and the simulation results showed the good performance of the scheme. Phillips [5] used the scheme as gliding algorithm to expand the range of a guided projectile.

This chapter studies the glide-range problem over a spherical Earth. The chapter is organized as following: In Sect. 2, firstly, a mathematical proof is given to show that if a hypersonic vehicle glides at the specific angle of attack that maximizes the L/D , the glide range over a spherical Earth also is nearly as far as the maximum glide range. Then a guidance scheme is provided to maximize the glide range of a hypersonic vehicle and suppress the oscillation by adding a damping component, which is opposite to the velocity in the vertical direction, to the lift force. Finally, the scheme is extended to control the glide range by regulating the profile of the L/D' when the initial and final mechanical energy of the vehicle are specified. In Sect. 3, a simplified model of a hypersonic vehicle used in this chapter is presented. In Sect. 4, firstly, some examples are given to show the performance of the scheme.

In these examples, the simulation results are compared with the optimal control results obtained by using the Gauss Pseudospectral Method (GPM) [6–8]. Then, an application of the extended guidance scheme is provided to show the scheme’s ability of controlling the glide range of the vehicle. Finally, Sect. 5 gives the conclusions.

9.2 Guidance Scheme

9.2.1 Mathematical Proof

This section begins by proving that the L/D_{\max} operation is approximately glide-range-optimal over a spherical Earth through a variable-density atmosphere. Regarding a hypersonic vehicle as a particle, the equations of motion for flight in a vertical plane over the non-rotating spherical Earth are

$$\frac{dH}{dt} = V \sin(\gamma) \quad (9.1)$$

$$\frac{dR}{dt} = V \cos(\gamma) \frac{R_0}{R_0 + H} \quad (9.2)$$

$$\frac{dV}{dt} = -\frac{D}{m} - g \sin(\gamma) \quad (9.3)$$

$$\frac{d\gamma}{dt} = \frac{L}{mV} - \frac{g \cos(\gamma)}{V} + \frac{V \cos(\gamma)}{R_0 + H} \quad (9.4)$$

Here, the third term of the right side of Eq. (9.4) is due to the centrifugal force. H is altitude (in meter). R is downrange (in meter). V is speed (in meter per second). γ is flight-path angle (in rad). m is a constant mass (in kg). R_0 is the average radius of earth and has an approximately value of 6 356.766 km. L is lift and D is drag (in Newton). g is the acceleration of gravity and can be calculated by Eq. (9.5).

$$g = \frac{\mu}{(R_0 + H)^2} \quad (9.5)$$

Here, μ is a constant and has an approximately value of $3.962\,72 \times 10^{14}\text{m}^3/\text{s}^2$.

Regarding the infinite point as the zero point of the gravitational potential energy, the special energy E , which is defined as the mechanical energy per unit mass, can be calculated by Eq. (9.6).

$$E = \frac{1}{2} V^2 - \frac{\mu}{R_0 + H} \quad (9.6)$$

In the glide phase of the hypersonic vehicle, the speed usually is less than the first cosmic velocity (i.e. approximately 7.9 km/s) and the altitude ranges from 0 km to 100 km in general. So the range of E is from $-6.32 \times 10^7 \text{ J/kg}$ to $-3.11 \times 10^7 \text{ J/kg}$. E decreases due to the drag force and its change rate is shown in Eq. (9.7).

$$\frac{dE}{dt} = V \frac{dV}{dt} + \frac{\mu}{(R_0 + H)^2} \frac{dH}{dt} = -\frac{D V}{m} \quad (9.7)$$

Dividing Eq. (9.2) by Eq. (9.7), then obtain

$$dR = -\frac{m R_0 \cos(\gamma)}{D(R_0 + H)} dE \quad (9.8)$$

The proof process assumes that the vehicle glides in the quasi-steady vertical equilibrium condition which means that the components of the lift, gravity, and centrifugal force perpendicular to the velocity are approximately balanced, then the left side in Eq. (9.4) can be treated as zero and Eq. (9.9) is obtained.

$$L - mg \cos(\gamma) + \frac{m V^2 \cos(\gamma)}{R_0 + H} \approx 0 \quad (9.9)$$

After some algebra, the cosine of the flight-path angle can be obtained

$$\cos(\gamma) = \frac{L}{mg - \frac{mV^2}{R_0 + H}} \quad (9.10)$$

Substituting Eq. (9.10) into Eq. (9.8), then obtain

$$dR = -\frac{L}{D} \frac{R_0}{g(R_0 + H) - V^2} dE = -\frac{L}{D} \frac{R_0}{\frac{\mu}{R_0 + H} - V^2} dE \quad (9.11)$$

From Eq. (9.6), obtain

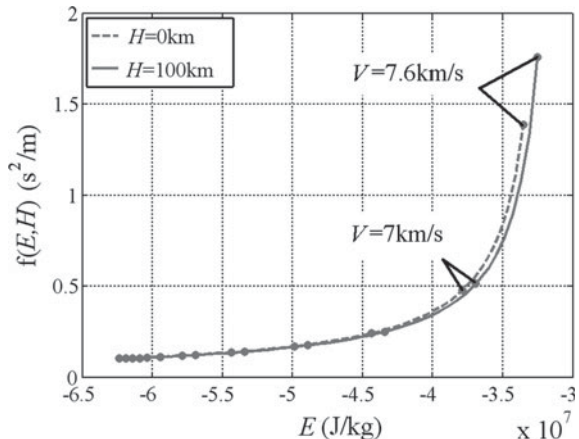
$$V^2 = 2E + \frac{2\mu}{R_0 + H} \quad (9.12)$$

Substituting Eq. (9.12) into Eq. (9.11), then obtain

$$dR = -\frac{L}{D} \frac{R_0}{-2E - \frac{\mu}{R_0 + H}} dE = -\frac{L}{D} \cdot f(E, H) dE \quad (9.13)$$

The function f in Eq. (9.13) has two variables which are E and H . The value of $f(E, H)$ increases with increasing E and decreasing H . Although the L/D , E , and H are not independent in a real situation and change with speed, it can be assumed that H is a constant in analysis. Figure 9.1 shows the curves of $f(E, H)$ as functions of

Fig. 9.1 H has little effect on the value of $f(E, H)$ since $H \ll R_0$



E when H equals 0 km and 100 km respectively. It should be noted that the value of E at the first cosmic velocity is a singular point in $f(E, H)$. If the speed tends to the first cosmic velocity, the value of $f(E, H)$ tends to infinity, which means the vehicle will never come back to earth theoretically. In order to avoid the singular point, the speed, which directly affects the value of E in Fig. 9.1, ranges from 0 to 7.6 km/s. It can be seen from Fig. 9.1 that the altitude has little effect on the value of $f(E, H)$, especially when the speed is less than 7 km/s. The reason is that the altitude H is much smaller than the average radius of earth R_0 .

The glide range can be calculated by integrating the right side of Eq. (9.13) from the initial special energy E_0 to the final special energy E_f and it is shown in Eq. (9.14).

$$R = \int_{E_0}^{E_f} -\frac{L}{D} f(E, H) dE \quad (9.14)$$

Since the altitude has little effect on the value of $f(E, H)$, the L/D has a critical influence on the glide range. Thus, it is proved that, if the L/D is maximized at each Mach number (Ma), the glide range is nearly as far as the maximum glide range when the initial special energy E_0 and the final special energy E_f are specified.

9.2.2 Command Flight-Path Angle for L/D_{max}

In the glide phase of a hypersonic vehicle, the flight-path angle at L/D_{max} in the quasi-steady vertical equilibrium condition is named the command flight-path angle for L/D_{max} (γ^*). In the following text, a formula, which is a function of current states, is derived to approximate the value of γ^* accurately.

Kelley derives the formula of γ^* by assuming that the required dynamic pressure is a constant on a flat Earth [4]. However, in the glide phase of a hypersonic vehicle,

since the centrifugal force is taken into account and decreases with decreasing the speed gradually, the required lift, which approximately balances the composition of the gravity and centrifugal force, increases with time, thereby, the required dynamic pressure, which is proportional to the required lift, cannot be assumed as a constant. Here, an improved method is used to derive the formula of γ^* . From Eq. (9.9), obtain

$$\frac{C_l^* \cdot 0.5\rho V^2 \cdot S}{m} - g \cos(\gamma^*) + \frac{V^2 \cos(\gamma^*)}{R_0 + H} = 0 \quad (9.15)$$

Here, C_l^* is the lift coefficient for L/D_{\max} . Since the vehicle is regarded as a particle, the aerodynamic coefficients can be simplified as the functions of Ma and the angle of attack (α) in general. However, C_l^* is only a function of Ma . ρ is the atmospheric density which is a function of H . S is the reference area. As we know, Ma is equal to the speed of the vehicle divided by the local sound speed. Since the sound speed changes with H according to the U.S. Standard Atmosphere 1976 [9], Ma is a function of V and H . Take the derivative of Eq. (9.15) with respect to time t , then obtain

$$\begin{aligned} & \frac{1}{m} \frac{dC_l^*}{dMa} \left(\frac{\partial Ma}{\partial V} \frac{dV}{dt} + \frac{\partial Ma}{\partial H} \frac{dH}{dt} \right) \frac{1}{2} \rho V^2 S + \frac{1}{m} C_l^* \frac{1}{2} \frac{d\rho}{dH} \frac{dH}{dt} V^2 S + \frac{1}{m} C_l^* \rho V \frac{dV}{dt} S \\ & - \frac{dg}{dH} \frac{dH}{dt} \cos(\gamma^*) + g \frac{d\gamma^*}{dt} \sin(\gamma^*) + \frac{1}{R_0 + H} [2V \frac{dV}{dt} \cos(\gamma^*) \\ & - V^2 \sin(\gamma^*) \frac{d\gamma^*}{dt}] - \frac{1}{(R_0 + H)^2} V^2 \frac{dH}{dt} \cos(\gamma^*) = 0 \end{aligned} \quad (9.16)$$

In order to simplify Eq. (9.16), two assumptions are taken: One is that the terms of Eq. (9.16), which contain either the derivative of gravity with respect to altitude or the derivative of γ^* with respect to t , are neglected because their absolute values can be treated as zero; the other one assumes that $\sin(\gamma^*) \approx \gamma^*$ and $\cos(\gamma^*) \approx 1$ because γ^* is close to zero. Using these assumptions and substituting Eq. (9.1) and Eq. (9.3) into Eq. (9.16), an expression of the command flight-path angle for L/D_{\max} is obtained by Eq. (9.17).

$$\begin{aligned} \gamma^* = & - \frac{D^*}{mg} \frac{1}{1 - a_{11} - a_{12} + a_{13} + a_{14} + a_{15}} \\ & - \frac{D^*}{mg} \frac{1}{1 - a_{21} - a_{22} + a_{23} + a_{24} + a_{25}} \\ & - \frac{D^*}{mg} \frac{1}{1 - a_{31} - a_{32} + a_{33} + a_{34} + a_{35}} \end{aligned} \quad (9.17)$$

Here, the drag force $D^* = C_d^* \cdot 0.5\rho V^2 \cdot S$. C_d^* is the drag coefficient for L/D_{\max} . The expressions of these coefficients $\{a_{ij} | i = 1, 2, 3; j = 1, 2, \dots, 5\}$ are as follows.

$$\begin{aligned}
a_{11} &= \frac{d\rho}{dH} \frac{C_l^* V}{\frac{dC_l^*}{dMa} \frac{\partial Ma}{\partial V} \rho g} & a_{21} &= \frac{d\rho}{dH} \frac{V^2}{2\rho g} & a_{31} &= \frac{d\rho}{dH} \frac{C_l^* V^2 S(R_0+H)}{4mg} \\
a_{12} &= \left(\frac{\partial Ma}{\partial H} \right) / \left(\frac{\partial Ma}{\partial V} g \right) & a_{22} &= \frac{dC_l^*}{dMa} \frac{\partial Ma}{\partial H} \frac{V^2}{2C_l^* g} & a_{32} &= \frac{dC_l^*}{dMa} \frac{\partial Ma}{\partial H} \frac{\rho V^2 S(R_0+H)}{4mg} \\
a_{13} &= \frac{2C_l^*}{\frac{dC_l^*}{dMa} \frac{\partial Ma}{\partial V} V} & a_{23} &= 1/a_{13} & a_{33} &= 1/a_{14} \\
a_{14} &= \frac{4m}{\frac{dC_l^*}{dMa} \frac{\partial Ma}{\partial V} \rho V S(R_0+H)} & a_{24} &= \frac{2m}{C_l^* \rho S(R_0+H)} & a_{34} &= 1/a_{24} \\
a_{15} &= \frac{2Vm}{\frac{dC_l^*}{dMa} \frac{\partial Ma}{\partial V} \rho Sg (R_0+H)^2} & a_{25} &= \frac{mV^2}{C_l^* \rho g S(R_0+H)^2} & a_{35} &= \frac{V^2}{2g(R_0+H)}
\end{aligned}$$

In general, the partial derivatives of the aerodynamic coefficients with respect to Ma are close to zero when a vehicle glides at hypersonic speed. So if it can be assumed that the aerodynamic coefficients are independent of Ma , Eq. (9.17) can be simplified to Eq. (9.18).

$$\gamma^* = -\frac{D^*}{mg} \frac{1}{1 - a_{21} + a_{24} + a_{25}} - \frac{D^*}{mg} \frac{1}{1 - a_{31} + a_{34} + a_{35}} \quad (9.18)$$

9.2.3 Guidance Scheme for Range Maximization and Trajectory Damping Control

Under the control of the L/D_{\max} operation, the trajectory of a hypersonic vehicle usually has a phugoid oscillation with a poor degree of damping. As we know that, if the speed and angle of attack are specified, the magnitude of lift is a function of altitude, and the higher altitude tends to decrease the lift force since the atmospheric density decreases. So in the vertical direction, the motion of the vehicle can be regarded as that of a nonlinear spring system affected by a damping force and an external force. Here, the lift force for L/D_{\max} is the nonlinear restoring force and causes the oscillation of the trajectory. The vertical component of the drag force (i.e. $-D^* \sin(\gamma)$) can be regarded as the damping force since it has an opposite direction with the vertical component of the velocity (i.e. $V \sin(\gamma)$). However, the degree of damping is poor because γ is close to zero. The composition of gravity and the centrifugal force can be regarded as the external force acting on the nonlinear spring system. Under the actions of the restoring force and external force, the vehicle oscillates around the equilibrium altitude which approximately meets the equality constraint Eq. (9.15) with $\gamma = \gamma^*$. In order to suppress oscillation, a damping component is added to the lift force, which has sufficient vertical component. Thus, the lift force consists of two parts: one is of the L/D_{\max} operation and can be regarded as the restoring component; the other is the damping component which is proportional to $(\gamma^* - \gamma)$ and opposite to the vertical component of the velocity. So the command angle of attack of the scheme is obtained by Eq. (9.19) in which the flight-path angle γ is the negative feedback signal.

$$\alpha = \alpha^* + k_\gamma (\gamma^* - \gamma) \quad (9.19)$$

Here, α^* is the angle of attack for L/D_{\max} . The formula of γ^* is selected from Eq. (9.17) and Eq. (9.18) according to the actual situation. k_γ is a positive constant. The greater k_γ tends to increase the degree of damping. Under the control of this scheme, the amplitude of the oscillation decreases rapidly due to the damping component of lift, or even there is no oscillation when k_γ is large enough, then γ converges to γ^* and the hypersonic vehicle glides at L/D_{\max} in the quasi-steady vertical equilibrium condition.

9.2.4 Extended Guidance Scheme for Glide Range Control

In most cases, the required glide range is less than the maximum glide range, and in order to decrease the heating rate and increase the flight time in the terminal guidance phase, it is desired to decrease the final speed in the midcourse phase. In other words, it is needed to glide the vehicle to the destination with consuming sufficient energy. Furthermore, since Eq. (9.14) indicates that the L/D has a critical influence on the glide range, the scheme is extended to control the glide range by planning the profile of the L/D' when E_0 and E_f are specified. Equation (9.20) and Eq. (9.21) show a simple and rapid method of planning the profile of the L/D' .

$$L/D' = k_{L/D} L/D_{\max} \quad (9.20)$$

$$k_{L/D} = \frac{R'_f}{R_{f\max}} \quad (9.21)$$

Here, $k_{L/D}$ is a constant. R'_f represents the required glide range, and $R_{f\max}$ is the maximum glide range and can be precalculated by Eq. (9.19). Then, the extended guidance scheme can be expressed as

$$\alpha = \alpha' + k_\gamma (\gamma' - \gamma) \quad (9.22)$$

Here, α' is the angle of attack for L/D' . Obviously, if $L/D' < L/D_{\max}$, α' has two solutions: one is greater than α^* ; while, the other is less than α^* . Since the larger α' tends to increase the glide altitude and thereby decrease the maximum heating rate, the scheme lets $\alpha' > \alpha^*$. Similar to the L/D_{\max} flight, γ' is the command flight-path angle for L/D' and can be calculated by replacing C_l^* , C_d^* , and the derivative of C_l^* with the lift coefficient for L/D' (C_l^*), the drag coefficient for L/D' (C_d^*), and the derivative of C_l^* respectively in Eq. (9.17) or Eq. (9.18).

9.3 Hypersonic Vehicle Model

The vehicle used for showing the performance of the guidance scheme is similar to the model of a space shuttle. The model is given in [3 and 10], and some changes of the aerodynamic data are made. In the glide phase, the mass of the vehicle is a constant and has a value of 50 000 kg. The drag and lift models are expressed as the following equations.

$$L = C_l \cdot \frac{1}{2} \rho V^2 \cdot S \quad (9.23)$$

$$D = C_d \cdot \frac{1}{2} \rho V^2 \cdot S \quad (9.24)$$

$$C_l = C_{l0}(Ma) + C_l^\alpha(Ma) \cdot \alpha \quad (9.25)$$

$$C_d = C_{d0}(Ma) + K(Ma) \cdot C_l^2 \quad (9.26)$$

Here, C_l is the lift coefficient. C_d is the drag coefficient. The reference area S is 100 m^2 . $C_{l0}(Ma)$, $C_l^\alpha(Ma)$, $C_{d0}(Ma)$, and $K(Ma)$ are showed in Figs. 9.2, 9.3, 9.4 and 9.5. In this model, C_l^* and its derivative can be obtained by

$$C_l^* = \sqrt{\frac{C_{d0}}{K}} \quad (9.27)$$

$$\frac{dC_l^*}{dMa} = \frac{1}{2} \left(\frac{1}{\sqrt{C_{d0}K}} \frac{dC_{d0}}{dMa} - \sqrt{\frac{C_{d0}}{K^3}} \frac{dK}{dMa} \right) \quad (9.28)$$

Fig. 9.2 C_{l0} as a function of Ma

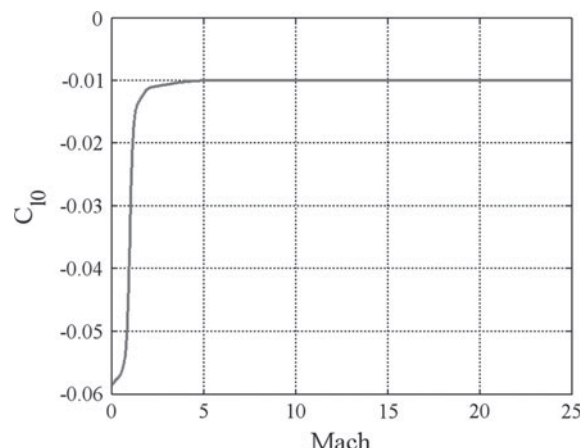


Fig. 9.3 C_l^α as a function of Ma

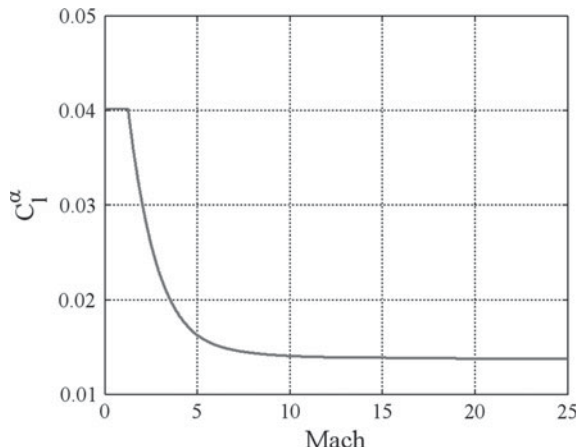


Fig. 9.4 C_{d0} as a function of Ma

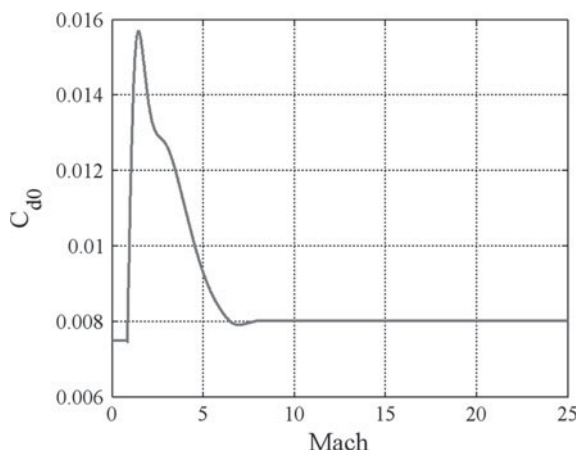
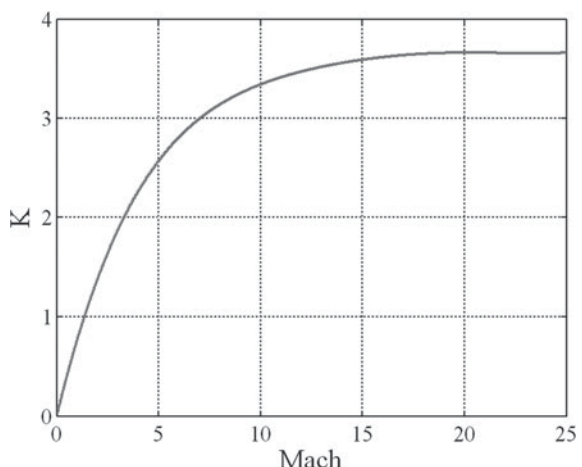


Fig. 9.5 K as a function of Ma



Then, α^* and C_d^* can be obtained by substituting Eq. (9.27) into Eqs. (9.25) and (9.26). The heating rate (in W/cm^2) can be calculated by Eq. (9.29).

$$\dot{Q} = (3 \times 10^{-8}) \cdot \sqrt{\rho} V^3 \quad (9.29)$$

Here, the atmospheric density ρ (in kg/m^3) is simply modeled by Eq. (9.30), and the magnitude of ρ will be virtually halved if the altitude increases every 4.62 km.

$$\rho = 1.225e^{-0.00015H} \quad (9.30)$$

9.4 Results and Discussion

9.4.1 Performance of Guidance Scheme

This part gives some examples to show the performance of the scheme. The initial altitude, speed, and flight-path angle are $H_0 = 100 \text{ km}$, $V_0 = 6800 \text{ km/s}$ and $\gamma_0 = 0 \text{ rad}$ respectively. The final altitude is $H_f = 10 \text{ km}$. Equation (9.19) is used in the glide phase where γ^* is computed by Eq. (9.17) because the aerodynamic coefficients change with Ma . Figure 9.6 shows the trajectories for the scheme with different values of k_γ . Table 9.1 lists the values of k_γ and the final glide ranges corresponding to the cases shown in Fig. 9.6. Figure 9.7 shows the final glide range as a function of k_γ . It can be seen that the largest glide range for this scheme is obtained at $k_\gamma = 0.15$ and has a value of about 13 711.573 km. Figure 9.8 shows that the maximum heating rate is a decreasing function of k_γ . Figure 9.9 shows that the maximum dynamic pressure also is a decreasing function of k_γ . Figure 9.10 shows the maximum load

Fig. 9.6 Trajectories with different values of k_γ

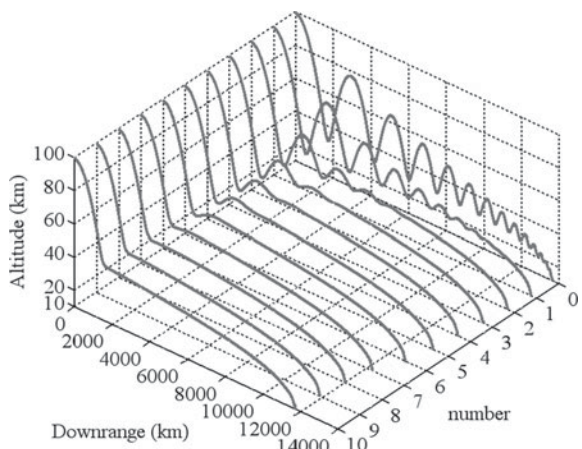


Table 9.1 Values of k_γ and Downrange

Number	k_γ	Downrange, km
0	0	13 673.113
1	0.15	13 711.573
2	0.5	13 647.217
3	1	13 504.486
4	2	13 207.200
5	3	12 912.065
6	4	12 618.807
7	5	12 341.008
8	7	12 071.766
9	10	11 889.561
10	15	11 754.342

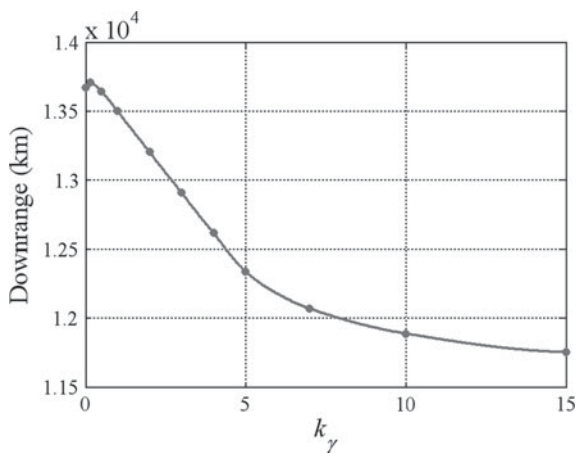
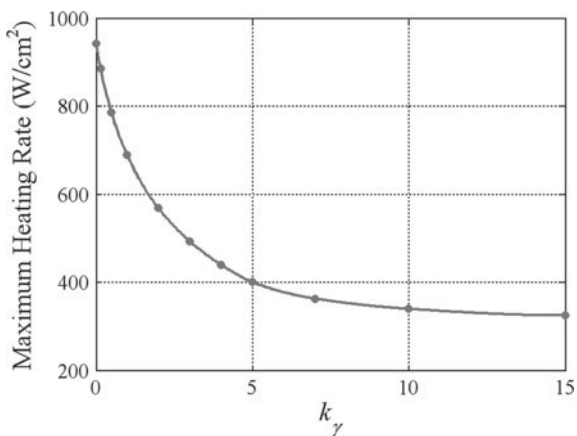
Fig. 9.7 Glide range as a function of k_γ **Fig. 9.8** Maximum heating rate as a function of k_γ 

Fig. 9.9 Maximum dynamic pressure as a function of k_γ

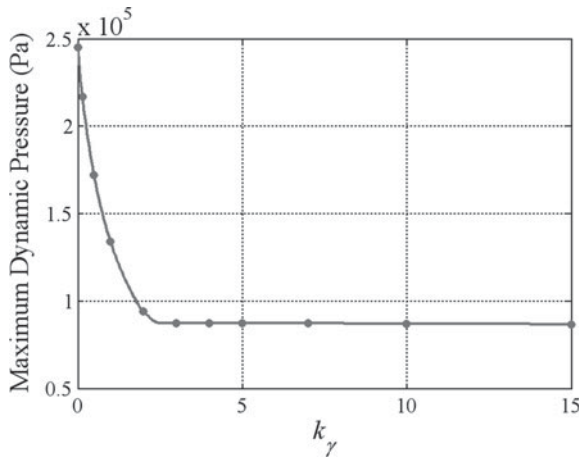
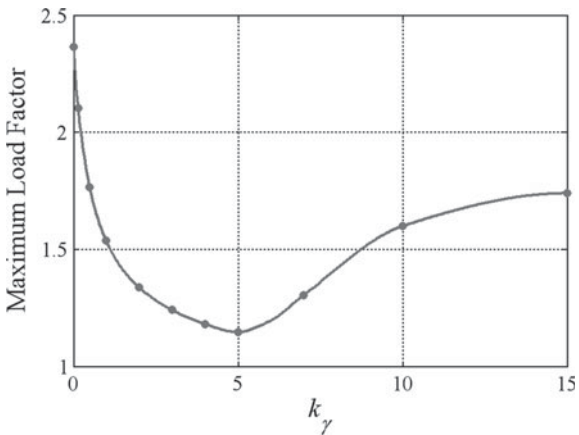


Fig. 9.10 Maximum load factor as a function of k_γ



factor as a function of k_γ . The points in Figs. 9.7, 9.8, 9.9 and 9.10 correspond to the trajectories shown in Fig. 9.6 respectively.

As previously mentioned, in the vertical direction, the motion of the vehicle can be treated as the oscillation of a nonlinear spring system affected by a damping force and an external force, and only when the speed and altitude approximately meet the special constraint Eq. (9.15) with $\gamma = \gamma^*$, the vehicle can glide at L/D_{\max} in the quasi-steady vertical equilibrium condition. As can be seen from Fig. 9.6, in the beginning, because of the thin atmosphere at 100 km altitude, the dynamic pressure is small and the lift force is less than the composition of the gravitational force and centrifugal force, therefore, the vehicle loses height rapidly. Since the lift component for L/D_{\max} increases with decreasing the altitude and thereby can be treated as a restoring force, the vehicle oscillates around the equilibrium altitude. When $k_\gamma = 0$, the oscillation amplitude decreases slowly because the damping

force ($-D \sin(\gamma)$) is poor. When $k_\gamma > 0$, lift contains a damping component which has an opposite direction with velocity in the vertical direction, then the oscillation amplitude decreases quickly, or even there is no oscillation when k_γ is large enough. As can be seen from Fig. 9.7, 9.8, 9.9 and 9.10, although the greater k_γ tends to decrease the final glide range slightly, it causes that the maximum heating rate, dynamic pressure, and load factor decrease quickly. However, when the value of k_γ is greater than 3 and still increases, the maximum dynamic pressure becomes steady. It is because that the maximum dynamic pressure is occurred in the quasi-steady equilibrium condition when $k_\gamma > 3$, rather than at the first bottom of the oscillation when $k_\gamma < 3$. Overall, setting an appropriate value of k_γ is an effective way to limit the values of these physical quantities.

In order to show that the glide range for the guidance scheme is nearly as far as the maximum glide range, the results for the scheme are compared with the optimal results that maximize the glide range by using the Gauss Pseudospectral Method. The analysis has two aspects: one case has no path constraint; while, the other case limits the heating rate to be less than 500 W/cm^2 during the glide phase.

In the first case, the results for the optimal control, which have the same boundary conditions as mentioned earlier, are compared with that for the scheme when $k_\gamma = 0.15$. Figure 9.11 shows the trajectories for the optimal control and the scheme. Figure 9.12 shows the histories of the angle of attack for the optimal control and the scheme. The other characteristics of the results for the scheme are shown in Figs. 9.13, 9.14, 9.15 and 9.16. The maximum glide range for the optimal control is 13 754.851 km and slightly further than that for the scheme which is 13 711.573 km. Overall, the results for the scheme are very similar with that for the optimal control. However, there is a small jump at the end of the trajectory for the optimal control, and it is the main reason why the optimal glide range is further than that for the scheme. As can be seen from these Figures, the results coincide with the expectation

Fig. 9.11 Trajectories without path constraint

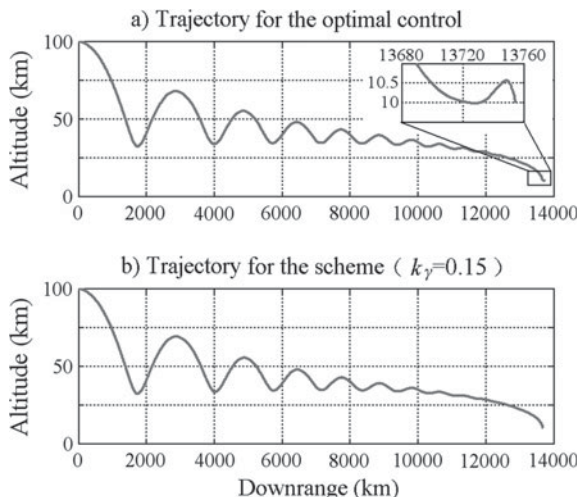


Fig. 9.12 Angle of attack histories without path constraint

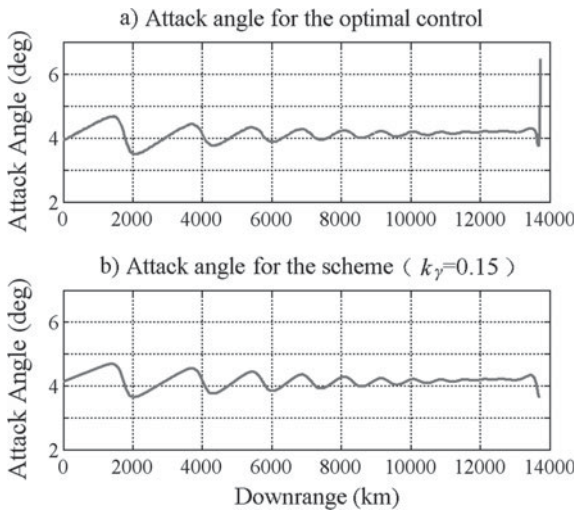


Fig. 9.13 Speed history for the scheme when $k_\gamma = 0.15$

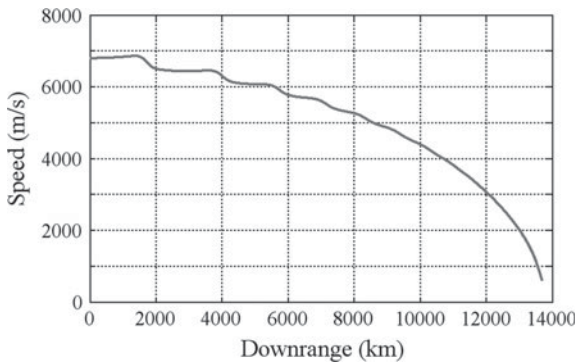


Fig. 9.14 Flight-path angle history for the scheme when $k_\gamma = 0.15$

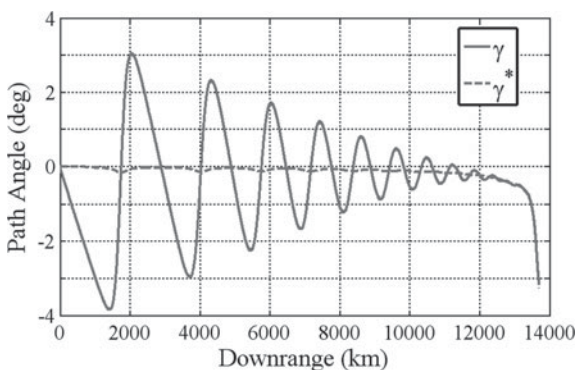


Fig. 9.15 L/D history for the scheme when $k_\gamma = 0.15$

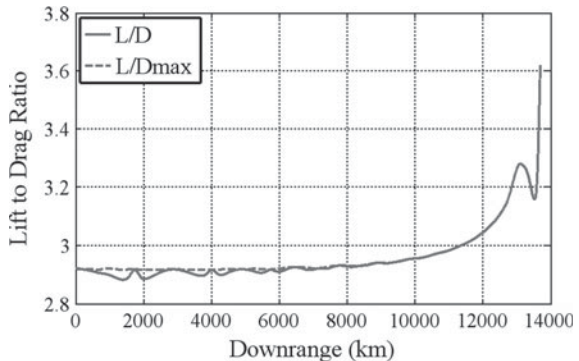
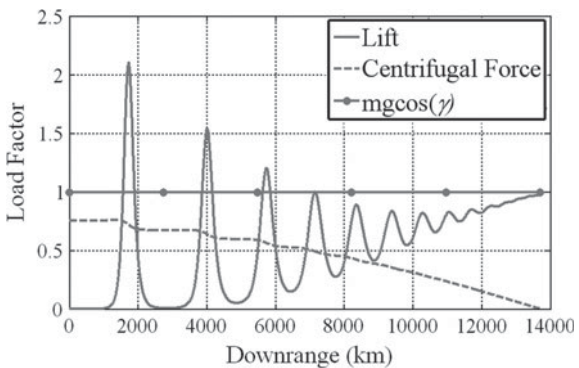


Fig. 9.16 Load factor history for the scheme when $k_\gamma = 0.15$



of the performance of the scheme: as the oscillation amplitude decreases to zero, γ converges to γ^* (Fig. 9.14), then α maximizes L/D (Fig. 9.15), and the lift force is approximately in equilibrium with the composition of the gravitational force and centrifugal force (Fig. 9.16).

In the second case, with limiting the maximum heating rate (\dot{Q}_{\max}) to be not greater than 500 W/cm^2 , the results for the optimal control are also compared with that for the scheme when $k_\gamma = 3$. Figure 9.17 shows the trajectories of the optimal control and the scheme. Figure 9.18 shows the histories of α . More characteristics of the results for both the optimal control and the scheme are shown in Figs. 9.19, 9.20, 9.21, 9.22, 9.23 and 9.24. The maximum glide range for the optimal control is 13 098.319 km and also slightly further than that for the scheme which is 12 912.065 km. As can be seen from these Figures, the lift to drag ratio for the optimal control is maximized as well as that for the scheme most of the time. The vibration decay rate for the optimal control is slower than that for the scheme which has a high degree of damping. According to the lift formula (i.e. Eq. (9.23)), the dynamic pressure is proportional to the lift force and inversely proportional to the lift coefficient. Therefore, from Fig. 9.24, it can be seen that the dynamic pressure for the scheme increases with time when $3000 \text{ km} < R < 12000 \text{ km}$ because the required lift

Fig. 9.17 Trajectories with $\dot{Q}_{\max} \leq 500 \text{ W/cm}^2$

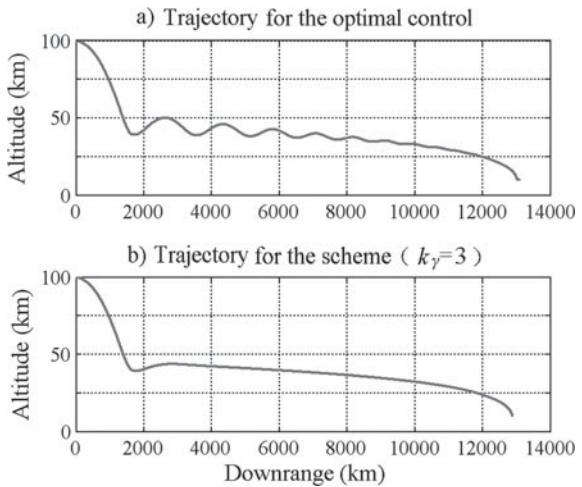
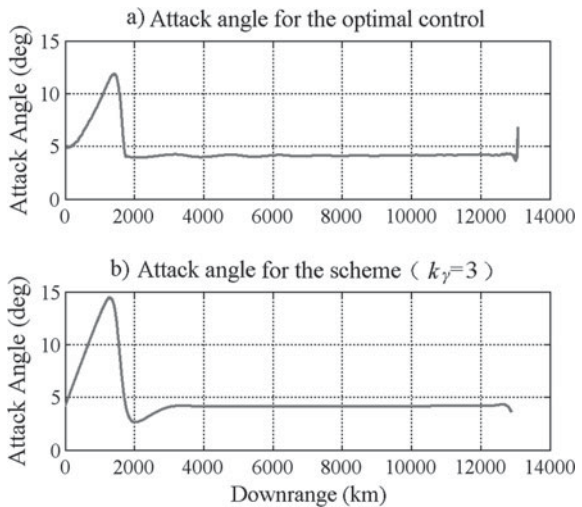


Fig. 9.18 Angle of attack histories with $\dot{Q}_{\max} \leq 500 \text{ W/cm}^2$



force increases (Fig. 9.22), and decreases when $R > 12\,000 \text{ km}$ because C_l^* rapidly increases. As with the previous results, there is also a small jump at the end of the trajectory for the optimal control, then the dynamic pressure decreases quickly. It causes that the vehicle loses lift greatly, and therefore the curves of the flight-path angle and lift load factor for the optimal control drop rapidly after the jump. It should be noted that there is a fact contrary to our experience: when the glide range is near 1 800 km, the flight-path angle increases with decreasing the angle of attack. It is because that, even though the angle of attack decreases, the atmospheric density increases rapidly with decreasing the altitude, then the lift force increases and be

Fig. 9.19 Speed histories with $\dot{Q}_{\max} \leq 500 \text{ W/cm}^2$

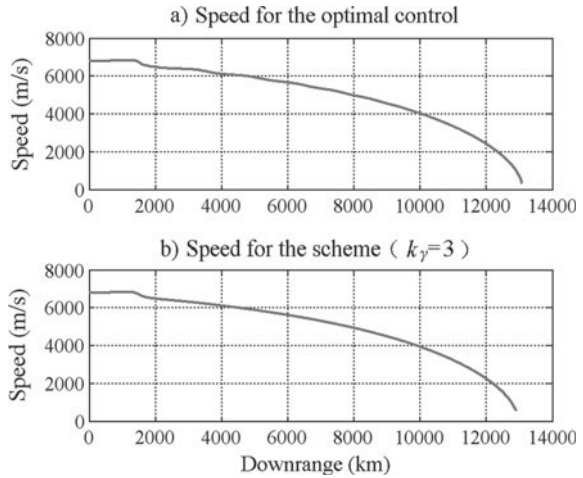
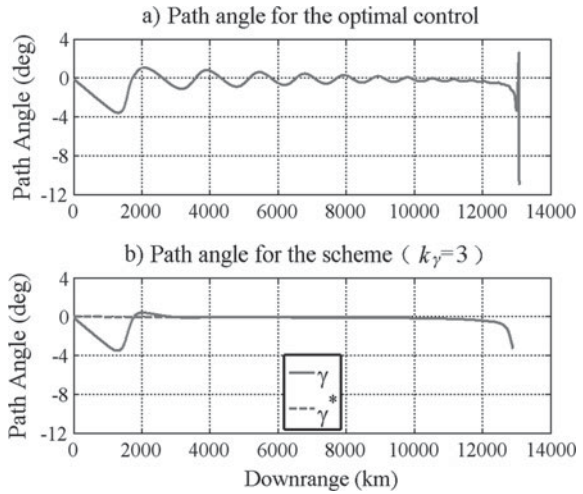


Fig. 9.20 Flight-path angle histories with $\dot{Q}_{\max} \leq 500 \text{ W/cm}^2$



greater than the composition of the other two forces (Fig. 9.22). Therefore, the lift force pulls the flight-path angle up.

9.4.2 Application of the Extended Guidance Scheme

This part shows the extension of the scheme which is to control the glide range by planning the profile of the L/D' . Here, under the control of the extended guidance scheme, the vehicle glides at L/D' , rather than at L/D_{\max} , in quasi-steady equilibrium condition. Where, L/D' is determined by Eq. (9.20) and Eq. (9.21). According to

Fig. 9.21 L/D histories with $\dot{Q}_{\max} \leq 500 \text{ W/cm}^2$

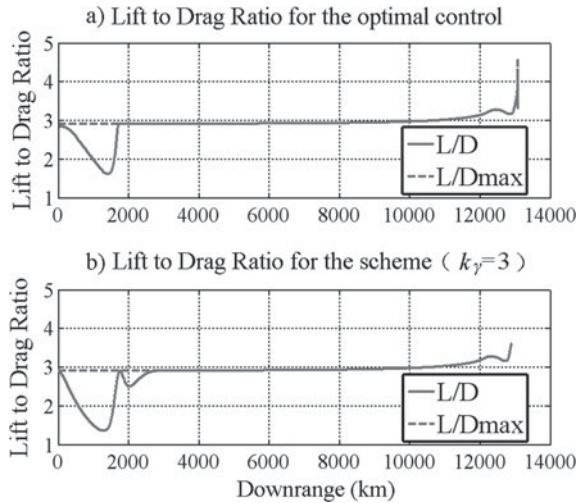
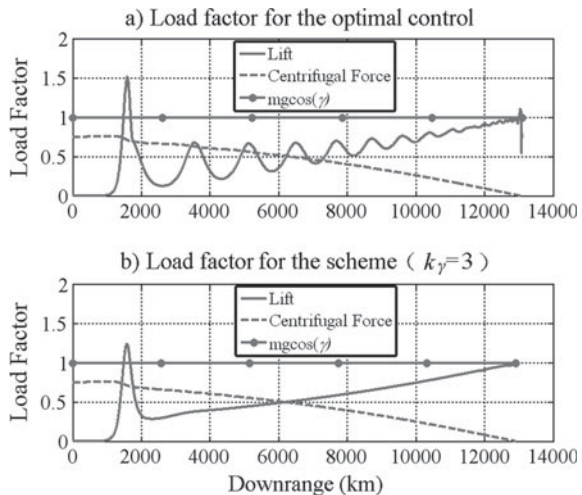


Fig. 9.22 Load factor histories with $\dot{Q}_{\max} \leq 500 \text{ W/cm}^2$



the simplified vehicle model, the lift coefficient for $L/D'(C'_l)$ and its derivative can be calculated by

$$C'_l = \frac{1 + \sqrt{1 - k_{L/D}^2}}{k_{L/D}} C_l^* \quad (9.31)$$

$$\frac{dC'_l}{dMa} = \frac{1 + \sqrt{1 - k_{L/D}^2}}{k_{L/D}} \frac{dC_l^*}{dMa} \quad (9.32)$$

Fig. 9.23 Heating rate histories with $\dot{Q}_{\max} \leq 500 \text{ W/cm}^2$

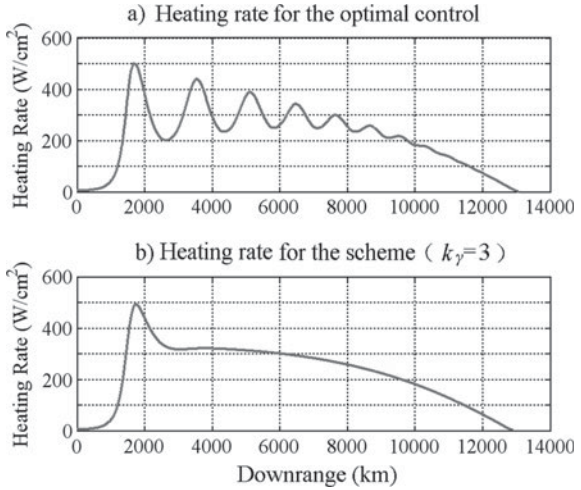
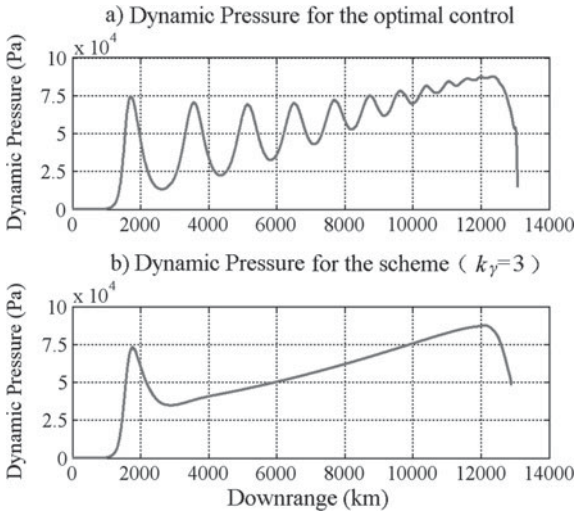


Fig. 9.24 Dynamic pressure histories with $\dot{Q}_{\max} \leq 500 \text{ W/cm}^2$



Here, the formulas of C_l^* and its derivative can be found in Eq. (9.27) and Eq. (9.28). Then, α' and C_d' can be obtained by substituting Eq. (9.31) into Eq. (9.25) and Eq. (9.26).

The preceding example shows that, the maximum glide range for the scheme is 12 912.065 km when $k_\gamma = 3$, the initial and final special energy are about $-3.83 \times 10^7 \text{ J/kg}$ and $-6.21 \times 10^7 \text{ J/kg}$ respectively. When the initial conditions and final special energy are the same as that of the preceding example, under the control of Eq. (9.22), Figs. 9.25 and 9.26 show that the final glide range and the maximum heating rate are functions of $k_{L/D}$. It can be seen that when $k_{L/D} > 0.4$, the glide range is approximately proportional to $k_{L/D}$. Due to the limitation of the angle of

Fig. 9.25 Glide range as a function of $k_{L/D}$

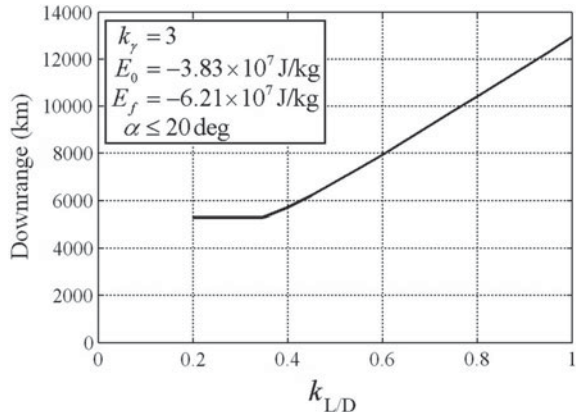
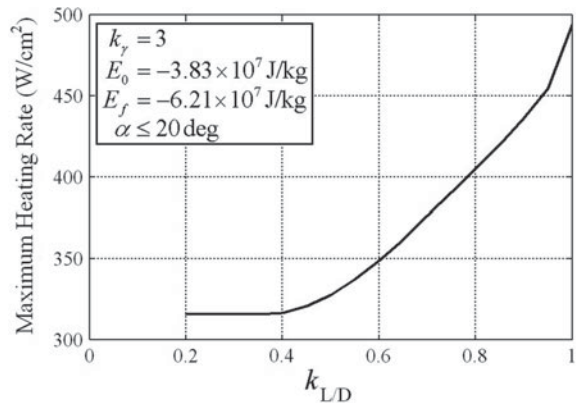


Fig. 9.26 Maximum heating rate as a function of $k_{L/D}$



attack, the glide range and maximum heating rate have no change with $k_{L/D}$ when $k_{L/D}$ is near 0.2.

In this example, it is needed to steer the vehicle to glide 10 000 km with $E_f = -6.21 \times 10^7 \text{ J/kg}$. In this respect, let $k_{L/D}$ be equal to the ratio of the required glide range and the maximum glide range for the scheme, which is about 0.7743, set $k_\gamma = 3$, and then glide the vehicle under the control of Eq. (9.22). The simulation results compared with that of the maximum glide flight (i.e. $k_{L/D} = 1$) are shown in Figs. 9.27, 9.28, 9.29, 9.30, 9.31 and 9.32. The final glide range with $k_{L/D} = 0.7743$ is 10 104.317 km and has an error of about 1%. From Fig. 9.29, it can be seen that γ' still accurately approximates the flight-path angle at the L/D' in quasi-steady equilibrium condition.

Fig. 9.27 Trajectories when $k_\gamma = 3$

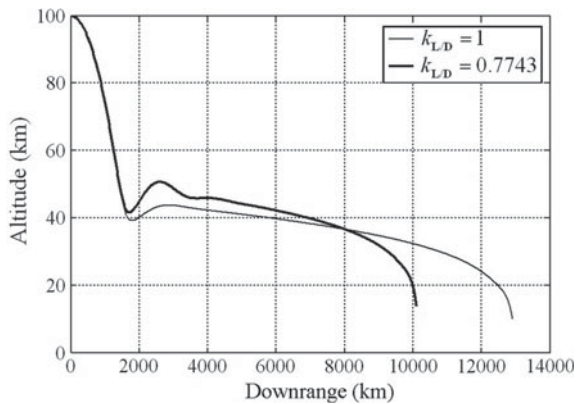


Fig. 9.28 Special energy histories when $k_\gamma = 3$

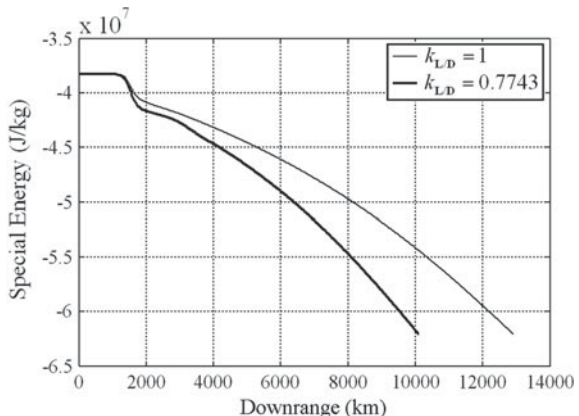


Fig. 9.29 Angle of attack histories when $k_\gamma = 3$

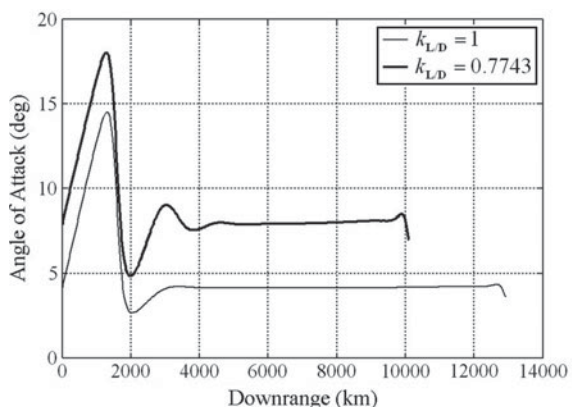


Fig. 9.30 Speed histories when $k_\gamma = 3$

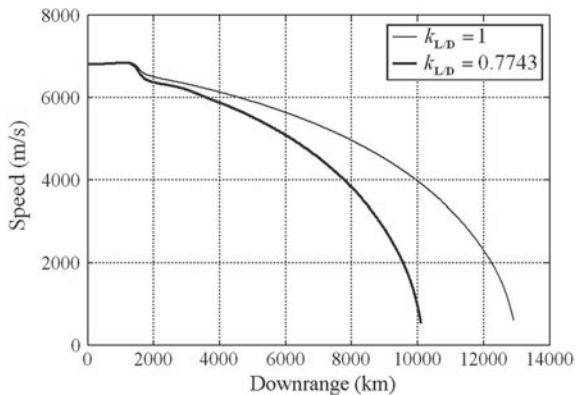


Fig. 9.31 Flight-path angle histories when $k_\gamma = 3$

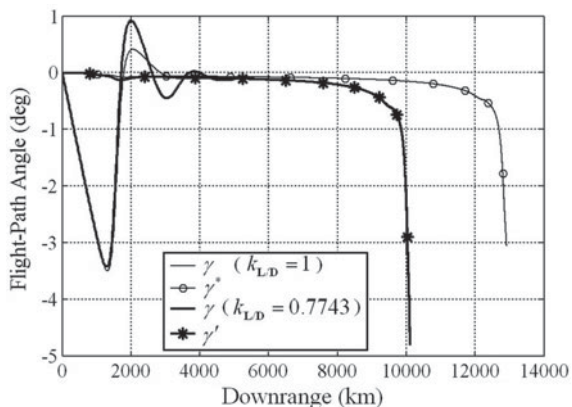
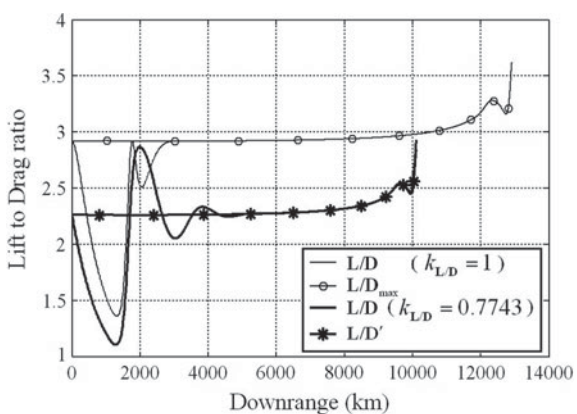


Fig. 9.32 L/D histories when $k_\gamma = 3$



9.5 Conclusions

The study proves that the L/D_{\max} operation in a decelerating glide phase of a hypersonic vehicle is approximately glide-range-optimal over a spherical Earth. Then a guidance scheme based on the theory is provided to maximize the glide range. In the scheme, a damping component is added to the lift force. Therefore the oscillation is suppressed. The maximum heating rate, dynamic pressure and load factor also decreases quickly with increasing the feedback gain. In addition, the scheme is extended to control the glide range of the vehicle by planning the profile of the required L/D . A simple and rapid method of planning the required L/D is introduced and the simulation results show that the glide range is nearly proportional to $k_{L/D}$.

References

1. Yu, W., Chen, W.: Guidance scheme for glide range maximization of a hypersonic vehicle. AIAA Guidance, Navigation, and Control Conference, Portland (2011)
2. Sheu, D., Chen, Y.M., Chern, J.S.: Optimal three-dimensional glide for maximum reachable domain. 24th Atmospheric Flight Mechanics Conference, Portland (1999)
3. Morimoto, H., Chuang, J.C.H.: Minimum-fuel trajectory along entire flight profile for a hypersonic vehicle with constraint. AIAA Guidance, Navigation, and Control Conference and Exhibit, Boston (1998)
4. Kelley, H.J., Cliff, E.M., Lutze, F.H.: Boost-glide range-optimal guidance. Optimal Control Applications and Methods **3**(3), 293–298 (1982)
5. Phillips, C.A.: Guidance algorithm for range maximization and time-of-flight control of a guided projectile. J. Guid. Control Dyn. **31**(5), 1447–1455 (2008)
6. Fornberg, B.: A practical guide to pseudospectral methods. Cambridge University Press, Cambridge (1998)
7. Rao, A.V.: User's manual for GPOPS version 3.0: a MATLAB software for solving multiple-phase optimal control problems using pseudospectral methods. Publications Dept, ACM Inc, New York (2008)
8. Rao, A.V.: Algorithm 902: GPOPS, a MATLAB software for solving multiple-phase optimal control problems using the gauss pseudospectral methods. Publications Dept, ACM Inc, New York (2008)
9. Sissenwine, N., et al.: U.S. Standard Atmosphere, 1976. U.S. Government Printing Office, Washington D.C. (1976)
10. Ware, G.M., Cruz, C.I.: Aerodynamic characteristics of the HL-20. Journal of Spacecraft & Rockets **30**(5), 529–536 (1993)

Chapter 10

Steady Glide Dynamic Modeling and Trajectory Optimization for High Lift-To-Drag Ratio Reentry Vehicle



10.1 Introduction

Entry guidance plays an important role in generating the steering command to guide the vehicle from its initial condition to reach the destination safely and accurately [1]. In general, traditional reentry guidance divides into two parts. The first part is the generation of a feasible reference trajectory. The second part is the tracking of this reference trajectory [2]. This chapter focuses on generating a feasible steady glide reference trajectory, especially for high lift-to-drag ratio reentry vehicle, using numerical optimal method. Previous researches in reentry trajectory optimization are summarized as follows. Scott applied the Legendre Pseudospectral method into the trajectory optimization of reentry vehicles. In Josselyn's work [3], covector mapping theorem of Legendre Pseudospectral method was used to verify the first-order optimality condition arising in the path-constraints trajectory optimization. Anil Rao [4] also studied the problem of reentry trajectory optimization using Legendre Pseudospectral method. The key features of the optimal trajectory and quality of trajectory obtained from the Legendre Pseudospectral method were discussed. Jorris and Zhao [5, 6] employed the Gauss Pseudospectral method to optimize the 2-D and 3-D reentry trajectory for Common Aero Vehicle (CAV), in which waypoint and no-fly zone constraints were considered as inner-point constraints in optimal process. Rahimi [7] applied the particle swarm optimization into spacecraft reentry optimization. High-order polynomials were used to approximate the angle of attack and bank angle in problem formulation. The coefficients of both polynomials were considered as input variables in optimal process. It should be noted that, because of not considering the trajectory-oscillation suppressing scheme, the optimal trajectories generated from above methods are naturally oscillatory. In steady glide, the heating rate will not change sharply and the steady state will greatly release the burden of control system. Therefore, steady glide trajectory is the best reference trajectory for the reentry guidance. Actually, quasi-equilibrium-glide condition (QEBC) is a well-known "soft" path constraint that makes the trajectory change monotonously. However, complicated reentry dynamics, especially for high lift-to-drag ratio vehicle,

is so sensitive to the “soft” path constraint that it is very difficult for numerical optimization method to converge when QEGC is considered in optimal process. Generally speaking, this constraint is suitable for the trajectory planning in which one or two parameters are searched by secant method so as to generate a feasible trajectory [8–10]. Therefore, steady glide trajectory optimization for the high lift-to-drag ratio vehicle is always a challenge for numerical optimization.

The objective of this chapter is to investigate the steady glide dynamic modeling and trajectory optimization for the high lift-to-drag ratio vehicle. A new steady glide dynamic modeling is formulated by extending a trajectory-oscillation suppressing scheme, which is presented by Yu in [11], into three-dimensional reentry dynamics. Firstly, a special flight-path angle which is able to keep the vehicle flying in a steady glide is calculated from the command angle of attack, command bank angle and current states. Then, the trajectory-oscillation is suppressed via regulating the longitudinal acceleration in negative feedback form and keeping the lateral acceleration invariant. It should be noted that the negative feedback signal is the deviation between the special flight path angle and actual flight path angle. Simulation result shows that this scheme performs well in suppressing trajectory-oscillation and guides the vehicle into steady glide as soon as possible. Additionally, a study on steady glide trajectory optimization is investigated based on this new modeling. The derivatives of command angle of attack and bank angle are chosen as the control variables. And the performance index is the weighted squares sum of those derivatives. The limits on actual angle of attack and bank angle are considered as the path constraints. In fact, steady glide trajectory optimization is a typical optimal control problem whose solutions change rapidly in certain regions. Therefore, hp-adaptive Gaussian quadrature collocation method [12], which performs well in dealing with this kind of problem, is chosen to transfer the optimal control problem into a standard nonlinear programming problem and solve it. The notable difference from the Yu’s method is that the scheme is suitable for the three-dimensional reentry dynamics. Another notable difference is that the scheme comprehensively considers all factors (including the derivatives of reference angle of attack and reference bank angle) acting on the flight path angle. That makes it easy to integrate into the motion dynamics by the choice of those derivatives as the control variables. Two classical numerical optimal examples (with and without bank reversal) are taken to evaluate the performance of the steady glide trajectory optimization. In order to demonstrate the superior performance in applicability and computational efficiency, a comparison with the traditional method is also provided. Furthermore, a comparison between optimal trajectory and integral trajectory is carried out to verify the feasibility of the pseudospectral solution. The results show that the new method not only significantly improves the computational efficiency of trajectory optimization since using fewer nodes will achieve a higher accuracy for the steady glide reentry trajectory, but also has an extensive applicability in considering more final constraints even with the bank reversal. Most importantly, it is capable of providing more stable and safer optimal steady glide trajectory with high precision, which would be a better choice for tracking guidance.

This chapter is organized as follows: entry dynamics including entry trajectory constraints and vehicle model are described in Sect. 10.2; three-dimensional reentry trajectory-oscillation suppressing scheme is presented in Sect. 10.3; steady glide dynamic modeling and trajectory optimization are presented in detail in Sect. 10.4.

10.2 Dynamics and Vehicle Description

10.2.1 Entry Dynamics

The 3 DOF point mass dynamics of the reentry vehicle over a spherical, rotating Earth is described as follows [13]:

$$\dot{r} = V \sin \gamma \quad (10.1)$$

$$\dot{\theta} = \frac{V \cos \gamma \sin \psi}{r \cos \varphi} \quad (10.2)$$

$$\dot{\varphi} = \frac{V \cos \gamma \cos \psi}{r} \quad (10.3)$$

$$\dot{V} = -\frac{D}{m} - g \sin \gamma + \omega^2 r \cos \varphi (\sin \gamma \cos \varphi - \cos \gamma \sin \varphi \cos \psi) \quad (10.4)$$

$$\dot{\gamma} = \frac{1}{V} \left(\left(\frac{L \cos \sigma}{m} + \left(\frac{V^2}{r} - g \right) \cos \gamma + 2\omega V \cos \varphi \sin \psi \right) + \omega^2 r \cos \varphi (\cos \gamma \cos \varphi + \sin \gamma \sin \varphi \cos \psi) \right) \quad (10.5)$$

$$\dot{\psi} = \frac{1}{V} \left(\frac{L \sin \sigma}{m} + \frac{V^2}{r} \cos \gamma \sin \psi \tan \varphi - 2\omega V (\cos \varphi \tan \gamma \cos \psi - \sin \varphi) + \frac{\omega^2 r}{\cos \gamma} \sin \varphi \cos \varphi \sin \psi \right) \quad (10.6)$$

where, r is the radial distance from the center of the Earth to the vehicle. In the later, h denotes the altitude. The radius of the Earth is 6 378 145 m. θ and φ are the longitude and latitude, respectively. V is the Earth-relative velocity. γ is the flight-path angle of the Earth-relative velocity. ψ is the azimuth angle of the Earth-relative velocity. m is the mass of the vehicle. $g = \mu/r^2$ is the gravity acceleration, where μ is Earth's gravitational constant. ω denotes the Earth self-rotation rate. The aerodynamic lift L and drag D are given as follows:

$$\begin{aligned} L &= \frac{1}{2} \rho V^2 C_l S_{ref} \\ D &= \frac{1}{2} \rho V^2 C_d S_{ref} \end{aligned} \quad (10.7)$$

where, $\rho = \rho_0 \exp(-h/H)$ is the atmospheric density, where ρ_0 is the standard atmospheric pressure from the sea-level. S_{ref} is the reference area of the vehicle. C_l and C_d are lift and drag coefficients which are dependent on the vehicle configuration.

10.2.2 Entry Trajectory Constraints

Typical entry trajectory inequality path constraints for hypersonic vehicle include

$$k\sqrt{\rho}V^{3.15} \leq \dot{Q}_{\max} \quad (10.8)$$

$$|L \cos \alpha + D \sin \alpha| \leq n_{\max} \quad (10.9)$$

$$\frac{1}{2}\rho V^2 \leq q_{\max} \quad (10.10)$$

where, Eq. (10.8) is the heating rate at a stagnation point on the surface of the vehicle. Equation (10.9) is the aerodynamic acceleration in the body-normal direction. Equation (10.10) is the dynamic pressure. The heating limit value is \dot{Q}_{\max} , the load factor limit value is n_{\max} , and the dynamic pressure limit value is q_{\max} . These are dependent on the vehicle configuration and mission. Those three constraints are considered to be ‘hard’ constraints that should be enforced strictly.

10.2.3 Vehicle Description and Model Assumption

Common Aero Vehicle (CAV) is one of the most representative hypersonic entry vehicles with high lift-to-drag ratio. Relaying on aerodynamic control, this vehicle is able to glide without power through the atmosphere. There are two types of CAV in the report of Phillips [14], the low-lift CAV and the high-lift CAV. The high-lift CAV, namely CAV-H, is modeled here to extend the trajectory optimization. The weight of CAV-H is 907 kg, the area reference is 0.483 9 m², and the maximum Lift-to-Drag ratio is about 3.5. In order to make derivation analysis more intuitive and easier to follow, it is assumed that the lift and drag coefficients are only dependent on the angle of attack. They can be expressed in the form as

$$\begin{cases} C_l = k_{l1}\alpha + k_{l2} \\ C_d = k_{d1}\alpha^2 + k_{d2}\alpha + k_{d3} \end{cases} \quad (10.11)$$

where, $k_{l1} = 0.04675$, $k_{l2} = -0.10568$, $k_{d1} = 0.000508$, $k_{d2} = 0.004228$, $k_{d3} = 0.0161$. Moreover, because the angle of attack having the maximum lift-to-drag ratio

is about 10 Deg, the scope of angle of attack is extended to $[5^\circ, 20^\circ]$. The scope of bank angle is limited within $[-60^\circ, 60^\circ]$. The limiting values of heating rate, dynamic pressure and normal load factor are 400 W/cm^2 , 60 kPa and 2 g respectively.

10.3 Trajectory-Oscillation Suppressing Scheme

The objective of trajectory-oscillation suppressing scheme is to make the vehicle flying in a steady glide so that the heating rate won't change sharply, which also will significantly release the burden of control system. In this section, a trajectory-oscillation suppressing scheme using the flight path angle feedback is extended. Firstly, the command angle of attack and bank angle are used to calculate the special flight path angle that keeps the two-order derivative of flight path angle zero. Then, the trajectory-oscillation is suppressed via regulating the longitudinal acceleration in negative feedback form and keeping the lateral acceleration invariant. The negative feedback signal is the deviation between the special flight path angle and actual flight path angle. Simulation results show that the scheme is capable of guiding the vehicle into a steady condition in which the command angle of attack and bank angle can generate enough vertical lift to sustain the vehicle glide.

10.3.1 Generic Theory for the Oscillation Suppressing Scheme

Let us pay attention to the Eq. (10.5). While the flight path angle is small and varies relatively slow, it is assumed that $\cos\gamma = 1$ and $\sin\gamma = \gamma$. Therefore, the Eq. (10.5) without considering the earth rotation is formulated as

$$\dot{\gamma} = \frac{1}{V} \left(\frac{L \cos \sigma}{m} + \left(\frac{V^2}{r} - g \right) \right) \quad (10.12)$$

where, $L = \frac{1}{2} \rho V^2 C_l S_{ref}$, $g = \frac{\mu}{r^2}$. Substitute them into Eq. (10.12), then, Eq. (10.13) is the derivative of the Eq. (10.12) with respect to time.

$$\ddot{\gamma} = \frac{1}{V} \frac{d \left(\frac{\rho V^2 C_l S_{ref} \cos \sigma}{2m} + \left(\frac{V^2}{r} - \frac{\mu}{r^2} \right) \right)}{dt} + \left(\frac{D}{m} + g\gamma \right) \left(\frac{\rho C_l S_{ref} \cos \sigma}{2m} + \left(\frac{1}{r} - \frac{g}{V^2} \right) \right) \quad (10.13)$$

where,

$$\begin{aligned} \frac{d\left(\frac{\rho V^2 C_l S_{ref} \cos \sigma}{2m} + \left(\frac{V^2}{r} - \frac{\mu}{r^2}\right)\right)}{dt} &= \frac{V^2 C_l S_{ref} \cos \sigma}{2m} \dot{r} + \frac{\rho V C_l S_{ref} \cos \sigma}{m} \dot{V} \\ &\quad + \frac{\rho V 2 S_{ref}}{2m} (\dot{C}_l \cos \sigma - C_l \sin \sigma \dot{\sigma}) + \frac{2V}{r^2} \dot{V} - \frac{V^2}{r^2} \dot{r} + 2 \frac{\mu}{r^3} \dot{r} \end{aligned} \quad (10.14)$$

Substitute Eq. (10.1), Eq. (10.4) and the derivative of the atmospheric density into Eq. (10.14). Then, substitute Eq. (10.14) into Eq. (10.13). The two-order derivative of flight path angle can be rewritten as

$$\begin{aligned} \ddot{\gamma} &= -\frac{\rho V^2 C_l S_{ref} \cos \sigma}{2mH} \gamma - \frac{\rho C_l S_{ref} \cos \sigma D}{2m^2} - \frac{\rho C_l S_{ref} \cos \sigma g}{2m} \gamma \\ &\quad + \frac{\rho V S_{ref}}{2m} (\dot{C}_l \cos \sigma - C_l \sin \sigma \dot{\sigma}) - \frac{D}{rm} - \frac{V^2}{r_2} \gamma - \frac{Dg}{mV^2} + \frac{g}{r} \gamma - \frac{g^2}{V^2} \gamma \end{aligned} \quad (10.15)$$

where, the derivative of lift coefficient is formulated as follow

$$\dot{C}_l = \frac{\partial C_l}{\partial \alpha} \cdot \frac{\partial \alpha}{\partial t} + \frac{\partial C_l}{\partial Ma} \cdot \frac{\partial Ma}{\partial r} \cdot \frac{\partial r}{\partial t} \quad (10.16)$$

For reentry vehicle, the Mach number is much larger than five. Therefore, the aerodynamic coefficients are often assumed to be not dependent on the Mach number. Then, the last term in Eq. (10.16) can be neglected.

Now, consider that the vehicle is in a certain condition of reentry process, if the command angle of attack and bank angle are given, the special flight path angle that keeps the two-order derivative of flight path angle zero can be formulated as follow.

$$\begin{aligned} \gamma_m &= \frac{D^*}{-mV^2 - mg - \frac{2m^2 V^2}{r^2 \rho C_l^* S_{ref} \cos \sigma} + \frac{2m^2 g}{r \rho C_l^* S_{ref} \cos \sigma} - \frac{2m^2 g^2}{V^2 \rho C_l^* S_{ref} \cos \sigma}} \\ &\quad + \frac{(\dot{C}_l^* \cos \sigma - C_l^* \sin \sigma \dot{\sigma})}{\frac{VC_l^* \cos \sigma}{H} + \frac{C_l^* \cos \sigma g}{V} + \frac{2mV}{r^2 \rho S_{ref}} - \frac{2mg}{r \rho V S_{ref}} + \frac{2mg^2}{V^3 \rho S_{ref}}} \\ &\quad + \frac{D^*}{-\frac{\rho V^2 C_l^* S_{ref} \cos \sigma r}{2H} - \frac{\rho C_l^* S_{ref} \cos \sigma gr}{2} - \frac{V^2}{r} m + mg - \frac{g^2 rm}{V^2}} \\ &\quad + \frac{D^*}{-\frac{\rho V^4 C_l^* S_{ref} \cos \sigma}{2Hg} - \frac{\rho V^2 C_l^* S_{ref} \cos \sigma}{2} - \frac{mV^4}{r^2 g} + \frac{mV^2}{r} - mg} \end{aligned} \quad (10.17)$$

where, superscript “*” denotes the lift and drag coefficients dominated by the command angle of attack and bank angle. The notable difference from the Yu's work is that the special flight path angle is derived from the three-dimensional reentry dynamics and comprehensively considers all factors including the derivatives of command angle of attack and bank angle. In the later section, the special flight path angle is easily calculated in the trajectory optimization when consider the derivatives

of command angle of attack and bank angle as control variables. Then, trajectory-oscillation is suppressed via regulating the longitudinal acceleration in negative feedback form and keeping the lateral acceleration invariant. The flight path angle also tends to the special flight path angle as soon as possible.

$$\begin{cases} C_{l2} \cos \sigma_2 = C_{l1} \cos \sigma_1 + K(\gamma - \gamma_m) \\ C_{l2} \sin \sigma_2 = C_{l1} \sin \sigma_1 \end{cases} \quad (10.18)$$

where, C_{l2} is the actual lift coefficient, C_{l1} is the command lift coefficient dominated by the command angle of attack. σ_2 is the actual bank angle. σ_1 is the command bank angle. K is a negative feedback gain, it should be noted that a better K will perform well in suppressing the trajectory oscillation. Then, a numerical simulation of entry process is carried out to evaluate the performance of the proposed scheme.

10.3.2 Performance of the Trajectory-Oscillation Suppressing Scheme

In this subsection, the proposed scheme is applied into reentry simulation with constant command angle of attack and bank angle. The simulation model, aerodynamic data and some key parameters are stated in Sect. 10.2.3. The command angle of attack is 10 Deg. The command bank angle is also 10 Deg. If the assumptions mentioned in Sect. 10.2.3 are hold, the actual angle of attack and bank angle suppressing the trajectory-oscillation can be calculated as follows.

$$\sigma_2 = \arctan\left(\frac{C_{l1} \sin \sigma_1}{C_{l1} \cos \sigma_1 + K(\gamma - \gamma_m)}\right) \quad (10.19)$$

$$\alpha_2 = \frac{1}{k_{l1}} \left(\frac{C_{l1} \cos \sigma_1 + K(\gamma - \gamma_m)}{\cos \sigma_2} - k_{l2} \right) \quad (10.20)$$

The initial states are $h_0 = 60$ km, $\theta_0 = 0$ Deg, $\varphi_0 = 0$ Deg, $V_0 = 7100$ m/s, $\gamma_0 = 0$ Deg, $\psi_0 = 90$ Deg. All programs run on a personal computer with a 3.3 GHz processor and MATLAB 2008b. The solver of integral is ODE-45. The simulation stops when the altitude reduces to 30 km. Another worthy note is the negative feedback gain. After some attempts, it is easy to find that the trajectory-oscillation will be suppressed perfectly when K is -16. Figure 10.1 shows the three-dimensional view of reentry trajectories. Note that the reference trajectory is the integral trajectory using the constant angle of attack and bank angle. It is obvious that the vehicle glides through the atmosphere in a great performance. Moreover, the glide trajectory is similar to the reference trajectory except that the trajectory-oscillation is suppressed.

Figure 10.2 shows the time histories of angle of attack and bank angle respectively. The actual angle of attack and bank angle change substantially at the beginning of

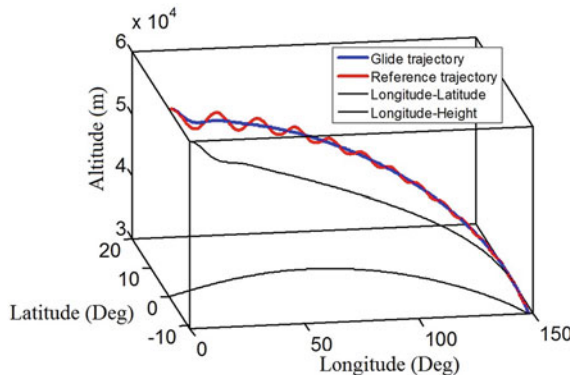


Fig. 10.1 Three-dimensional view of trajectory

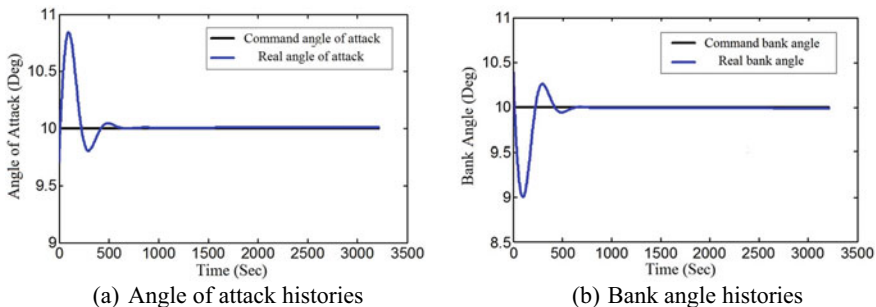


Fig. 10.2 Histories of angle of attack and bank angle

the flight and converge into the command angle of attack and bank angle quickly. Therefore, it is easy to conclude that applying the proposed scheme will guide the vehicle into a special condition in which the command angle of attack and bank angle will keep the vehicle glide steadily. Another point should be noted is that the strict mathematical proof of convergence for this proposed method is absent. The future work will focus on this point.

10.4 Steady Glide Dynamic Modeling and Trajectory Optimization

In this section, the steady glide trajectory optimization is carried out to find the optimal controls satisfying path and final constraints. Firstly, a new steady glide dynamic modeling is formulated via integrating the trajectory-oscillation suppressing

scheme into the motion dynamics while remaining the intrinsic properties. Secondly, the steady glide trajectory optimization is formulated based on this new modeling. The derivatives of command angle of attack and bank angle used to determine the special flight-path angle are considered as control variables, and a performance index used to provide the stable controls is selected. Because steady glide trajectory optimization is a typical control problem whose solutions change rapidly in certain regions or are discontinuous, the hp-adaptive Gaussian quadrature collocation method is naturally selected to transfer it into a nonlinear programming problem. Finally, two numerical examples with and without bank reversal are used to evaluate the performance and applicability of the new method. In order to demonstrate its superior performance in computational efficiency, a comparison with the traditional method is also provided. Moreover, a comparison between the optimal trajectory and integral trajectory is carried out to further verify the feasibility of the solution provided by the pseudospectral solver.

10.4.1 Steady Glide Dynamic Modeling

In previous section, the trajectory-oscillation suppressing scheme is presented in Sect. 10.3.1. The performance of this scheme is evaluated by the simulation in Sect. 10.3.2. Now, the steady glide dynamic modeling is formulated via integrating the trajectory-oscillation suppressing scheme into the three-dimensional reentry dynamics in Sect. 10.2.1.

$$\left\{ \begin{array}{l} \dot{r} = V \sin \gamma; \dot{\theta} = \frac{V \cos \gamma \sin \psi}{r \cos \varphi}; \dot{\varphi} = \frac{V \cos \gamma \cos \psi}{r} \\ \dot{V} = -\frac{D_2}{m} - g \sin \gamma + \omega^2 r \cos \varphi (\sin \gamma \cos \varphi - \cos \gamma \sin \varphi \cos \psi) \\ \dot{\gamma} = \frac{1}{V} \left(\frac{L_2 \cos \sigma_2}{m} + \left(\frac{V^2}{r} - g \right) \cos \gamma + 2\omega V \cos \varphi \sin \psi \right. \\ \quad \left. + \omega^2 r \cos \varphi (\cos \gamma \cos \varphi + \sin \gamma \sin \varphi \cos \psi) \right) \\ \dot{\psi} = \frac{1}{V} \left(\frac{L_2 \sin \sigma_2}{m} + \frac{V^2}{r} \cos \gamma \sin \psi \tan \varphi - 2\omega V (\cos \varphi \tan \gamma \cos \psi - \sin \varphi) \right. \\ \quad \left. + \frac{\omega^2 r}{\cos \gamma} \sin \varphi \cos \varphi \sin \psi \right) \\ \sigma_2 = \text{atan} \left(\frac{C_{I1} \sin \sigma_1}{C_{I1} \cos \sigma_1 + K(\gamma - \gamma_m)} \right); \alpha_2 = \frac{1}{k_{I1}} \left(\frac{C_{I1} \cos \sigma_1 + K(\gamma - \gamma_m)}{\cos \sigma_2} - k_{I2} \right) \\ \gamma_m = f(r, V, \alpha_1, \sigma_1, \dot{\alpha}_1, \dot{\sigma}_1); \dot{\alpha}_1 = u_1; \dot{\sigma}_1 = u_2 \end{array} \right. \quad (10.21)$$

where, L_2 is the actual aerodynamic lift dominated by the command angle of attack, $\dot{\alpha}_1$, $\dot{\sigma}_1$ are the derivatives of command angle of attack and bank angle, α_1 , σ_1 and σ_2 are defined in previous sections. If $\dot{\alpha}_1$ and $\dot{\sigma}_1$ are given, there exists a specific steady

glide trajectory determined by the steady glide dynamic modeling. Thus, steady glide trajectory optimization is continued based on this modeling in the next section so as to find the optimal control satisfying path and final constraints. Another point should be noted is that there is analytical solution for the actual angle of attack and bank angle because of the simplification of aerodynamic coefficients. However, if complex aerodynamic coefficients are considered in the steady glide trajectory optimization, it only needs to regard the complex function of aerodynamic coefficients as the equality constraint in optimal process.

10.4.2 *H_p-Adaptive Gaussian Quadrature Collocation Method*

H_p-adaptive Gaussian quadrature collocation method is an efficient tool for solving multiple-phase optimal control problems using variable-order Gaussian quadrature collocation methods [15, 16]. Because an adaptive mesh refinement scheme [17, 18] is implemented to achieve a specified accuracy, this method performs well in solving the optimal control problem whose solutions change rapidly in certain regions or are discontinuous. In each mesh interval, the dynamics and constraints are transferred into a set of nonlinear algebraic constraints by employing a Legendre-Gauss-Radau quadrature collocation method. Therefore, the continuous-time optimal control problem is transferred to a large sparse nonlinear programming problem that is solved using well-established techniques. This method takes the advantage of the exponential convergence in regions where the solution is smooth and places mesh points only near potential discontinuities or in regions where the solution changes rapidly.

Steady glide trajectory optimization problem for high lift-drag ratio reentry vehicle is a complex constrained continuous-time optimal control problem. What's more, there exist several regions where the state and control variables change rapidly. At the beginning of the reentry, because the vehicle has not enough control capacity at high altitude, the altitude decreases rapidly in this phase. When the vehicle decreases to an appropriate height in which the vehicle has enough vertical lift to sustain the vehicle glide, the state and control variables also change rapidly. At the end of flying, it only takes a short time to steer the vehicle to meet the final requirements. The state and control variables also change rapidly. However, the vehicle glides in a steady and smooth condition for most of the flight duration. Naturally, hp-adaptive Gaussian quadrature collocation method is suitable for solving the steady glide trajectory optimization problem. The later numerical results also show that hp-adaptive Gaussian quadrature collocation method performs well in various glide trajectory optimizations.

10.4.3 Numerical Example of Trajectory Optimization Without Bank Reversal

In this subsection, hp-adaptive Gaussian quadrature collocation method is applied to solve the steady glide trajectory optimization problem. Meanwhile, a comparison with the traditional entry trajectory optimization using the dynamics of motion in Eqs. (10.1)–(10.6) is also provided so as to further demonstrate the superior performance of the new method. Some of the simulation parameters are the same as those mentioned in above sections. For steady glide trajectory optimization, the motion dynamics are formulated in Eq. (10.18). In optimization process, the derivatives of command angle of attack and bank angle are chosen as the control variables, and the angle of attack and bank angle are considered as procedure variables. In order to make the trajectory state and optimal control as smooth and stable as possible, the performance index is selected as follow.

$$J = \int_{t_0}^{t_f} K_1 \dot{\alpha}_1^2 + K_2 \dot{\sigma}_1^2 dt \quad (10.22)$$

where, K_1 and K_2 are control weighting coefficients. The limits on actual angle of attack and actual bank-angle are considered as path constraints and presented as follows.

$$\sigma_{\min} \leq \arctan\left(\frac{Cl_1 \sin \sigma_1}{Cl_1 \cos \sigma_1 + K(\gamma - \gamma_m)}\right) \leq \sigma_{\max} \quad (10.23)$$

$$\alpha_{\min} \leq \frac{1}{k_{l1}} \left(\frac{Cl_1 \cos \sigma_1 + K(\gamma - \gamma_m)}{\cos \sigma_2} - k_{l2} \right) \leq \alpha_{\max} \quad (10.24)$$

For the traditional trajectory optimization, the control variables are the derivatives of angle of attack and bank angle, and the performance index is the weighted square sum of those derivatives. The initial and final conditions for both methods are listed in Table 10.1. It should be noted that the traditional trajectory optimization will fail

Table 10.1 Initial and final conditions for different methods

Initial condition						
	θ_0 (Deg)	φ_0 (Deg)	h_0 (m)	V_0 (m/s)	γ_0 (Deg)	ψ_0 (Deg)
Traditional method	0	0	70 000	6 900	0	65
New method	0	0	70 000	6 900	0	65
Final condition						
	θ_f (Deg)	φ_f (Deg)	h_f (m)	V_f (m/s)	γ_f (Deg)	ψ_f (Deg)
Traditional method	–	0	30 000	2 400	0	–
New method	156.6	0	30 000	2 400	0	–

to converge due to considering too many final constraints. So, the final longitude is set to be free. However, the new method is capable of addressing the problem with all final constraints. Therefore, the final longitude for such optimization is fixed at the optimal longitude provided by the traditional method. Another point should be noted is that both optimal results come from the same initial guess.

In the procedure of optimization, finite difference method is used to provide the derivatives of nonlinear programming problem for both optimizations. Because the flight-path angle is so sensitive, it is necessary to set the step of finite difference method to be a small value. The step is then set at 10^{-9} . In addition, the feasible and optimal tolerances are set at 10^{-8} respectively.

Numerical results for the case without bank reversal are presented in Fig. 10.3. As seen from those figures, it is apparent that a perfect steady glide optimal trajectory satisfying all constraints is provided via the new method, around which the entry trajectory provided by the traditional method appears some damped oscillation with a decreasing period. Moreover, the angle of attack and bank angle provided by the new method are very smooth and stable except at the beginning and end of the flight. The angle of attack and bank angle provided by the traditional method also appear to oscillate around that provided by the new method. It should be noted that, because the angle of attack, bank angle, and the flight-path angle are plotted over a large time scale (it is from 0 to 4000 s), they seem to vary very sharply at the end of flight. In fact, those angles vary very slowly and completely meet the control requirements. The derivative of flight-path angle is less than 1 Deg/s. Another significant phenomenon depicted in Fig. 10.3h–j is that the path constraints generated by the traditional method are much larger than that provided by the new method due to the trajectory oscillation. It is obvious that the heating rate for the traditional method is much larger than the limit (the maximum is up to 430 W/cm^2), but the one for the new method is within the safe range.

The distribution of mesh nodes for both methods is shown in Fig. 10.4. It is clear that the initial mesh nodes are the same for both methods. After several iterations, the mesh nodes for the traditional method are distributed with a high density, but the ones for the new method are distributed sparsely.

Table 10.2 shows the statistics of optimal results by the NLP solver (SNOPT [19]). It is apparent that it only takes 4 times of mesh refine to achieve the required feasible and optimal tolerances for both methods. However, the number of total nodes for the traditional method is much more than that for the new method, which is 498 for the traditional method, but 285 for the new method. Moreover, because the time-consuming will increase exponentially with the increase in the number of total nodes, the computational efficiency has been significantly improved for the new method. It only costs 82.06 s to finish the optimization for the new method, which is only one third of that for traditional method. Therefore, it is concluded that the new method is not only capable of solving the problem that the traditional method cannot solve, but also has high computational efficiency since it will use less nodes to achieve a

higher accuracy. Importantly, it will also provide more stable and safer optimal entry trajectory. It should be noted that it only takes half the time if “forward-difference” or “back-difference” is used in optimization. Applying more efficient resources is another way to reduce the computing time.

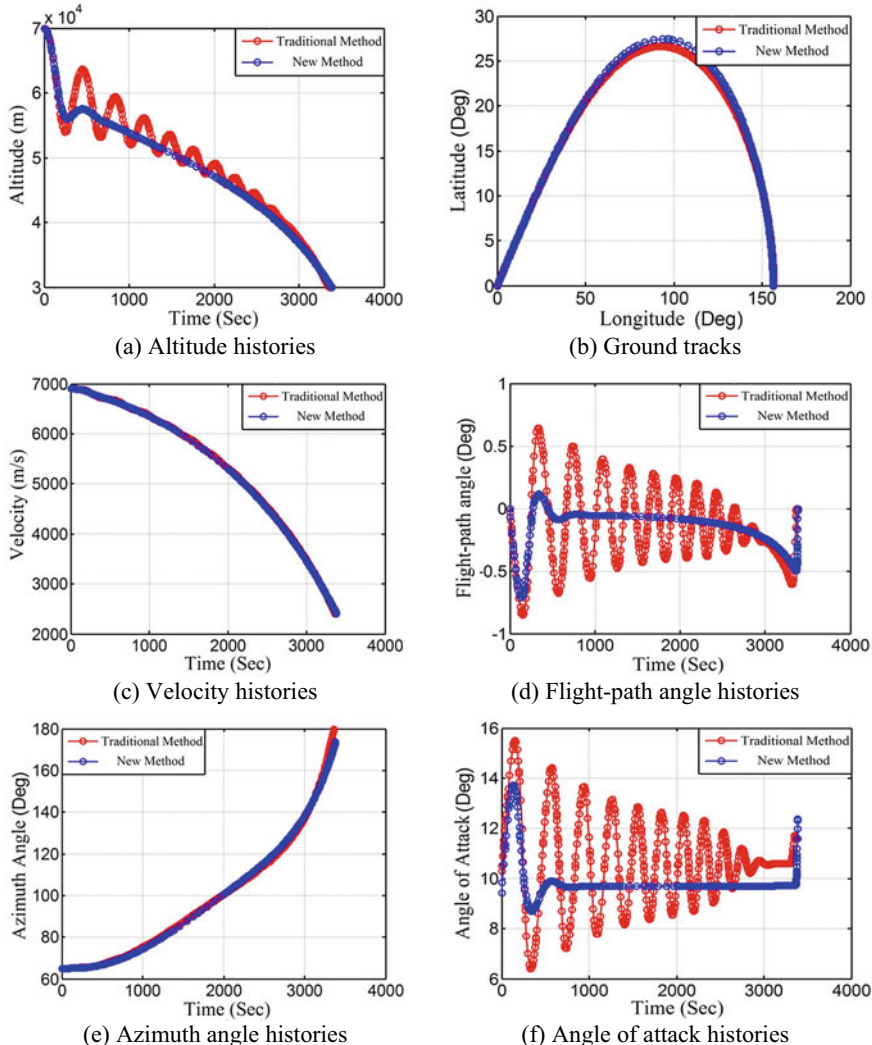


Fig. 10.3 Numeric results of steady glide trajectory optimization without bank reversal

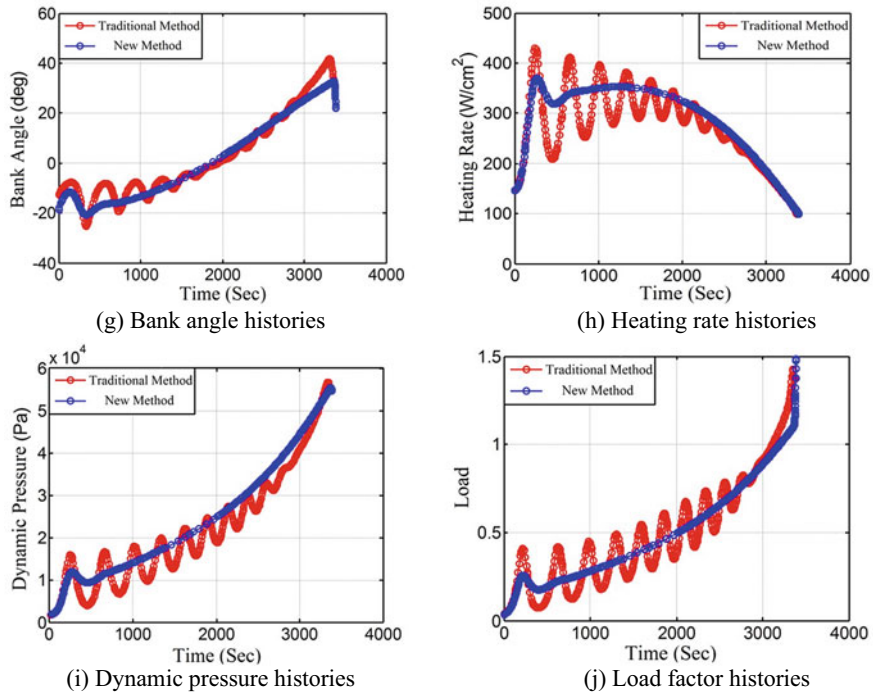
**Fig. 10.3** (continued)

Fig. 10.4 Distribution of mesh nodes (Blue: new method, Red: traditional method)

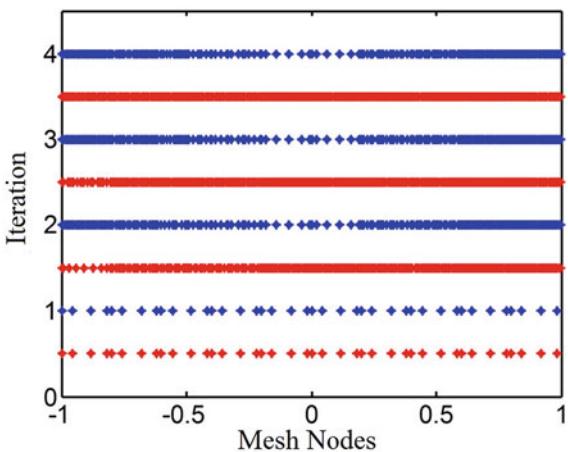


Table 10.2 Optimal results by SNOPT

Traditional method						
Mesh iteration	Node	Feasible	Optimal	Maximum relative error for each mesh	Time-consuming in each iteration	Time (s)
1	41	9.2E-15	6.8E-9	0.148 390 0	37.17	222.04
2	287	3.4E-15	3.2E-9	1.823 4E-5	88.02	
3	473	2.3E-15	6.7E-9	5.619 4E-7	82.58	
4	498	2.3E-15	7.5E-9	9.315 1E-9	14.27	
New method						
Mesh iteration	Node	Feasible	Optimal	Maximum relative error for each mesh	Time-consuming in each iteration	Time (s)
1	41	5.1E-15	3.7E-9	0.019 311 0	1.61	82.06
2	209	2.5E-15	4.5E-9	0.001 524 4	24.91	
3	278	2.2E-15	8.7E-9	3.962 4E-7	41.56	
4	285	1.9E-15	1.0E-9	9.048 8E-9	13.98	

10.4.4 Numerical Example of Trajectory Optimization with Bank Reversal

Generally speaking, the objective of steady glide trajectory optimization is to provide reference trajectory for traditional entry guidance such as linear-quadratic regulator tracking laws. Those laws focus on tracking only the reference longitudinal profile. The bank reversal is used to null the lateral errors. Meanwhile, reentry flight with bank reversal will significantly increase the trajectory shaping capability for the vehicle and provide more smooth control commands except when the bank reversal is happened. Therefore, in order to provide the available reference trajectory, steady glide trajectory optimization with bank reversal is considered in this subsection. It is assumed that there is only one bank reversal during the reentry flight. Therefore, the optimal control problem divides into two phases. And the sign of the bank angles before and after the bank reversal are opposite. The interior point constraints used to maintain continuity in the state at the phase boundaries are presented as

$$\begin{aligned} t^+ &= t^-, r(t^+) = r(t^-), \theta(t^+) = \theta(t^-), \varphi(t^+) = \varphi(t^-), v(t^+) = v(t^-), \\ \gamma(t^+) &= \gamma(t^-), \psi(t^+) = \psi(t^-), \alpha(t^+) = \alpha(t^-), \sigma(t^+) = -\sigma(t^-), \end{aligned} \quad (10.25)$$

where, t denotes the switching time for two phases. The performance index is stated in Eq. (10.22), and the motion dynamics are also stated in Eq. (10.21). All simulation environments are the same as that in Sect. 10.4.1. Initial states for glide vehicle are: $h_0 = 70\ 000$ m, $\theta_0 = 0$ Deg, $\varphi_0 = 0$ Deg, $V_0 = 7\ 100$ m/s, $\gamma_0 = 0$ Deg, $\psi_0 =$

Table 10.3 Different terminal states for various cases

Case	Longitude (Deg)	Latitude (Deg)	Velocity (m/s)	Flight-path angle (Deg)
Case1	155	0	2 400	0
Case2	165	0	2 400	0
Case3	175	0	2 400	0
Case4	185	0	2 400	0
Case5	195	0	2 400	0

90 Deg. In addition, various cases for different cross-ranges are done to evaluate the applicability of the new method. The final longitude, latitude, velocity, and flight-path angle are listed in Table 10.3.

Numerical results for the cases with bank reversal are presented in Fig. 10.5. Obviously, the new method is applicable for the cases with the bank reversal in different cross-ranges. All trajectories are optimal steady glide trajectories and meet all constraints. And it is very easy to find the bank reversal in the time history of bank angle. And another point should be noted is that the magnitudes of the bank angle vary more stably and linearly than that without bank reversal. The meshes for various cases are placed perfectly in regions where the state and control change substantially. Additionally, the maximum heating rate in case-1 reaches the limit.

The statistics for optimal results are presented in Table 10.4 as follows. It has been seen that the number of mesh iterations are 7 for case-1, case-2 and case-3, 4 for case-4, and 5 for case-5. The total node for various cases is about 190. All tolerances satisfy the stop criterions that are set at the beginning of optimization. From the statistics of CPU time, it only takes 2–3 min to successfully finish the steady glide optimization with high numerical precision.

10.4.5 Verification of Feasibility for the Pseudospectral Solution

According to the results obtained above, it is not difficult to conclude that the proposed scheme not only performs well in suppressing the trajectory oscillation, but also has high efficiency in three-dimensional steady glide optimization with and without bank reversal. However, there are three reasons that an elementary check on should be conducted to validate the solution provided by the pseudospectral method. First, the feasible tolerance listed in Table 10.4 is for NLP [20]. Second, hp-adaptive gaussian quadrature collocation method has some deficiency that it is unable to solve some special simple problems [21]. Third, the solution provided by the pseudospectral method meets dynamics only at a limited number of nodes. Therefore, a comparison between the optimal trajectories and integral trajectories is carried out to verify the feasibility of the resulted optimal trajectories.

Figure 10.6 shows the results comparing between the optimal trajectories provided by the pseudospectral solver and integral trajectories generated by integrating the equations of motion using the optimal controls presented in Sect. 10.4.3 with variable step (the min step size is 0.001 s and the max step size is 0.1 s). The comparison includes altitude, flight path angle, velocity, and ground footprint. It is apparent that those trajectories are practically the same even though the flight-path angle varies within the range from -0.5 to 0.1 Deg.

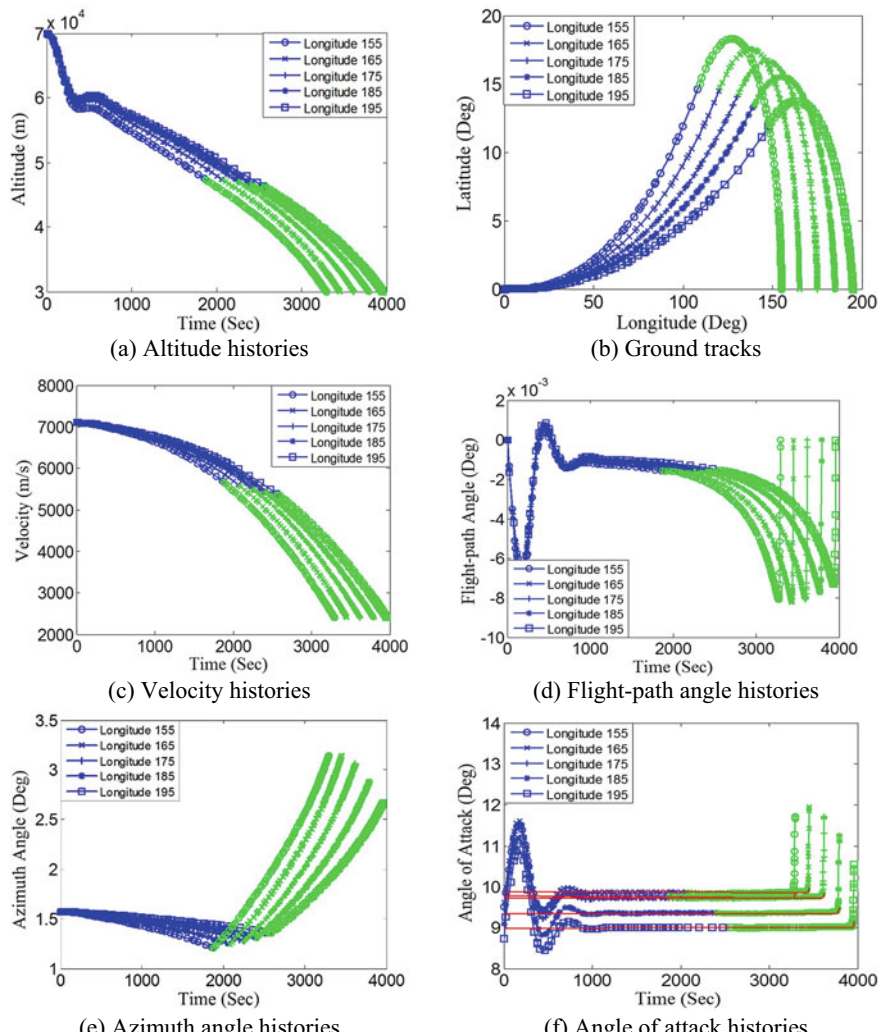
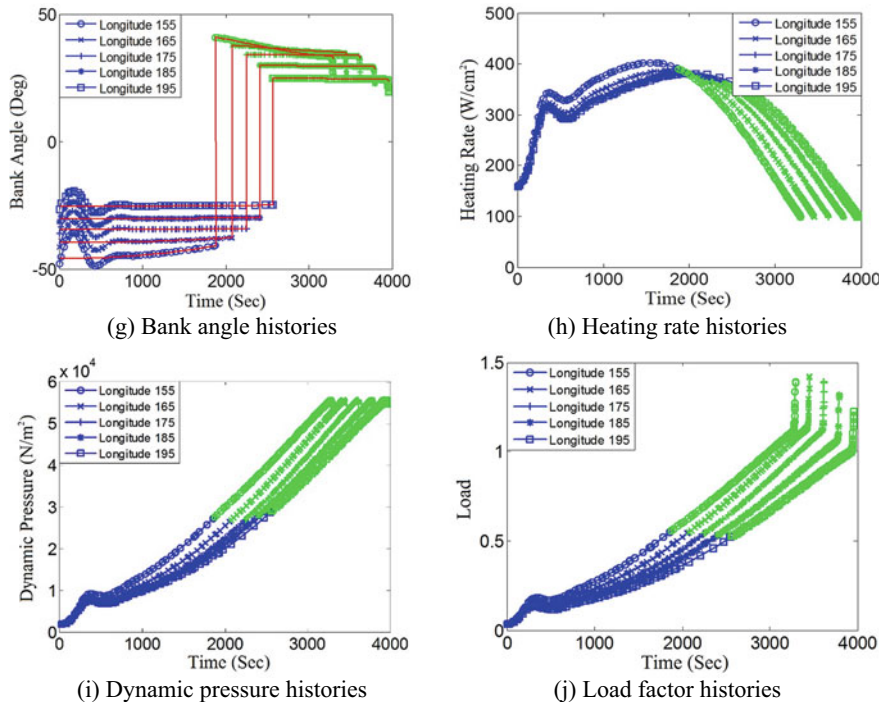


Fig. 10.5 Numeric results of steady glide trajectory optimization with bank reversal

**Fig. 10.5** (continued)**Table 10.4** Optimal results by SNOPT

Mesh iterations	Total node	Feasible	Optimal	Maximum relative error for each mesh	Time (s)
7	179	2.6E-15	7.8E-9	9.538 8E-7	170.77
7	188	2.5E-15	9.2E-8	6.889 1E-7	168.96
7	196	3.4E-15	6.1E-8	1.926 0E-7	204.70
4	192	3.2E-15	6.4E-8	8.068 1E-7	96.56
5	187	2.6E-15	8.0E-8	6.569 6E-7	135.68

The statistic on final errors for various integral trajectories is presented in Table 10.5. The maximal error for altitude is 2.519 3 m, the maximal error for velocity is 0.171 4 m/s, the maximal error for flight-path angle is $-0.003\ 006$ Deg, the maximal error for longitude is 0.002 742 Deg and the maximal error for latitude is 0.002 329 Deg. Obviously, the steady glide trajectory optimal control problem formulated in this chapter can be solved by hp-adaptive pseudospectral solver with a very high efficiency. And the solution is of high precision that it is suitable to be considered as the reference trajectory for the tracking reentry guidance law.

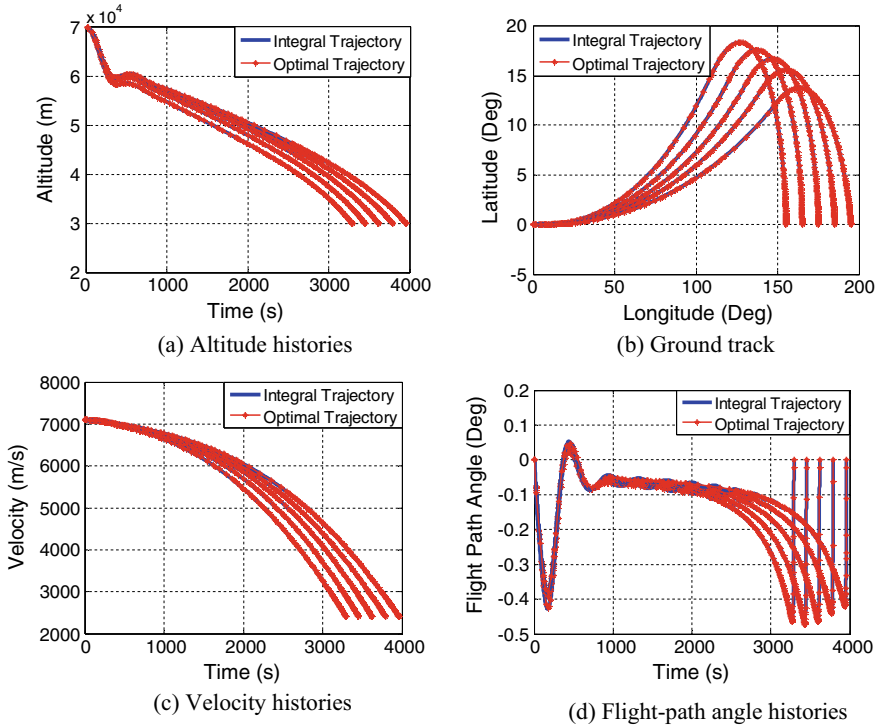


Fig. 10.6 Comparison between Numerical Optimal Trajectories and Integral Trajectories

Table 10.5 Final errors for various integral trajectories

Cases	Altitude (m)	Velocity (m/s)	Flight-path angle (Deg)	Longitude (Deg)	Latitude (Deg)
1	0.285 8	0.139 8	-0.001 026	0.002 742	0.002 329
2	2.519 3	0.171 4	0.001 847	0.002 007	0.001 763
3	1.382 0	0.153 8	-0.001 858	0.002 772	0.001 763
4	2.187 6	0.005 8	0.001 411	0.000 452	0.001 763
5	-1.117 3	0.168 6	-0.003 006	0.002 534	0.001 690

10.5 Conclusion

In this chapter, a new steady glide dynamic modeling for high lift-to-drag ratio reentry vehicle is presented via extending the trajectory-oscillation suppressing scheme into three-dimensional reentry dynamics. Simulation shows that this scheme performs well in trajectory oscillation suppressing. Based on this new modeling, a study on steady glide trajectory optimization with multiple final constraints is investigated. The derivatives of command angle of attack and bank angle are chosen as the control

variables. And the weighted square sum of those derivatives is selected as the performance index so as to achieve the smoothest controls. Then, because the steady glide trajectory optimization is a typical optimal control problem whose solutions change rapidly in certain regions or are discontinuous, hp-adaptive Gaussian quadrature collocation method is selected to solve it. Two classical optimization examples (with and without bank reversal) are conducted to show that the new method performs well in providing optimal steady glide trajectory even considering multiple final constraints. A comparison with the traditional method is done to demonstrate that the new method significantly improves the computational efficiency since the steady glide trajectory can be discretized with fewer nodes. And a comparison between optimal trajectory and integral trajectory is also carried out to verify that the solution provided by the pseudospectral method is of very high accuracy.

References

1. Yang, L., Chen, W.C., Liu, X.M., Zhou, H. Steady glide dynamic modeling and trajectory optimization for high lift-to-drag ratio reentry vehicle. International Journal of Aerospace Engineering. (2016)
2. Dukeman, G.A. Profile-following entry guidance using linear quadratic regulator theory. AIAA Paper 2002-4457. (2002)
3. Josselyn, S., Ross, I.M.: Rapid verification method for trajectory optimization of reentry vehicle. J. Guidance, Control, Dyn. **25**(3), 505–508 (2002)
4. Rao, A.V., Clarke, K.A. Performance optimization of a maneuvering re-entry vehicle using a legendre pseudospectral method. AIAA Paper 2002-4885. (2002)
5. Jorries, T.R., Cobb, R.G.: Three-dimensional trajectory optimization satisfying waypoint and no-fly zone constraints. J. Guidance, Control, Dyn. **32**(2), 551–572 (2009)
6. Jiang, Z., Rui, Z.: Reentry trajectory optimization for hypersonic vehicle satisfying complex constraints. Chin. J. Aeronaut. **26**(6), 1544–1553 (2013)
7. Rahimi, A., Kumar, K.D., Alighanbari, H.: Particle swarm optimization applied to spacecraft reentry trajectory. J. Guidance, Control, Dyn. **36**(1), 307–310 (2013)
8. Shen, Z., Lu, P.: On-board generation of three-dimensional constrained entry trajectories. J. Guidance, Control, Dyn. **26**(1), 111–121 (2003)
9. Mease, K.D., Chen, D.T., Teufel, P., et al.: Reduced-order entry trajectory planning for acceleration guidance. J. Guidance, Control, Dyn. **25**(2), 257–266 (2002)
10. Lu, P.: Entry guidance: a unified method. J. Guidance, Control, Dyn. **37**(3), 713–728 (2014)
11. Yu, W.B., Chen, W.C. Guidance scheme for glide range maximization of a hypersonic vehicle. AIAA Paper 2011-6714, (Aug. 2011)
12. Patterson, M.A., Rao, A.V.: GPOPS-II: a matlab software for solving multiple-phase optimal control problems using hp-adaptive gaussian quadrature collocation methods and sparse nonlinear programming. ACM Trans. Math. Softw. **41**(1), 1–37 (2014)
13. Vinh, N.X., Busemann, A., Culp, R.D. Hypersonic and planetary entry flight mechanics. Ann Arbor MI: Univ. of Michigan Press. (1980). chap. 7
14. Phillips, T.H. A common aero vehicle (CAV) model, description, and employment guide. Schafer Corp. for Air Force Research Laboratory and Air Force Command. (2003)
15. Benson, D.A. A gauss pseudospectral transcription for optimal control. Ph.D Thesis, Department of Aeronautics and Astronautics, MIT. (2004)
16. Garg, D., Patterson, M.A., Hager, W.W., et al.: A unified framework for the numerical solution of optimal control problems using pseudospectral methods. Automatica **46**(11), 1843–1851 (2010)

17. Darby, C.L., Hager, W.W., Rao, A.V.: An hp-adaptive pseudospectral method for solving optimal control problems. *Optimal Control Appl. Methods* **32**(4), 476–502 (2010)
18. Darby, C.L., Hager, W.W., Rao, A.V.: Direct trajectory optimization by a variable low-order hp-adaptive pseudospectral method. *J. Spacecraft Rockets* **48**(3), 433–445 (2011)
19. Gill, P.E., Murray, W., Saunders, M.A.: SNOPT: an SQP algorithm for large-scale constrained optimization. *SIAM Rev.* **47**(1), 99–131 (2002)
20. Betts, J.T. Practical methods for optimal control and estimation using nonlinear programming, 2nd edn. *Advance in Design and Control Series*, US: SIAM, (2009)
21. Ross, I.M., Karpenko, M.: A review of pseudospectral optimal control: from theory to flight. *Ann. Rev. Control* **36**, 182–197 (2012)

Chapter 11

Singular Perturbation Guidance of Hypersonic Glide Reentry



11.1 Singular Perturbation Guidance for Range Maximization of a Hypersonic Glider

In the previous chapter, the trajectory optimization for maximum range of hypersonic glider with no constraints has been finished by collocation method and sequential quadratic programming method. Then, a guidance law can be designed for tracking the optimal trajectory. However, in practice, the off-line calculations are very time consuming, and the original optimal trajectory may lose its optimality due to the changes in flight conditions caused by various disturbances or unexpected external forces.

Therefore, in order to solve this problem fundamentally, it is necessary to develop an online algorithm capable of sloving the optimal or near-optimal trajectory in real time. In this chapter, an analytical guidance law based on singular perturbation theory is proposed for the maximum gliding range problem of hypersonic vehicle [1].

11.1.1 Problem Formulation (Dimensionless Model)

Consider the three-dimensional dynamics of the center of mass in Chap. 3, where the dynamic equation about velocity is replaced by the following dynamic equation about specific energy.

$$\frac{dE}{dt} = -DV \quad (11.1)$$

Based on the analysis of the time-scales of state variables, altitude h is assumed as a faster variable in comparison with the range x and specific energy E . Flight-path angle γ is considered as an even faster variable in comparison with the altitude [2, 3].

In this chapter, the slowest variables will be treated in the outer solution while slow and fast boundary-layer corrections will be provided for the altitude and flight-path angle dynamics, respectively. Thus, the original system can be represented by a three time-scales system as follows:

$$\frac{dx}{dt} = V \cos \gamma \frac{R_0}{R_0 + h} \quad (11.2)$$

$$\varepsilon \frac{dh}{dt} = V \sin \gamma \quad (11.3)$$

$$\frac{dE}{dt} = -DV \quad (11.4)$$

$$\varepsilon^2 \frac{d\gamma}{dt} = \frac{L - \cos \gamma}{V} + \frac{V \cos \gamma}{R_0 + h} \quad (11.5)$$

which satisfying the boundary conditions $\{x, h, E, \gamma\}(t_0) = \{x_0, h_0, E_0, \gamma_0\}$ and $h(t_f) = h_f$. The parameters ε and ε^2 appended on the left side of Eqs. (11.3) and (11.5) serve to denote that these variables evolve on a faster time-scale than others.

The maximum range problem analyzed in this chapter may be defined as: find the optimal control L subject to the differential constraints Eqs. (11.2)–(11.5) with the boundary conditions while maximizing the following performance index.

$$J = x_f \quad (11.6)$$

The Hamiltonian is

$$H = \lambda_x V \cos \gamma \frac{R_0}{R_0 + h} + \lambda_h V \sin \gamma - \lambda_E DV + \lambda_\gamma \left(\frac{L - \cos \gamma}{V} + \frac{V \cos \gamma}{R_0 + h} \right) \quad (11.7)$$

Corresponding costate equations are

$$\frac{d\lambda_x}{dt} = -\frac{\partial H}{\partial x} = 0 \quad (11.8)$$

$$\begin{aligned} \varepsilon \frac{d\lambda_h}{dt} &= -\frac{\partial H}{\partial h} = \lambda_x \cos \gamma \left[\frac{1}{V} \cdot \frac{R_0}{R_0 + h} + \frac{VR_0}{(R_0 + h)^2} \right] + \lambda_h \frac{\sin \gamma}{V} - \lambda_E \left(\frac{D}{V} - V \frac{\partial D}{\partial h} \right) \\ &\quad - \lambda_\gamma \left[\frac{L - \cos \gamma}{V^3} + \frac{1}{V} \cdot \frac{\partial L}{\partial h} - \frac{1}{V} \cdot \frac{\cos \gamma}{R_0 + h} - \frac{V \cos \gamma}{(R_0 + h)^2} \right] \end{aligned} \quad (11.9)$$

$$\begin{aligned} \frac{d\lambda_E}{dt} &= -\frac{\partial H}{\partial E} = -\lambda_x \frac{R_0}{R_0 + h} \cdot \frac{\cos \gamma}{V} - \lambda_h \frac{\sin \gamma}{V} + \lambda_E \left(\frac{D}{V} + V \frac{\partial D}{\partial E} \right) \\ &\quad - \lambda_\gamma \left(\frac{-L + \cos \gamma}{V^3} + \frac{1}{V} \cdot \frac{\partial L}{\partial E} + \frac{1}{V} \cdot \frac{\cos \gamma}{R_0 + h} \right) \end{aligned} \quad (11.10)$$

$$\varepsilon^2 \frac{d\lambda_\gamma}{dt} = -\frac{\partial H}{\partial \gamma} = -\lambda_x V \sin \gamma \frac{R_0}{R_0 + h} - \lambda_h V \cos \gamma - \lambda_\gamma \left(\frac{\sin \gamma}{V} - \frac{V \sin \gamma}{R_0 + h} \right) \quad (11.11)$$

The optimality condition is

$$\frac{\partial H}{\partial L} = -\lambda_E \frac{2VKL}{q} + \lambda_r \frac{1}{V} = 0 \quad (11.12)$$

According to the performance index Eq. (11.6), the transversality condition can be obtained as

$$\lambda_x(t_f) = 1 \quad (11.13)$$

Because the derivation of λ_γ is equal to zero as shown in Eq. (11.8), λ_γ is a constant. Thus, $\lambda_\gamma = 1$. Additionally, since the final time is free and the Hamiltonian does not depend on the time explicitly, there is

$$H(t) = 0 \quad (11.14)$$

11.1.2 Reduced-Order System Solutions

Setting $\varepsilon = 0$ in Eqs. (11.2)–(11.5), we can obtain the reduced-order system

$$\gamma = 0 \quad (11.15)$$

$$L = 1 - \frac{V^2}{R_0 + h} \quad (11.16)$$

$$\frac{dx}{dt} = V \frac{R_0}{R_0 + h} \quad (11.17)$$

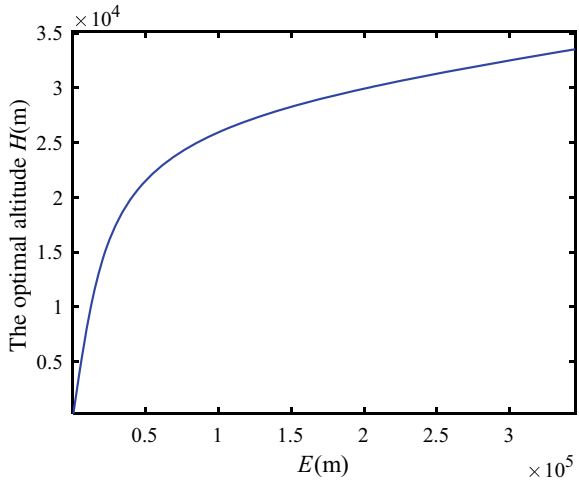
$$\frac{dE}{dt} = -DV \quad (11.18)$$

and then the Hamiltonian in this time scale can be reduced to

$$H = V \frac{R_0}{R_0 + h} - \lambda_E DV \quad (11.19)$$

There is $H = 0$ because all variables in Eq. (11.19) are independent of time. Thus the expression of λ_E can be obtained as

Fig. 11.1 The relationship between the optimal altitude and specific energy



$$\lambda_E = \frac{R_0}{R_0 + h} \cdot \frac{1}{D} \quad (11.20)$$

Control variable in this time scale is altitude h . From the optimality condition $\partial H / \partial h = 0$, one has

$$\frac{\partial D}{\partial h} = -\frac{D}{R_0 + h} \quad (11.21)$$

By solving Eqs. (11.16)–(11.18) and (11.20)–(11.21), the optimal control of the reduced-order system, i.e. the optimal altitude, can be obtained with respect to the current specific energy, as shown in Fig. 11.1. In reality, the relationship between the optimal altitude and specific energy can be precomputed off-line and stored on-board in the form of two-dimensional tables for interpolation.

In the following sections, the superscript “0” denotes the values of state and control variables in the slowest time-scale.

11.1.3 Slow-Boundary Layer Solutions

This boundary layer system is formally obtained by introducing a time stretching transformation $\tau_1 = t/\varepsilon$ into Eqs. (11.2)–(11.5), which leads to:

$$\frac{dx}{d\tau_1} = \varepsilon V \cos \gamma \frac{R_0}{R_0 + h} \quad (11.22)$$

$$\frac{dh}{d\tau_1} = V \sin \gamma \quad (11.23)$$

$$\frac{dE}{d\tau_1} = -\varepsilon DV \quad (11.24)$$

$$\varepsilon \frac{d\gamma}{d\tau_1} = \frac{L - \cos \gamma}{V} + \frac{V \cos \gamma}{R_0 + h} \quad (11.25)$$

The corresponding costate Eqs. (11.8)–(11.11) can be rewritten as

$$\frac{d\lambda_x}{d\tau_1} = 0 \quad (11.26)$$

$$\begin{aligned} \frac{d\lambda_h}{d\tau_1} &= \lambda_x \cos \gamma \left(\frac{g}{V} \cdot \frac{R_0}{R_0 + h} + \frac{VR_0}{(R_0 + h)^2} \right) + \lambda_h \sin \gamma \frac{g}{V} - \lambda_E \left(\frac{g}{V} D - V \frac{\partial D}{\partial H} \right) \\ &\quad - \lambda_\gamma \left[\frac{(L - \cos \gamma)g}{V^3} + \frac{1}{V} \cdot \frac{\partial L}{\partial H} - \frac{g}{V} \cdot \frac{\cos \gamma}{R_0 + h} - \frac{V \cos \gamma}{(R_0 + h)^2} \right] \end{aligned} \quad (11.27)$$

$$\begin{aligned} \frac{d\lambda_E}{d\tau_1} &= \varepsilon \left[-\lambda_\gamma \cos \gamma \frac{R_0}{R_0 + h} \cdot \frac{g}{V} - \lambda_h \sin \gamma \frac{g}{V} + \lambda_E \left(D \frac{g}{V} + V \frac{\partial D}{\partial E} \right) \right] \\ &\quad - \varepsilon \lambda_\gamma \left[\frac{(-L + \cos \gamma)g}{V^3} + \frac{1}{V} \cdot \frac{\partial L}{\partial E} + \frac{g}{V} \cdot \frac{\cos \gamma}{R_0 + h} \right] \end{aligned} \quad (11.28)$$

$$\varepsilon \frac{d\lambda_\gamma}{d\tau_1} = \lambda_\gamma V \sin \gamma \frac{R_0}{R_0 + h} - \lambda_h V \cos \gamma - \lambda_\gamma \left(\frac{\sin \gamma}{V} - \frac{V \sin \gamma}{R_0 + h} \right) \quad (11.29)$$

Letting $\varepsilon = 0$ in Eqs. (11.22)–(11.29) yields

$$\frac{dx}{d\tau_1} = 0 \quad (11.30)$$

$$\frac{dE}{d\tau_1} = 0 \quad (11.31)$$

$$L = \cos \gamma \left(1 - \frac{V^2}{R_0 + h} \right) \quad (11.32)$$

$$\frac{d\lambda_E}{d\tau_1} = 0 \quad (11.33)$$

$$0 = \lambda_x V \sin \gamma \frac{R_0}{R_0 + h} - \lambda_h V \cos \gamma - \lambda_\gamma \left(\frac{\sin \gamma}{V} - \frac{V \sin \gamma}{R_0 + h} \right) \quad (11.34)$$

From Eqs. (11.30), (11.31) and (11.33), we can obtain that $x(\tau_1) = r_0$, $E(\tau_1) = E_0$, $\lambda_E(\tau_1) = \lambda_{E0}$. Now the Hamiltonian in this time-scale becomes

$$\begin{aligned}
H &= \lambda_x V \cos \gamma \frac{R_0}{R_0 + h} + \lambda_h V \sin \gamma - \lambda_E D V \\
&= V \cos \gamma \frac{R_0}{R_0 + h} + \lambda_h V \sin \gamma - \lambda_E V \left[q C_{D0} + \frac{K \cos^2 \gamma}{q} \left(1 - \frac{V^2}{R_0 + h} \right)^2 \right] \\
&= 0
\end{aligned} \tag{11.35}$$

which is obtained by substituting Eq. (11.32) into Eq. (11.7).

In the slow-boundary layer, the control variable is the flight-path angle γ . Thus the optimal condition is

$$\frac{\partial H}{\partial \gamma} = -V \sin \gamma \frac{R_0}{R_0 + h} + \lambda_h V \cos \gamma + \frac{2\lambda_E V K \cos \gamma \sin \gamma}{q} \left(1 - \frac{V^2}{R_0 + h} \right)^2 = 0 \tag{11.36}$$

In principle, the optimal control γ and the adjoint variable λ_h of the slow-boundary layer solutions can be determined by solving Eqs. (11.35) and (11.36) simultaneously. However, in order to offset the computation error, we replace Eq. (11.35) with the following equation.

$$H - H^0 = \cos \gamma \left(V \frac{R_0}{R_0 + h} - V^0 \frac{R_0}{R_0 + h^0} \right) + \lambda_h V \sin \gamma - \lambda_E (D V - D^0 V^0) = 0 \tag{11.37}$$

Solving Eqs. (11.36) and (11.37), the expressions of λ_h and $\cos \gamma$ can be obtained by

$$\cos \gamma = \frac{R_0}{R_0 + h} \cdot \frac{1}{\lambda_E [q C_{D0} + KB^2 (2 - \cos^2 \gamma) / q] + H^0 / V} \tag{11.38}$$

$$\lambda_h = \lambda_E \sin \gamma (q C_{D0} - KB^2 \cos^2 \gamma / q) + H^0 \sin \gamma / V \tag{11.39}$$

where $\lambda_E = \frac{R_0}{R_0 + h^0} \cdot \frac{1}{D^0}$, $B = 1 - \frac{V^2}{R_0 + h}$. After several iterations, we can obtain the control variable γ in the slow-boundary layer. In addition, if $h^0 > h$, $\gamma > 0$; otherwise, if $h^0 < h$, $\gamma < 0$.

In the following sections, the superscript “i1” will be used to denote the variables in the slow-boundary layer.

11.1.4 Fast-Boundary Layer Solutions

Applying the time stretching transformation $\tau_2 = t/\varepsilon^2$ to Eqs. (11.2)–(11.5), we can obtain the dynamics in the fast-boundary layer.

$$\frac{dx}{d\tau_2} = \varepsilon^2 V \cos \gamma \frac{R_0}{R_0 + h} \quad (11.40)$$

$$\frac{dh}{d\tau_2} = \varepsilon V \sin \gamma \quad (11.41)$$

$$\frac{dE}{d\tau_2} = -\varepsilon^2 DV \quad (11.42)$$

$$\frac{d\gamma}{d\tau_2} = \frac{L - \cos \gamma}{V} + \frac{V \cos \gamma}{R_0 + h} \quad (11.43)$$

Similarly, introducing the time stretching transformation into Eqs. (11.8)–(11.11) yields

$$\frac{d\lambda_x}{d\tau_2} = 0 \quad (11.44)$$

$$\begin{aligned} \frac{d\lambda_h}{d\tau_2} &= \varepsilon \left[\lambda_x \cos \gamma \left(\frac{g}{V} \cdot \frac{R_0}{R_0 + h} + \frac{VR_0}{(R_0 + h)^2} \right) + \lambda_h \sin \gamma \frac{g}{V} - \lambda_E \left(\frac{g}{V} D - V \frac{\partial D}{\partial h} \right) \right] \\ &\quad - \varepsilon \lambda_\gamma \left[\frac{g(L - \cos \gamma)}{V^3} + \frac{1}{V} \cdot \frac{\partial L}{\partial h} - \frac{g}{V} \cdot \frac{\cos \gamma}{R_0 + h} - \frac{V \cos \gamma}{(R_0 + h)^2} \right] \end{aligned} \quad (11.45)$$

$$\begin{aligned} \frac{d\lambda_E}{d\tau_2} &= \varepsilon^2 \left[-\lambda_x \cos \gamma \frac{R_0}{R_0 + h} \cdot \frac{g}{V} - \lambda_h \sin \gamma \frac{g}{V} + \lambda_E \left(D \frac{g}{V} + V \frac{\partial D}{\partial E} \right) \right] \\ &\quad - \varepsilon^2 \lambda_\gamma \left[\frac{g(-L + \cos \gamma)}{V^3} + \frac{1}{V} \cdot \frac{\partial L}{\partial E} + \frac{g}{V} \cdot \frac{\cos \gamma}{R_0 + h} \right] \end{aligned} \quad (11.46)$$

$$\frac{d\lambda_\gamma}{d\tau_2} = \lambda_x V \sin \gamma \frac{R_0}{R_0 + h} - \lambda_h V \cos \gamma - \lambda_\gamma \left(\frac{\sin \gamma}{V} - \frac{V \sin \gamma}{R_0 + h} \right) \quad (11.47)$$

Setting $\varepsilon = 0$ in above equations gives

$$\frac{dx}{d\tau_2} = 0 \quad (11.48)$$

$$\frac{dh}{d\tau_2} = 0 \quad (11.49)$$

$$\frac{dE}{d\tau_2} = 0 \quad (11.50)$$

$$\frac{d\lambda_h}{d\tau_2} = 0 \quad (11.51)$$

$$\frac{d\lambda_E}{d\tau_2} = 0 \quad (11.52)$$

The solutions for Eqs. (11.48)–(11.52) are $x(\tau_2) = x_0$, $h(\tau_2) = h_0$, $E(\tau_2) = E_0$, $\lambda_h(\tau_2) = \lambda_{h0}$, $\lambda_E(\tau_2) = \lambda_{E0}$. The Hamiltonian now becomes

$$H = \lambda_\gamma V \cos \gamma \frac{R_0}{R_0 + h} + \lambda_h V \sin \gamma - \lambda_E DV + \lambda_\gamma \left(\frac{L - \cos \gamma}{V} + \frac{V \cos \gamma}{R_0 + h} \right) = 0 \quad (11.53)$$

In this layer, lift L is the control variable. Thus, the optimal condition is

$$\frac{\partial H}{\partial L} = -\lambda_E \frac{2VKL}{q} + \lambda_\gamma \frac{1}{V} = 0 \quad (11.54)$$

In order to offset the computation error, Eq. (11.53) is replaced by $H - H^{i1} = 0$.

$$\begin{aligned} H - H^{i1} &= \lambda_\gamma V \frac{R_0}{R_0 + h} (\cos \gamma - \cos \gamma^{i1}) + \lambda_h V (\sin \gamma - \sin \gamma^{i1}) - \lambda_E V (D - D^{i1}) \\ &\quad + \lambda_\gamma \left(\frac{L - \cos \gamma}{V} + \frac{V \cos \gamma}{R_0 + h} \right) = 0 \end{aligned} \quad (11.55)$$

Solving Eqs. (11.54) and (11.55) simultaneously gives

$$\lambda_\gamma = \lambda_E \frac{2KV^2L}{q} \quad (11.56)$$

$$(L - B \cos \gamma)^2 = F \quad (11.57)$$

where $\lambda_E = \frac{R_0}{R_0 + h} \cdot \frac{1}{D_0}$, $F = \frac{q}{\lambda_E K} \left[\frac{R_0}{R_0 + h} (\cos \gamma^{i1} - \cos \gamma) + \lambda_h (\sin \gamma^{i1} - \sin \gamma) \right] + B^2 (\cos \gamma^{i1} - \cos \gamma)$, $\lambda_h = \lambda_E (qC_{D0} + KB^2 \cos^2 \gamma^{i1} / q) \sin \gamma^{i1}$, $B = 1 - \frac{V^2}{R_0 + h}$.

From Eq. (11.57), one has

$$L = B \cos \gamma \pm \sqrt{F} \quad (11.58)$$

In Eq. (11.58), if $\gamma^{i1} \geq \gamma$, “+” is used, and vice versa. The corresponding angle of attack (deg) can be calculated by

$$\alpha = \frac{L/q - C_{L0}}{C_{L\alpha}} \quad (11.59)$$

11.1.5 Simulation Results

In this section, we implement the obtained singular perturbation guidance (SPG) on the flight vehicle introduced in Sect. 6.4.2. The boundary conditions are the same as

Fig. 11.2 The maximum glide range trajectory for SPG

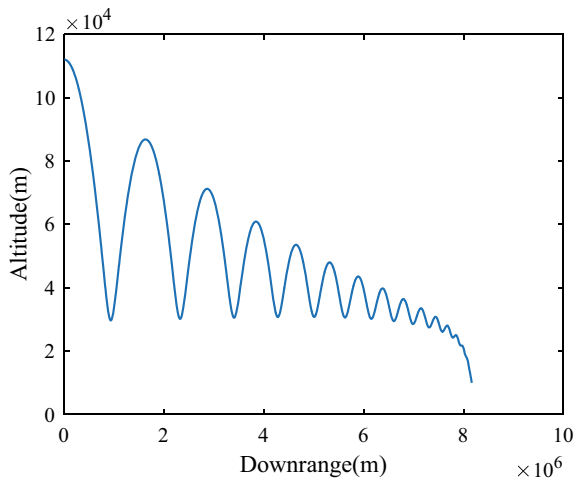
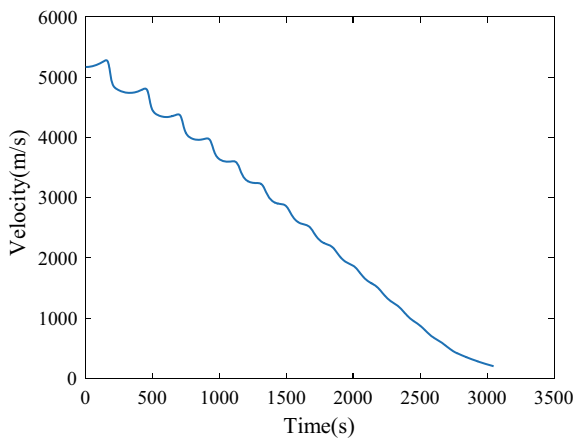


Fig. 11.3 The velocity histories for SPG



those in Sect. 6.4.2. The simulation results are shown in Figs. 11.2, 11.3, 11.4, 11.5, 11.6.

The terminal states of the CAV are: total flight time $t_f = 3048.0$ s, downrange $x_f = 8,165,786.0$ m, velocity $V_f = 201.6$ m/s, specific energy $E_f = 30,319.2$ m.

11.1.6 Comparison and Analysis

In reference [1], maximum lift-drag ratio method (MLDRM), Gauss pseudospectral method (GPM), and collocation method (CM) are used to obtain the maximum glide range trajectory for hypersonic vehicle. Here, the results of the proposed

Fig. 11.4 The flight-path angle histories for SPG

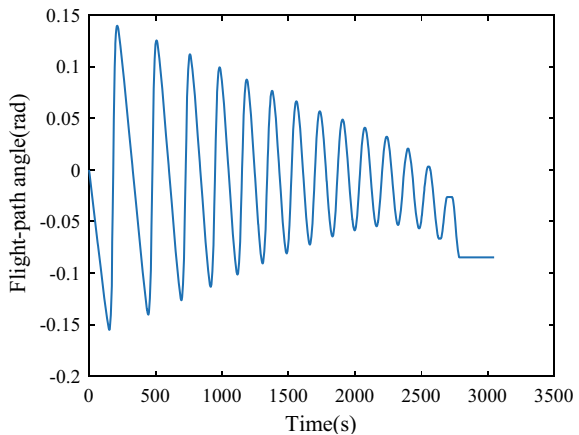


Fig. 11.5 The command load histories for SPG

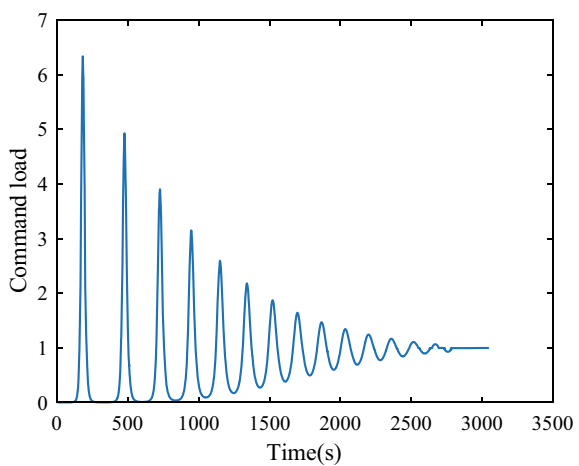
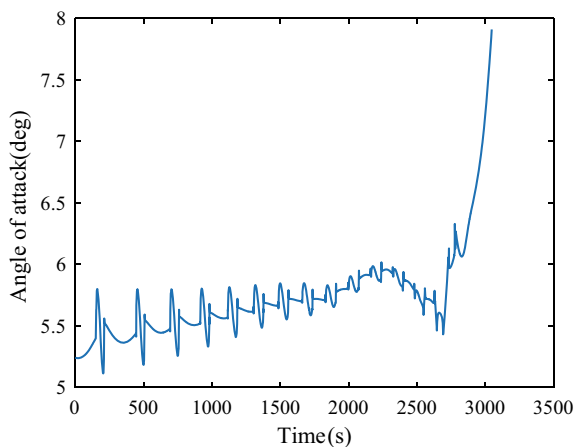


Fig. 11.6 The angle of attack histories for SPG



singular perturbed method (SPM) are compared with those of the MLDRM and GPM methods. As shown in Fig. 11.7, there are weakly-damped phugoid oscillations in all the three trajectories, where MLDRM has the largest amplitude, SPM has the moderate amplitude, and GPM has the least amplitude. In addition, the results also indicate that the guidance derived by SPM can obtain a trajectory closer to the optimal trajectory than that by the MLDRM. The velocity histories of the three methods are shown in Fig. 11.8. As can be seen from the figure, the energy management is very well during the entry process such that the vehicle is able to achieve the maximum glide range. Figure 11.9 shows the angle of attack histories of the hypersonic vehicle.

Due to the super high speed, heating rate is a factor that must be taken into account in the hypersonic vehicle design. The formula for calculating the heating rate is

Fig. 11.7 The trajectories

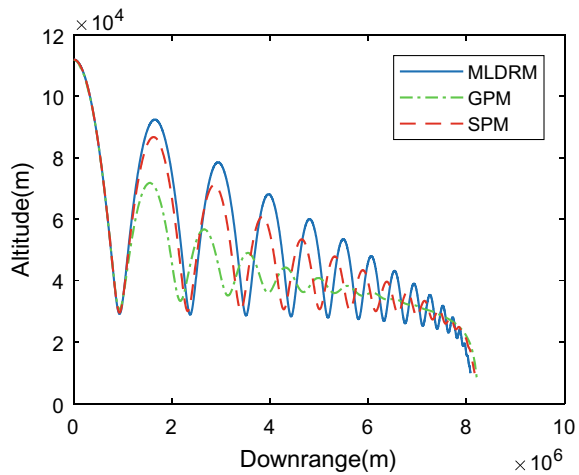


Fig. 11.8 The velocity histories

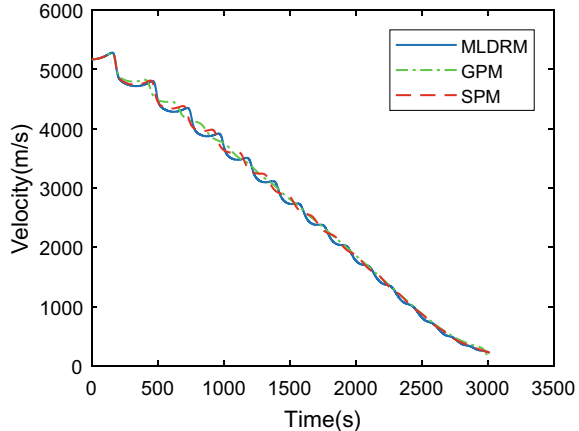
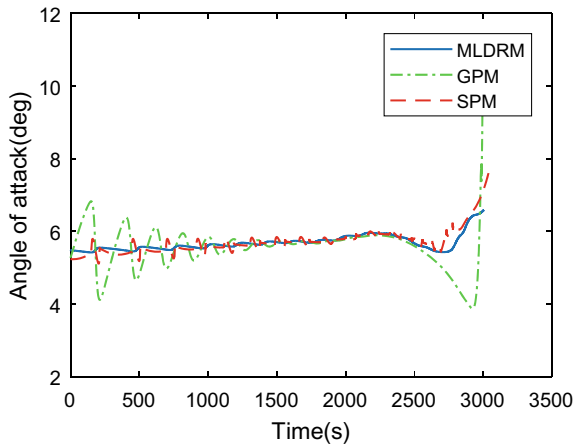


Fig. 11.9 The angle of attack histories



$$\dot{Q} = 5.188 \times 10^{-8} \rho^{0.5} V^3 \quad (11.60)$$

The heating rate histories with respect to downrange of the three methods are shown in Fig. 11.10. It can be seen that GPM has the minimal heating rate peak, followed by SPM, and MLDRM has the maximal heating rate peak. The comparison of the terminal states of the three methods is presented in Table 11.1.

Fig. 11.10 The heating rate histories with respect to the downrange

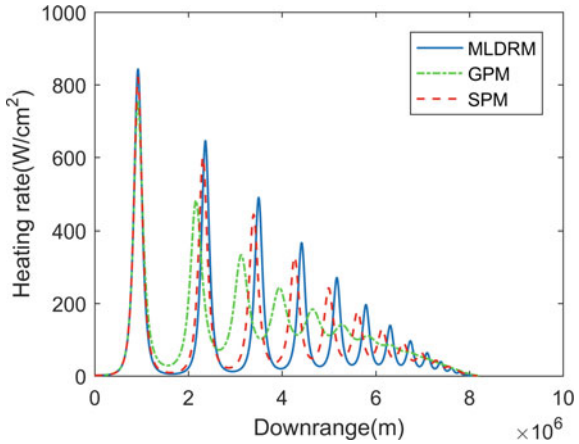


Table 11.1 The flight time, downrange, terminal velocity, and maximal heating rate

Method	Flight time (s)	Downrange (km)	Terminal velocity (m/s)	Maximal heating rate (W/cm ²)
MLDRM	3006.0	8084.3	225.3	843.2
GPM	3000.0	8219.3	151.4	755.5
SPM	3048.0	8165.8	201.6	820.6

11.2 Improved Singular Perturbation Guidance for Maximum Glide Range

In previous section, we developed the guidance law for maximum glide range of hypersonic vehicle by using singular perturbation technique, and compared its performance with GPM and MLDRM. However, the maximum heating rate peak is still very high because there is no constraint on heating rate during the derivation.

As a matter of experience, the high heating rate peak is caused by the violently oscillation of the trajectory. Therefore, the flight trajectory should be as smooth as possible so as to reduce the heating rate peak. Of course, the optimal trajectory with heating rate constraint can be obtained by some numerical optimization methods. But, the huge amount of calculation and heavy computational loads prevent its application in real-time. Moreover, there are many kinds of disturbances that may change the states of the vehicle such that the vehicle cannot meet the requirements for tracking the optimal values.

The singular perturbation technique provides a relatively simple and effective analytical method to obtain the optimal trajectory and guidance in real-time. Firstly, we can get a basic understanding of the trajectory characteristics from the solutions of the reduced-order model, called outer solutions. Then after finishing the boundary layer correction, we can obtain the ultimate guidance law that will permit the vehicle to follow the outer solutions. That is to say, most of the vehicle performance arises from the dynamics of outer variables, with boundary layer correction providing relatively minor performance improvement [2]. Therefore, without affecting the optimality of the outer solutions, we can make the hypersonic vehicle satisfy the heating rate constraint during the entry phase through some proper method to handle the boundary layer correction.

In this section, an improved guidance (ISPG) is developed which using the dynamic inverse technique to deal with the boundary layer corrections [4, 5]. The method may sacrifice some performance but can significantly reduce the heating rate peak.

11.2.1 Dynamic Model and Solutions to the Reduced-Order System

Consider the same dynamic model and singular perturbation system [i.e. Equations (11.2)–(11.5)] as presented in the previous section. The initial conditions and final conditions are

$$\{x, h, E, \gamma\}(t_0) = \{x_0, h_0, E_0, \gamma_0\} \quad (11.61)$$

$$h(t_f) = h_f \quad (11.62)$$

The performance index for the optimal control problem of the maximum glide range trajectory is

$$J = -x_f \quad (11.63)$$

Setting $\varepsilon_1 = \varepsilon_2 = 0$ yields $\gamma = 0$ and $L = 1 - \frac{V^2}{R_0 + h}$. Substituting these variables and parameters into the original singular perturbation system, we can obtain the reduced-order system as

$$\frac{dx}{dt} = V \frac{R_0}{R_0 + h} \quad (11.64)$$

$$\frac{dE}{dt} = -DV \quad (11.65)$$

where $D = D_0 + K \left(1 - \frac{V^2}{R_0 + h} \right) / q$. The control variable for the reduced-order system is altitude h . Now the Hamiltonian is

$$H = \lambda_x V \frac{R_0}{R_0 + h} - \lambda_E DV \quad (11.66)$$

From the costate equations

$$\frac{d\lambda_x}{dt} = -\frac{\partial H}{\partial x} = 0 \quad (11.67)$$

it can be seen that λ_x is a constant, and from the transversely condition

$$\lambda_x(t_f) = -1 \quad (11.68)$$

we can get that $\lambda_x = -1$. Since the final time is free, there is

$$H(t_f) = 0 \quad (11.69)$$

Besides, the Hamiltonian is independent with time t . Hence,

$$H(t) = 0 \quad (11.70)$$

Thus, the expression of the costate λ_E can be calculated by

$$\lambda_E = -\frac{R_0}{R_0 + h} \cdot \frac{1}{D} \quad (11.71)$$

From the optimal condition $\partial H / \partial h = 0$, we can obtain

$$\frac{\partial H}{\partial h} = -\frac{D}{R_0 + h} \quad (11.72)$$

which has implicit dependence on h and E . By solving the equation above, the optimal altitude h^0 can be obtained, which is the same as the results of the reduced-order system in the previous section. In the following, superscript “0” is used to denote the variables in the reduced-order system.

11.2.2 Boundary Layer Correction

Under the condition of constant mass and certain velocity, the drag of the vehicle is closely related to the local atmospheric density. On the one hand, the higher the altitude is, the smaller the air density is, and the smaller the drag independent of lift is. On the other hand, with the decrease of the air density, it needs to increase the deflection angle of the control surface to obtain the same control force. However, it will cause significant increase of the drag with respect to the overload. Therefore, if the overload is not zero, the drag of the vehicle will first decrease and then increase with the increase of altitude. There is an altitude at which the drag reaches a minimum.

From Eq. (11.72), we can see that the optimal altitude of the reduced-order system is the altitude at which the drag is minimized. Because the altitude decreases slowly, the optimal altitude determined by Eq. (11.72) can be regarded as the altitude which minimizes the energy loss of the vehicle. In this way, we only need to make the vehicle fly at the optimal altitude of the reduce-order system when carrying out the boundary-layer correction.

11.2.3 Slow Boundary-Layer Correction

The slow boundary layer is composed of the altitude dynamics, which regards the slow variables as constant. The control variable is the flight-path angle γ that changes the altitude from its initial value to the optimal altitude h^0 . A dynamic inverse

controller is designed for the hypersonic vehicle as follows.

$$\gamma^{i1} = \arcsin \frac{k_h(h^0 - h)}{V} \quad (11.73)$$

where k_h is a undetermined parameter.

11.2.4 Fast Boundary-Layer Correction

The fast boundary layer consists of the flight-path angle dynamics. The control variable is the overload n that leads the flight-path angle from its initial value to the value required by the slow boundary layer. Similarly, a dynamic inverse controller can be designed for the hypersonic vehicle as follows.

$$n = \left[k_\gamma (\gamma^{i1} - \gamma) - \frac{V \cos \gamma}{R_0 + h} \right] V + \cos \gamma \quad (11.74)$$

where k_γ is a undetermined parameter.

This completes the corrections of the slow and fast boundary layers.

11.2.5 Guidance Law Derivation

Accord to the dynamic inverse theory, the undetermined parameters k_h and k_γ in Eqs. (11.73) and (11.74) are actually the reciprocal of the time constant of the altitude flight-path angle, respectively. The method described in reference [4] can be used to estimate the time constant of a variable. However, it should be noted that since this method can only roughly estimate the range of the time constant, the specific value also depends on the design or engineering experience to select manually.

In the initial entry phase, because the actual altitude of the hypersonic vehicle differs greatly from the optimal altitude, the dynamic inverse controller will generate an excessive command overload. For one thing, it is prone to cause control problems. For another, the drag is relatively large at this time, causing the energy to be rapidly lost. Therefore, we set the command overload to zero directly in the initial entry phase. When the vehicle falls back to a relatively low altitude, the dynamic inverse controller will be activated to adjust the velocity direction and pull up the vehicle.

11.2.6 Simulation Results and Analyses

The previous case is rerun by the improved singular perturbation guidance. Set the command overload zero if the altitude is higher than 92.27 km. The parameters of the dynamic inverse controller is set to $k_h = 0.5$ and $k_\gamma = 1.2$. The results are shown in Figs. 11.11, 11.12, 11.13, 11.14, 11.15 and 11.16.

From Figs. 11.11 and 11.12, we can see that ISPG can steer the vehicle along a smooth trajectory. At first, the altitude of the vehicle decreases quickly and adjusts its altitude to the optimal altitude of the reduced-order system. Then, the vehicle will fly along the optimal altitude. Figure 11.13 shows that the velocity decreases

Fig. 11.11 The maximum glide-range trajectory for ISPG

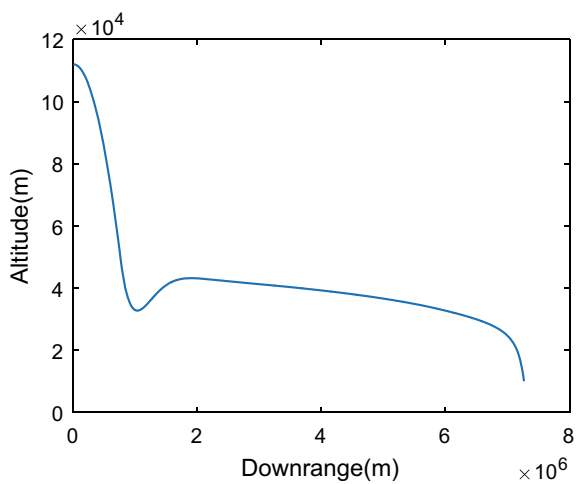


Fig. 11.12 The actual and optimal altitude histories

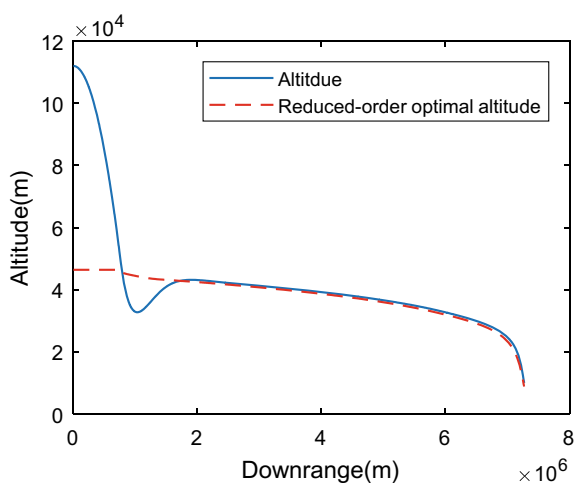


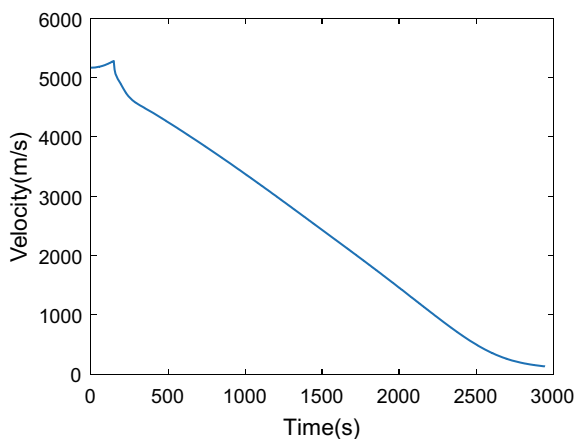
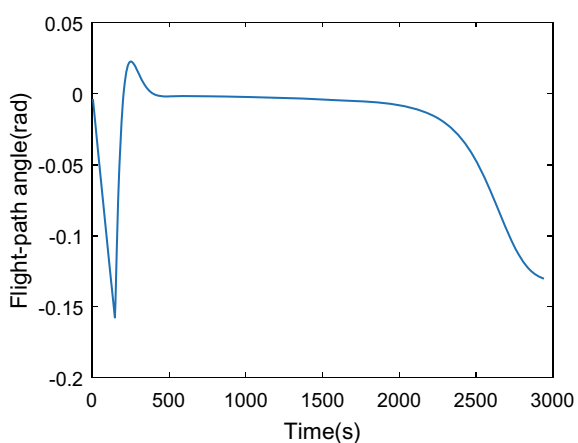
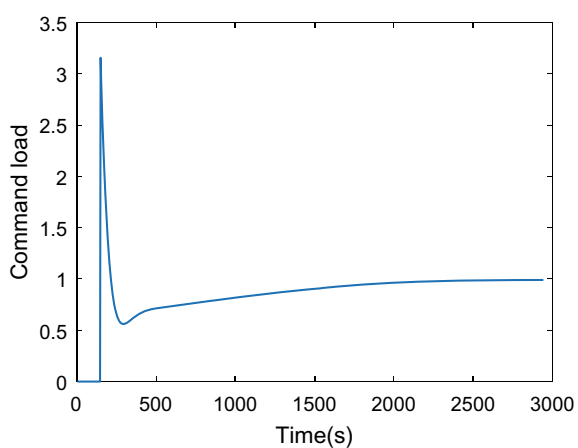
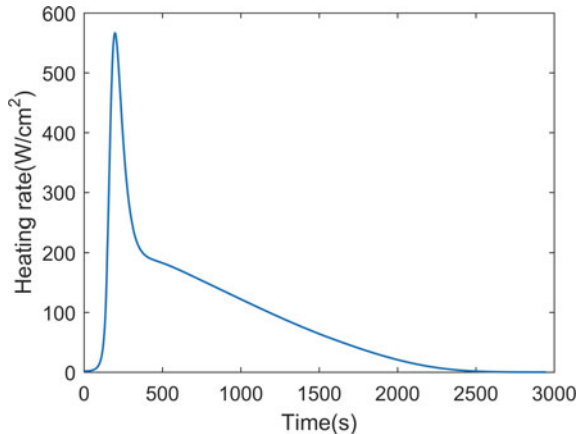
Fig. 11.13 Velocity histories**Fig. 11.14** The flight-path angle histories**Fig. 11.15** The command overload histories

Fig. 11.16 The heating rate histories



almost linearly, except for the initial descent phase. As a result, there will be no sudden increase in the heating rate. Figure 11.15 provides the command overload histories. After a short zero-overload free fall, the command overload increases to its maximum immediately. Because the speed of hypersonic vehicle is very high and its mass is quite heavy as well, the control force required to achieve a high overload is huge, which means that the vehicle will suffer a large drag force. Therefore, it should be further studied to reduce the maximum command load. Figure 11.16 displays the heating rate histories. The heating rate decreases smoothly without sudden change after the maximum heating rate peak. The comparison of the results before and after the improvement of the singular perturbation guidance is shown in Table 11.2.

Compared with the results of SPM, by using ISPG, the maximum heating rate is greatly reduced, reaching 68.97% of that of SPM. It should be noted that by adjusting the parameters of the dynamic inverse controller, smaller heating rate peak and altitude overshoot can be obtained to meet the requirements of engineering applications. In addition, due to the constraints on the maximum heating rate, the downrange of ISPG is shorter than that of SPM (about 89% of SPM).

Table 11.2 The comparison of the terminal states before and after improvement

Methods	Flight time (s)	Downrange (km)	Terminal velocity (m/s)	Maximum heating rate (W/cm²)
SPM	3048.0	8165.8	201.6	820.6
ISPG	2943.0	7267.9	131.6	566.0

11.3 Summary

In this chapter two singular-perturbation-based methods are proposed for the hypersonic vehicle over a spherical, nonrotating Earth in the vertical plane.

The performance of the first guidance SPM is similar to that of the numerical method GPM. However, it does not consider the constraint on the heating rate. Therefore, the improved guidance ISPG is proposed to reduce the maximum heating rate peak. The dynamic inverse technique is used for the boundary layer correction such that the vehicle is able to track the optimal altitude of the reduced-order system. But, because the drag of the vehicle is very sensitive to the overload due to the high velocity and altitude, the two parameters of the dynamic inverse controller must be carefully selected. The simulation results show that ISPG can achieve a smooth trajectory and reduce the maximum heating rate peak significantly.

References

1. Qiao, Q.: Guidance algorithm for long range air-to-air missile attacking slow maneuver target. Beihang University, Beijing (2013)
2. Menon, P.K.A., Briggs, M.M.: A midcourse guidance law for air-to-air missiles. In: Guidance, Navigation and Control Conference, Monterey, pp. 1070–1079 (1987)
3. Shen, D., Chen, Y.M., Cheng, Y.J., et al.: Optimal glide for maximum range. In: 23rd Atmosphere Flight Mechanics Conference, Boston, pp. 771–781 (1998)
4. Qiao, Q., Chen, W.: Singular perturbation midcourse guidance law based on dynamic inversion for air-to-air missile. *J. Beijing Univ. Aeronaut Astronaut* **37**(11), 1365–1371 (2011)
5. Qiao, Q., Chen, W.: Near-optimal midcourse guidance law for hypersonic missile. *Flight Dyn.* **32**(1), 48–52 (2014)

Chapter 12

3-D Reentry Guidance with Real-Time Planning of Reference using New Analytical Solutions Based on Spectral Decomposition Method



12.1 Introduction

A Common Aero Vehicle (CAV) [1] is a hypersonic gliding vehicle that is boosted to the speed of about Mach 20 by a launch vehicle and reenters the atmosphere without power. The flight of CAV can be roughly divided into two phases: the entry and terminal guidance phases. The entry phase starts shortly after the CAV is separated from the launch vehicle and ends at a specified distance from the target. In the entry phase, the CAV performs lateral maneuvers under the heating rate, dynamic pressure and load factor constraints to manage its energy. In the terminal guidance phase, the CAV attacks the ground target from a near-vertical orientation. In this paper, we study the guidance problem in the entry phase.

There are two categories of entry guidance: reference-tracking guidance and predictor-corrector guidance. Shuttle entry guidance [2] is the benchmark for reference-tracking guidance. This guidance plans a longitudinal reference in the drag-vs-speed corridor using an offline calculation. The reference is tracked by modulating the bank angle. To eliminate the crossrange error, the sign of the bank angle changes when the heading error exceeds a pre-defined threshold. Hanson et al. [3] applied shuttle entry guidance to the X-33 program. Mease et al. [4] proposed a fast drag-profile planning method that predicts the final states by integrating a reduced-order system and then corrects the reference profile. Later, Dukeman [5] used the Linear-Quadratic Regulator (LQR) method to simultaneously track the reference profiles of the range to go s_{go} , altitude H and flight-path angle γ with respect to the specific energy E . Simulation results demonstrated the good performance of the method. Shen and Lu [6] presented an onboard planning method that can quickly plan the $V(s_{go})$, $H(s_{go})$ and $\gamma(s_{go})$ profiles (where V is speed), and also used the LQR method to track these references. In the traditional guidance laws, using a heading error threshold

Reprinted from Advances in Space Research, Vol. 55, Yu Wenbin, Chen Wanchun, Entry guidance with real-time planning of reference based on analytical solutions, Pages 2325, Copyright (2015), with permission from Elsevier.

to determine the bank reversals may result in a large crossrange error if there are large aerodynamic dispersions. To overcome the problem, Shen and Lu [7] proposed a new lateral guidance logic that uses the crossrange error threshold to determine the bank reversals. The other type of entry guidance is the predictor-corrector guidance [8, 9], in which the control profiles are typically parameterized to simplify the complexity of the algorithm and increase its robustness. Later, Zimmerman et al. [10] proposed a predictor-corrector entry guidance that satisfies the heating rate constraint by breaking the entry trajectory into two parts. Additionally, Yu and Chen proposed a guidance scheme that can effectively suppresses the trajectory oscillations [11]. Lu et al. [12] simplified the scheme by neglecting the effects of the Earth curvature and then applied it to adaptive predictor-corrector entry guidance. In [13, 14], Li et al. proposed an optimization method for planning the reference trajectory, and then designed an adaptive tracking guidance to track it. In [15], Xia et al. proposed a new tracking law named active disturbance rejection control.

Many analytical solutions to hypersonic gliding problems exist. In [2] and [16–23], only the longitudinal motion is considered. In [16, 17], the downrange analytical solution is obtained as a function of V by assuming that the Lift to Drag ratio (L/D) is constant and γ is zero. In [18–20], three kinds of analytical relations among V , H and γ are presented. In [21], the relationships among the analytical solutions presented in [18–20] are revealed. In [22], Loh obtained the downrange analytical solutions to three different entry problems: (1) ρV^n is constant where ρ is the air density and n is a positive constant; (2) γ is constant; and (3) γ is a special function of ρ . In [23], Cohen obtained the downrange solutions where the lift and drag are special functions of V and ρ . In [24–26], all the authors considered lateral motion and almost simultaneously derived the same analytical solutions for downrange, crossrange and heading angle. In the derivation, the L/D and bank angle are limited to constants, and the influence of the Earth's curvature on the heading angle is neglected. Chen [26] obtained the analytical solutions to the constant-deceleration gliding problem.

In this paper, we first develop the new analytical solutions for downrange, cross-range, and heading angle where the L/D and bank angle are functions of energy. To improve the accuracy of the analytical solutions for crossrange and heading angle, we consider the effect of the Earth curvature on the heading angle and then obtain a linear system with variable coefficients by linearization. However, this system cannot be solved by traditional methods such as the Laplace transform. This is why the Earth curvature is neglected in the derivation of the traditional analytical solutions [24–26]. To solve such a system, we propose an innovative method based on spectral decomposition [27]. Next, we design an entry guidance based on the new solutions. The analytical solutions show that the profile of the vertical Lift to Drag ratio (L_1/D), the ratio of the vertical component of the lift to the drag, has a significant effect on the downrange. Therefore, the entry guidance plans the L_1/D profile using the downrange expression in real time to satisfy the downrange requirement, and tracks this profile by modulating the bank angle. For the sake of lessening the demands on the Flight Control System (FCS), the trajectory is planned with only two bank reversals. Different from the traditional guidance laws, the proposed entry guidance does not need a heading or crossrange error threshold to control the bank reversals. As the

new analytical solutions have sufficient accuracy, we propose a new scheme for bank reversals based on these solutions: If there are more bank reversals, the crossrange expression is used to plan all the bank reversals, and after the penultimate reversal is performed, the trajectory simulation is used to correct the last bank reversal slightly and accurately. Such a scheme avoids the repeated simulations of the whole trajectory and thus significantly reduces the computational load. Since the CAV trajectory has a weakly-damped phugoid oscillation, we extend the scheme used for suppressing the oscillation, presented in [11], to a 3-Dimensional (3-D) scheme and then apply it to the entry guidance. Because no offline planning is needed for specific mission, the entry guidance can handle various urgent tasks and deal well with large aerodynamic and atmospheric dispersions.

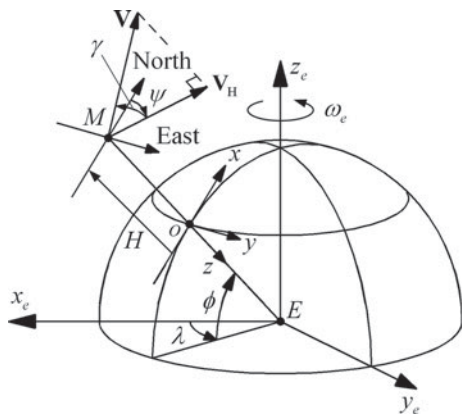
The structure of this paper is as follows. Section 12.2 shows the equations of motion considering the rotation of the Earth. Section 12.3 illustrates the entry guidance problem. Section 12.4 derives the new analytical solutions to the entry problem. Section 12.5 presents the new entry guidance based on these analytical solutions. Section 12.6 gives some examples to show the performance of the entry guidance. Section 12.7 summarizes the major contributions of the paper. Appendix shows the method of getting the states of motion relative to an auxiliary frame.

12.2 Equations of Motion

Before introducing the equations of motion, we need to define two coordinate systems first, as shown in Fig. 12.1.

Geocentric Equatorial Rotating (GER) frame: The origin E is at the Earth's center; the z_e axis is along the north polar axis; and the x_e and y_e axes are perpendicular to each other in the equatorial plane. The GER frame rotates around the z_e axis with an angular velocity $\omega_e = 7.292\ 116 \times 10^{-5}$ rad/s.

Fig. 12.1 Geocentric Equatorial Rotating (GER) frame: $E-x_Ey_Ez_E$ and local North-East-Down (NED) frame: $o-xyz$



Local North-East-Down (NED) frame: The origin o is at the intersection of the Earth surface with the line segment ME , where the point M is at the center of mass of the vehicle; the x axis points to the local north, the y axis points to the local east, and the z axis points to the Earth's center.

Regarding the vehicle as a particle, the equations of motion for flight over the rotating spherical Earth are

$$\frac{d\lambda}{dt} = \frac{V \cos(\gamma) \sin(\psi)}{(R_e + H) \cos(\phi)} \quad (12.1)$$

$$\frac{d\phi}{dt} = \frac{V \cos(\gamma) \cos(\psi)}{(R_e + H)} \quad (12.2)$$

$$\frac{dH}{dt} = V \sin(\gamma) \quad (12.3)$$

$$\begin{aligned} \frac{dV}{dt} = & -\frac{D}{m} - g \sin(\gamma) + \omega_e^2 (R_e + H) \cos^2(\phi) \sin(\gamma) \\ & - \omega_e^2 (R_e + H) \sin(\phi) \cos(\phi) \cos(\gamma) \cos(\psi) \end{aligned} \quad (12.4)$$

$$\begin{aligned} \frac{d\gamma}{dt} = & \frac{1}{V} \left[\frac{L \cos(\sigma)}{m} - g \cos(\gamma) + \frac{V^2 \cos(\gamma)}{R_e + H} + \omega_e^2 (R_e + H) \cos^2(\phi) \cos(\gamma) \right. \\ & \left. + 2V \omega_e \cos(\phi) \sin(\psi) + \omega_e^2 (R_e + H) \sin(\phi) \cos(\phi) \sin(\gamma) \cos(\psi) \right] \end{aligned} \quad (12.5)$$

$$\begin{aligned} \frac{d\psi}{dt} = & \frac{1}{V} \left[\frac{L \sin(\sigma)}{m \cos(\gamma)} + \frac{V^2 \cos(\gamma) \sin(\psi) \tan(\phi)}{R_e + H} - \frac{\omega_e^2 (R_e + H) \sin(\phi) \cos(\phi) \sin(\psi)}{\cos(\gamma)} \right. \\ & \left. + 2V \omega_e \sin(\phi) - 2V \omega_e \cos(\phi) \tan(\gamma) \cos(\psi) \right] \end{aligned} \quad (12.6)$$

where, as shown in Fig. 12.1, λ is the longitude, ϕ is the latitude, H is the altitude, V is the speed relative to the rotating Earth, γ is the flight-path angle, ψ is the heading angle, m is the mass, σ is the bank angle, and $R_e = 6356.766$ km is the average radius of the Earth. L is the lift, D is the drag, and g is the local gravitational acceleration. The coordinate transformation matrix $\mathbf{T}_{\text{GER}}^{\text{NED}}$ from the GER frame to the NED frame is

$$\mathbf{T}_{\text{GER}}^{\text{NED}} = \begin{bmatrix} -\cos(\lambda) \sin(\phi) & -\sin(\lambda) \sin(\phi) & \cos(\phi) \\ -\sin(\lambda) & \cos(\lambda) & 0 \\ -\cos(\lambda) \cos(\phi) & -\sin(\lambda) \cos(\phi) & -\sin(\phi) \end{bmatrix} \quad (12.7)$$

12.3 Entry Trajectory Constraints

12.3.1 Path Constraints

In general, the entry trajectory should satisfy the following constraints on the heating rate \dot{Q} , dynamic pressure q and load factor n as

$$q = \frac{1}{2} \rho V^2 \leq q_{\max} \quad (12.8)$$

$$\dot{Q} = k_Q \sqrt{\rho} V^{3.15} \leq \dot{Q}_{\max} \quad (12.9)$$

$$n = \frac{L}{mg_0} \leq n_{\max} \quad (12.10)$$

where, for CAV, $k_Q = 1.5 \times 10^{-8}$, $q_{\max} = 150 \text{ kPa}$, $\dot{Q}_{\max} = 500 \text{ W/cm}^2$, and $n_{\max} = 2g$. g_0 is the gravitational acceleration at sea level.

12.3.2 Terminal Conditions

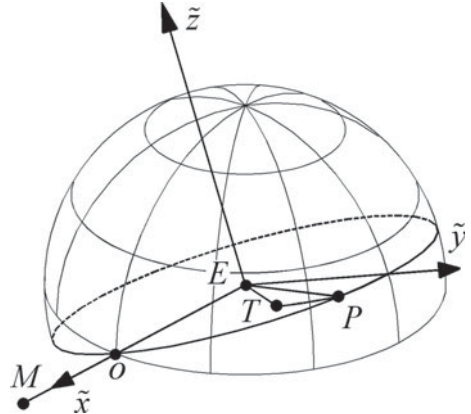
When the horizontal distance between the CAV and target reduces to a specified value $S_{\text{TEAM}} = 50 \text{ km}$, the entry phase ends and the terminal guidance phase begins. The desired terminal conditions of the entry phase are the heading error, $|\Delta\psi_{\text{STEM}}| \leq 5 \text{ deg}$, the speed relative to the rotating Earth $V_{\text{TEAM}} = 2000 \text{ m/s}$, the altitude $H_{\text{TAEM}} = 25 \text{ km}$ and the bank angle $|\sigma_{\text{TAEM}}| \leq 30 \text{ deg}$. Note that the subscript “TAEM” is widely used to represent the requirements of the interface of the Terminal Area Energy Management phase for a Reusable Launch Vehicle (RLV) [3], so we also use it here. Different from the RLV, the accuracy requirement of the CAV on H_{TAEM} is relatively loose because the CAV attacks the ground target from a near-vertical orientation, rather than lands horizontally. Therefore, the major factors contributing to success are S_{TAEM} , $\Delta\psi_{\text{TAEM}}$, and V_{TAEM} .

12.4 Analytical Solutions to Hypersonic Gliding Problem

12.4.1 Auxiliary Geocentric Inertial (AGI) Frame

In this subsection, we establish a frame called the AGI frame used for deriving and applying the analytical solutions. In the derivation of these solutions, the AGI frame is fixed in the inertial space. In the entry guidance, the AGI frame is updated once

Fig. 12.2 The AGI frame $E - \tilde{x}\tilde{y}\tilde{z}$ is static during each guidance cycle



according to the current states of the CAV in each guidance cycle, and remains stationary during the guidance cycle. The following shows how to establish the AGI frame.

As observed from the inertial space, the ground fixed target T moves with the rotating Earth. Therefore, as shown in Fig. 12.2, the collision point P , where the vehicle M hits the target, is not at the current target position. The position of P can be predicted by

$$\lambda_P = \lambda_T + \omega_e t_{\text{go}}, \quad \phi_P = \phi_T, \quad H_P = H_T \quad (12.11)$$

where, λ_P , ϕ_P and H_P are the longitude, latitude and altitude of P . λ_T , ϕ_T and H_T are the longitude, latitude and altitude of the target. t_{go} is the time to go. If we observe the vehicle's motion from the rotating Earth and assume that the vehicle's speed relative to the rotating Earth changes linearly with time, then t_{go} can be estimated roughly by

$$t_{\text{go}} = \frac{2s_{\text{go}}}{V + V_{\text{TAEM}}} \quad (12.12)$$

where s_{go} is the range to go observed from the rotating Earth and defined as the length of the great circle arc between the points o and T . s_{go} can be calculated by

$$s_{\text{go}} = R_e \arccos(\hat{\mathbf{x}}_{EM} \cdot \hat{\mathbf{x}}_{ET}) \quad (12.13)$$

Here, $\hat{\mathbf{x}}_{EM}$ and $\hat{\mathbf{x}}_{ET}$ are the unit vectors of \overrightarrow{EM} and \overrightarrow{ET} , where \overrightarrow{EM} is the vector from E to M , and \overrightarrow{ET} is the vector from E to T .

As shown in Fig. 12.2, the AGI frame is updated once in each guidance cycle. The origin is at the Earth's center; the \tilde{x} -axis points to M ; the \tilde{y} -axis is in the MEP plane which passes through M , E , and P ; and the \tilde{z} -axis is determined by the right-hand rule.

We define the generalized equator as the intersection of the Earth's surface with the *MEP* plane, and define the generalized meridian as half the great circle with both endpoints on the \tilde{z} -axis. The generalized meridian through the point o is chosen as the generalized prime meridian. Then, the position of an object can be expressed using the generalized longitude $\tilde{\lambda}$, generalized latitude $\tilde{\phi}$ and generalized altitude \tilde{H} . In each guidance cycle, because the entry guidance uses the current states as the initial states in the analytical solutions, the initial position relative to the AGI frame is $\tilde{\lambda}_0 = 0$, $\tilde{\phi}_0 = 0$, and $\tilde{H}_0 = H$.

Because the AGI frame is fixed with respect to the inertial space during each guidance cycle, the velocity vector of the CAV relative to this frame ($\tilde{\mathbf{V}}$) is the vector sum of the velocity relative to the Earth and the velocity due to the Earth's rotation. Define the generalized speed \tilde{V} as the magnitude of $\tilde{\mathbf{V}}$. Define the generalized flight path angle $\tilde{\gamma}$ as the angle between the local horizontal plane and $\tilde{\mathbf{V}}$, where $\tilde{\gamma}$ is negative when the altitude decreases. Define the generalized heading angle $\tilde{\psi}$ as the angle of the horizontal component of $\tilde{\mathbf{V}}$, measured clockwise from the vector that is parallel to the local generalized meridian and has a positive component on the \tilde{z} -axis. Appendix shows how to get the above generalized states from the states of motion relative to the GER frame.

12.4.2 Linearization of the Equations of Motion

There are two benefits to deriving the analytical solutions in the AGI frame. First, because the AGI frame is fixed with respect to the inertial space, we can obtain the equations of motion without complex nonlinear terms related to the Earth's rotation, as shown in Eqs. (12.14)–(12.19). Second, $\tilde{\phi} \approx 0$ and $\tilde{\psi} \approx \pi/2$ because the entry guidance approximately steers the vehicle to P along the generalized equator, which helps improve the accuracy of linearization.

$$\frac{d\tilde{\lambda}}{dt} = \frac{\tilde{V} \cos(\tilde{\gamma}) \sin(\tilde{\psi})}{(R_e + \tilde{H}) \cos(\tilde{\phi})} \quad (12.14)$$

$$\frac{d\tilde{\phi}}{dt} = \frac{\tilde{V} \cos(\tilde{\gamma}) \cos(\tilde{\psi})}{(R_e + \tilde{H})} \quad (12.15)$$

$$\frac{d\tilde{H}}{dt} = \tilde{V} \sin(\tilde{\gamma}) \quad (12.16)$$

$$\frac{d\tilde{V}}{dt} = -\frac{D}{m} - g \sin(\tilde{\gamma}) \quad (12.17)$$

$$\frac{d\tilde{\gamma}}{dt} = \frac{1}{\tilde{V}} \left[\frac{L \cos(\sigma)}{m} - g \cos(\tilde{\gamma}) + \frac{\tilde{V}^2 \cos(\tilde{\gamma})}{R_e + \tilde{H}} \right] \quad (12.18)$$

$$\frac{d\tilde{\psi}}{dt} = \frac{1}{\tilde{V}} \left[\frac{L \sin(\sigma)}{m \cos(\tilde{\gamma})} + \frac{\tilde{V}^2 \cos(\tilde{\gamma}) \sin(\tilde{\psi}) \tan(\tilde{\phi})}{R_e + \tilde{H}} \right] \quad (12.19)$$

As shown in Eq. (12.20), the specific absolute energy \tilde{E} is defined as the mechanical energy per unit mass relative to the AGI frame.

$$\tilde{E} = \frac{1}{2} \tilde{V}^2 - \frac{\mu}{R_e + \tilde{H}} \quad (12.20)$$

The time derivative of \tilde{E} is

$$\frac{d\tilde{E}}{dt} = \tilde{V} \dot{\tilde{V}} + g \dot{\tilde{H}} = -\frac{D \tilde{V}}{m} \quad (12.21)$$

Define the downrange (x_D) as $\tilde{\lambda} R_e$ and the crossrange (x_C) as $\tilde{\phi} R_e$. Dividing Eqs. (12.14)–(12.15) and Eq. (12.19) by Eq. (12.21) yields

$$\frac{dx_D}{d\tilde{E}} = -\frac{m \cos(\tilde{\gamma}) \sin(\tilde{\psi})}{D \cos(\tilde{\phi})} \frac{R_e}{(R_e + \tilde{H})} \quad (12.22)$$

$$\frac{dx_C}{d\tilde{E}} = -\frac{m \cos(\tilde{\gamma}) \cos(\tilde{\psi})}{D} \frac{R_e}{(R_e + \tilde{H})} \quad (12.23)$$

$$\frac{d\tilde{\psi}}{d\tilde{E}} = -\frac{\tilde{m}}{D \tilde{V}^2} \left[\frac{L \sin(\sigma)}{m \cos(\tilde{\gamma})} + \frac{\tilde{V}^2 \cos(\tilde{\gamma}) \sin(\tilde{\psi})}{R_e + \tilde{H}} \tan\left(\frac{x_C}{R_e}\right) \right] \quad (12.24)$$

Let $L_1 = L \cos(\sigma)$ and $L_2 = L \sin(\sigma)$. We assume that the vehicle glides in the Quasi-Equilibrium Glide Condition (QEGC) [6] which means that $d\tilde{\gamma}/dt \approx 0$. Then, from Eq. (12.18), we get

$$\frac{L_1}{m} - g \cos(\tilde{\gamma}) + \frac{\tilde{V}^2 \cos(\tilde{\gamma})}{R_e + \tilde{H}} = 0 \quad (12.25)$$

After some algebra, we obtain

$$\cos(\tilde{\gamma}) = \frac{L_1}{mg - \frac{m\tilde{V}^2}{R_e + \tilde{H}}} \quad (12.26)$$

From Eq. (12.20), we get

$$\tilde{V}^2 = 2\tilde{E} + \frac{2\mu}{R_e + \tilde{H}} \quad (12.27)$$

In the AGI frame, $\tilde{\psi} \approx \pi/2$ and $\tilde{\phi} = x_C/R_e \approx 0$ because the entry guidance steers the vehicle to P approximately along the generalized equator. Therefore, we can assume that $\cos(\tilde{\psi}) = \pi/2 - \tilde{\psi}$, $\sin(\tilde{\psi}) = 1$, $\cos(\tilde{\phi}) = 1$, and $\tan(x_C/R_e) = x_C/R_e$. Note that the graph of $y = \pi/2 - \tilde{\psi}$ is the tangent line to the graph of $y = \cos(\tilde{\psi})$ at $\tilde{\psi} = \pi/2$. Substituting Eqs. (12.26)–(12.27) into Eqs. (12.22)–(12.24) and using these assumptions, we obtain

$$\frac{dx_D}{d\tilde{E}} = -\frac{L_1}{D} \frac{R_e}{-\frac{\mu}{(R_e+\tilde{H})} - 2\tilde{E}} \quad (12.28)$$

$$\frac{dx_C}{d\tilde{E}} = \frac{L_1}{D} \frac{R_e \tilde{\psi}}{-\frac{\mu}{R_e+\tilde{H}} - 2\tilde{E}} - \frac{\pi}{2} \frac{L_1}{D} \frac{R_e}{-\frac{\mu}{R_e+\tilde{H}} - 2\tilde{E}} \quad (12.29)$$

$$\frac{d\tilde{\psi}}{d\tilde{E}} = \frac{L_1}{D} \frac{1}{\frac{\mu}{R_e+\tilde{H}} + 2\tilde{E}} \frac{x_C}{R_e} - \frac{L_2}{D} \frac{1}{2\tilde{E} + \frac{2\mu}{R_e+\tilde{H}}} \quad (12.30)$$

Note that, to facilitate the following derivation, $\cos(\tilde{\gamma})$ in the denominator of Eq. (12.24) is assumed to be 1.

12.4.3 Analytical Solutions

Because $\tilde{H} \ll R_e$, \tilde{H} has little influence on the solutions of Eqs. (12.28)–(12.30). Thus, we set \tilde{H} to a constant $H^* = (\tilde{H}_0 + H_{TAEM}/2)$. Let $R^* = R_e + H^*$ and $L_1/D = L \cos(\sigma)/D$. Because the low order polynomials are commonly used functions, and in the proposed entry guidance, L_1/D is designed as a piecewise function consisting of low order polynomials, for general, we let

$$L_1/D = a_2 \tilde{E}^2 + a_1 \tilde{E} + a_0 \quad (12.31)$$

Define the horizontal Lift to Drag ratio as $L_2/D = L \sin(\sigma)/D$. Also for general, let

$$L_2/D = b_2 \tilde{E}^2 + b_1 \tilde{E} + b_0 \quad (12.32)$$

where the L_1/D and L_2/D profiles can be tracked by simultaneously modulating the Angle of Attack (AOA) and bank angle. By substituting Eq. (12.31) into Eq. (12.28), we obtain the downrange expression as

$$\begin{aligned} x_D(\tilde{E}, \tilde{E}_0) = & \frac{1}{4} a_2 R_e (\tilde{E}^2 - \tilde{E}_0^2) + \frac{1}{2} \left(a_1 - \frac{a_2 \mu}{2R^*} \right) R_e (\tilde{E} - \tilde{E}_0) \\ & + \frac{4a_0(R^*)^2 - 2\mu R^* a_1 + \mu^2 a_2}{8(R^*)^2} R_e \ln \left(\frac{2R^* \tilde{E} + \mu}{2R^* \tilde{E}_0 + \mu} \right) \end{aligned} \quad (12.33)$$

Combining Eqs. (12.29)–(12.30) together yields

$$\begin{bmatrix} \frac{dx_C}{d\tilde{E}} \\ \frac{d\tilde{\psi}}{d\tilde{E}} \end{bmatrix} = \frac{L_1}{D} \frac{1}{\frac{\mu}{R^*} + 2\tilde{E}} \begin{bmatrix} 0 & -R_e \\ \frac{1}{R_e} & 0 \end{bmatrix} \begin{bmatrix} x_C \\ \tilde{\psi} \end{bmatrix} + \begin{bmatrix} \frac{\pi}{2} \frac{L_1}{D} \frac{R_e}{\frac{\mu}{R^*} + 2\tilde{E}} \\ -\frac{L_2}{D} \frac{1}{2\tilde{E} + \frac{2\mu}{R^*}} \end{bmatrix}^T \quad (12.34)$$

Let

$$f_1(\tilde{E}) = \frac{L_1}{D} \frac{1}{\frac{\mu}{R^*} + 2\tilde{E}} \quad (12.35)$$

$$f_2(\tilde{E}) = \frac{\pi R_e}{2} f_1(\tilde{E}) \quad (12.36)$$

$$f_3(\tilde{E}) = -\frac{L_2}{D} \frac{1}{2\tilde{E} + \frac{2\mu}{R^*}} \quad (12.37)$$

$$f_4(\tilde{E}, \tilde{E}_0) = \int_{\tilde{E}_0}^{\tilde{E}} f_1(\tilde{x}_E) d\tilde{x}_E = \frac{x_D(\tilde{E}, \tilde{E}_0)}{R_e} \quad (12.38)$$

$$\mathbf{A} = \begin{bmatrix} 0 & -R_e \\ 1/R_e & 0 \end{bmatrix} \quad (12.39)$$

Then, Eq. (12.34) can be rewritten as

$$\begin{bmatrix} \frac{dx_C}{d\tilde{E}} \\ \frac{d\tilde{\psi}}{d\tilde{E}} \end{bmatrix} = f_1(\tilde{E}) \mathbf{A} \begin{bmatrix} x_C \\ \tilde{\psi} \end{bmatrix} + \begin{bmatrix} f_2(\tilde{E}) \\ f_3(\tilde{E}) \end{bmatrix} \quad (12.40)$$

This system cannot be solved by traditional methods such as the Laplace transform. To address this problem, in [24–26], x_C and $\tilde{\psi}$ were decoupled by neglecting the second term in the brackets of Eq. (12.19). However, this results in apparent errors in the solutions for crossrange and heading angle. To solve the above system, we propose an innovative method based on spectral decomposition. We define $\mathbf{Q}(\tilde{E}, \tilde{E}_0)$ as

$$\mathbf{Q}(\tilde{E}, \tilde{E}_0) = \exp \left(- \int_{\tilde{E}_0}^{\tilde{E}} \mathbf{A} f_1(\tilde{x}_E) d\tilde{x}_E \right) = \exp(-\mathbf{A} f_4(\tilde{E}, \tilde{E}_0)) \quad (12.41)$$

Left multiplying both sides of Eq. (12.40) by $\mathbf{Q}(\tilde{E}, \tilde{E}_0)$ yields

$$\begin{aligned} \exp(-\mathbf{A}f_4(\tilde{E}, \tilde{E}_0)) \begin{bmatrix} \frac{dx_C}{d\tilde{E}} \\ \frac{d\psi}{d\tilde{E}} \end{bmatrix} - \exp(-\mathbf{A}f_4(\tilde{E}, \tilde{E}_0)) f_1(\tilde{E}) \mathbf{A} \begin{bmatrix} x_C \\ \tilde{\psi} \end{bmatrix} \\ = \exp(-\mathbf{A}f_4(\tilde{E}, \tilde{E}_0)) \begin{bmatrix} f_2(\tilde{E}) \\ f_3(\tilde{E}) \end{bmatrix} \end{aligned} \quad (12.42)$$

Equation (12.42) can be rewritten as

$$\begin{aligned} \exp(-\mathbf{A}f_4(\tilde{E}, \tilde{E}_0)) \begin{bmatrix} \frac{dx_C}{d\tilde{E}} \\ \frac{d\psi}{d\tilde{E}} \end{bmatrix} + \frac{d}{d\tilde{E}} \left[\exp(-\mathbf{A}f_4(\tilde{E}, \tilde{E}_0)) \right] \begin{bmatrix} x_C \\ \tilde{\psi} \end{bmatrix} \\ = \exp(-\mathbf{A}f_4(\tilde{E}, \tilde{E}_0)) \begin{bmatrix} f_2(\tilde{E}) \\ f_3(\tilde{E}) \end{bmatrix} \end{aligned} \quad (12.43)$$

Inversely using the product rule for finding the derivative, we have

$$\frac{d}{d\tilde{E}} \left[\exp(-\mathbf{A}f_4(\tilde{E}, \tilde{E}_0)) \begin{bmatrix} x_C \\ \tilde{\psi} \end{bmatrix} \right] = \exp(-\mathbf{A}f_4(\tilde{E}, \tilde{E}_0)) \begin{bmatrix} f_2(\tilde{E}) \\ f_3(\tilde{E}) \end{bmatrix} \quad (12.44)$$

Integrating both sides of Eq. (12.44) yields

$$\begin{aligned} \exp(-\mathbf{A}f_4(\tilde{E}, \tilde{E}_0)) \begin{bmatrix} x_C \\ \tilde{\psi} \end{bmatrix} - \exp(-\mathbf{A}f_4(\tilde{E}_0, \tilde{E}_0)) \begin{bmatrix} x_{C0} \\ \tilde{\psi}_0 \end{bmatrix} \\ = \int_{\tilde{E}_0}^{\tilde{E}} \exp(-\mathbf{A}f_4(\tilde{x}_E, \tilde{E}_0)) \begin{bmatrix} f_2(\tilde{x}_E) \\ f_3(\tilde{x}_E) \end{bmatrix} d\tilde{x}_E \end{aligned} \quad (12.45)$$

Note that $\exp(-\mathbf{A}f_4(\tilde{E}_0, \tilde{E}_0)) = \exp(\mathbf{0}_{2 \times 2}) = \mathbf{I}_{2 \times 2}$, where $\mathbf{0}_{2 \times 2}$ is the 2×2 zero matrix and $\mathbf{I}_{2 \times 2}$ is the 2×2 unit matrix. The inverse of $\mathbf{Q}(\tilde{E}, \tilde{E}_0)$ is

$$\Phi(\tilde{E}, \tilde{E}_0) = \left[\mathbf{Q}(\tilde{E}, \tilde{E}_0) \right]^{-1} = \exp(\mathbf{A}f_4(\tilde{E}, \tilde{E}_0)) \quad (12.46)$$

Left multiplying Eq. (12.45) by Eq. (12.46) yields

$$\begin{bmatrix} x_C \\ \tilde{\psi} \end{bmatrix} = \Phi(\tilde{E}, \tilde{E}_0) \begin{bmatrix} x_{C0} \\ \tilde{\psi}_0 \end{bmatrix} + \int_{\tilde{E}_0}^{\tilde{E}} \Phi(\tilde{E}, \tilde{x}_E) \begin{bmatrix} f_2(\tilde{x}_E) \\ f_3(\tilde{x}_E) \end{bmatrix} d\tilde{x}_E \quad (12.47)$$

where $\Phi(\tilde{E}, \tilde{E}_0)$ is the so-called state transition matrix and can be solved by innovatively using the spectral decomposition of \mathbf{A} .

$$\Phi(\tilde{E}, \tilde{E}_0) = \exp(\lambda_1 f_4(\tilde{E}, \tilde{E}_0)) \mathbf{G}_1 + \exp(\lambda_2 f_4(\tilde{E}, \tilde{E}_0)) \mathbf{G}_2 \quad (12.48)$$

where $\lambda_1 = i$ and $\lambda_2 = -i$ are the eigenvalues of \mathbf{A} where $i = \sqrt{-1}$. \mathbf{G}_1 and \mathbf{G}_2 are the spectral projectors of \mathbf{A} and can be calculated using

$$\mathbf{G}_1 = \frac{\mathbf{A} - \lambda_2 \mathbf{I}}{\lambda_1 - \lambda_2} = \begin{bmatrix} 1/2 & R_e i/2 \\ -i/(2R_e) & 1/2 \end{bmatrix} \quad (12.49)$$

$$\mathbf{G}_2 = \frac{\mathbf{A} - \lambda_1 \mathbf{I}}{\lambda_2 - \lambda_1} = \begin{bmatrix} 1/2 & -R_e i/2 \\ i/(2R_e) & 1/2 \end{bmatrix} \quad (12.50)$$

Then, we obtain

$$\Phi(\tilde{E}, \tilde{E}_0) = \begin{bmatrix} \cos(f_4(\tilde{E}, \tilde{E}_0)) & -R_e \sin(f_4(\tilde{E}, \tilde{E}_0)) \\ \sin(f_4(\tilde{E}, \tilde{E}_0))/R_e & \cos(f_4(\tilde{E}, \tilde{E}_0)) \end{bmatrix} \quad (12.51)$$

And

$$\int_{\tilde{E}_0}^{\tilde{E}} \Phi(\tilde{E}, \tilde{x}_E) \begin{bmatrix} f_2(\tilde{x}_E) \\ f_3(\tilde{x}_E) \end{bmatrix} d\tilde{x}_E = \int_{\tilde{E}_0}^{\tilde{E}} \begin{bmatrix} \cos(f_4(\tilde{E}, \tilde{x}_E))f_2(\tilde{x}_E) - R_e \sin(f_4(\tilde{E}, \tilde{x}_E))f_3(\tilde{x}_E) \\ \sin(f_4(\tilde{E}, \tilde{x}_E))f_2(\tilde{x}_E)/R_e + \cos(f_4(\tilde{E}, \tilde{x}_E))f_3(\tilde{x}_E) \end{bmatrix} d\tilde{x}_E \quad (12.52)$$

From Eqs. (12.36) and (12.38), we have

$$\begin{aligned} \int_{\tilde{E}_0}^{\tilde{E}} \cos(f_4(\tilde{E}, \tilde{x}_E))f_2(\tilde{x}_E) d\tilde{x}_E &= -\frac{\pi R_e}{2} \int_{\tilde{E}_0}^{\tilde{E}} \cos(f_4(\tilde{E}, \tilde{x}_E)) df_4(\tilde{E}, \tilde{x}_E) \\ &= \frac{\pi R_e}{2} \sin(f_4(\tilde{E}, \tilde{E}_0)) \end{aligned} \quad (12.53)$$

$$\begin{aligned} \frac{1}{R_e} \int_{\tilde{E}_0}^{\tilde{E}} \sin(f_4(\tilde{E}, \tilde{x}_E))f_2(\tilde{x}_E) d\tilde{x}_E &= -\frac{\pi}{2} \int_{\tilde{E}_0}^{\tilde{E}} \sin(f_4(\tilde{E}, \tilde{x}_E)) df_4(\tilde{E}, \tilde{x}_E) \\ &= \frac{\pi}{2} - \frac{\pi}{2} \cos(f_4(\tilde{E}, \tilde{E}_0)) \end{aligned} \quad (12.54)$$

Then, the analytical solutions for crossrange and heading angle are

$$x_C(\tilde{E}, \tilde{E}_0) = x_{C0} \cos(f_4(\tilde{E}, \tilde{E}_0)) - R_e \tilde{\psi}_0 \sin(f_4(\tilde{E}, \tilde{E}_0)) + \frac{\pi R_e}{2} \sin(f_4(\tilde{E}, \tilde{E}_0)) \\ - R_e \int_{\tilde{E}_0}^{\tilde{E}} \sin(f_4(\tilde{E}, \tilde{x}_E)) f_3(\tilde{x}_E) d\tilde{x}_E \quad (12.55)$$

$$\tilde{\psi}(\tilde{E}, \tilde{E}_0) = \frac{x_{C0}}{R_e} \sin(f_4(\tilde{E}, \tilde{E}_0)) + \tilde{\psi}_0 \cos(f_4(\tilde{E}, \tilde{E}_0)) + \frac{\pi}{2} - \frac{\pi}{2} \cos(f_4(\tilde{E}, \tilde{E}_0)) \\ + \int_{\tilde{E}_0}^{\tilde{E}} \cos(f_4(\tilde{E}, \tilde{x}_E)) f_3(\tilde{x}_E) d\tilde{x}_E \quad (12.56)$$

Note that the proposed entry guidance steers the vehicle along a pre-designed AOA profile and tracks a planned L_1/D profile by modulating the bank angle. This means that the L_2/D profile cannot be arbitrarily designed and cannot even be expressed as a finite term polynomial such as Eq. (12.32). However, the above solutions still hold, because the expression of L_2/D is only contained in $f_3(\tilde{x}_E)$ and is not used in the derivation.

12.4.4 Example for Accuracy Verification

An example is provided to compare the results of the analytical solutions and trajectory simulations, where the CAV model is used. The initial conditions are $\tilde{V}_0 = 7200$ m/s, $\tilde{H}_0 = 60$ km, $\tilde{\gamma}_0 = 0$ deg and $\tilde{\psi}_0 = 90$ deg. The final condition is $\tilde{E}_f = -5.5 \times 10^4$ kJ/kg. We consider two typical cases. In Case 1, the CAV achieves a long glide range, where the planned reference profiles are

$$L_1/D = 2.5 \quad (12.57)$$

$$L_2/D = \begin{cases} 1.5 & \text{if } \tilde{E} \geq -4.5 \times 10^4 \text{ kJ/kg} \\ -1.5 & \text{if } \tilde{E} < -4.5 \times 10^4 \text{ kJ/kg} \end{cases} \quad (12.58)$$

In Case 2, the CAV achieves a short glide range. The planned reference profiles are

$$L_1/D = 1.5 \quad (12.59)$$

$$L_2/D = \begin{cases} -2.5 & \text{if } \tilde{E} \geq -4.5 \times 10^4 \text{ kJ/kg} \\ 2.5 & \text{if } \tilde{E} < -4.5 \times 10^4 \text{ kJ/kg} \end{cases} \quad (12.60)$$

In [25], Bell obtained the analytical solutions for downrange, crossrange and heading angle, denoted as x_D^{Bell} , x_C^{Bell} and $\tilde{\psi}^{\text{Bell}}$ respectively, by limiting the L/D and σ to constants and neglecting the second term in the brackets of Eq. (12.19), which reflects the effects of the Earth's curvature on the heading angle and creates difficulty in obtaining the entry solutions. To identify the two kinds of solutions, we refer to the analytical solutions presented in this paper as Yu-Chen's Glide Formulas (YCGF), and the analytical solutions presented in [25] as Bell's Glide Formulas (BGF). According to the piecewise reference profiles, we modify BGF to

$$x_D^{\text{Bell}}(\tilde{V}, \tilde{V}_0) = L_1/D \frac{(R^*)^2}{\mu} \int_{\tilde{V}}^{\tilde{V}_0} \frac{\mu v \cos(\tilde{\psi}^{\text{Bell}}(v, \tilde{V}_0) - \pi/2)}{\mu - v^2 R^*} dv \quad (12.61)$$

$$x_C^{\text{Bell}}(\tilde{V}, \tilde{V}_0) = -L_1/D \frac{(R^*)^2}{\mu} \int_{\tilde{V}}^{\tilde{V}_0} \frac{\mu v \sin(\tilde{\psi}^{\text{Bell}}(v, \tilde{V}_0) - \pi/2)}{\mu - v^2 R^*} dv \quad (12.62)$$

$$\tilde{\psi}^{\text{Bell}}(\tilde{V}, \tilde{V}_0) = \begin{cases} \tilde{\psi}_0 + k_{\text{sgn}} |L_2/D| \ln\left(\tilde{V}_0/\tilde{V}\right); & \text{if } \tilde{V} \geq \tilde{V}_s \\ \tilde{\psi}_0 + k_{\text{sgn}} |L_2/D| \ln\left(\tilde{V}_0/\tilde{V}_s\right) - k_{\text{sgn}} |L_2/D| \ln\left(\tilde{V}_s/\tilde{V}\right); & \text{if } \tilde{V} < \tilde{V}_s \end{cases} \quad (12.63)$$

where $\tilde{V}_s = 5802.29$ m/s at $\tilde{E} = -4.5 \times 10^4$ kJ/kg in the trajectory simulation. The final speed in the trajectory simulation is $\tilde{V}_f = 3721.68$ m/s. In Case 1, $k_{\text{sgn}} = 1$, and in Case 2, $k_{\text{sgn}} = -1$. The 20-point Gauss-Legendre quadrature rule [28] is used to calculate the integrals in the analytical solutions. In the trajectory simulation, the oscillation-suppressing scheme shown in Sect. 5.2 is used to suppress the trajectory oscillation. The limitation on the change rate of the bank angle is neglected to closely track the reference profiles. The programs are written in the C programming language.

From Table 12.1 and Figs. 12.3, 12.4 and 12.5, we can see that YCGF are very accurate and the computation time of YCGF is at least two orders of magnitude less than that of the trajectory simulation.

First, we analyze the downrange expressions. Because we assume that $\sin(\tilde{\psi}) = 1$ in the derivation, the effect of the heading error on the downrange is neglected. This causes the downrange result of YCGF to be greater than that of the trajectory

Fig. 12.3 Downrange results

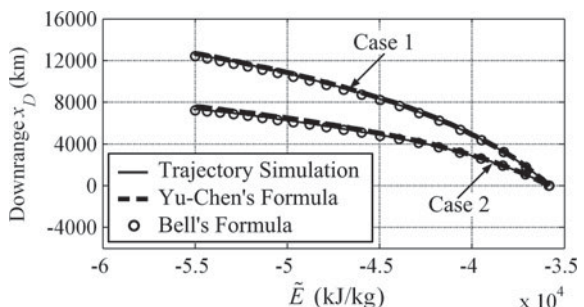
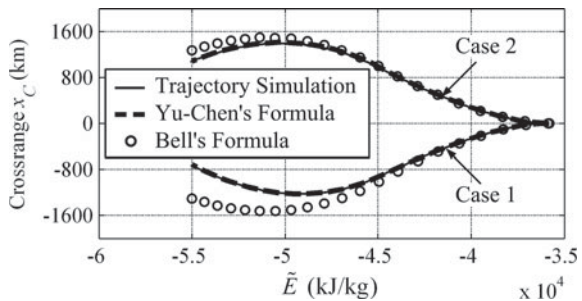
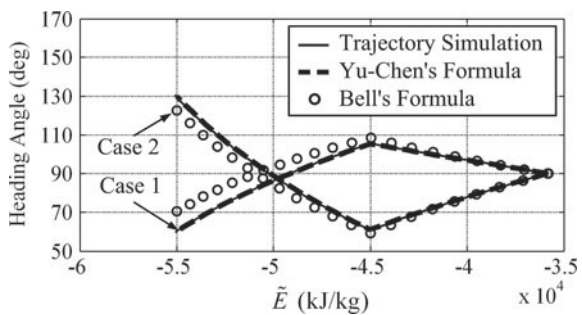


Fig. 12.4 Crossrange results**Fig. 12.5** Generalized heading angle results

simulation. However, in practical applications, the entry guidance can reduce the heading error by performing more bank reversals, and can thus improve the accuracy of the YCGF for downrange. The BGF results are also given here as a comparison. Because BGF takes into account the effect of the heading error on the downrange, its accuracy is higher than that of YCGF, especially in Case 2. However, compared with YCGF, BGF requires more computational effort if it is used by the entry guidance to plan the L_1/D profile in real time, because (1) BGF needs an iterative procedure to determine the profile's parameters due to the coupling of the downrange and heading angle expressions, and (2) it also needs the numerical integration method to calculate the integral term.

Next, we analyze the crossrange and heading angle expressions. The results show that the accuracy of BGF for crossrange and heading angle is much lower than YCGF, especially in the long range case. This is because the second term in the brackets of Eq. (12.19) is removed in the derivation of BGF. Additionally, although the crossrange expression of YCGF has an integral term, the computational load of the entry guidance is small because, using the crossrange expression, the bank reversals are only updated several times rather than in real time (Table 12.1).

Table 12.1 Comparison of the analytical solutions and trajectory simulation

Case	Method	$x_D(\tilde{E}_f, \tilde{E}_0)$ (km)	$x_C(\tilde{E}_f, \tilde{E}_0)$ (km)	$\tilde{\psi}(\tilde{E}_f, \tilde{E}_0)$ (deg)	Computing time (s)
Case 1	Trajectory simulation	12,544.10	-728.55	60.23	0.05626
Case 1	Yu-Chen's formulas	12,662.03	-714.98	60.03	1.1554×10^{-4}
Case 1	Bell's formulas	12,394.07	-1302.87	70.38	1.2549×10^{-4}
Case 2	Trajectory simulation	7314.01	1080.22	129.46	0.03578
Case 2	Yu-Chen's formulas	7573.54	1079.83	130.04	1.1340×10^{-4}
Case 2	Bell's formulas	7225.20	1271.57	122.68	1.2522×10^{-4}

12.5 Entry Guidance

In this section, we design a new entry guidance based on the analytical solutions. Different from the traditional guidance laws, the new guidance does not need to conduct any offline planning for specific mission. Therefore, this guidance can handle various urgent tasks. The entry guidance divides the entry flight into three phases: Descent Phase (DP), Quasi-Equilibrium Glide Phase (QEGP), and Altitude Adjustment Phase (AAP).

12.5.1 Descent Phase

The descent phase starts shortly after the CAV separates from the launch vehicle and ends when the vehicle can glide in the QEGC. In the early part of this phase, because the air density ρ is quite small, the vehicle loses altitude quickly and the heating rate increases rapidly with increasing ρ . The local maximum heating rate occurs near the end of the DP. As shown in Fig. 12.6, to satisfy the heating rate constraint, we let the AOA be its maximum allowable value (α_{\max}) and let the bank angle (σ) be zero, such that the vehicle glides as high as possible and the heating rate is minimized. When $\dot{\gamma} \geq 0$, the lift is sufficient to support the vehicle to glide in the QEGC. Thus, as shown in the second sub-equation of Eq. (12.64), we use a transition scheme to smoothly change the AOA to the planned value in the QEGP. Therefore, the AOA and bank angle commands are

$$\alpha_{\text{cmd}} = \begin{cases} \alpha_{\max} & \text{If } \dot{\gamma} < 0 \text{ deg/s} \\ \frac{\Delta\gamma}{\Delta\gamma_1} \alpha_{\max} + \frac{\Delta\gamma_1 - \Delta\gamma}{\Delta\gamma_1} (\alpha_{\text{plan}} + k_\gamma \Delta\gamma) & \text{If } \dot{\gamma} \geq 0 \text{ deg/s} \end{cases} \quad (12.64)$$

$$\sigma_{\text{cmd}} = 0 \text{ deg} \quad (12.65)$$

$$\Delta\gamma = \gamma_{\text{plan}} - \gamma \quad (12.66)$$

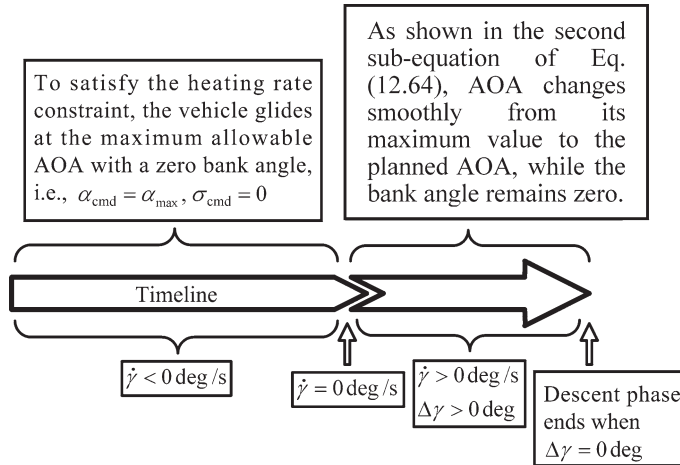


Fig. 12.6 Entry guidance timeline in descent phase

where α_{plan} is the planned AOA, and γ_{plan} is the flight-path angle corresponding to quasi-equilibrium glide. α_{plan} and γ_{plan} will be described in detail in Sect. 12.5.2. $\Delta\gamma_1$ is the value of $\Delta\gamma$ at $\dot{\gamma} = 0 \text{ deg/s}$, and k_γ is a constant. As $\Delta\gamma$ changes from $\Delta\gamma_1$ to 0, α_{cmd} changes smoothly from α_{max} to α_{plan} . When $\Delta\gamma = 0$ and $\dot{\gamma} \geq 0 \text{ deg/s}$, the descent phase ends because the vehicle will ascend later. The specific absolute energy at this moment is denoted as \tilde{E}_1 .

12.5.2 Quasi-Equilibrium Glide Phase

As shown in Fig. 12.7, the whole trajectory is planned with two bank reversals where the second bank reversal is at a specified point near the end of the trajectory. After the second bank reversal, the vehicle dives into the dense atmosphere by reducing α and the QEGC is no longer satisfied. So the QEGP ends when the second bank reversal occurs. As shown in the box located in the upper left of Fig. 12.7, in the QEGP, the vehicle glides along a planned AOA (α_{plan}) profile in the QEGC. The entry guidance uses the downrange expression to update the L_1/D profile in real time such that the downrange requirement is satisfied, and tracks this profile by modulating σ . The second terms on the right of the formulas of α_{cmd} and σ_{cmd} are due to the 3-D oscillation suppressing scheme. As shown in the box located in the upper right of Fig. 12.7, in the AAP, because the QEGC is no longer satisfied, we proposed a new guidance scheme based on Proportional Navigation (PN) [29], which can well meet the requirements on final heading error and speed in the presence of various disturbances. Different from the traditional guidance laws, the proposed entry guidance does not use a heading or crossrange error threshold to control the bank reversals. As shown in the bottom of Fig. 12.7, a new scheme is proposed for bank

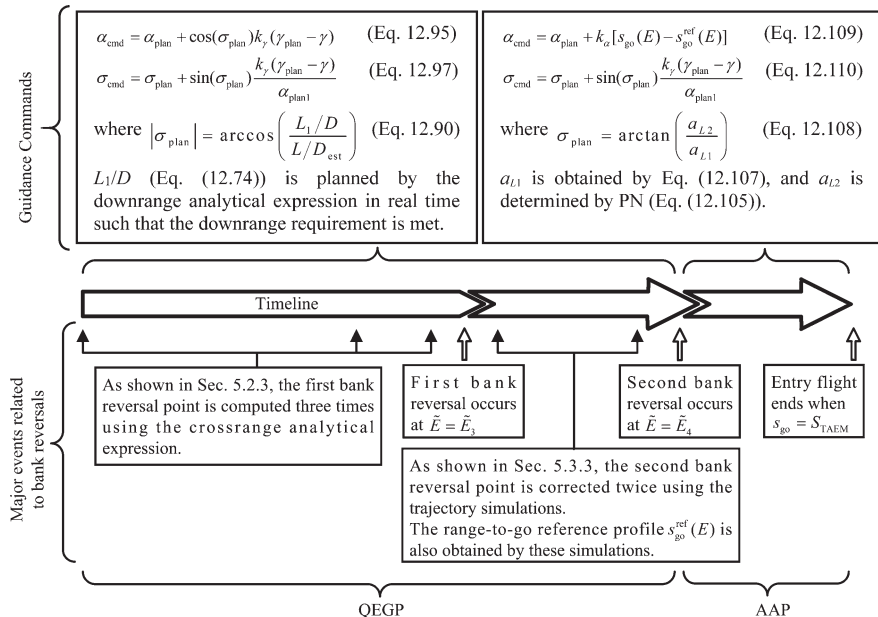


Fig. 12.7 Entry guidance timeline during the QEGP and AAP

reversals. In this scheme, the crossrange expression is used to correct the first bank reversal point three times such that the second bank reversal will occur at a specified point near the end of the entry flight. After the first bank reversal is performed, the second bank reversal is corrected twice by the trajectory simulations based on the proposed entry guidance. Letting the second bank reversal be near the end of the flight has a benefit: The correction of the second bank reversal can eliminate the errors accumulated before the second bank reversal, and the errors accumulated in the AAP are small because the remaining trajectory is short, while most of them can also be eliminated. In addition, because only the latter part of the flight is simulated several times for correcting the second bank reversal, the entry guidance will not result in a heavy computational load of the onboard computer.

Note that although the guidance uses a different scheme in the AAP, the guidance plans the L_1/D profile and first bank reversal in the QEGP under the assumption that the vehicle always tracks the L_1/D profile during the remaining glide flight. There are two reasons for this. First, it aids the implementation of the analytical solutions because it is easy to get the desired final states of the entry flight relative to the AGI frame. Second, it lets the vehicle be in appropriate initial states in the AAP, so that the commands in the AAP will not exceed the limitations on α and σ .

12.5.2.1 Planned AOA and Planned Lift to Drag Ratio (L/D_{plan})

Now we show the α_{plan} profile and some other preparatory works related to α_{plan} . L/D_{plan} is the L/D profile corresponding to α_{plan} . It is known that the L/D generally varies with the AOA and Mach number (Ma). Because Ma is affected by the motion of the atmosphere which can approximately be regarded as static in the rotating Earth, we design the α_{plan} and L/D_{plan} profiles as functions of the specific relative energy E , which is defined as the mechanical energy per unit mass relative to the rotating Earth and can be obtained by Eq. (12.67). The benefit is that no modification of the α_{plan} and L/D_{plan} profiles is needed for various missions.

$$E = \frac{1}{2} V^2 - \frac{\mu}{R_e + H} \quad (12.67)$$

The α_{plan} profile is shown in Eq. (12.68). To achieve a long glide range, we let the vehicle glide at $\alpha_1 = 10$ deg in the QEGP because this AOA approximately corresponds to the maximum L/D (L/D_{max}). In the AAP, we decrease H to H_{TAEM} smoothly by reducing α_{plan} to α_2 in order that the vehicle has enough dynamic pressure to perform maneuvers in the terminal guidance phase. As found from the trajectory simulation trials, if $\alpha_2 = 6$ deg, then the final altitude H_f is approximate to H_{TAEM} . Therefore, we let α_2 be 6 deg.

$$\alpha_{\text{plan}} = \begin{cases} \alpha_1; & E_2 \leq E \leq E_0 \\ \left(\frac{E_2 - E}{E_2 - E_f}\right)^2 (\alpha_2 - \alpha_1) + \alpha_1; & E_f \leq E < E_2 \end{cases} \quad (12.68)$$

where E_0 is the initial specific relative energy, $E_2 = -5.6 \times 10^7 \text{ J/kg}$ is approximately at the dividing point between the QEGP and AAP, and E_f is the desired final specific relative energy and can be obtained by substituting V_{TAEM} and H_{TAEM} into Eq. (12.67).

As shown in Fig. 12.8, after specifying the α_{plan} profile, we can determine the altitude corridor. The lower boundary of the altitude (H_{\min}) is obtained by the path constraints shown in Sect. 12.3. The upper boundary of the altitude (H_{\max}) is obtained

Fig. 12.8 Altitude corridor

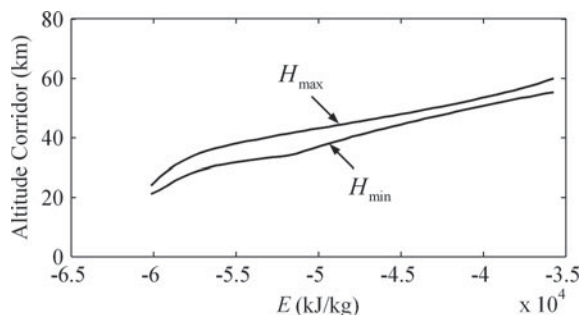
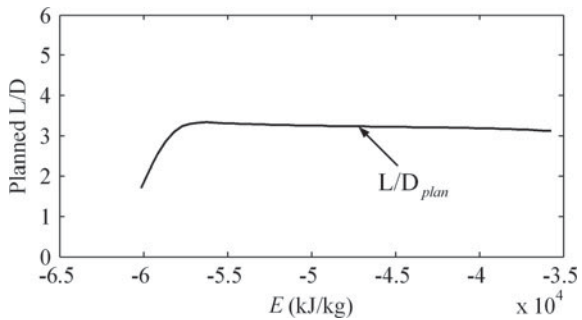


Fig. 12.9 Planned L/D profile with respect to E



by ignoring the Earth's rotation, assuming that $\sigma = 0$ deg and $d\gamma/dt = 0$, and then solving Eq. (12.5).

Now we determine the L/D_{plan} profile with respect to E . As the α_{plan} profile is specified, L/D_{plan} is a function of Ma (which is a function of V and H). Therefore, if the altitude profile is specified, we can determine the L/D_{plan} profile. In fact, when the vehicle glides at hypersonic speed, L/D changes slightly with Ma , and because H is limited in the narrow altitude corridor and the speed of sound varies slightly with H , H has little effect on Ma . Thus, the altitude profile has little effect on the L/D_{plan} profile. Therefore, we can assume that the vehicle glides in the middle of the altitude corridor. Under this assumption, V , H , and Ma are determined at any specified E . Further, by the α_{plan} and Ma profiles, we can obtain the L/D_{plan} profile with respect to E as shown in Fig. 12.9. From this figure, we can see that the maximum value of L/D_{plan} is up to 3.

We also need to obtain the relationship between \tilde{E} and E because the analytical solutions are implemented in the AGI frame. From Eqs. [(12.20), (12.67) and (12.115)], the exact relationship between E and \tilde{E} is

$$\tilde{E} = E + V\omega_e(R_e + H) \cos(\phi) \cos(\gamma) \sin(\psi) + 0.5\omega_e^2(R_e + H)^2 \cos^2(\phi) \quad (12.69)$$

However, this relationship is not practical because the states in the remaining trajectory are unknown. For a typical suborbital entry mission, if $V_0 = 7000$ m/s, $H_0 = 80$ km, $V_f = 2000$ m/s, and $H_f = 25$ km, then $E_0 \approx -3.7 \times 10^4$ kJ/kg, $E_f \approx -6 \times 10^4$ kJ/kg, $V_0\omega_e(R_e + H_0) \approx 3.3 \times 10^3$ kJ/kg, $V_f\omega_e(R_e + H_f) \approx 0.93 \times 10^3$ kJ/kg, and $\omega_e^2(R_e + H_0)^2 \approx 0.22 \times 10^3$ kJ/kg. We can see that the magnitude of the nonlinear terms in Eq. (12.69) is much smaller than that of the linear term. Thus, the linear term plays a dominant role in Eq. (12.69), which causes the profile of \tilde{E} with respect to E to look like a straight line in the simulation results. Therefore, we innovatively use a linear fitting formula to approximate the relationship between the specific relative and absolute energies as follows

$$x_E = \frac{E_f - E}{\tilde{E}_f - \tilde{E}} (\tilde{x}_E - \tilde{E}) + E \quad (12.70)$$

where E and \tilde{E} are the current specific relative and absolute energies, E_f and \tilde{E}_f are the desired final specific relative and absolute energies, and x_E and \tilde{x}_E are the specific relative and absolute energies at any moment. Here, \tilde{E}_f is obtained by Eq. (12.123) in Appendix. For identification, we put a hat (“~”) on L/D_{plan} to represent the L/D_{plan} profile with respect to \tilde{E} , i.e., $\tilde{L}/D_{\text{plan}}(\tilde{x}_E)$, which can be obtained by substituting Eq. (12.70) into $L/D_{\text{plan}}(\tilde{x}_E)$.

Additionally, as shown in Eq. (12.71), after determining the altitude corridor, we can compute the maximum allowable bank angle σ_{\max} in real time using the method presented in [6]. It is known that if the vehicle glides in the QEGC, H decreases with increasing $|\sigma|$. Therefore, σ_{\max} is achieved if the vehicle glides along H_{\min} . As shown in Eq. (12.72), for quasi-equilibrium glide, L_1 is almost equal to the net force of the gravity and centrifugal force. As shown in Eq. (12.73), if the vehicle glides along H_{\min} , then L is maximized because ρ is maximized. Then, for quasi-equilibrium glide, σ_{\max} can be obtained from the first term on the right side of Eq. (12.71). To facilitate our discussion, we denote the derivative of a function f with respect to E by $(f)_E$. If there is an oscillation in the trajectory, then we need the second term on the right sight of Eq. (12.71). For instance, if H decreases rapidly and $(H)_E - (H_{\min})_E > 0$, then σ_{\max} is reduced by the second term so that the vehicle will not fall below H_{\min} .

$$\sigma_{\max} = \arccos\left(\frac{L_1}{L_{\max}}\right) + k_{\sigma}\left(\frac{dH}{dE} - \frac{dH_{\min}}{dE}\right) \quad (12.71)$$

$$L_1 = m\left(g - \frac{\tilde{V}_0^2}{R_e + H_{\min}(E)}\right) \quad (12.72)$$

$$L_{\max} = C_{\text{Lest}}[0.5\rho(H_{\min})V^2]S_{\text{ref}} \quad (12.73)$$

where C_{Lest} is the current estimated lift coefficient measured by the Inertial Navigation System (INS), S_{ref} is the reference area, and $k_{\sigma} = -50$. The value of k_{σ} is determined by analyzing the simulation trials and means that if $(H)_E = 2(H_{\min})_E$ near the maximum heating rate point, the correction of σ_{\max} is about 5 deg.

12.5.2.2 L_1/D Profile

The L_1/D profile satisfying the downrange requirement is planned by the downrange expression in real time. Because the analytical solutions are validated in the AGI frame, we design the L_1/D profile as a function of the specific absolute energy. As shown in Fig. 12.9, when $E > E_2$, L/D_{plan} is approximately a constant. So we design the L_1/D profile for $\tilde{E} > \tilde{E}_2$ as a constant, where \tilde{E}_2 is obtained by substituting $x_E = E_2$ into Eq. (12.70). When $E < E_2$, L/D_{plan} decreases with decreasing E . Thus, we let L_1/D change linearly to L_1/D_2 , which is not greater than the final L/D . So the L_1/D profile is

$$L_1/D(\tilde{x}_E) = \begin{cases} L_1/D_1; & \tilde{E}_2 \leq \tilde{x}_E \leq \tilde{E}_1 \\ \frac{\tilde{x}_E - \tilde{E}_f}{\tilde{E}_2 - \tilde{E}_f} L_1/D_1 + \frac{\tilde{E}_2 - \tilde{x}_E}{\tilde{E}_2 - \tilde{E}_f} L_1/D_2; & \tilde{E}_f \leq \tilde{x}_E < \tilde{E}_2 \end{cases} \quad (12.74)$$

where the two parameters L_1/D_1 and L_1/D_2 are updated in real time. To reduce the planning complexity, we neglect the path constraints. As a result, a problem arises: because the bank angle command is limited in the allowable range, the L_1/D profile cannot be tracked sometimes, especially in the early part of the QEGP. However, the resulting downrange error can be eliminated by updating the L_1/D profile in the latter part of the QEGP, where the path constraints are relatively relaxed. Because the cosine of σ is equal to the ratio of L_1/D to L/D , and we desire that the final bank angle is zero, we let L_1/D_2 be equal to the estimated final L/D as

$$L_1/D_2 = L/D_{\text{plan}}(E_f) \frac{L/D_{\text{est}}(E)}{L/D_{\text{plan}}(E)} \quad (12.75)$$

where $L/D_{\text{plan}}(E)$ is the estimated current L/D obtained by the INS, $L/D_{\text{plan}}(E)$ is the current L/D_{plan} , and $L/D_{\text{plan}}(E_f)$ is the final L/D_{plan} . As observed in the AGI frame, the entry guidance steers the vehicle to P and the end point of the trajectory is approximately S_{TAEM} from P . Therefore, the required downrange is

$$x_{Df} = R_e \tilde{\lambda}_P - S_{\text{TAEM}} \quad (12.76)$$

where $\tilde{\lambda}_P$ is obtained by Eq. (12.120). L_1/D_1 is found to meet the above downrange requirement as

(1) When $\tilde{E} \geq \tilde{E}_2$

By substituting Eq. (12.74) into Eq. (12.28) and then integrating Eq. (12.28), we can obtain

$$x_D(\tilde{E}_2, \tilde{E}) + x_D(\tilde{E}_f, \tilde{E}_2) = x_{Df} \quad (12.77)$$

where

$$x_D(\tilde{E}_2, \tilde{E}) = \frac{L_1/D_1 R_e}{2} \ln \left(\frac{2R^* \tilde{E}_2 + \mu}{2R^* \tilde{E} + \mu} \right) \quad \text{for } \tilde{E} \geq \tilde{E}_2 \quad (12.78)$$

$$\begin{aligned} x_D(\tilde{E}_f, \tilde{E}) &= \frac{R_e(L_1/D_1 - L_1/D_2)(\tilde{E}_f - \tilde{E})}{2(\tilde{E}_2 - \tilde{E}_f)} - \frac{R_e L_1/D_1}{2(\tilde{E}_2 - \tilde{E}_f)} \left(\tilde{E}_f + \frac{\mu}{2R^*} \right) \ln \left(\frac{2R^* \tilde{E}_f + \mu}{2R^* \tilde{E} + \mu} \right) \\ &\quad + \frac{R_e L_1/D_2}{2(\tilde{E}_2 - \tilde{E}_f)} \left(\tilde{E}_2 + \frac{\mu}{2R^*} \right) \ln \left(\frac{2R^* \tilde{E}_f + \mu}{2R^* \tilde{E} + \mu} \right); \quad \text{for } \tilde{E} \leq \tilde{E}_2 \end{aligned} \quad (12.79)$$

Here, $x_D(\tilde{E}_f, \tilde{E}_2)$ can be obtained by substituting $\tilde{E} = \tilde{E}_2$ into Eq. (12.79). Solving Eq. (12.77), we get

$$L_1/D_1 = c_1/c_2 \quad (12.80)$$

where

$$c_1 = x_{Df} - \frac{1}{2}R_e L_1/D_2 - \frac{R_e L_1/D_2}{2(\tilde{E}_2 - \tilde{E}_f)} \left(\tilde{E}_2 + \frac{\mu}{2R^*} \right) \ln \left(\frac{2R^* \tilde{E}_f + \mu}{2R^* \tilde{E}_2 + \mu} \right) \quad (12.81)$$

$$c_2 = \frac{R_e}{2} \ln \left(\frac{2R^* \tilde{E}_2 + \mu}{2R^* \tilde{E}_f + \mu} \right) - \frac{1}{2}R_e - \frac{1}{2} \frac{R_e}{\tilde{E}_2 - \tilde{E}_f} \left(\tilde{E}_f + \frac{\mu}{2R^*} \right) \ln \left(\frac{2R^* \tilde{E}_f + \mu}{2R^* \tilde{E}_2 + \mu} \right) \quad (12.82)$$

(2) When $\tilde{E} < \tilde{E}_2$

We do not need to update L_1/D_1 because the vehicle mostly glides in the AAP where the L_1/D profile is no longer tracked.

12.5.2.3 First Bank Reversal

Different from the traditional guidance laws, the proposed entry guidance does not need a bank reversal threshold to control the bank reversals. The first bank reversal point is planned by the crossrange expression here. From the crossrange expression, we know that the L_2/D profile has a significant impact on the crossrange. This profile can be obtained by

$$L_2/D(\tilde{x}_E) = \begin{cases} \text{sgn} \cdot |L_2/D(\tilde{x}_E)| & \text{if } \tilde{x}_E > \tilde{E}_3 \text{ or } \tilde{E}_f \leq \tilde{x}_E \leq \tilde{E}_4 \\ -\text{sgn} \cdot |L_2/D(\tilde{x}_E)| & \text{if } \tilde{E}_4 < \tilde{x}_E \leq \tilde{E}_3 \end{cases} \quad (12.83)$$

where \tilde{E}_3 and \tilde{E}_4 are the specific absolute energies at which the two bank reversals occur. sgn is used to determine the sign of the bank angle such that the heading error decreases in the beginning. Assuming that the unknown percentage deviation of the L/D in the remaining trajectory is a constant and equal to the current one measured by the INS, $|L_2/D(\tilde{x}_E)|$ can be predicted by

$$|L_2/D(\tilde{x}_E)| = \sqrt{\left(\widetilde{L/D}_{\text{plan}}(\tilde{x}_E) \frac{L/D_{\text{est}}(E)}{L/D_{\text{plan}}(E)} \right)^2 - L_1/D(\tilde{x}_E)^2} \quad (12.84)$$

Define an integral function as

$$F(\tilde{x}_{E2}, \tilde{x}_{E1}) = - \int_{\tilde{x}_{E1}}^{\tilde{x}_{E2}} \sin(f_4(\tilde{E}_f, \tilde{x}_E)) |f_3(\tilde{x}_E)| d\tilde{x}_E \quad (12.85)$$

The integral function is similar to the integral term of the crossrange expression [i.e., Equation (12.55)]. Because the L_1/D profile is a piecewise function, $f_4(\tilde{E}_f, \tilde{x}_E)$ is also a piecewise function as

$$f_4(\tilde{E}_f, \tilde{x}_E) = \begin{cases} [x_D(\tilde{E}_f, \tilde{E}_2) + x_D(\tilde{E}_2, \tilde{x}_E)]/R_e; & \text{for } \tilde{x}_E \geq \tilde{E}_2 \\ x_D(\tilde{E}_f, \tilde{x}_E)/R_e; & \text{for } \tilde{x}_E < \tilde{E}_2 \end{cases} \quad (12.86)$$

where $x_D(\tilde{E}_f, \tilde{E}_2)$ and $x_D(\tilde{E}_f, \tilde{x}_E)$ can be obtained by Eq. (12.79), and $x_D(\tilde{E}_2, \tilde{x}_E)$ can be obtained by Eq. (12.78). When planning \tilde{E}_3 , we let \tilde{E}_4 be equal to \tilde{E}_2 . Thus, from Eq. (12.55) and Eq. (12.83), the final crossrange is only a function of \tilde{E}_3 as

$$x_{Cf}(\tilde{E}_3) = \left(\frac{\pi}{2} - \tilde{\psi}_0 \right) R_e \sin\left(\frac{x_{Df}}{R_e} \right) - \text{sgn}R_e F(\tilde{E}_f, \tilde{E}) + 2\text{sgn}R_e F(\tilde{E}_4, \tilde{E}_3) \quad (12.87)$$

where $\tilde{\psi}_0$ is calculated by Eq. (12.117) in Appendix. The derivative of x_{Cf} with respect to \tilde{E}_3 is

$$x'_{Cf}(\tilde{E}_3) = 2\text{sgn}R_e \sin[f_4(\tilde{E}_f, \tilde{E}_3)]|f_3(\tilde{E}_3)| \quad (12.88)$$

As observed in the AGI frame, the entry guidance steers the vehicle to P which is on the generalized equator. We assume that the end point of the trajectory is over P because S_{TAEM} is much smaller than the total glide range, so the desired final crossrange is zero. Then, Newton's method [28] is used to solve $x_{Cf}(\tilde{E}_3) = 0$ as

$$\tilde{E}_3^{(k+1)} = \tilde{E}_3^{(k)} - \frac{x_{Cf}(\tilde{E}_3^{(k)})}{x'_{Cf}(\tilde{E}_3^{(k)})} \quad (12.89)$$

As shown in Fig. 12.7, to cope with the interference, we compute \tilde{E}_3 three times. The first computation is conducted at the beginning of the QEGP and the result is $\tilde{E}_3 = \tilde{E}_3^{(m1)}$. The second is conducted about 200 s before the first bank reversal, i.e., when $\tilde{E} = \tilde{E}_3^{(m1)} + \Delta\tilde{E} + a_D \tilde{V}_0 T_1$ where $T_1 = 200$ s, and the result is $\tilde{E}_3 = \tilde{E}_3^{(m2)}$. The third is conducted when $\tilde{E} = \tilde{E}_3^{(m2)} + \Delta\tilde{E} + a_D \tilde{V}_0 T_2$ where $T_2 = 30$ s, and the result is $\tilde{E}_3 = \tilde{E}_3^{(m3)}$. Here, $\Delta\tilde{E}$ is used to account for the lag due to the limitation on the change rate of σ , and will be shown in Eq. (12.91). a_D is the drag acceleration measured by the INS.

12.5.2.4 Planned Bank Angle in the QEGP

After determining the L_1/D profile and the bank reversals, we can obtain the planned bank angle in the QEGP as

$$\sigma_{\text{plan}} = \begin{cases} \text{sgn} \cdot \arccos\left(\frac{L_1/D}{L/D_{\text{est}}} \right) & \text{if } \tilde{E} > \tilde{E}_3 + \Delta\tilde{E} \\ -\text{sgn} \cdot \arccos\left(\frac{L_1/D}{L/D_{\text{est}}} \right) & \text{if } \tilde{E}_4 + \Delta\tilde{E} < \tilde{E} \leq \tilde{E}_3 + \Delta\tilde{E} \end{cases} \quad (12.90)$$

where $\Delta\tilde{E}$ is half the specific absolute energy consumed during one bank reversal. To overcome the lag due to the limitation on the change rate of the bank angle, the bank reversals start $\Delta\tilde{E}$ ahead of schedule. Assuming that a_D and \tilde{V}_0 are constant over a short period of time, we have

$$\Delta\tilde{E} = a_D \tilde{V}_0 \Delta t \quad (12.91)$$

where Δt is half the time required to complete one bank reversal and can be estimated by $\Delta t = |\sigma/\dot{\sigma}_{\max}|$, where σ is the current bank angle, and $\dot{\sigma}_{\max}$ is the maximum allowable change rate of the bank angle.

12.5.2.5 AOA and Bank Angle Commands in the QEGP

As shown by the dashed line in Fig. 12.10, if α_{plan} and σ_{plan} are directly used as the commands, the entry trajectory will have a weakly-damped phugoid oscillation. In [11], a guidance scheme was proposed for suppressing the oscillation by adjusting the AOA. The simulation results demonstrated the good performance of this scheme. We extend the scheme to a 3-dimensional one where both the AOA and bank angle are adjusted to suppress the oscillation. As shown in Fig. 12.11, the vertical and horizontal components of the lift coefficient (C_{L1} and C_{L2}) are determined by α_{plan} and σ_{plan} . To suppress the oscillation, we add ΔC_{L1} to C_{L1} where

Fig. 12.10 Weakly-damped phugoid oscillation

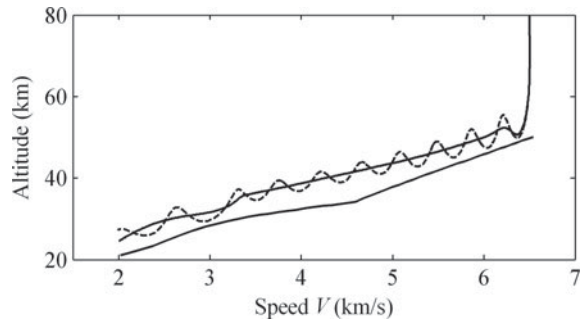
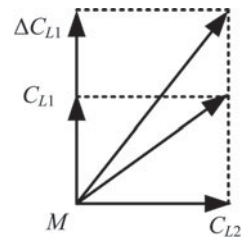


Fig. 12.11 3-D oscillation suppressing scheme



$$\Delta C_{L1} = C_L^\alpha k_\gamma (\gamma_{\text{plan}} - \gamma) \quad (12.92)$$

where C_L^α is the lift-curve slope and the feedback gain k_γ is set to 5. The value of k_γ is obtained by observing the simulation trials. γ_{plan} is the planned flight-path angle and will be shown later. The principle of the scheme is as: If the vehicle quickly ascends, then $\gamma_{\text{plan}} - \gamma < 0$, and thus $\Delta C_{L1} < 0$, which causes a reduction in L_1 and thus prevents the vehicle from ascending too quickly. Similarly, if the vehicle quickly descends, ΔC_{L1} can prevent it from descending too quickly. Finally, the vehicle glides in the QEGC, as shown by the solid line in Fig. 12.10.

(1) AOA Command

If Ma is given, the AOA is a function of the lift coefficient C_L , denoted as $\alpha = f_\alpha(C_L)$. Its first order Taylor approximation is

$$\alpha_{\text{cmd}} = f_\alpha(\sqrt{(C_{L1} + \Delta C_{L1})^2 + C_{L2}^2}) \approx f_\alpha(\sqrt{C_{L1}^2 + C_{L2}^2}) + \frac{f'_\alpha(\sqrt{C_{L1}^2 + C_{L2}^2})C_{L1}}{\sqrt{C_{L1}^2 + C_{L2}^2}} \Delta C_{L1} \quad (12.93)$$

Note that

$$f'_\alpha(\sqrt{C_{L1}^2 + C_{L2}^2}) = \frac{d\alpha}{dC_L} = \frac{1}{C_L^\alpha} \quad (12.94)$$

Substituting Eqs. [(12.92), (12.94)] into Eq. (12.93) yields

$$\alpha_{\text{cmd}} = \alpha_{\text{plan}} + \cos(\sigma_{\text{plan}})k_\gamma(\gamma_{\text{plan}} - \gamma) \quad (12.95)$$

(2) Bank Angle Command

From Fig. 12.11, we have

$$\sigma_{\text{cmd}} = \arctan\left(\frac{C_{L2}}{C_{L1} + \Delta C_{L1}}\right) \quad (12.96)$$

Its first order Taylor approximation is

$$\begin{aligned} \sigma_{\text{cmd}} &\approx \arctan\left(\frac{C_{L2}}{C_{L1}}\right) - \frac{C_{L2}}{C_{L1}^2 + C_{L2}^2} \Delta C_{L1} = \sigma_{\text{plan}} - \frac{C_{L2}}{C_L} \frac{C_L^\alpha}{C_L} k_\gamma (\gamma_{\text{plan}} - \gamma) \\ &\approx \sigma_{\text{plan}} - \sin(\sigma_{\text{plan}}) \frac{k_\gamma (\gamma_{\text{plan}} - \gamma)}{\alpha_{\text{plan}1}} \end{aligned} \quad (12.97)$$

where we let $\alpha_{\text{plan}1} = 10 \text{ deg}$ for CAV. To ensure that the path constraints are satisfied, we let

$$\sigma_{\text{cmd}} = \begin{cases} \sigma_{\max} & \text{if } \sigma_{\text{cmd}} > \sigma_{\max} \\ -\sigma_{\max} & \text{if } \sigma_{\text{cmd}} < -\sigma_{\max} \end{cases} \quad (12.98)$$

(3) Planned Flight-Path Angle

γ_{plan} is a high-precision approximation of the flight-path angle corresponding to quasi-equilibrium glide. We use the method proposed in [11] to obtain the formula of γ_{plan} . From Eq. (12.5), by assuming that $d\gamma/dt = 0$ deg/s and neglecting the Earth's rotation, we obtain

$$L_{\text{plan}} \cos(\sigma_{\text{plan}}) - mg \cos(\gamma_{\text{plan}}) + \frac{mV^2 \cos(\gamma_{\text{plan}})}{R_e + H} = 0 \quad (12.99)$$

By taking the time derivative of Eq. (12.99), and assuming that $dg/dt \approx 0$, $\cos(\gamma_{\text{plan}}) \approx 1$, and $\sin(\gamma_{\text{plan}}) \approx \gamma_{\text{plan}}$, after a lot of algebra, we can obtain

$$\gamma_{\text{plan}} = -\frac{D_{\text{plan}}}{mg} \frac{d_1}{d_2} \quad (12.100)$$

Here, $D_{\text{plan}} = C_{D_{\text{plan}}} q S_{\text{ref}}$ where $C_{D_{\text{plan}}}$ is the drag coefficient at α_{plan} .

$$\begin{aligned} d_1 = & \frac{\rho V^2 S_{\text{ref}} \cos(\sigma_{\text{plan}})}{2m} \frac{dC_{L_{\text{plan}}}}{dE} + \frac{2}{R_0 + H} + \frac{C_{L_{\text{plan}}} \rho S_{\text{ref}} \cos(\sigma_{\text{plan}})}{m} \\ & + \frac{L_{\text{plan}}}{m} \frac{d}{dE} [\cos(\sigma_{\text{plan}})] \end{aligned} \quad (12.101)$$

$$\begin{aligned} d_2 = & -\frac{C_{L_{\text{plan}}} V^2 S_{\text{ref}} \cos(\sigma_{\text{plan}})}{2mg} \frac{d\rho}{dH} + \frac{2}{R_0 + H} + \frac{C_{L_{\text{plan}}} \rho S_{\text{ref}} \cos(\sigma_{\text{plan}})}{m} \\ & + \frac{V^2}{(R_0 + H)^2 g} \end{aligned} \quad (12.102)$$

where $[\cos(\sigma_{\text{plan}})]_E$ is obtained by Eq. (12.103) in the QEGP, but we use the difference quotient of $\cos(\sigma_{\text{plan}})$ to approximate its derivative in the AAP since $[\cos(\sigma_{\text{plan}})]_E$ is very complex.

$$\frac{d}{dE} [\cos(\sigma_{\text{plan}})] = \frac{d}{dE} \left[\frac{L_1/D}{L/D_{\text{est}}} \right] = \frac{1}{L/D_{\text{est}}} \frac{dL_1/D}{dE} - \frac{L_1/D}{L/D_{\text{est}} L/D_{\text{plan}}} \frac{dL/D_{\text{plan}}}{dE} \quad (12.103)$$

where $(L_1/D)_E$ can be calculated by Eqs. (12.70) and (12.74).

12.5.3 Altitude Adjustment Phase

When the last bank reversal is performed, the AAP starts. In this phase, the vehicle dives into the dense atmosphere by reducing the AOA, so that the vehicle has enough dynamic pressure to perform maneuver in the terminal guidance phase. However, this causes that dy/dt cannot be approximated by zero. Thus, the analytical solutions are not sufficiently accurate to satisfy the terminal conditions. Therefore, we propose a new guidance scheme here. In this scheme, before the last bank reversal, \tilde{E}_4 is corrected twice by the onboard trajectory simulations to achieve the desired final speed, as shown in Fig. 12.7. After the last bank reversal, PN is used to eliminate the crossrange error. Before introducing the correction method of \tilde{E}_4 , we need to show the guidance commands in the AAP first, because this helps explain why the desired final speed can be achieved by adjusting \tilde{E}_4 .

12.5.3.1 Planned Bank Angle in the AAP

In the AAP, the α_{plan} profile is the same as that in the QEGP, but the planned bank angle is determined by PN. We neglect the Earth's curvature here because the vehicle is close enough to the target. Thus, from Fig. 12.2, we can find that the change rate of the azimuth angle of MP , the segment between M and P , is equal to the ratio of the component of $\dot{\mathbf{V}}$ perpendicular to the generalized equatorial plane to the horizontal distance between M and P as

$$\dot{\psi}_{MP} = \frac{\tilde{V}_0 \cos(\tilde{\gamma}_0) \sin(\pi/2 - \tilde{\psi}_0)}{x_{DP}} \quad (12.104)$$

where $x_{DP} = R_e \tilde{\lambda}_P$. The formulas of $\tilde{\lambda}_P$, \tilde{V}_0 , $\tilde{\gamma}_0$, and $\tilde{\psi}_0$ are shown in Appendix. The lateral acceleration command of PN is

$$a_{L2} = k_{PN} \dot{\psi}_{MP} \tilde{V}_0 \cos(\tilde{\gamma}_0) \quad (12.105)$$

To prevent the initial bank angle from saturation, we let k_{PN} change from 2 to 4 as

$$k_{PN} = 2 \frac{x_{DP}}{x_{DP}^{E4}} + 4 \left(1 - \frac{x_{DP}}{x_{DP}^{E4}}\right) \quad (12.106)$$

where x_{DP}^{E4} is the value of x_{DP} at the second bank reversal. Additionally, we assume that the vertical component of the lift is equal to the resultant force of the gravity and centrifugal force as

$$a_{L1} \approx g - \frac{\tilde{V}_0^2}{R_e + H} \quad (12.107)$$

Then, we let the planned bank angle be

$$\sigma_{\text{plan}} = \arctan\left(\frac{a_{L2}}{a_{L1}}\right) \quad \text{for } \tilde{E} \leq \tilde{E}_4 + \Delta\tilde{E} \quad (12.108)$$

12.5.3.2 AOA and Bank Angle Commands in the AAP

Before the vehicle enters the AAP, the onboard trajectory simulations are conducted to correct \tilde{E}_4 and obtain the range-to-go reference profile with respect to energy, denoted as $s_{\text{go}}^{\text{ref}}(E)$. Although the correction of \tilde{E}_4 eliminates the errors accumulated before the second bank reversal, there still exists the final speed error in the AAP due to the interference. As shown in Eq. (12.109), we propose a scheme to track $s_{\text{go}}^{\text{ref}}(E)$ closely by modulating the AOA such that most of the final speed error accumulated in the AAP can be eliminated. For instance, if $s_{\text{go}}(E)$ is greater than $s_{\text{go}}^{\text{ref}}(E)$, then we need to increase L/D to extend the glide range. Because L/D increases significantly with the AOA increasing in the AAP, we increase the AOA to raise L/D . Generally, the correction of the AOA is small because the errors accumulated in the short remaining trajectory are also small. To suppress the oscillation, we let σ_{cmd} be the same as that in the QEGP.

$$\alpha_{\text{cmd}} = \alpha_{\text{plan}} + k_\alpha [s_{\text{go}}(E) - s_{\text{go}}^{\text{ref}}(E)] \quad (12.109)$$

$$\sigma_{\text{cmd}} = \sigma_{\text{plan}} - \sin(\sigma_{\text{plan}}) \frac{k_\gamma (\gamma_{\text{plan}} - \gamma)}{\alpha_{\text{plan1}}} \quad (12.110)$$

where $k_\alpha = (5\pi/18) \times 10^{-6}$, which means that a 0.5 deg correction of the AOA accounts for 10 km dispersion in range. To satisfy the path constraints, the measure shown in Eq. (12.98) is also taken here.

12.5.3.3 Second Bank Reversal

Before the last bank reversal is performed, we need to adjust \tilde{E}_4 to achieve the desired final speed, because the L_1/D profile is no longer tracked in the AAP. Now we analyze the relationship between \tilde{E}_4 and V_f : If \tilde{E}_4 is reduced, the reversal time is postponed and the heading error at \tilde{E}_4 increase. Thus, PN generates a greater lateral acceleration to eliminate the heading error, and thus increases the magnitude of the bank angle. This reduces the L_1/D and hence reduces the final speed. Therefore, we can conclude that V_f decreases with decreasing \tilde{E}_4 .

After the first bank reversal is performed, we use an iterative method to correct \tilde{E}_4 where the major steps are as follows:

- (1) The onboard trajectory simulation is conducted to predict the final speed $V_f(\tilde{E}_4^{(k)})$, where $\tilde{E}_4^{(k)}$ represents the value of \tilde{E}_4 used in the k -th simulation. In the simulation, Eqs. (12.1)–(12.6) are integrated numerically with the proposed entry guidance as control. The simulation starts from the current states of motion and assumes that the unknown percentage deviations of the aerodynamic coefficients in the remaining trajectory are equal to the estimated current percentage deviations measured by the INS. When $s_{go} = s_{TAEM}$, the simulation stops and obtains $V_f(\tilde{E}_4^{(k)})$.
- (2) As shown in Eq. (12.111), the secant method [28] is used to update \tilde{E}_4 .

$$\tilde{E}_4^{(k+1)} = \tilde{E}_4^{(k)} - \frac{(V_f(\tilde{E}_4^{(k)}) - V_{TAEM})(\tilde{E}_4^{(k)} - \tilde{E}_4^{(k-1)})}{(V_f(\tilde{E}_4^{(k)}) - V_f(\tilde{E}_4^{(k-1)}))} \quad (12.111)$$

- (3) Repeat Steps (1)–(2) until $|V_f(\tilde{E}_4^{(k)}) - V_{TAEM}| < 1 \text{ m/s}$.

Because V_f changes monotonously and smoothly with \tilde{E}_4 , and the correction of \tilde{E}_4 is small, the above process can generally be accomplished within 5 iterations. As shown in Fig. 12.7, to cope with the interference and minimize the computational load, \tilde{E}_4 is corrected twice by the iterative method. The first correction is conducted shortly after the first bank reversal, and the result is $\tilde{E}_4^{(n1)}$. The second is conducted about 1 min before the last bank reversal, i.e., when $\tilde{E} = \tilde{E}_4^{(n1)} + \Delta\tilde{E} + a_D \tilde{V}_0 T_1$ with $T_1 = 60 \text{ s}$, and the result is $\tilde{E}_4^{(n2)}$. Then, we let $\tilde{E}_4 = \tilde{E}_4^{(n2)}$.

12.5.4 Results and Discussion

The CAV model [1] with L/D_{\max} up to 3 is used to demonstrate the performance of the proposed entry guidance. Because of the limitation on the flight-control system, the constraints on the AOA are $|\dot{\alpha}| \leq 4 \text{ deg/s}$ and $|\ddot{\alpha}| \leq 8 \text{ deg/s}^2$, and the constraints on the bank angle are $|\sigma| \leq 80 \text{ deg}$, $|\dot{\sigma}| \leq 8 \text{ deg/s}$ and $|\ddot{\sigma}| \leq 10 \text{ deg/s}^2$. The initial conditions are $H_0 = 80 \text{ km}$, $\lambda_0 = 0 \text{ rad}$, $\phi_0 = 0 \text{ rad}$, $V_0 = 6500 \text{ m/s}$, $\gamma_0 = 0 \text{ rad}$ and $\psi_0 = \pi/2 \text{ rad}$.

12.5.5 Nominal Cases

First we observe three nominal cases where there is no interference and the targets are far apart. In Case 1, the target position is $\lambda_{T1}R_e = 7500 \text{ km}$ and $\phi_{T1}R_e = 1000 \text{ km}$. In Case 2, $\lambda_{T2}R_e = 10,000 \text{ km}$ and $\phi_{T2}R_e = 0 \text{ km}$. In Case 3, $\lambda_{T3}R_e = 12,000 \text{ km}$ and $\phi_{T3}R_e = 2000 \text{ km}$. As shown in Figs. 12.12, 12.13, 12.14, 12.15, 12.16, 12.17, 12.18 and 12.19, a shorter glide range tends to increase the magnitude of σ to track

Fig. 12.12 Altitude versus speed histories

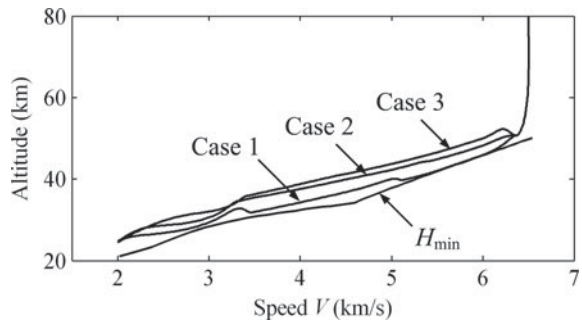


Fig. 12.13 Ground tracks

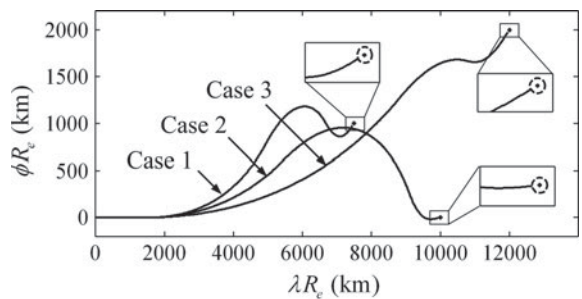


Fig. 12.14 Flight-path angle histories

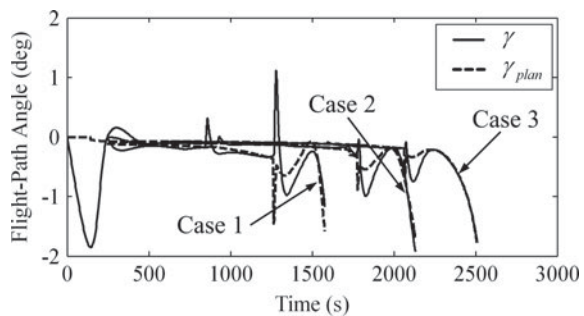


Fig. 12.15 \tilde{E} versus E profiles look like straight lines

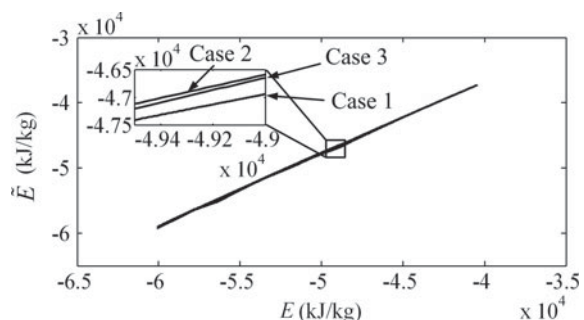


Fig. 12.16 Angle of attack histories

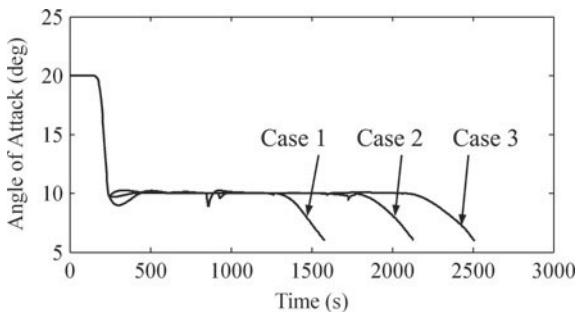


Fig. 12.17 Bank angle histories

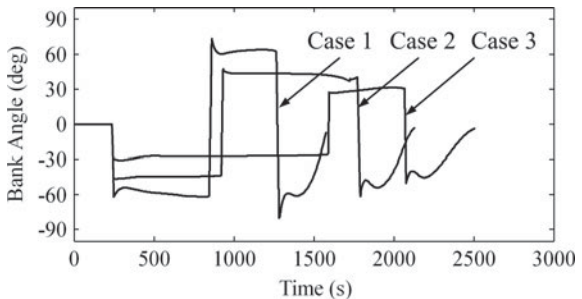


Fig. 12.18 Heating rate histories

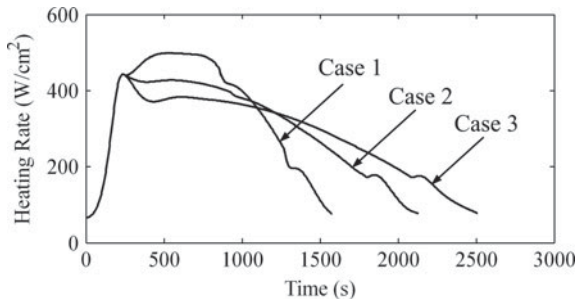


Fig. 12.19 Dynamic pressure histories

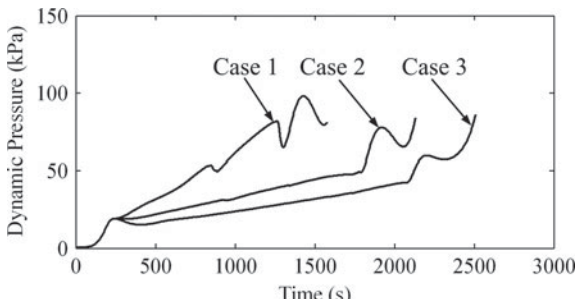


Table 12.2 Simulation results for nominal cases

	\tilde{E}_3 (kJ/kg)	\tilde{E}_4 (kJ/kg)	V_f (m/s)	H_f (km)	$\Delta\psi_f$ (deg)	σ_f (deg)
Case 1	-46,875	-54,674	2000	24.87	-0.124	-6.84
Case 2	-44,897	-55,158	2000	24.62	-0.090	-3.08
Case 3	-49,714	-54,409	2000	24.46	-0.043	-3.74

the L_1/D profile, and then decrease H . This causes the heating rate and dynamic pressure to increase. Figure 12.14 shows that γ_{plan} is a good approximation of γ and the oscillation-suppressing scheme can effectively suppress the trajectory oscillation. Figure 12.15 shows that the profiles of \tilde{E} with respect to E look like straight lines. So the linear fitting formula [i.e. Equation (12.70)] is a reasonable approximation of the relationship between E and \tilde{E} . Figure 12.17 shows that for Cases 2 and 3, although the L_1/D profiles are updated in real time, the corresponding bank angles in the QEGP are almost unchanged with time. This indirectly indicates that the downrange expression is sufficiently accurate and thus the L_1/D profile is only adjusted slightly. From Table 12.2, although the three cases are very different, the differences of \tilde{E}_4 are within 650 kJ/kg. This demonstrates that the accuracy of the crossrange expression is also sufficient. As can be seen from Fig. 12.19, in the QEGP, as the centrifugal force decreases gradually with the speed decreasing, the dynamic pressure, required to generate enough lift such that the lift, gravity and centrifugal force are balanced in the vertical direction, increases smoothly with time. In the AAP, the dynamic pressure increases rapidly as the vehicle dives into the dense atmosphere by reducing the AOA, especially in Cases 2 and 3.

12.5.5.1 Aerodynamic Dispersion Cases

There generally exist aerodynamic dispersions in the first flight. The percentage deviations of the aerodynamic coefficients typically change with Ma and the AOA. For simplicity, we use a linear aerodynamic dispersion model to demonstrate the performance of the entry guidance as follows

$$\delta_{CL} = \delta_{CL0} + k_{\delta CL}^{Ma} \frac{Ma - 15}{17} + k_{\delta CL}^{\alpha} \frac{18}{\pi} \left(\alpha - \frac{\pi}{18} \right) \quad (12.112)$$

$$\delta_{CD} = \delta_{CD0} + k_{\delta CD}^{Ma} \frac{Ma - 15}{17} + k_{\delta CD}^{\alpha} \frac{18}{\pi} \left(\alpha - \frac{\pi}{18} \right) \quad (12.113)$$

where δ_{CL} and δ_{CD} are the percentage deviations of the lift and drag coefficients, respectively. As can be concluded from the analytical solutions, L/D has an important impact on the glide range. Thus we consider two cases with large percentage deviations of L/D . Here, the dispersion in C_L is not considered, i.e., $\delta_{CL} = 0$. In Case 1, let $\delta_{CD0} = -20\%$, $k_{\delta CD}^{Ma} = 10\%$, and $k_{\delta CD}^{\alpha} = 5\%$; In Case 2, let $\delta_{CD0} = 25\%$,

$k_{\delta CD}^{Ma} = -20\%$, and $k_{\delta CD}^{\alpha} = -5\%$. The target position is $\lambda_{T4}R_e = 9000$ km and $\phi_{T4}R_e = 1000$ km.

Figure 12.20 shows the histories of the percentage deviations of L/D . Figure 12.21 shows the altitude-vs-speed profiles. As shown in Figs. 12.22, 12.23 and 12.24, as C_D increases, L/D decreases and thus the magnitude of σ is also reduced. This results in a decrease in the lateral maneuver capability, and thus the first bank reversal time is postponed to achieve the desired crossrange. After the second bank reversal, α is slightly adjusted to track the $s_{go}^{\text{ref}}(E)$ profile. In addition, as shown in Fig. 12.21 and Figs. 12.25, 12.26, reducing the magnitude of σ tends to increase the altitude, which causes the heating rate and dynamic pressure to decrease. Table 12.3 shows

Fig. 12.20 Percentage deviations of the L/D over time

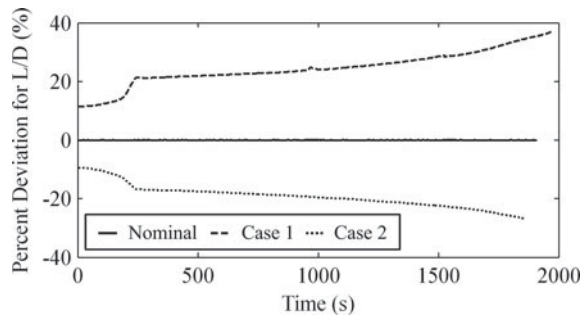


Fig. 12.21 Altitude versus speed profiles

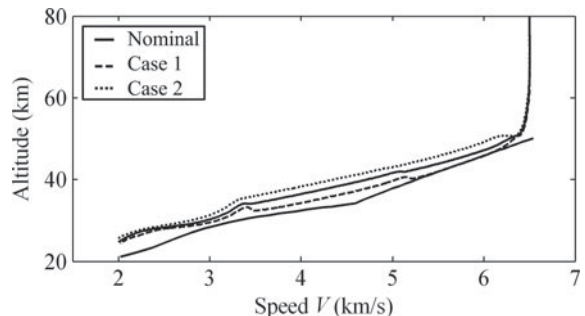


Fig. 12.22 Ground tracks

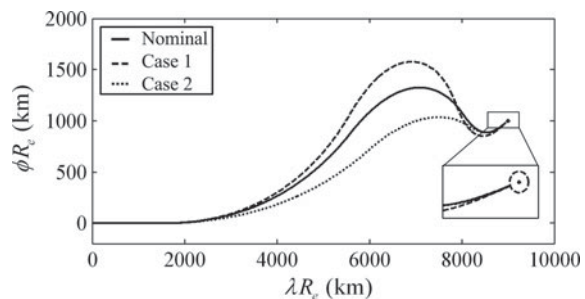


Fig. 12.23 Angle of attack histories

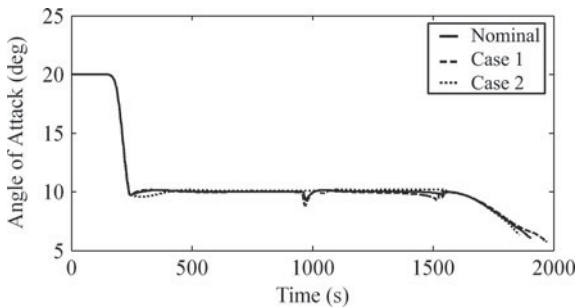


Fig. 12.24 Bank angle histories

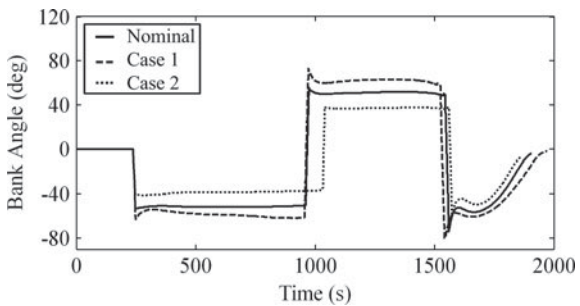


Fig. 12.25 Heating rate histories

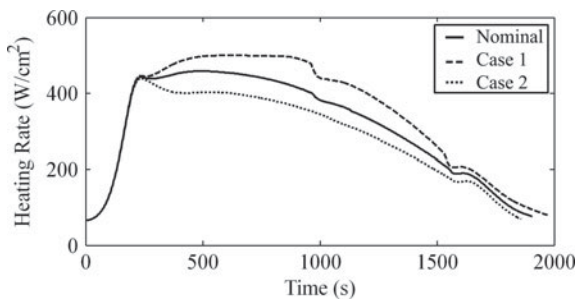


Fig. 12.26 Dynamic pressure histories

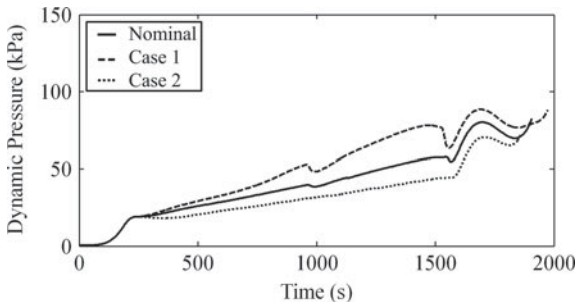


Table 12.3 Simulation results for aerodynamic dispersion cases

	\tilde{E}_3 (kJ/kg)	\tilde{E}_4 (kJ/kg)	V_f (m/s)	H_f (km)	$\Delta\psi_f$ (deg)	σ_f (deg)
Case 1	-46,401	-54,850	2017.65	24.42	-0.0236	-1.841
Case 2	-47,438	-54,690	1979.97	25.48	-0.2046	-7.192
Nominal	-46,648	-54,715	2000.00	24.73	-0.0710	-3.730

Table 12.4 Numerical characteristics of the normally distributed random variables

Variable	Mean	3 times standard deviation	Variable	Mean	3 times standard deviation (%)
H_0 (km)	80	3	δ_{CL0}	0	15
λ_0 (deg)	0	0.45	$k_{\delta CL}^{Ma}$	0	10
ϕ_0 (deg)	0	0.45	$k_{\delta CL}^{\alpha}$	0	5
V_0 (m/s)	6500	200	δ_{CD0}	0	15
γ_0 (deg)	0	1	$k_{\delta CD}^{Ma}$	0	10
ψ_0 (deg)	90	1	$k_{\delta CD}^{\alpha}$	0	5
V_{wind}^{EW} (m/s)	0	100	δ_p	0	20
V_{wind}^{NS} (m/s)	0	100			

that the entry guidance can still perform well in the presence of the large percentage deviations of L/D .

12.5.5.2 Monte Carlo Simulations

The Monte Carlo simulations are conducted to test the robustness of the proposed entry guidance. As shown in Table 12.4, the dispersions in the initial conditions, aerodynamic model, and atmospheric model are considered here. The aerodynamic dispersion model is shown in Eqs. (12.112) and (12.113). δ_p represents the percentage deviation of the air density. V_{wind}^{EW} represents the wind speed in the East-West direction, and V_{wind}^{NS} represents the wind speed in the North-South direction. δ_p , V_{wind}^{EW} and V_{wind}^{NS} are assumed to be constant throughout each flight. Although the dispersion model is simple and does not match actual situations, it can be used to test the robustness of the entry guidance because it is more challenging than a real situation. As a comparison, the Monte Carlo simulation results for the gliding guidance presented in [12] are also given here. We refer to the entry guidance presented in this paper as the Entry Guidance based on Analytical Solutions (EGAS), and refer to the gliding guidance presented in [12] as the Predictor-Corrector Gliding Guidance (PCGG). To satisfy the heating rate constraint, we have slightly modified the PCGG so that the vehicle glides at α_{max} with $\sigma = 0$ when the vehicle drops down quickly in the early part of the trajectory. Additionally, the AOA profile for the PCGG is also given by Eq. (12.68).

However, we set α_2 to 7 deg such that H_{TAEM} can be achieved, because the final bank angle for PCGG is approximately 30 deg, instead of zero.

Figure 12.27 shows that EGAS can effectively suppress the oscillations caused by the bank reversals. The PCGG also uses the method presented in [11] for suppressing the trajectory oscillation, but the γ_{plan} formula is simplified by neglecting the effect of the Earth curvature. This reduces the accuracy of γ_{plan} . Therefore, in order not to disturb the gliding guidance, the gain of the oscillation suppressing term decreases to zero finally. This means that the PCGG cannot effectively suppress the oscillations in the latter part of some trajectories, as shown in Fig. 12.28. Figures 12.29 and 12.30 show the ground tracks for the two methods. Figures 12.31 and 12.32 show the AOA profiles for the two methods. Figure 12.33 shows that the EGAS only performs two bank reversals in all trajectories, and they are relatively concentrated. Figure 12.34 shows the bank angles for the PCGG. The PCGG needs 3–5 bank reversals, where the exact number of bank reversals depends on the L/D dispersion. A greater L/D tends to increase the number of the bank reversals. Figures 12.35 and 12.36 show the heating rate histories. Figures 12.37 and 12.38 show the dynamic pressure histories. As shown in Figs. 12.39 and 12.40, the final heading error for the EGAS is much smaller than that for the PCGG. In a few cases, H is slightly below H_{\min} for both approaches, mainly because of the decreases in ρ . However, the path constraints are still satisfied.

Fig. 12.27 Altitude versus speed for the EGAS

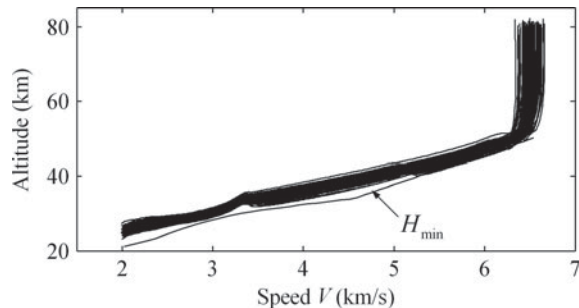


Fig. 12.28 Altitude versus speed for the PCGG

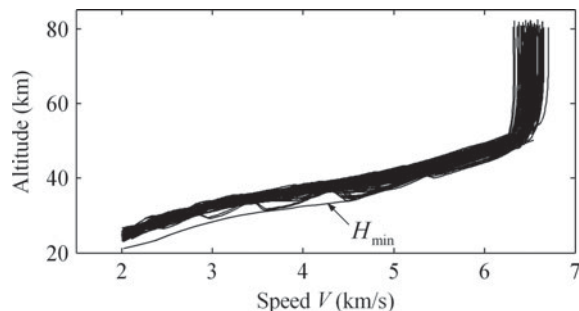


Fig. 12.29 Ground tracks for the EGAS

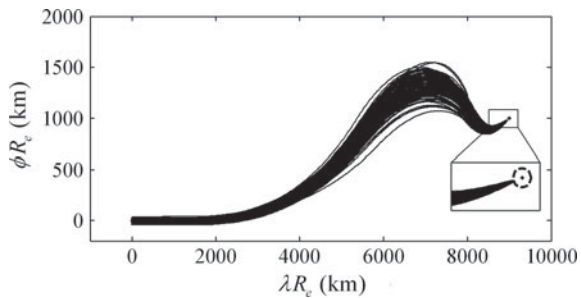


Fig. 12.30 Ground tracks for the PCGG

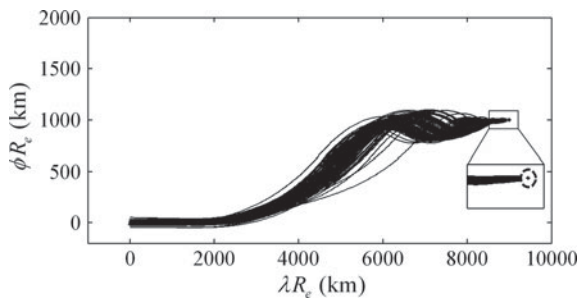


Fig. 12.31 AOA for the EGAS

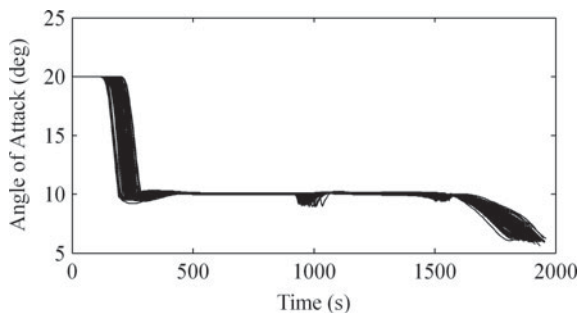


Fig. 12.32 AOA for the PCGG

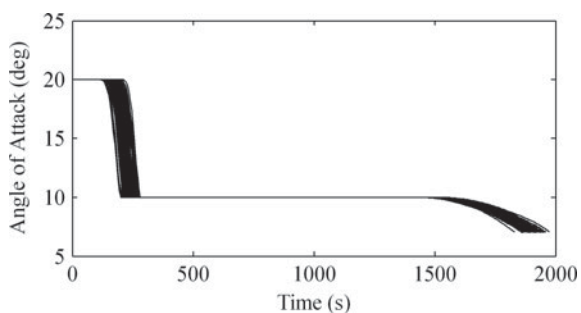


Fig. 12.33 Bank angle for the EGAS

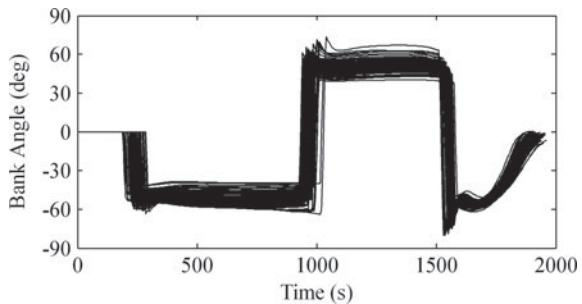


Fig. 12.34 Bank angle for the PCGG

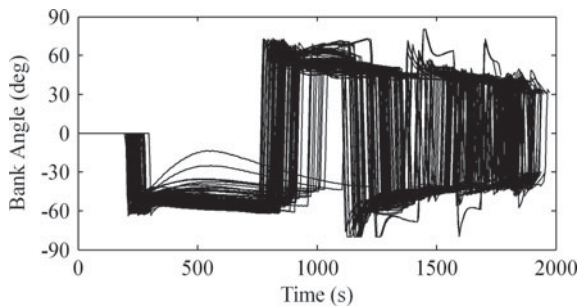


Fig. 12.35 Heating rate for the EGAS

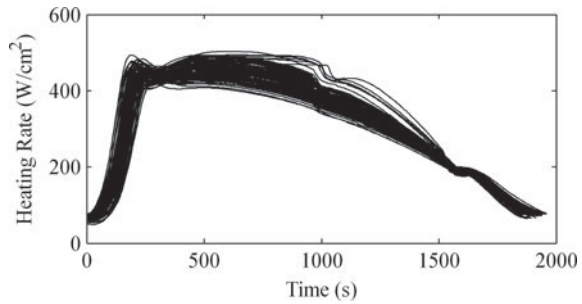


Fig. 12.36 Heating rate for the PCGG

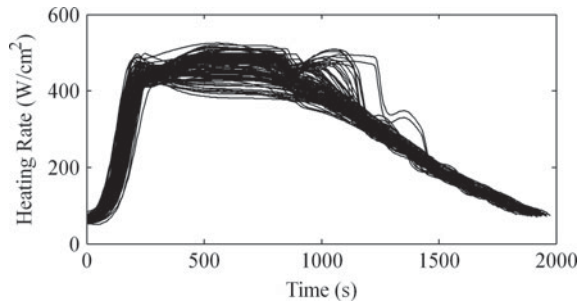


Fig. 12.37 Dynamic pressure for the EGAS

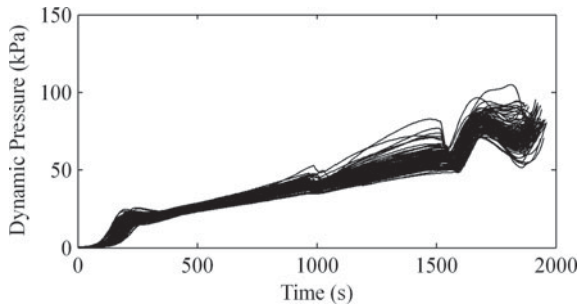


Fig. 12.38 Dynamic pressure for the PCGG

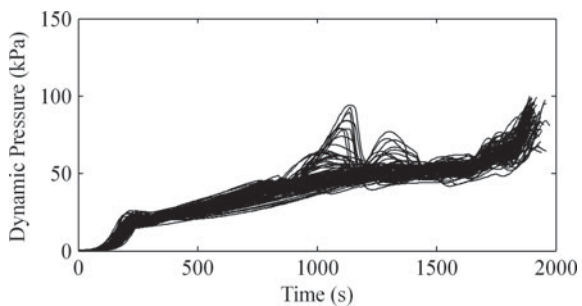


Fig. 12.39 Final states for the EGAS

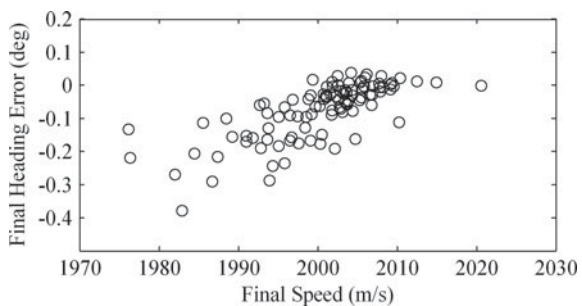
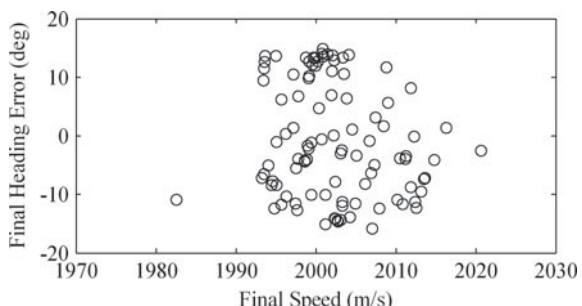


Fig. 12.40 Final states for the PCGG



12.6 Conclusions

The major contributions of this paper are summarized as follows.

- (1) In Sect. 12.4, we develop the new analytical solutions to hypersonic gliding problem where the effect of the Earth curvature is taken into account. This greatly improves the accuracy of the crossrange and heading angle expressions, compared with the traditional solutions. Therefore, these new solutions can be used to plan bank reversals.
- (2) In the derivation of these new solutions, we obtain a special type of linear system with variable coefficients. However, this system cannot be solved by conventional approaches such as the Laplace transform. To solve such a system, we propose an innovative method based on spectral decomposition.
- (3) A new entry guidance based on the analytical solutions is proposed, where the longitudinal reference profile and bank reversals are planned autonomously and quickly using the new solutions. Different from the traditional guidance laws, the proposed entry guidance does not need to conduct any offline planning for specific mission, such as the design of the bank reversal threshold. Therefore, the guidance can deal with various urgent tasks.
- (4) In Sect. 12.5.2.5, we extend the scheme for suppressing trajectory oscillations proposed in [11] to a three dimensional scheme, which can effectively suppress the trajectory oscillation while not interfering with the work of the entry guidance.
- (5) In Sect. 12.5.3, we propose a guidance scheme for the AAP by innovatively combining PN and a reference tracking law. This scheme can well satisfy the requirements on final heading angle and speed in the presence of various disturbances.

Appendix

In the entry guidance, when the analytical solutions are used to plan the L_1/D profile and bank reversals, the states of motion relative to the AGI frame are required. Therefore, in this appendix, we show how to get the states of motion relative to the AGI frame from that relative to the GER frame. As stated in Sect. 12.4.1, because the AGI frame is fixed with respect to the inertial space, the velocity vector relative to the AGI frame ($\tilde{\mathbf{V}}$) is the vector sum of the velocity relative to the Earth and the velocity due to the Earth's rotation. Because the entry guidance uses the current states as the initial states in the analytical solutions, the initial value of $\tilde{\mathbf{V}}$ used in the current guidance cycle is

$$\tilde{\mathbf{V}}_0^{\text{NED}} = \left[V \cos(\gamma) \cos(\psi) \quad V \cos(\gamma) \sin(\psi) + \omega_e(R_e + H) \cos(\phi) \quad -V \sin(\gamma) \right]^T \quad (12.114)$$

where the superscript “NED” represents that the coordinates of a vector are in the NED frame. From Eq. (12.114), the initial values of \tilde{V} and $\tilde{\gamma}$ in the current guidance cycle are

$$\tilde{V}_0 = \sqrt{V^2 + 2V\omega_e(R_e + H)\cos(\phi)\cos(\gamma)\sin(\psi) + \omega_e^2(R_e + H)^2\cos^2(\phi)} \quad (12.115)$$

$$\tilde{\gamma}_0 = \arcsin(V\sin(\gamma)/\tilde{V}_0) \quad (12.116)$$

As shown in Fig. 12.2, because the tangent line to the generalized prime meridian at o is parallel to $\tilde{\mathbf{z}}^{\text{GER}}$, which is the unit vector along the \tilde{z} -axis of the AGI frame, the initial value of $\tilde{\psi}$ is just equal to the angle between the local horizontal component of $\tilde{\mathbf{V}}_0$ (denoted as $\tilde{\mathbf{V}}_{H0}^{\text{GER}}$) and $\tilde{\mathbf{z}}^{\text{GER}}$, as shown in Eq. (12.117). Here, the superscript “GER” represents that the coordinates of a vector are in the GER frame.

$$\tilde{\psi}_0 = \begin{cases} \arccos(\tilde{\mathbf{z}}^{\text{GER}} \cdot \tilde{\mathbf{V}}_{H0}^{\text{GER}} / ||\tilde{\mathbf{V}}_{H0}^{\text{GER}}||); & \text{if } \tilde{\mathbf{V}}_{H0}^{\text{GER}} \cdot \tilde{\mathbf{y}}^{\text{GER}} \geq 0 \\ -\arccos(\tilde{\mathbf{z}}^{\text{GER}} \cdot \tilde{\mathbf{V}}_{H0}^{\text{GER}} / ||\tilde{\mathbf{V}}_{H0}^{\text{GER}}||); & \text{if } \tilde{\mathbf{V}}_{H0}^{\text{GER}} \cdot \tilde{\mathbf{y}}^{\text{GER}} < 0 \end{cases} \quad (12.117)$$

where $\tilde{\mathbf{y}}^{\text{GER}}$ is the unit vector along the \tilde{y} -axis of the AGI frame, and $\tilde{\mathbf{V}}_{H0}^{\text{GER}}$ is calculated by

$$\tilde{\mathbf{V}}_{H0}^{\text{GER}} = (\mathbf{T}_{\text{GER}}^{\text{NED}})^T \tilde{\mathbf{V}}_{H0}^{\text{NED}} \quad (12.118)$$

$$\tilde{\mathbf{V}}_{H0}^{\text{NED}} = [V \cos(\gamma) \cos(\psi) \ V \cos(\gamma) \sin(\psi) + \omega_e(R_e + H) \cos(\phi) \ 0]^T \quad (12.119)$$

From Fig. 12.2, we can find that the generalized longitude, latitude and altitude of P are

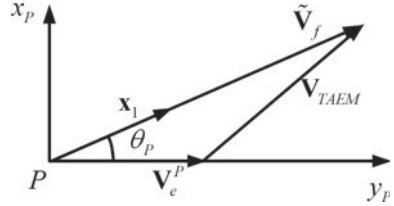
$$\tilde{\lambda}_P = \arccos(\hat{\mathbf{x}}_{EP}^{\text{GER}} \cdot \tilde{\mathbf{x}}^{\text{GER}}), \ \tilde{\phi}_P = 0, \ \tilde{H}_P = H_T \quad (12.120)$$

where $\hat{\mathbf{x}}_{EP}^{\text{GER}}$ is the unit vector pointing from E to P , and $\hat{\mathbf{x}}_{EP}^{\text{GER}}$ is the unit vector along the \tilde{x} -axis of the AGI frame.

Section 12.3 shows the terminal conditions relative to the rotating Earth. Now we need to convert these conditions into that relative to the AGI frame, as the analytical solutions are implemented in this frame. As observed from the AGI frame, the horizontal distance between the end point of the glide trajectory and P is approximately S_{TAEM} . To facilitate the derivation, we assume that the end point of the glide trajectory is over P because S_{TAEM} is much smaller than the total glide range and Earth’s radius.

As shown in Fig. 12.41, \mathbf{x}_1 is the unit vector parallel to the tangent line to the generalized equator at P , \mathbf{V}_{TAEM} is the desired final velocity vector relative to the rotating Earth, $\tilde{\mathbf{V}}_f$ is the desired final velocity vector relative to the AGI frame, and

Fig. 12.41 Assuming that $\tilde{\mathbf{V}}_f$ is parallel to \mathbf{x}_1



\mathbf{V}_e^P is the velocity due to the Earth rotation and points to the local east. We assume that $\tilde{\mathbf{V}}_f$ is parallel to \mathbf{x}_1 as the entry guidance approximately steers the vehicle to P along the generalized equator, and the generalized flight path angle is small. Note that, although this assumption may be inaccurate, the entry guidance will eliminate any resulting error using the trajectory simulations to correct the last bank reversal. The magnitude of \mathbf{V}_e^P is

$$V_e^P = \omega_e(R_e + H_{\text{TAEM}}) \cos(\phi_P) \quad (12.121)$$

The magnitude of $\tilde{\mathbf{V}}_f$ is denoted as \tilde{V}_f . Using geometry, we can obtain

$$\tilde{V}_f = V_e^P \cos(\theta_P) + \sqrt{(V_e^P)^2(\cos^2(\theta_P) - 1) + V_{\text{TAEM}}^2} \quad (12.122)$$

where θ_P is the angle of \mathbf{x}_1 measured counterclockwise from the local east. Then, the desired final specific absolute energy, required by the analytical solutions in the entry guidance, can be estimated by

$$\tilde{E}_f = \frac{1}{2} \tilde{V}_f^2 - \frac{\mu}{R_e + H_{\text{TAEM}}} \quad (12.123)$$

References

1. Phillips, T.H.: A Common Aero Vehicle (CAV) Model, Description, and Employment Guide. Schafer Corporation for AFRL and AFSPC, Arlington (2003)
2. Harbold, J.C., Graves, C.A.: Shuttle entry guidance. *J. Astronaut. Sci.* **27**(3), 239–268 (1979)
3. Hanson, J.M., Coughlin, D.J., Dukeman, G.A., et al.: Ascent, transition, entry, and abort guidance algorithm design for the X-33 vehicle. In: AIAA Guidance, Navigation, and Control Conference and Exhibit. Boston (1998)
4. Mease, K.D., Chen, D.T., Schnenberger, H., et al.: Reduced-order entry trajectory planning for acceleration guidance. *J. Guidance Control Dyn.* **25**(2), 257–266 (2002)
5. Dukeman, G.A.: Profile-following entry guidance using linear quadratic regulator theory. In: AIAA Guidance, Navigation, and Control Conference and Exhibit. Monterey (2002)
6. Shen, Z., Lu, P.: Onboard generation of three-dimensional constrained entry trajectories. *J. Guidance Control Dyn.* **26**(1), 111–121 (2003)
7. Shen, Z., Lu, P.: Dynamic lateral entry guidance logic. *J. Guidance, Control Dyn.* **27**, 949–959 (2004)

8. Powell, R.W.: Six-degree-of-freedom guidance and control-entry analysis of the HL-20. *J. Spacecraft Rockets* **30**(5), 537–542 (1993)
9. Graesslin, M.H., Telhaar, J., Schottle, U.M.: Ascent and reentry guidance concept based on NLP-methods. *Acta Astronaut.* **55**(3–9), 461–471 (2004)
10. Zimmerman, C., Dukeman, G., Hanson, J.: Automated method to compute orbital reentry trajectories with heating constraints. *J Guidance Control Dyn* **26**(4), 523–529 (2003)
11. Yu, W., Chen, W.: Guidance scheme for glide range maximization of a hypersonic vehicle. In: AIAA Guidance, Navigation, and Control Conference. Portland (2011)
12. Lu, P., Forbes, S., Baldwin, M.: Gliding guidance of high L/D hypersonic vehicles. In: AIAA Guidance, Navigation, and Control (GNC) Conference. Boston (2013)
13. Li, S., Peng, Y.: Mars entry trajectory optimization using DOC and DCNLP. *Adv. Space Res.* **47**(3), 440–452 (2011)
14. Li, S., Peng, Y.: Command generator tracker based direct model reference adaptive tracking guidance for Mars atmospheric entry. *Adv. Space Res.* **49**(1), 49–63 (2012)
15. Xia, Y., Chen, R., Pu, F., et al.: Active disturbance rejection control for drag tracking in mars entry guidance. *Adv. Space Res.* **53**(5), 853–861 (2014)
16. Eggers, A.J., Allen, H.J., Neice, S.E.A.: Comparative analysis of the performance of long-range hypervelocity vehicles. *NACA TN 4046* (1957)
17. Gazley, C.: Atmospheric entry. The RAND Corporation, Santa Monica (1960)
18. Lees, L., Hartwig, F.W., Cohen, C.B.: Use of aerodynamic lift during entry into the earth's atmosphere. *Ars J.* **29**(9), 633–641 (1959)
19. Ting, L., Wang, K.: An approximate analytic solution of re-entry trajectory with aerodynamic forces. *ARS J.* **30**(6), 565–566 (1960)
20. Loh, W.H.T.: Dynamics and thermodynamics of planetary entry. Prentice Hall Inc., Englewood Cliffs (1963)
21. Vinh, N.X., Busemann, A., Culp, R.D.: Hypersonic and planetary entry flight mechanics. University of Michigan Press, Ann Arbor (1980)
22. Loh, W.H.T.: Some exact analytical solutions of planetary entry. *AIAA J.* **1**(4), 836–842 (1963)
23. Cohen, M.J.: Some closed form solutions to the problem of re-entry of lifting and non-lifting vehicles. In: 2nd Aerospace Sciences Meeting, New York (1965)
24. Nyland, F.S.: Hypersonic turning with constant bank angle control. The RAND Corporation, Santa Monica (1965)
25. Bell, R.N.: A Closed-Form Solution to Lifting Reentry, AFFDL-TR65-65 (1965)
26. Chen, S.Y.: The Longitudinal and Lateral Range of Hypersonic Glide Vehicles with Constant Bank Angle. The RAND Corporation, Santa Monica (1966)
27. Meyer, C.D.: Matrix Analysis and Applied Linear Algebra. The Society for Industrial and Applied Mathematics, Philadelphia (2000)
28. Burden, R.L., Faires, J.D.: Numerical Analysis. Cengage Learning, Boston (2010)
29. Zarchan, P.: Tactical and Strategic Missile Guidance. AIAA Progress in Aeronautics and Astronautics, Reston (2007)

Chapter 13

Omnidirectional Autonomous Reentry Guidance Based on 3-D Analytical Glide Formulae Considering Influence of Earth's Rotation



13.1 Introduction

Common Aero Vehicle (CAV) [1] is a high-L/D hypersonic vehicle gliding in the region of the Earth's atmosphere with altitude of 20 km to 100 km. CAV is sent into a sub-orbital trajectory by a launch vehicle. After separating from the launch vehicle, CAV reenters the atmosphere with initial Mach number of about 20. As the maximum L/D (L/D_{max}) is up to 3, CAV can travel more than ten thousand kilometers, while its lateral maneuver range can also be up to thousands of kilometers. The flight of CAV can be roughly divided into entry and nosedive phases. In the entry phase, CAV manages the flight energy by performing proper lateral maneuvers, and eliminates the heading error by conducting several bank reversals. During the entry flight, the glide trajectory should satisfy the constraints on heating rate, dynamic pressure, and load factor. In the nosedive phase, CAV dives into the dense atmosphere and impacts its intended target almost vertically [2–4]. This paper is aimed at developing a fully-automated guidance law used in the entry phase and capable of steering CAV to any place of the world.

Investigating the analytical solutions to entry problems [5–16] is an important way to explore and discover the rules of hypersonic glide trajectory, especially in the early days when the computer technique was not advanced. However, as the entry dynamics are strongly nonlinear and coupled, most of the analytical solutions [5–12] only consider the longitudinal motion and are obtained under special flight conditions. For example, there are two common solutions developed for predicting the glide range and expressed as functions of speed: one is obtained by letting the drag profile be a polynomial of speed [5]; the other assumes that the flight path angle γ is zero and lets L/D be constant [6–7]. In [13–16], there are two kinds of the analytical solutions that consider the lateral motion and are capable of predicting the

Reprinted from ISA Transactions, Vol 65, Yu Wenbin, Chen Wanchun, Jiang Zhiguo, Liu Xiaoming, Zhou Hao, Omnidirectional autonomous entry guidance based on 3-D analytical glide formulas, Pages 487–503, Copyright (2016), with permission from Elsevier.

downrange, crossrange, and heading angle of hypersonic glide trajectory. In the first kind of the solutions [13–15], the bank angle (σ) and L/D are designed to be constant, which limits the scope of application of the solutions. To develop the solutions, the effect of the Earth's curvature on the heading angle is neglected so as to decouple the equations of lateral motion. However, this significantly decreases the solutions' accuracy. By contrast, in the second kind of solutions [16], $L/D \cos(\sigma)$ and $L/D \sin(\sigma)$ are designed as polynomials of energy in order to extend the scope of application, and the effect of the Earth's curvature on the heading angle is considered so as to improve the accuracy. However, this greatly increases the difficulty of developing the new solutions, because a complex Linear Time-Varying (LTV) system is obtained by linearization whereas there is no universal method for solving LTV systems. By observing and analyzing the characteristics of the obtained system, an innovative method based on spectral decomposition is proposed for solving this system, and thus the high-precision solutions are obtained successfully.

Entry guidance laws are generally classified as reference-tracking guidance and predictor–corrector guidance. Shuttle entry guidance [5] is the typical representative of reference-tracking guidance and provides a foundation for the skeleton process of the entry guidance laws. Shuttle entry guidance consists of four parts: (1) determine the entry corridor satisfying all path constraints; (2) plan a reference profile meeting terminal conditions in the entry corridor; (3) properly adjust AOA and bank angle to track the reference profile; (4) design a bank reversal threshold to eliminate heading error.[17] verifies that shuttle entry guidance can also be applied to the X-33 entry mission by simulation testing. In [18], reduced-order entry dynamics are developed and then an iterative method based on these dynamics is proposed for fast planning the drag acceleration profile and bank reversals, whereas the planning method presented in [5] can only plan the drag acceleration profile. In [19], a new tracking method is designed based on the linear quadratic regulator and the simulation results show that this method can closely track the planned profiles of range to go, altitude, and flight-path angle with respect to energy. In [20], a method is developed for directly planning the bank angle profile where the path constraints are converted into the bank angle limitation. In [21], also using the reduced-order entry dynamics developed in [18], an approach is developed for planning 3-D drag profiles where both the AOA and bank angle are adjusted to track these profiles. In the predictor–corrector guidance laws [22–24], the onboard trajectory simulation is generally conducted in real time to predict the final state errors, and then the parametric command profiles are corrected so as to eliminate the predicted errors. Compared with the reference-tracking guidance laws, the predictor–corrector guidance laws can cope with large disturbances, but require extremely heavy computational loads. In [25–26], the entry-trajectory planning methods take into account the no-fly-zone constraints. In [27–28], the neural network control is used to track the flight path angle and velocity of hypersonic flight vehicle. Such a control law excels at handling the problem with unknown dynamics. In [29], an attitude tracking control is developed by combining the trajectory linearization control and alternative active disturbance rejection control. Here, to estimate the uncertainties acting on the linearized entry control system, linear

extended state observers are constructed. In [30], an integrated guidance and control scheme is developed for entry flight, which can strictly satisfy the path constraints.

Note that the conventional guidance laws [5, 17–30] mentioned above are designed for the low- to mid-L/D re-entry vehicles, the L/Ds of which are near 1, but cannot be used to steer the high-L/D CAV. Compared with the low- to mid-L/D re-entry vehicles, the glide trajectory of CAV has noticeable phugoid oscillations [31–32], which count against the close tracking of reference profiles if there are large disturbances and greatly increase the peak values of heating rate and dynamic pressure [32]. However, the conventional guidance laws [5, 17–30] cannot eliminate the phugoid oscillations and thus are unable to handle the entry mission of CAV. In [33], a scheme termed Trajectory Damping Control Technique (TDCT) is proposed for suppressing the trajectory oscillations. By adopting TDCT, the entry guidance laws presented in [16] and [32] are capable of steering CAV reliably. In [32], TDCT is simplified and applied in coordination with Predictor–Corrector Gliding Guidance (PCGG). In [16], an entry guidance is developed based on analytical solutions and denoted as EGAS. After comprehensive and in-depth study, we reveal some drawbacks of the two guidance laws. For PCGG, the final heading error is too large and sometimes can be up to 20 deg. In addition, the computational load is extremely heavy because a reduced-order dynamic system need be simulated numerically in real time. In [16], because the 3-D analytical glide formulas are developed without considering the effects of the Earth’s rotation, and EGAS fails to compensate these effects adequately when utilizing these formulas, EGAS cannot handle some special cases, especially that CAV flies along the north or south direction.

This paper is aimed at developing an autonomous entry guidance that can steer CAV to any place of the world accurately. Thus, this guidance is referred to as Omnidirectional Autonomous Entry Guidance (OAEG). In the guidance, the downrange formula [16] is used to plan the longitudinal reference profile in order to meet the downrange and final energy requirements, and the crossrange formula [16] is used to regulate the bank reversals in order to eliminate the crossrange error. To compensate the effects of the Earth’s rotation, we observe the motion of the vehicle from the inertial space, rather than from the rotating Earth, and introduce the generalized aerodynamic forces. As the generalized aerodynamic profiles are tracked using AOA and bank angle, planning the generalized aerodynamic profile arbitrarily will result in violent swings in AOA and bank angle and may even cause them to exceed their available ranges. To keep the AOA and bank angle commands almost constant in the SGP, we need evaluate the effects of the Earth’s rotation on the generalized aerodynamic profiles. However, this is difficult because the states are yet unknown in the remaining flight. Therefore, we carefully design a series of strategies to plan the generalized aerodynamic profiles. As viewed from the inertial space, the atmosphere almost moves together with the rotating Earth. Considering this regular motion, we can roughly obtain the relation between the generalized and conventional aerodynamic profiles over the whole flight. Then, using this relation, we can determine the parametric formulas of the generalized aerodynamic profiles based on the baseline aerodynamic profile. After using the analytical glide formulas to determine the

formula parameters, the guidance adjusts the baseline AOA and bank angle to accurately track the planned profiles. As verified by trajectory simulations, the strategies can fully compensate the effects of the Earth's rotation and will not result in drastic adjustments in the AOA and bank angle. In addition, the iterative algorithms for correcting the last bank reversal proposed here has two advantages compared with that presented in [16]: (1) the new algorithms improve the accuracy of final altitude by slightly adjusting the baseline AOA profile; (2) the new algorithms is able to deal with the case that the last bank reversal has a large error.

The chapter is structured as: Sect. 13.2 illustrates the entry guidance problem; Sect. 13.3 presents the development of the new entry guidance; Sect. 13.4 gives some examples to demonstrate the performance of the guidance; Sect. 13.5 draws the conclusions; Appendix 1 shows the generalized states of motion; Appendix 2 shows the generalized aerodynamic forces; References are listed finally.

13.2 Entry Guidance Problem

13.2.1 Equations of Motion

Treating the vehicle as a particle, the equations of motion for entry flight over the spherical, rotating Earth are [34]

$$\frac{d\lambda}{dt} = \frac{V \cos(\gamma) \sin(\psi)}{(R_e + H) \cos(\phi)} \quad (13.1)$$

$$\frac{d\phi}{dt} = \frac{V \cos(\gamma) \cos(\psi)}{(R_e + H)} \quad (13.2)$$

$$\frac{dH}{dt} = V \sin(\gamma) \quad (13.3)$$

$$\begin{aligned} \frac{dV}{dt} = & -\frac{D}{m} - g \sin(\gamma) + \omega_e^2 (R_e + H) \cos^2(\phi) \sin(\gamma) \\ & - \omega_e^2 (R_e + H) \sin(\phi) \cos(\phi) \cos(\gamma) \cos(\psi) \end{aligned} \quad (13.4)$$

$$\begin{aligned} \frac{d\gamma}{dt} = & \frac{1}{V} \left[\frac{L \cos(\sigma)}{m} - g \cos(\gamma) + \frac{V^2 \cos(\gamma)}{R_e + H} \right. \\ & + \omega_e^2 (R_e + H) \cos^2(\phi) \cos(\gamma) \\ & \left. + 2V \omega_e \cos(\phi) \sin(\psi) + \omega_e^2 (R_e + H) \sin(\phi) \cos(\phi) \sin(\gamma) \cos(\psi) \right] \end{aligned} \quad (13.5)$$

$$\frac{d\psi}{dt} = \frac{1}{V} \left[\frac{L \sin(\sigma)}{m \cos(\gamma)} + \frac{V^2 \cos(\gamma) \sin(\psi) \tan(\phi)}{R_e + H} \right]$$

$$\begin{aligned}
& - \frac{\omega_e^2(R_e + H) \sin(\phi) \cos(\phi) \sin(\psi)}{\cos(\gamma)} \\
& + 2V\omega_e \sin(\phi) - 2V\omega_e \cos(\phi) \tan(\gamma) \cos(\psi) \]
\end{aligned} \tag{13.6}$$

where λ is the longitude, ϕ is the latitude, H is the altitude, V is the speed relative to the rotating Earth, γ is the flight-path angle, and ψ is the heading angle measured clockwise from the local north. m is the mass, σ is the bank angle, and g is the gravitational acceleration. R_e is the average radius of Earth with a value of 6 356.766 km, and ω_e is the rotation rate of Earth with a value of $7.292\ 116 \times 10^{-5}$ rad/s. L is the lift and D is the drag.

13.2.2 Path Constraints

Generally, due to the limitations of the thermal protection system and lightweight structure, the entry trajectory of CAV is constrained by heating rate \dot{Q} , dynamic pressure q and load factor n , as follows

$$\dot{Q} = k_Q \sqrt{\rho(H)} V^{3.15} \leq \dot{Q}_{\max} \tag{13.7}$$

$$q = \frac{1}{2} \rho(H) V^2 \leq q_{\max} \tag{13.8}$$

$$n = \frac{L}{mg_0} \leq n_{\max} \tag{13.9}$$

where k_Q is a parameter related to heating rate. \dot{Q}_{\max} , q_{\max} , and n_{\max} are the maximum allowable values of \dot{Q} , q , and n , respectively. g_0 is the gravitational acceleration at sea level. In addition, considering the capacity constraints of Flight Control System (FCS), we limit the change rates of AOA and bank angle as follows.

$$|\dot{\alpha}| \leq 4\text{deg/s}, |\ddot{\alpha}| \leq 16\text{deg/s}^2 \tag{13.10}$$

$$|\dot{\sigma}| \leq 8\text{deg/s}, |\ddot{\sigma}| \leq 40\text{deg/s}^2 \tag{13.11}$$

13.2.3 Terminal Conditions

The termination condition of the entry phase is that the vehicle reaches the circle centered at the target with radius of $S_{\text{TAEM}} = 50\text{km}$. Because the subscript “TAEM” is widely used to represent the required conditions of Reusable Launch Vehicle (RLV) for Terminal Area Energy Management, it is also used here to represent the desired terminal conditions of CAV in the entry phase. Define $\Delta\psi_{\text{TAEM}}$ as the desired final heading error, V_{TAEM} as the desired final speed, H_{TAEM} as the desired final altitude, and σ_{TAEM} as the desired final bank angle. In the entry phase, the desired terminal conditions of CAV are $|\Delta\psi_{\text{TAEM}}| \leq 5\text{ deg}$, $V_{\text{TAEM}} = 2000\text{m/s}$, $H_{\text{TAEM}} = 25\text{km}$, and $|\sigma_{\text{TAEM}}| \leq 30\text{ deg}$.

13.3 Omnidirectional Autonomous Entry Guidance

13.3.1 Overview

This section presents the design of Omnidirectional Autonomous Entry Guidance (OAEG). Figure 13.1 shows an entry trajectory of CAV guided by OAEG, where the upper curve is the altitude-vs-longitude profile and the lower curve is the latitude-vs-longitude profile, commonly termed ground track. As can be seen from this figure, according to the trajectory characteristics, we divide the entry flight into three phases: Descent Phase (DP), Steady Glide [35] Phase (SGP), and Altitude Adjustment Phase (AAP). To make clear the overall guidance process, the following briefly describes the trajectory characteristics and guidance strategies of the three phases, respectively.

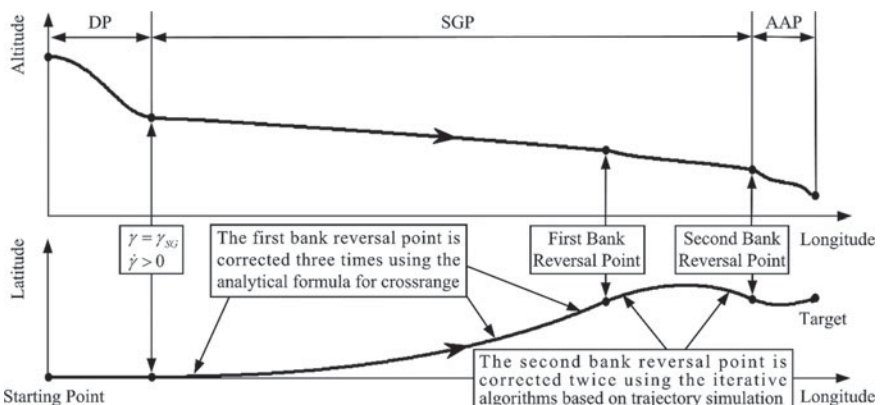


Fig. 13.1 Entry trajectory of CAV guided by OAEG

(1) Descent Phase

The DP begins shortly after CAV separates from the launch vehicle. In this phase, CAV loses altitude quickly since the atmosphere density is extremely thin at the separation altitude. As CAV drops into the dense atmosphere, the heating rate increases rapidly and reaches peak value near the end of this phase. To satisfy the heating rate constraint, we let the AOA be its maximum allowable value while maintaining a zero bank angle, such that CAV can glide as high as possible and thus minimize the peak value of the heating rate. Define γ_{SG} as the flight path angle corresponding to steady glide trajectory. γ_{SG} is an explicit function of the current states and will be shown in detail in Sect. 13.3.3.7. As shown in Fig. 13.1, when $\gamma = \gamma_{SG}$ and $\dot{\gamma} > 0$, the lift is large enough and the altitude no longer decreases rapidly. Thus, the DP ends at this moment.

(2) Steady Glide Phase

As shown in Fig. 13.1, the SGP is the largest part of the entry flight, where the lift is large enough to prevent CAV from dropping quickly. In this phase, the guidance uses the 3-D analytical glide formulas, capable of predicting the downrange, crossrange, and heading angle of hypersonic glide trajectory, to plan the reference profiles, and then modulates AOA and bank angle to track these profiles. As these glide formulas are developed without considering the effects of the Earth's rotation, we need observe the motion of CAV from the inertial space, in which the entry dynamics do not contain the complex terms related to the Earth's rotation. Denote the velocity vectors relative to the inertial space and rotating Earth as \tilde{V} and V , respectively. Define the generalized lift \tilde{L} as the component of the aerodynamic force \mathbf{F}_{aero} perpendicular to \tilde{V} , the generalized drag \tilde{D} as the component of \mathbf{F}_{aero} along $-\tilde{V}$, and the generalized lift to drag ratio ($\widetilde{L}/\widetilde{D}$) as the ratio of \tilde{L} to \tilde{D} . By contrast, according to the conventional definitions, if there is no wind, the lift L is the component of \mathbf{F}_{aero} perpendicular to V , the drag D is the component of \mathbf{F}_{aero} along $-V$, and the lift to drag ratio (L/D) is the ratio of L to D . Because there is a small angle between \tilde{V} and V due to the Earth's rotation, the generalized aerodynamic forces are slightly different from the conventional ones. By choosing the profiles of the generalized aerodynamic forces as the reference profiles, and then using the 3-D analytical glide formulas to plan and track these profiles, the entry guidance can fully compensate the effects of the Earth's rotation. The following briefly shows the guidance process in the SGP.

- Step 1: Offline design the baseline AOA (α_{bsl}) profile and then determine the corresponding baseline L/D (L/D_{bsl}) profile. These two profiles are pre-stored in the onboard computer and no modification is needed for different missions.
- Step 2: Obtain the generalized L/D profile ($\widetilde{L}/\widetilde{D}_{\text{ref}}$) based on L/D_{bsl} by roughly evaluating the effects of the Earth's rotation on the aerodynamic forces over the whole flight.
- Step 3: Define the generalized vertical lift to drag ratio $\widetilde{L}_1/\widetilde{D}$ as the ratio of the vertical component of \tilde{L} to \tilde{D} . The entry guidance uses the downrange formula to plan the $\widetilde{L}_1/\widetilde{D}$ profile, denoted as $\widetilde{L}_1/\widetilde{D}_{\text{ref}}$, so as to meet the downrange and terminal energy requirements.

- Step 4: Define the generalized horizontal lift to drag ratio \widetilde{L}_2/D as the ratio of the horizontal component of \tilde{L} to \tilde{D} . The profile of the absolute value of \widetilde{L}_2/D , denoted as $|\widetilde{L}_2/D_{\text{ref}}|$, can be obtained by $\widetilde{L}/D_{\text{ref}}$ and $\widetilde{L}_1/D_{\text{ref}}$. As \widetilde{L}_2/D has a significant impact on crossrange, the profile of $|\widetilde{L}_2/D_{\text{ref}}|$ will be used by the crossrange formula to regulate the bank reversals.
- Step 5: As shown in Fig. 13.1, the vehicle need only perform two bank reversals to eliminate the crossrange error. Before the first bank reversal occurs, the second bank reversal is set properly near the target, and then the first bank reversal is corrected three times using the crossrange formula. After the first bank reversal is performed, the guidance uses the iterative algorithms based on trajectory simulation to correct the second bank reversal slightly but accurately. As the second bank reversal is close to the target, correcting this point can eliminate the errors accumulated during most of flight. Note that the iterative algorithms will not result in a heavy computational load, because only the remaining short trajectory needs to be numerically simulated and the second bank reversal is only corrected twice, rather than in real time.
- Step 6: Modulate the baseline bank angle σ_{bsl} to track $\widetilde{L}_1/D_{\text{ref}}$ and actualize the bank reversals.
- Step 7: To suppress trajectory oscillations, the feedback generated by TDCT [33] is added to α_{bsl} and σ_{bsl} , which yields the AOA and bank angle commands, denoted as α_{cmd} and σ_{cmd} respectively. Once the oscillations are eliminated, the feedback becomes almost zero, and thus TDCT will not disturb the tracking of the reference profiles.
- Step 8: To satisfy the constraints on heating rate, dynamic pressure and load factor, convert these constraints into the allowable range of the bank angle, and then limit the bank angle command within the allowable range.
- Step 9: Repeat the above steps 2–8 until the SGP ends.

Note that due to careful design, the above strategies proposed for compensating the effects of the Earth's rotation will not result in rapid changes in the AOA, and can keep the bank angle approximately constant in the SGP. This has three major benefits. First, it helps to manage the flight energy rationally and thus prevents the commands from saturation in the AAP. Second, it also helps to improve the tracking accuracy of the FCS as the guidance commands vary smoothly and slowly. Finally, as the aerodynamic dispersions are generally sensitive to AOA, avoiding drastic changes in the AOA contributes to evaluating the effects of the aerodynamic dispersions accurately, which can enhance the robustness of the guidance and also improve its accuracy.

(3) Altitude Adjustment Phase

As shown in Fig. 13.1, after the second bank reversal is performed, the vehicle enters the AAP, where the altitude is adjusted to the desired value by properly reducing the baseline AOA. In this phase, because the change rate of the flight path angle is relatively large, the accuracy of the analytical glide formulas is insufficient to meet

the terminal conditions. Therefore, we use a different guidance scheme here, where Proportional Navigation (PN) is used to determine the baseline bank angle so as to eliminate the heading error. In order to meet the final speed requirement, the guidance modulates the AOA to follow the reference range-to-go profile ($s_{\text{go}}^{\text{ref}}$) with respect to energy, which is obtained from the last onboard trajectory simulation conducted for correcting the second bank reversal. Because the trajectory of this phase is relatively short, the accumulated errors are small and thus the AOA need only be adjusted slightly to eliminate these errors.

The following subsections show the entry guidance in detail.

13.3.2 Descent Phase

In this phase, due to the thin atmosphere, the vehicle loses altitude quickly. As the vehicle drops into the dense atmosphere, the heating rate increases rapidly and achieves the local maximum near the end of the phase. As shown in Eq. (13.12), to satisfy the constraints on heating rate and dynamic pressure, we adopt the most conservative scheme [16] which commands the vehicle to fly along $\alpha = \alpha_{\max}$ with $\sigma = 0$, where α_{\max} is the maximum allowable value of AOA. This can increase the glide altitude as high as possible, and thus minimizes the local maximum value of the heating rate. As the lift increases with the dynamic pressure increasing, $\dot{\gamma}$ gets greater gradually. When $\dot{\gamma} = 0$, the lift is large enough to make the vehicle glide steadily. Thus, as shown in the second sub-equation of Eq. (13.12), the AOA changes to the baseline AOA (α_{bsl}) gradually.

$$\alpha_{\text{cmd}} = \begin{cases} \alpha_{\max} & \text{if } \dot{\gamma} < 0 \text{deg/s} \\ \frac{\Delta\gamma}{\Delta\gamma_1} \alpha_{\max} + \frac{\Delta\gamma_1 - \Delta\gamma}{\Delta\gamma_1} [\alpha_{\text{bsl}} + k_{\gamma} \Delta\gamma] & \text{if } \dot{\gamma} \geq 0 \text{deg/s} \end{cases} \quad (13.12)$$

$$\sigma_{\text{cmd}} = 0 \text{ deg} \quad (13.13)$$

$$\Delta\gamma = \gamma_{SG} - \gamma \quad (13.14)$$

where γ_{SG} is the flight path angle corresponding to steady glide and will be shown in detail in Sect. 13.3.3.7. $\Delta\gamma_1$ is the value of $\Delta\gamma$ when $\dot{\gamma} = 0 \text{deg/s}$. k_{γ} is a constant. When $\Delta\gamma = 0$, the descent phase ends because the altitude no longer decreases rapidly.

13.3.3 Steady Glide Phase

Section 13.3.1 briefly showed the trajectory characteristics and guidance process in the SGP. Now we present the guidance process in detail.

13.3.3.1 Baseline AOA and L/D Profiles

In the SGP and AAP, we let the vehicle glide along the baseline AOA (α_{bsl}) profile. As shown in Eq. (13.15), we design this profile as a function of the specific relative energy E , which is defined as the mechanical energy per unit mass relative to the rotating Earth and can be obtained by Eq. (13.16).

$$\alpha_{\text{bsl}} = \begin{cases} \alpha_1; & \text{for } E_\alpha \leq E \leq E_0 \\ \left(\frac{E_\alpha - E}{E_\alpha - E_{\text{TAEM}}} \right)^2 (\alpha_2 - \alpha_1) + \alpha_1; & \text{for } E_{\text{TAEM}} \leq E < E_\alpha \end{cases} \quad (13.15)$$

$$E = \frac{1}{2} V^2 - \frac{\mu}{R_e + H} \quad (13.16)$$

In Eq. (13.15), E_0 is the initial value of E , E_α is set to $-5.6 \times 10^7 \text{ J/kg}$, which is close to the second bank reversal, i.e. the handover point between the SGP and AAP, and E_{TAEM} is the desired final value of E and can be obtained by substituting V_{TAEM} and H_{TAEM} into Eq. (13.16). To reach the full potential of the vehicle, α_1 is set to 10 deg because the L/D is almost maximized at this angle. In the AAP, to achieve the desired final altitude H_{TAEM} , we reduce α_{bsl} to α_2 smoothly. α_2 is initially set to 6 deg and will be corrected slightly using the iterative algorithms based on trajectory simulation presented in Sect. 13.4.1.

Figure 13.2 shows the altitude corridor corresponding to the α_{bsl} profile. The lower bound of this corridor H_{\min} is determined by the path constraints presented in Sect. 13.2.2. As the altitude for steady-glide increases with the magnitude of the bank angle decreasing, the upper bound H_{\max} is achieved by setting the bank angle to zero.

Fig. 13.2 Altitude corridor

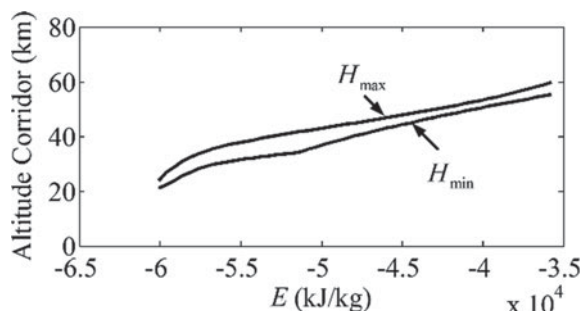
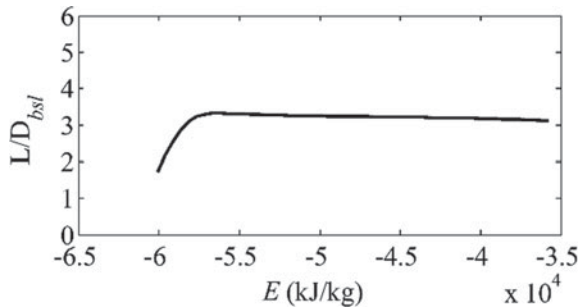


Fig. 13.3 Baseline L/D profile with respect to E



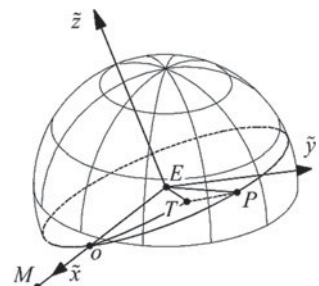
Now we determine the baseline L/D (L/D_{bsl}) profile, the L/D profile corresponding to α_{bsl} . In general, L/D is a function of AOA and Mach number (Ma). However, for hypersonic glide, the aerodynamic coefficients are insensitive to Ma . Meanwhile, as the altitude corridor is narrow, changes in glide altitude have little effect on Ma . Therefore, the L/D_{bsl} profile is insensitive to the glide altitude. Assuming that the vehicle glides along the middle of the corridor, we can determine the profile of Ma with respect to E . Combining this profile with the α_{bsl} profile, we can obtain the L/D_{bsl} profile with respect to E , as shown in Fig. 13.3. From this figure, we can see that the maximum L/D of CAV is up to 3, whereas the practical L/Ds of the space shuttle and X-33 RLV are only about 1.

13.3.3.2 Auxiliary Geocentric Inertial Frame

As the 3-D analytical glide formulas [16] are developed without considering the effects of the Earth's rotation, the entry guidance implements these formulas in the inertial space in order to compensate these effects. As shown in Fig. 13.4, we use the Auxiliary Geocentric Inertial (AGI) frame [16] as the frame of reference, because it helps to improve the accuracy of the analytical formulas. The following shows the details of this frame.

Define point P as the point at which the vehicle M collides with its target T , as viewed from the inertial space. As the target is always moving with the rotating Earth,

Fig. 13.4 Auxiliary geocentric inertial frame:
 $E - \tilde{x}\tilde{y}\tilde{z}$



the collision point P is not at the current position of T . Its position can be predicted by

$$\lambda_P = \lambda_T + \omega_e t_{\text{go}}, \phi_P = \phi_T, H_P = H_T \quad (13.17)$$

where λ_P , ϕ_P , and H_P are the longitude, latitude, and altitude of P , and λ_T , ϕ_T , and H_T are the longitude, latitude, and altitude of T . t_{go} is the time to go. Now we temporarily return to the Earth and observe the motion of the vehicle from the Earth, where we can see that the vehicle flies towards the target. Denote s_{go} as the range to go observed from the Earth, i.e. the length of the arc between the points o and T , as shown in Fig. 13.4. Assuming that the speed of the vehicle relative to the rotating Earth varies linearly with time, we can roughly predict t_{go} by

$$t_{\text{go}} = \frac{2s_{\text{go}}}{V + V_{\text{TAEM}}} \quad (13.18)$$

As shown in Fig. 13.4, define the generalized equator as the great circle passing through the points o and P , where great circle refers to a circle centered at the Earth's center E with the same radius as the Earth. Based upon the generalized equator, we can create the AGI frame. The origin of this frame is at the Earth's center. The x -axis is denoted as \tilde{x} and points towards M . The y -axis (\tilde{y}) is in the generalized equatorial plane and perpendicular to \tilde{x} . The z -axis (\tilde{z}) is determined by the right hand rule. Denote the unit vectors pointing in the directions of the positive \tilde{x} -, \tilde{y} -, and \tilde{z} -axes as $\hat{\mathbf{x}}$, $\hat{\mathbf{y}}$, and $\hat{\mathbf{z}}$, respectively.

Note that although the AGI frame is updated once using the current states of motion in each guidance cycle, it is treated as an inertial frame throughout the guidance cycle.

Define the generalized meridian as half of the great circle with both end points on the \tilde{z} -axis. Obviously, the plane containing the generalized meridian is perpendicular to the generalized equatorial plane. Let the generalized meridian passing through the point o be the generalized prime meridian. Thus, the position of an object can be described by the generalized longitude $\tilde{\lambda}$, generalized latitude $\tilde{\phi}$, and generalized altitude \tilde{H} . In each guidance cycle, because the AGI frame is updated once, the initial values of the generalized states appearing in the analytical formulas are $\tilde{\lambda}_0 = 0$, $\tilde{\phi}_0 = 0$, and $\tilde{H}_0 = H$.

Define the generalized speed \tilde{V} as the magnitude of the velocity vector relative to the AGI frame $\tilde{\mathbf{V}}$, define the generalized flight-path angle $\tilde{\gamma}$ as the angle between $\tilde{\mathbf{V}}$ and the local horizontal plane, and define the generalized heading angle $\tilde{\psi}$ as the angle between $\tilde{\mathbf{V}}$ and the local generalized meridian. Additionally, define downrange as $x_D = \tilde{\lambda}R_e$ and crossrange as $x_C = \tilde{\phi}R_e$. Appendix 1 shows the relationships between the conventional and generalized states of motion.

As previously defined in Sect. 13.3.1, the generalized lift \tilde{L} is the component of the aerodynamic force \mathbf{F}_{aero} perpendicular to $\tilde{\mathbf{V}}$, the generalized drag \tilde{D} is the component of \mathbf{F}_{aero} along $-\tilde{\mathbf{V}}$, and the generalized lift to drag ratio (\tilde{L}/\tilde{D}) as the ratio of \tilde{L} to \tilde{D} . Define \tilde{L}_1 as the component of \tilde{L} in the local vertical plane containing $\tilde{\mathbf{V}}$, and \tilde{L}_2

as the component of \tilde{L} in the local horizontal plane. Define the generalized vertical lift to drag ratio as $\widetilde{L_1/D} = \tilde{L}_1/\tilde{D}$ and the generalized horizontal lift to drag ratio as $\widetilde{L_2/D} = \tilde{L}_2/\tilde{D}$. Appendix 2 shows the relationships between the conventional and generalized aerodynamic forces.

To compensate the effects of the Earth's rotation, the new guidance chooses the generalized aerodynamic profiles as the reference profiles and then uses the 3-D analytical glide formulas to plan them. Because CAV glides to the predicted collision point P approximately along the generalized equator, there are $\tilde{\phi} \approx 0$ deg and $\tilde{\psi} \approx 90$ deg, at which the reduced-order dynamic equations are linearized for developing the analytical glide formulas. Thus, using the AGI frame as the frame of reference helps to improve the accuracy of these formulas.

13.3.3.3 Generalized L/D Profile

Based upon the baseline L/D profile, we plan the generalized L/D profile with respect to the specific absolute energy \tilde{E} , denoted as $\widetilde{L/D}_{\text{ref}}(\tilde{E})$, where \tilde{E} is defined as

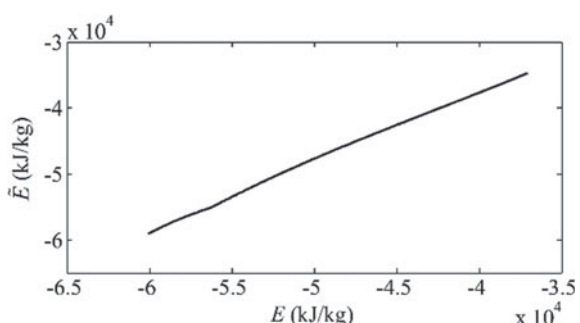
$$\tilde{E} = \frac{1}{2} \tilde{V}^2 - \frac{\mu}{R_e + \tilde{H}} \quad (13.19)$$

First, we need to obtain the relationship between \tilde{E} and E . The exact relationship can be obtained from Eq. (13.87) as

$$\tilde{E} = E + V\omega_e(R_e + H) \cos(\phi) \cos(\gamma) \sin(\psi) + 0.5\omega_e^2(R_e + H)^2 \cos^2(\phi) \quad (13.20)$$

However, this complex relationship is useless because the states of motion in the remaining trajectory are not yet known. By quantitative analysis, we find that the first term on the right side of Eq. (13.20) is one to two orders of magnitude higher than the other two terms. Thus, the linear part plays a dominant role in the relationship, which makes the profile of \tilde{E} with respect to E look like a straight line, as shown in Fig. 13.5.

Fig. 13.5 The \tilde{E} -vs- E profile looks like a straight line



Therefore, it is reasonable to use the following linear formula to approximate the relationship.

$$x_E = \frac{E_{\text{TAEM}} - E}{\tilde{E}_{\text{TAEM}} - \tilde{E}} (\tilde{x}_E - \tilde{E}) + E \quad (13.21)$$

Here, E and \tilde{E} represent the current values of the specific relative and absolute energies, respectively. E_{TAEM} and \tilde{E}_{TAEM} represent the desired terminal values of the specific relative and absolute energies, respectively, where E_{TAEM} is calculated by Eq. (13.102). x_E and \tilde{x}_E represent the values of the specific relative and absolute energies at any moment, respectively. Using the linear relationship, we can get the profile of L/D_{bsl} with respect to \tilde{x}_E , i.e., $L/D_{\text{bsl}}(\tilde{x}_E) = L/D_{\text{bsl}}[x_E(\tilde{x}_E)]$.

From Eq. (13.113) in Appendix 2, we can obtain $\widetilde{L/D}_{\text{ref}}(\tilde{x}_E)$ by

$$\widetilde{L/D}_{\text{ref}}(\tilde{x}_E) = \frac{k_{L/D} L/D_{\text{bsl}}(\tilde{x}_E) + \sin(\bar{\sigma}(\tilde{x}_E)) \bar{\theta}_V(\tilde{x}_E)}{\cos(\bar{\theta}_V(\tilde{x}_E)) - k_{L/D} L/D_{\text{bsl}}(\tilde{x}_E) \sin(\bar{\sigma}(\tilde{x}_E)) \sin(\bar{\theta}_V(\tilde{x}_E))} \quad (13.22)$$

where $k_{L/D}$ is determined by Eq. (13.23) and used to compensate the effects of the aerodynamic dispersions.

$$k_{L/D} = \frac{L/D_{\text{est}}(E)}{L/D_{\text{ideal}}(E)} \quad (13.23)$$

where $L/D_{\text{est}}(E)$ is the current actual L/D estimated by the in-flight aerodynamic identification technique [36], and $L/D_{\text{ideal}}(E)$ is the current L/D corresponding to the ideal aerodynamic model. Here, Eq. (13.23) implies that the deviation percentage of L/D in the rest of flight is assumed to be equal to the current one, in spite of that this percentage generally varies with the flight circumstances. This is because the actual L/D dispersion in the remaining flight is unknown yet.

In Eq. (13.22), $\bar{\theta}_V(\tilde{x}_E)$ is a linear fitting of θ_V , the angle between $\tilde{\mathbf{V}}$ and \mathbf{V} , and $\bar{\sigma}(\tilde{x}_E)$ is the predicted bank angle profile. Also because the states of motion in the remaining flight are unknown, we have to use these fittings to approximate $\theta_V(\tilde{x}_E)$ and $\sigma(\tilde{x}_E)$. The planned profile $\widetilde{L/D}_{\text{ref}}(\tilde{x}_E)$ based on $\bar{\theta}_V(\tilde{x}_E)$ and $\bar{\sigma}(\tilde{x}_E)$ can still be accurately tracked by slightly adjusting the baseline AOA. The following shows $\bar{\theta}_V(\tilde{x}_E)$ and $\bar{\sigma}(\tilde{x}_E)$ in detail.

As shown in Fig. 13.4, define oT as the arc between the points o and T . As viewed from the rotating Earth, by assuming that the vehicle flies to the target T approximately along oT , we can use Eq. (13.103) to calculate the current and final values of $\bar{\theta}_V$, denoted as $\bar{\theta}_V(\tilde{E})$ and $\bar{\theta}_V(\tilde{E}_{\text{TAEM}})$ respectively. Then, we design $\bar{\theta}_V(\tilde{x}_E)$ as

$$\bar{\theta}_V(\tilde{x}_E) = \frac{\bar{\theta}_V(\tilde{E}) - \bar{\theta}_V(\tilde{E}_{\text{TAEM}})}{\tilde{E} - \tilde{E}_{\text{TAEM}}} (\tilde{x}_E - \tilde{E}) + \bar{\theta}_V(\tilde{E}) \quad (13.24)$$

Next, we plan the profile of $\bar{\sigma}(\tilde{x}_E)$. Because we desire that the magnitude of the bank angle keeps constant in the SGP, but reduces to zero smoothly in the AAP, we design $\bar{\sigma}(\tilde{x}_E)$ as a piecewise function as follows.

$$\bar{\sigma}(\tilde{x}_E) = \begin{cases} \text{sgn} \cdot |\sigma_{\text{bsl}}(E)|; & \text{if } \tilde{x}_E \geq \tilde{E}_{BR1} \\ -\text{sgn} \cdot |\sigma_{\text{bsl}}(E)|; & \text{if } \tilde{E}_{BR2} \leq \tilde{x}_E < \tilde{E}_{BR1} \\ \text{sgn} \cdot |\sigma_{\text{bsl}}(E)| \frac{\tilde{x}_E - \tilde{E}_{TAEM}}{\tilde{E}_{BR2} - \tilde{E}_{TAEM}}; & \text{if } \tilde{x}_E < \tilde{E}_{BR2} \end{cases} \quad (13.25)$$

where $\sigma_{\text{bsl}}(E)$ is the current value of the baseline bank angle. sgn is a sign function used to determine the sign of the bank angle. This sign function lets the vehicle initially turn to the direction making the heading error decrease. \tilde{E}_{BR1} and \tilde{E}_{BR2} represent the specific absolute energies at which the first and second bank reversals occur, respectively.

13.3.3.4 Generalized Vertical L/D Profile

In [16], the general form of the analytical formula for downrange ($x_D = \tilde{\lambda}R_e$) is developed as

$$x_D(\tilde{E}, \tilde{E}_0) = \int_{\tilde{E}_0}^{\tilde{E}} \frac{R_e \widetilde{L_1/D}(\tilde{x}_E)}{2\tilde{x}_E + \mu/R^*} d\tilde{x}_E \quad (13.26)$$

where \tilde{E}_0 and \tilde{E} represent the initial and current specific absolute energies, respectively, and $R^* = R_e + (\tilde{H}_0 + \tilde{H}_{TAEM})/2$ is a constant. Obviously, downrange increases with increasing $\widetilde{L_1/D}$.

The above equation is used to onboard plan the profile of $\widetilde{L_1/D}_{\text{ref}}$ meeting the downrange and terminal energy requirements. First, we need to parameterize the profile of $\widetilde{L_1/D}_{\text{ref}}(\tilde{x}_E)$. As can be seen from Fig. 13.3, for $E \geq E_\alpha$, L/D_{bsl} is approximately constant, and for $E < E_\alpha$, L/D_{bsl} decreases with E decreasing. To make the bank angle change smoothly, we want that the profile of $\widetilde{L_1/D}_{\text{ref}}$ has a similar shape to that of L/D_{bsl} . Therefore, as shown in Eq. (13.27), we design the profile of $\widetilde{L_1/D}_{\text{ref}}$ as a piecewise function: for $\tilde{x}_E \geq \tilde{E}_\alpha$, $\widetilde{L_1/D}_{\text{ref}}$ is constant, and for $\tilde{x}_E < \tilde{E}_\alpha$, $\widetilde{L_1/D}_{\text{ref}}$ reduces to $\widetilde{L_1/D}_2$ smoothly, where \tilde{E}_α is obtained by substituting $x_E = E_\alpha$ into Eq. (13.21).

$$\widetilde{L_1/D}_{\text{ref}}(\tilde{x}_E) = \begin{cases} \widetilde{L_1/D}_1; & \tilde{E}_\alpha \leq \tilde{x}_E \leq \tilde{E}_0 \\ \widetilde{L_1/D}_1 + \left(\frac{\tilde{E}_\alpha - \tilde{x}_E}{\tilde{E}_\alpha - \tilde{E}_{TAEM}} \right)^2 \left(\widetilde{L_1/D}_2 - \widetilde{L_1/D}_1 \right); & \tilde{E}_{TAEM} \leq \tilde{x}_E < \tilde{E}_\alpha \end{cases} \quad (13.27)$$

Here, in order to achieve a near-zero final bank angle, we let \widetilde{L}_1/D_2 be equal to $\widetilde{L}/D_{\text{ref}}(\tilde{E}_{\text{TAEM}})$. As viewed from the AGI frame, the required downrange is

$$x_{Df} = R_e \tilde{\lambda}_P - S_{\text{TAEM}} \quad (13.28)$$

where $\tilde{\lambda}_P$ is the generalized longitude of P and can be calculated by Eq. (13.95). \widetilde{L}_1/D_1 is determined by x_{Df} , as follows.

(1) If $\tilde{E} \geq \tilde{E}_\alpha$, we have

$$x_D(\tilde{E}_\alpha, \tilde{E}) + x_D(\tilde{E}_{\text{TAEM}}, \tilde{E}_\alpha) = x_{Df} \quad (13.29)$$

Substituting Eq. (13.27) into Eq. (13.26) and then integrating it, we have. For $\tilde{E} \geq \tilde{E}_\alpha$,

$$x_D(\tilde{E}_\alpha, \tilde{E}) = \frac{\widetilde{L}_1/D_1 R_e}{2} \ln \left(\frac{2R^* \tilde{E}_\alpha + \mu}{2R^* \tilde{E} + \mu} \right) \quad (13.30)$$

For $\tilde{E} \leq \tilde{E}_\alpha$,

$$\begin{aligned} x_D(\tilde{E}_{\text{TAEM}}, \tilde{E}) &= \frac{1}{4} a_2 R_e (\tilde{E}_{\text{TAEM}}^2 - \tilde{E}^2) + \frac{1}{2} \left(a_1 - \frac{a_2 \mu}{2R^*} \right) R_e (\tilde{E}_{\text{TAEM}} - \tilde{E}) \\ &\quad + \frac{4a_0(R^*)^2 - 2\mu R^* a_1 + \mu^2 a_2}{8(R^*)^2} R_e \ln \left(\frac{2R^* \tilde{E}_{\text{TAEM}} + \mu}{2R^* \tilde{E} + \mu} \right) \end{aligned} \quad (13.31)$$

where

$$a_2 = \frac{\widetilde{L}_1/D_2 - \widetilde{L}_1/D_1}{\left(\tilde{E}_\alpha - \tilde{E}_{\text{TAEM}} \right)^2} \quad (13.32)$$

$$a_1 = \frac{2\tilde{E}_\alpha \left(\widetilde{L}_1/D_1 - \widetilde{L}_1/D_2 \right)}{\left(\tilde{E}_\alpha - \tilde{E}_{\text{TAEM}} \right)^2} \quad (13.33)$$

$$a_0 = \widetilde{L}_1/D_1 \left[1 - \frac{\tilde{E}_\alpha^2}{\left(\tilde{E}_\alpha - \tilde{E}_{\text{TAEM}} \right)^2} \right] + \widetilde{L}_1/D_2 \frac{\tilde{E}_\alpha^2}{\left(\tilde{E}_\alpha - \tilde{E}_{\text{TAEM}} \right)^2} \quad (13.34)$$

Solving Eq. (13.29) yields

$$\widetilde{L_1/D_1} = \frac{c_1}{c_2} \quad (13.35)$$

where

$$c_1 = x_{Df} + \frac{R_e \widetilde{L_1/D_2}}{4(\tilde{E}_\alpha - \tilde{E}_{TAEM})} \left[\tilde{E}_{TAEM} - 3\tilde{E}_\alpha - \frac{\mu}{R^*} \right] - \frac{R_e \widetilde{L_1/D_2}}{(\tilde{E}_\alpha - \tilde{E}_{TAEM})^2} \left[\frac{\tilde{E}_\alpha^2}{2} + \frac{\mu \tilde{E}_\alpha}{2R^*} + \frac{\mu^2}{8(R^*)^2} \right] \ln \left(\frac{2R^* \tilde{E}_{TAEM} + \mu}{2R^* \tilde{E}_\alpha + \mu} \right) \quad (13.36)$$

$$c_2 = \frac{1}{4} \frac{R_e}{(\tilde{E}_\alpha - \tilde{E}_{TAEM})} \left[\tilde{E}_{TAEM} - 3\tilde{E}_\alpha - \frac{\mu}{R^*} \right] + \frac{R_e}{2} \ln \left(\frac{2R^* \tilde{E}_\alpha + \mu}{2R^* \tilde{E}_\alpha + \mu} \right) + \frac{R_e}{2(\tilde{E}_\alpha - \tilde{E}_{TAEM})^2} \left[-2\tilde{E}_\alpha \tilde{E}_{TAEM} + \tilde{E}_{TAEM}^2 - \frac{\mu \tilde{E}_\alpha}{R^*} - \frac{\mu^2}{4(R^*)^2} \right] \ln \left(\frac{2R^* \tilde{E}_{TAEM} + \mu}{2R^* \tilde{E}_\alpha + \mu} \right) \quad (13.37)$$

- (2) If $\tilde{E} < \tilde{E}_\alpha$, $\widetilde{L_1/D_1}$ no longer needs to be updated since the vehicle is mainly in the AAP, where a different guidance scheme is used.

13.3.3.5 Regulation of Bank Reversals

As the vehicle is inclined laterally at a proper angle to track the profile of $\widetilde{L_1/D}_{ref}$, it will travel a long lateral range. To eliminate the resulting crossrange error, the vehicle needs to conduct several bank reversals in due time. As previously shown In Fig. 13.1, to release the demands on FCS, the whole trajectory is planned with only two bank reversals, where the corresponding specific absolute energies are denoted as \tilde{E}_{BR1} and \tilde{E}_{BR2} respectively. To reduce the computational load, the bank reversals are corrected only several times, rather than in real time. Note that as the method of correcting the second bank reversal needs to be accompanied by the guidance scheme used in the AAP, we will show this method in Sect. 3.4.1. Here, we only introduce the method of correcting the first bank reversal, in which \tilde{E}_{BR2} is set to a specified value.

The analytical formula for crossrange [16] shows that the generalized lateral L/D has a significant impact on crossrange. Considering the bank reversals, the profile of $\widetilde{L_2/D}$ is

$$\widetilde{L_2/D_{\text{ref}}}(\tilde{x}_E) = \begin{cases} \text{sgn} \cdot |\widetilde{L_2/D_{\text{ref}}}(\tilde{x}_E)| & \text{for } \tilde{x}_E > \tilde{E}_{BR1} \text{ or } \tilde{x}_E \leq \tilde{E}_{BR2} \\ -\text{sgn} \cdot |\widetilde{L_2/D_{\text{ref}}}(\tilde{x}_E)| & \text{for } \tilde{E}_{BR2} < \tilde{x}_E \leq \tilde{E}_{BR1} \end{cases} \quad (13.38)$$

where $|\widetilde{L_2/D_{\text{ref}}}|$ can be obtained by

$$|\widetilde{L_2/D_{\text{ref}}}(\tilde{x}_E)| = \sqrt{\left[\widetilde{L_1/D_{\text{ref}}}(\tilde{x}_E)\right]^2 - \left[\widetilde{L_2/D_{\text{ref}}}(\tilde{x}_E)\right]^2} \quad (13.39)$$

As $\widetilde{L_2/D_{\text{ref}}}$ is a piecewise function, the form of the analytical formula for crossrange is quite complicate. To facilitate the writing, define a function as

$$F(\tilde{x}_{E2}, \tilde{x}_{E1}) = - \int_{\tilde{x}_{E1}}^{\tilde{x}_{E2}} \sin(f_1(\tilde{E}_{\text{TAEM}}, \tilde{x}_E)) |f_2(\tilde{x}_E)| d\tilde{x}_E \quad (13.40)$$

Here, since $\widetilde{L_1/D_{\text{ref}}}$ (Eq. (13.27)) is a piecewise function, $f_1(\tilde{E}_{\text{TAEM}}, \tilde{x}_E)$ is also a piecewise function as

$$f_1(\tilde{E}_{\text{TAEM}}, \tilde{x}_E) = \begin{cases} [x_D(\tilde{E}_{\text{TAEM}}, \tilde{E}_\alpha) + x_D(\tilde{E}_\alpha, \tilde{x}_E)]/R_e; & \text{for } \tilde{x}_E \geq \tilde{E}_\alpha \\ x_D(\tilde{E}_{\text{TAEM}}, \tilde{x}_E)/R_e; x_D(\tilde{E}_{\text{TAEM}}, \tilde{x}_E)/R_e; & \text{for } \tilde{x}_E < \tilde{E}_\alpha \end{cases} \quad (13.41)$$

where $x_D(\tilde{E}_{\text{TAEM}}, \tilde{E}_\alpha)$ and $x_D(\tilde{E}_{\text{TAEM}}, \tilde{x}_E)$ are calculated by Eq. (13.31), and $x_D(\tilde{E}_\alpha, \tilde{x}_E)$ is obtained by Eq. (13.30). The formula of $f_2(\tilde{x}_E)$ is

$$f_2(\tilde{x}_E) = - \frac{\widetilde{L_2/D_{\text{ref}}}(\tilde{x}_E)}{2(\tilde{x}_E + \mu/R^*)} \quad (13.42)$$

When regulating \tilde{E}_{BR1} , we let $\tilde{E}_{BR2} = \tilde{E}_\alpha$ such that the second bank reversal point is properly near the destination. The benefit is that correcting the second bank reversal can eliminate the errors accumulated during most of flight, and the errors accumulated in the remaining flight will be relatively small. From [16], the final crossrange can be predicted by

$$\begin{aligned} x_{Cf}(\tilde{E}_{BR1}) = & \left(\frac{\pi}{2} - \tilde{\psi}_0 \right) R_e \sin\left(\frac{x_{Df}}{R_e}\right) - \text{sgn}R_e F(\tilde{E}_{\text{TAEM}}, \tilde{E}_{BR2}) \\ & + \text{sgn}R_e F(\tilde{E}_{BR2}, \tilde{E}_{BR1}) - \text{sgn}R_e F(\tilde{E}_{BR1}, \tilde{E}) \end{aligned} \quad (13.43)$$

The derivative of x_{Cf} with respect to \tilde{E}_{BR1} is

$$\begin{aligned} x'_{Cf}(\tilde{E}_{BR1}) = & \text{sgn}R_e \sin[f_1(\tilde{E}_{\text{TAEM}}, \tilde{E}_{BR1})] \cdot \left| f_2^+(\tilde{E}_{BR1}) \right| \\ & + \text{sgn}R_e \sin[f_1(\tilde{E}_{\text{TAEM}}, \tilde{E}_{BR1})] \cdot \left| f_2^-(\tilde{E}_{BR1}) \right| \end{aligned} \quad (13.44)$$

where $f_2^+(\tilde{E}_{BR1})$ is the right-sided limit of $f_2(\tilde{x}_E)$ at $\tilde{x}_E = \tilde{E}_{BR1}$, and $f_2^-(\tilde{E}_{BR1})$ is the left-sided limit of $f_2(\tilde{x}_E)$ at $\tilde{x}_E = \tilde{E}_{BR1}$. Note that $|f_2^+(\tilde{E}_{BR1})| \neq |f_2^-(\tilde{E}_{BR1})|$ because it can be found from Eqs. (13.22), (13.25) and (13.39) that the profile of $|\widetilde{L_2/D_{ref}}|$ is discontinuous at $\tilde{x}_E = \tilde{E}_{BR1}$.

As shown in Fig. 13.4, because the predicted collision point P is on the generalized equatorial plane, the desired final crossrange is zero. Thus, we use the Newton iteration [37] to solve the equation $x_{Cf}(\tilde{E}_{BR1}) = 0$.

$$\tilde{E}_{BR1}^{(k+1)} = \tilde{E}_{BR1}^{(k)} - \frac{x_{Cf}(\tilde{E}_{BR1}^{(k)})}{x'_{Cf}(\tilde{E}_{BR1}^{(k)})} \quad (13.45)$$

As the final crossrange changes monotonously with \tilde{E}_{BR1} , the convergence rate of the iterative process is quite fast, and generally only four or five iterations are needed to achieve enough accuracy. As shown in Fig. 13.1, we correct \tilde{E}_{BR1} three times. The first happens shortly after the vehicle enters the SGP, the second occurs about 3 min before the first bank reversal, and the third is about 1 min before the first bank reversal.

13.3.3.6 Baseline Bank Angle in SGP

The entry guidance tracks the profile of $\widetilde{L_1/D_{ref}}$ by modulating the baseline bank angle σ_{bsl} . From Eq. (13.109) in Appendix 2, we have

$$\widetilde{L_1/D_{ref}} = \frac{L/D_{est} \cos(\sigma_{bsl})}{\cos(\theta_V) - \sin(\theta_V)L/D_{est} \sin(\sigma_{bsl})} \quad (13.46)$$

This equation can be transformed into

$$\cos(\Delta\sigma) \cos(\sigma_{bsl}) + \sin(\Delta\sigma) \sin(\sigma_{bsl}) = \frac{\widetilde{L_1/D_{ref}}}{L/D_{est}} \frac{\cos(\theta_V)}{\sqrt{1 + [\widetilde{L_1/D_{ref}} \sin(\theta_V)]^2}} \quad (13.47)$$

where

$$\cos(\Delta\sigma) = \frac{1}{\sqrt{1 + [\widetilde{L_1/D_{ref}} \sin(\theta_V)]^2}} \quad (13.48)$$

$$\sin(\Delta\sigma) = \frac{\widetilde{L_1/D_{ref}} \sin(\theta_V)}{\sqrt{1 + [\widetilde{L_1/D_{ref}} \sin(\theta_V)]^2}} \quad (13.49)$$

Solving Eq. (13.47) for σ_{bsl} yields

$$|\sigma_{bsl} - \Delta\sigma| = \arccos \left(\frac{\widetilde{L_1/D}_{ref}}{L/D_{est}} \frac{\cos(\theta_V)}{\sqrt{1 + (\widetilde{L_1/D}_{ref} \sin(\theta_V))^2}} \right) \quad (13.50)$$

Considering the bank reversals, we have

$$\sigma_{bsl} = \begin{cases} \text{sgn} \cdot \arccos \left(\frac{\widetilde{L_1/D}_{ref}}{L/D_{est}} \frac{\cos(\theta_V)}{\sqrt{1 + (\widetilde{L_1/D}_{ref} \sin(\theta_V))^2}} \right) + \Delta\sigma & \text{for } \tilde{E} > \tilde{E}_{BR1} + \Delta\tilde{E} \\ -\text{sgn} \cdot \arccos \left(\frac{\widetilde{L_1/D}_{ref}}{L/D_{est}} \frac{\cos(\theta_V)}{\sqrt{1 + (\widetilde{L_1/D}_{ref} \sin(\theta_V))^2}} \right) + \Delta\sigma & \text{for } \tilde{E}_{BR2} + \Delta\tilde{E} < \tilde{E} \leq \tilde{E}_{BR1} + \Delta\tilde{E} \end{cases} \quad (13.51)$$

Note that for $\tilde{E} \leq \tilde{E}_{BR2} + \Delta\tilde{E}$, the vehicle is in the AAP, where a different guidance scheme is used to determine the baseline bank angle. Since the roll rate is limited, we let the bank reversal occur $\Delta\tilde{E}$ ahead of schedule, where $\Delta\tilde{E}$ is determined by

$$\Delta\tilde{E} = a_D \tilde{V}_0 \Delta t \quad (13.52)$$

where a_D is the drag acceleration, \tilde{V}_0 is calculated by Eq. (13.87), and

$$\Delta t = \left| \frac{\sigma}{\dot{\sigma}_{max}} \right| \quad (13.53)$$

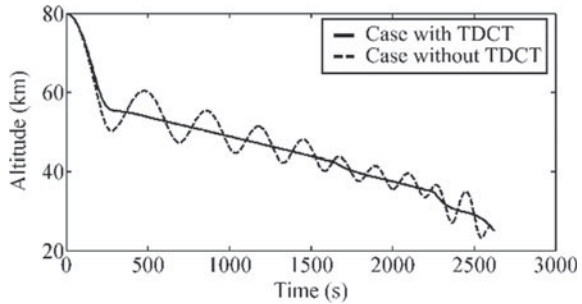
where σ is the current bank angle, and $\dot{\sigma}_{max}$ is the maximum allowable roll rate, as shown in Eq. (13.11).

13.3.3.7 AOA and Bank Angle Commands in SGP

As shown by the dashed line in Fig. 13.6, if α_{bsl} and σ_{bsl} are directly used as the guidance commands, the trajectory naturally has weakly-damped phugoid oscillations, which greatly reduces the accuracy of the analytical glide formulas and have a negative effect on the tracking of the reference profiles. Therefore, we adopt the Trajectory Damping Control Technique (TDCT) [16, 33] to suppress the oscillations. For $\sigma = \sigma_{bsl}$, the vertical and horizontal components of the lift coefficient corresponding to α_{bsl} are denoted as C_{L1} and C_{L2} , respectively. The TDCT generates the following feedback and adds it to C_{L1} .

$$\Delta C_{L1} = C_L^\alpha k_\gamma (\gamma_{SG} - \gamma) \quad (13.54)$$

Fig. 13.6 The natural trajectory of CAV has weakly-damped phugoid oscillations



where C_L^α is the slope of the lift curve, γ_{SG} is an approximation of the flight path angle corresponding to steady glide trajectory and will be shown in detail later, and k_γ is a constant.

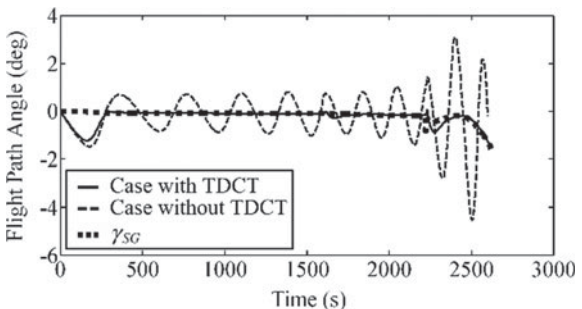
We briefly explain the principle of the TDCT. If the altitude of the vehicle drops quickly, then $\gamma_{SG} - \gamma > 0$. Thus Eq. (13.54) generates a positive signal to prevent the vehicle from descending rapidly. Inversely, if the vehicle climbs up quickly, then Eq. (13.54) generates a negative signal to prevent the vehicle from ascending rapidly. Finally, as shown by the solid lines in Figs. 13.6 and 13.7, the vehicle achieves the steady glide while γ approaches γ_{SG} tightly. As $\gamma_{SG} - \gamma \approx 0$, ΔC_{L1} is almost zero. Thus, the TDCT does not hinder the close tracking of the reference profiles. The following shows the guidance commands.

(1) AOA command

In general, the lift coefficient C_L is a function of α . Conversely, α can also be treated as a function of C_L , denoted as $\alpha = f_\alpha(C_L)$. Use the first order Taylor expansion to simplify the formula of the AOA command, as follows.

$$\begin{aligned}\alpha_{cmd} &= f_\alpha(\sqrt{(C_{L1} + \Delta C_{L1})^2 + C_{L2}^2}) \\ &\approx f_\alpha(\sqrt{C_{L1}^2 + C_{L2}^2}) + \frac{f'_\alpha(\sqrt{C_{L1}^2 + C_{L2}^2})C_{L1}}{\sqrt{C_{L1}^2 + C_{L2}^2}}\Delta C_{L1}\end{aligned}$$

Fig. 13.7 γ_{SG} is a perfect approximation of the flight-path angle corresponding to steady glide trajectory



$$= \alpha_{\text{bsl}} + \frac{C_{L1}}{C_{L(\text{bsl})}} \frac{\Delta C_{L1}}{C_L^\alpha} \quad (13.55)$$

where $C_{L(\text{bsl})}$ is the lift coefficient corresponding to α_{bsl} . Substituting Eq. (13.54) into the above equation yields

$$\alpha_{\text{cmd}} = \alpha_{\text{bsl}} + \cos(\sigma_{\text{bsl}}) k_\gamma (\gamma_{SG} - \gamma) \quad (13.56)$$

(2) Bank Angle Command

Considering ΔC_{L1} , the bank angle command is

$$\sigma_{\text{cmd}} = \arctan\left(\frac{C_{L2}}{C_{L1} + \Delta C_{L1}}\right) \quad (13.57)$$

Also using the first order Taylor expansion yields

$$\begin{aligned} \sigma_{\text{cmd}} &\approx \arctan\left(\frac{C_{L2}}{C_{L1}}\right) - \frac{C_{L2}}{C_{L1}^2 + C_{L2}^2} \Delta C_{L1} \\ &= \sigma_{\text{bsl}} - \frac{C_{L2}}{C_{L(\text{bsl})}} \frac{C_L^\alpha}{C_{L(\text{bsl})}} k_\gamma (\gamma_{SG} - \gamma) \\ &\approx \sigma_{\text{bsl}} - \sin(\sigma_{\text{bsl}}) \frac{k_\gamma (\gamma_{SG} - \gamma)}{\alpha_1} \end{aligned} \quad (13.58)$$

As can be seen from Eq. (13.56) and Eq. (13.58), because of the weights $\cos(\sigma_{\text{bsl}})$ and $\sin(\sigma_{\text{bsl}})$, if $|\sigma_{\text{bsl}}|$ is about 90 deg, the TDCT uses the bank angle as the major means to suppress the oscillations, whereas if $|\sigma_{\text{bsl}}|$ is near zero, the TDCT uses the AOA as the major means.

(3) Flight-Path Angle for Steady Glide

In [16] and [33], using the differentiation technique, the high-precision formula of γ_{SG} is developed as an explicit function of states, as follows.

$$\gamma_{SG} = -\frac{D_{\text{bsl}}}{mg} \frac{d_1}{d_2} \quad (13.59)$$

where $D_{\text{bsl}} = C_{D(\text{bsl})} q S_{\text{ref}}$ is the drag corresponding to α_{bsl} . Here, $C_{D(\text{bsl})}$ is the drag coefficient corresponding to α_{bsl} , ρ is the atmospheric density, and S_{ref} is the aerodynamic reference area. The formulas of d_1 and d_2 are

$$d_1 = \frac{\rho V^2 S_{\text{ref}} \cos(\sigma_{\text{bsl}})}{2m} \frac{dC_{L(\text{bsl})}}{dE} + \frac{2}{R_0 + H} + \frac{C_{L(\text{bsl})} \rho S_{\text{ref}} \cos(\sigma_{\text{bsl}})}{m} \quad (13.60)$$

$$d_2 = -\frac{C_{L(\text{bsl})} V^2 S_{\text{ref}} \cos(\sigma_{\text{bsl}})}{2mg} \frac{d\rho}{dH} + \frac{2}{R_0 + H} + \frac{C_{L(\text{bsl})} \rho S_{\text{ref}} \cos(\sigma_{\text{bsl}})}{m} + \frac{V^2}{(R_0 + H)^2 g} \quad (13.61)$$

where $L_{\text{bsl}} = C_{L(\text{bsl})} q S_{\text{ref}}$ is the lift corresponding to α_{bsl} , and $C_{L(\text{bsl})}$ is the corresponding lift coefficient. $dC_{L(\text{bsl})}/dE$ can be obtained after the baseline AOA profile is designed.

To prevent the path constraints from being violated, we need to limit the bank angle command. For steady glide, if the magnitude of the bank angle increases, the glide altitude decreases and the atmospheric density increases. This leads to the increases of the heating rate, dynamic pressure, and load factor. Therefore, the maximum bank angle is achieved if one of the stress and thermal parameters reaches its constraint boundary [16, 20]. In such a case, the maximum allowable bank angle is determined by the first term on the right side of Eq. (13.62). Here, L_1 is the vertical component of the lift and almost balances other forces due to $\dot{\gamma} \approx 0$, as shown in Eq. (13.63). Meanwhile, the lift is maximized since the atmospheric density is maximized, as shown in Eq. (13.64). The second term on the right side of Eq. (13.62) is used to cope with trajectory oscillations. For example, if the vehicle drops down quickly, this term will properly reduce σ_{\max} in order to prevent the vehicle from falling below H_{\min} .

$$\sigma_{\max} = \arccos\left(\frac{L_1}{L_{\max}}\right) + k_{\sigma}\left(\frac{dH_{\min}}{dE} - \frac{dH}{dE}\right) \quad (13.62)$$

where

$$L_1 = mg - \frac{mV^2}{R_e + H_{\min}(E)} - m\omega_e^2(R_e + H_{\min}) \cos^2(\phi) - 2mV\omega_e \cos(\phi) \sin(\psi) \quad (13.63)$$

$$L_{\max} = C_{L(\text{est})}[0.5\rho(H_{\min})V^2]S_{\text{ref}} \quad (13.64)$$

$$\frac{dH}{dE} \approx -\frac{m \sin(\gamma)}{D} \quad (13.65)$$

where $C_{L(\text{est})}$ is the current actual lift coefficient obtained by the aerodynamic identification technique, and k_{σ} is a constant. To satisfy the path constraints, we take the following measure

$$\sigma_{cmd} = \begin{cases} \sigma_{\max} & \text{if } \sigma_{cmd} > \sigma_{\max} \\ -\sigma_{\max} & \text{if } \sigma_{cmd} < -\sigma_{\max} \end{cases} \quad (13.66)$$

Although this measure may hinder the close tracking of the reference profile, it will not result in a failure of the guidance. As greater speed tends to increase the heating rate, dynamic pressure, and load factor greatly, the vehicle is more likely to violate the path constraints, especially on heating rate, in the high-speed phase. If the above measure is activated to ensure that all path constraints are satisfied, it will prevent the reference profile from being tracked closely. However this does not affect the effectiveness of the guidance, because in the low-speed phase, the entry corridor becomes wide, and the command gradually gets away from the boundary constructed by the constraints. Thus, in the low-speed phase, the reference profiles will be re-planned to eliminate the tracking errors accumulated in the high-speed phase.

13.4 Altitude Adjustment Phase

As previously shown in Fig. 13.1, after the second bank reversal, the vehicle flies in the AAP, where the altitude is properly reduced by decreasing the AOA. However, the altitude adjustment enlarges the change rate of flight path angle and thus causes the analytical glide formulas to be inaccurate to meet the terminal conditions. Therefore, we have to use a different guidance scheme here, which is an improvement of the guidance scheme for the AAP presented in [16]. In this phase, the baseline bank angle is determined by Proportional Navigation (PN) [38] so as to eliminate the crossrange error. Because the $\widehat{L_1/D}_{\text{ref}}$ profile is no longer tracked, we need use new strategies to achieve the desired final speed. These strategies can be divided into two parts: (1) before the second bank reversal, this reversal point is corrected by the iterative algorithms based on trajectory simulation to eliminate the energy errors accumulated before the AAP; (2) after the second bank reversal, the AOA is slightly adjusted to track the profile of the reference range to go with respect to energy $s_{\text{go}}^{\text{ref}}(E)$, which is obtained from the last onboard trajectory simulation, in order to null the energy errors accumulated in the AAP. Compared with the iterative algorithms presented in [16], the new iterative algorithms can handle the case that \tilde{E}_{BR2} has a large error, and improve the accuracy of the final altitude by slightly modifying the baseline AOA profile.

13.4.1 Correction of Baseline AOA Profile and Second Bank Reversal

Before entering the AAP, the guidance uses some iterative algorithms based on trajectory simulation to correct the baseline AOA profile and second bank reversal so as to meet the final altitude and speed requirements. As shown in Fig. 13.1, to lighten the burden on the guidance computer, these algorithms are executed twice:

One happens shortly after the first bank reversal occurs, and the other happens about 2 min before the second bank reversal.

Before introducing the iterative algorithms, we show the onboard trajectory simulation first. In the trajectory simulation, the ideal aerodynamic model is roughly modified by considering the current aerodynamic dispersions evaluated by the aerodynamic identification technique, and then Eqs. (13.1–13.6) are integrated numerically with the new guidance as control. The simulation stops when $s_{go}^{(n)} = S_{TAEM}$, or when $V^{(n)} = V_{TAEM}$ and $s_{go}^{(n)} > 100\text{km}$. The latter condition is activated in some extreme cases that the vehicle cannot reach the target. Here, we use the superscript “ (n) ” to represent the ordinal number of the trajectory simulation.

There are three different iterative algorithms used here. The first algorithm is named α_{bsl} -correction algorithm used to slightly adjust α_2 , a parameter of the baseline AOA profile, so as to improve the final altitude accuracy. This algorithm need only conduct the trajectory simulation once. The second algorithm is called reversal-correction algorithm 1 and used to correct \tilde{E}_{BR2} roughly if \tilde{E}_{BR2} has a large error. The third algorithm is termed reversal-correction algorithm 2 and used to correct \tilde{E}_{BR2} slightly but accurately so as to eliminate the final speed error. Note that the simulation termination condition for reversal-correction algorithm 1 is $V^{(n)} = V_{TAEM}$ and $s_{go}^{(n)} > 100\text{km}$, whereas that condition for reversal-correction algorithm 2 is $s_{go}^{(n)} = S_{TAEM}$.

Figure 13.8 shows the process of calling these iterative algorithms. First, if \tilde{E}_{BR2} has a large error, reversal-correction algorithm 1 is called to roughly correct \tilde{E}_{BR2} . Next, α_{bsl} -correction algorithm is called to adjust α_2 so as to improve the final altitude accuracy. Finally, reversal-correction algorithm 2 is called to correct \tilde{E}_{BR2} accurately in order to achieve the desired final speed.

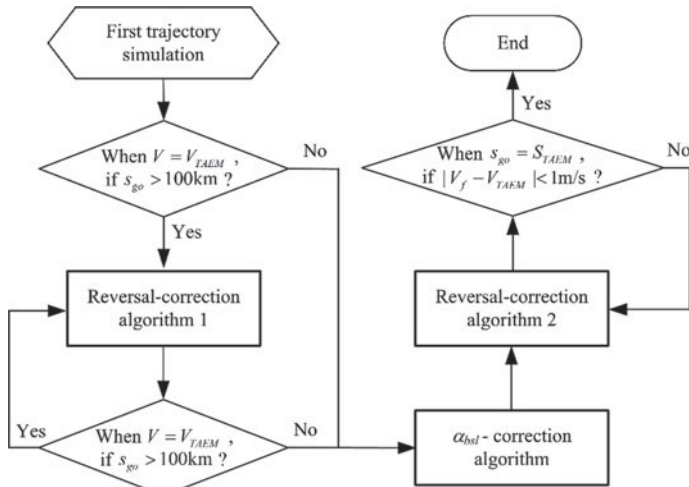


Fig. 13.8 Process of calling the three iterative algorithms

The following shows the details of the three algorithms.

(1) α_{bsl} - correction algorithm

This algorithm need only conduct the trajectory simulation once. Among the simulation results, the final flight path angle $\gamma_f^{(1)}$, final bank angle $\sigma_f^{(1)}$, and change rate of γ are close to zero. Therefore, we can assume that $\cos(\gamma_f^{(1)}) = 1$, $\cos(\sigma_f^{(1)}) = 1$, and $\dot{\gamma}_f^{(1)} = 0$. Then from Eq. (13.5), we get

$$\begin{aligned} \frac{C_{L(\text{est})}\left(\alpha_{\text{bsl}}^{(1)}(E_f^{(1)})\right)q_f^{(1)}S_{\text{ref}}}{m} - g + \frac{(V_f^{(1)})^2}{R_e + H_f^{(1)}} \\ + \omega_e^2(R_e + H_f^{(1)})\cos^2(\phi_f^{(1)}) \\ + \omega_e^2(R_e + H_f^{(1)})\sin(\phi_f^{(1)}) \\ \cos(\phi_f^{(1)})\cos(\psi_f^{(1)}) \\ + 2V_f^{(1)}\omega_e\cos(\phi_f^{(1)})\sin(\psi_f^{(1)}) = 0 \end{aligned} \quad (13.67)$$

where $C_{L(\text{est})}\left[\alpha_{\text{bsl}}^{(1)}(E_f^{(1)})\right]$ is the estimated actual final lift coefficient. However, according to the terminal conditions shown in Sect. 13.2.3, we desire that

$$\begin{aligned} \frac{C_{L(\text{est})}\left(\alpha_{\text{bsl}}^{(2)}(E_{TAEM})\right)q_{TAEM}S_{\text{ref}}}{m} - g + \frac{V_{TAEM}^2}{R_e + H_{TAEM}} \\ + \omega_e^2(R_e + H_{TAEM})\cos^2(\phi_f^{(1)}) \\ + \omega_e^2(R_e + H_{TAEM})\sin(\phi_f^{(1)}) \\ \cos(\phi_f^{(1)})\cos(\psi_f^{(1)}) \\ + 2V_{TAEM}\omega_e\cos(\phi_f^{(1)})\sin(\psi_f^{(1)}) = 0 \end{aligned} \quad (13.68)$$

where $\alpha_{\text{bsl}}^{(2)}$ represents the corrected baseline AOA profile, and q_{TAEM} is determined by V_{TAEM} and H_{TAEM} . Since the altitude is much smaller than the Earth's radius, we assume that $R_e + H_f^{(1)} \approx R_e + H_{TAEM}$. Subtracting Eq. (13.68) from Eq. (13.67) obtains

$$\begin{aligned} & \frac{\left[C_{L(\text{est})}\left(\alpha_{\text{bsl}}^{(1)}(E_f^{(1)})\right) - C_{L(\text{est})}\left(\alpha_{\text{bsl}}^{(2)}(E_{TAEM})\right)\right]q_{TAEM}S_{\text{ref}}}{m} \\ &= \frac{C_{L(\text{est})}\left(\alpha^{(1)}(E_f^{(1)})\right)\left[q_{TAEM} - q_f^{(1)}\right]S_{\text{ref}}}{m} \\ &+ \frac{V_{TAEM}^2 - (V_f^{(1)})^2}{R_e + H_f^{(1)}} \end{aligned}$$

$$+ 2(V_{\text{TAEM}} - V_f^{(1)})\omega_e \cos(\phi_f^{(1)}) \sin(\psi_f^{(1)}) \quad (13.69)$$

Linearize the following term.

$$\begin{aligned} & C_{L(\text{est})}\left(\alpha_{\text{bsl}}^{(1)}(E_f^{(1)})\right) - C_{L(\text{est})}\left(\alpha_{\text{bsl}}^{(2)}(E_{\text{TAEM}})\right) \\ & \approx C_{L(\text{est})}^\alpha \cdot \left[\alpha_{\text{bsl}}^{(1)}(E_f^{(1)}) - \alpha_{\text{bsl}}^{(2)}(E_{\text{TAEM}}) \right] \\ & = C_{L(\text{est})}^\alpha \cdot \left[\alpha_{\text{bsl}}^{(1)}(E_f^{(1)}) - \alpha_{\text{bsl}}^{(1)}(E_{\text{TAEM}}) + \alpha_{\text{bsl}}^{(1)}(E_{\text{TAEM}}) - \alpha_{\text{bsl}}^{(2)}(E_{\text{TAEM}}) \right] \\ & = C_{L(\text{est})}^\alpha \cdot \left[\alpha_{\text{bsl}}^{(1)}(E_f^{(1)}) - \alpha_2^{(1)} - \Delta\alpha_2 \right] \end{aligned} \quad (13.70)$$

where $\alpha_{\text{bsl}}^{(1)}(E_{\text{TAEM}}) = \alpha_2^{(1)}$ and $\Delta\alpha_2 = \alpha_{\text{bsl}}^{(2)}(E_{\text{TAEM}}) - \alpha_{\text{bsl}}^{(1)}(E_{\text{TAEM}})$ is the correction of α_2 . $C_{L(\text{est})}^\alpha$ is the slope of the lift curve corresponding to the modified aerodynamic model. Solving Eqs. (13.69–13.70) for $\Delta\alpha_2$ yields

$$\begin{aligned} \Delta\alpha_2 &= \alpha_{\text{bsl}}^{(1)}(E_f^{(1)}) - \alpha_2^{(1)} + \frac{C_{L(\text{est})}\left(\alpha^{(1)}(E_f^{(1)})\right)[q_f^{(1)} - q_{\text{TAEM}}]}{C_{L(\text{est})}^\alpha q_{\text{TAEM}}} \\ &+ \frac{m[(V_f^{(1)})^2 - V_{\text{TAEM}}^2]}{C_{L(\text{est})}^\alpha q_{\text{TAEM}} S_{\text{ref}}(R_e + H_f^{(1)})} \\ &+ \frac{2m(V_f^{(1)} - V_{\text{TAEM}})\omega_e \cos(\phi_f^{(1)}) \sin(\psi_f^{(1)})}{C_{L(\text{est})}^\alpha q_{\text{TAEM}} S_{\text{ref}}} \end{aligned} \quad (13.71)$$

Thus, we get the corrected parameter of the baseline AOA profile $\alpha_2^{(2)} = \alpha_2^{(1)} + \Delta\alpha_2$.

(2) Reversal-correction algorithm 1

This algorithm is designed to correct the second bank reversal roughly in order to deal with some extreme cases that the vehicle cannot reach its destination. In this algorithm, the stop condition of the trajectory simulation is $V^{(n)} = V_{\text{TAEM}}$ and $s_{\text{go}}^{(n)} > 100\text{km}$. The final range to go for the n -th simulation is denoted as $s_{\text{go}(f)}^{(n)}$. The following analyzes the relationship between \tilde{E}_{BR2} and $s_{\text{go}(f)}^{(n)}$.

If \tilde{E}_{BR2} gets greater, the second bank reversal will occur earlier, which makes the heading error at \tilde{E}_{BR2} decrease. Thus, after this reversal occurs, smaller bank angle is required to eliminate the heading error. This causes L_1/D to increase and thus extends the glide range, which indicates that $s_{\text{go}(f)}^{(n)}$ is reduced.

Due to the above monotonic relation, the secant method [37] is reliable and efficient to solve $s_{\text{go}(f)}(E_{BR2}) = S_{\text{TAEM}}$ for \tilde{E}_{BR2} , as follows

$$\tilde{E}_{BR2}^{(n+1)} = \tilde{E}_{BR2}^{(n)} - (s_{go(f)}^{(n)} - S_{TAEM}) \frac{(\tilde{E}_{BR2}^{(n)} - \tilde{E}_{BR2}^{(n-1)})}{(s_{go(f)}^{(n)} - s_{go(f)}^{(n-1)})} \quad (13.72)$$

Repeat the above process until $s_{go(f)}^{(n)} < 100\text{km}$.

(3) Reversal-correction algorithm 2

This algorithm is used to correct the second bank reversal accurately so as to achieve the desired final speed. In this algorithm, the stop condition of the simulation is $s_{go} = S_{TAEM}$. By similar analysis, we can conclude that V_f is an increasing function of \tilde{E}_{BR2} .

Therefore, reversal-correction algorithm 2 uses the trajectory simulation to predict $V_f^{(n)}$, and then uses the secant method [37] to correct \tilde{E}_{BR2} , as follows

$$\tilde{E}_{BR2}^{(n+1)} = \tilde{E}_{BR2}^{(n)} - (V_f^{(n)} - V_{TAEM}) \frac{(\tilde{E}_{BR2}^{(n)} - \tilde{E}_{BR2}^{(n-1)})}{(V_f^{(n)} - V_f^{(n-1)})} \quad (13.73)$$

Repeat the above process until $|V_f^{(n)} - V_{TAEM}| < 1\text{ m/s}$.

13.4.2 Baseline Bank Angle in AAP

In the AAP, the baseline AOA profile is still in the form of Eq. (13.15), but the parameter α_2 is slightly adjusted using the above iterative algorithms. To eliminate the heading error, the baseline bank angle is determined by PN [16]. As viewed from the AGI frame, the change rate of the azimuth angle of LOS is

$$\dot{\psi}_{LOS} = \frac{\tilde{V}_0 \cos(\tilde{\gamma}_0) \sin(\pi/2 - \tilde{\psi}_0)}{x_{DP}} \quad (13.74)$$

where $x_{DP} = R_e \tilde{\lambda}_P$. The required lateral maneuvering acceleration generated by PN is

$$a_{L2} = k_{PN} \dot{\psi}_{LOS} \tilde{V}_0 \cos(\tilde{\gamma}_0) \quad (13.75)$$

To prevent the initial bank angle from saturation, we let k_{PN} change from 2 to 4, as follows.

$$k_{PN} = 2 \frac{x_{DP}}{x_{BR2}^{BR2}} + 4 \left(1 - \frac{x_{DP}}{x_{BR2}^{BR2}}\right) \quad (13.76)$$

where x_{DP}^{BR2} is the value of x_{DP} at the second bank reversal. Because the forces in the vertical direction are almost balanced, the vertical component of the lift acceleration can be approximated by

$$a_{L1} \approx g - \frac{\tilde{V}_0^2}{R_e + H} \quad (13.77)$$

Then the baseline bank angle is

$$\sigma_{bsl} = \arctan\left(\frac{a_{L2}}{a_{L1}}\right) \quad \text{for } \tilde{E} \leq \tilde{E}_{BR2} + \Delta\tilde{E} \quad (13.78)$$

13.4.3 AOA and Bank Angle Commands in AAP

In the AAP, AOA is an increasing function of L/D. Therefore, as shown in Eq. (13.79), in order to eliminate the errors accumulated in this phase, we adjust the AOA command to track the profile of the reference range to go with respect to energy, which is denoted as $s_{go}^{ref}(E)$ and obtained from the last onboard trajectory simulation,. Since the second bank reversal is close to the destination, the accumulated errors in the AAP are relatively small. Thus the AOA adjustment is small and will not result in a large error in final altitude. The bank angle command is determined by Eq. (13.80), where the second term on the right side is used to suppress the trajectory oscillations.

$$\alpha_{cmd} = \alpha_{bsl} + k_\alpha[s_{go}(E) - s_{go}^{ref}(E)] \quad (13.79)$$

$$\sigma_{cmd} = \sigma_{bsl} - \sin(\sigma_{bsl}) \frac{k_\gamma(\gamma_{SG} - \gamma)}{\alpha_{bsl0}} \quad (13.80)$$

where k_α is a constant. To ensure that the path constraints are satisfied, we also take the measure as

$$\sigma_{cmd} = \begin{cases} \sigma_{max} & \text{if } \sigma_{cmd} > \sigma_{max} \\ -\sigma_{max} & \text{if } \sigma_{cmd} < -\sigma_{max} \end{cases} \quad (13.81)$$

where σ_{max} is the maximum allowable bank angle and determined by Eq. (13.62).

13.5 Results and Discussion

13.5.1 Nominal Cases

Four nominal cases with different flight directions are given to demonstrate that the new entry guidance is capable of steering CAV to any place of the world automatically and accurately, where the initial and terminal conditions are listed in Table 13.1.

The simulation results are shown in Table 13.2 and Figs. 13.9, 13.10, 13.11, 13.12, 13.13 and 13.14. Table 13.2 shows the corrected values of α_2 and the achieved final states of motion, where $s_{go(f)}$ represents the final range to go. The results show that all the missions are successful. Figure 13.9 shows the ground tracks of the trajectories, where we can see that the vehicles fly along four typical directions. Note that in Case 4, the trajectory in high latitude area is stretched and distorted due to the problem of projection. Here we can find a phenomenon that the glide range for flying to the east is longer than the other cases. Figure 13.10 shows the altitude-vs-speed profiles, where we can see that the vehicle has to suffer a high heat load in the high-speed part of flight. Figure 13.11 presents the AOA histories, where we can clearly identify the three phases of the entry flight. Figure 13.12 shows that before the last bank reversal point, the bank angle almost keeps constant, and after the last bank reversal, the bank angle tends to zero gradually. Figure 13.13 and Fig. 13.14 show the histories

Table 13.1 The initial and terminal conditions of the four cases

Case	1	2	3	4
H_0 (km)	80	80	80	80
λ_0 (deg)	0	0	0	0
ϕ_0 (deg)	45	45	45	45
V_0 (m/s)	7000	7000	7000	7000
γ_0 (deg)	0	0	0	0
ψ_0 (deg)	90	180	-110	20
λ_T (deg)	130	0	-90	165
ϕ_T (deg)	0	-50	0	30

Table 13.2 The simulation results of the four cases

Case	1	2	3	4
α_2 (deg)	6.147	6.376	6.583	6.405
$s_{go(f)}$ (km)	50.00	50.00	50.00	50.00
V_f (m/s)	2000.00	2000.00	2000.00	2000.00
H_f (km)	24.98	25.03	25.01	24.97
$\Delta\psi_f$ (deg)	-0.0591	-0.0519	0.1101	0.1084
σ_f (deg)	-2.242	1.802	5.396	3.047

Fig. 13.9 Ground tracks of the entry trajectories

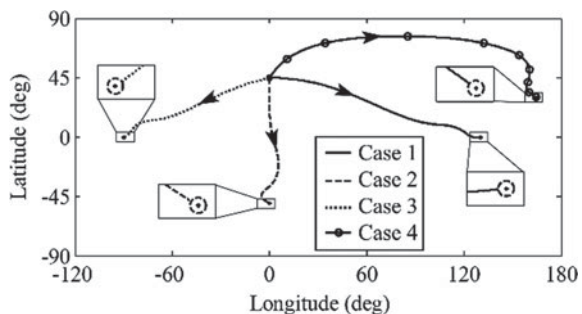


Fig. 13.10 Altitude-vs-speed profiles

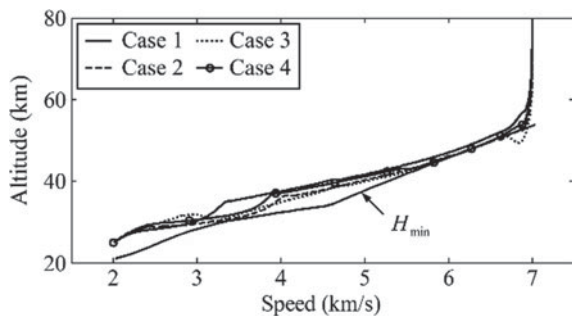


Fig. 13.11 Histories of the AOA

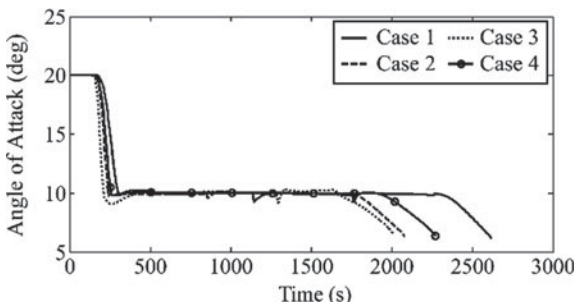


Fig. 13.12 Histories of the bank angle

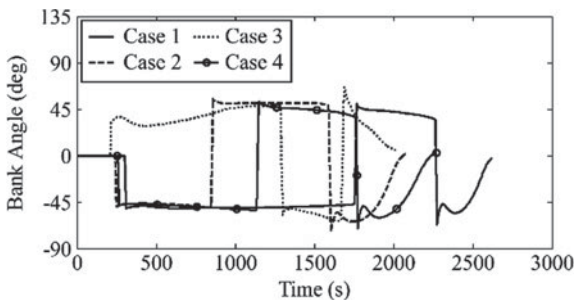


Fig. 13.13 Histories of the heating rate

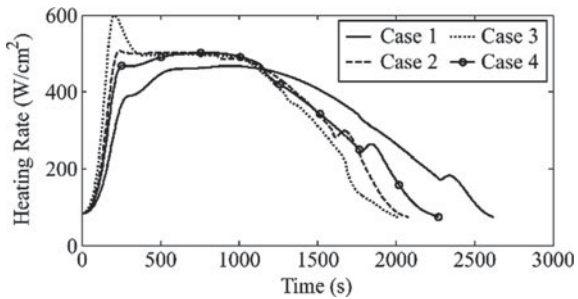
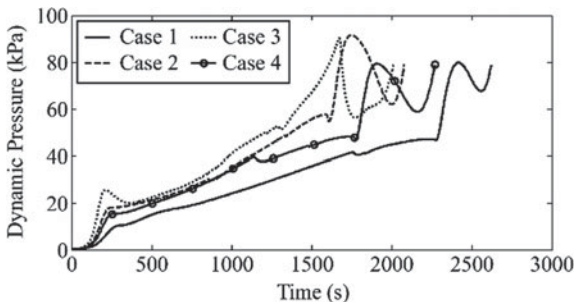


Fig. 13.14 Histories of the dynamic pressure



of the heating rate and dynamic pressure, respectively. As shown in Fig. 13.10 and Fig. 13.13, if the vehicle flies towards the west, the glide altitude is the lowest because the last term on the right side of Eq. (13.5) is negative, which causes that the maximum heating rate is the largest and even exceeds its limitation.

As a comparison, the simulation results of the entry guidance developed in [16] are also provided here. From Table 13.3, we can find that this guidance fails to handle Cases 2 and 3. In these two cases, the angle between \tilde{V} and V , denoted as θ_V , is large, which indicates that the Earth's rotation has noticeable interference effects on the tracking of the reference profiles, whereas the guidance fails to consider these effects adequately. In Cases 1 and 4, θ_V is small. This is because in Case 1, as the vehicle flies to the east, V has almost the same direction as \mathbf{V}_e , the velocity vector due to the

Table 13.3 Simulation results for the guidance developed in [16]

Case	1	2	3	4
α_2 (deg)	6	6	6	6
$s_{go(f)}$ (km)	50.00	50.00	584.59	50.00
V_f (m/s)	2000.00	2752.54	1812.22	2000.00
H_f (km)	24.63	30.75	19.92	24.85
$\Delta\psi_f$ (deg)	- 0.0283	0.9890	40.3666	0.1588
σ_f (deg)	- 0.909	20.025	45.471	4.398

Earth's rotation, and in Case 4, as the vehicle flies over the high latitude region, \mathbf{V}_e is small. Therefore, the guidance handles Cases 1 and 4 successfully. Additionally, by comparing Table 13.2 with Table 13.3, we can find that the achieved final altitudes of the new guidance are more accurate than that of the guidance presented in [16], because α_2 is slightly corrected using the improved iterative algorithms in the new guidance.

13.5.2 Monte Carlo Simulations

To test the robustness of the new entry guidance, the Monte Carlo simulations are conducted here, where the dispersions in initial states, aerodynamic model and atmospheric model are considered. The dispersions in aerodynamic model generally exist in the early flight tests, and the percent deviations of the aerodynamics coefficients vary with AOA and Mach number. For simplicity, we use the following linear dispersion model.

$$\delta_{CL} = \delta_{CL0} + k_{\delta CL}^{\text{Ma}} \frac{\text{Ma} - 15}{17} + k_{\delta CL}^{\alpha} \frac{18}{\pi} \left(\alpha - \frac{\pi}{18} \right) \quad (13.82)$$

$$\delta_{CD} = \delta_{CD0} + k_{\delta CD}^{\text{Ma}} \frac{\text{Ma} - 15}{17} + k_{\delta CD}^{\alpha} \frac{18}{\pi} \left(\alpha - \frac{\pi}{18} \right) \quad (13.83)$$

where δ_{CL} and δ_{CD} are the percent deviations of the lift and drag coefficients, respectively. δ_{CL0} , $k_{\delta CL}^{\text{Ma}}$, $k_{\delta CL}^{\alpha}$, δ_{CD0} , $k_{\delta CD}^{\text{Ma}}$, and $k_{\delta CD}^{\alpha}$ are the related coefficients (Figs. 13.15 and 13.16).

Figure 13.17 show the profile of the maximum possible wind speed and Fig. 13.18 show the profile of the maximum possible percent deviation of the atmospheric density [39–40]. Here, we can see that the maximum possible wind speed is up to 170 m/s and the maximum possible percent deviation of the atmospheric density is up to 50%.

Fig. 13.15 Ground tracks of the trajectories

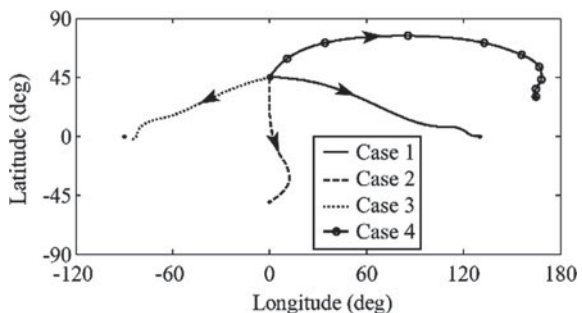


Fig. 13.16 Histories of the bank angle

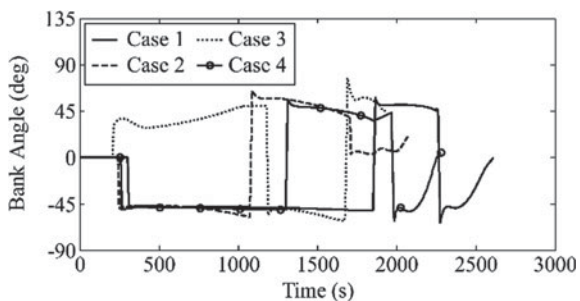


Fig. 13.17 Profile of the maximum possible wind speed

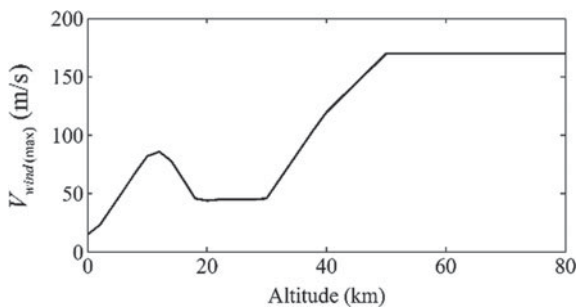
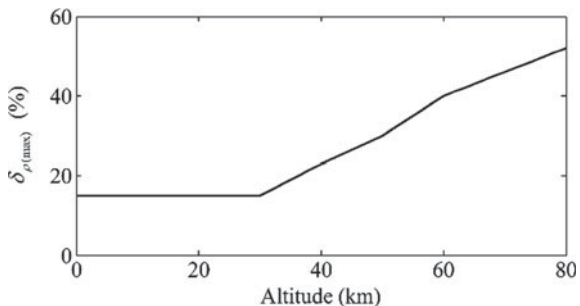


Fig. 13.18 Profile of maximum possible percent deviation of the atmospheric density



We assume that the wind speed and the percent deviation of the atmospheric density are

$$V_{\text{wind}}^{\text{EW}} = k_{\text{wind}}^{\text{EW}} V_{\text{wind}(\text{max})} \quad (13.84)$$

$$V_{\text{wind}}^{\text{NS}} = k_{\text{wind}}^{\text{NS}} V_{\text{wind}(\text{max})} \quad (13.85)$$

$$\delta_{\rho} = k_{\rho} \delta_{\rho(\text{max})} \quad (13.86)$$

Table 13.4 Statistical characteristics of the normally distributed random parameters

Variable	Mean	3TSD	Variable	Mean	3TSD(%)
H_0 (km)	80	3	δ_{CL0}	0	15
λ_0 (deg)	0	0.45	$k_{\delta CL}^{Ma}$	0	10
ϕ_0 (deg)	50	0.45	$k_{\delta CL}^{\alpha}$	0	5
V_0 (m/s)	7000	200	δ_{CD0}	0	15
γ_0 (deg)	0	1	$k_{\delta CD}^{Ma}$	0	10
ψ_0 (deg)	180	1	$k_{\delta CD}^{\alpha}$	0	5
λ_T (deg)	10	0	k_{wind}^{EW}	0	100
ϕ_T (deg)	-50	0	k_{wind}^{NS}	0	100
			k_{ρ}	0	100

where V_{wind}^{EW} represents the wind speed in the east or west direction, V_{wind}^{NS} represents the wind speed in the north or south direction, and δ_{ρ} is the percent deviation of the atmospheric density. k_{wind}^{EW} , k_{wind}^{NS} , and k_{ρ} are the related coefficients between -1 and 1.

The coefficients related to the dispersion models are normally distributed, and their statistical characteristics are shown in Table 13.4, where 3TSD refers to 3 Times Standard Deviation. Although the dispersion models are simple and not in conformity with the actual situation, they are more challenge for the guidance than the real dispersions, because the percent deviation of L/D can be up to $\pm 30\%$ and changes substantially during flight.

In [32], Lu simplified TDCT and applied it to develop the Predictor–Corrector Gliding Guidance (PCGG) for steering CAV. The Monte Carlo simulation results of PCGG are also provided here for comparison. To satisfy the path constraints, we modify PCGG partly: (1) in the descent phase, the modified PCGG adopts the guidance scheme shown in Sect. 13.3.2, and (2) in the glide phase, Eqs. (13.62–13.66) is used to limit the bank angle command.

For convenience, the new entry guidance is abbreviated as OAEG. The simulation programs are written in Matlab programming language. The average computing time per one simulation for OAEG is about 56.16 s, whereas that for PCGG is up to 404.96 s and much longer than that of OAEG. This is because PCGG needs to integrate a reduced-order longitudinal dynamic model numerically in real time.

Figures 13.19 and 13.20 show the ground tracks of the two guidance laws and their local enlarged views near the destination, where we can see that all the trajectories end on the circle centered at the target with radius of 50 km. Figures 13.21 and 13.22 show the altitude-vs-speed profiles of the two guidance laws. From Fig. 13.22, we can see that some trajectories of PCGG have serious oscillations in the low-speed part of flight. This is because the accuracy of γ_{SG} for the simplified TDCT is low and thus the feedback gain of the simplified TDCT has to tend to zero gradually in order not to hinder the tracking of reference, which significantly weakens the capability of suppressing oscillations. Figures 13.23 and 13.24 show the AOA histories,

Fig. 13.19 Ground tracks for OAEG

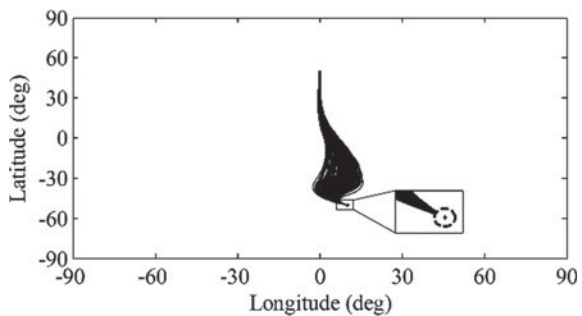


Fig. 13.20 Ground tracks for PCGG

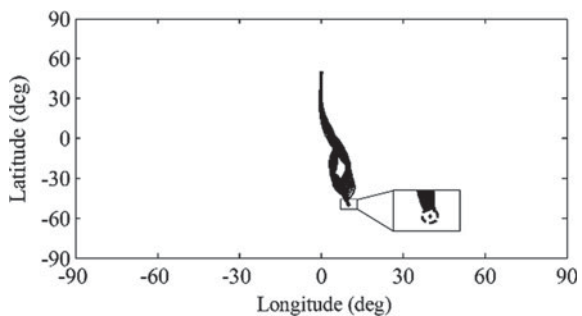


Fig. 13.21 Altitude versus speed histories for OAEG

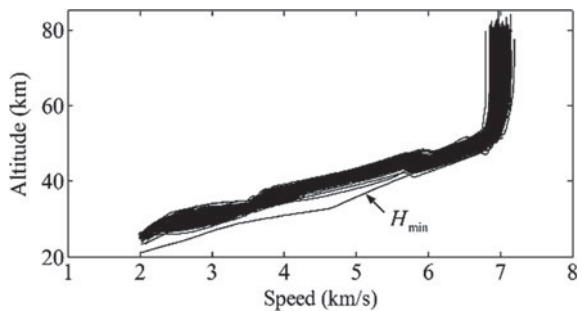


Fig. 13.22 Altitude versus speed histories for PCGG

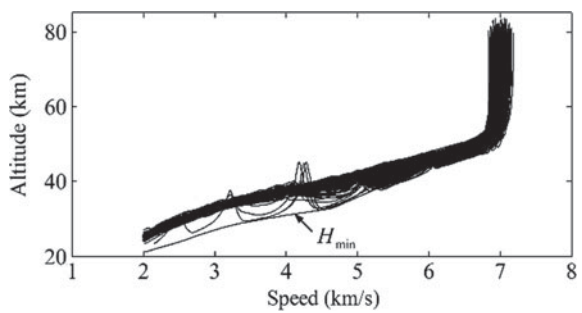


Fig. 13.23 AOA histories for OAEG

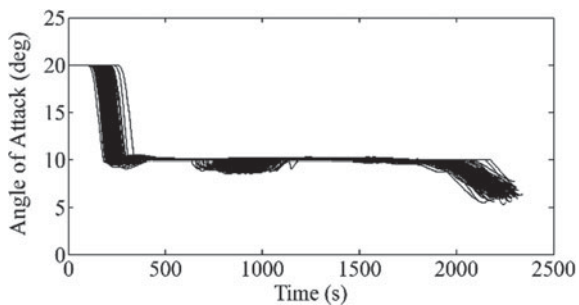
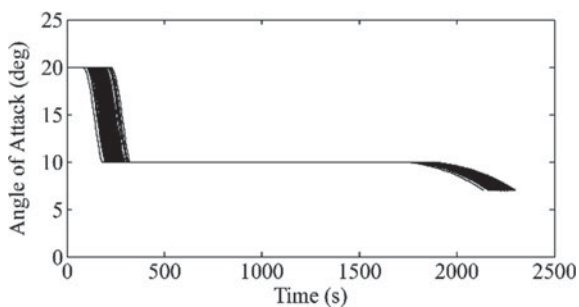


Fig. 13.24 AOA histories for PCGG



where the modified PCGG adopts the baseline AOA profile of OAEG. Figures 13.25 and 13.26 show the bank angle histories, where we can see that OAEG only needs two bank reversals, but PCGG requires 4–7 bank reversals distributing in disorder. Additionally, as expected, the bank angles of OAEG keep almost constant in the SGP and converge to zero gradually in the AAP. Figures 13.27 and 13.28 show the distributions of the final speeds and heading errors, where we can see that although PCGG conducts more bank reversals, the final heading errors for PCGG are much greater than that of OAEG.

Fig. 13.25 Bank angle histories for OAEG

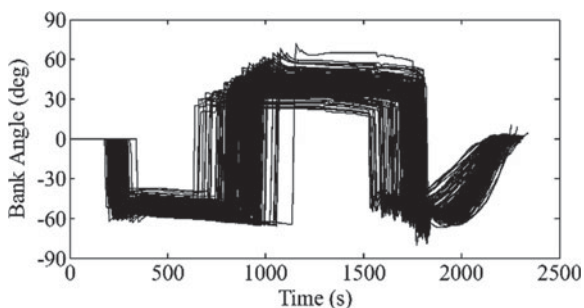


Fig. 13.26 Bank angle histories for PCGG

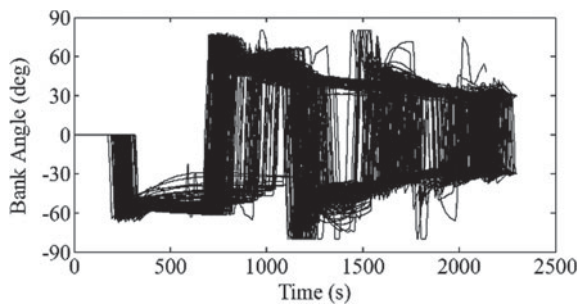


Fig. 13.27 Distribution of final speeds and heading errors for OAEG

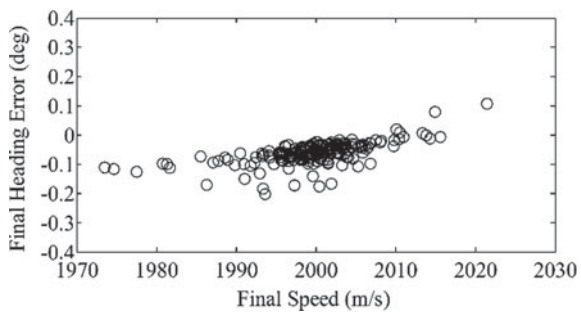
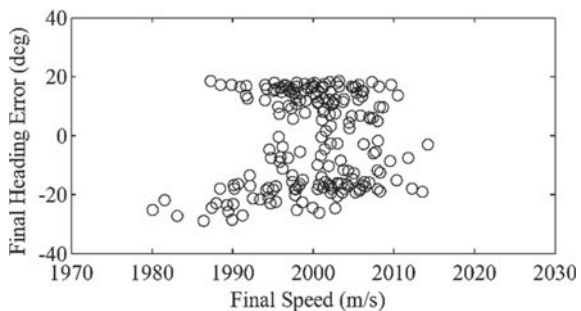


Fig. 13.28 Distribution of final speeds and heading errors for PCGG



13.6 Conclusions

In this paper, we develop the omnidirectional autonomous entry guidance, which can steer the hypersonic glide vehicle with high L/D to any place of the world automatically and accurately. To compensate the effects of the Earth's rotation, the generalized aerodynamic forces are innovatively introduced and used as the reference profiles, which are planned onboard using 3-D analytical glide formulas. As verified by the Monte Carlo simulations, the guidance has a very high accuracy in the presence of large disturbances.

Appendix 1: Generalized States of Motion

Before introducing the way of converting the conventional states of motion $\{\lambda, \phi, H, V, \gamma, \psi\}$ into the generalized states $\{\tilde{\lambda}, \tilde{\phi}, \tilde{H}, \tilde{V}, \tilde{\gamma}, \tilde{\psi}\}$, we need introduce two frames of reference: one is called the Geocentric Equatorial Rotating (GER) frame and the other is called the local North-East-Down (NED) frame [16].

The GER frame is a frame with origin at the Earth's center E . The x_e and y_e axes are in the equatorial plane while the x_e axis intersects with the prime meridian. The z_e axis points towards the north polar. The GER frame rotates together with Earth.

The origin of the NED frame, denoted as o , is at the intersection of the Earth's surface and the segment connecting the Earth's center with the mass center of the vehicle, denoted as M . The x axis points to the local north, the y axis points to the local east, and the z axis points to the Earth's center.

The coordinate transformation matrix from the GER frame to the NED frame can be calculated by

$$\mathbf{T}_{\text{GER}}^{\text{NEDP}} = \begin{bmatrix} -\cos(\lambda) \sin(\phi) & -\sin(\lambda) \sin(\phi) & \cos(\phi) \\ -\sin(\lambda) & \cos(\lambda) & 0 \\ -\cos(\lambda) \cos(\phi) & -\sin(\lambda) \cos(\phi) & -\sin(\phi) \end{bmatrix} \quad (13.87)$$

As shown in Sect. 13.3.3.2, the entry guidance updates the AGI frame once in each guidance cycle and uses the current conventional states to determine the initial generalized states appearing in the analytical glide formulas. Therefore, we have.

$$\tilde{\lambda}_0 = 0, \tilde{\phi}_0 = 0, \tilde{H}_0 = H \quad (13.88)$$

$\tilde{\mathbf{V}}$ and \mathbf{V} are the velocity vectors of the vehicle relative to the AGI frame and the rotating Earth, respectively. Since the AGI frame is an inertial frame, $\tilde{\mathbf{V}}$ is equal to the sum of \mathbf{V} and the velocity vector due to the Earth's rotation, as follows.

$$\tilde{\mathbf{V}}_0^{\text{NED}} = [V \cos(\gamma) \cos(\psi) \ V \cos(\gamma) \sin(\psi) + \omega_e(R_e + H) \cos(\phi) \ -V \sin(\gamma)]^T \quad (13.89)$$

where the superscript “NED” means the coordinates are with respect to the NED frame, and the superscript “ T ” represents the transform of vector or matrix. According to the definitions of the generalized states of motion shown in Sect. 13.3.3.2, from Eq. (13.86), we have

$$\tilde{V}_0 = \sqrt{V^2 + 2V\omega_e(R_e + H) \cos(\phi) \cos(\gamma) \sin(\psi) + \omega_e^2(R_e + H)^2 \cos^2(\phi)} \quad (13.90)$$

$$\tilde{\gamma}_0 = \arcsin\left(\frac{V \sin(\gamma)}{\tilde{V}_0}\right) \quad (13.91)$$

$$\tilde{\psi}_0 = \begin{cases} \arccos\left(\frac{\tilde{\mathbf{z}}^{\text{GER}} \cdot \tilde{\mathbf{V}}_{H0}^{\text{GER}}}{\|\tilde{\mathbf{V}}_{H0}^{\text{GER}}\|}\right); & (\tilde{\mathbf{V}}_{H0}^{\text{GER}} \times \tilde{\mathbf{z}}^{\text{GER}}) \cdot \tilde{\mathbf{x}}^{\text{GER}} \geq 0 \\ -\arccos\left(\frac{\tilde{\mathbf{z}}^{\text{GER}} \cdot \tilde{\mathbf{V}}_{H0}^{\text{GER}}}{\|\tilde{\mathbf{V}}_{H0}^{\text{GER}}\|}\right); & (\tilde{\mathbf{V}}_{H0}^{\text{GER}} \times \tilde{\mathbf{z}}^{\text{GER}}) \cdot \tilde{\mathbf{x}}^{\text{GER}} < 0 \end{cases} \quad (13.92)$$

where $\tilde{\mathbf{V}}_{H0}^{\text{GER}}$ is the horizontal component of $\tilde{\mathbf{V}}_0^{\text{GER}}$ and calculated by the following equations, and $\tilde{\mathbf{x}}^{\text{GER}}$ and $\tilde{\mathbf{z}}^{\text{GER}}$ are the unit vectors along the positive directions of the \tilde{x} - and \tilde{z} -axes of the AGI frame, respectively. The superscript “GER” represents the coordinates are with respect to the GER frame.

$$\tilde{\mathbf{V}}_{H0}^{\text{GER}} = (\mathbf{T}_{\text{GER}}^{\text{NED}})^T \tilde{\mathbf{V}}_{H0}^{\text{NED}} \quad (13.93)$$

$$\tilde{\mathbf{V}}_{H0}^{\text{NED}} = \begin{bmatrix} V \cos(\gamma) \cos(\psi) \\ V \cos(\gamma) \sin(\psi) + \omega_e (R_e + H) \cos(\phi) \\ 0 \end{bmatrix} \quad (13.94)$$

Now we determine the desired final generalized states of motion. As the dot product of two unit vectors is just equal to the cosine of the angle between the two vectors, the generalized longitude, latitude, and altitude of the predicted collision point P , as shown in Fig. 13.4, can be calculated by.

$$\tilde{\lambda}_P = \arccos(\hat{\mathbf{x}}_{EP}^{\text{GER}} \cdot \tilde{\mathbf{x}}^{\text{GER}}), \tilde{\phi}_P = 0, \tilde{H}_P = H_T \quad (13.95)$$

where $\hat{\mathbf{x}}_{EP}^{\text{GER}}$ is the unit vector pointing from E to P , and $\tilde{\mathbf{x}}^{\text{GER}}$ is the unit vector along the \tilde{x} -axis of the AGI frame.

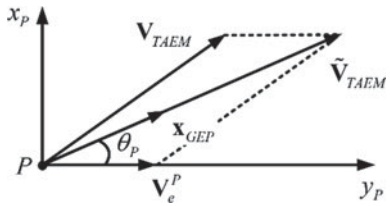
The desired final generalized speed is denoted as \tilde{V}_{TAEM} . Apparently, due to the effect of the Earth’s rotation, there are $\tilde{V}_{\text{TAEM}} \neq V_{\text{TAEM}}$. As shown in Fig. 13.4, since the vehicle flies to the point P approximately along the generalized equator, we assume that the desired final generalized velocity vector $\tilde{\mathbf{V}}_{\text{TAEM}}$ is parallel to the generalized equator, where the unit vector along the generalized equator at the point P , denoted as \mathbf{x}_{GEP} , can be calculated using the following equations.

$$\mathbf{x}_1^{\text{GER}} = \hat{\mathbf{x}}_{EP}^{\text{GER}} - \tilde{\mathbf{x}}^{\text{GER}} \quad (13.96)$$

$$\mathbf{x}_2^{\text{GER}} = \mathbf{x}_1^{\text{GER}} - (\mathbf{x}_1^{\text{GER}} \cdot \hat{\mathbf{x}}_{EP}^{\text{GER}}) \hat{\mathbf{x}}_{EP}^{\text{GER}} \quad (13.97)$$

$$\mathbf{x}_{GEP}^{\text{GER}} = \frac{\mathbf{x}_2^{\text{GER}}}{\|\mathbf{x}_2^{\text{GER}}\|} \quad (13.98)$$

Fig. 13.29 $\tilde{\mathbf{V}}_{\text{TAEM}}$ is assumed to be tangent to the generalized equator



$$\mathbf{x}_{GEP}^{\text{NEDP}} = \mathbf{T}_{\text{GER}}^{\text{NEDP}} \mathbf{x}_{GEP}^{\text{GER}} \quad (13.99)$$

where the superscript “NEDP” represents the NED frame at the point P , and $\mathbf{T}_{\text{GER}}^{\text{NEDP}}$ is the transform matrix from the GER frame to the NEDP frame (Fig. 13.29).

\mathbf{V}_e^P is the velocity vector due to the Earth’s rotation at the point P . \mathbf{V}_e^P points towards the local East and has a magnitude of

$$V_e^P = \omega_e (R_e + H_{\text{TAEM}}) \cos(\phi_P) \quad (13.100)$$

Using the assumption that $\tilde{\mathbf{V}}_{\text{TAEM}}$ is parallel to \mathbf{x}_{GEP} , we have

$$\tilde{\mathbf{V}}_{\text{TAEM}} = \tilde{V}_{\text{TAEM}} \mathbf{x}_{GEP} \quad (13.101)$$

$$\cos(\theta_P) = \mathbf{x}_{GEP}^{\text{NEDP}}|_y \quad (13.102)$$

Then we have

$$(\tilde{\mathbf{V}}_{\text{TAEM}} - \mathbf{V}_e^P)^2 = (\mathbf{V}_{\text{TAEM}})^2 \quad (13.103)$$

Expanding the above equation yields

$$\tilde{V}_{\text{TAEM}}^2 - 2\tilde{V}_{\text{TAEM}} V_e^P \cos(\theta_P) + (V_e^P)^2 = V_{\text{TAEM}}^2 \quad (13.104)$$

Solving the above equation for \tilde{V}_{TAEM} yields

$$\tilde{V}_{\text{TAEM}} = V_e^P \cos(\theta_P) + \sqrt{(V_e^P)^2 (\cos^2(\theta_P) - 1) + V_{\text{TAEM}}^2} \quad (13.105)$$

Further, the desired final absolute specific energy can be calculated by

$$\tilde{E}_{\text{TAEM}} = \frac{\tilde{V}_{\text{TAEM}}^2}{2} - \frac{\mu}{R_e + H_{\text{TAEM}}} \quad (13.106)$$

Appendix 2: Generalized Aerodynamic Forces

In this appendix, we show the relationship between the conventional aerodynamic forces $\{L_1, L_2, D\}$ and the generalized aerodynamic forces $\{\tilde{L}_1, \tilde{L}_2, \tilde{D}\}$. To reduce the complexity of derivation, we assume that $\gamma = 0$. In Fig. 13.30, \mathbf{V}_e is the velocity vector due to the Earth's rotation and θ_V is the angle between $\tilde{\mathbf{V}}$ and \mathbf{V} , which can be calculated by

$$\sin(\theta_V) = \frac{(\mathbf{V} \times \tilde{\mathbf{V}}) \cdot \tilde{\mathbf{z}}}{||\mathbf{V}|| \cdot ||\tilde{\mathbf{V}}||} = \frac{\omega_e(R_e + H) \cos(\psi) \cos(\phi)}{\tilde{V}_0} \quad (13.107)$$

From Fig. 13.30, we have

$$L_1 = \tilde{L}_1 \quad (13.108)$$

$$L_2 = \tilde{L}_2 \cos(\theta_V) - \tilde{D} \sin(\theta_V) \quad (13.109)$$

$$D = \tilde{D} \cos(\theta_V) + \tilde{L}_2 \sin(\theta_V) \quad (13.110)$$

Then we can convert $\widetilde{L_1/D}$ and $\widetilde{L_2/D}$ into L_1/D and L_2/D , as follows

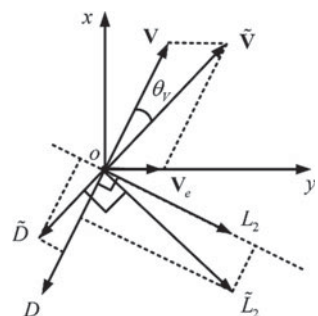
$$L_1/D = \frac{\widetilde{L_1/D}}{\cos(\theta_V) + \widetilde{L_2/D} \sin(\theta_V)} \quad (13.111)$$

$$L_2/D = \frac{\widetilde{L_2/D} \cos(\theta_V) - \sin(\theta_V)}{\cos(\theta_V) + \widetilde{L_2/D} \sin(\theta_V)} \quad (13.112)$$

Conversely, we can also convert L_1/D and L_2/D into $\widetilde{L_1/D}$ and $\widetilde{L_2/D}$, as follows

$$\widetilde{L_1/D} = \frac{L_1/D}{\cos(\theta_V) - \sin(\theta_V)L_2/D} \quad (13.113)$$

Fig. 13.30 Relationship between the conventional and generalized aerodynamic forces



$$\widetilde{L_2/D} = \frac{\cos(\theta_V)L_2/D + \sin(\theta_V)}{\cos(\theta_V) - \sin(\theta_V)L_2/D} \quad (13.114)$$

Now we investigate the relationship between L/D and $\widetilde{L/D}$. From Eqs. (13.107–13.108), we have

$$L/D = \frac{\sqrt{\left(\widetilde{L_1/D}\right)^2 + \left(\widetilde{L_2/D} \cos(\theta_V) - \sin(\theta_V)\right)^2}}{\cos(\theta_V) + \widetilde{L_2/D} \sin(\theta_V)} \quad (13.115)$$

From Eqs. (13.109–13.110), we have

$$\widetilde{L/D} = \frac{\sqrt{(L_1/D)^2 + (L_2/D \cos(\theta_V) + \sin(\theta_V))^2}}{\cos(\theta_V) - L_2/D \sin(\theta_V)} \quad (13.116)$$

Because θ_V is near zero, we approximate the numerator of Eq. (13.112) by the first-order Taylor series at $\theta_V = 0$, as follows

$$\widetilde{L/D} \approx \frac{L/D + \sin(\sigma)\theta_V}{\cos(\theta_V) - L/D \sin(\sigma) \sin(\theta_V)} \quad (13.117)$$

Thus, we get the approximation relation between L/D and $\widetilde{L/D}$.

References

1. Phillips T.H. A common aero vehicle (CAV) model, description, and employment guide. Schafer Corporation for AFRL and AFSPC. (2003)
2. Xiong, S., Wang, W., Liu, X., et al.: Guidance law against maneuvering targets with intercept angle constraint. ISA Trans. **53**(4), 1332–1342 (2014)
3. Yu, W., Chen, W.: Trajectory-shaping guidance with final speed and load factor constraints. ISA Trans. **56**, 42–52 (2015a)
4. Wang, X., Zhang, Y., Wu, H.: Sliding mode control based impact angle control guidance considering the seeker's field-of-view constraint. ISA Trans. **61**, 49–59 (2016)
5. Harpold, J.C., Graves, C.A.: Shuttle Entry Guidance. NASA Lyndon B. Johnson Space Center, Houston (1979)
6. Eggers, A.J., Allen, H.J., Neice, S.E. A Comparative Analysis of the Performance of Long-range Hypervelocity Vehicles. National Advisory Committee for Aeronautics. (1957)
7. Gazley, C. Atmospheric entry. The RAND Corporation (1960)
8. Lees, L., Hastwig, F.W., Cohen, C.B.: Use of aerodynamic lift during entry into the earth's atmosphere. ARS J. **29**(9), 633–641 (1959)
9. Ting, L., Wang, K.: An approximate analytic solution of re-entry trajectory with aerodynamic forces. ARS J. **30**(6), 565–566 (1960)
10. Loh, W.H.T.: Dynamics and Thermodynamics of Planetary Entry. Prentice Hall, Englewood Cliffs (1963a)
11. Loh, W.H.T.: Some exact analytical solutions of planetary entry. AIAA J. **1**(4), 836–842 (1963b)

12. Cohen, M. Some Closed Form Solutions to the Problem of Re-entry of Lifting and Non-lifting Vehicles//2nd Aerospace Sciences Meeting. New York, p. 46. (1965)
13. Nyland, F.S. Hypersonic turning with constant bank angle control. The RAND Corporation. (1965)
14. Bell, R.N. A closed-form solution to lifting reentry. Defense Technical Information Center. (1965)
15. Chen, S.Y. The longitudinal and lateral range of hypersonic glide vehicles with constant bank angle. The RAND Corporation. (1966)
16. Yu, W., Chen, W.: Entry guidance with real-time planning of reference based on analytical solutions. *Adv. Space Res.* **55**(9), 2325–2345 (2015b)
17. Hanson, J.M., Coughlin, D.J., Dukeman, G. et al. Ascent, Transition, Entry, and Abort Guidance Algorithm Design for the X-33 Vehicle//Guidance, Navigation, and Control Conference and Exhibit. Boston. 4409 (1998)
18. Mease, K.D., Chen, D.T., Teufel, P., et al.: Reduced-order entry trajectory planning for acceleration guidance. *J. Guidance, Control, Dyn.* **25**(2), 257–266 (2002)
19. Dukeman, G.A. Profile-following Entry Guidance Using Linear Quadratic Regulator Theory//AIAA Guidance, Navigation, and Control Conference and Exhibit. Monterey. 4457 (2002)
20. Shen, Z., Lu, P.: On-board generation of three-dimensional constrained entry trajectories. *J. Guidance, Control, Dyn.* **26**(1), 111–121 (2003)
21. Zhang, Y.L., Chen, K.J., Liu, L., et al.: Entry trajectory planning based on three-dimensional acceleration profile guidance. *Aerospace Sci. Technol.* **48**, 131–139 (2016)
22. Powell, R.W.: Six-degree-of-freedom guidance and control-entry analysis of the HL-20. *J. Spacecraft Rockets* **30**(5), 537–542 (1993)
23. Graesslin, M.H., Telaar, J., Schottle, U.M.: Ascent and reentry guidance concept based on NLP-methods. *Acta Astronaut.* **55**(3–9), 461–471 (2004)
24. Zimmerman, C., Dukeman, G., Hanson, J.: Automated method to compute orbital reentry trajectories with heating constraints. *J. Guidance, Control, Dyn.* **26**(4), 523–529 (2003)
25. Xie, Y., Liu, L., Tang, G., et al.: Highly constrained entry trajectory generation. *Acta Astronaut.* **88**, 44–60 (2013)
26. Zhao, J., Zhou, R.: Reentry trajectory optimization for hypersonic vehicle satisfying complex constraints. *Chin. J. Aeronaut.* **26**(6), 1544–1553 (2013)
27. Xu, B., Wang, D., Sun, F., et al.: Direct neural discrete control of hypersonic flight vehicle. *Nonlinear Dyn.* **70**(1), 269–278 (2012)
28. Bu, X., Wu, X., Zhu, F., et al.: Novel prescribed performance neural control of a flexible air-breathing hypersonic vehicle with unknown initial errors. *ISA Trans.* **59**, 149–159 (2015)
29. Shao, X., Wang, H.: Active disturbance rejection based trajectory linearization control for hypersonic reentry vehicle with bounded uncertainties. *ISA Trans.* **54**, 27–38 (2015)
30. Tian, B., Fan, W., Zong, Q.: Integrated guidance and control for reusable launch vehicle in reentry phase. *Nonlinear Dyn.* **80**(1–2), 397–412 (2015)
31. Zhao, J., Zhou, R.: Pigeon-inspired optimization applied to constrained gliding trajectories. *Nonlinear Dyn.* **82**(4), 1781–1795 (2015)
32. Lu, P.: Entry guidance: a unified method. *J. Guidance, Control, Dyn.* **37**(3), 713–728 (2014)
33. Yu, W., Chen, W. Guidance Scheme for Glide Range Maximization of a Hypersonic Vehicle//AIAA Guidance, Navigation, and Control Conference. Portland. 6714 (2011)
34. Kermode, A.C.: Mechanics of Flight, 11th edn. Prentice Hall, London (2006)
35. Hu, J., Li, J., Chen, W. Longitudinal Characteristics of Steady Glide Trajectory for Hypersonic Vehicle//IEEE International Conference on Control, Automation and Information Sciences. Changshu. 272–279 (2015)
36. Chowdhary, G., Jategaonkar, R.: Aerodynamic parameter estimation from flight data applying extended and unscented Kalman filter. *Aerospace Sci. Technol.* **14**(2), 106–117 (2010)
37. Burden, R.L., Faires, J.D.: Numerical Analysis, 9th edn. Cengage Learning, Boston (2010)
38. Zarchan, P. Tactical and Strategic Missile Guidance, 5th ed. AIAA Progress in Aeronautics and Astronautics (2007)

39. Kidiyarova, V.G., Tarasenko, D.A., Schereia, I.A. Influence of Longitudinal Variations of the Structure of the Temperature, Pressure and Wind Fields in the Stratosphere and Mesosphere of the Northern Hemisphere//16 th COSPAR Plenary Meeting. Konstanz. (1973)
40. Zeilik, M.A., Gregory, S.A. Introductory Astronomy and Astrophysics, 4th ed. Saunders College Publishing (1998)

Chapter 14

Analytical Steady-Gliding Guidance Employing Pseudo-Aerodynamic Profiles



14.1 Introduction

Common Aero Vehicle (CAV) [1] is a Hypersonic Glide Vehicle (HGV) featuring a hypersonic-L/D of up to 3, whereas the in-flight L/Ds of the space shuttle and X-33 Reusable Launch Vehicle (RLV) are only about 1. The high L/D allows CAV to travel more than 10, 000 km and cover crossrange of thousands of kilometers. The entry phase is the longest and most critical flight phase of CAV, where the vehicle glides in the atmosphere with altitude of 20 to 100 km. In this phase, the Mach number (Ma) is initially as high as 20 and then reduces to about 6 gradually. One of the main challenges for CAV is the design of highly constrained entry guidance because: (1) different from homing guidance [2, 3], entry guidance needs to dissipate the flight energy by performing proper lateral maneuvers as well as guiding the vehicle to destination; (2) the entry corridor is very narrow as the Thermal Protection System (TPS), Flight Control System (FCS), and lightweight structure have harsh requirements on flight environment; (3) the entry trajectory of CAV has under-damped, phugoid natural oscillations due to the high L/D, which will seriously deteriorate the stress and thermal environments and interfere with the tracking of reference profiles.

Shuttle entry guidance [4] is the first guidance that has been successfully applied in lifting atmospheric entry missions. The key to its success is to use bank angle, instead of AOA, as the major means to manage the energy of motion, because there exists a clear, monotonous relation between drag and bank angle, i.e., greater bank angle tends to decrease glide altitude and thus increase atmospheric density, which then results in an increase in drag. The guidance has four parts: (1) Determine the entry corridor satisfying all path constraints, (2) plan a reference trajectory meeting terminal requirements in the corridor, (3) modulate the magnitude of the bank angle to track the reference trajectory, and (4) design a threshold to reverse the bank angle

Reprinted from Aerospace Science and Technology, Vol 66, Yu Wenbin, Chen Wanchun, Jiang Zhiguo, Zhou Hao, Liu Xiaoming, Liu Ming, Analytical entry guidance based on pseudo-aerodynamic profiles, Pages 315-331, Copyright (2017), with permission from Elsevier.

timely so as to eliminate heading error. These four parts makes up the skeleton of all lifting entry guidance laws [4–16]. Mease et al. developed a method for planning drag and lateral acceleration profiles using reduced-order entry dynamics [5]. However, these two profiles cannot be tracked simultaneously if there are large disturbances, especially in the case that the actual L/D is smaller than its ideal value. In practice, only the drag profile will be closely tracked and the tracking errors of the lateral acceleration profile will be offset by properly adjusting the bank reversals. Dukeman et al. [6] designed a reference-following scheme by only considering the longitudinal motion. In this scheme, the Linear-Quadratic Regulator (LQR) is applied to simultaneously track the reference profiles of altitude, range to go, and flight-path angle. Monte Carlo simulations were conducted to demonstrate the good performance of the scheme. Shen et al. [7] converted the path constraints into the bank angle limitation and then employed trajectory simulation to directly plan the reference profile of bank angle. Zhang et al. [8] modified the method presented in [5] for planning 3-D acceleration profiles, where AOA as well as bank angle are used to track the planned profiles. However, this method is further challenged by a problem that the aerodynamic uncertainties are sensitive to AOA and changes unpredictably with it. Zhao and Zhou [9] applied the pigeon-inspired optimization to generate the reference entry trajectory and proposed a reversal logic for calculating footprint roughly. In predictor-corrector entry guidance laws [10, 11], the onboard trajectory simulation is applied to predict the final states in real time and then the secant method is used to properly adjust the control profiles by comparing the predicted and desired final states, where the control profiles are generally parameterized in order to reduce the computing complexity. As a large amount of trajectory simulations is conducted, these guidance laws have high accuracy but require very heavy computational loads. In [12, 13], the entry trajectory planning problems with the no-fly-zone constraints were studied.

Compared with the mid-L/D space shuttle and X-33 RLV, the entry-guidance design for CAV faces more severe challenges. As the L/D of CAV is up to 3, the trajectory of CAV has poor damped, phugoid oscillations [14, 15], which have three detrimental effects: (1) The stress and thermal loads suffered by the vehicle get very large and are likely to exceed their limits at the bottoms of the oscillated trajectory, (2) if there are large disturbances, the resulting tracking errors cannot be removed at the oscillation peaks because the drag is almost zero due to the thin atmosphere and thus has no margin for adjustment, and (3) the autopilot becomes inefficient to follow the guidance commands at the altitude peaks also because of the very tiny atmospheric density. However, the conventional entry guidance laws [4–13] cannot eliminate the oscillations. Thus, they fail to steer the high-L/D CAV safely and reliably. In [15], Yu and Chen found that the vehicle's vertical motion can be analogous to that of a nonlinear, underdamped oscillator and then proposed an effective technique termed Trajectory Damping Control Technique (TDCT) for enhancing the damping. By adopting the TDCT, two entry guidance laws [14, 16] were developed for steering CAV. The guidance law shown in [14] is a predictor-corrector guidance with the assistance of a simplified TDCT and denoted as PCGG. The simulation results show that PCGG has a low accuracy of the final heading error, which sometimes can be

greater than 20 deg. In [16], Yu and Chen obtained 3-D analytical glide formulas, which fully consider the effects of the Earth's curvature but neglect that of the Earth's rotation, and then designed an autonomous entry guidance denoted as EGAS using these formulas to real-time plan reference profiles. To compensate the effects of the Earth's rotation, some measures based on generalized longitude and latitude were proposed by observing the vehicle's motion from the inertial space. However, after in-depth study, we find that EGAS fails in some special cases, especially if the vehicle flies across the equator in north or south direction, because the Earth rotation effects are substantial under these circumstances but EGAS fails to fully compensate them.

This chapter is aimed at developing a high-precision entry guidance capable of steering the high-L/D CAV to any place on the Earth safely and reliably. The guidance is also based on the analytical glide formulas [16]. Different from [16], the entry flight is always observed from the rotation Earth. To compensate the Earth rotation effects, pseudo-aerodynamic forces are introduced as the combinations of the aerodynamic and inertial forces, and their profiles are used as the reference profiles. To avoid drastic changes in commands, we need carefully forecast the change trends of the inertial forces. However, this is quite difficult because the remaining states of motion are unknown yet. Thus, under the circumstance of steady glide [17], we have to simplify the relation between the conventional and pseudo aerodynamic forces by neglecting small terms and properly using the linearization technique. After that, we find that the pseudo-aerodynamic profiles for constant angles of attack and bank can be well approximated by inversely proportional functions. Subsequently, on the basis of the existing work [16], we derive new 3-D analytical glide formulas for the inversely-proportional pseudo-aerodynamic profiles, and then use the new formulas to plan these profiles. In addition, the TDCT [15] is utilized here to suppress the trajectory oscillations. As verified by a large amount of trajectory simulations, the guidance can compensate the Earth rotation effects completely and achieve a high accuracy even in the presence of large disturbances. Meanwhile, as expected, the AOA and bank angle remain almost constant during the steady glide phase, the major phase of entry flight.

The chapter is structured as: Sect. 14.2 describes the entry guidance problem; Sect. 14.3 develops the analytical entry guidance based on the pseudo-aerodynamic profiles; Sect. 14.4 demonstrates the guidance performance by providing sufficient examples; Sect. 14.5 draws the conclusions; References are listed finally.

14.2 Entry Guidance Problem

14.2.1 Equations of Motion

The equations of motion for entry flight considering the effects of the Earth's curvature and rotation [16] are

$$\frac{d\lambda}{dt} = \frac{V \cos(\gamma) \sin(\psi)}{(R_e + H) \cos(\phi)} \quad (14.1)$$

$$\frac{d\phi}{dt} = \frac{V \cos(\gamma) \cos(\psi)}{(R_e + H)} \quad (14.2)$$

$$\frac{dH}{dt} = V \sin(\gamma) \quad (14.3)$$

$$\begin{aligned} \frac{dV}{dt} = & -\frac{D}{m} - g \sin(\gamma) + \omega_e^2 (R_e + H) \cos^2(\phi) \sin(\gamma) \\ & - \omega_e^2 (R_e + H) \sin(\phi) \cos(\phi) \cos(\gamma) \cos(\psi) \end{aligned} \quad (14.4)$$

$$\begin{aligned} \frac{d\gamma}{dt} = & \frac{1}{V} \left[\frac{L \cos(\sigma)}{m} - g \cos(\gamma) + \frac{V^2 \cos(\gamma)}{R_e + H} \right. \\ & + \omega_e^2 (R_e + H) \cos^2(\phi) \cos(\gamma) + 2V \omega_e \cos(\phi) \sin(\psi) \\ & \left. + \omega_e^2 (R_e + H) \sin(\phi) \cos(\phi) \sin(\gamma) \cos(\psi) \right] \end{aligned} \quad (14.5)$$

$$\begin{aligned} \frac{d\psi}{dt} = & \frac{1}{V} \left[\frac{L \sin(\sigma)}{m \cos(\gamma)} + \frac{V^2 \cos(\gamma) \sin(\psi) \tan(\phi)}{R_e + H} \right. \\ & - \frac{\omega_e^2 (R_e + H) \sin(\phi) \cos(\phi) \sin(\psi)}{\cos(\gamma)} \\ & \left. + 2V \omega_e \sin(\phi) - 2V \omega_e \cos(\phi) \tan(\gamma) \cos(\psi) \right] \end{aligned} \quad (14.6)$$

where λ is the longitude, ϕ is the latitude, H is the altitude, V is the speed relative to the rotating Earth, γ is the flight-path angle, ψ is the heading angle measured clockwise from the local north, m is the mass, σ is the bank angle, g is the gravitational acceleration, R_e is the average radius of Earth, ω_e is the rotation rate of Earth, L is the lift, and D is the drag.

14.2.2 Path Constraints

Due to the limitations of TPS, FCS, and lightweight structure, the entry trajectory of CAV is constrained by heating rate \dot{Q} , dynamic pressure q and load factor n , as follows

$$\dot{Q} = k_Q \sqrt{\rho(H)} V^{3.15} \leq \dot{Q}_{\max} \quad (14.7)$$

$$q = \frac{1}{2} \rho(H) V^2 \leq q_{\max} \quad (14.8)$$

$$n = \frac{L}{mg_0} \leq n_{\max} \quad (14.9)$$

where \dot{Q}_{\max} , q_{\max} , and n_{\max} are the maximum allowable values of \dot{Q} , q , and n , respectively. k_Q is a constant, and g_0 is the gravitational acceleration at sea level. In addition, considering the limited capacity of FCS, we restrain the change rates of the AOA and bank angle by $|\dot{\alpha}| \leq 4\text{deg/s}$, $|\ddot{\alpha}| \leq 16\text{deg/s}^2$, $|\dot{\sigma}| \leq 8\text{deg/s}$, and $|\ddot{\sigma}| \leq 40\text{deg/s}^2$.

14.2.3 Terminal Conditions

The entry phase ends when the range to go reduces to 50 km, i.e. $s_{\text{go}} = S_{\text{TAEM}} = 50\text{km}$. At this moment, the desired conditions are $|\Delta\psi_{\text{TAEM}}| \leq 5\text{ deg}$, $V_{\text{TAEM}} = 2000\text{ m/s}$, $H_{\text{TAEM}} = 25\text{km}$, and $|\sigma_{\text{TAEM}}| \leq 30\text{ deg}$, where $\Delta\psi_{\text{TAEM}}$, V_{TAEM} , H_{TAEM} , and σ_{TAEM} are the desired final heading error, speed, altitude, and bank angle, respectively. Note that the subscript “TAEM” is widely used to represent the required conditions of Reusable Launch Vehicle (RLV) for Terminal Area Energy Management, and therefore it is also used here to represent the desired terminal conditions of CAV in the entry phase.

14.3 Analytical Entry Guidance Design

As shown in Fig. 14.1, in consideration of the entry trajectory characteristics, the entry flight is divided into three phases: Descent Phase (DP), Steady Glide Phase (SGP), and Altitude Adjustment Phase (AAP). In the DP, as the atmosphere

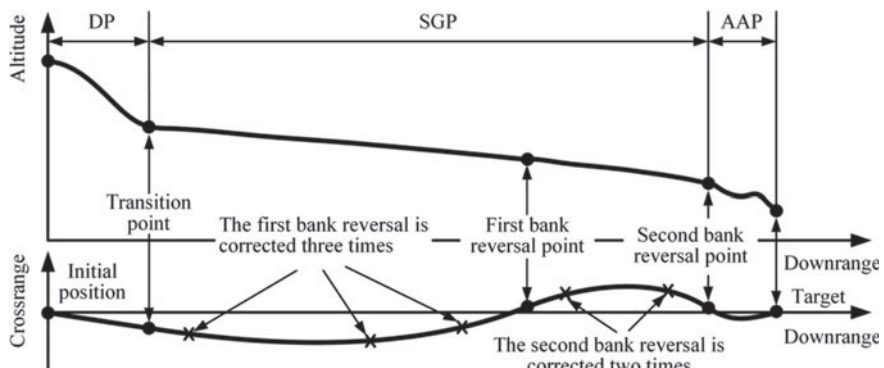


Fig. 14.1 Entry trajectory of CAV corresponding to the proposed guidance

is too thin, the vehicle loses altitude quickly. In the SGP, the lift is large enough to prevent the altitude from decreasing rapidly. In this phase, new 3-D analytical glide formulas are used to plan reference profiles and regulate bank reversals. To lighten the burden on FCS, the guidance only conducts two bank reversals, the second of which is properly near the target and also the end point of the SGP. In the AAP, the altitude is adjusted to the desired value by properly reducing the AOA. The following shows the guidance scheme of each phases in detail.

14.3.1 Descent Phase

The entry flight generally starts from the edge of the atmosphere where the atmospheric density is too tiny and thus the altitude drops rapidly. With the vehicle falling into the dense atmosphere, the heating rate increases rapidly and reaches its peak near the end of the DP. To ensure the satisfaction of the path constraints, we adopt the most conservative scheme [16] which commands the vehicle to glide along $\alpha = \alpha_{\max}$ with $\sigma = 0$, where α_{\max} is the maximum allowable AOA. Such a scheme can raise the altitude as high as possible and thus minimizes the peak of heating rate. Once the lift becomes large enough, the AOA will be adjusted to the baseline AOA (α_{bsl}) smoothly and the flight will enter the SGP soon afterwards.

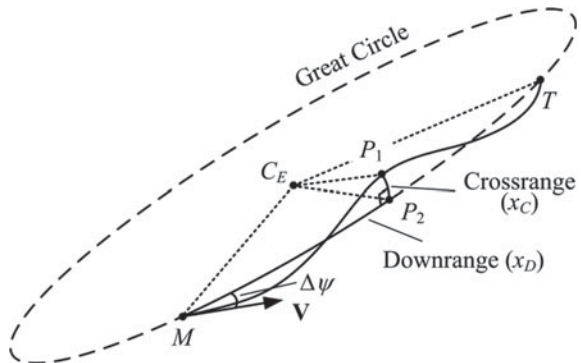
14.3.2 Steady Glide Phase

14.3.2.1 Overview

Figure 14.1, we can see that the SGP starts immediately after the DP and ends at the second bank reversal point. This phase constitutes the major part of entry flight. In this phase, as the lift is sufficient to counteract other external forces, the glide altitude decreases slowly and smoothly under the action of the TDCT. Since the vehicle tilts sideways at a proper angle to track the longitudinal reference profile and reverses the bank angle twice to remove the heading error, the ground track looks like an S-maneuvering snake. In this section, new analytical glide formulas will be developed on the basis of the previous work [16] and used to plan the reference profiles. Thus, the following briefly shows some key results obtained in [16] first.

Now we need introduce some notations and concepts. In Fig. 14.2, C_E is the Earth center, M represents the vehicle, and T represents the target. In the plane EMT determined by these three points, we construct the great circle GC_1 , a circle centered at C_E with radius of R_e . \mathbf{V} is the velocity vector of the vehicle relative to the rotating Earth. $\Delta\psi$ is the angle of \mathbf{V} measured counterclockwise from the tangent line to the circle GC_1 at M and called heading error. Thus, it is just negative for the case shown in Fig. 14.2. The curve shown in Fig. 14.2 is a schematic entry trajectory and P_1 is a point on the trajectory. Passing through P_1 , we construct a new great circle GC_2 that

Fig. 14.2 Definitions of downrange and crossrange



is perpendicular to the plane EMT . The circles GC_1 and GC_2 intersect at the point P_2 . Define downrange x_D as the length of the arc between M and P_2 and crossrange x_C as the length of the arc between P_1 and P_2 .

Define L_1 and L_2 as the vertical and horizontal components of the lift L , respectively, i.e., $L_1 = L \cos(\sigma)$ and $L_2 = L \sin(\sigma)$. Define the vertical lift to drag ratio L_1/D as the ratio of L_1 to drag D and the horizontal lift to drag ratio L_2/D as the ratio of L_2 to D . The mechanical energy of the vehicle per unit mass is determined by

$$E = \frac{1}{2}V^2 - \frac{\mu}{R_e + H} \quad (14.10)$$

In [16], designating L_1/D and L_2/D as control variables, 3-D analytical glide formulas are developed, as shown in Eqs. (14.11)–(14.13). Note again that these formulas fully consider the Earth-curvature effects but ignore the Earth-rotation effects.

$$x_D(E, E_0) = \int_{E_0}^E \frac{L_1}{D} \frac{R_e}{2x_E + \mu/R^*} dx_E \quad (14.11)$$

$$\begin{aligned} x_C(E, E_0) &= x_{C0} \cos(x_D(E, E_0)/R_e) + R_e \Delta\psi_0 \sin(x_D(E, E_0)/R_e) \\ &\quad - R_e \int_{E_0}^E \sin(x_D(E, x_E)/R_e) f_1(x_E) dx_E \end{aligned} \quad (14.12)$$

$$\begin{aligned} \Delta\psi(E, E_0) &= \Delta\psi_0 \cos(x_D(E, E_0)/R_e) - \frac{x_{C0}}{R_e} \sin(x_D(E, E_0)/R_e) \\ &\quad - \int_{E_0}^E \cos(x_D(E, x_E)/R_e) f_1(x_E) dx_E \end{aligned} \quad (14.13)$$

where E_0 is the initial energy, E is the current energy, and x_E represents the energy at any moment. R^* is set to $R_e + H^*$ where H^* is the average glide altitude. $f_1(x_E)$ is defined as

$$f_1(x_E) = -\frac{L_2}{D} \frac{1}{2x_E + 2\mu/R^*} \quad (14.14)$$

From these formulas, we can see that x_D is proportional to L_1/D while x_C varies linearly with L_2/D .

The following briefly describes the guidance process of the SGP based on the above analytical formulas.

- Step 1: Offline design a baseline AOA (α_{bsl}) profile and then determine the corresponding baseline L/D (L/D_{bsl}) profile.
- Step 2: Design the L_1/D profile as a piecewise polynomial function that has a similar shape with the L/D_{bsl} profile such that the bank angle magnitude remains almost constant in the SGP. Afterwards, we can get the parametric profile of the absolute value of L_2/D .
- Step 3: To compensate the Earth-rotation effects, introduce pseudo- L_1/D ($\overline{L_1/D}$) and pseudo- L_2/D ($\overline{L_2/D}$) as the modified L_1/D and L_2/D considering the effects of the inertial forces, respectively. By carefully forecasting the change trends of the inertial forces, design the $\overline{L_1/D}$ and $\overline{L_2/D}$ profiles as inversely proportional functions.
- Step 4: Develop new 3-D analytical glide formulas for these inversely proportional profiles, and then use the new downrange formula to determine the parameter of the $\overline{L_1/D}$ profile according to the downrange and final energy requirements.
- Step 5: To remove the crossrange error, use the new crossrange formula to regulate the bank reversals in due time, rather than in real time, as shown in Fig. 14.1.
- Step 6: Modulate the baseline bank angle (α_{bsl}) to track the $\overline{L_1/D}$ profile and perform the bank reversals.
- Step 7: Apply the TDCT to suppress the trajectory oscillations. Thus, the AOA and bank angle commands α_{cmd} and σ_{cmd} are generated by merging the feedback signals of the TDCT into α_{bsl} and σ_{bsl} .
- Step 8: Determine the allowable range of bank angle from the path constraints and then limit σ_{cmd} within this range.
- Step 9: Repeat the above process from Step 2 until the SGP ends.

Although the guidance scheme designs the $\overline{L_1/D}$ and $\overline{L_2/D}$ profiles to be in complex forms and thus makes the analytical glide formulas complicated, it is developed on the basis of thorough analysis and reasonable assumptions and thereby conforms to the natures of hypersonic glide trajectory. It is verified by simulation results that, as expected, the guidance scheme can overcome the Earth-rotation effects completely while remaining the AOA and bank angle almost constant in the SGP. This brings three benefits: (1) The flight energy is dissipated evenly, which helps to avoid the command saturation in the AAP, (2) the almost-invariant guidance commands help

to improve the tracking accuracy of FCS, and (3) as the aerodynamic dispersions are generally sensitive to AOA, constant AOA helps to evaluate the influence of the aerodynamic dispersions more accurately, which can further improve the guidance accuracy and enhance the robustness. The following presents the guidance scheme of the SGP in detail.

14.3.2.2 Baseline AOA and L/D Profiles

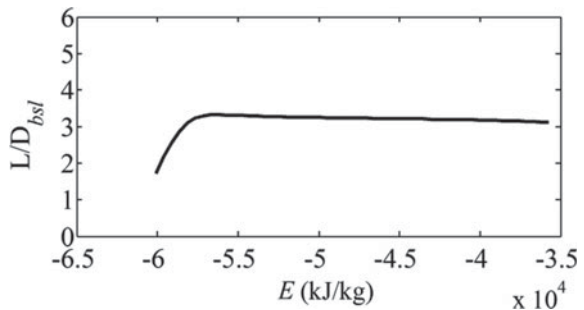
For the sake of utilizing the analytical glide formulas, all the reference profiles required by the new guidance are designed as functions of E . The baseline AOA (α_{bsl}) profile is the benchmark of AOA for the SGP and AAP as

$$\alpha_{bsl} = \begin{cases} \alpha_1 & \text{for } E \geq E_\alpha \\ \left(\frac{E_\alpha - E}{E_\alpha - E_{TAEM}} \right)^2 (\alpha_2 - \alpha_1) + \alpha_1 & \text{for } E < E_\alpha \end{cases} \quad (14.15)$$

where $E_\alpha = -5.55 \times 10^7 \text{ J/kg}$, which is near the transition point from the SGP to the AAP, and E_{TAEM} is the desired final energy and obtained by substituting V_{TAEM} and H_{TAEM} into Eq. (14.10). For $E \geq E_\alpha$, the flight is major in the SGP. Because the L/D is approximately maximized at the AOA of 10 deg, we let $\alpha_1 = 10 \text{ deg}$ in order to make full use of the vehicle's ability. In the AAP, to adjust the altitude to H_{TAEM} , we reduce α_{bsl} to α_2 smoothly, where α_2 is initially set to 6 deg and will be slightly modulated using an iterative algorithm based on trajectory simulation in Sect. 6.3.3.1. In some cases with large disturbances, E may be smaller than E_{TAEM} , which will cause α_{bsl} to be smaller than α_2 and even become negative. To sustain the flight, we pose an additional constraint that.

Subsequently, using the method presented in [16], we can determine the profile of the baseline L/D (L/D_{bsl}), the L/D corresponding to α_{bsl} , as shown in Fig. 14.3.

Fig. 14.3 Baseline L/D profile corresponding to α_{bsl}



14.3.2.3 L1/D and L2/D Profiles

In view of the shape of the L/D_{bsl} profile, we design the L₁/D profile as

$$L_1/D = \begin{cases} L_1/D_1 & \text{for } E \geq E_\alpha \\ \left(\frac{E_\alpha - E}{E_\alpha - E_{TAEM}}\right)^2 (L_1/D_2 - L_1/D_1) + L_1/D_1 & \text{for } E < E_\alpha \end{cases} \quad (14.16)$$

Because L₁/D = L/D cos(σ) and L/D_{bsl} is almost constant in the SGP, we let L₁/D be a constant of L₁/D₁ for E ≥ E_α in order to keep the bank angle approximately constant in the SGP. For E < E_α, in order to follow the trend of L/D_{bsl}, we reduce L₁/D to L₁/D₂ smoothly. The parameter L₁/D₁ is used to adjust the glide range and will be determined in Sect. 6.3.2.5. In order that the bank angle tends to zero finally, we let L₁/D₂ = k_{L/D}L/D_{bsl}(E_{TAEM}), where k_{L/D} = L/D_{real}(E)/L/D_{ideal}(E) is used to roughly compensate the aerodynamic dispersion effects, L/D_{real}(E) is the current real L/D measured onboard by aerodynamic identification technology [18, 19], and L/D_{ideal}(E) is the current L/D corresponding to the ideal aerodynamic model. After determining the L₁/D profile, we can obtain the parametric profile of the absolute value of L₂/D by

$$|L_2/D| = \sqrt{(k_{L/D}L/D_{bsl})^2 - (L_1/D)^2} \quad (14.17)$$

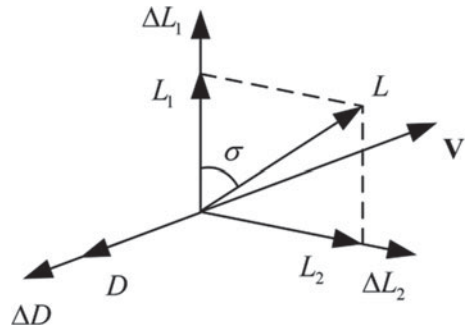
14.3.2.4 Pseudo-L1/D and Pseudo-L2/D Profiles

Equations (14.4)–(14.6) show that the inertial forces caused by the Earth's rotation have complex effects on the entry motion. To compensate these effects, pseudo-aerodynamic forces are introduced here by merging the inertial and aerodynamic forces. By carefully predicting the change trends of the inertial forces, we design the pseudo-aerodynamic profiles as inversely proportional functions, then derive new 3-D analytical glide formulas for these inversely proportional profiles, and finally apply these formulas to determine the parameters of the pseudo-aerodynamic profiles. Although the pseudo-aerodynamic profiles for constant AOA and bank angle are not strictly consistent with inversely proportional functions, the planned profiles can still be closely tracked by slightly adjusting the AOA and bank angle.

In Fig. 14.4, ΔL₁, ΔL₂, and ΔD are the mutually orthogonal inertial forces. From Eqs. (14.4)–(14.6), we have

$$\begin{aligned} \Delta L_1 = & m\omega_e^2(R_e + H) \cos^2(\phi) \cos(\gamma) + m\omega_e^2(R_e \\ & + H) \sin(\phi) \cos(\phi) \sin(\gamma) \cos(\psi) \\ & + 2mV\omega_e \cos(\phi) \sin(\psi) \end{aligned} \quad (14.18)$$

Fig. 14.4 Aerodynamic and inertial forces are merged as pseudo-aerodynamic forces



$$\begin{aligned}\Delta L_2 &= -m\omega_e^2(R_e + H) \sin(\phi) \cos(\phi) \sin(\psi) \\ &\quad + 2mV\omega_e \cos(\gamma)(\sin(\phi) - \cos(\phi) \tan(\gamma) \cos(\psi))\end{aligned}\quad (14.19)$$

$$\begin{aligned}\Delta D &= -m\omega_e^2(R_e + H) \cos^2(\phi) \sin(\gamma) \\ &\quad + m\omega_e^2(R_e + H) \sin(\phi) \cos(\phi) \cos(\gamma) \cos(\psi)\end{aligned}\quad (14.20)$$

Since $\gamma \approx 0$, assume that $\sin(\gamma) = 0$ and $\cos(\gamma) = 1$. Thus the above equations can be simplified as

$$\Delta L_1 = m\omega_e^2(R_e + H) \cos^2(\phi) + 2mV\omega_e \cos(\phi) \sin(\psi) \quad (14.21)$$

$$\Delta L_2 = -m\omega_e^2(R_e + H) \sin(\phi) \cos(\phi) \sin(\psi) + 2mV\omega_e \sin(\phi) \quad (14.22)$$

$$\Delta D = m\omega_e^2(R_e + H) \sin(\phi) \cos(\phi) \cos(\psi) \quad (14.23)$$

As $2V$ is much greater than $\omega_e(R_e + H) \cos(\phi)$, ΔL_1 and ΔL_2 can be further simplified as

$$\Delta L_1 = 2mV\omega_e \cos(\phi) \sin(\psi) \quad (14.24)$$

$$\Delta L_2 = 2mV\omega_e \sin(\phi) \quad (14.25)$$

Define pseudo-L₁/D and pseudo-L₂/D as

$$\overline{L_1/D} = \frac{L_1 + \Delta L_1}{D + \Delta D} \quad (14.26)$$

$$\overline{L_2/D} = \frac{L_2 + \Delta L_2}{D + \Delta D} \quad (14.27)$$

Their first-order Taylor expansions are

$$\overline{L_1/D} = L_1/D + \frac{1}{D} \Delta L_1 - \frac{L_1/D}{D} \Delta D \quad (14.28)$$

$$\overline{L_2/D} = L_2/D + \frac{1}{D} \Delta L_2 - \frac{L_2/D}{D} \Delta D \quad (14.29)$$

Note that $\overline{L_1/D}$ and $\overline{L_2/D}$ are very sensitive to D as D appears in the denominators. Here, we let D be the value corresponding to the steady glide, which is denoted as D_{SG} . Thus we have

$$\overline{L_1/D} = L_1/D + \frac{1}{D_{SG}} \Delta L_1 - \frac{L_1/D}{D_{SG}} \Delta D \quad (14.30)$$

$$\overline{L_2/D} = L_2/D + \frac{1}{D_{SG}} \Delta L_2 - \frac{L_2/D}{D_{SG}} \Delta D \quad (14.31)$$

Ignoring the Earth's rotation and assuming that $\gamma \approx 0$ and $\dot{\gamma} \approx 0$, from Eqs. (14.5) and (14.10), the vertical component of lift for steady glide can be approximated by

$$L_{1(SG)} \approx mg - \frac{mV^2}{R_e + H} = -\frac{m}{R^*} \left(2E + \frac{\mu}{R^*} \right) \quad (14.32)$$

Using L_1/D , D_{SG} can be calculated by

$$D_{SG} = \frac{L_{1(SG)}}{L_1/D} \approx -\frac{m}{R^*} \left(2E + \frac{\mu}{R^*} \right) / L_1/D \quad (14.33)$$

Substituting Eqs. (14.23)–(14.25) and (14.33) into Eqs. (14.30)–(14.31), we can obtain

$$\overline{L_1/D} = L_1/D(1 + h_1) \quad (14.34)$$

$$\overline{L_2/D} = L_2/D(1 + h_2) + L_1/Dh_3 \quad (14.35)$$

Here, h_1 , h_2 , and h_3 are expressed as

$$h_1 = \frac{h_{z1}}{h_m}, h_2 = \frac{h_{z2}}{h_m}, h_3 = \frac{h_{z3}}{h_m} \quad (14.36)$$

where

$$h_{z1} = -\frac{R^*}{m} (\Delta L_1 - L_1/D \cdot \Delta D) \quad (14.37)$$

$$h_{z2} = \frac{R^* L_1/D}{m} \Delta D \quad (14.38)$$

$$h_{z3} = -\frac{R^*}{m} \Delta L_2 \quad (14.39)$$

$$h_m = 2E + \frac{\mu}{R^*} \quad (14.40)$$

To implement the analytical glide formulas, we need to obtain the profiles of h_1 , h_2 , and h_3 with respect to E . However, this is impossible because the remaining states of motion are unknown yet. Therefore, we have to approximate them appropriately. As h_m has already been a function of E , we need only determine the approximation formulas of h_{z1} , h_{z2} , and h_{z3} . By observing the simulation results, we find an interesting phenomenon that $\cos(\phi) \sin(\psi)$ remains approximately constant during entry flight, despite that $\cos(\phi)$ and $\sin(\psi)$ vary nonlinearly with time. This helps to simplify the formula of ΔL_1 . The interpretation of the phenomenon is given by proving the following proposition.

Proposition 1 *If a vehicle flies strictly along a great circle, then the following identity holds throughout the flight.*

$$\cos(\phi) \sin(\psi) \equiv \text{Constant} \quad (14.41)$$

Proof Inasmuch as the usual proof process is very long and complicated, we prove the proposition in a skillful and concise way. Note that Eq. (14.41) is independent of speed. Thus, we can assume that the vehicle undergoes uniform circular motion only under the action of gravity. As the extension line of gravity intersects with the Earth's axis of rotation z_e , the moment of gravity about z_e -axis is zero and thus according to the angular momentum theorem, the angular momentum of the vehicle about z_e -axis remains constant. Here, this angular momentum is just equal to the product of the eastward component of the velocity vector ($V \sin(\psi)$) and the distance of the vehicle from z_e -axis ($R_e \cos(\phi)$), as follows

$$H_{Ze} = V R_e \sin(\psi) \cos(\phi) \quad (14.42)$$

As H_{Ze} , V and R_e are constant, Eq. (14.41) has been proved to be true for any great circle.

Consequently, as the hypersonic vehicle glides to the destination approximately along the great circle shown in Fig. 14.2, $\cos(\phi) \sin(\psi)$ keeps almost constant for entry flight.

Next, we further simplify other terms in ΔL_1 , ΔL_2 , and ΔD . In Eqs. (14.23)–(14.25), we approximate V and $\sin(\phi)$ by linear functions, and thus use a quadratic polynomial to approximate $V \sin(\phi)$. Since $2V \gg \omega_e(R_e + H) \cos(\phi)$, the influence of ΔD is much smaller than that of ΔL_1 and ΔL_2 . Thereby, despite that ΔD changes irregularly, we use a linear function to approximate it. All in all, ΔL_1 and ΔD are approximated by linear functions but ΔL_2 is approximated by a quadratic polynomial due to $V \sin(\phi)$. Further, from Eqs. (14.37)–(14.39), the approximation formulas of h_{z1} , h_{z2} , and h_{z3} are designed as

$$\bar{h}_{z1}(x_E) = k_{h1(0)} + k_{h1(1)}x_E \quad (14.43)$$

$$\bar{h}_{z2}(x_E) = k_{h2(0)} + k_{h2(1)}x_E \quad (14.44)$$

$$\bar{h}_{z3}(x_E) = k_{h3(0)} + k_{h3(1)}x_E + k_{h3(2)}x_E^2 \quad (14.45)$$

where the parameters are determined by the boundary points. Specifically, for $i = 1, 2$, $k_{hi(0)}$ and $k_{hi(1)}$ are determined by

$$k_{hi(0)} = \frac{h_{zi}(E_{\text{TAEM}})E - h_{zi}(E)E_{\text{TAEM}}}{E - E_{\text{TAEM}}} \quad (14.46)$$

$$k_{hi(1)} = \frac{h_{zi}(E) - h_{zi}(E_{\text{TAEM}})}{E - E_{\text{TAEM}}} \quad (14.47)$$

where

$$h_{z1}(E) = 2mV\omega_e \cos(\phi) \sin(\bar{\psi}) \\ + m\omega_e^2(R_e + H) \cos(\phi) [\cos(\phi) - L_1/D^{pre} \sin(\phi) \cos(\bar{\psi})] \quad (14.48)$$

$$h_{z1}(E_{\text{TAEM}}) = 2mV_{\text{TAEM}}\omega_e \cos(\phi_T) \sin(\bar{\psi}_T) \\ + m\omega_e^2(R_e + H_{\text{TAEM}}) \cos(\phi_T) \\ \times [\cos(\phi_T) - L_1/D_{\text{TAEM}} \sin(\phi_T) \cos(\bar{\psi}_T)] \quad (14.49)$$

$$h_{z2}(E) = \omega_e^2 R^*(R_e + H)L_1/D^{pre} \sin(\phi) \cos(\phi) \cos(\bar{\psi}) \quad (14.50)$$

$$h_{z2}(E_{\text{TAEM}}) = \omega_e^2 R^*(R_e + H_{\text{TAEM}})L_1/D_{\text{TAEM}} \sin(\phi_T) \cos(\phi_T) \cos(\bar{\psi}_T) \quad (14.51)$$

where L_1/D^{pre} is the value of L_1/D obtained in the last guidance cycle, and $L_1/D_{\text{TAEM}} = L_1/D_2$ is the planned final value of L_1/D . ϕ_T is the latitude of the target. $\bar{\psi}$ is a weighted average of ψ in some sense and obtained under the assumption that the vehicle flies strictly along the great circle passing through the target. $\bar{\psi}_T$ is the weighted average of ψ at the target.

From Eqs. (14.25) and (14.39), h_{z3} can be approximated by

$$\bar{h}_{z3}(x_E) = -2\omega_e R^* \left[\frac{V - V_{\text{TAEM}}}{E - E_{\text{TAEM}}} (x_E - E) + V \right] \\ \left[\frac{\sin(\phi) - \sin(\phi_T)}{E - E_{\text{TAEM}}} (x_E - E) + \sin(\phi) \right] \quad (14.52)$$

Expanding Eq. (14.52), we can obtain the parameters of Eq. (14.45) as

$$k_{h3(0)} = -2\omega_e R^* \frac{(V_{\text{TAEM}} E - V E_{\text{TAEM}})[\sin(\phi_T)E - \sin(\phi)E_{\text{TAEM}}]}{(E - E_{\text{TAEM}})^2} \quad (14.53)$$

$$\begin{aligned} k_{h3(1)} &= -2\omega_e R^* \frac{[V_{\text{TAEM}} \sin(\phi) + V \sin(\phi_T)](E + E_{\text{TAEM}})}{(E - E_{\text{TAEM}})^2} \\ &\quad + 4\omega_e R^* \frac{V_{\text{TAEM}} \sin(\phi_T)E + V \sin(\phi)E_{\text{TAEM}}}{(E - E_{\text{TAEM}})^2} \end{aligned} \quad (14.54)$$

$$k_{h3(2)} = -2\omega_e R^* \frac{(V - V_{\text{TAEM}})[\sin(\phi) - \sin(\phi_T)]}{(E - E_{\text{TAEM}})^2} \quad (14.55)$$

14.3.2.5 Calculation of L1/D1

The above has determined the expressions of $\overline{L_1/D}$ and $\overline{L_2/D}$ where there are two parameters L_1/D_1 and L_1/D_2 . In Sect. 6.3.2.3, to achieve a near-zero final bank angle, L_1/D_2 is set to $k_{L/D} D_{\text{bsl}}(E_{\text{TAEM}})$. In this subsection, we derive new analytical glide formulas for the inversely-proportional $\overline{L_1/D}$ and $\overline{L_2/D}$ profiles, and then use the new downrange formula to determine L_1/D_1 in consideration of the range-to-go and final energy requirements. From Eqs. (14.16) and (14.34), the $\overline{L_1/D}$ profile can be expressed as

$$\overline{L_1/D} = \begin{cases} L_1/D_1[1+h_1(x_E)]; & \text{for } x_E \geq E_\alpha \\ \left[\left(\frac{E_\alpha - x_E}{E_\alpha - E_{\text{TAEM}}} \right)^2 (L_1/D_2 - L_1/D_1) + L_1/D_1 \right] [1+h_1(x_E)]; & \text{for } x_E < E_\alpha \end{cases} \quad (14.56)$$

Replacing L_1/D in Eq. (14.11) by $\overline{L_1/D}$ and then integrating Eq. (14.11), we can obtain the new downrange formula through a long and complex derivation process. Since the $\overline{L_1/D}$ profile is segmented, this formula is also a piecewise function as follows:

(1) If $E_\alpha \leq E_2 \leq E_1$, there is

$$\begin{aligned} x_D(E_2, E_1) &= \frac{R_e L_1/D_1}{2} \left(1 + \frac{k_{h1(1)}}{2} \right) \ln \left(\frac{2E_2 + \mu/R^*}{2E_1 + \mu/R^*} \right) \\ &\quad - \frac{R_e L_1/D_1}{2} \left(k_{h1(0)} - \frac{\mu k_{h1(1)}}{2R^*} \right) \left(\frac{1}{2E_2 + \mu/R^*} - \frac{1}{2E_1 + \mu/R^*} \right) \end{aligned} \quad (14.57)$$

(2) If $E_2 \leq E_1 \leq E_\alpha$, there is

$$\begin{aligned}
x_D(E_2, E_1) = & \left(1 + \frac{k_{h1(1)}}{2}\right) \frac{R_e a_2}{4} (E_2^2 - E_1^2) \\
& + \frac{1}{2} R_e \left[\left(1 + \frac{k_{h1(1)}}{2}\right) a_1 + \left(-1 - k_{h1(1)} + \frac{R^* k_{h1(0)}}{\mu}\right) \frac{\mu a_2}{2R^*} \right] \\
& (E_2 - E_1) \\
& + \frac{1}{2} R_e \left[\left(1 + \frac{k_{h1(1)}}{2}\right) a_0 + \frac{-\mu(1+k_{h1(1)}) + R^* k_{h1(0)}}{2R^*} a_1 \right] \\
& \ln \left(\frac{2E_2 + \mu/R^*}{2E_1 + \mu/R^*} \right) \\
& + \frac{1}{2} R_e \frac{\mu^2(2 + 3k_{h1(1)}) - 4\mu R^* k_{h1(0)}}{8(R^*)^2} a_2 \ln \left(\frac{2E_2 + \mu/R^*}{2E_1 + \mu/R^*} \right) \\
& - \frac{1}{2} R_e \left(k_{h1(0)} - \frac{\mu k_{h1(1)}}{2R^*} \right) \left(a_0 - \frac{1}{2} \frac{\mu}{R^*} a_1 + \frac{\mu^2}{4(R^*)^2} a_2 \right) \\
& \times \left(\frac{1}{2E_2 + \mu/R^*} - \frac{1}{2E_1 + \mu/R^*} \right)
\end{aligned} \tag{14.58}$$

where

$$a_0 = \frac{(L_1/D_2 - L_1/D_1)E_\alpha^2}{(E_\alpha - E_{TAEM})^2} + L_1/D_1 \tag{14.59}$$

$$a_1 = -\frac{2(L_1/D_2 - L_1/D_1)E_\alpha}{(E_\alpha - E_{TAEM})^2} \tag{14.60}$$

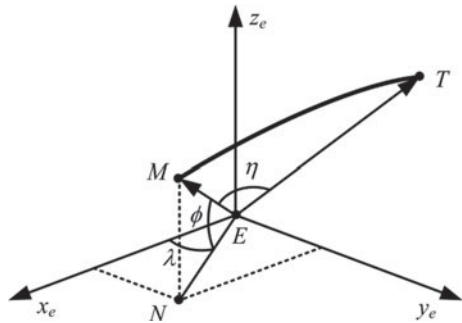
$$a_2 = \frac{(L_1/D_2 - L_1/D_1)}{(E_\alpha - E_{TAEM})^2} \tag{14.61}$$

(3) If $E_2 \leq E_\alpha \leq E_1$, the downrange can be calculated by

$$x_D(E_2, E_1) = x_D(E_\alpha, E_1) + x_D(E_2, E_\alpha) \tag{14.62}$$

Before determining L_1/D_1 , we need calculate s_{go} first. The reference frame $E-x_e y_e z_e$ shown in Fig. 14.5 is called the Geocentric Equatorial Rotating (GER) frame [16]. The origin of this frame is at the Earth's center E . The x_e - and y_e -axes are in the equatorial plane while the x_e -axis intersects with the prime meridian. The z_e -axis points toward the North Pole. In Fig. 14.5, M represents the vehicle, N is the vertical projection of M onto the equatorial plane, and T represents the target. s_{go} is defined as the length of the arc between M and T . Define \overrightarrow{EM} as the vector from E to M , \overrightarrow{ET} as the vector from E to T , and η as the angle between \overrightarrow{EM} and \overrightarrow{ET} . Thus s_{go} can be calculated by

Fig. 14.5 Calculation of range to go s_{go}



$$s_{\text{go}} = R_e \eta \quad (14.63)$$

Now we need to calculate η . Denote \mathbf{x}_{EM} as the unit vector of \overrightarrow{EM} and \mathbf{x}_{ET} as the unit vector of \overrightarrow{ET} . As can be seen from Fig. 14.5, the component of \mathbf{x}_{EM} in the equatorial plane is $\cos(\phi)$ and the component along z_e -axis is $\sin(\phi)$. Further, since the angle between the segment EN and x_e -axis is λ , we can obtain the x_e —component of \mathbf{x}_{EM} as $\cos(\lambda) \cos(\phi)$ and the y_e —component as $\sin(\lambda) \cos(\phi)$. Thereby, the coordinates of \mathbf{x}_{EM} in the GER frame are

$$\mathbf{x}_{EM}^{\text{GER}} = [\cos(\lambda) \cos(\phi), \sin(\lambda) \cos(\phi), \sin(\phi)]^T \quad (14.64)$$

Similarly, we can obtain the coordinates of \mathbf{x}_{ET} as

$$\mathbf{x}_{ET}^{\text{GER}} = [\cos(\lambda_T) \cos(\phi_T), \sin(\lambda_T) \cos(\phi_T), \sin(\phi_T)]^T \quad (14.65)$$

where λ_T and ϕ_T represent the longitude and latitude of the target respectively. Because the dot product of two unit vectors are geometrically equal to the cosine of the angle between the two vectors, η is calculated by

$$\eta = \arccos(\mathbf{x}_{EM}^{\text{GER}} \cdot \mathbf{x}_{ET}^{\text{GER}}) \quad (14.66)$$

Next, we can determine L_1/D_1 using s_{go} . As the pseudo- L_1/D profile is a piecewise function, we need consider the following two cases:

(1) If $E > E_\alpha$, we have

$$x_D(E_{\text{TAEM}}, E_\alpha) + x_D(E_\alpha, E) = s_{\text{go}} - S_{\text{TAEM}} \quad (14.67)$$

where $x_D(E_{\text{TAEM}}, E_\alpha)$ is calculated by Eq. (14.58) while $x_D(E_\alpha, E)$ is obtained by Eq. (14.57). By solving Eq. (14.67), we can get L_1/D_1 as

$$L_1/D_1 = \frac{s_{go} - S_{TAEM} - k_{xD1}L_1/D_2}{-k_{xD1} + k_{xD2}} \quad (14.68)$$

where

$$\begin{aligned} k_{xD1} = & -\frac{R_e}{4} \left(1 + \frac{k_{h1(1)}}{2} \right) \frac{(E_\alpha + E_{TAEM})}{(E_\alpha - E_{TAEM})} \\ & + \frac{R_e}{2(E_\alpha - E_{TAEM})} \left[2E_\alpha + \frac{\mu}{2R^*} + \left(E_\alpha + \frac{\mu}{2R^*} \right) k_{h1(1)} - \frac{k_{h1(0)}}{2} \right] \\ & + \frac{R_e(2E_\alpha R^* + \mu)}{2(E_\alpha - E_{TAEM})^2} \left[\frac{2E_\alpha R^* + \mu}{4(R^*)^2} - \frac{k_{h1(0)}}{2R^*} \right] \ln \left(\frac{2E_{TAEM} + \mu/R^*}{2E_\alpha + \mu/R^*} \right) \\ & + \frac{R_e(2E_\alpha R^* + \mu)}{2(E_\alpha - E_{TAEM})^2} \left(\frac{(2E_\alpha R^* + 3\mu)}{8(R^*)^2} \right) k_{h1(1)} \ln \left(\frac{2E_{TAEM} + \mu/R^*}{2E_\alpha + \mu/R^*} \right) \\ & - \frac{R_e(2E_\alpha R^* + \mu)^2}{8(R^*)^2(E_\alpha - E_{TAEM})^2} \left(k_{h1(0)} - \frac{\mu k_{h1(1)}}{2R^*} \right) \\ & \times \left(\frac{1}{2E_{TAEM} + \mu/R^*} - \frac{1}{2E_\alpha + \mu/R^*} \right) \end{aligned} \quad (14.69)$$

$$\begin{aligned} k_{xD2} = & \frac{1}{2} R_e \left(1 + \frac{k_{h1(1)}}{2} \right) \ln \left(\frac{2E_{TAEM} + \mu/R^*}{2E + \mu/R^*} \right) \\ & - \frac{1}{2} R_e \left(k_{h1(0)} - \frac{\mu k_{h1(1)}}{2R^*} \right) \left(\frac{1}{2E_{TAEM} + \mu/R^*} - \frac{1}{2E + \mu/R^*} \right) \end{aligned} \quad (14.70)$$

- (2) If $E \leq E_\alpha$, we need not update L_1/D_1 , because, most of time, the vehicle flies in the AAP where a different guidance scheme is used.

14.3.2.6 Regulation of Bank Reversals

As the vehicle banks at a proper angle to track the $\overline{L_1/D}$ profile, the vehicle always maneuvers laterally and the crossrange can be up to thousands of kilometers. In order to reach the destination, the vehicle needs reverse the bank angle properly to eliminate the crossrange error. As shown in Fig. 14.1, the guidance requires only two bank reversals, which helps to lessen the demands on FCS. Denote the energies corresponding to the two bank reversals as E_{BR1} and E_{BR2} , respectively. When $E > E_{BR1}$, the guidance lets $E_{BR2} = E_\alpha$ and then uses the new crossrange formula to regulate E_{BR1} . When $E_{BR2} < E < E_{BR1}$, an iterative algorithm based on trajectory simulation is used to fine-tune E_{BR2} . The iterative algorithm will be shown in Sect. 6.3.3.1 because it needs the guidance scheme of the AAP.

From Eq. (14.35), by considering the bank reversals, the $\overline{L_2/D}$ profile can be expressed as

$$\overline{L_2/D}(x_E) = (-1)^{k_{BR}} \operatorname{sgn}|L_2/D(x_E)|[1 + \bar{h}_2(x_E)] + L_1/D\bar{h}_3(x_E) \quad (14.71)$$

where sgn is a sign function of initial heading error and its output makes the vehicle initially turn to the direction making the heading error decrease, k_{BR} refers to the number of the bank reversals having been performed, and $|L_2/D(x_E)|$ can be determined by Eq. (14.17).

By substituting Eq. (14.71) into the crossrange formula (Eq. (14.12)) and letting the definite integral be over the interval $[E, E_{TAEM}]$, we can predict the final crossrange as

$$\begin{aligned} x_{Cf} &= R_e \Delta\psi \sin(x_D(E_{TAEM}, E)/R_e) \\ &+ R_e \int_E^{E_{TAEM}} \sin(x_D(E_{TAEM}, x_E)/R_e) \frac{L_1/D\bar{h}_3(x_E)}{2x_E + 2\mu/R^*} dx_E \\ &- \operatorname{sgn}R_e [F(E_{BR1}, E) - F(E_{BR2}, E_{BR1}) + F(E_{TAEM}, E_{BR2})] \end{aligned} \quad (14.72)$$

Note that x_{C0} in Eq. (14.12) is zero here because the great circle is updated once in each guidance cycle according to the current states. $F(x_{E2}, x_{E1})$ is defined as

$$F(x_{E2}, x_{E1}) = \int_{x_{E1}}^{x_{E2}} \sin(x_D(E_{TAEM}, x_E)/R_e) f_2(x_E) dx_E \quad (14.73)$$

Different from $f_1(x_E)$ (Eq. (14)), $f_2(x_E)$ is defined as

$$f_2(x_E) = -\frac{|L_2/D(x_E)|[1 + \bar{h}_2(x_E)]}{2x_E + 2\mu/R^*} \quad (14.74)$$

Due to the segmented $\overline{L_1/D}$ profile, $x_D(E_{TAEM}, x_E)$ is a piecewise function as

$$x_D(E_{TAEM}, x_E) = \begin{cases} [x_D(E_{TAEM}, E_\alpha) + x_D(E_\alpha, x_E)]; & x_E \geq E_\alpha \\ x_D(E_{TAEM}, x_E); & x_E < E_\alpha \end{cases} \quad (14.75)$$

where $x_D(E_{TAEM}, E_\alpha)$ and $x_D(E_{TAEM}, x_E)$ are calculated by Eq. (14.58), and $x_D(E_\alpha, x_E)$ is obtained by Eq. (14.57). The derivative of x_{Cf} with respect to E_{BR1} is

$$x'_{Cf} = \frac{dx_{Cf}}{dE_{BR1}} = -2\operatorname{sgn}R_e \sin(x_D(E_{TAEM}, E_{BR1})/R_e) f_2(E_{BR1}) \quad (14.76)$$

As shown in Fig. 14.2, we desire that $x_{Cf} = 0$ and use the Newton's method [20] to solve this equation for E_{BR1} as

$$E_{BR1}^{(k+1)} = E_{BR1}^{(k)} - \frac{x_{Cf}(E_{BR1}^{(k)})}{x'_{Cf}(E_{BR1}^{(k)})} \quad (14.77)$$

Due to the monotonic variation of x_{Cf} with respect to E_{BR1} , Eq. (14.77) generally need only be iterated several times to achieve the termination condition that $|x_{Cf}| < 1\text{m}$. As shown in Fig. 14.1, to lighten the computational load, we only correct E_{BR1} at three proper time points, rather than in real time.

14.3.2.7 Baseline Bank Angle in SGP

The entry guidance modulates the magnitude of the baseline bank angle to track the L/D profile and reverses its direction on schedule, as follows

$$\sigma_{bsl} = \begin{cases} \text{sgn} \cdot \arccos\left(\frac{L_1/D}{L/D_{\text{real}}}\right); & E > E_{BR1} + \Delta E \\ -\text{sgn} \cdot \arccos\left(\frac{L_1/D}{L/D_{\text{real}}}\right); & E_{BR2} + \Delta E < E \leq E_{BR1} + \Delta E \end{cases} \quad (14.78)$$

where L/D_{real} is the current real L/D measured by aerodynamic identification technology [18, 19], and ΔE is used to compensate for the roll rate limitation and determined by

$$\Delta E = a_D V \Delta t \quad (14.79)$$

where a_D is the drag acceleration, and

$$\Delta t = \left| \frac{\sigma}{\dot{\sigma}_{\max}} \right| \quad (14.80)$$

where σ is the current bank angle and s is the maximum allowable roll rate as shown in Sect. 6.2.2. Therefore, the above measurement makes the vehicle perform the bank reversals Δt ahead of schedule.

Note that for $E \leq E_{BR2} + \Delta E$, as the flight is in the AAP, a different guidance scheme is used to determine σ_{bsl} .

14.3.2.8 AOA and Bank Angle Commands in SGP

In [15], it has been revealed that the entry trajectory for the high-L/D vehicle has weakly-damped, phugoid natural oscillations, which can lead to substantial deterioration of the stress and thermal environments and thus pose serious challenges to the lightweight structure and thermal protection system. In addition, the trajectory oscillations have detrimental effects on tracking reference profiles. Thus, the TDCT

[15, 16] is also adopted here to eliminate the trajectory oscillations. In this technique, a high-precision approximation formula is developed for the flight-path angle corresponding to steady glide (γ_{SG}) and then a lift feedback signal proportional to $\gamma_{SG} - \gamma$ is returned and merged with α_{bsl} and σ_{bsl} . For instance, if $\gamma > \gamma_{SG}$, which means that the altitude decreases too slowly or may even increase, the TDCT returns a negative lift feedback signal to accelerate the decreasing rate or prevent the ascent. Conversely, if $\gamma < \gamma_{SG}$, a positive lift feedback signal is returned to prevent the vehicle from descending too fast. Finally, γ closely follows γ_{SG} and the feedback signal becomes almost zero. Therefore, once the trajectory oscillations are eliminated, the TDCT will not interfere with the tracking of references. From [16], the AOA and bank angle commands are

$$\alpha_{cmd} = \alpha_{bsl} + \cos(\sigma_{bsl})k_\gamma(\gamma_{SG} - \gamma) \quad (14.81)$$

$$\sigma_{cmd} = \sigma_{bsl} - \sin(\sigma_{bsl})\frac{k_\gamma(\gamma_{SG} - \gamma)}{\alpha_1} \quad (14.82)$$

where k_γ is constant. In [15], by conducting a large number of simulation trails, it is found that if k_γ is set to 3, the trajectory oscillations can be well suppressed. α_1 is the parameter of the α_{bsl} profile, and γ_{SG} is calculated by

$$\gamma_{SG} = -\frac{D_{bsl}}{mg}\frac{d_1}{d_2} \quad (14.83)$$

where $D_{bsl} = C_{D(bsl)}qS_{ref}$, $C_{D(bsl)}$ is the drag coefficient corresponding to α_{bsl} , and S_{ref} is the aerodynamic reference area. The formulas of d_1 and d_2 are

$$d_1 = \frac{\rho V^2 S_{ref} \cos(\sigma_{bsl})}{2m} \frac{dC_{L(bsl)}}{dE} + \frac{2}{R_0 + H} + \frac{C_{L(bsl)}\rho S_{ref} \cos(\sigma_{bsl})}{m} \quad (14.84)$$

$$d_2 = -\frac{C_{L(bsl)}V^2 S_{ref} \cos(\sigma_{bsl})}{2mg} \frac{d\rho}{dH} + \frac{2}{R_0 + H} + \frac{C_{L(bsl)}\rho S_{ref} \cos(\sigma_{bsl})}{m} \\ + \frac{V^2}{(R_0 + H)^2 g} \quad (14.85)$$

where $L_{bsl} = C_{L(bsl)}qS_{ref}$ and $C_{L(bsl)}$ is the lift coefficient corresponding to α_{bsl} . ρ is the atmospheric density and $dC_{L(bsl)}/dE$ can be obtained from the α_{bsl} profile.

To ensure the satisfaction of the path constraints, we adopt the measures shown in [16]. For steady glide, greater bank angle tends to decrease H and thus increase ρ , which further cause \dot{Q} , q , and n to increase. Thereby the path constraints determine the maximum allowable bank angle σ_{max} as well as the minimum allowable altitude H_{min} , as shown by the first term on the right side of Eq. (14.86). The second term on the right side of Eq. (14.86) is used to cope with trajectory oscillations. For example,

if the vehicle drops down rapidly, this term will properly reduce σ_{\max} in order to prevent the vehicle from falling below H_{\min} .

$$\sigma_{\max} = \arccos\left(\frac{L_1}{L_{\max}}\right) + k_{\sigma}\left(\frac{dH_{\min}}{dE} - \frac{dH}{dE}\right) \quad (14.86)$$

where $k_{\sigma} = -50$, which indicates that if $dH/dE = 2(dH_{\min}/dE)$, the correction of σ_{\max} is about 5 deg. For steady glide, due to $\dot{\gamma} \approx 0$, from Eq. (14.5), L_1 can be approximated by

$$L_1 = mg - \frac{mV^2}{R_e + H_{\min}(E)} - m\omega_e^2(R_e + H_{\min})\cos^2(\phi) - 2mV\omega_e \cos(\phi) \sin(\psi) \quad (14.87)$$

At H_{\min} , the lift is maximized since the atmospheric density is also maximized.

$$L_{\max} = C_{L(\text{real})}[0.5\rho(H_{\min})V^2]S_{\text{ref}} \quad (14.88)$$

where $C_{L(\text{real})}$ is the current real lift coefficient. dH_{\min}/dE can be determined from the H_{\min} profile. dH/dE is calculated by

$$\frac{dH}{dE} \approx -\frac{m \sin(\gamma)}{D} \quad (14.89)$$

To satisfy the path constraints, we limit σ_{cmd} within its allowable range as

$$\sigma_{\text{cmd}} = \begin{cases} \sigma_{\max} & \text{if } \sigma_{\text{cmd}} > \sigma_{\max} \\ -\sigma_{\max} & \text{if } \sigma_{\text{cmd}} < -\sigma_{\max} \end{cases} \quad (14.90)$$

Although this measure may prevent the reference profile from being tracked closely, it will not result in a failure of the guidance. As the heating rate, dynamic pressure, and load factor increase largely with increasing speed, the entry corridor is narrow in the high-speed phase but becomes wide in the low-speed phase. Therefore the above measure is more likely to be enabled in the high-speed phase, and in the low-speed phase, by re-planning the reference profiles, the tracking errors accumulated in the high-speed phase can be eliminated.

14.3.3 Altitude Adjustment Phase

As shown in Fig. 14.1, for $E < E_{BR2}$, the flight is in the AAP where the altitude is adjusted by properly reducing α_{bsl} . In this phase, due to the relatively large change

rate of altitude, the analytical glide formulas become inaccurate to meet the terminal requirements. Here, we adopt the guidance scheme of the AAP presented in [16] and slightly improve it. In this guidance, α_{bsl} is still planned as Eq. (14.15) but σ_{bsl} is determined by Proportional Navigation (PN) [2], which can remove the heading error almost completely. However, no longer tracking the $\overline{L_1/D}$ profile would result in a final speed error of about 50 m/s. By qualitative analysis, it is found that reducing E_{BR2} can decrease V_f . Therefore, before the last bank reversal, an iterative algorithm based on trajectory simulation is used to correct E_{BR2} slightly according to the final speed requirement. In the AAP, there are still energy errors caused by interferences. To eliminate these errors, the AOA is slightly adjusted to track the reference profile of s_{go} with respect to E , which is denoted as $s_{go}^{ref}(E)$ and obtained from the last onboard trajectory simulation. As the remaining trajectory is short and needs only be simulated numerically several times, the iterative algorithm only requires a light computational load. Additionally, compared with [16], the improved iterative algorithm is able to fine-tune α_2 , a parameter of the α_{bsl} profile, in order to improve the final altitude accuracy.

14.3.3.1 Correction of α_2 and EBR2

As mentioned above, before entering the AAP, the guidance uses an iterative algorithm based on trajectory simulation to slightly correct α_2 and E_{BR2} . To lighten the computational load, the correction is conducted only twice: One is shortly after the first bank reversal occurs and the other is about 2 min before the second bank reversal.

Before introducing the iterative algorithm, we describe the onboard trajectory simulation first. In the n -th trajectory simulation, Eqs. (14.1)–(14.6) are integrated numerically from the current condition with the proposed guidance as control until $s_{go}^{(n)} = S_{TAEM}$, where the aerodynamic model is roughly updated by considering the information on aerodynamic dispersions having been measured by aerodynamic identification technology. Here, the superscript “ (n) ” represents the ordinal number of the trajectory simulation.

The iterative algorithm has two sub-algorithms: α_2 —correction algorithm and E_{BR2} —correction algorithm. α_2 —correction algorithm is used first to slightly adjust α_2 in order to improve the final altitude accuracy, and then E_{BR2} —correction algorithm is employed to correct E_{BR2} so as to meet the final speed requirement. The following describes these two sub-algorithms in detail.

(1) α_2 —correction algorithm

This sub-algorithm needs only conduct the trajectory simulation once, and then corrects α_2 according to the difference between $H_f^{(1)}$ and H_{TAEM} . Here, care should be taken to distinguish the subscripts “ f ” and “TAEM”: “ f ” represents the achieved final states in the onboard trajectory simulation whereas “TAEM” refers to the desired final states of the entry phase.

As $\gamma_f^{(1)}$, $\sigma_f^{(1)}$, and $\dot{\gamma}$ are near zero, assume that $\cos(\gamma_f^{(1)}) = 1$, $\cos(\sigma_f^{(1)}) = 1$, and $\dot{\gamma}_f^{(1)} = 0$. Using these assumptions, from Eq. (14.5), we have

$$\begin{aligned} & \frac{C_{L(\text{est})} \left(\alpha_{\text{bsl}}^{(1)}(E_f^{(1)}) \right) q_f^{(1)} S_{\text{ref}}}{m} - g + \frac{(V_f^{(1)})^2}{R_e + H_f^{(1)}} + \omega_e^2(R_e + H_f^{(1)}) \cos^2(\phi_f^{(1)}) \\ & + \omega_e^2(R_e + H_f^{(1)}) \sin(\phi_f^{(1)}) \cos(\phi_f^{(1)}) \cos(\psi_f^{(1)}) + 2V_f^{(1)}\omega_e \cos(\phi_f^{(1)}) \sin(\psi_f^{(1)}) = 0 \end{aligned} \quad (14.91)$$

where $C_{L(\text{est})} \left[\alpha_{\text{bsl}}^{(1)}(E_f^{(1)}) \right]$ is the final lift coefficient estimated using the information on aerodynamic dispersions having been measured by aerodynamic identification technique. However, according to Sect. 6.2.3, the desired equation is

$$\begin{aligned} & \frac{C_{L(\text{est})} \left(\alpha_{\text{bsl}}^{(2)}(E_{\text{TAEM}}) \right) q_{\text{TAEM}} S_{\text{ref}}}{m} - g + \frac{V_{\text{TAEM}}^2}{R_e + H_{\text{TAEM}}} + \omega_e^2(R_e + H_{\text{TAEM}}) \cos^2(\phi_f^{(1)}) \\ & + \omega_e^2(R_e + H_{\text{TAEM}}) \sin(\phi_f^{(1)}) \cos(\phi_f^{(1)}) \cos(\psi_f^{(1)}) \\ & + 2V_{\text{TAEM}}\omega_e \cos(\phi_f^{(1)}) \sin(\psi_f^{(1)}) = 0 \end{aligned} \quad (14.92)$$

where $\alpha_{\text{bsl}}^{(2)}$ refers to the corrected α_{bsl} profile, and q_{TAEM} is the dynamic pressure corresponding to V_{TAEM} and H_{TAEM} . Since H is much less than R_e , assume that $R_e + H_f^{(1)} \approx R_e + H_{\text{TAEM}}$. Subtracting Eq. (14.92) from Eq. (14.91) yields

$$\begin{aligned} & \frac{\left[C_{L(\text{est})} \left(\alpha_{\text{bsl}}^{(1)}(E_f^{(1)}) \right) - C_{L(\text{est})} \left(\alpha_{\text{bsl}}^{(2)}(E_{\text{TAEM}}) \right) \right] q_{\text{TAEM}} S_{\text{ref}}}{m} \\ & = \frac{C_{L(\text{est})} \left(\alpha^{(1)}(E_f^{(1)}) \right) \left[q_{\text{TAEM}} - q_f^{(1)} \right] S_{\text{ref}}}{m} + \frac{V_{\text{TAEM}}^2 - (V_f^{(1)})^2}{R_e + H_f^{(1)}} \\ & + 2(V_{\text{TAEM}} - V_f^{(1)})\omega_e \cos(\phi_f^{(1)}) \sin(\psi_f^{(1)}) \end{aligned} \quad (14.93)$$

Linearize the following expression

$$\begin{aligned} & C_{L(\text{est})} \left(\alpha_{\text{bsl}}^{(1)}(E_f^{(1)}) \right) - C_{L(\text{est})} \left(\alpha_{\text{bsl}}^{(2)}(E_{\text{TAEM}}) \right) \\ & \approx C_{L(\text{est})}^\alpha \cdot \left[\alpha_{\text{bsl}}^{(1)}(E_f^{(1)}) - \alpha_{\text{bsl}}^{(2)}(E_{\text{TAEM}}) \right] \\ & = C_{L(\text{est})}^\alpha \cdot \left[\alpha_{\text{bsl}}^{(1)}(E_f^{(1)}) - \alpha_{\text{bsl}}^{(1)}(E_{\text{TAEM}}) + \alpha_{\text{bsl}}^{(1)}(E_{\text{TAEM}}) - \alpha_{\text{bsl}}^{(2)}(E_{\text{TAEM}}) \right] \\ & = C_{L(\text{est})}^\alpha \cdot \left[\alpha_{\text{bsl}}^{(1)}(E_f^{(1)}) - \alpha_2^{(1)} - \Delta\alpha_2 \right] \end{aligned} \quad (14.94)$$

where $\alpha_{\text{bsl}}^{(1)}(E_{\text{TAEM}}) = \alpha_2^{(1)}$ and $\Delta\alpha_2 = \alpha_{\text{bsl}}^{(2)}(E_{\text{TAEM}}) - \alpha_{\text{bsl}}^{(1)}(E_{\text{TAEM}})$. $C_{L(\text{est})}^\alpha$ is the estimated lift curve slope. Solving Eqs. (14.93)–(14.94) for $\Delta\alpha_2$ yields

$$\begin{aligned}\Delta\alpha_2 &= \alpha_{\text{bsl}}^{(1)}(E_f^{(1)}) - \alpha_2^{(1)} + \frac{C_{L(\text{est})}\left(\alpha^{(1)}(E_f^{(1)})\right)\left[q_f^{(1)} - q_{\text{TAEM}}\right]}{C_{L(\text{est})}^\alpha q_{\text{TAEM}}} \\ &+ \frac{m\left[(V_f^{(1)})^2 - V_{\text{TAEM}}^2\right]}{C_{L(\text{est})}^\alpha q_{\text{TAEM}} S_{\text{ref}}\left(R_e + H_f^{(1)}\right)} + \frac{2m(V_f^{(1)} - V_{\text{TAEM}})\omega_e \cos(\phi_f^{(1)}) \sin(\psi_f^{(1)})}{C_{L(\text{est})}^\alpha q_{\text{TAEM}} S_{\text{ref}}}\end{aligned}\quad (14.95)$$

Thus, we get the corrected value of α_2 , i.e. $\alpha_2^{(2)} = \alpha_2^{(1)} + \Delta\alpha_2$.

(2) E_{BR2} —correction algorithm

This algorithm is used to fine-tune E_{BR2} in order to meet the final speed requirement. The following analyzes the relationship between E_{BR2} and V_f .

Decreasing E_{BR2} postpones the occurrence of the second bank reversal and thus causes the heading error at $E = E_{BR2}$ to increase. Consequently, in the AAP, greater bank angle is required by PN to remove the heading error. This results in a decrease in L_1/D . Further, the energy dissipation rate is accelerated and thus V_f is reduced.

Due to the monotonic relation, the secant method [20] is quite suitable for iteratively solving $V_f(E_{BR2}) = V_{\text{TAEM}}$ as

$$E_{BR2}^{(n+1)} = E_{BR2}^{(n)} - (V_f^{(n)} - V_{\text{TAEM}}) \frac{(E_{BR2}^{(n)} - E_{BR2}^{(n-1)})}{(V_f^{(n)} - V_f^{(n-1)})} \quad (14.96)$$

where $V_f^{(n)}$ is the value of V_f obtained in the n -th trajectory simulation and $E_{BR2}^{(n)}$ is the value of E_{BR2} used in the n -th trajectory simulation. In general, Eq. (14.96) needs only be iterated 4–5 times to meet the condition that $|V_f^{(n)} - V_{\text{TAEM}}| < 1 \text{ m/s}$.

14.3.3.2 Baseline Bank Angle in AAP

PN is employed here to determine σ_{bsl} . The time derivative of the azimuth angle of the Line Of Sight (LOS) is

$$\dot{\psi}_{\text{LOS}} = \frac{V \cos(\gamma) \sin(\Delta\psi)}{s_{\text{go}}} \quad (14.97)$$

Then the lateral acceleration command generated by PN is

$$a_{L2} = k_{PN} \dot{\psi}_{\text{LOS}} V \cos(\gamma) - \Delta L_2/m \quad (14.98)$$

where ΔL_2 is due to the inertial forces and calculated by Eq. (14.22). The corresponding term is used to counteract the inertial force. To avoid the saturation of the initial bank angle, we let the navigation ratio k_{PN} increase from 2 to 4 as

$$k_{PN} = 2 \frac{s_{go}(E)}{s_{go}(E_{BR2})} + 4 \left(1 - \frac{s_{go}(E)}{s_{go}(E_{BR2})} \right) \quad (14.99)$$

By assuming that $\dot{\gamma} \approx 0$, the vertical component of the lift acceleration a_{L1} can be approximated by

$$a_{L1} \approx g - \frac{V^2}{R_e + H} - \frac{\Delta L_1}{m} \quad (14.100)$$

where ΔL_1 is calculated by Eq. (14.21). Then the baseline bank angle is determined by

$$\sigma_{bsl} = \arctan\left(\frac{a_{L2}}{a_{L1}}\right) \quad \text{for } E \leq E_{BR2} + \Delta E \quad (14.101)$$

14.3.3.3 AOA and Bank Angle Commands in AAP

In the AAP, the AOA and bank angle commands are

$$\alpha_{cmd} = \alpha_{bsl} + k_\alpha [s_{go}(E) - s_{go}^{ref}(E)] \quad (14.102)$$

$$\sigma_{cmd} = \sigma_{bsl} - \sin(\sigma_{bsl}) \frac{k_\gamma (\gamma_{SG} - \gamma)}{\alpha_1} \quad (14.103)$$

where $s_{go}^{ref}(E)$ is the reference profile of s_{go} with respect to E and obtained from the last onboard trajectory simulation. The constant k_α is set to $5\pi/(1.8 \times 10^7)$, which means that, for instance, if s_{go} is 1 km longer than s_{go}^{ref} , AOA will be increased by 0.05 deg. The purpose is to increase L/D and thus reduce energy dissipation rate in order that s_{go} can catch up with s_{go}^{ref} . Thereby, the corresponding term is used to cope with the disturbances occurring in the AAP. Since the trajectory in the AAP is relatively short, the errors accumulated in this phase are small and thus only a small adjustment of AOA is required. The second term of Eq. (14.103) is also used to eliminate the trajectory oscillations. To ensure the satisfaction of the path constraints, the measures shown in Eqs. (14.86)–(14.90) are also taken here.

14.4 Results and Discussion

14.4.1 Nominal Cases

To confirm that the proposed entry guidance, denoted as AEG, is able to compensate the Earth rotation effects completely, seven nominal cases with different flight directions are given here. The initial conditions of these cases are $H_0 = 80\text{km}$, $\lambda_0 = 0\text{ deg}$, $\phi_0 = 50\text{ deg}$, $V_0 = 7000\text{ m/s}$, and $\gamma_0 = 0\text{ deg}$. The initial heading angle ψ_0 depends on the target position, as shown in Table 14.1. As AEG is a substantial improvement of the entry guidance developed in [16], denoted as EGAS, the simulation results of EGAS are also provided here for comparison.

The simulation results are shown in Tables 14.2, 14.3 and Figs. 14.6, 14.7, 14.8, 14.9, 14.10, 14.11 and 14.12. As can be seen from these figures, the result curves are distributed closely and difficult to be distinguished. Therefore, for the sake of brevity, we do not mark out the corresponding cases for these curves except Cases T4 and T5, the heating rates of which exceed the limitation temporarily. Even so, the trajectory characteristics are still clear without labeling the results. In Cases T4 and T5, because the vehicles fly westwards, the dominant component of the inertial force, i.e. $2V\omega_e \cos(\phi) \sin(\psi)$ in Eq. (14.5), is negative, which indicates that the

Table 14.1 Simulation conditions for nominal cases

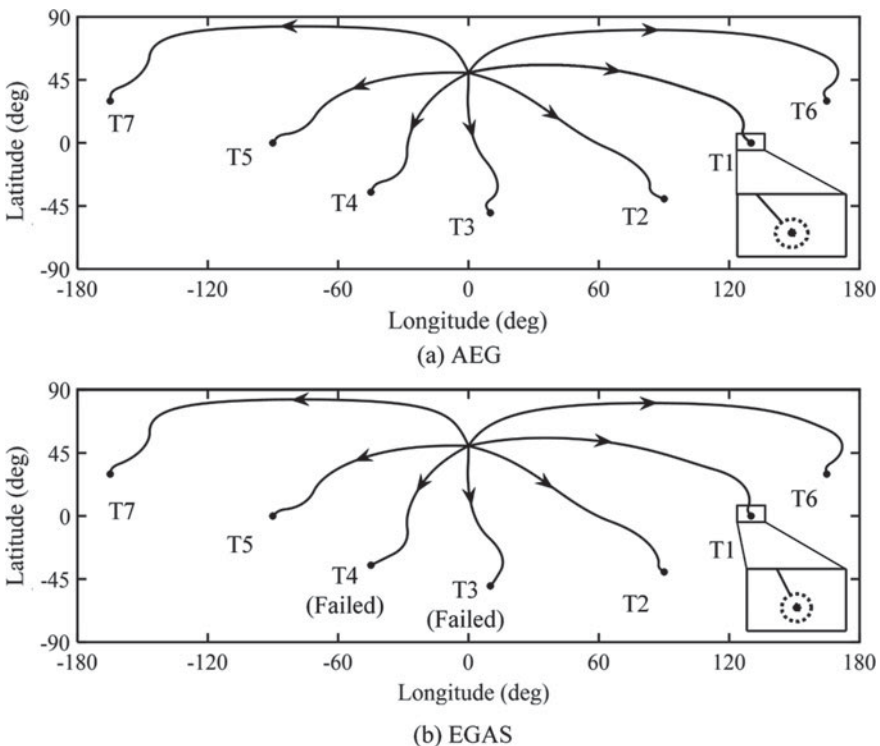
Case	λ_T (deg)	ϕ_T (deg)	ψ_0 (deg)
T1	130	0	60
T2	90	-40	120
T3	10	-50	180
T4	-50	-40	-140
T5	-90	0	-85
T6	165	30	15
T7	-165	30	-10

Table 14.2 Nominal terminal results of AEG

Case	t_f (s)	$s_{go(f)}$ (km)	V_f (m/s)	H_f (km)	$\Delta\psi_f$ (deg)	α_2 (deg)	E_{BR1} (kJ/kg)	E_{BR2} (kJ/kg)
T1	2464.61	50.00	2000.00	25.01	-0.0041	6.32	-46,865.68	-55,593.68
T2	2569.41	50.00	2000.00	25.03	-0.0106	6.35	-45,859.15	-55,701.34
T3	2202.71	50.00	2000.00	25.01	-0.0160	6.55	-46,547.89	-55,707.88
T4	2060.51	50.00	2000.00	24.99	-0.0165	6.88	-46,899.17	-55,716.89
T5	1968.18	50.00	2000.00	24.85	-0.0082	7.26	-47,951.05	-55,678.58
T6	2162.31	50.00	2000.00	25.03	0.0034	6.59	-47,152.14	-55,573.11
T7	2177.21	50.00	2000.00	24.96	0.0015	6.43	-47,619.14	-55,597.49

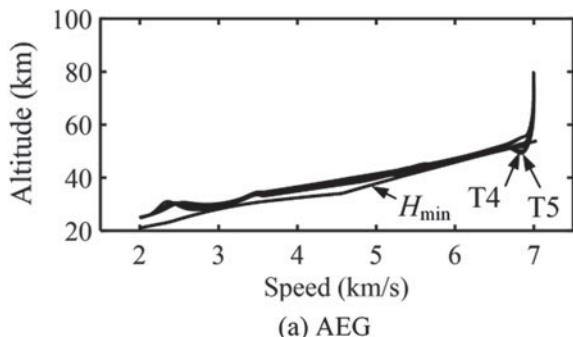
Table 14.3 Nominal terminal results of EGAS

Case	t_f (s)	$s_{go(f)}$ (km)	V_f (m/s)	H_f (km)	$\Delta\psi_f$ (deg)	α_2 (deg)	E_{BR1} (kJ/kg)	E_{BR2} (kJ/kg)
T1	2500.12	50.00	2000.00	25.54	0.09490	6.00	-47,679.21	-57,073.02
T2	2611.32	50.00	2000.00	25.62	-0.04800	6.00	-46,676.00	-57,426.91
T3	2185.90	50.00	2601.62	30.48	0.95640	6.00	-47,556.74	-55,614.81
T4	2030.90	50.00	2665.18	3057	0.94790	6.00	-47,841.77	-55,457.39
T5	1979.10	50.00	2000.00	25.10	0.11504	6.00	-48,708.36	-56,476.10
T6	2181.10	50.00	2000.00	25.32	0.14233	6.00	-47,809.40	-56,521.45
T7	2192.91	50.00	2000.00	25.07	0.15187	6.00	-48,225.78	-56,539.78

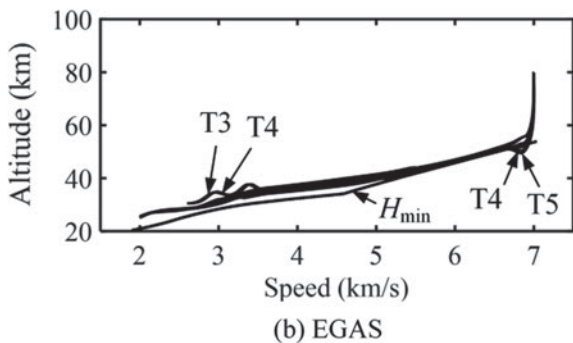
**Fig. 14.6** Nominal ground tracks

inertial force points downwards and thus depresses the glide altitude. This causes the heating rate constraint to be violated even if the AOA has been maximized. From Tables 14.2, 14.3 and Fig. 14.6, we can see that AEG is successful for all cases, but EGAS fails in Cases T3 and T4 where the achieved final speed is much greater than V_{TAEM} . The reason for failure is that EGAS compensates the effects of the Earth's

Fig. 14.7 Nominal altitude versus speed histories

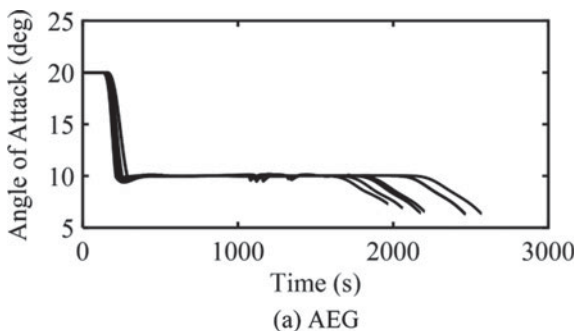


(a) AEG

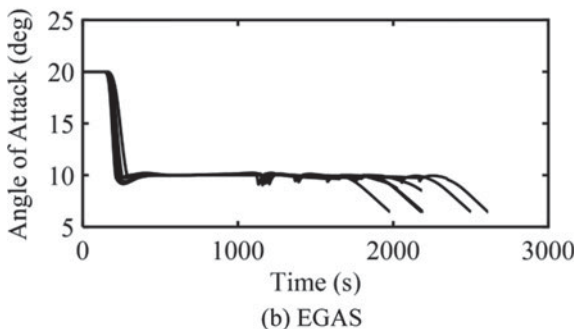


(b) EGAS

Fig. 14.8 Nominal AOA histories



(a) AEG



(b) EGAS

Fig. 14.9 Nominal bank angle histories

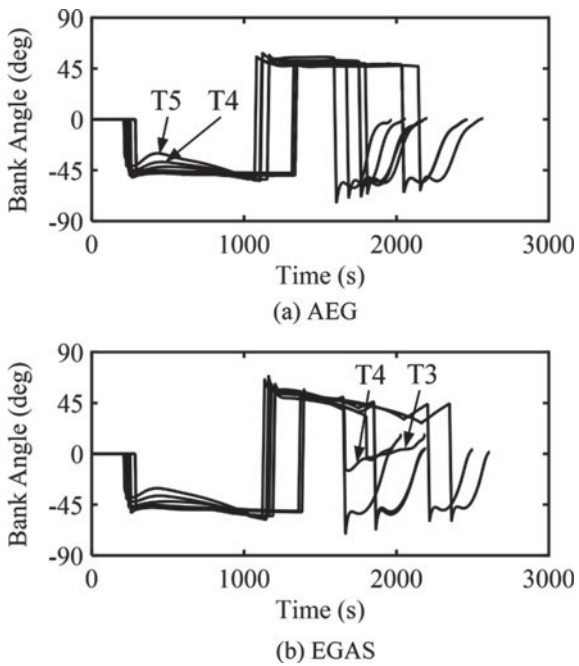


Fig. 14.10 Nominal heating rate histories

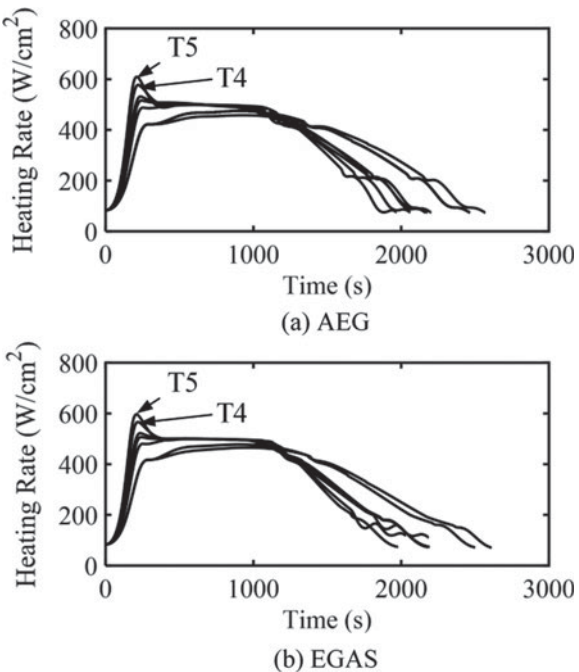
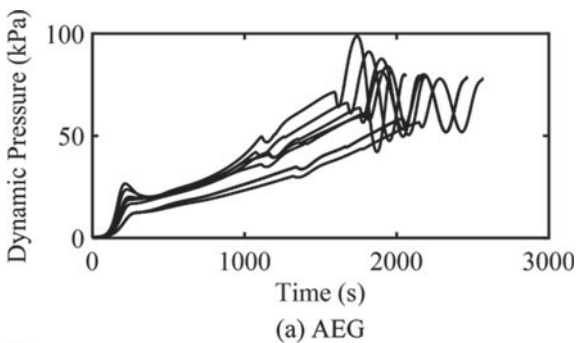
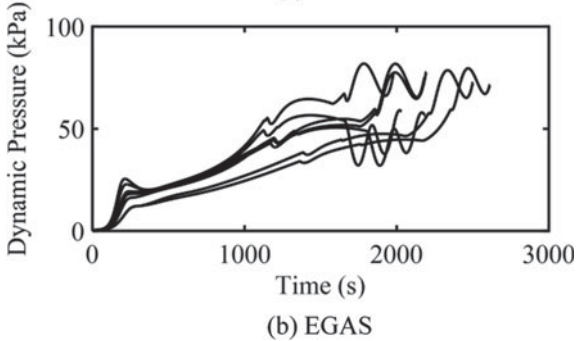


Fig. 14.11 Nominal dynamic pressure histories

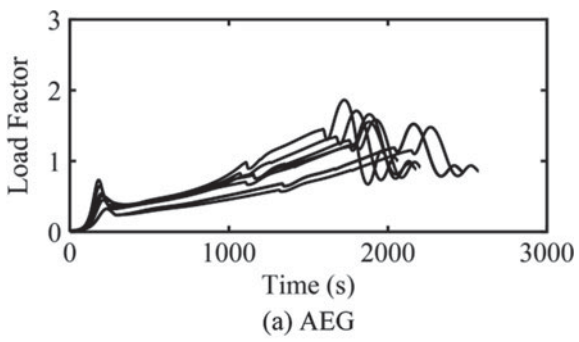


(a) AEG

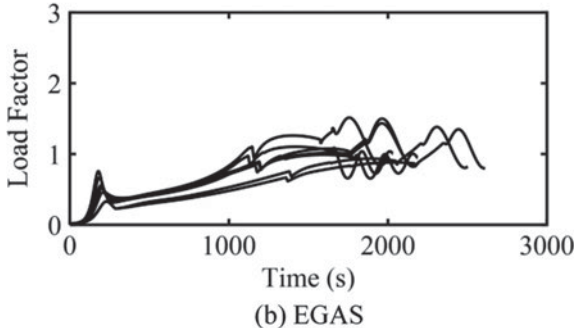


(b) EGAS

Fig. 14.12 Nominal load factor histories



(a) AEG



(b) EGAS

rotation insufficiently and thus has apparent reference-tracking errors, especially if the vehicle flies northwards or southwards near the equator. By comparing Table 14.2 with Table 14.3, we can find that the accuracy of H_f for AEG is one order of magnitude higher than that for EGAS. This is because in AEG, α_2 is slightly adjusted by α_2 -correction algorithm presented in Sect. 6.3.3.1 according to the predicted final altitude error. Additionally, the distribution of E_{BR2} for AEG is more concentrated than that of EGAS. This indirectly indicates that, compared with EGAS, AEG can compensate the effects of the Earth's rotation more reasonably and adequately. Figure 14.6 shows the ground tracks for the two guidance laws. From the magnification of the ground track for Case 1, we can see that the entry flight ends at the circle centered at the target with radius of 50 km while the vehicle has a clear trend of heading toward its target. Figure 14.6b marks out Cases T3 and T4 where EGAS fails. Figure 14.7 presents the H -vs- V histories and verifies that the trajectory oscillations are effectively suppressed by the TDCT. Figure 14.8 shows the AOA histories where we can clearly distinguish the three phases of entry flight. Figure 14.9 displays the bank angle histories. For AEG, in most of the cases, the bank angle remains almost constant in the SGP and gradually converges to zero in the AAP, which is in line with our expectation. For EGAS, in the failed Cases T3 and T4, the bank angles change abnormally in the AAP. Figures 14.10, 14.11 and 14.12 show the histories of the heating rates, dynamic pressures, and load factors, respectively. As the load factor n is proportional to the dynamic pressure q , the load factor profiles have similar shapes with that of the dynamic pressures. Additionally, we can also see that n and q increase gradually with time in the SGP. This is because the centrifugal force caused by the Earth's curvature decreases with decreasing speed and thus the lift gets increased to resist the gravity.

14.4.2 Monte Carlo Simulations

Monte Carlo simulations are conducted here to verify the robustness of the proposed guidance. The considered disturbances include initial state dispersions, aerodynamic uncertainties, and atmospheric perturbations. The aerodynamic uncertainties generally exist in early flight tests and vary with AOA and Mach number (Ma) [21]. For simplicity, we assume that the percentage variations in the lift and drag coefficients, denoted as δ_{CL} and δ_{CD} respectively, are linear functions of α and Ma , as follows

$$\delta_{CL} = \delta_{CL0} + k_{\delta CL}^{Ma} \frac{Ma - 15}{17} + k_{\delta CL}^{\alpha} \frac{18}{\pi} \left(\alpha - \frac{\pi}{18} \right) \quad (14.104)$$

$$\delta_{CD} = \delta_{CD0} + k_{\delta CD}^{Ma} \frac{Ma - 15}{17} + k_{\delta CD}^{\alpha} \frac{18}{\pi} \left(\alpha - \frac{\pi}{18} \right) \quad (14.105)$$

where δ_{CL0} , $k_{\delta CL}^{Ma}$, $k_{\delta CL}^{\alpha}$, δ_{CD0} , $k_{\delta CD}^{Ma}$, and $k_{\delta CD}^{\alpha}$ are coefficients.

Fig. 14.13 Profile of $V_{\text{wind}(max)}$

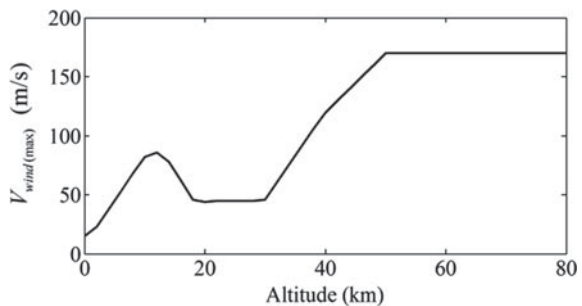
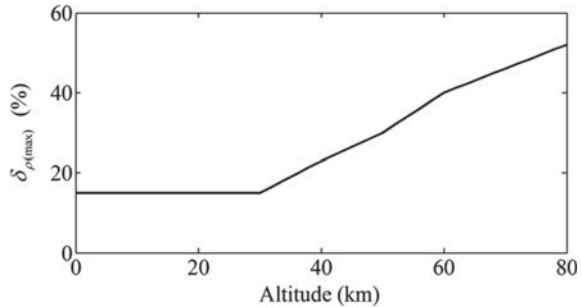


Fig. 14.14 Profile of $\delta_{\rho(max)}$



The atmosphere is not static as viewed from the rotating Earth, but constantly flows, expands with heat, or contracts with cold. This produces winds and causes changes in the atmospheric density. Denote the maximum possible wind speed as $V_{\text{wind}(max)}$ and the maximum possible percent deviation of the atmospheric density as $\delta_{\rho(max)}$. Figures 14.13 and 14.14 show the $V_{\text{wind}(max)}$ and $\delta_{\rho(max)}$ profiles with respect to H , respectively. Here, we can see that $V_{\text{wind}(max)}$ can be up to 170 m/s and $\delta_{\rho(max)}$ is more than 50% at high altitudes.

The wind model and the dispersion model of atmospheric density are established by

$$V_{\text{wind}}^{EW} = k_{\text{wind}}^{EW} V_{\text{wind}(max)} \quad (14.106)$$

$$V_{\text{wind}}^{NS} = k_{\text{wind}}^{NS} V_{\text{wind}(max)} \quad (14.107)$$

$$\delta_{\rho} = k_{\rho} \delta_{\rho(max)} \quad (14.108)$$

where V_{wind}^{EW} is the wind speed in local east or west direction, V_{wind}^{NS} is the wind speed in local north or south direction, and δ_{ρ} is the percent deviation of the atmospheric density. k_{wind}^{EW} , k_{wind}^{NS} , and k_{ρ} are coefficients with values between -1 and 1.

Table 14.4 Statistical characteristics of the normally distributed random parameters

Uncertainty	3TSD	Uncertainty	3TSD	Uncertainty	3TSD
ΔH_0 (km)	3	δ_{CL0}	15%	k_{wind}^{EW}	100%
$\Delta \lambda_0$ (deg)	0.45	$k_{\delta CL}^{Ma}$	5%	k_{wind}^{NS}	100%
$\Delta \phi_0$ (deg)	0.45	$k_{\delta CL}^{\alpha}$	5%	k_{ρ}	100%
ΔV_0 (m/s)	100	δ_{CD0}	15%		
$\Delta \gamma_0$ (deg)	1	$k_{\delta CD}^{Ma}$	5%		
$\Delta \psi_0$ (deg)	1	$k_{\delta CD}^{\alpha}$	5%		

Cases T2, T3, T4, and T6 introduced in Sect. 6.4.1 are also considered here. In the Monte Carlo simulations, all the random variables are normally distributed with zero means, and their 3 Times Standard Deviations (3TSD) are listed in Table 14.4, where ΔH_0 , $\Delta \lambda_0$, $\Delta \phi_0$, ΔV_0 , $\Delta \gamma_0$, and $\Delta \psi_0$ are the deviations of H_0 , λ_0 , ϕ_0 , V_0 , γ_0 , and ψ_0 from their nominal values.

Predictor-Corrector Gliding Guidance (PCGG) with assistance of a simplified TDCT was developed for steering CAV [14]. The Monte Carlo simulation results of PCGG are also provided here. To satisfy the path constraints, we modify PCGG partly: (1) In the descent phase, the scheme presented in Sect. 6.3.2 is adopted, which commands the vehicle to fly along α_{max} with $\sigma = 0$, and (2) in the glide phase, the measures described by Eqs. (14.86)–(14.90) are also taken here to limit the bank angle command.

Additionally, as a classical entry guidance law, Shuttle Entry Guidance (SEG) is applied to steer the high-L/D CAV here. According to the needs of the missions, some changes are made to SEG: (1) The guidance scheme of AEG used in the DP is also adopted by SEG, and (2) the AOA profile of AEG is also applied to SEG.

The simulation results are shown in Figs. 14.15, 14.16, 14.17, 14.18, 14.19, 14.20 and 14.21. Figure 14.15 presents the ground tracks of AEG, PCGG and SEG for the four considered cases. From the local enlarged drawings, we can clearly see that the trajectories of AEG near the ends are distributed closely and regularly while the vehicles have clear trends of heading toward their destinations. By contrast, the trajectories of PCGG and SEG are distributed relatively disorderly and their final heading errors are large. Additionally, PCGG and SEG fail in some extreme cases with large aerodynamic uncertainties and strong side-winds. From this figure, we can find a strange phenomenon: There exist some blank regions surrounded by the ground tracks of PCGG and SEG. This is essentially due to the discontinuity of the bank reversal thresholds.

To prevent the paper length from growing too large, the following graphs only display the results for Case T6. Figure 14.16 shows the altitude profiles with respect to speed. Due to the TDCT, the altitudes of AEG in the SGP and AAP decrease slowly and smoothly. Some results of PCGG have apparent adverse oscillations. This is because PCGG adopts the simplified TDCT, where the formula of γ_{SG} has a relatively low accuracy and thus the feedback gain has to decay to zero as the

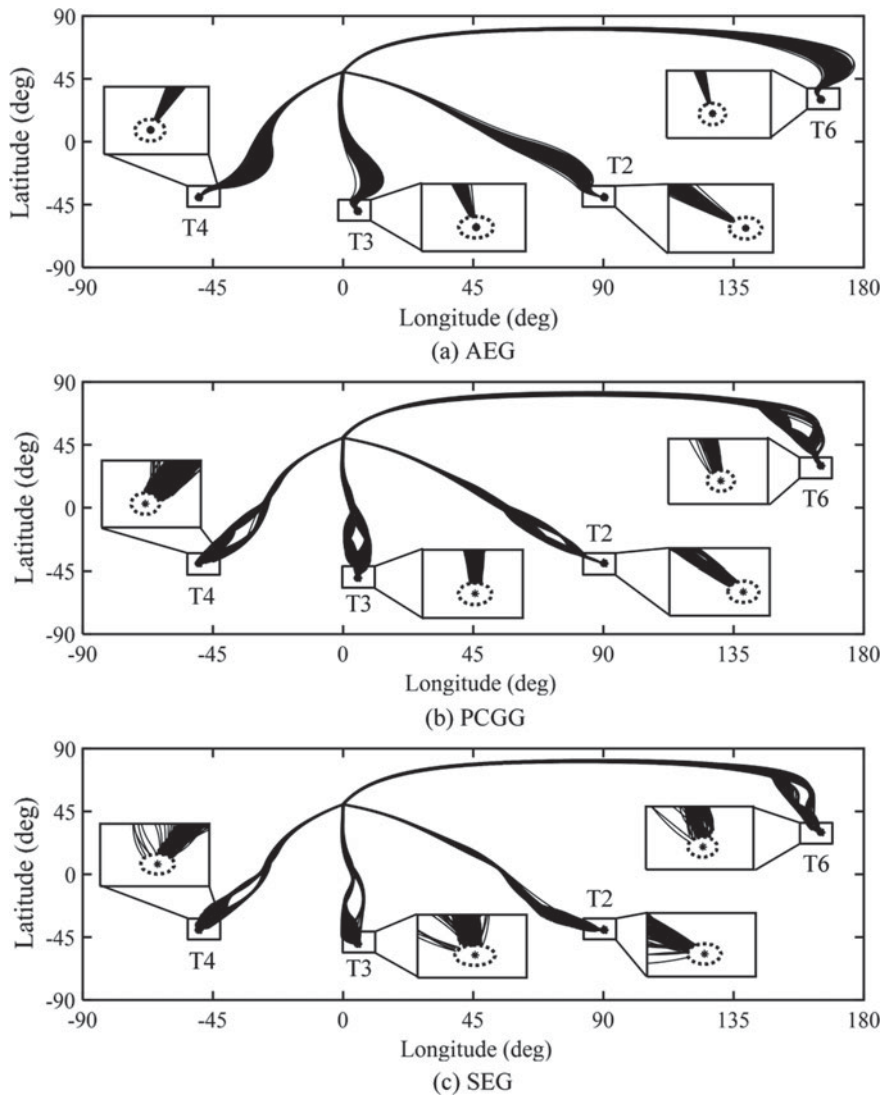
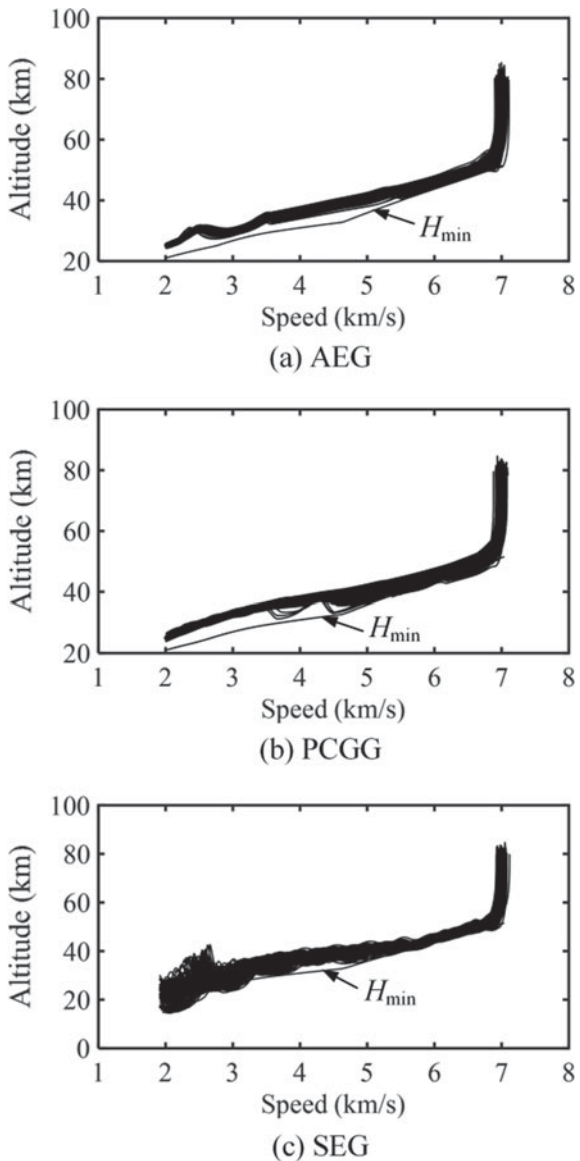


Fig. 14.15 Ground tracks of AEG, PCGG, and SEG for Cases T2, T3, T4, and T6

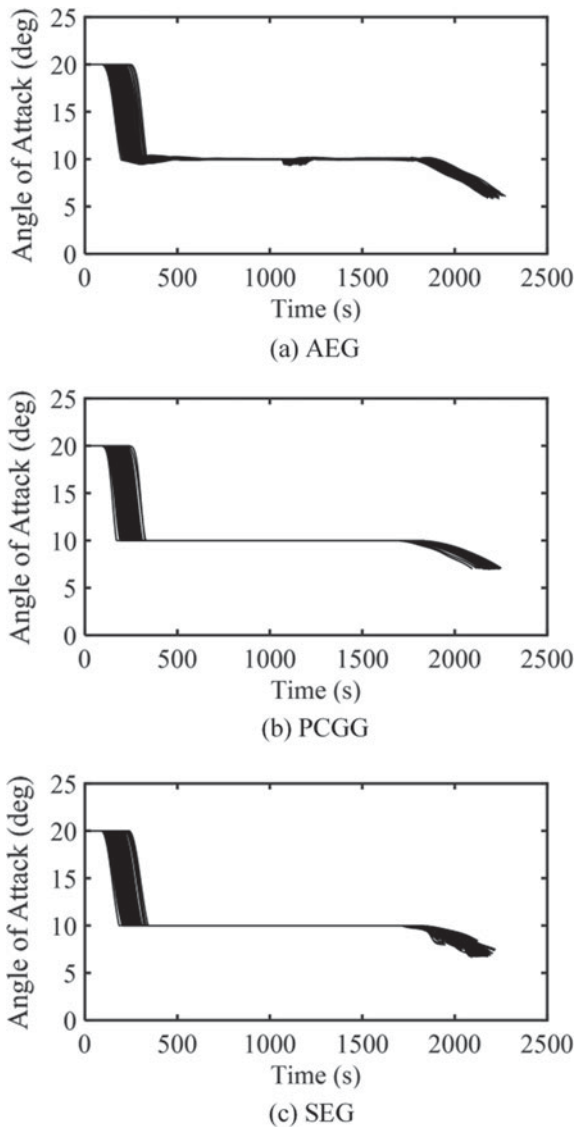
vehicle gets close to the target in order not to interfere the tracking of reference. However, reducing the feedback gain will weaken the effectiveness of suppressing the trajectory oscillations. SEG has a very weak capacity of suppressing the oscillations, and thus the oscillations become more and more intense. From the following results, we will see that the oscillations significantly reduce the accuracy of SEG, seriously impede flight safety, and even lead to failures of some flight missions. Figure 14.17 shows the AOA histories. Due to the modifications of PCGG and SEG made here,

Fig. 14.16 Altitude versus speed histories for Case T6



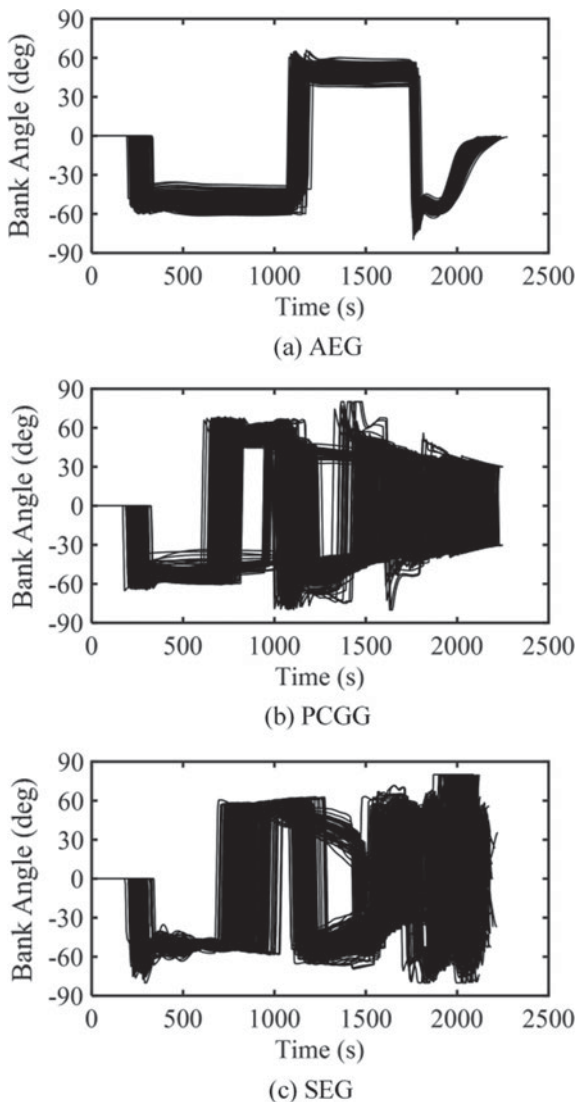
the AOA histories of PCGG and SEG are similar to that of AEG. Figure 14.18 shows that AEG only requires two bank reversals distributed regularly, whereas PCGG and SEG perform more bank reversals and sometimes the reversal number can be even up to 9. Figure 14.19 presents the distributions of the final speeds and heading errors. Here we can see that the final heading errors for PCGG and SEG are almost 1000 times larger than that of AEG even though there are much more bank

Fig. 14.17 AOA histories for Case T6



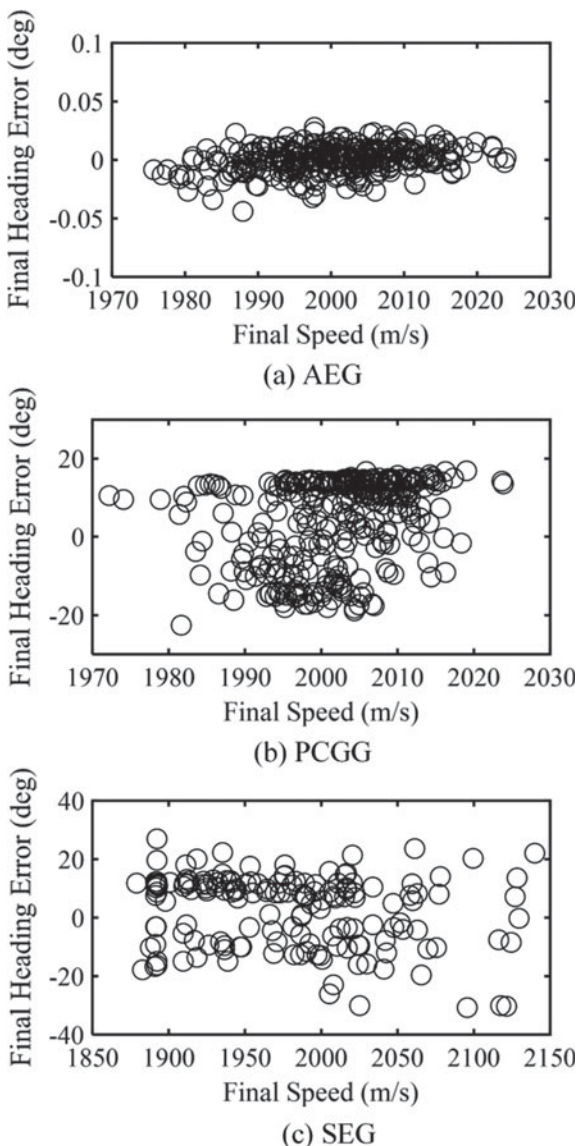
reversals performed by PCGG and SEG to eliminate the heading errors. In addition, the trajectory oscillations result in a serious reduction in the final speed accuracy of SEG, where the final speed errors of SEG are almost 3–5 times larger than that of AEG and PCGG. Figure 14.20 displays the distribution of the final altitudes and bank angles, where we can see that the final bank angles of AEG are almost zero, PCGG are distributed near ± 30 deg, and SEG are randomly distributed over the range of -60 deg to 60 deg. The final altitude accuracy of AEG is also much higher than that of PCGG

Fig. 14.18 Bank angle histories for Case T6



and SEG. Due to the trajectory oscillations, the final altitudes of SEG are distributed in a wide range. Figure 14.21 compares the computing times per one simulation of AEG, PCGG and SEG, where all the simulation programs are written in Matlab programming language. As PCGG needs to simulate the reduced-order equations of longitudinal motion numerically in real time, PCGG has the heaviest computational load. Conversely, because SEG need not conduct any onboard trajectory simulation and all commands are generated by explicit functions, the computing time for SEG is the shortest.

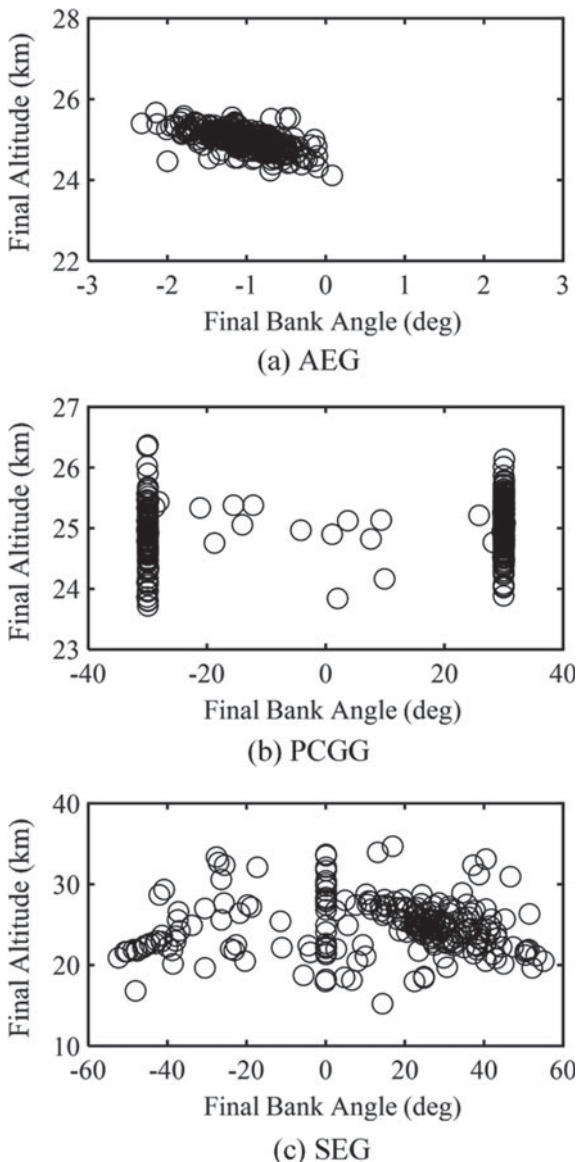
Fig. 14.19 Distribution of final speeds and heading errors for Case T6



14.5 Conclusions

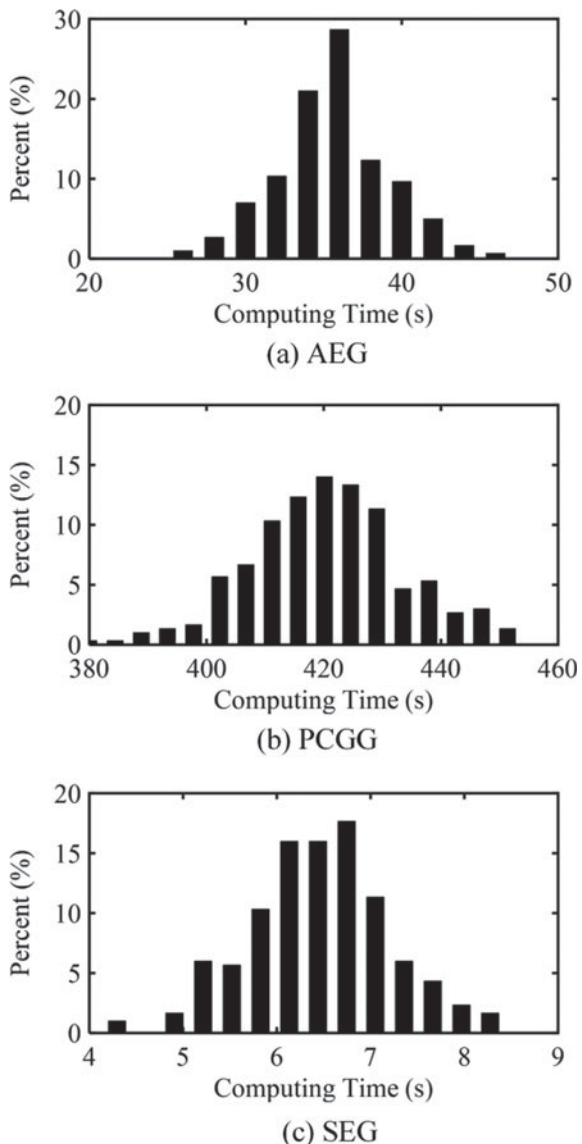
An analytical entry guidance is developed for high-L/D hypersonic glide vehicle and capable of steering the vehicle to any place on the Earth. As the adopted 3-D analytical glide formulas ignore the effects of the Earth's rotation, we introduce the pseudo-aerodynamic forces by merging the conventional aerodynamic forces with

Fig. 14.20 Distribution of final bank angles and altitudes for Case T6



the inertial forces to compensate these effects. To remain the AOA and bank angle almost constant in the SGP, by carefully forecast the change trends of the inertial forces, we design the pseudo-aerodynamic profiles elaborately as inversely proportional functions. Further, we derive the new 3-D analytical glide formulas for these inversely proportional profiles and then use them to determine the profiles' parameters and bank reversals. By simulating the scenarios with different flight directions,

Fig. 14.21 Distribution of computing time per one simulation for Case T6



it is verified that the guidance can fully compensate the effects of the Earth's rotation while remaining the AOA and bank angle almost constant in the SGP. The Monte Carlo simulations are conducted to demonstrate the high accuracy and strong robustness of the proposed guidance, where some challenging interferences including initial state dispersions, aerodynamic uncertainties, and atmosphere perturbations are imposed to test the guidance.

References

1. Phillips, T.H.: A common aero vehicle (CAV) model, description, and employment guide. Schafer Corporation for AFRL and AFSPC, (2003)
2. Zarchan, P.: Tactical and strategic missile guidance, 5th edn. AIAA Progress in Aeronautics and Astronautics (2007)
3. Bryson, A.E., Ho, Y.C.: Applied optimal control. Blaisdell, Waltham (1969)
4. Harpold, J.C., Graves, C.A.: Shuttle entry guidance. NASA Lyndon B. Johnson Space Center, Houston (1979)
5. Mease, K.D., Chen, D.T., Teufel, P., et al.: Reduced-order entry trajectory planning for acceleration guidance. *J. Guidance Control Dyn.* **25**(2), 257–266 (2002)
6. Dukeman, G.A.: Profile-following entry guidance using linear quadratic regulator theory. AIAA Guidance, Navigation, and Control Conference and Exhibit. Monterey, 4457 (2002)
7. Shen, Z., Lu, P.: On-board generation of three-dimensional constrained entry trajectories. *J. Guidance Control Dyn.* **26**(1), 111–121 (2003)
8. Zhang, Y.L., Chen, K.J., Liu, L., et al.: Entry trajectory planning based on three-dimensional acceleration profile guidance. *Aerosp. Sci. Technol.* **48**, 131–139 (2016)
9. Zhou, J., Zhao, R.: Pigeon-inspired optimization applied to constrained gliding trajectories. *Nonlinear Dyn.* **82**(4), 1781–1795 (2015)
10. Powell, R.W.: Six-degree-of-freedom guidance and control-entry analysis of the HL-20. *Journal of Spacecraft and Rockets* **30**(5), 537–542 (1993)
11. Zimmerman, C., Dukeman, G., Hanson, J.: Automated method to compute orbital reentry trajectories with heating constraints. *J. Guidance Control Dyn.* **26**(4), 523–529 (2003)
12. Xie, Y., Liu, L., Tang, G., et al.: Highly constrained entry trajectory generation. *Acta Astronaut.* **88**, 44–60 (2013)
13. Zhao, J., Zhou, R.: Reentry trajectory optimization for hypersonic vehicle satisfying complex constraints. *Chin. J. Aeronaut.* **26**(6), 1544–1553 (2013)
14. Lu, P.: Entry guidance: a unified method. *J. Guidance Control Dyn.* **37**(3), 713–728 (2014)
15. Yu, W., Chen, W.: Guidance scheme for glide range maximization of a hypersonic vehicle. AIAA Guidance, Navigation, and Control Conference. Portland, p. 6714 (2011)
16. Yu, W., Chen, W.: Entry guidance with real-time planning of reference based on analytical solutions. *Adv. Space Res.* **55**(9), 2325–2345 (2015)
17. Hu, J., Li, J., Chen, W.: Longitudinal characteristics of steady glide trajectory for hypersonic vehicle. IEEE International Conference on Control, Automation And Information Sciences. Changshu, pp. 272–279 (2015)
18. Chowdhary, G., Jategaonkar, R.: Aerodynamic parameter estimation from flight data applying extended and unscented Kalman filter. *Aerosp. Sci. Technol.* **14**(2), 106–117 (2010)
19. Whitmore, S.A., Cobleigh, B.R., Haering, E.A.: Design and calibration of the X-33 flush airdata sensing (FADS) system. 36th AIAA Aerospace Sciences Meeting and Exhibit. Reno, p. 201 (1998)
20. Burden, R.L., Faires, J.D.: Numerical analysis, 9th edn. Cengage Learning, Boston (2010)
21. Cobleigh, B.R.: Development of the X-33 aerodynamic uncertainty model. NASA Dryden Flight Research Center, Edwards (1998)

Chapter 15

Linear Pseudospectral Guidance Method for Eliminating General Nominal Effort Miss Distance



15.1 Introduction

Model predictive control (MPC) is a form of control in which the current control is obtained by on-line solving a finite horizon open-loop optimal control problem, using the current state of the plant as the initial state in the calculation [1]. It has had a tremendous impact on industrial application development in the last decades. Now, an increasing number of researchers focus their attention on the development of “fast MPC”. Different from the off-line control policy, which is devoted to obtain the control by solving a full nonlinear optimal control problem. MPC usually involves employing the neighboring optimal control problem based on linearized dynamics. In general, a two-point boundary value problem (TPBVP) is formulated to calculate the current control. In order to reduce the consumption of time, Ohtsuka and Fujii have extended the stabilized continuation method to get a real-time optimization algorithm for nonlinear system [2]. A suitable continuation parameter is preselected to ensure satisfactory convergence. Lu Ping proposed a closed-form control law for trajectory tracking, in which a multi-step expansion is used to predict the state and Euler-Simpson approximation is employed to integral cost. Then, a quadratic programming problem is detected in analytically obtaining the current control [3]. Yan has applied the Legendre Pseudospectral method to solve the linear quadratic optimal control problem [4, 5]. A set of linear algebraic equations transferred from the original problem can be easily solved to obtain the current control. And this method has been successfully applied in magnetic attitude stabilization of satellite. It is noted that these methods are based on the assumption that the deviations from the reference trajectory are small. Paul Williams has proposed a new method to overcome this drawback [6]. This method approximates the original problem with successive linear approximation via quasi-linearization, and a Jacobi pseudospectral scheme is used to transfer the linear optimal control problem into solving a set of linear algebraic equations. An explicit integration for short horizon is used to overcome the comparatively large deviations. Another noteworthy point is that all these methods are receding horizon control that only solves a local optimal control from a finite

short time. Therefore, the solution can be obtained quickly but is not globally optimal. Consequently, those methods are suitable for tracking a desired trajectory.¹

To solve the nonlinear optimal control problem with hard terminal constraints and quadratic performance index, a new nonlinear optimal control design called model predictive static programming (MPSP) is proposed by Padhi [7–9]. This method combines the idea of nonlinear model predictive theory with the approximation dynamic programming. It can obtain the global optimal control. The current control is obtained via successively solving the static programming problem. However, this method should select a large number of nodes to ensure the Euler integration within a satisfactory tolerance.

In this chapter, a method for solving the same problem of MPSP is presented. This method combines the philosophies of the nonlinear approximation model predictive control, linear quadrature optimal control and the Gauss Pseudospectral method [10]. Therefore, the proposed method is called Linear Gauss Pseudospectral Model Predictive Control (LGPMPc). Current control is obtained by successively solving a set of linear algebraic equations transferred from the original nonlinear control problem via linearization and the Gauss Pseudospectral method. This method is attractive from the point of view of computational efficiency, high accuracy with fewer discrete points and character that the solution can be expressed in a smooth function with control at discrete points. It is suitable for on-line implementation. The most notable difference from the Paul's method is that this method is used to solve the global optimal control problem with hard terminal constraints. Therefore, the horizon is not fixed; the linearization is not designed to track a desired trajectory. Another important difference is that the approximation differential matrix of the Gauss Pseudospectral method is not default rank compared with that of Legendre and Jacobi Pseudospectral methods. The recent study shows that these methods may result in a null space in solving optimal control problem [11]. A design of terminal impact with a specified direction is carried out to evaluate the performance of the proposed method. The results of simulations suggest that, comparing with MPSP and adaptive terminal guidance, the proposed method is not only applicable in the framework of guidance design, but also of high efficiency and accuracy in terminal guidance.

15.2 Generic Theory of LGPMPc

In this section, the generic theory of LGPMPc is presented in five parts. A brief description on some of the relevant concepts in linearization of nonlinear dynamic system and linear optimal control problem is stated in Sect. 15.2.1. And a linear

¹Reprinted from Acta Astronautica, Vol 96, Yang Liang, Zhou Hao, Chen Wanchun, Application of linear gauss pseudospectral method in model predictive control, Pages 175–187, Copyright (2014), with permission from Elsevier.

two-point boundary value problem (TPBVP) using the deviations from the reference trajectory as the independent variables is formulated. Sect. 15.2.2 describes the linear Gauss Pseudospectral Method in detail, which transfers the linear TPBVP into solving a set of linear algebraic equations. Sect. 15.2.3 is devoted to the discussion on the singularity of differential approximation matrices for different pseudospectral methods. The boundary controls of linear Gauss Pseudospectral Method are discussed in Sect. 15.2.4. In the final part, the procedure of implementation of LGPMPC is presented in detail.

15.2.1 Linearization of Nonlinear Dynamic System and Formulation of Linear Optimal Control Problem

Linearization of the nonlinear dynamic system is one of the most common methods in industrial application. Although a large sum of literatures have described the linearization in detail, it is still necessary to provide a brief description of it at the beginning of this subsection. Consider the general nonlinear dynamical system with hard terminal constraints as follow

$$\dot{\mathbf{x}} = \mathbf{f}(\mathbf{x}, \mathbf{u}, t) \quad (15.1)$$

$$\Psi(\mathbf{x}(t_f)) = 0 \quad (15.2)$$

where, $\mathbf{x} \in \mathbb{R}^n$ is the state vector, $\mathbf{u} \in \mathbb{R}^m$ is the control vector, $t \in \mathbb{R}$ is the time variable, $\Psi \in \mathbb{R}^s$ is the vector of the terminal constraint functions. Equation (15.1) is expanded in Taylor series with high-order differentiation around a nominal trajectory. Then, a set of linear dynamic equations, Eq. (15.3), using the deviations from the nominal trajectory as the independent variables are formulated by neglecting the higher order terms.

$$\delta\dot{\mathbf{x}} = \mathbf{A}\delta\mathbf{x} + \mathbf{B}\delta\mathbf{u} \quad (15.3)$$

where, $\mathbf{A} = \mathbf{f}_x(\mathbf{x}_p, \mathbf{u}_p)$ and $\mathbf{B} = \mathbf{f}_u(\mathbf{x}_p, \mathbf{u}_p)$, \mathbf{x}_p and \mathbf{u}_p are the nominal state and control vectors, $\delta\mathbf{x}$ is the deviation vector from the nominal trajectory. It should be noted that, in linearizing the nonlinear dynamic equations, the relation between the real states and nominal states is assumed to be $\mathbf{x} = \mathbf{x}_p - \delta\mathbf{x}$ rather than $\mathbf{x} = \mathbf{x}_p + \delta\mathbf{x}$ used in lots of literatures.

Now, consider a linear optimal control problem with the following performance index which subjects to Eq. (15.3).

$$J = \delta\mathbf{x}^T(t_f)\mathbf{P}_f\delta\mathbf{x}(t_f) + \mathbf{v}^T\left(\frac{\partial\Psi}{\partial\mathbf{x}_f}\delta\mathbf{x}(t_f) - d\Psi\right)$$

$$+ \frac{1}{2} \int_{t_0}^{t_f} (\mathbf{x}_p - \delta \mathbf{x})^T \mathbf{Q} (\mathbf{x}_p - \delta \mathbf{x}) + (\mathbf{u}_p - \delta \mathbf{u})^T \mathbf{R} (\mathbf{u}_p - \delta \mathbf{u}) dt \quad (15.4)$$

The first two terms are the terminal cost function. \mathbf{P}_f is the positive semidefinite weighting matrix. $d\psi$ is the vector of deviations between the values of terminal state constraints, which is generated by predictive integration, and the desired ones. \mathbf{Q} and \mathbf{R} are the positive semidefinite matrices respectively. It should be noted that the performance index is the minimization of the weighted square sum of actual control and state variables rather than that of deviations. According to the first-order necessary condition of an optimal control problem, a set of Eqs. (15.5)~(15.8) are obtained as

$$H = \frac{1}{2} (\mathbf{x}_p - \delta \mathbf{x})^T \mathbf{Q} (\mathbf{x}_p - \delta \mathbf{x}) + \frac{1}{2} (\mathbf{u}_p - \delta \mathbf{u})^T \mathbf{R} (\mathbf{u}_p - \delta \mathbf{u}) + \boldsymbol{\lambda}^T (\mathbf{A} \delta \mathbf{x} + \mathbf{B} \delta \mathbf{u}) \quad (15.5)$$

$$\frac{\partial H}{\partial \delta \mathbf{u}} = -\mathbf{R} (\mathbf{u}_p - \delta \mathbf{u}) + \mathbf{B}^T \boldsymbol{\lambda} = \mathbf{0} \rightarrow \delta \mathbf{u} = \mathbf{u}_p - \mathbf{R}^{-1} \mathbf{B}^T \boldsymbol{\lambda} \quad (15.6)$$

$$-\dot{\lambda} = \frac{\partial H}{\partial \delta \mathbf{x}} = -\mathbf{Q} (\mathbf{x}_p - \delta \mathbf{x}) + \mathbf{A}^T \boldsymbol{\lambda} \rightarrow \dot{\lambda} = -\mathbf{Q} \delta \mathbf{x} - \mathbf{A}^T \boldsymbol{\lambda} + \mathbf{Q} \mathbf{x}_p \quad (15.7)$$

$$\delta \dot{\mathbf{x}} = \mathbf{A} \delta \mathbf{x} - \mathbf{B} \mathbf{R}^{-1} \mathbf{B}^T \boldsymbol{\lambda} + \mathbf{B} \mathbf{u}_p \quad (15.8)$$

where, H is the Hamiltonian for the linear optimal control problem, $\boldsymbol{\lambda}$ is the costate vector for the current iteration. There are two types of transversality conditions. One is when \mathbf{x}_f is the variable of terminal cost function. Then, following Eq. (15.9) is used to calculate the corresponding boundary costate.

$$\boldsymbol{\lambda}(t_f) = \mathbf{P}_f \delta \mathbf{x}(t_f) + \mathbf{v}^T \left(\frac{\partial \Psi}{\partial \mathbf{x}_f} \right) \quad (15.9)$$

The other one is when \mathbf{x}_f is not the variable of terminal cost function. In order to eliminate the effect of corresponding terminal state, it is assumed that the corresponding part of \mathbf{P}_f is zero. Then, the boundary costate is known as follow.

$$\boldsymbol{\lambda}(t_f) = \mathbf{0} \quad (15.10)$$

If the terminal state is restricted to a specific value, it is equivalent to the first one. The function of terminal state constraint is regarded as $\mathbf{x}(t_f) = \mathbf{x}_f$. As the terminal state is known, the corresponding transversality condition is

$$\boldsymbol{\lambda}(t_f) = \mathbf{v} \quad (15.11)$$

where \mathbf{v} is a Lagrange Multiplier.

In general, the linear optimal control problem is transferred into a TPBVP with the dynamic equations Eq. (15.12). The transversality conditions are decided by the terminal constraints Eq. (15.2).

$$\begin{bmatrix} \delta\dot{\mathbf{x}} \\ \lambda \end{bmatrix} = \begin{bmatrix} \mathbf{A} & -\mathbf{BR}^{-1}\mathbf{B}^T \\ -\mathbf{Q} & -\mathbf{A}^T \end{bmatrix} \begin{bmatrix} \delta\mathbf{x} \\ \lambda \end{bmatrix} + \begin{bmatrix} \mathbf{Bu}_p \\ \mathbf{Qx}_p \end{bmatrix} \quad (15.12)$$

The optimal state and costate variables are obtained by solving TPBVP with initial and terminal conditions. The corresponding control can also be obtained by Eq. (15.6).

15.2.2 Linear Gauss Pseudospectral Method

In Linear Gauss Pseudospectral Method, the state and control variables are approximated using a basis of Lagrange interpolating polynomials; the differential-algebraic equations are approximated via orthogonal collocation. Thus, the linear optimal control problem with quadratic performance index is transferred into the problem of solving a set of linear algebraic equations. Compared with the time of numerically solving the nonlinear programming problem, the time of solving a set of linear algebraic equations is only a fraction of a second. The concrete procedure of discretization through Linear Gauss Pseudospectral method is given as follows.

Without loss of generality, consider a linear time-varying system such as the one mentioned in Sect. 15.2.1. Its dynamic equations and performance index are Eqs. (15.3) and (15.4) respectively. Because the points of Lagrange interpolating polynomials are orthogonal points, which lie in the computational interval $[-1, 1]$, the first step is to transfer the time domain from the time interval $[t_0, t_f]$ to the time interval $[-1, 1]$ via the following Eq. (15.13).

$$t = \frac{t_f - t_0}{2}\tau + \frac{t_f + t_0}{2} \quad (15.13)$$

The original performance index and linear dynamic equations are also transferred into Eqs. (15.14), and (15.15).

$$\begin{aligned} J &= \delta\mathbf{x}^T(1)\mathbf{P}_f\delta\mathbf{x}(1) + \mathbf{v}^T\left(\frac{\partial\Psi}{\partial\mathbf{x}_f}\delta\mathbf{x}(1) - d\Psi\right) \\ &\quad + \frac{t_f - t_0}{4} \int_{-1}^1 (\mathbf{x}_p - \delta\mathbf{x})^T \mathbf{Q} (\mathbf{x}_p - \delta\mathbf{x}) + (\mathbf{u}_p - \delta\mathbf{u})^T \mathbf{R} (\mathbf{u}_p - \delta\mathbf{u}) d\tau \end{aligned} \quad (15.14)$$

$$\delta\dot{\mathbf{x}} = \frac{t_f - t_0}{2}\mathbf{A}\delta\mathbf{x} + \frac{t_f - t_0}{2}\mathbf{B}\delta\mathbf{u} \quad (15.15)$$

The corresponding TPBVP is also transferred into Eqs. (15.16)~(15.18).

$$\begin{bmatrix} \delta\dot{\mathbf{x}} \\ \dot{\lambda} \end{bmatrix} = \frac{t_f - t_0}{2} \begin{bmatrix} \mathbf{A} & -\mathbf{B}\mathbf{R}^{-1}\mathbf{B}^T \\ -\mathbf{Q} & -\mathbf{A}^T \end{bmatrix} \begin{bmatrix} \delta\mathbf{x} \\ \boldsymbol{\lambda} \end{bmatrix} + \frac{t_f - t_0}{2} \begin{bmatrix} \mathbf{B}\mathbf{u}_p \\ \mathbf{Q}\mathbf{x}_p \end{bmatrix} \quad (15.16)$$

$$\delta\mathbf{x}(-1) = \delta\mathbf{x}_0 \quad (15.17)$$

$$\boldsymbol{\lambda}(1) = \mathbf{P}_f \delta\mathbf{x}(1) + \mathbf{v}^T \left(\frac{\partial \boldsymbol{\Psi}}{\partial \mathbf{x}_f} \right) \quad (15.18)$$

$\delta\mathbf{x}_0$ is a state vector of initial deviations from a nominal trajectory. The solution to the original nonlinear optimal control problem is obtained by solving the sequence of resulting linear optimal control problems, which are formulated via linearization around the nominal predictive trajectory from the current state. Therefore, there are no deviations in initial values. This means that $\delta\mathbf{x}_0$ is always a zero vector in each control period.

$L_N(\tau)$ and $L_N^*(\tau)$ are Lagrange interpolating polynomials of degree N . τ_l ($l = 1, 2, \dots, N$) are the roots of Legendre Polynomial of degree N named Legendre-Gauss (LG) points. It is noted that there is no analytical solution for such roots. Consequently, a numerical algorithm is used to calculate the LG points. And then, the state, control and costate variables are approximated by using a basis of Lagrange interpolating polynomials of degree N as

$$\delta\mathbf{x}^N(\tau) = \sum_{l=0}^N \delta\mathbf{x}(\tau_l) L_l(\tau); \delta\mathbf{u}^N(\tau) = \sum_{l=0}^N \delta\mathbf{u}(\tau_l) L_l(\tau); \boldsymbol{\lambda}^N(\tau) = \sum_{l=1}^{N+1} \boldsymbol{\lambda}(\tau_l) L_l^*(\tau) \quad (15.19)$$

According to the basic theory of Lagrange interpolating polynomial, $L_N(\tau)$ and $L_N^*(\tau)$ satisfy the properties

$$L_l(\tau_k) = \begin{cases} 1, & \text{when } l = k \\ 0, & \text{when } l \neq k \end{cases}; L_l^*(\tau_k) = \begin{cases} 1, & \text{when } l = k \\ 0, & \text{when } l \neq k \end{cases} \quad (15.20)$$

$$\delta\mathbf{x}^N(\tau_l) = \delta\mathbf{x}(\tau_l); \delta\mathbf{u}^N(\tau_l) = \delta\mathbf{u}(\tau_l); \boldsymbol{\lambda}^N(\tau_l) = \boldsymbol{\lambda}(\tau_l) \quad (15.21)$$

At the LG points, the derivative of \mathbf{x}^N can be expressed in a differential approximation matrix form as following Eq. (15.22). The differential approximation matrix \mathbf{D} is a $N \times (N+1)$ matrix and obtained by the derivative of each Lagrange Polynomial at the LG points. The elements of \mathbf{D} are determined as Eq. (15.23).

$$\delta\dot{\mathbf{x}}^N(\tau_k) = \sum_{l=0}^N D_{kl} \delta\mathbf{x}(\tau_l); \dot{\lambda}^N(\tau_k) = \sum_{l=1}^{N+1} D_{kl}^* \boldsymbol{\lambda}(\tau_l) \quad (15.22)$$

$$D_{kl} = \dot{L}_l(\tau_k) = \sum_{i=0}^N \frac{\prod_{j=0, j \neq i, l}^N (\tau_k - \tau_j)}{\prod_{j=0, j \neq l}^N (\tau_l - \tau_j)} \quad (15.23)$$

Lemma 1 Relation between the differential approximation matrix \mathbf{D} and its adjoint \mathbf{D}^* is

$$D_{ik}^* = -\frac{\omega_k}{\omega_i} D_{ki} \quad (15.24)$$

Lemma 2 The differential approximation matrix \mathbf{D} is related to $\bar{\mathbf{D}}$ by the following relation

$$\bar{D}_i = -\sum_{k=1}^N D_{ik} \quad (15.25)$$

Where, $\bar{\mathbf{D}}$ is the first column of differential approximation matrix \mathbf{D} . According to these two lemmas, adjoint differential approximation matrix \mathbf{D}^* is directly determined by the approximation matrix \mathbf{D} [12]. The appendix gives the proof of those two lemmas.

It is assumed that the state and costate variables are given as follows.

$$\delta x = (\delta x_1^T \ \delta x_2^T \ \dots \ \delta x_{N+1}^T); \lambda = (\lambda_0^T \ \lambda_1^T \ \lambda_2^T \ \dots \ \lambda_{N+1}^T) \quad (15.26)$$

By substituting Eq. (15.22) into Eq. (15.16), the dynamic equations and adjoint dynamic equations are not only transferred into a set of algebraic Eq. (15.27), but also represented by the state and costate variables at the LG points.

$$\left\{ \begin{array}{l} \sum_{l=0}^N D_{kl} \delta \mathbf{x}_l - \frac{t_f - t_0}{2} (\mathbf{A}_k \delta \mathbf{x}_k - \mathbf{B}_k \mathbf{R}^{-1} \mathbf{B}_k^T \lambda_k) = \frac{t_f - t_0}{2} \mathbf{B}_k \mathbf{u}_{pk} \\ \delta \mathbf{x}_{N+1} = \delta \mathbf{x}_0 + \frac{t_f - t_0}{2} \sum_{k=1}^N \omega_k (\mathbf{A}_k \delta \mathbf{x}_k - \mathbf{B}_k \mathbf{R}^{-1} \mathbf{B}_k^T \lambda_k + \mathbf{B}_k \mathbf{u}_{pk}) \\ \sum_{l=1}^{N+1} D_{kl}^* \lambda_l + \frac{t_f - t_0}{2} (\mathbf{Q}_k \delta \mathbf{x}_k + \mathbf{A}_k^T \lambda_k) = \frac{t_f - t_0}{2} \mathbf{Q}_k \mathbf{x}_{pk} \\ \lambda_0 = \lambda_{N+1} + \frac{t_f - t_0}{2} \sum_{k=1}^N \omega_k (\mathbf{Q}_k \delta \mathbf{x}_k + \mathbf{A}_k^T \lambda_k - \mathbf{Q}_k \mathbf{x}_{pk}) \end{array} \right. \quad (15.27)$$

Where $k = 1, 2, \dots, N$. Note that the dynamic constraint is collocated only at the LG points and not at the boundary points. Thus, two additional constraints in

the discretization are added into Eq. (15.22) to keep the boundary state and costate variables on the constraints of dynamic equations via Gauss quadrature.

Now, the linear optimal control problem is transferred into solving a set of linear algebraic equations by sampling Eq. (15.27). The explicit expression of the solutions can be represented in the following form.

$$\mathbf{S}\mathbf{z} = \mathbf{K} \quad (15.28)$$

Where, \mathbf{z} is a column vector including the unknown state and costate variables.

$$\mathbf{z} = [\delta\mathbf{x} \ \boldsymbol{\lambda}]^T = [\delta\mathbf{x}_1^T \ \delta\mathbf{x}_2^T \ \dots \ \delta\mathbf{x}_{N+1}^T \ \boldsymbol{\lambda}_0^T \ \boldsymbol{\lambda}_1^T \ \boldsymbol{\lambda}_2^T \ \dots \ \boldsymbol{\lambda}_{N+1}^T]^T_{(2N+3)s \times 1} \quad (15.29)$$

The elements of \mathbf{S} and \mathbf{K} are defined as

$$\mathbf{S} = \begin{bmatrix} \mathbf{S}^{xx} & \mathbf{S}^{x\lambda} \\ \mathbf{S}^{\lambda x} & \mathbf{S}^{\lambda\lambda} \end{bmatrix}; \mathbf{K} = \begin{bmatrix} (\mathbf{K}^x)^T & (\mathbf{K}^\lambda)^T \end{bmatrix}^T \quad (15.30)$$

$$\mathbf{S}^{xx} = \begin{bmatrix} D_{11} - \frac{t_f-t_0}{2}\mathbf{A}_1 & D_{12} & \dots & D_{1N} & O \\ D_{21} & D_{22} - \frac{t_f-t_0}{2}\mathbf{A}_2 & \dots & D_{2N} & O \\ \vdots & \dots & \ddots & \vdots & O \\ D_{N1} & D_{N2} & \dots & D_{NN} - \frac{t_f-t_0}{2}\mathbf{A}_N & O \\ -\omega_1 \frac{t_f-t_0}{2}\mathbf{A}_1 & -\omega_2 \frac{t_f-t_0}{2}\mathbf{A}_2 & \dots & -\omega_N \frac{t_f-t_0}{2}\mathbf{A}_N & \mathbf{I} \end{bmatrix} \quad (15.31)$$

$$\mathbf{S}^{x\lambda} = \begin{bmatrix} O & \frac{t_f-t_0}{2}\mathbf{B}_1\mathbf{R}_1^{-1}\mathbf{B}_1^T & O & O & O \\ O & O & \frac{t_f-t_0}{2}\mathbf{B}_2\mathbf{R}_2^{-1}\mathbf{B}_2^T & \dots & O \\ O & \vdots & \dots & \ddots & \vdots \\ O & O & O & \dots & \frac{t_f-t_0}{2}\mathbf{B}_N\mathbf{R}_N^{-1}\mathbf{B}_N^T \\ O & \omega_1 \frac{t_f-t_0}{2}\mathbf{B}_1\mathbf{R}_1^{-1}\mathbf{B}_1^T & \omega_2 \frac{t_f-t_0}{2}\mathbf{B}_1\mathbf{R}_1^{-1}\mathbf{B}_1^T & \dots & \omega_N \frac{t_f-t_0}{2}\mathbf{B}_N\mathbf{R}_N^{-1}\mathbf{B}_N^T \end{bmatrix} \quad (15.32)$$

$$\mathbf{S}^{\lambda x} = \begin{bmatrix} -\omega_1 \frac{t_f-t_0}{2}\mathbf{Q}_1 & -\omega_2 \frac{t_f-t_0}{2}\mathbf{Q}_2 & \dots & -\omega_N \frac{t_f-t_0}{2}\mathbf{Q}_N & O \\ \frac{t_f-t_0}{2}\mathbf{Q}_1 & O & \dots & O & O \\ O & \frac{t_f-t_0}{2}\mathbf{Q}_2 & \dots & O & O \\ \vdots & \vdots & \ddots & \vdots & \vdots \\ O & O & \dots & \frac{t_f-t_0}{2}\mathbf{Q}_N & O \end{bmatrix} \quad (15.33)$$

$$\mathbf{S}^{\lambda\lambda} = \begin{bmatrix} \mathbf{I} & -\frac{t_f-t_0}{2}\omega_1\mathbf{A}_1^T & -\frac{t_f-t_0}{2}\omega_2\mathbf{A}_2^T & \dots & -\frac{t_f-t_0}{2}\omega_N\mathbf{A}_N^T & -\mathbf{I} \\ O & D_{11}^* + \frac{t_f-t_0}{2}\mathbf{A}_1^T & D_{12}^* & \dots & D_{1N}^* & D_{1(N+1)}^* \\ O & D_{21}^* & D_{22}^* + \frac{t_f-t_0}{2}\mathbf{A}_2^T & \dots & D_{2N}^* & D_{2(N+1)}^* \\ \vdots & \vdots & \vdots & \ddots & \vdots & \vdots \\ O & D_{N1}^* & D_{N2}^* & \dots & D_{NN}^* + \frac{t_f-t_0}{2}\mathbf{A}_N^T & D_{N(N+1)}^* \end{bmatrix} \quad (15.34)$$

K is composed of constant elements in linear algebraic equations and divides into two parts. One is determined by the terminal state variables that are restricted to specific values. The other is determined by the nominal trajectory at LG points.

$$\mathbf{K}^x = \begin{bmatrix} \frac{t_f - t_0}{2} \mathbf{B}_1 \mathbf{u}_{p1} \\ \frac{t_f - t_0}{2} \mathbf{B}_2 \mathbf{u}_{p2} \\ \vdots \\ \frac{t_f - t_0}{2} \mathbf{B}_N \mathbf{u}_{pN} \\ \frac{t_f - t_0}{2} \sum_{k=1}^N \omega_k \mathbf{B}_k \mathbf{u}_{pk} \end{bmatrix}; \mathbf{K}^\lambda = \begin{bmatrix} -\frac{t_f - t_0}{2} \sum_{k=1}^N \omega_k \mathbf{Q}_k \mathbf{x}_{pk} \\ \frac{t_f - t_0}{2} \mathbf{Q}_1 \mathbf{x}_{p1} \\ \vdots \\ \frac{t_f - t_0}{2} \mathbf{Q}_N \mathbf{x}_{pN} \end{bmatrix} \quad (15.35)$$

Where, notation s denotes the number of state variables of plant, notation m denotes the number of terminal state variables that are restricted to the specific values.

Note that the terminal constraints in linear optimal control problem should be expressed in a specified form according to the concrete nonlinear terminal constraint functions. Thus, it is difficult to express in a fixed manner in above matrix. However, if the nonlinear terminal constraints are restricted to some specific values, it only regards the corresponding costate variables as the independent variables. And then, a unique solution exists because the number of unknowns equals the number of equations. It is noted that if the number of state variables that are not the variables of terminal cost function is k , the corresponding costate variables are known according to the transversality conditions. The number of unknowns reduces to $(2N + 3)s - m - k$ and equals the number of equations. Also, the state and costate variables at the LG points are obtained by solving the above linear algebraic equations. The corresponding control variables at the LG points can be determined by following formula.

$$\mathbf{u}_k = \mathbf{u}_{pk} - \delta \mathbf{u}_k = \mathbf{R}_k^{-1} \mathbf{B}_k^T \boldsymbol{\lambda}_k, k = 1, 2, \dots, N \quad (15.36)$$

Two main points have been given for choosing adjoint differential approximation matrix. (1) The algebraic matrix constraints transferred from the costate dynamic equations are only determined by the costate variables at the LG points and the end of the time. And the transversality conditions mainly act on the last point. (2) It can establish the equivalence between the discrete linear programming problem and continuous optimal control problem for this kind of problem. In Sect. 15.2.3, existence of solution for the discrete optimal control problem is discussed via analysis in singularity of differential approximation matrices. Gauss scheme ensures that, if the continuous optimal control problem is feasible, there exists the solution for the discrete optimal control problem. In Sect. 15.2.4, because the control variables do not include the boundary control in conventional Gauss scheme, a discussion on how to get the boundary control for linear Gauss Pseudospectral method is presented. As soon as the control iterations have been updated in LGPMPC, the boundary control will apply to the real plant.

15.2.3 Singularity of Differential Approximation Matrices for Different Pseudospectral Methods

Recent studies have shown that if the differential approximation matrix is singular, the equivalence between the differential and integral formation is not established [11]. The fact is that there will be a determined trajectory for the unique initial state and dynamic equations. However, further study finds out that if the approximation matrix is singular such as Legendre Pseudospectral method, there will be no solution in discrete formation for some special initial state. Therefore, there exists a null space for this kind of schemes.

Suppose that \mathbf{D} is the differential approximation matrix of Legend pseudospectral scheme [13, 14]. The initial state and dynamical equation are zeros, and the relation can be given as

$$\mathbf{D}_1 \mathbf{0} + \mathbf{D}_{2:N} \mathbf{X} = \mathbf{0} \quad (15.37)$$

\mathbf{X} must be zero at the LGL points, so, $\text{rank}(\mathbf{D}_{2:N}) = N - 1$.

If the initial state is not zero, we can get the following relation.

$$\mathbf{D}_{2:N} \mathbf{X} = \mathbf{f}(\mathbf{X}) - \mathbf{D}_1 \mathbf{X}_0 \quad (15.38)$$

$$\mathbf{D}_{2:N} \mathbf{X} = \mathbf{F}(\mathbf{X}) \quad (15.39)$$

Thus, the existence of the solution is dependent on the rank of $[\mathbf{D}_{2:N} \mathbf{F}(\mathbf{X})]$. If the rank is full, there is no solution, and if not, $\mathbf{F}(\mathbf{X})$ is the combination of $\mathbf{D}_{2:N}$. There exists a unique solution. The existence of null space will result in the singularity of solving the algebraic equations for some special conditions. However, because the size of $\mathbf{D}_{2:N}$, which is generated via Gauss scheme and is non-singular, is $N \times N$, the existence of the solution is dependent on the rank of $\mathbf{D}_{2:N}$. There always exists a unique solution for non-singular differential approximation matrix such as Gauss and Radau schemes [15].

15.2.4 Boundary Control of Linear Gauss Pseudospectral Method

LG points are roots of Legendre Polynomial and lie in the time interval $(-1,1)$. They do not include the boundary points. Thus, the solution to the nonlinear programming problem directly transferred from original problem via Gauss Pseudospectral scheme only includes the control variables at the LG points. According to the maximum principle, two additional boundary Hamiltonians are formulated to obtain the boundary

control. And these Hamiltonians are functions of boundary state and costate variables. Those maximum optimizations are also nonlinear programming problems due to the nonlinear dynamic system. Therefore, in the Gauss Pseudospectral Method, there are three nonlinear programming problems that should be numerically solved for the nonlinear optimal control problem.

Being different with the nonlinear dynamic system, there is an analytic maximum solution of Hamiltonian in the boundary points for the linear dynamic system. Consider the Hamiltonian as follow

$$J[\mathbf{u}(\cdot)] = \min\{H\} = \min \left\{ \frac{1}{2} \left[(\mathbf{x}_p - \delta \mathbf{x})^T \mathbf{Q} (\mathbf{x}_p - \delta \mathbf{x}) + (\mathbf{u}_p - \delta \mathbf{u})^T \mathbf{R} (\mathbf{u}_p - \delta \mathbf{u}) \right] + \lambda^T (\mathbf{A} \delta \mathbf{x} + \mathbf{B} \delta \mathbf{u}) \right\} \quad (15.40)$$

If there is not any constraint on control variables, the optimal solution is unique and can be obtained by deriving Eq. (15.40).

$$\frac{\partial H}{\partial \delta \mathbf{u}} = \mathbf{0} \rightarrow (\mathbf{u}_p - \delta \mathbf{u})_{0,N+1} = \mathbf{R}_{0,N+1}^{-1} \mathbf{B}_{0,N+1}^T(t_{0,N+1}) \boldsymbol{\lambda}(t_{0,N+1}) \quad (15.41)$$

Thus, it is not necessary to obtain the boundary control through numerically solving additional NLP for linear optimal control with quadrature performance index.

15.2.5 Implementation of LGPMPC

The objective of LGPMPC is to obtain the solution of a nonlinear optimal control problem with the hard terminal constraints by successively solving the linear optimal control problem. At the beginning, the predictive integration using the current control iterations is reproduced to obtain the terminal deviations $d\psi$ and trajectory information. Then, the linearization around the predictive trajectory is employed to formulate the linear optimal control problem. The solution eliminating the terminal deviations is obtained by solving a set of linear matrix equations, which is transferred via the Gauss pseudospectral scheme. Update the control iterations and repeat the steps until the solution for nonlinear dynamic equation meets the terminal conditions.

The procedure for implementing the LGPMPC is included in the flowchart in Fig. 15.1 and summarized in detail as follows.

- (1) Initialization: set initial simulation parameters and select a suitable initial guess that can be produced from off-board trajectory optimization or certain guidance law.
- (2) Predictive integration using current control iterations: calculate the deviations $d\psi$ and store the trajectory information date X_k, U_k .

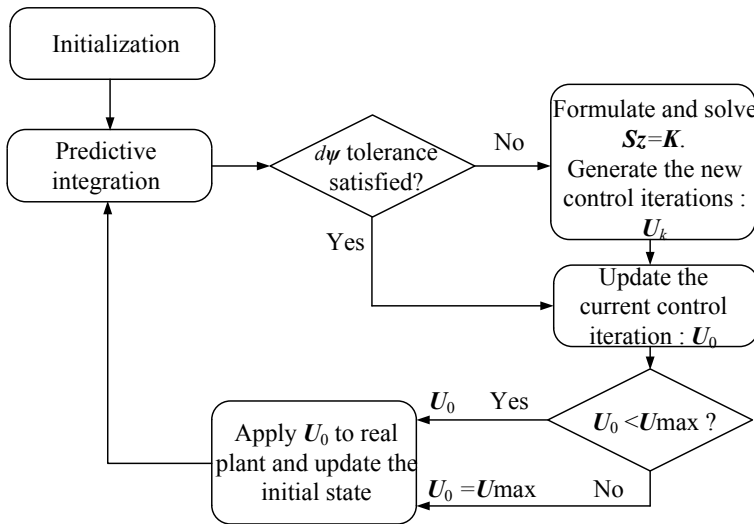


Fig. 15.1 Flowchart for implementing the LGPMPC

- (3) Judgment on the satisfaction of $d\psi$ tolerance: if deviation $d\psi$ is within the prescribed tolerance, go to next step; if not, go to step 6.
- (4) Update the current control U_0 and judge on the saturation of U_0 : if U_0 is larger than U_{\max} , U_0 equals U_{\max} ; if not, U_0 equals U_0 . Then, go to next step.
- (5) Apply U_0 to the real plant and return step 2. Also, those control iterations are the results of simulations and will be applied to the next predictive integration as input.
- (6) Apply the method of linearization around the current predictive trajectory to formulate the matrices S and K , and update the control iterations by numerically solving linear algebraic equations, then go to step 4.

The solution to a nonlinear problem is obtained by repeating the above steps. When the real plant is approaching the destination, the number of LG points is decreasing with the decrease of the number of predictive integral steps. This method is very easy to implement and combines the Gauss Pseudospectral method with the linearization of nonlinear dynamical system and model predictive control. Therefore, it not only retains the accuracy of indirect trajectory optimization, but also is of high efficiency without solving a nonlinear programming problem. Another worthy note is the sufficient condition for the existence of a solution. The dynamic system is continuously differentiable, P_f and Q are positive semi-definite, R is positive definite.

15.3 Application to Terminal Guidance

In this section, LGPMPC is applied to guide the vehicle to impact the ground target from a specified direction by using three-dimensional nonlinear engagement dynamics. Applicability of the proposed method in different terminal angles is evaluated by various cases for target with straight-line movements. The simulations with different LG points are conducted to demonstrate the effect of LG nodes on the accuracy and efficiency. The performance of the method is compared with that of other methods. It is noted that the augmented PN guidance law is used to produce the initial guess in all cases. And the commanded accelerations are generated at 20 Hz rate. All programs are implemented on a personal computer with 3.3 GHz processor and MATLAB 2008b. The computation time can be reduced by applying more efficient resources.

15.3.1 Terminal Guidance Problem and Three-Dimensional Mode

The standard three-dimensional equations of motion of a terminal guidance vehicle over a flat earth can be given as:

$$\begin{aligned}\dot{x}_m &= V_m \cos \gamma_m \cos \psi_m; \dot{y}_m = V_m \cos \gamma_m \sin \psi_m; \dot{z}_m = V_m \sin \gamma_m; \\ \dot{V}_m &= -\frac{D_m}{m_m} - g \sin \gamma_m; \dot{\gamma}_m = \frac{-a_z - g \cos \gamma_m}{V_m}; \dot{\psi}_m = \frac{-a_y}{V_m \cos \gamma_m}; \\ \dot{a}_y &= \frac{a_{yc} - a_y}{t_\tau}; \dot{a}_z = \frac{a_{zc} - a_z}{t_\tau};\end{aligned}\quad (15.42)$$

Note that a first-order autopilot lag is considered in the dynamic equations. Where, a_{zc} and a_{yc} are commanded accelerations in z and y directions, a_z and a_y are achieved accelerations in z and y directions which act in the XZ and XY plane respectively. All accelerations are perpendicular to the velocity vector V_m . Noted that the first-order autopilot lag is not considered in applying the proposed method to calculate the commanded accelerations. It is only considered in the real plant. x_m , y_m , z_m are coordinates of the vehicle over flat earth. γ_m is the flight-path angle between the relative velocity vector and the horizontal XY plane. ψ_m is the heading angle between the horizontal projection of the velocity vector and x axes. In order to better understand the notations of motion, three-dimensional motion of flight vehicle is demonstrated in Fig. 15.2.

Simulation parameters of the vehicle such as mass, reference area and so on refer to [16]. All state variables are normalized by the normalizing quantities as Eq. (15.43). The main reason for the normalization is better numerical condition for solving linear algebraic equations.

Fig. 15.2 Three-dimensional motion of flight vehicle over a flat earth

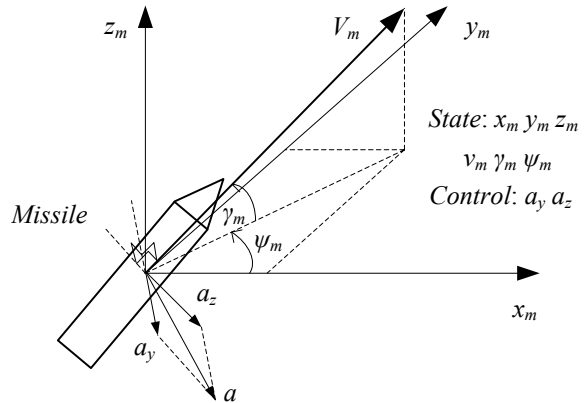


Table 15.1 Simulation parameters

Parameter and units	Value
Convergence condition threshold	10^{-10}
Initial velocity, V_{m0} (Ma)	1.5
State weighting matrix, Q	$O_{6 \times 6}$
Control weighting matrix, R	$I_{2 \times 2}$
Initial coordinates, x, y, z (km)	(0, 2, 6)
Initial flight-path angle, γ_0 (Deg)	15
Initial azimuth angle, ψ_0 (Deg)	15
Normalizing Velocity value, V_* (m/s)	600
Normalizing angle value, γ_*, ψ_* (Deg)	50
Normalizing coordinates value, x_*, y_*, z_* (km)	5
Normalizing acceleration value, a_{y*}, a_{z*} (m/s^2)	9.81
Mass of flight vehicle, m_m (kg)	150
Surface area, $surf$ (m^2)	0.032 4
First order lag, t_τ	0.2

$$\begin{aligned} x_n &= \frac{x_m}{x_*}; y_n = \frac{y_m}{y_*}; z_n = \frac{z_m}{z_*}; a_{yn} = \frac{a_{ym}}{a_{y*}}; \\ a_{zn} &= \frac{a_{zm}}{a_{z*}}; V_n = \frac{V_m}{V_*}; \gamma_n = \frac{\gamma_m}{\gamma_*}; \psi_n = \frac{\psi_m}{\psi_*}; \end{aligned} \quad (15.43)$$

Where, the subscript n denotes the normalized values of corresponding state variables, superscript ‘*’ denotes the normalizing quantities. It is found out that the values of normalizing quantities should be selected carefully to keep the magnitude of all state variables in a similar level. Normalizing quantities and some of the key simulation parameters are listed in Table 15.1.

Because the air density is so rarefied in the high altitude that the acceleration produced from the vehicle is very limit, a path constraint on acceleration should be considered in the terminal guidance. It is assumed that the acceleration limit in longitudinal plane or lateral plane varies with the height of vehicle as follows.

$$a_{\max} = \begin{cases} 2, & \text{if } z > 4000 \\ -\frac{z}{2000} + 4, & \text{if } z \leq 4000 \end{cases} \quad (15.44)$$

Consideration of limit constraints in acceleration not only reflects the influence of air environment, but also provides a good opportunity to evaluate the performance of LGPMPC.

15.3.2 Initial Guess and Target Model

In this chapter, augmented PN guidance law is applied to produce the initial guess for LGPMPC. Since this guidance is one of the most famous guidance laws and has been under investigation in many papers, it is not necessary to repeat the description in detail here. Equations (15.45) and (15.46) are commanded accelerations in z and y directions respectively.

$$a_{zc} = \begin{cases} N_e V_c \dot{\sigma}_{\text{pitch}} + \frac{1}{2} a_{tpitch} + g \cos \gamma_m, & \text{if } |a_{zc}| \leq a_{c\max} \\ a_{c\max} \text{sign}(a_{zc}), & \text{if } |a_{zc}| > a_{c\max} \end{cases} \quad (15.45)$$

$$a_{yc} = \begin{cases} N_e V_c \dot{\sigma}_{\text{yaw}} + \frac{1}{2} a_{tyaw}, & \text{if } |a_{yc}| \leq a_{c\max} \\ a_{c\max} \text{sign}(a_{yc}), & \text{if } |a_{yc}| > a_{c\max} \end{cases} \quad (15.46)$$

Where, $\dot{\sigma}_{\text{pitch}}$ and $\dot{\sigma}_{\text{yaw}}$ are rates of line-of-sight from the target to the vehicle, V_c is the closing velocity, N_e is the proportional constant for augmented PN guidance, $a_{c\max}$ is the acceleration limit for the vehicle, a_{tpitch} and a_{tyaw} are functions of the accelerations of the target and given as follows:

$$\begin{aligned} a_{tpitch} &= -\sin \gamma_m (\cos \psi_m \ddot{x}_t + \sin \psi_m \ddot{y}_t) \\ a_{tyaw} &= -\sin \gamma_m \ddot{x}_t + \cos \gamma_m \ddot{y}_t \end{aligned} \quad (15.47)$$

The key assumptions for the target model are that the velocity is constant; there is only a commanded acceleration being perpendicular to the target velocity vector. The target dynamic equations are presented as

$$\dot{x}_t = V_t \cos \psi_t; \dot{y}_t = V_t \sin \psi_t; \dot{\psi}_t = \frac{a_{yt}}{V_t} \quad (15.48)$$

15.3.3 Cases for Target with Straight-Line Movements

In this subsection, some cases for target with straight-line movements are used to demonstrate the applicability of the proposed method in different terminal angles. In addition to the constraints on the final coordinates, the vehicle must also impact the target from a specified direction. Initial conditions of the vehicle and the target, the desired terminal angles and LG nodes for cases are listed in Table 15.2.

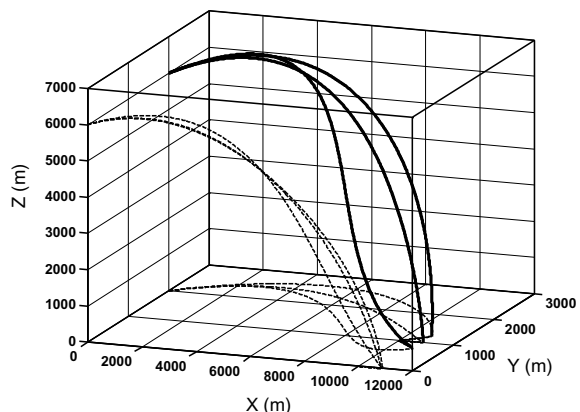
The three-dimensional flight paths for different cases are depicted in Fig. 15.3. The proposed method can guide the vehicle to impact the target in different directions. Initial heading angles of the target for different cases are 15° , 0° and -10° .

Figure 15.4 shows the time histories of the accelerations for various cases. It is obvious that the accelerations change greatly at the beginning of flight, not only because the initial accelerations of the vehicle are zeros, but also because the terminal errors between the vehicle and the target are the biggest in the beginning. It is observed that the accelerations also change greatly at the time of impact. The reason is that all cases consider the first-order autopilot lag in its response to the commanded accelerations. If the commanded acceleration is not zero, the effect of errors resulting from the difference between the commanded acceleration and actual acceleration will deteriorate when the vehicle is approximating the target. And the vehicle will need more acceleration to eliminate the errors. However, when the guidance commands are produced at an adaptive rate, the miss distance resulting from 0.2 s lag constant will be small. This conclusion can be proved by the later miss distance statistics in

Table 15.2 Initial and final state condition for different cases

Cases	ψ_{t0} ($^\circ$)	γ_{mf} ($^\circ$)	ψ_{mf} ($^\circ$)	LG node
Case-1	15	-65	-40	10
Case-2	0	-75	-15	10
Case-3	-10	-30	20	10

Fig. 15.3 Three-dimensional view of various trajectories



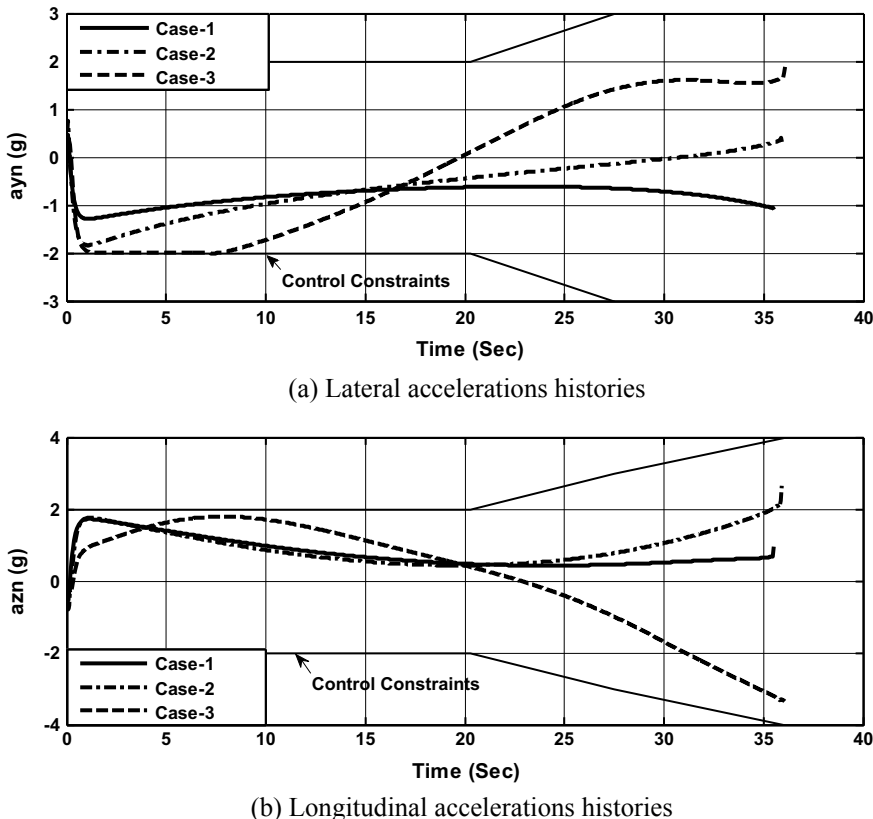


Fig. 15.4 Time histories of lateral and longitudinal accelerations for various cases

Table 15.3. Those figures also reveal that the energy management for the terminal constraints on both flight-path angle and heading angle mainly occur at the later stage of flight. For the three cases, the accelerations tend to be violently different after about 20 s. Another point should be noted is that the lateral acceleration in Case-3 touches the boundary of limit constraint at the early stage of flying. After about 6 s on the flying with the maximum of lateral acceleration, the proposed method finds the appropriate commanded acceleration to guide the vehicle. Finally, the vehicle impacts the target from the specified direction. The simulation results suggest that,

Table 15.3 Miss distances for different cases

Cases	Coordinates (m)	Flight-path angle (°)	Azimuth angle (°)
Case-1	0.001 132	0.003 15	-0.003 54
Case-2	0.009 108	-0.004 21	0.037 13
Case-3	0.015 731	-0.021 63	-0.047 27

even under the consideration of limit constraints in control inputs, the proposed method can work well.

Figure 15.5 shows the time histories of flight-path angle and heading angle. It is clear that all the terminal angles satisfy the required constraints, $\gamma_{mf} = -65^\circ$, $\psi_{mf} = -40^\circ$; $\gamma_{mf} = -75^\circ$, $\psi_{mf} = -15^\circ$; $\gamma_{mf} = -30^\circ$, $\psi_{mf} = 20^\circ$. Also, comparing with the acceleration figures, it is easy to find out that both angles tend to be greatly different at the later stage. But the time of occurrence in the angles figure is later than that in the accelerations figure. That means that the energy management for the terminal constraints on both angles is a long-period control process.

In order to study the convergence rate of the proposed method, another set of simulations is also carried out. The simulation parameters are the same as those listed in Tables 15.1 and 15.2. However, the first-order autopilot is not considered in the simulation. Figure 15.6 shows the histories of the convergence rate. Note that dYN^2 is the sum of square errors of different terminal constraints. It takes a few steps to reach a high accuracy. Consequently, the proposed method has a fast convergence rate.

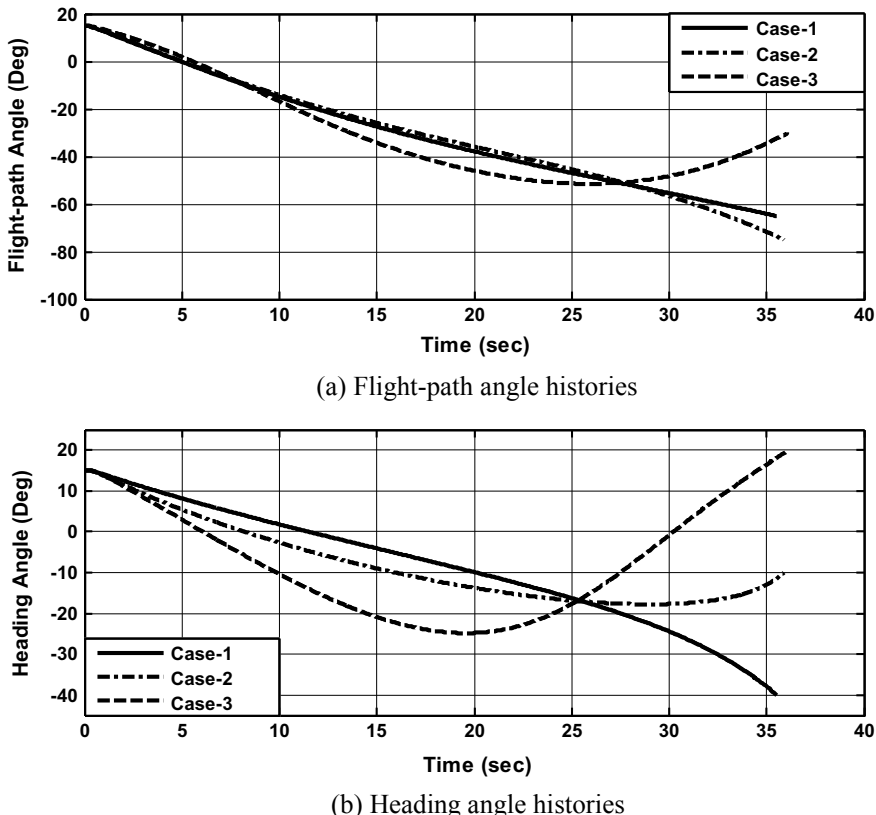


Fig. 15.5 Time histories of flight-path angle and heading angle for various cases

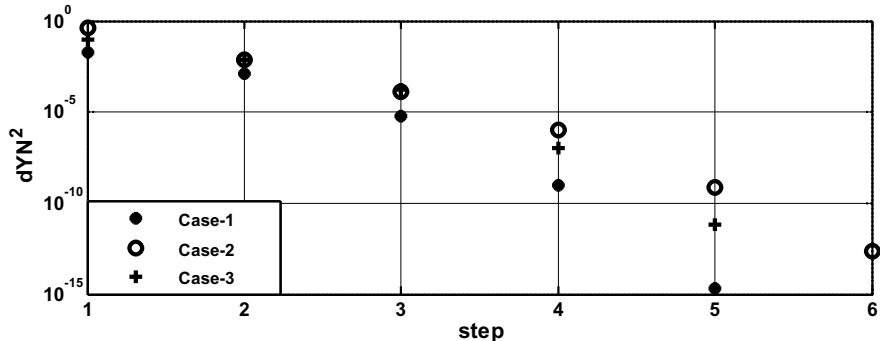


Fig. 15.6 Convergence rate histories for various cases

Table 15.3 shows the miss distance statistics including the final position coordinates, terminal flight-path angle and heading angle. To ensure the vehicle to impact the target from a specified direction, the terminal state variables are restricted to some specific values. The miss distances of the impact are less than 0.02 m, and the miss distances of both angles are less than 0.05°. These observations lead to an important conjecture: the less required terminal angles especially in flight-path angle will result in the less miss distance of final position coordinates and both terminal angles.

Another point note is the number of LG points. Generally speaking, the number of LG points, which is dependent on the optimal state, determines the size of linear algebraic matrix equations. If the optimal state variables are smooth enough to be approximated by using a less order Lagrange interpolating polynomials, the solution with a high precision can be obtained via the Gauss pseudospectral scheme with the less LG points. It also means that it can take the less time to reach the higher accuracy. Therefore, the number of LG points is one of the most important parameters and should be carefully decided by the designer. To demonstrate the speed of the proposed method, comparison of computing time between different LG points cases and the MPSP method is presented in Table 15.4.

The initial and terminal conditions for the proposed method and the MPSP method are the same as those of case-1. The time step of simulation is fixed in 50 ms. The statistical results indicate that the mean computing time of the proposed method decreases exponentially with the decrease of LG points. When there are 6 LG points, the mean computing time is only 0.011 31 s. These results also reveal that the size of linear algebraic matrix equations decreases exponentially with the decrease in

Table 15.4 Comparison of CPU time for terminal impact example

	MPSP	Proposed method		
Step/LG node	50 ms	6	10	20
Mean time (s)	0.021 21	0.011 31	0.012 80	0.029 34
Final dYN^2	5.301e-7	4.7e-7	2.04e-7	1.972e-7

the number of LG points. It is noted that the sum of square terminal errors for the MPSP and the proposed method stand at a lower level. Consequently, by comparing with the MPSP method, the proposed method applied in terminal guidance has better performance in effectiveness and accuracy.

15.3.4 Comparison with Adaptive Terminal Guidance

Adaptive terminal guidance, which is in a proportional-navigation form, is designed to guide the vehicle to impact the target in a specified direction. The commanded accelerations are generated by adjusting the proportional constants according to the current state between the vehicle and the target and the desired terminal angles [17]. Proportional navigation guidance laws for the commanded heading angle ψ_{com} and the flight-path γ_{com} are given as

$$\dot{\psi}_{com} = -\lambda_1 \dot{\theta} \quad (15.49)$$

$$\dot{\gamma}_{com} = -\lambda_2 \dot{\phi} \quad (15.50)$$

Where λ_1 and λ_2 are adaptive proportional parameters in different planes. θ and ϕ are the angles of the line-of-sight in XY plane and XZ plane. Their rates can be calculated from the current state between the vehicle and the target. It should be noted that the validity of adaptive guidance laws is when the initial λ_1 and λ_2 are greater than two. Those two parameters are determined by the current position and velocity direction of the vehicle. Therefore, two terminal guidance logics are applied to guide the vehicle to meet above conditions respectively. Once the computed value λ_1 or λ_2 is greater than two, the corresponding guidance law will be activated to guide the vehicle to impact the target in the specified terminal angle. The detailed description on the adaptive terminal guidance is given in [17].

In this subsection, a comparison between the proposed method and adaptive terminal guidance is done to demonstrate the performance of required loads. The simulation parameters are the same as those listed in Table 15.1. Note that the target is stationary without any movements. Terminal angles are $\gamma_{mf} = -65^\circ$, $\psi_{mf} = -40^\circ$. A 2 g constant commanded acceleration is applied as the lateral guidance logic. The prespecified constant for the vehicle ending the heading alignment phase is 40 Deg. At the heading alignment phase, the vehicle flies a longitudinal load profile as

$$n_{com} = 2 - 2e^{-t/T_{trans}} \quad (15.51)$$

Where, t is flight time, T_{trans} is a preselected parameter to ensure reasonably fast transition from 0 g to 2 g. The miss distances for the two methods are less than 0.2 m. It meets the requirement of impact.

Figure 15.7 shows the time histories of the flight-path angle and heading angle of both methods. Terminal angles for proposed method: $\gamma_f = -65.020^\circ$, $\psi_f = -40.008^\circ$; Terminal angles for adaptive terminal guidance: $\gamma_f = -64.996^\circ$, $\psi_f = -39.997^\circ$. It is observed that the proposed method performs as well as the adaptive terminal guidance. Two figures also clearly indicate that the vehicle is activated at about 3 s and 12 s into the corresponding terminal flight respectively. It can be noted that the proposed method will result in the smoother curves of both angles.

Figure 15.8 shows the range histories of lateral and longitudinal accelerations and total load of both methods. For adaptive terminal guidance, the changes resulting from the switch from the logic guidance to terminal guidance are presented more obviously in the accelerations figure. At the time of switch, the accelerations jump from -2 g to 2 g in lateral guidance plane and from 2 g to -6 g in the longitudinal guidance plane respectively. For the proposed method, however, both accelerations vary more smoothly. There is not great change during the guidance except at the time of impact. Another important point revealed from the figure of total load is that the required total load of the proposed method is less than that of adaptive terminal

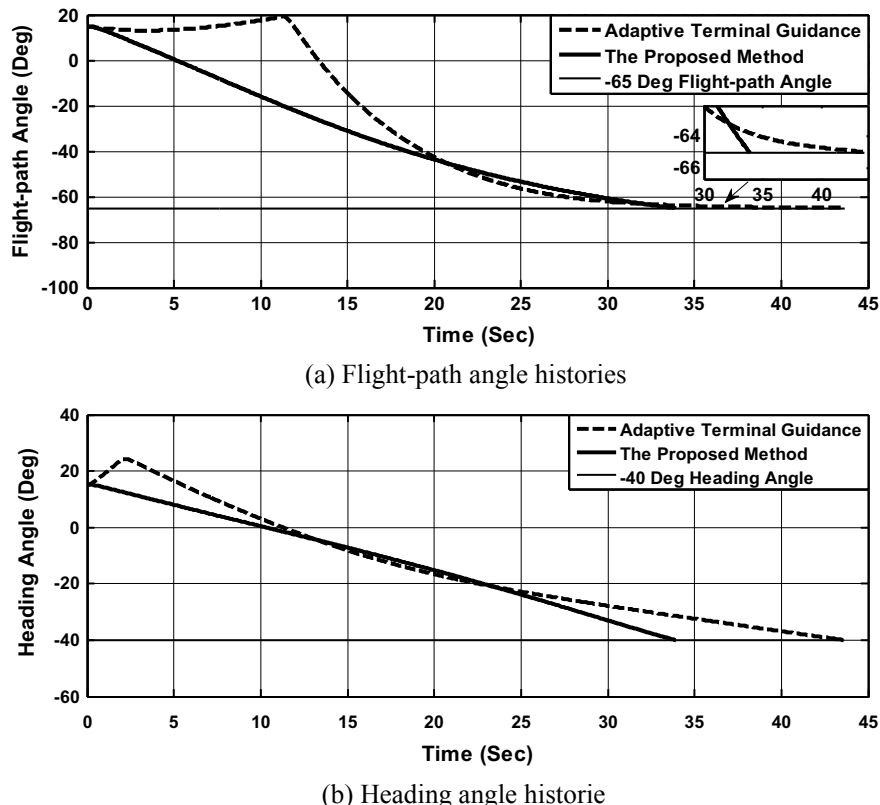


Fig. 15.7 Comparison of the proposed method and adaptive terminal guidance

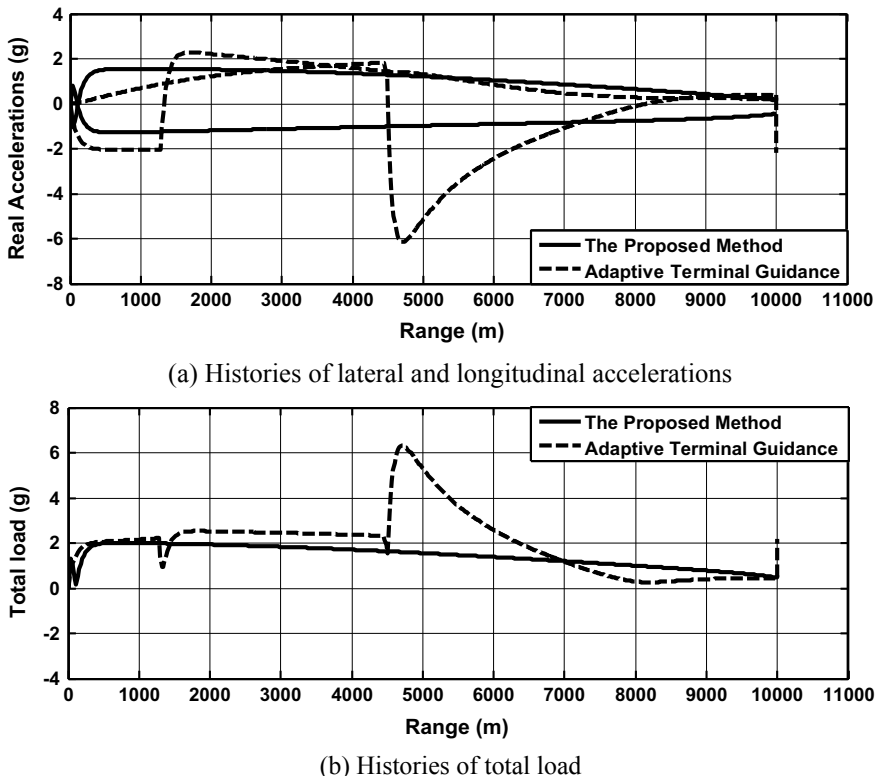


Fig. 15.8 Comparison of the proposed method and adaptive terminal guidance

guidance during most of the guidance time. With this fact, it is easy to conclude that the proposed method is superior to adaptive terminal guidance in resulting in the smoother and fewer required commands that the vehicle can be easy to track.

15.4 Conclusion

A new kind of Model Predictive Control (MPC) method for solving a nonlinear quadratic optimal control problem with hard terminal constraints is presented in this chapter. It combines the philosophies of linearization of nonlinear dynamic system, model predictive control and the Gauss pseudospectral method. It has a fast convergence rate for the solution from successively solving the two-point boundary value problem via linear Gauss pseudospectral scheme. This method is successfully applied in the terminal impact in a specified direction. Some cases for the target with straight-line movements are carried out to demonstrate that the proposed method has a wider

area of applicability in different terminal angles constraints. Meanwhile, simulation results have shown that, comparing with the different Legendre-Gauss (LG) points and the Model Predictive Static Programming (MPSP) method, the proposed method is of high effectiveness and accuracy. Additionally, another comparison with the adaptive terminal method is provided to demonstrate that the commanded accelerations generated by the proposed method are smoother and smaller than that of adaptive terminal guidance.

Appendix

The Proof of Two Key Lemmas [12]

Lemma 1 Relation between the differential approximation matrix \mathbf{D} and its adjoint \mathbf{D}^* is

$$D_{ik}^* = -\frac{\omega_k}{\omega_i} D_{ki} \quad (15.51)$$

Proof Consider the integration by parts formulas for two N order polynomials, $f(t), g(t)$, so,

$$\int_{-1}^1 \dot{f}(t)g(t)dt = f(t)g(t)|_{-1}^1 - \int_{-1}^1 f(t)\dot{g}(t)dt \quad (15.52)$$

The polynomials within the integration are $2N-1$ order so that the integrals can be replaced exactly by Gauss quadrature formulas, and the derivative of $f(t)$ and $g(t)$ are replaced by differential approximation matrixes. Eq. (15.52) can be rewritten as

$$\sum_{k=1}^N \left[\sum_{i=0}^N f(t_i) \cdot D_{ki} \right] g(t_k) \omega_k = f(t) \cdot g(t)|_{-1}^1 - \sum_{k=1}^N f(t_k) \left[\sum_{i=1}^{N+1} g(t_i) D_{ki}^* \right] \omega_k \quad (15.53)$$

It defines $f(t) = L_l(t)$, $g(t) = L_j^*(t)$, so that

$$\omega_i D_{ik}^* = -\omega_k D_{ki} \quad (15.54)$$

Lemma 2. The differential approximation matrix \mathbf{D} is related to $\bar{\mathbf{D}}$ by the relation

$$\bar{D}_i = - \sum_{k=1}^N D_{ik} \quad (15.55)$$

Proof It is assumed that $f(t) = c$, c is a constant and the $f(t)$ is a constant function, the relation can be found by applying the differential approximation matrices to the

derivative of that function, so

$$c\bar{D}_i + c \sum_{k=1}^N D_{ik} = \dot{f}(t_i) = 0 \quad (15.56)$$

The result can be simplified to obtain Eq. (15.55).

References

1. Mayne, D.Q., Rawlings, J.B., Rao, C.V., et al.: Constrained model predictive control: stability and optimality. *Automatica* **36**, 789–814 (2000)
2. Ohtsuka, T., Fujii, H.A.: Real-time optimization algorithm for nonlinear receding horizon control. *Automatica* **33**(6), 1147–1154 (1997)
3. Lu, P.: Regulation about time-varying trajectories: precision entry guidance illustrated. *J. Guid. Control Dyn.* **22**(6), 784–790 (1999)
4. Yan, H., Fahroo, F., Ross, I. M.: Optimal feedback control laws by legendre pseudospectral approximations. In: Proceeding of the American Control Conference, Piscataway (2001)
5. Yan, H., Ross, I.M., Alfriend, K.T.: Pseudospectral feedback control for three-axis magnetic attitude stabilization in elliptic orbits. *J. Guid. Control Dyn.* **30**(4), 1107–1115 (2007)
6. Williams, P.: Application of pseudospectral methods for receding horizon control. *J. Guid. Control Dyn.* **27**(2), 310–314 (2004)
7. Padhi, R., Kothari, M.: Model predictive static programming: a computationally efficient technique for suboptimal control design. *Int. J. Innov. Comput. Inf. Control* **5**(2), 399–411 (2009)
8. Oza, H.B., Padhi, R.: Impact-angle-constrained suboptimal model predictive static programming guidance of air-to-ground missiles. *J. Guid. Control Dyn.* **35**(1), 153–164 (2012)
9. Chawla, C., Sarmah, P., Padhi, R.: Suboptimal midcourse guidance of interceptors for high speed targets with alignment angle constraint. *Aerospace Sci. Technol.* **14**(6), 377–386 (2010)
10. Benson, D.A., Huntington, G.T., Thorvaldsen, T.P., et al.: Direct trajectory optimization and costate estimation via an orthogonal collocation method. *J. Guid. Control Dyn.* **29**(1), 1435–1440 (2006)
11. Garg, D., Patterson, M., Hager, W.W., et al.: A unified framework for the numerical solution of optimal control problems using pseudospectral methods. *Automatica* **46**, 1843–1851 (2010)
12. Benson, D. A. A.: gauss pseudospectral transcription for optimal control, Ph.D. thesis, Department of Aeronautics and Astronautics, MIT (2004)
13. Elnagar, J., Kazemi, M.A., Razzaghi, M.: The pseudospectral legendre method for discretizing optimal control problem. *IEEE Trans. Autom. Control* **40**(10), 1793–1796 (1995)
14. Fahroo, F., Ross, I.M.: Costate estimation by a legendre pseudospectral method. *J. Guid. Control Dyn.* **24**(2), 270–277 (2001)
15. Garg, D., Patterson, M., Darby, C., et al.: Direct trajectory optimization and costate estimation of general optimal control problems using a radau pseudospectral method//AIAA Guidance, Navigation, and Control Conference, pp. 10–13. Illinois, Chicago (2009)
16. Imado, F., Kuroda, T., Tahk, M. J.: A new missile guidance algorithm against a maneuvering target. In: Proceeding of the AIAA Guidance, Navigation, and Control Conference and Exhibit, Boston, MA (1998)
17. Lu, P., Doman, D., Schierman, J.: Adaptive terminal guidance for hypervelocity impact in specified direction. *J. Guid. Control Dyn.* **29**(2), 269–278 (2006)

Chapter 16

Linear Pseudospectral Reentry Guidance with Adaptive Flight Phase Segmentation and Eliminating General Nominal Effort Miss Distance



16.1 Introduction

Since the successful flights of Apollo capsule and Space Shuttle, researches on entry guidance algorithm have made impressive and remarkable progress [1]. Although there are many different types of entry guidance algorithms, the most famous one is the Space Shuttle Entry Guidance [2] which is the benchmark in reference-tracking guidance. This algorithm consists of two parts. One is to plan a reference drag-acceleration profile within a safe corridor according to the range requirement. The other is to design a profile tracking law based on linearization in simplified drag dynamical model. The magnitude of bank angle is modulated so as to eliminate the drag deviation and its sign is used to reduce the heading error via a pre-selected threshold corridor (named heading error corridor). In order to enhance the performance, Mease and Kremer [3] revisited the shuttle guidance law in the framework of feedback linearization and argued that the nonlinearity in the dynamics could be compensated if the modeling was accurate enough. Bharadwaj and Rao [4] applied approximate feedback linearization theory into reference trajectory tracking law design, in which the downrange and crossrange served as the output variables. Mease [5] proposed a reduced-order entry trajectory planning method for acceleration guidance, which was used to provide the drag profile considering both longitudinal and lateral motions. Dukeman [6] extended the Linear Quadratic Regulator (LQR) into tracking the reference longitudinal states including altitude, flight-path angle and range-to-go. The results showed that this algorithm was very robust with respect to different missions. Further efforts on reference tracking guidance can be found in references [7–9].

Note that, although the reference tracking entry guidance law is highly successful, it relies on reference trajectory generated off-line. Therefore, reference tracking method lacks from adaptability to large and unexpected trajectory dispersions. In order to overcome this drawback, numerous researchers have diverted their attentions to the predictor–corrector algorithm over the years. This algorithm aims at iteratively determining the control parameters onboard to eliminate the predicted

errors. Zimmerman [10] has proposed an automated method for computing feasible reentry trajectory on-line with heating constraints. Shen and Lu [11] have developed a fast method for planning onboard a feasible entry trajectory using quasi-equilibrium glide condition (QEGC). Furthermore, predictor–corrector algorithms also use the conventional heading error corridor to control the lateral trajectory. For medium L/D ratio vehicle, this results in large cross-range error. Therefore, more efficient lateral guidance logic for determining the bank reversal point was investigated [12]. Other researches seeking to improve the robustness have been discussed in [13].

It should be pointed out that the computation time for predictor–corrector algorithms increases exponentially as the number of control parameters increase. This is because the gradient information used to improve the control parameters is got via secant method which employs numerical integration. Therefore, in order to reduce the complexity and increase the robustness for numerical process, these algorithms iterate only one or two control parameters. And therefore only a few terminal constraints can be satisfied. Furthermore, those algorithms use a pre-selected threshold corridor or logic to reduce the heading error. For high lift-to-drag ratio entry vehicle, it will not only significantly limit the lateral maneuvering capability, but also cause larger heading error and more bank reversals. Additionally, driven by the need of better handover, it needs to consider more final requirements comparing with traditional vehicles. Obviously, it is necessary to develop a more robust and capable entry guidance algorithm that would be applicable to large cross-range entries and more final requirements. Yu and Chen [14, 15] have proposed an efficient entry guidance algorithm on the foundation of trajectory damping control scheme and analytical solution, in which the spectral decomposition is applied into the linearized reduced-order entry dynamics, and thereby successfully obtaining the decoupled longitudinal and lateral analytical solutions.

Inspired by the idea of parameterization in [16], a novel entry guidance algorithm is proposed in this chapter. This algorithm combines the philosophies of nonlinear model predictive control, multi-segment linear pseudospectral method and calculus of variations. The presented method differs from the method of [15] because of the iterative solution to the coupled nonlinear reduced order dynamics. Furthermore, added terminal constraints such as flight-path angle and altitude are considered. The main contributions of our research are:

- (1) A multi-segment linear pseudospectral model predictive control (MLPMPC) is proposed based on the previous works [17, 18]. Because the control is parametrized, the resulting matrix used to eliminate the predicted error is simpler and solvable. Moreover, this method is capable of handling the multi-segment problem whose states and controls are discontinuous and providing the precise switching time in combination with calculus of variation if that is considered as control parameter. Note that the method in [16] cannot solve this kind of problem.
- (2) This chapter proposes an entry guidance law which is based on MLPMPC. Here a series of analytical formulas have been developed to update the longitudinal L/D and bank reversal commands in accordance with the predicted trajectory

errors. Therefore, this method is not only capable of providing the precise bank reversal point so as to fully exploit the great capability of lateral maneuver, but also of high efficiency since orthogonal polynomials are used to approximate the state and control variables.

- (3) Additionally, proportional guidance and polynomial guidance are investigated. These are designed in longitudinal and lateral guidance planes respectively in order to meet multiple terminal requirements accurately after the last bank reversal.

The proposed method is evaluated via high fidelity simulations with various destinations. Its superior performance and robustness are verified in comparison with other typical method through Monte Carlo simulation. The results indicate that the proposed method has high computational efficiency and guidance accuracy, besides being stable and robust even under multiple terminal constraints. Furthermore, it is capable of providing the precise bank reversal point so as to significantly increase the lateral trajectory shaping capability.

16.2 Entry Dynamics, Entry Trajectory Constraints and Vehicle Description

16.2.1 Entry Dynamics

The 3 DOF point mass dynamics of the reentry vehicle over a spherical, rotating Earth is described as follows [19].

$$\dot{r} = v \sin \gamma; \dot{\theta} = \frac{v \cos \gamma \sin \psi}{r \cos \phi}; \dot{\phi} = \frac{v \cos \gamma \cos \psi}{r}; \quad (16.1)$$

$$\dot{v} = -\frac{D}{m} - g \sin \gamma + \omega^2 r \cos \phi (\sin \gamma \cos \phi - \cos \gamma \cos \psi \sin \phi); \quad (16.2)$$

$$\begin{aligned} \dot{\gamma} &= \frac{L \cos \sigma}{mv} - \left(\frac{g}{v} - \frac{v}{r} \right) \cos \gamma + 2\omega \sin \psi \cos \phi \\ &\quad + \frac{\omega^2 r}{v} \cos \phi (\cos \gamma \cos \phi + \sin \gamma \cos \psi \sin \phi); \end{aligned} \quad (16.3)$$

$$\begin{aligned} \dot{\psi} &= \frac{L \sin \sigma}{vm \cos \gamma} + \frac{v}{r} \cos \gamma \sin \psi \tan \phi \\ &\quad - 2\omega (\tan \gamma \cos \psi \cos \phi - \sin \phi) \\ &\quad + \frac{\omega^2 r}{v \cos \gamma} \sin \psi \sin \phi \cos \phi; \end{aligned} \quad (16.4)$$

where, r is the radial distance from the center of the Earth to the vehicle. h denotes the altitude. θ and ϕ are the longitude and latitude. v is the Earth-relative velocity. γ is the flight-path angle (FPA) of the Earth-relative velocity. ψ is the azimuth angle of the Earth-relative velocity which is defined as a clockwise rotation angle starting at due north. m is the vehicle mass. $g = \mu/r^2$ is the acceleration from gravity, where μ is the Earth's gravitational constant. The relative energy, e , is defined as $e = -r/\mu + v^2/2$. The bank angle, σ , is defined such that the lift vector in the lateral plane is zero at zero bank angle and positive corresponding to the right. ω denotes the Earth self-rotation rate. The aerodynamic lift L and drag D are given as

$$\begin{aligned} L &= \frac{1}{2} \rho v^2 C_l S_{ref} \\ D &= \frac{1}{2} \rho v^2 C_d S_{ref} \end{aligned} \quad (16.5)$$

where, $\rho = \rho_0 \exp(-h/H)$ is the atmospheric density, ρ_0 is the standard atmospheric pressure at sea-level, H is an atmospheric constant. S_{ref} presents the reference area for the vehicle. C_l and C_d are the lift and drag coefficients which are generally dependent on the Mach number and angle of attack (AOA).

16.2.2 Entry Trajectory Constraints

16.2.2.1 Path Constraints

Typical entry trajectory path constraints are heating rate, dynamical pressure and load factor as follows.

$$\dot{Q} = K_Q(\rho)^{0.5} V^{3.15} \leq \dot{Q}_{\max} \quad (16.6)$$

$$q = 0.5 \rho V^2 \leq q_{\max} \quad (16.7)$$

$$n = \frac{L}{g_0} \leq n_{\max} \quad (16.8)$$

where, $K_Q = 1.5e^{-8}$ is used for the numerical simulations. \dot{Q}_{\max} , q_{\max} and n_{\max} are limit values which are dependent on the vehicle configuration and mission. And those three constraints are considered to be “hard” constraints that should be enforced strictly during the flight.

16.2.2.2 Terminal Constraints

In this chapter, the terminal constraints for horizontal landing vehicles such as RLV and X-33 [11] are considered. It calls for the entry phase to terminate at some specified distance from the destination where it is feasible to hand over to the terminal area energy management (TAEM) guidance system. The final constraints at the TAEM interface are defined in terms of altitude, velocity, flight path angle and bank angle. In addition, the relative velocity vector is preferred to closely point to the destination.

$$\begin{aligned} h(e_f) &= h_f, v(e_f) = v_f, s(e_f) = s_f, \gamma(e_f) = 0, \\ \sigma(e_f) &= 0, \Delta\psi = \psi(e_f) - \psi_{los}(e_f) = 0 \end{aligned} \quad (16.9)$$

where, e_f denotes the relative energy at the TAEM interface, s_f represents the final range between the vehicle and the destination, and $\Delta\psi$ is the heading error between the azimuth angel and the line of sight (LOS) angle.

16.2.3 Vehicle Description and Model Assumption

Common Aero Vehicle (CAV) is one of the most representative entry vehicles with high lift-to-drag ratio. CAV-H introduced in the report of Phillips [20] is modeled to evaluate the proposed method. Its weight is 907 kg, its area reference is 0.4839 m^2 and its maximum lift-to-drag ratio is around 3.5. The lift and drag coefficients are approximated by high order polynomials which are functions of the AOA and Mach number. Because the AOA having the maximum lift-to-drag ratio is at around 10 Deg, the range of AOA is from 5 to 20 Deg. The limiting values of heating rate, dynamic pressure and normal load factor are 500 W/cm^2 , 100 kPa, and 2 g respectively. In addition, the following nominal AOA profile is scheduled for all missions.

$$\begin{cases} \alpha = 10, e \geq e_{mid} \\ \alpha = a_{\alpha 1}(e - e_f)^2 + a_{\alpha 2}(e - e_f) + 7, e \leq e_{mid} \end{cases} \quad (16.10)$$

where, e_{mid} is a pre-selected bank reversal point (the velocity is 3500 m/s and the altitude is 35,000 m), and $a_{\alpha 1}$ and $a_{\alpha 2}$ are chosen to make this piecewise function smooth and continuous.

16.2.4 Auxiliary Geocentric Inertial Frame and Emotion Dynamics

In this subsection, the Auxiliary Geocentric Inertial (AGI) Frame discussed in [11] is used to simplify the calculation for guidance commands. This frame is fixed in the

inertial space and updated once according to the current condition of the vehicle and a virtual destination which is estimated as follows.

$$\lambda_p = \lambda_T + \omega t_{go}, \phi_p = \phi_T, h_p = h_T, t_{go} = S_{go}/(v + v_f) \quad (16.11)$$

where, λ_p , ϕ_p and h_p are the longitude, latitude and altitude of the virtual destination, S_{go} is the range along the great circle connecting the vehicle and the virtual destination. Then, the AGI frame is defined such that the first axis coincides with the current position vector, the second axis is orthogonal to the first axis and directs to the virtual destination, the third axis directs to the new pole. The states in AGI frame can be transformed from the states defined in Sect. 16.2.1 via the LOS angle. The motion dynamics in AGI frame are formulated as

$$\begin{aligned} \dot{r} &= v \sin \gamma; \dot{\tilde{\theta}} = \frac{\tilde{v} \cos \tilde{\gamma} \sin \tilde{\psi}}{r \cos \tilde{\phi}}; \dot{\tilde{\phi}} = \frac{\tilde{v} \cos \tilde{\gamma} \cos \tilde{\psi}}{r}; \\ \dot{\tilde{v}} &= -\frac{D}{m} - g \sin \tilde{\gamma}; \dot{\tilde{\gamma}} = \frac{L \cos \sigma}{m \tilde{v}} - \left(\frac{g}{\tilde{v}} - \frac{\tilde{v}}{r} \right) \cos \tilde{\gamma}; \\ \dot{\tilde{\psi}} &= \frac{L \sin \sigma}{\tilde{v} m \cos \tilde{\gamma}} + \frac{\tilde{v}}{r} \cos \tilde{\gamma} \sin \tilde{\psi} \tan \tilde{\phi}; \end{aligned} \quad (16.12)$$

where, $\tilde{\theta}$ and $\tilde{\phi}$ are the longitude and latitude in AGI frame, \tilde{v} presents the absolute velocity and is the vector sum of the relative velocity and the velocity due to the Earth's rotation. $\tilde{\gamma}$ and $\tilde{\psi}$ are the FPA and azimuth angle with respect to absolute velocity in AGI frame. The absolute energy is defined as

$$E = -\frac{r}{\mu} + \frac{\tilde{v}^2}{2} \quad (16.13)$$

And its derivative is

$$\dot{E} = -D\tilde{v} \quad (16.14)$$

Note that the initial longitude and latitude in AGI are zeros.

16.3 Linear Pseudospectral Model Predictive Entry Guidance

A robust entry guidance algorithm using multi-segment linear pseudospectral model predictive control is proposed in this section. According to the trajectory characteristic of entry vehicle, the entry flight is divided into three phases: descent phase, glide phase and terminal adjustment phase. In descent phase, the control scheme

is designed to transit the vehicle from its initial altitude to the glide altitude. In glide phase, multi-segment linear pseudospectral model predictive control is used to update the steering commands. The aim is not only to glide towards destination but also successful transition to the terminal adjustment phase. In terminal adjustment phase, the Proportional Navigation and Polynomial guidance are developed to accurately guide the vehicle towards the TAEM interface while satisfying all terminal constraints.

16.3.1 Descent Phase Guidance

Descent phase ranges from the initial altitude to an altitude where the derivative of altitude equals zero. It also means that the aerodynamic lift is sufficiently built up to support the vehicle to glide. In this phase, because of the high velocity and the rapid increase in the atmospheric density, the magnitudes of AOA and bank angle have great impact on the local heating rate and subsequent trajectory. Generally, the local maximum heating rate will happen at the end of this phase. Therefore, in order to limit hearting rate and leave the vehicle enough energy to regulate, the vehicle drops with maximum allowable AOA and 0 Deg bank angle.

$$\begin{aligned}\alpha_{\text{cmd}} &= \alpha_{\text{max}}; \\ \sigma_{\text{cmd}} &= 0 \text{ deg};\end{aligned}\quad (16.15)$$

Note that the stop criterion in this phase is presented as

$$\dot{h} = v \sin \gamma = 0 \quad (16.16)$$

where, v and γ signify the relative velocity and FPA provided by the Inertial Measurement Unit (IMU). It may be noted that, this phase is ended not exactly when the derivative of altitude is zero but at a point just before the derivative is positive. This is done to exclude the case where the initial FPA is positive. The terminal state of descent phase is the initial state of glide phase.

16.3.2 Glide Phase Entry Guidance

16.3.2.1 Reduced-Order Dynamics in Model Predictive Integration

The entry dynamics in AGI frame can be simplified into a set of reduced order entry equations as in Eq. (16.17). In doing that, the Coriolis force and centripetal acceleration has been ignored and it is assumed that the vehicle flies over a fixed radius sphere. It is also assumed that the derivative of FPA is small enough to be ignored.

$$\begin{aligned}\frac{d\tilde{\theta}}{dE} &= \frac{\sin \tilde{\psi}}{\cos \phi \left(\frac{\mu}{r} + 2E\right)} U; \quad \frac{d\tilde{\phi}}{dE} = \frac{\cos \tilde{\psi}}{\left(\frac{\mu}{r} + 2E\right)} U; \\ \frac{d\tilde{\psi}}{dE} &= \mp \frac{1}{2(E + \frac{\mu}{r})} \sqrt{[k_{ld}F(e)]^2 - U^2} + \frac{\sin \tilde{\psi} \tan \tilde{\phi}}{\left(\frac{\mu}{r} + 2E\right)} U;\end{aligned}\quad (16.17)$$

where, E is the absolute energy, F denotes the total lift-to-drag ratio, which is a function of relative energy and is generated off-line using AOA profile. Control variable, U , represents the longitudinal L/D that is the vertical component of F , k_{ld} is the estimation to the L/D ratio deviation provided by the IMU and is assumed to be a constant in predictive integration, r denotes constant altitude which is the average of the current and final altitudes in each guidance circle. The relationship between the absolute energy and the relative energy is approximated by a linear function.

16.3.2.2 Parameterization of Control Command

Because AOA profile is determined off-line, the control command parameterization refers to the planning of longitudinal L/D profile using several parameters. In fact, the longitudinal L/D profile is equivalent with the bank angle profile since there is a one to one mapping relationship between them. Two bank reversals are planned to guarantee enough scope to eliminate errors and provide adequate lateral maneuvering. The first bank reversal is performed intermediately, and the second bank reversal is done near the TAEM interface. Finally, the control command is designed as a piecewise function divided into three parts.

$$U = \begin{cases} u, & E \geq E_{re1}; \\ u, & E_{re2} \leq E \leq E_{re1}; \\ c_1(E - E_f)^2 + c_2(E - E_f) + k_{ld} \frac{L}{D}(e_f), & E_f \leq E \leq E_{re2}; \end{cases} . \quad (16.18)$$

where, E_{re1} and E_{re2} are bank reversal points, u is a scalar control parameter. The reason for having two constant bank reversals is to keep the vehicle in a steady glide and have enough L/D margin to eliminate longitudinal disturbance. After the last bank reversal, the vehicle comes into the terminal adjustment phase. It is obvious that the L/D in this phase is approximated via a quadratic function. And its final value equals the L/D at the TAEM interface. c_1 and c_2 are function coefficients which are chosen to make the piecewise function smooth and continuous. Analytically, c_1 and c_2 are expressed as

$$\begin{aligned}c_1 &= - \left(k_1 - k_{ld} \frac{L}{D}(e_f) \right) / (E_{re2} - E_f)^2 \\ c_2 &= 2 \left(k_1 - k_{ld} \frac{L}{D}(e_f) \right) / (E_{re2} - E_f)\end{aligned}\quad (16.19)$$

Therefore, if u , E_{re1} and E_{re2} are given, the entry trajectory is determined by the nonlinear reduced-order entry dynamics with an initial state.

16.3.2.3 Linearization of Multi-segment Nonlinear Dynamics

Without loss of generality, let us consider the reduced-order entry dynamics with hard terminal constraints as follows.

$$\begin{aligned}\dot{\mathbf{x}} &= \mathbf{f}(\mathbf{x}, \mathbf{u}) \\ \theta(E_f) &= \theta_f, \phi(E_f) = \phi_f\end{aligned}\quad (16.20)$$

where, $\mathbf{x} = (\theta \ \phi \ \psi)^T$. If initial guess values are given, numerical integration methods such as Euler or Runge–Kutta can be used to predict the states in all regions. The terminal deviations from the desired states are expressed as $d\mathbf{x}_f = \mathbf{x}(E_f) - \mathbf{x}_f$. Then, Eq. (16.20) is expanded in Taylor series with high-order differentiation around the integral trajectory. Thus, a set of linear dynamics equations using the deviations as the independent variables are formulated by neglecting the higher order terms

$$\begin{aligned}\delta\dot{\mathbf{x}} &= \mathbf{A}_1(E)\delta\mathbf{x} + \mathbf{B}_1(E)\delta\mathbf{u}, E > E_{re1} \\ \delta\dot{\mathbf{x}} &= \mathbf{A}_2(E)\delta\mathbf{x} + \mathbf{B}_2(E)\delta\mathbf{u}, E_{re2} \leq E \leq E_{re1} \\ \delta\dot{\mathbf{x}} &= \mathbf{A}_3(E)\delta\mathbf{x} + \tilde{\mathbf{B}}_3(E)\delta\mathbf{u}, E_f \leq E \leq E_{re2} \\ \tilde{\mathbf{B}}_3(E) &= \mathbf{B}_3(E) \left(\frac{2(E - E_f)}{(E_{re2} - E_f)} - \frac{(E - E_f)^2}{(E_{re2} - E_f)^2} \right)\end{aligned}\quad (16.21)$$

where, $\delta\mathbf{x} = \mathbf{x}_{ref} - \mathbf{x}$, $\delta\mathbf{u} = \mathbf{u}_{ref} - \mathbf{u}$. Note that matrix \mathbf{A}_i is 3 by 3, matrix \mathbf{B}_i is 3 by 1. The elements of those matrices are derived as

$$\mathbf{A}_i(E) = \begin{bmatrix} 0 & \frac{\sin \tilde{\psi} \sin \tilde{\phi}}{\cos^2 \tilde{\phi} (\frac{\mu}{r} + 2E)} u & \frac{\cos \tilde{\psi}}{\cos \tilde{\phi} (\frac{\mu}{r} + 2E)} u \\ 0 & 0 & -\frac{\sin \tilde{\psi}}{(\frac{\mu}{r} + 2E)} u \\ 0 & \frac{\sin \tilde{\psi} \sec^2 \tilde{\phi}}{(\frac{\mu}{r} + 2E)} u & \frac{\cos \tilde{\psi} \tan \tilde{\phi}}{(\frac{\mu}{r} + 2E)} u \end{bmatrix} \quad (16.22)$$

And

$$\mathbf{B}_i(E) = \begin{bmatrix} \frac{\sin \tilde{\psi}}{\cos \tilde{\phi} (\frac{\mu}{r} + 2E)} \\ \frac{\cos \tilde{\psi}}{(\frac{\mu}{r} + 2E)} u \\ \pm \frac{u}{2(E + \frac{\mu}{r})\sqrt{[k_{ld}F(e)]^2 - u^2}} + \frac{\sin \tilde{\psi} \tan \tilde{\phi}}{(\frac{\mu}{r} + 2E)} \end{bmatrix} \quad (16.23)$$

Note that, the first sign of the third element in matrix \mathbf{B}_1 is the same as that in matrix \mathbf{B}_3 and different from that in matrix \mathbf{B}_2 . Additionally, the initial deviation vector,

$\delta\mathbf{x}(E_0)$, is always a zero vector since the predictive integration starts from the current states in each calculation. Finally, in combination with both initial and terminal deviations, a linear multi-segment control problem is built up. Next, multi-segment linear pseudospectral method and calculus of variations are used to efficiently discretize the problem to provide a series of analytical correction formulas.

16.3.2.4 Correction Using Multi-segment Linear Pseudospectral Model Predictive Control

In linear pseudospectral method, the state and control variables are approximated using a basis of Lagrange interpolating polynomials, and the differential–algebraic equations are approximated via orthogonal collocation. Thus, the optimal control problem is transferred into the problem of solving a set of linear algebraic equations. And it only takes a fraction of a second to solve this problem. In this subsection, linear pseudospectral method is extended into the linear multi-segment control problem with parameterized control command. Generally, there are three popularly used sets of collocation points, Legendre–Gauss (LG) [21, 22], Legendre–Gauss–Radau (LGR) [23] and Legendre–Gauss–Lobatto (LGL) [24–26] points. And those three sets of points are roots of a Legendre polynomial and/or linear combination of a Legendre polynomial and its derivatives. Recent studies show that there exists a null space in LGL discretization due to the fact that the LG and LGR differentiation matrices are full rank whereas the LGL differentiation matrix is singular. So, LG collocation scheme, a Gauss Pseudospectral method, is chosen here.

Because the support points of Lagrange interpolating polynomials are orthogonal points and lie in the computational interval $[-1, 1]$, the first step is to transfer the time domain of each segment into $[-1, 1]$.

$$\begin{cases} E = \frac{E_{re1} - E_0}{2}\tau + \frac{E_{re1} + E_0}{2}, E_{re1} \leq E \leq E_0 \\ E = \frac{E_{re2} - E_{re1}}{2}\tau + \frac{E_{re2} + E_{re1}}{2}, E_{re2} \leq E \leq E_{re1} \\ E = \frac{E_f - E_{re2}}{2}\tau + \frac{E_f - E_{re2}}{2}, E_f \leq E \leq E_{re2} \end{cases} \quad (16.24)$$

Therefore, the original problem is transferred into Eq. (16.25)

$$\begin{aligned} \frac{d\delta\mathbf{x}}{d\tau} &= \frac{E_{re1} - E_0}{2}\mathbf{A}_1(E)\delta\mathbf{x} + \frac{E_{re1} - E_0}{2}\mathbf{B}_1(E)\delta u \\ \frac{d\delta\mathbf{x}}{d\tau} &= \frac{E_{re2} - E_{re1}}{2}\mathbf{A}_2(E)\delta\mathbf{x} + \frac{E_{re2} - E_{re1}}{2}\mathbf{B}_2(E)\delta u \\ \frac{d\delta\mathbf{x}}{d\tau} &= \frac{E_f - E_{re2}}{2}\mathbf{A}_3(E)\delta\mathbf{x} + \frac{E_f - E_{re2}}{2}\tilde{\mathbf{B}}_3(E)\delta u \end{aligned} \quad (16.25)$$

Next, let us define that $L_N(\tau)$ is a Lagrange interpolating polynomial of degree N . τ_i present the roots of Legendre Polynomial of degree N named LG points. Note that there is no analytical solution for such special roots, and a numerical algorithm is used to provide the LG points. Hence, the state variables in each phase are approximated by using a basis of Lagrange interpolating polynomials of degree N as

$$\delta\mathbf{x}^N(\tau) = \sum_{l=0}^N \delta\mathbf{x}(\tau_l) L_l(\tau) \quad (16.26)$$

According to the basic theory of Lagrange interpolating polynomial, $L_N(\tau)$ satisfies the properties

$$L_l(\tau_k) = \begin{cases} 1, & \text{when } l = k \\ 0, & \text{when } l \neq k \end{cases} \quad (16.27)$$

And

$$\delta\mathbf{x}^N(\tau_k) = \delta\mathbf{x}(\tau_k) \quad (16.28)$$

At the LG points, the derivative of $\delta\mathbf{x}$ can be expressed through a differential approximation matrix. The differential approximation matrix D is a $N \times (N + 1)$ matrix which is obtained by the derivative of each Lagrange Polynomial at the LG points. The elements of D are determined as

$$\delta\dot{\mathbf{x}}^N(\tau_k) = \sum_{l=0}^N D_{kl} \delta\mathbf{x}(\tau_l) \quad (16.29)$$

And

$$D_{ki} = \dot{L}_i(\tau_k) = \sum_{l=0}^N \frac{\prod_{j=0, j \neq i, l}^N (\tau_k - \tau_j)}{\prod_{j=0, j \neq i}^N (\tau_i - \tau_j)} \quad (16.30)$$

It is assumed that the state variables are given.

$$\delta\mathbf{x} = [\delta\mathbf{x}_1^T \ \delta\mathbf{x}_2^T \ \cdots \ \delta\mathbf{x}_N^T]^T \quad (16.31)$$

By substituting them into Eq. (16.25), the deviation dynamics are not only transferred into a set of algebraic equations, but also represented by the state deviations at the LG points.

$$\begin{aligned} \sum_{l=0}^N D_{kl} \delta x_l &= \frac{E_{re1} - E_0}{2} (\mathbf{A}_1(E_k) \delta x_k + \mathbf{B}_1(E_k) \delta u) \\ \sum_{l=0}^N D_{kl} \delta x_l &= \frac{E_{re2} - E_{re1}}{2} (\mathbf{A}_2(E_k) \delta x_k + \mathbf{B}_2(E_k) \delta u) \\ \sum_{l=0}^N D_{kl} \delta x_l &= \frac{E_f - E_{re2}}{2} (\mathbf{A}_3(E_k) \delta x_k + \tilde{\mathbf{B}}_3(E_k) \delta u) \end{aligned} \quad (16.32)$$

where, $k = 1, 2, \dots, N$. Rearranging the approximating matrix and state deviations in Eq. (16.32), a simple algebraic equation is formulated as

$$\mathbf{D}_1 \delta x_0 + \mathbf{D}_{2:n} \delta x = \frac{E_{re1} - E_0}{2} \mathbf{A}_1 \delta x + \frac{E_{re1} - E_0}{2} \mathbf{B}_1 \delta u \quad (16.33)$$

where, the element of \mathbf{D}_1 and $\mathbf{D}_{2:n}$ are

$$\mathbf{D}_1 = \begin{bmatrix} \mathbf{D}_{01}^{s \times s} \\ \vdots \\ \mathbf{D}_{0n}^{s \times s} \end{bmatrix}; \mathbf{D}_{2:n} = \begin{bmatrix} \mathbf{D}_{11}^{s \times s} \cdots \mathbf{D}_{n1}^{s \times s} \\ \vdots \quad \ddots \quad \vdots \\ \mathbf{D}_{1n}^{s \times s} \cdots \mathbf{D}_{nn}^{s \times s} \end{bmatrix}; \mathbf{D}_{ij}^{s \times s} = \begin{bmatrix} D_{ij} & \cdots & 0 \\ \vdots & \ddots & \vdots \\ 0 & \cdots & D_{ij} \end{bmatrix}; \quad (16.34)$$

Note that s denotes the number of state variables, and the matrices \mathbf{A}_1 and \mathbf{B}_1 are represented as

$$\mathbf{A}_1 = \begin{bmatrix} \mathbf{A}_1(E_1) & \cdots & 0 \\ \vdots & \ddots & \vdots \\ 0 & \cdots & \mathbf{A}_1(E_n) \end{bmatrix}, \mathbf{B}_1 = \begin{bmatrix} \mathbf{B}_1(E_1) \\ \vdots \\ \mathbf{B}_1(E_n) \end{bmatrix} \quad (16.35)$$

Rearranging the Eq. (16.33) again, state deviation vector can be analytically expressed as

$$\delta x = \left[\mathbf{D}_{2:n} - \frac{E_{re1} - E_0}{2} \mathbf{A}_1 \right]^{-1} \left[\frac{E_{re1} - E_0}{2} \mathbf{B}_1 \delta u - \mathbf{D}_1 \delta x_0 \right] \quad (16.36)$$

Note that the dynamic constraint is only collocated at the LG points and not at the boundary points. Thus, δx does not include the terminal state deviations. Actually, boundary deviations can be expressed as the function of the state deviations at the LG points and initial point via Gauss Quadrature.

$$\delta x_{re1} = \delta x_0 + \sum_{i=1}^n \omega_i \left(\frac{E_{re1} - E_0}{2} \mathbf{A}_1(E_i) \delta x_i + \frac{E_{re1} - E_0}{2} \mathbf{B}_1(E_i) \delta u \right) \quad (16.37)$$

where, ω is the weight of Gauss Quadrature. Adding Eq. (16.36) into Eq. (16.37) and rearranging it, the terminal state deviations are represented as

$$\delta\mathbf{x}_{re1} = \delta\mathbf{x}_0 + \frac{E_{re1} - E_0}{2} \mathbf{1}^T \mathbf{A}_1 \mathbf{W}_1 \delta\mathbf{x} + \frac{E_{re1} - E_0}{2} \mathbf{B}_1^T \mathbf{W}_1 \mathbf{1} \delta u \quad (16.38)$$

where, \mathbf{I} presents a column vector, \mathbf{W}_1 is a matrix of Gauss Quadrature weight represented as

$$\mathbf{W}_1 = \begin{bmatrix} \mathbf{W}_1^{s \times s} & \cdots & 0 \\ \vdots & \ddots & \vdots \\ 0 & \cdots & \mathbf{W}_n^{s \times s} \end{bmatrix}, \quad \mathbf{W}_1^{s \times s} = \begin{bmatrix} \omega_1 & \cdots & 0 \\ \vdots & \ddots & \vdots \\ 0 & \cdots & \omega_1 \end{bmatrix} \quad (16.39)$$

Finally, by substituting Eq. (16.36) into Eq. (16.38), the terminal state deviations in the first phase can be expressed as a explicit function of initial state deviations, $\delta\mathbf{x}_0$, and control improvement, δu .

$$\delta\mathbf{x}_{re1} = \mathbf{K}_1^x \delta\mathbf{x}_0 + \mathbf{K}_1^u \delta u \quad (16.40)$$

where, \mathbf{K}_1^x is a 3 by 3 matrix, \mathbf{K}_1^u is a 3 by 1 column vector, of which the elements are expressed as

$$\begin{aligned} \mathbf{K}_1^x &= \mathbf{L}^x(E_0, E_{re1}, \mathbf{A}_1, \mathbf{D}, \mathbf{W}_1) \\ \mathbf{K}_1^u &= \mathbf{L}^u(E_0, E_{re1}, \mathbf{A}_1, \mathbf{B}_1, \mathbf{D}, \mathbf{W}_1) \end{aligned} \quad (16.41)$$

where, the functions, $\mathbf{L}^x, \mathbf{L}^u$, are defined as

$$\begin{aligned} \mathbf{L}^x(E_0, E_{re1}, \mathbf{A}_1, \mathbf{D}, \mathbf{W}_1) &= \left\{ \mathbf{1} - \frac{E_{re1} - E_0}{2} \mathbf{1}^T \mathbf{A}_1 \mathbf{W}_1 \right. \\ &\quad \left[\mathbf{D}_{2:n} - \frac{E_{re1} - E_0}{2} \mathbf{A}_1 \right]^{-1} \mathbf{D}_1; \\ \mathbf{L}^u(E_0, E_{re1}, \mathbf{A}_1, \mathbf{B}_1, \mathbf{D}, \mathbf{W}_1) &= \left\{ \left(\frac{E_{re1} - E_0}{2} \right)^2 \mathbf{1}^T \mathbf{A}_1 \mathbf{W}_1 \right. \\ &\quad \left[\mathbf{D}_{2:n} - \frac{E_{re1} - E_0}{2} \mathbf{A}_1 \right]^{-1} \mathbf{B}_1 + \frac{E_{re1} - E_0}{2} \mathbf{B}_1^T \mathbf{W}_1 \mathbf{1} \right\} \end{aligned} \quad (16.42)$$

Similarly, the explicit function in the second segment is the same as that in the first segment and can be expressed by regarding the terminal state deviations in the first segment as the initial state deviations.

$$\begin{aligned} \mathbf{K}_2^x &= \mathbf{L}^x(E_{re1}, E_{re2}, \mathbf{A}_2, \mathbf{D}, \mathbf{W}_2) \\ \mathbf{K}_2^u &= \mathbf{L}^u(E_{re1}, E_{re2}, \mathbf{A}_2, \mathbf{B}_2, \mathbf{D}, \mathbf{W}_2) \end{aligned} \quad (16.43)$$

Also, the coefficient matrices in the third segment are given as

$$\begin{aligned}\mathbf{K}_3^x &= \mathbf{L}^x(E_{re2}, E_f, \mathbf{A}_3, \mathbf{D}, \mathbf{W}_3) \\ \mathbf{K}_3^u &= \mathbf{L}^u(E_{re2}, E_f, \mathbf{A}_3, \tilde{\mathbf{B}}_3, \mathbf{D}, \mathbf{W}_3)\end{aligned}\quad (16.44)$$

Then, the relationship among the initial state deviations, control improvement and terminal state deviations is formulated via superposition principle.

$$\delta\mathbf{x}_f = \mathbf{K}_3^x \mathbf{K}_2^x \mathbf{K}_1^x \delta\mathbf{x}_0 + (\mathbf{K}_3^x \mathbf{K}_2^x \mathbf{K}_1^u + \mathbf{K}_3^x \mathbf{K}_2^u + \mathbf{K}_3^u) \delta u \quad (16.45)$$

Note that the initial state deviations, $\delta\mathbf{x}_0$, are all zeros discussed in previous section. Therefore, the control improvement, which is used to eliminate predictive terminal deviations, are finally formulated as

$$\delta u = (\mathbf{K}_3^x \mathbf{K}_2^x \mathbf{K}_1^u + \mathbf{K}_3^x \mathbf{K}_2^u + \mathbf{K}_3^u)^{-1} \delta\mathbf{x}_f \quad (16.46)$$

Generally speaking, because of the irrelevance with the number of system segmentation, the explicit expression of control improvement can be extended into an arbitrary multi-segment nonlinear control problem with hard terminal constraints. Thus, a general multi-segment linear pseudospectral model predictive control is given.

Theorem 1 *For a general multi-segment nonlinear control problem with hard terminal constraints, assuming that the control variable can be expressed as a parametric function, the original problem is then able to be transferred into solving a set of multi-segment linear algebraic equations via linearization and gauss pseudospectral method, the relationship among the initial state deviations, terminal state deviations and control improvement is formulated as*

$$\delta\mathbf{x}_f = \prod_{i=1}^n \mathbf{K}_i^x \delta\mathbf{x}_0 + \left(\sum_{i=1}^n \left(\prod_{j=1}^{i-1} \mathbf{K}_{n+1-j}^x \right) \mathbf{K}_{n+1-j}^u \right) \delta u \quad (16.47)$$

where, n denotes the number of segments, $\prod_{j=1}^0 \mathbf{K}_{n+1-j}^x = \mathbf{I}$ and the elements of matrices \mathbf{K}_{n+1-j}^x and \mathbf{K}_{n+1-j}^u are expressed as

$$\begin{aligned}\mathbf{K}_i^x &= \mathbf{L}^x(E_{i-1}, E_i, \mathbf{A}_i, \mathbf{D}, \mathbf{W}_i) \\ \mathbf{K}_i^u &= \mathbf{L}^u(E_{i-1}, E_i, \mathbf{A}_i, \mathbf{B}_i, \mathbf{D}, \mathbf{W}_i)\end{aligned}\quad (16.48)$$

Note that there is only one parameter in parametric function such that only one terminal constraint can be corrected by the control improvement. In fact, longitudinal L/D is more sensitive to the terminal longitude than the others. Naturally, the control improvement is used to eliminate this deviation as in the case without considering the bank reversal point update.

$$\delta u = \frac{\delta \tilde{\theta}_f}{[\mathbf{1} \ 0 \ 0] (\mathbf{K}_3^x \mathbf{K}_2^x \mathbf{K}_1^u + \mathbf{K}_3^x \mathbf{K}_2^u + \mathbf{K}_3^u)} \quad (16.49)$$

In order to meet the final position requirement while keeping enough energy, the modulation of bank reversal point is chosen to eliminate the terminal lateral deviation. In combination with the Multi-segment linear pseudospectral method and calculus of variations, a novel and efficient predictor–corrector method used to simultaneously update the longitudinal L/D and bank reversal commands is presented. Now, let us consider the terminal state as follows.

$$\begin{aligned} \tilde{\theta}(E_f) &= f_1(u^k, E_{rel}^k) = \tilde{\theta}_0 + \int_{E_0}^{E_{rel}^k} f_1^1(\mathbf{x}, E, u^k) dE \\ &\quad + \int_{E_{rel}^k}^{E_{rel}^2} f_1^2(\mathbf{x}, E, u^k) dE + \int_{E_{rel}^2}^{E_f} f_1^1(\mathbf{x}, E, u^k) dE \\ \tilde{\phi}(E_f) &= f_2(u^k, E_{rel}^k) = \tilde{\phi}_0 + \int_{E_0}^{E_{rel}^k} f_2^1(\mathbf{x}, E, u^k) dE \\ &\quad + \int_{E_{rel}^k}^{E_{rel}^2} f_2^2(\mathbf{x}, E, u^k) dE + \int_{E_{rel}^2}^{E_f} f_2^1(\mathbf{x}, E, u^k) dE \end{aligned} \quad (16.50)$$

Assuming that δu and δE are small enough, the terminal state can be expressed as

$$\begin{aligned} f_1(u^k - \delta u, E_{rel}^k - \delta E^k) &= f_1(u^k, E_{rel}^k) - \frac{\partial f_1(u^k, E_{rel}^k)}{\partial u} \delta u \\ &\quad - \frac{\partial f_1(u^k, E_{rel}^k)}{\partial E_{rel}^k} \delta E^k + O(h^2) \\ f_2(u^k - \delta u, E_{rel}^k - \delta E^k) &= f_2(u^k, E_{rel}^k) - \frac{\partial f_2(u^k, E_{rel}^k)}{\partial u} \delta u \\ &\quad - \frac{\partial f_2(u^k, E_{rel}^k)}{\partial E_{rel}^k} \delta E^k + O(h^2) \end{aligned} \quad (16.51)$$

By neglecting the high-order terms, the relationship between the terminal deviations and control improvements is formulated around the integral trajectory.

$$\begin{aligned} \delta \tilde{\theta}_f &= \frac{\partial f_1(u^k, E_{rel}^k)}{\partial u} \delta u + \frac{\partial f_1(u^k, E_{rel}^k)}{\partial E_{rel}^k} \delta E^k \\ \delta \tilde{\phi}_f &= \frac{\partial f_2(u^k, E_{rel}^k)}{\partial u} \delta u + \frac{\partial f_2(u^k, E_{rel}^k)}{\partial E_{rel}^k} \delta E^k \end{aligned} \quad (16.52)$$

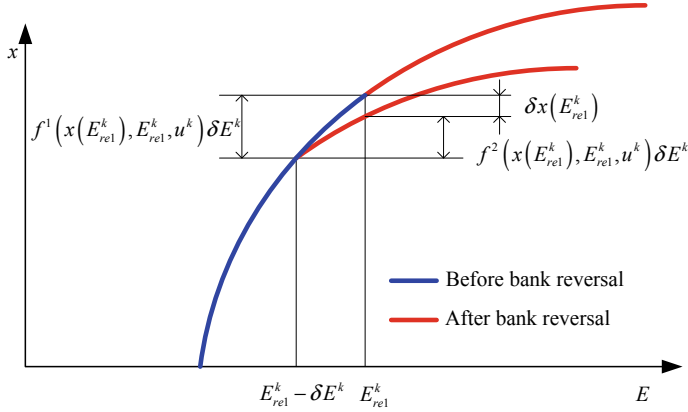


Fig. 16.1 State variation at the normal bank reversal point

Note that $\partial f_1(u^k, E_{rel}^k)/\partial u$ and $\partial f_2(u^k, E_{rel}^k)/\partial u$ are the partial derivatives with respect to the longitudinal L/D without considering the modulation of bank reversal point. They are provided via the multi-segment linear pseudospectral method.

$$\begin{bmatrix} \frac{\partial f_1(u^k, E_{rel}^k)}{\partial u} \delta u \\ \frac{\partial f_2(u^k, E_{rel}^k)}{\partial u} \delta u \end{bmatrix} = \begin{bmatrix} 1 & 0 & 0 \\ 0 & 1 & 0 \end{bmatrix} (\mathbf{K}_3^x \mathbf{K}_2^x \mathbf{K}_1^u + \mathbf{K}_3^x \mathbf{K}_2^u + \mathbf{K}_3^u) \quad (16.53)$$

$\partial f_1(u^k, E_{rel}^k)/\partial E_{rel}^k$ and $\partial f_2(u^k, E_{rel}^k)/\partial E_{rel}^k$ are the partial derivatives with respect to the bank reversal point without considering the modulation of longitudinal L/D . Modulation of bank reversal point will cause the state changes at the normal bank reversal point. The state variation at that point is shown in Fig. 16.1. Under the assumption of linearization, the state deviations before and after the normal bank reversal are $f^1(x(E_{rel}^k), E_{rel}^k, u^k)\delta E^k$ and $f^2(x(E_{rel}^k), E_{rel}^k, u^k)\delta E^k$. Therefore, the state variation at that point can be expressed as the function of the energy variation.

$$\delta \mathbf{x}(E_{rel}^k) = [f^1(x(E_{rel}^k), E_{rel}^k, u^k) - f^2(x(E_{rel}^k), E_{rel}^k, u^k)]\delta E^k \quad (16.54)$$

Without considering the longitudinal L/D modulation, the state deviation dynamics caused by bank reversal are formulated as

$$\begin{aligned} \frac{d\delta \mathbf{x}}{d\tau} &= \frac{E_{re2} - E_{rel1}}{2} \mathbf{A}_2(E) \delta \mathbf{x} \\ \frac{d\delta \mathbf{x}}{d\tau} &= \frac{E_f - E_{re2}}{2} \mathbf{A}_2(E) \delta \mathbf{x} \end{aligned} \quad (16.55)$$

Therefore, the relationship between the terminal state deviations and bank reversal point improvement can be analytically calculated via Eq. (16.45) without considering longitudinal L/D modulation.

$$\delta \mathbf{x}_f = \mathbf{K}_3^x \mathbf{K}_2^x \delta \mathbf{x}(E_{rel}^k) \quad (16.56)$$

The analytical expressions for the partial derivatives with respect to the bank reversal point are given as

$$\begin{aligned} [1 \ 0 \ 0] \mathbf{K}_3^x \mathbf{K}_2^x \begin{bmatrix} 0 \\ 0 \\ 1 \end{bmatrix} [f^1(\mathbf{x}(E_{rel}^k), E_{rel}^k, u^k) \\ - f^2(\mathbf{x}(E_{rel}^k), E_{rel}^k, u^k)] &= \frac{\partial f_1(u^k, E_{rel}^k)}{\partial E_{rel}^k} \\ [0 \ 1 \ 0] \mathbf{K}_3^x \mathbf{K}_2^x \begin{bmatrix} 0 \\ 0 \\ 1 \end{bmatrix} [f^1(\mathbf{x}(E_{rel}^k), E_{rel}^k, u^k) \\ - f^2(\mathbf{x}(E_{rel}^k), E_{rel}^k, u^k)] &= \frac{\partial f_2(u^k, E_{rel}^k)}{\partial E_{rel}^k} \end{aligned} \quad (16.57)$$

Finally, by substituting the Eqs. (16.52), (16.53) and (16.57), the improvements of the longitudinal L/D and bank reversal point used to eliminate the terminal errors are analytically determined as follows.

$$\begin{aligned} \delta u &= \frac{\frac{\partial f_1}{\partial E_{rel}^k} \delta \tilde{\phi}_f - \frac{\partial f_2}{\partial E_{rel}^k} \delta \tilde{\theta}_f}{\frac{\partial f_2}{\partial u} \frac{\partial f_1}{\partial E_{rel}^k} - \frac{\partial f_1}{\partial u} \frac{\partial f_2}{\partial E_{rel}^k}} \\ \delta E^k &= \frac{\frac{\partial f_1}{\partial u} \delta \tilde{\phi}_f - \frac{\partial f_2}{\partial u} \delta \tilde{\theta}_f}{\frac{\partial f_1}{\partial u} \frac{\partial f_2}{\partial E_{rel}^k} - \frac{\partial f_2}{\partial u} \frac{\partial f_1}{\partial E_{rel}^k}} \end{aligned} \quad (16.58)$$

The new longitudinal L/D and bank reversal commands are given as

$$\begin{aligned} u^{k+1} &= u^k - \delta u \\ E_{rel}^{k+1} &= E_{rel}^k - \delta E^k \end{aligned} \quad (16.59)$$

Also, the bank angle command is determined simultaneously as

$$\sigma_{com} = \tan^{-1} \frac{u^{k+1}}{(L/D)_{IMU}} \quad (16.60)$$

where, $(L/D)_{IMU}$ is the current L/D ratio measured by the IMU.

The above process is repeated until the precise control variable and the approaching bank reversal point are found. This method combines linear gauss pseudospectral method, linearization of multi-phase nonlinear dynamical system, model predictive control and calculus of variations. A series of analytical formulas are derived to correct longitudinal L/D and bank reversal point. Thus, this method not only retains the high accuracy of orthogonal discretization, but is also computationally efficient.

16.3.2.5 Example for the Efficiency and Convergence Verification

In this subsection, an example with various destinations and initial bank signs is employed to test the computational efficiency and convergence rate for the proposed method. The initial states for the two cases are listed in Table 16.1.

The numbers of LG nodes and predictive integral steps are 8 and 80 for the first two segments, 6 and 40 for the last segment. The ground tracks for both cases are shown in Fig. 16.2, where both trajectories meet the requirements. The azimuth angle histories are given in Fig. 16.3, it is easy to find the bank reversal points since the sign of its derivative will reverse when bank reversal is made.

Table 16.1 Initial states for various cases

	Case-1	Case-2
E_0	-3.7104E7	-3.7104E7
E_f	-5.7836E7	-5.7836E7
E_{re2}	-5.4515E7	-5.4515E7
θ_0 (Deg)	0	0
ψ_0 (Deg)	90	95
Sign (σ_0)	1	-1

Fig. 16.2 Ground tracks

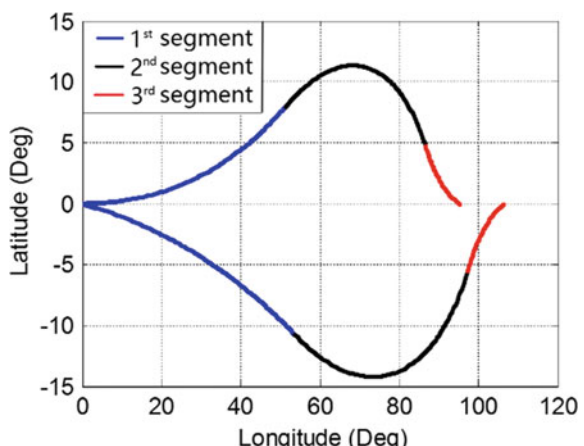
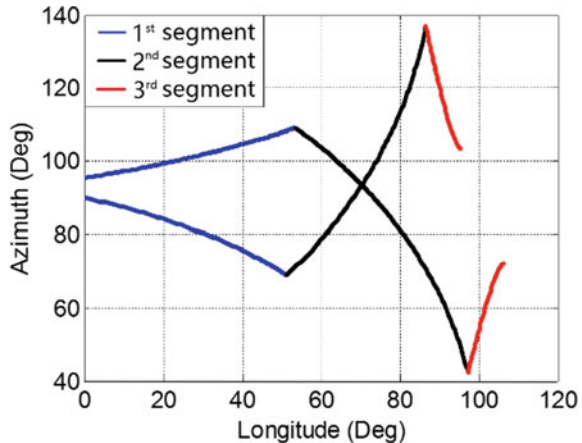


Fig. 16.3 Azimuth histories

The updating histories for longitudinal L/D and the first bank reversal commands are shown in Figs. 16.4 and 16.5. Obviously, both cases have the same initial values and it only takes few steps to converge to the steady values. The errors for the final latitude and longitude are presented in Figs. 16.6 and 16.7. It only takes few steps to achieve a high accuracy and verifies that the proposed method has a stable convergence rate.

The time taken for prediction using Runge–kutta method and calculation time are plotted in Figs. 16.8 and 16.9. It is obvious that the average time is around 0.03 s for predictive time, 0.01 s for calculation time. Conclusively, the proposed method not only has a fast convergence rate, but also is of high accuracy and efficiency. As such it may be said that the proposed method is suitable for online implementation.

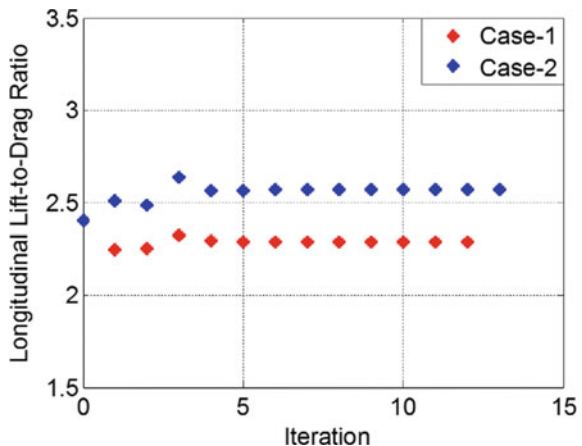
Fig. 16.4 Longitudinal L/D updating histories

Fig. 16.5 Bank reversal updating histories

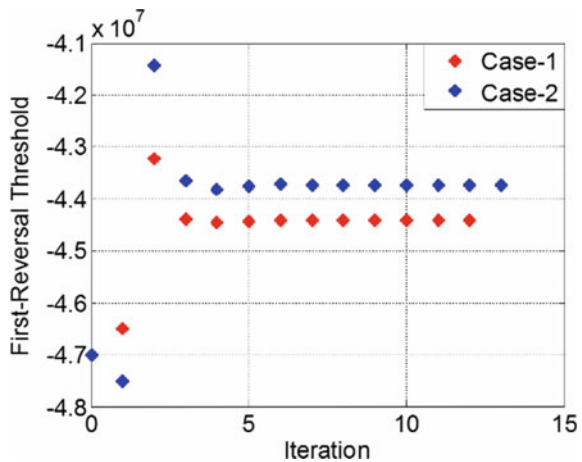


Fig. 16.6 Latitude error in each iteration

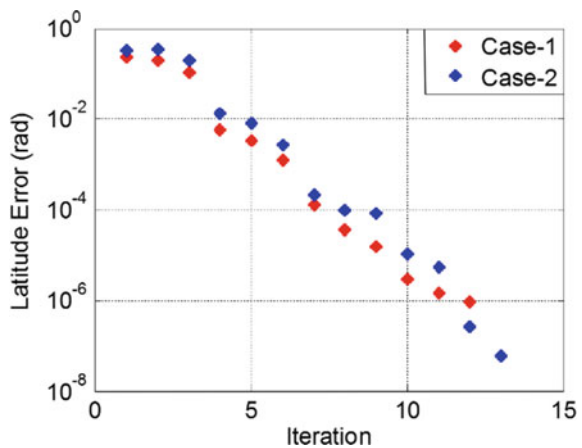


Fig. 16.7 Longitude error in each iteration

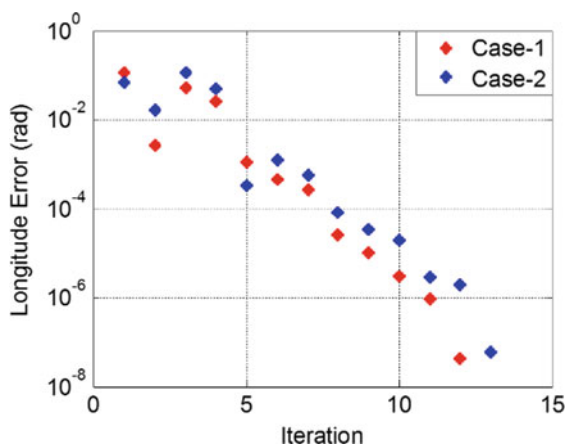


Fig. 16.8 Predictive time in each iteration

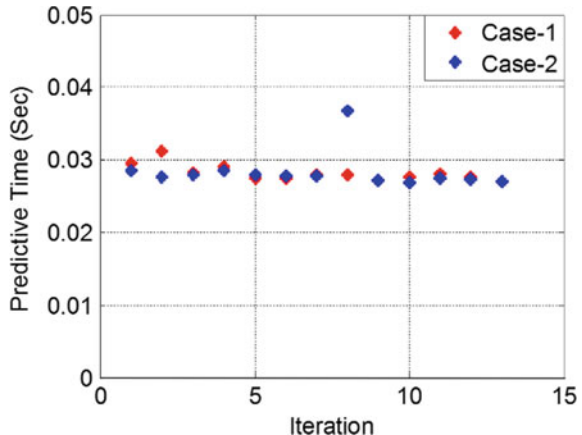
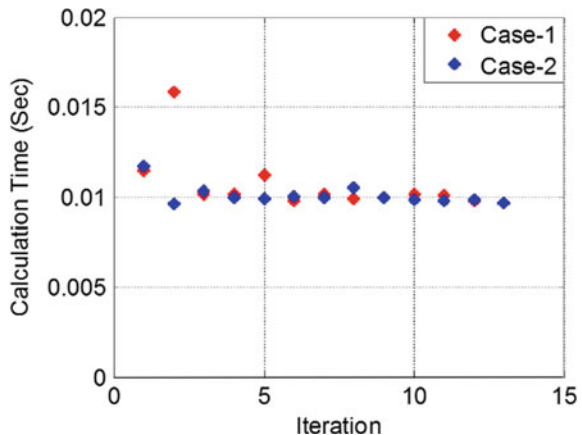


Fig. 16.9 Calculation time in each iteration



16.3.2.6 Path Constraints Management Strategy

The path constraints management strategy presented in [27] is applied here. During implementation, the path constraints given in Eqs. (16.6)–(16.8) are transferred into the maximum allowable magnitude of bank angle. By constraining the actual bank angle to this allowable value, the path constraints are absolutely satisfied. For example, considering the constraint on heating rate, the maximum allowable bank angle is given as follow.

$$\sigma_{\max}(v) = \cos\left(\frac{m(g(r_{\min}) - v^2/r_{\min})}{k_L L(r_{\min})} + k_{cst}\left(\frac{dr}{dv} - \frac{dr}{dv}\Big|_Q\right)\right) \quad (16.61)$$

where, r_{\min} is the minimum altitude which is determined by the heating rate limit and velocity, $k_L = L/\tilde{L}$, L is the lift force measured by accelerometer, \tilde{L} is the normal lift force measured by the IMU, dr/dv is the slope of altitude with respect to the velocity. $(dr/dv)|_Q$ is obtain by treating the altitude as a function of velocity from Eq. (16.6) and then taking the derivative with respect to the velocity. k_{csr} is a positive constant when the heating rate is dominant, and equals zero otherwise. Because the other constraints are also functions of altitude and velocity, the equivalent maximum allowable bank angle can be determined similarly. Therefore, the actual bank angle in glide phase is bounded by

$$\sigma(v) \leq \sigma_{\max}(v) \quad (16.62)$$

16.3.2.7 Trajectory Damping Control Scheme

The oscillation of entry trajectory of high lift-to-drag ratio vehicle has very low damping ratio. As such, directly implementing AOA and bank angle commands will result in phugoid oscillation. Hence the previous assumption on reduced order entry dynamics will not hold. For that reason, the trajectory damping control scheme proposed in [14] is extended to provide glide AOA and bank angle commands. Accordingly, we consider the 2nd order derivative of FPA as follows

$$\ddot{\gamma} = \frac{1}{V} \frac{d \left(\frac{\rho V^2 C_l S_{ref} \cos \sigma}{2m} + \left(\frac{V^2}{r} - \frac{\mu}{r^2} \right) \right)}{dt} + \left(\frac{D}{m} + g \gamma \right) \left(\frac{\rho C_l S_{ref} \cos \sigma}{2m} + \left(\frac{1}{r} - \frac{g}{V^2} \right) \right) \quad (16.63)$$

From Eq. (16.63), the special FPA can be calculated by equating the 2nd derivative of FPA to zero given the vehicle's flight state, AOA command and bank angle command as shown below.

$$\gamma_m = \frac{D^*}{C_1^{TOP}} + \frac{(\dot{C}_l^* \cos \sigma - C_l^* \sin \sigma \dot{\sigma})}{C_2^{TOP}} + \frac{D^*}{C_3^{TOP}} + \frac{D^*}{C_4^{TOP}} \quad (16.64)$$

where,

$$C_1^{TOP} = -mV^2 - mg - \frac{2m^2 V^2}{r^2 \rho C_l^* S_{ref} \cos \sigma} + \frac{2m^2 g}{r \rho C_l^* S_{ref} \cos \sigma} - \frac{2m^2 g^2}{V^2 \rho C_l^* S_{ref} \cos \sigma} \quad (16.65)$$

$$C_2^{TOP} = \frac{V C_l^* \cos \sigma}{H} + \frac{C_l^* \cos \sigma g}{V} + \frac{2mV}{r^2 \rho S_{ref}} - \frac{2mg}{r \rho V S_{ref}} + \frac{2mg^2}{V^3 \rho S_{ref}} \quad (16.66)$$

$$C_3^{TOP} = -\frac{\rho V^2 C_l^* S_{ref} \cos \sigma r}{2H} - \frac{\rho C_l^* S_{ref} \cos \sigma gr}{2} - \frac{V^2}{r} m + mg - \frac{g^2 rm}{V^2} \quad (16.67)$$

$$C_4^{TOP} = -\frac{\rho V^4 C_l^* S_{ref} \cos \sigma}{2Hg} - \frac{\rho V^2 C_l^* S_{ref} \cos \sigma}{2} - \frac{mV^4}{r^2 g} + \frac{mV^2}{r} - mg \quad (16.68)$$

where, superscript “*” denotes the lift and drag coefficients dominated by the AOA command. The trajectory-oscillation can then be suppressed by regulating the longitudinal acceleration in negative feedback form and keeping the lateral acceleration invariant as in Eq. (16.69).

$$\begin{cases} C_{l2} \cos \sigma_2 = C_l^* \cos \sigma_1 + K_\gamma (\gamma - \gamma_m) \\ C_{l2} \sin \sigma_2 = C_l^* \sin \sigma_1 \end{cases} \quad (16.69)$$

Here, subscript ‘2’ signifies the glide bank angle command and lift coefficient, K_γ is a feedback gain that determines the damping performance of suppressing, which is determined through some simulation attempts. Rearranging the Eq. (16.69) we get

$$\begin{aligned} \sigma_2 &= \tan^{-1} \left(\frac{C_l^* \sin \sigma_1}{C_l^* \cos \sigma_1 + K_\gamma (\gamma - \gamma_m)} \right); \\ C_{l2} &= \frac{C_l^* \cos \sigma_1 + K_\gamma (\gamma - \gamma_m)}{\cos \sigma_2} \end{aligned} \quad (16.70)$$

Then, the Newton method is applied to calculate the glide AOA command.

$$Alp_{com}^{k+1} = Alp_{com}^k - \frac{C_l(Alp_{com}^k) - C_{l2}}{C_{l\alpha}(Alp_{com}^k)} \quad (16.71)$$

It only takes few steps and several milliseconds to converge to the required tolerance if the AOA in last guidance period is considered as initial input. Note that, in entry guidance, the lift coefficients are scaled by an aerodynamic deviation estimation provided by the IMU.

16.3.3 Terminal Adjustment Phase

After the last bank reversal, only bank angle adjustment cannot satisfy multiple terminal requirements. Therefore, it is necessary to develop stable and reliable explicit guidance to issue both AOA and bank angle commands. As such, we employ lateral proportion navigational guidance and longitudinal polynomial guidance in this phase. These are capable of guiding the vehicle towards the TDEM interface while satisfying the final constraints on altitude, heading error, FPA, and bank angle.

16.3.3.1 Lateral Proportion Navigation Guidance

Proportional Navigation (PN) guidance [28], which is one of the most famous and robust guidance laws, is employed to steer the vehicle to glide towards the target with zero final lateral acceleration. The typical commanded acceleration for PN guidance is presented as.

$$n_1 = N_{pc} \dot{\lambda} v \cos \gamma \quad (16.72)$$

where, N_{pc} is the navigation ratio, $v \cos \gamma$ is the velocity projected in the lateral guidance plane. λ is the LOS angle on the spherical Earth, and its rate is formulated through the spherical trigonometry.

Consider the three-dimensional nonlinear engagement geometry in Fig. 16.10. It is easy to obtain A , B and c from the current state of vehicle and destination information.

$$A = \frac{\pi}{2} - \phi_m; B = \frac{\pi}{2} - \phi_f; c = \theta_f - \theta_0 \quad (16.73)$$

Therefore, the range between the vehicle and destination is expressed as

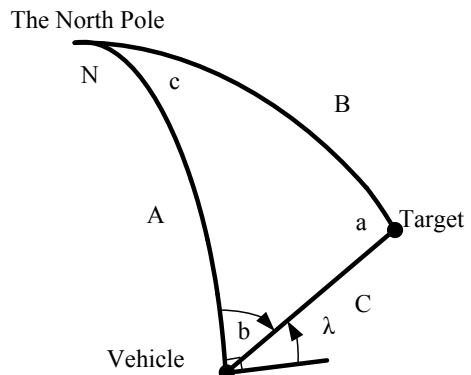
$$C = \cos^{-1}(\cos A \cos B + \sin A \sin B \cos c) \quad (16.74)$$

Now, the derivative of C with respect to time is determined.

$$\frac{dC}{dt} = -\frac{1}{\sqrt{1-f_1^2}} \frac{df_1}{dt} \quad (16.75)$$

where, $f_1 = \cos A \cos B + \sin A \sin B \cos c$, and its rate is generated according to the dynamics.

Fig. 16.10 Definition of the frames and sight-line angle



$$\frac{df_1}{dt} = -\sin A \cos B \frac{dA}{dt} + \cos A \sin B \cos c \frac{dA}{dt} - \sin A \sin B \sin c \frac{dc}{dt} \quad (16.76)$$

where,

$$\begin{cases} \frac{dA}{dt} = -\frac{d\phi_m}{dt} = -\frac{v \cos \gamma \sin \psi}{r} \\ \frac{dc}{dt} = -\frac{d\theta_m}{dt} = -\frac{v \cos \gamma \cos \psi}{r \cos \phi} \end{cases} \quad (16.77)$$

According to spherical trigonometry, b is the function of B , c and C as expressed below.

$$b = \sin^{-1} \left(\frac{\sin B \sin c}{\sin C} \right) \quad (16.78)$$

Now, let us define that the LOS angle, $\lambda = \pi/2 - b$, is anti-clockwise from the east. Its rate is provided by the derivative of each element with respect to time.

$$\frac{d\lambda}{dt} = -\frac{db}{dt} \Rightarrow \frac{d\lambda}{dt} = -\frac{1}{\sqrt{1-f_2^2}} \frac{df_2}{dt} \quad (16.79)$$

Similarly, $f_2 = \sin B \sin c / \sin C$, its rate is formulated as

$$\frac{df_2}{dt} = \frac{\sin B \cos c}{\sin C} \frac{dc}{dt} - \frac{\sin B \sin c \cos C}{\sin^2 C} \frac{dC}{dt} \quad (16.80)$$

Finally, the lateral acceleration is determined. A constant navigation ratio may make the initial bank angle too big to saturate. Therefore, it is better to set a varying value from 2 to 4 according to the range-to-go.

16.3.3.2 Longitudinal Polynomial Guidance

In this subsection, polynomial guidance, which was first proposed by Kim [29–31], is developed to steer the vehicle to glide to the TAEM interface with the desired altitude and FPA. Now, under the assumption that the flight vehicle velocity is constant and the influence of the earth rotation and curvature is neglected, let us consider the longitudinal dynamics and range-to-go dynamic.

$$\begin{cases} \dot{h} = v \sin \gamma \\ \dot{s} = v \cos \gamma \\ \dot{\gamma} = \frac{L \cos \sigma}{mv} - \frac{g}{v} \cos \gamma \end{cases} \quad (16.81)$$

Obviously, regarding the range-to-go as independent variable and assuming that FPA is a small value, a linear dynamical system can be formulated as.

$$\begin{cases} \frac{dh}{ds} = \gamma \\ \frac{d\gamma}{ds} = n_2 \end{cases} \quad (16.82)$$

where,

$$n_2 = \frac{L \cos \sigma}{mv^2 \cos \gamma} - \frac{g}{v^2} \quad (16.83)$$

Generally, guidance command is usually represented as the function of time-to-go. In view of the mission scenario, it is convenient to consider it as a function of range-to-go because it is not only a final constraint at the TAEM interface, but also easily measurable. Therefore, the guidance command can be defined as a polynomial function as

$$n_2 = a_1(s - s_f)^M + a_2(s - s_f)^K \quad (16.84)$$

where, s_f is the desired range-to-go at the TAEM interface, guidance gains, M and K , are arbitrary constants with $K > M > 0$. Analytically, the altitude and FPA are given as

$$\begin{aligned} \gamma &= a_1 \frac{(s - s_f)^{M+1}}{M + 1} + a_2 \frac{(s - s_f)^{K+1}}{K + 1} + a_3; \\ h &= a_1 \frac{(s - s_f)^{M+2}}{(M + 1)(M + 2)} + a_2 \frac{(s - s_f)^{K+2}}{(N + 1)(K + 2)} + a_3 s + a_4 \end{aligned} \quad (16.85)$$

where, a_1, a_2, a_3 and a_4 are integral constants which are determined analytically by boundary conditions.

$$\begin{aligned} a_1 &= \left((h_0 - h_f) - \gamma_f (s_0 - s_f) - \frac{(s_0 - s_f)(\gamma_0 - \gamma_f)}{(K + 2)} \right) \\ &\quad \frac{(M + 1)(M + 2)(K + 2)}{(N - M)(s_0 - s_f)^{M+2}}; \\ a_2 &= \frac{(K + 1)(K + 2)}{(K - M)(s_0 - s_f)^{K+1}} \left(\gamma_0 + (M + 1) - \frac{(h_0 - h_f)(M + 2)}{(s_0 - s_f)} \right); \\ a_3 &= \gamma_f; \quad a_4 = h_f - \gamma_f s_f \end{aligned} \quad (16.86)$$

where, s_f , h_f and γ_f are the desired range-to-go, altitude and FPA at the TAEM interface. And s_0 , h_0 , γ_0 are the equivalent values at initial state. Thus, the guidance command can be formulated analytically by substituting them into Eq. (16.84).

$$n_{20} = \frac{\gamma_0(M+K+3)}{(s_0 - s_f)} + \frac{\gamma_f(M+1)(K+1)}{(s_0 - s_f)} - (h_0 - h_f) \frac{(M+2)(K+2)}{(s_0 - s_f)^2} \quad (16.87)$$

Now, the longitudinal command, which guides the vehicle to the TAEM interface with the desired altitude and FPA, is determined. It is noted that, because the trajectory is expected to be smooth and simple so that the state won't change greatly, the appropriate guidance gains are chosen to make the degree of polynomial as less as possible. Therefore, $M = 2$, $K = 1$ are selected in all simulations.

16.3.3.3 Command Allocation

This subsection discusses how to regulate the AOA and bank angle to realize the acceleration commands in both guidance planes. Let us consider the entry dynamics with the earth curvature and ignoring the earth rotation. The lateral and longitudinal accelerations are expressed as

$$\begin{aligned} n_{\text{vertical}} &= \left(n_2 v^2 - \left(\frac{v^2}{r} - g \right) \right) \cos \gamma \\ n_{\text{lateral}} &= \left(-n_1 - 2 \frac{v^2}{r} \cos \gamma \sin \psi \tan \phi \right) \cos \gamma \end{aligned} \quad (16.88)$$

Because they are the components of total acceleration vector, it is easy to obtain the bank angle command.

$$Bank_{\text{com}} = \tan^{-1} \frac{n_{\text{lateral}}}{n_{\text{vertical}}} \quad (16.89)$$

Therefore, the lift coefficient is easily determined as

$$C_l = \frac{2mn_{\text{vertical}}}{\rho v^2 S_{\text{ref}} \cos(Bank_{\text{com}}) k_L} \quad (16.90)$$

where, k_L is defined in previous subsection. Then, Newton method is applied again to calculate the required AOA.

$$Alp_{\text{com}}^{k+1} = Alp_{\text{com}}^k - \frac{C_l(Alp_{\text{com}}^k) - C_l}{C_{l\alpha}(Alp_{\text{com}}^k)} \quad (16.91)$$

It may be noted that the previous AOA is considered as initial input in calculation.

16.3.4 Implementation of the Proposed Method

In order to simply and intuitively demonstrate the proposed algorithm, a flowchart for implementation is presented in Fig. 16.11. Note that, before the first bank reversal, the predictive trajectory and entry dynamics in glide phase consist of three segments. The multi-segment linear pseudospectral model predictive control is used to improve the first bank reversal and longitudinal L/D commands. However, after the first bank reversal, there are only two segments and the same method is used to improve the second bank reversal and longitudinal L/D commands. When the second bank reversal is made, the vehicle comes into the terminal adjustment phase, where the PN guidance and Polynomial guidance are applied to guide the vehicle to the TAEM interface while satisfying all final requirements. The procedure for implementing is summarized in detail as follows:

- (1) Initialization: set initial simulation parameters and select the suitable initial guess through off-line trajectory analysis.
- (2) Descent phase: drop with the allowable maximum AOA and zero bank angle commands until the stop criterion is triggered.
- (3) Judgment on whether to perform bank reversal in glide phase, if the relative energy is larger than the energy at bank reversal point, go to step 4; if it is less than that energy and it is not the last bank reversal, perform the bank reversal, rebuild the construction of nonlinear control problem, and go to step 4; if it is the last bank reversal, perform bank reversal and go to step 9.

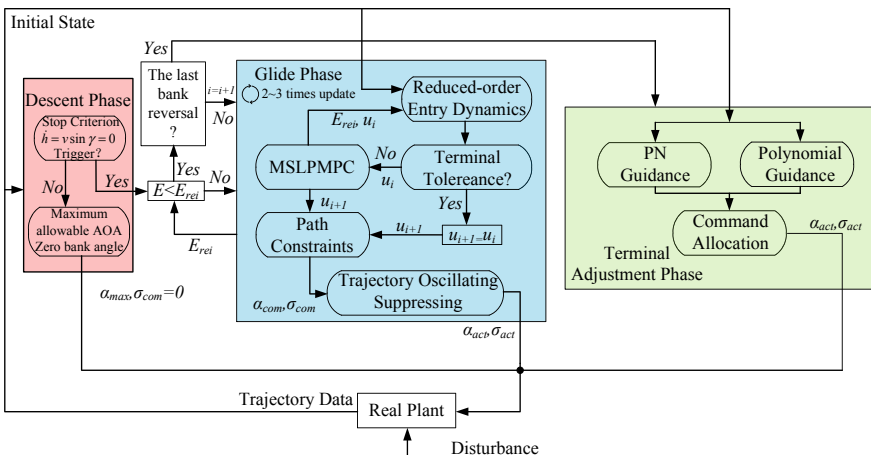


Fig. 16.11 Flowchart of implementation

- (4) Predictive integration using current control parameters and bank reversal points: calculate the final deviations and store the trajectory data. Then go to step 5.
- (5) Judgment on the satisfaction on final tolerance: If it is within the prescribed tolerance, go to next step, if not, go to step 8.
- (6) Path constraints: judge on the saturation of bank angle command. If it is larger than the maximum allowable bank angle determined by path constraints, set the bank angle command equals to the maximum, then go to step 7.
- (7) Apply the control command to the trajectory damping control scheme so as to obtain the glide AOA and bank angle commands. Then, apply them to the real plant and return step 3. Update the command and bank reversal point and put them as the input for the next predictive integration.
- (8) Apply the methods of linearization, multi-segment linear pseudospectral model predictive control and calculus of variations to improve the longitudinal L/D and bank reversal commands analytically according to predictive final deviations, then go to step 6.
- (9) Terminal adjustment phase: according to the current states and final requirements, calculate the commands using the improved PN guidance and Polynomial guidance. It will guide the vehicle toward the TAEM interface safely and accurately.

16.4 Numeric Results and Discussion

In this section, nominal cases, Monte Carlo simulations with dispersions and uncertainty, and comparison with a typical method are carried out to evaluate the performance and robustness of the proposed method using the model of CAV-H. In order to improve the fidelity of simulation, a first-order autopilot lag is considered to limit the bank angle rate $|\sigma| \leq 8 \text{ deg/s}$ and bank angle acceleration $|\dot{\sigma}| \leq 8 \text{ deg/s}^2$. All programs are implemented on a personal computer with 3.3 GHz processor and MATLAB 2008b. The computation efficiency can be enhanced by applying more efficient resources and advanced computers.

16.4.1 Normal Cases for Various Destinations

It is assumed that the destination is located within the shooting plane. Three nominal cases with various destinations are carried out to evaluate the applicability of the proposed method. Initial conditions are the same for all cases, $h_0 = 80.132 \text{ km}$, $\theta_0 = 0 \text{ Deg}$, $\varphi_0 = 0 \text{ Deg}$, $v_0 = 6700 \text{ m/s}$, $\gamma_0 = 0 \text{ Deg}$ and $\psi_0 = 0 \text{ Deg}$. Table 16.2 lists the terminal conditions for all cases. Additionally, the path constraints: heating rate, dynamic pressure and load factor should be enforced strictly during the flight.

Table 16.2 Terminal conditions for various cases

	h_f (km)	θ_f (Deg)	φ_f (Deg)	v_f (m/s)	γ_f (Deg)	$\Delta\psi_f$ (Deg)
Case-1	30.00	91	0	2 500	0	0
Case-2	30.00	101	0	2 500	0	0
Case-3	30.00	111	0	2 500	0	0

The altitude histories, ground tracks and velocity histories are plotted in Figs. 16.12, 16.13 and 16.14. It is obvious that all terminal constraints are satisfied. The vehicle is capable of performing a larger lateral maneuver so that the maximal latitude distance is more than 10 Deg. The FPA histories are shown in Fig. 16.15. It is clear that all FPAs tend to their special FPAs represented by the red-lines

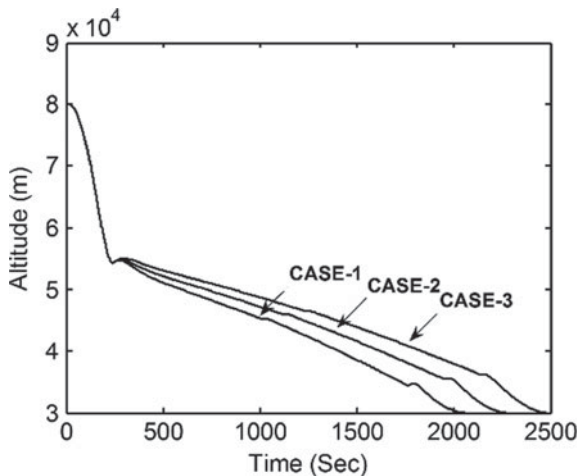
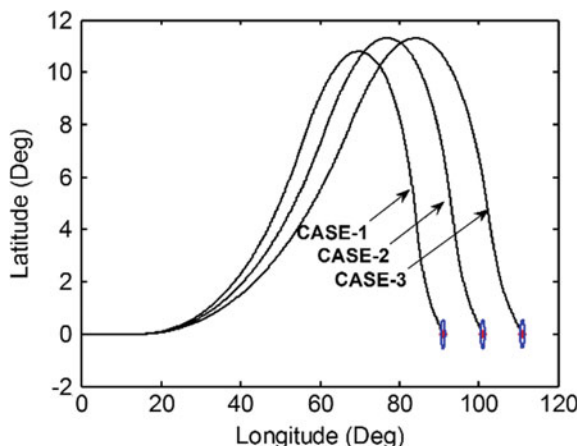
Fig. 16.12 Nominal altitude histories**Fig. 16.13** Nominal ground tracking

Fig. 16.14 Nominal velocity histories

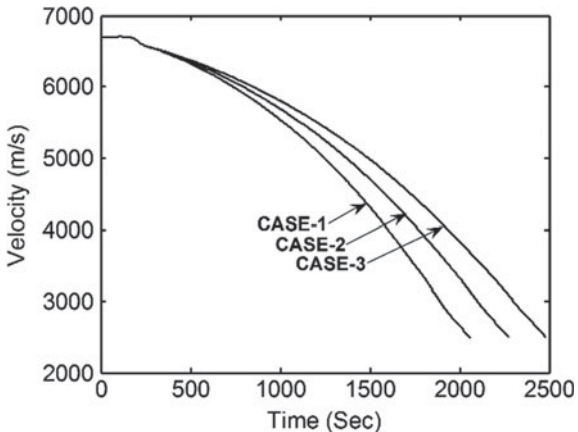
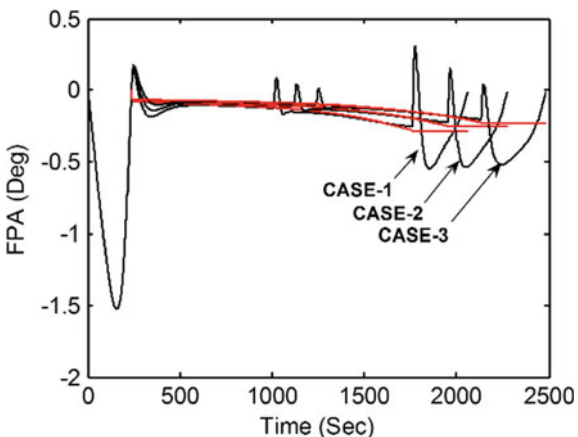


Fig. 16.15 Nominal FPA histories



and converge to zeros at the end. The AOA and bank angle histories are shown in Figs. 16.16 and 16.17. It is easy to find that the AOA slightly regulates at the beginning of glide phase or when the bank reversal is done. The magnitude of bank angle is almost unchanged in glide phase and successfully converges to zeros at the end.

The heading error histories and L/D histories are shown in Figs. 16.18 and 16.19. It reveals that the longitudinal L/D is proportional to the mission cross-range and varies slightly in glide phase. The path constraint histories are illustrated in Figs. 16.20, 16.21 and 16.22. It is apparent that none of cases exceed the limits.

The statistic of total CPU time including the predictive integral time and command update time is shown in Fig. 16.23. They are within the range from 0.06 to 0.11 s and are mostly concentrated on around 0.08 s. Note that the number of command update in each guidance period is set to 2 before the first bank reversal and 3 before the second bank reversal. Thus, total time consumed in computation is much more than that in Sect. 16.4.2.

Fig. 16.16 Nominal AOA histories

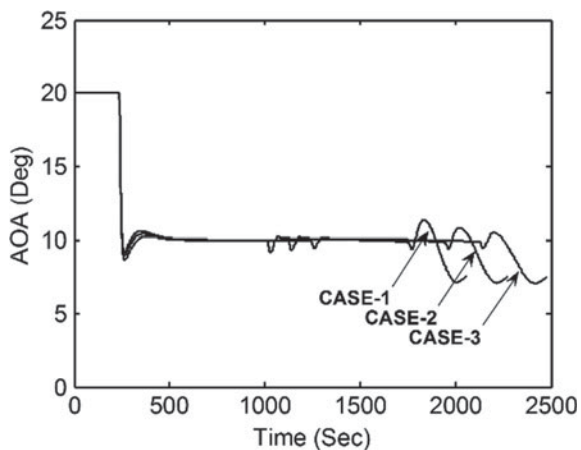


Fig. 16.17 Nominal bank angle histories

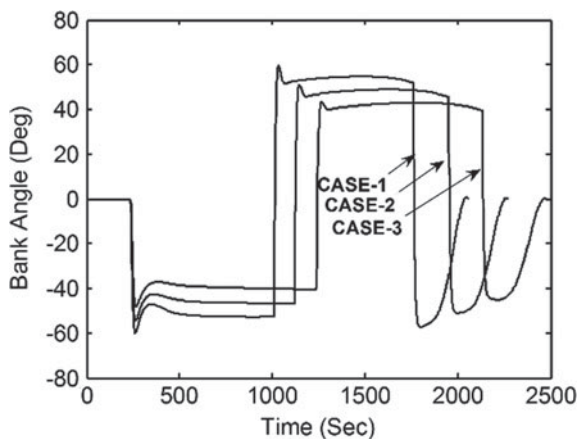


Fig. 16.18 Nominal heading error histories

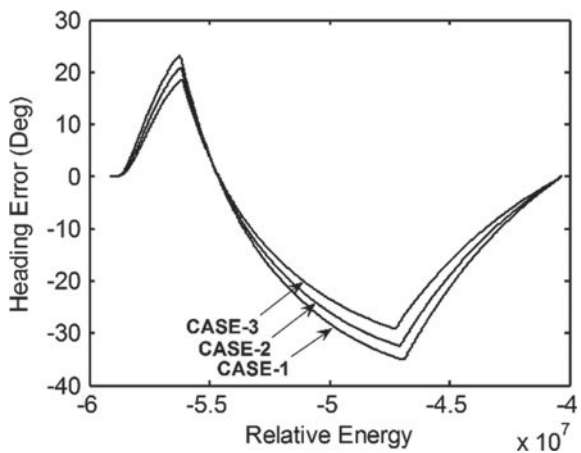


Fig. 16.19 Nominal L/D histories

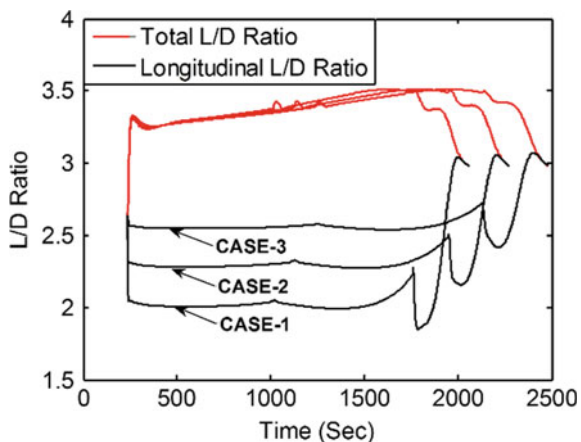


Fig. 16.20 Nominal heating rate histories

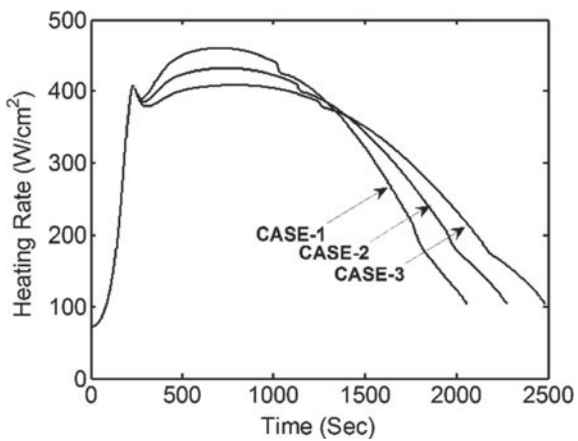


Fig. 16.21 Nominal dynamic pressure histories

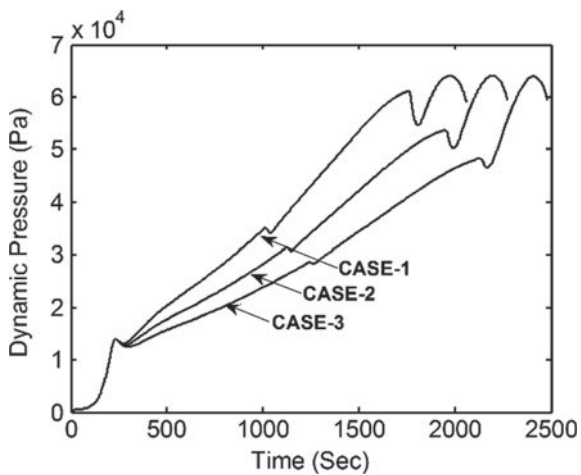


Fig. 16.22 Nominal load factor histories

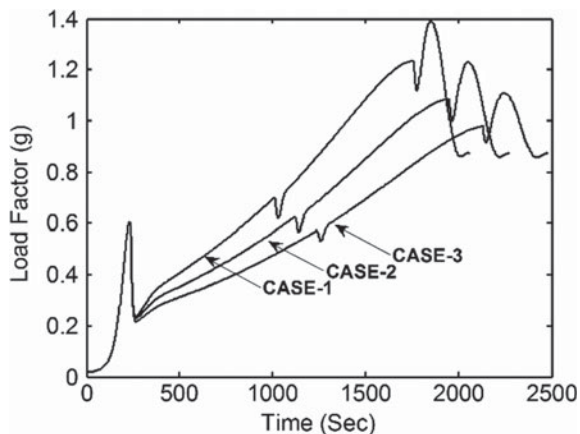
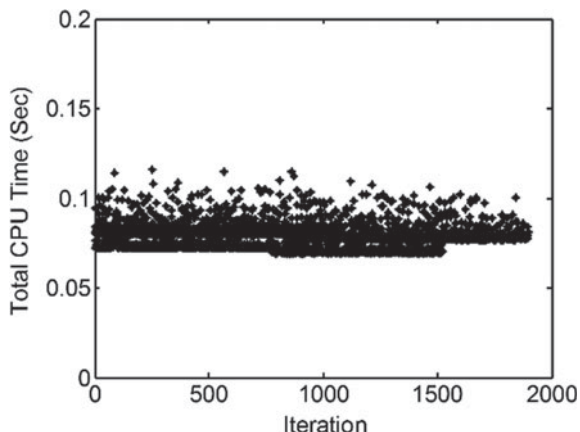


Fig. 16.23 Nominal total CPU time



The statistics on the final deviations are listed in Table 16.3. Because the range-to-go is considered as the stop criterion, its error is zero. All final requirements are so perfectly met that it may be concluded that the proposed method could be applicable for different mission scenarios.

Table 16.3 Statistics on the final deviations

	Case-1	Case-2	Case-3
ΔS (m)	0	0	0
δv_f (m/s)	1.0258	5.4318	-3.1177
$\delta \gamma_f$ (Deg)	-0.0125	-0.0156	-0.0162
$\Delta \psi_f$ (Deg)	-0.0132	-0.0082	-0.0050
$\Delta \sigma_f$ (Deg)	-0.4501	-0.3242	-0.2312
δh_f (m)	1.2123	1.2481	16.3092

16.4.2 Monte Carlo Simulations

In this subsection, Monte Carlo 3-DOF simulations are conducted to further evaluate the performance and robustness under a wide distribution of random dispersions and uncertainty. These dispersions and uncertainties include initial disturbance, wind disturbance, and disturbances in aerodynamic coefficients and atmospheric density. What's more, in order to further demonstrate the superior performance in computational efficiency, guidance accuracy and lateral trajectory shaping capability, a comparison with the typical predictor–corrector method [13] is also done. The initial and final conditions for those two methods are listed in Table 16.4. The dispersion parameters used in simulation are given in Table 16.5.

Even though the dispersion and uncertainty model is much simple, it is challenging enough to evaluate the performance and robustness of the proposed method. The maximum percentage deviation in L/D is up to 26.09% (-15% in C_l and 15% in C_d). Then, the 1000-run Monte Carlo simulations for the proposed method and 250-run Monte Carlo simulations for the existing method have been carried out. (Note that 250-run simulations are enough to demonstrate the feature of the existing method. In

Table 16.4 Initial and final conditions

Initial state		Final state	
h_0 (km)	80.132	h_f (km)	30
θ_0 (Deg)	0	θ_f (Deg)	97
φ_0 (Deg)	0	φ_f (Deg)	0
v_0 (m/s)	6700	v_f (m/s)	2500
γ_0 (Deg)	0	γ_f (Deg)	0
ψ_0 (Deg)	90	ψ_f (Deg)	–

Table 16.5 Dispersion parameters

Parameter	$3\sigma/\text{range}$	Distribution
δr_0 (m)	2000	Gaussian
$\delta\theta_0$ (Deg)	0.2	Gaussian
$\delta\varphi_0$ (Deg)	0.2	Gaussian
δv_0 (m/s)	100	Gaussian
$\delta\gamma_0$ (Deg)	0.1	Gaussian
$\delta\psi_0$ (Deg)	0.1	Gaussian
δC_l	$\pm 15\%$	Gaussian
δC_d	$\pm 15\%$	Gaussian
$\delta \rho$	$\pm 25\%$	Gaussian
W_{density}	100%	Gaussian
$W_{\text{direction}}$ (Deg)	± 180	Uniform

order to sufficiently show the stable performance for the proposed method, 1000-run simulations are carried out).

The ground tracks for both methods are given in Fig. 16.24. It shows that the potential of the lateral maneuvering for such vehicle has been fully exploited since the precise bank reversal points are found by the proposed method. The lateral maneuvering distances for the proposed method are widely distributed from 6 to 15 Deg while satisfying the final requirement. However, the equivalent ones for the existing method are not more than 2 Deg. Moreover, because the existing method uses a pre-selected threshold corridor to reduce the heading error, the number of bank reversal will rapidly increase when the vehicle is approaching the TAEM interface.

The altitude histories for both methods are shown in Fig. 16.25. Although those trajectories distributed widely, it is clear that the trajectories in the first plot are more stable than that in the second plot due to less bank reversals. Moreover, the final requirement on altitude is satisfied perfectly for the proposed method compared with

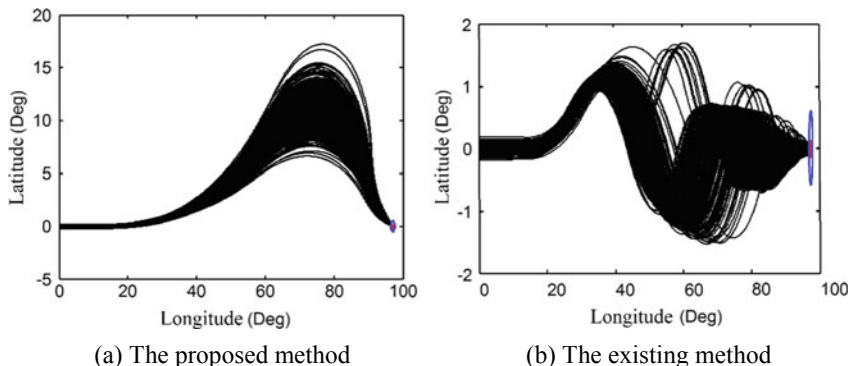


Fig. 16.24 Ground tracks

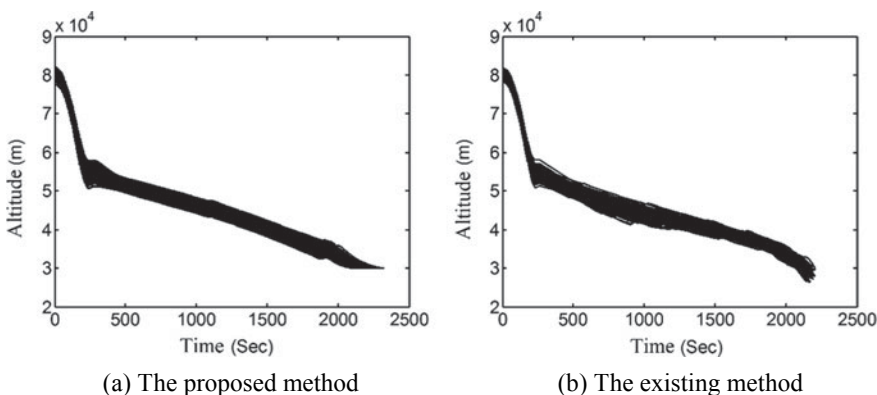
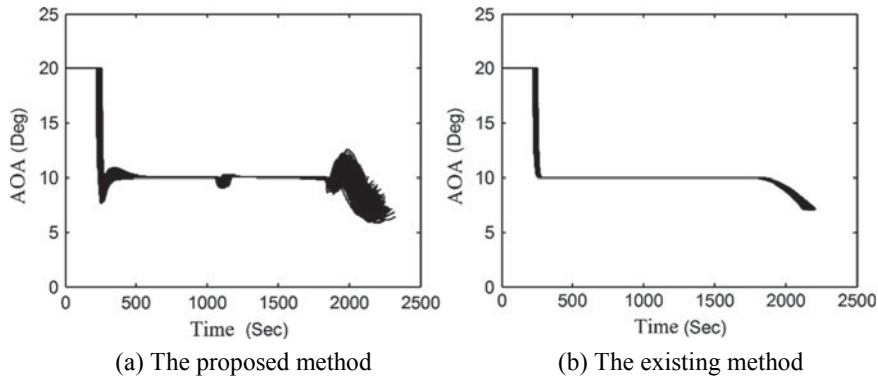
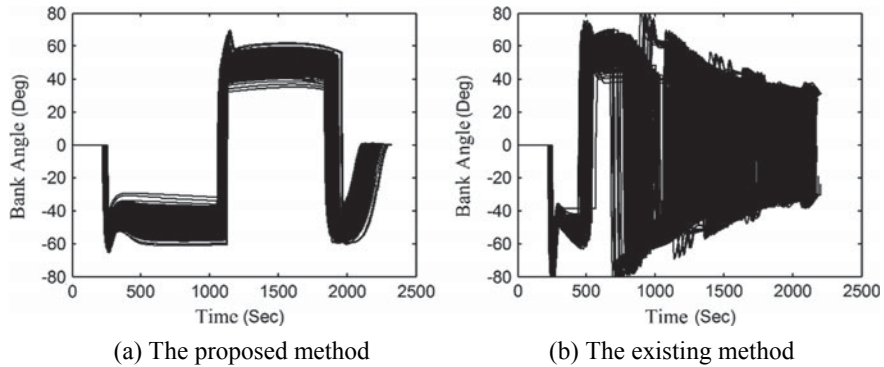


Fig. 16.25 Altitude histories

**Fig. 16.26** AOA histories**Fig. 16.27** Bank angle histories

the existing method. The first plot of Fig. 16.26 illustrates that the AOA provided by the proposed method varies slightly at the beginning of the glide phase or when the bank reversal is happened due to applying the trajectory damping control scheme. After the last bank reversal, the AOA associated with bank angle is used to realize the guidance commands so as to meet multiple final requirements. The second plot of Fig. 16.26 shows that the AOA provided by the existing method changes according to the AOA profile strictly.

The bank angle histories provided by the proposed method are shown in the first plot of Fig. 16.27. It is apparent that the bank angle varies greatly from 30 to 60 Deg due to the large dispersions and converges to zero at the TAEM interface. It also reveals that the proposed method is very reliable and robust in providing the guidance commands even in aforementioned large dispersions and uncertainties. Clearly, the bank angle provided by the existing method is more chaotic and irregular than that provided by the proposed method. Moreover, the existing method requires ever larger bank angle than the proposed method and does not ensure zero final bank angle. It

should be noted that the pre-selected threshold corridor using in [13] is not suitable for such mission because the large heading error threshold will lead to lateral guidance failure. Therefore, a smaller pre-selected threshold corridor is selected as

$$\psi_{LOS}^{Limit} = \begin{cases} 12, & 6000 \geq v \geq 4000; \\ 12 + \frac{6(v - 4000)}{1300}, & 4000 \geq v \geq 2700; \\ 6, & v \leq 2700, \text{ or, } v \geq 6000; \end{cases} \quad (16.92)$$

The heating rate histories and dynamic pressure histories for both methods are shown in Figs. 16.28 and 16.29. None of them exceeds the limits for the proposed method. However, the maximum heating rate for the existing method is much larger than that for the proposed method and exceeds the limit. The reason is that the large

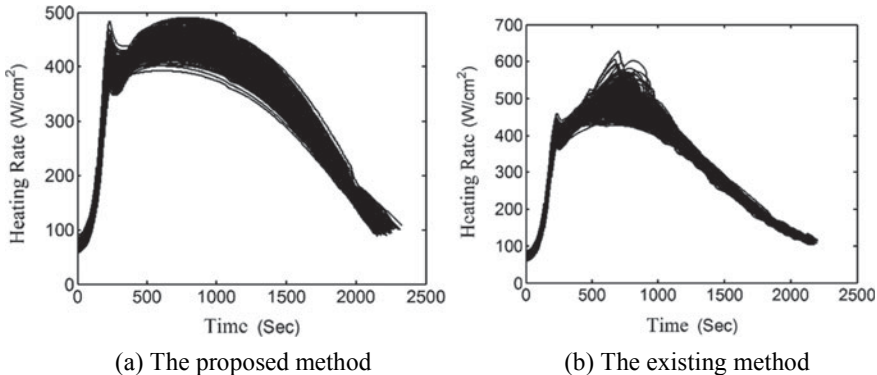


Fig. 16.28 Heating rate histories

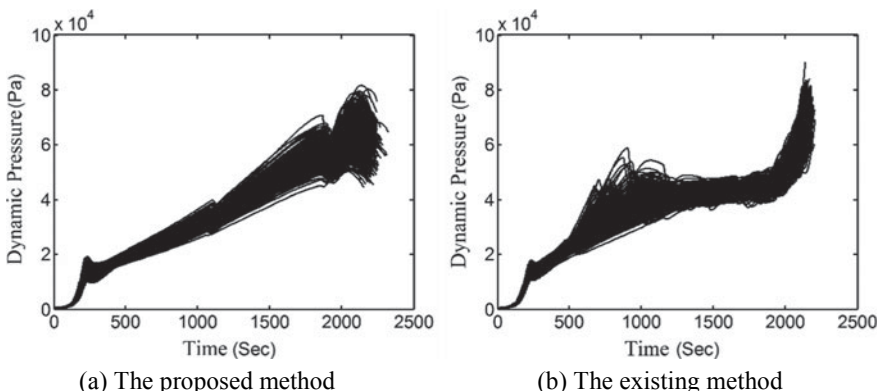


Fig. 16.29 Dynamic pressure histories

bank angle makes the vehicle gliding at relatively lower altitude so that it will suffer the worse atmospheric density. Although the maximum heating rate may be restricted by applying path constraints management strategy, the existing method will guide the vehicle flying at more harsh environments.

Other important state histories for the proposed method are plotted in Figs. 16.30, 16.31 and 16.32. The load factor histories in Fig. 16.30 show that the maximum load factor is much less than 2 g. the heading error histories are shown in Fig. 16.31. It has been seen that all heading errors successively converge to zeros. FPA histories are plotted in Fig. 16.32. It is clear that, even in highly dispersed case, all FPA curves

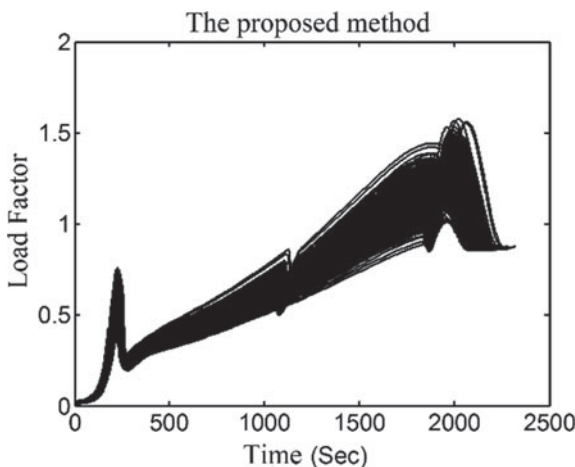


Fig. 16.30 Load factor histories

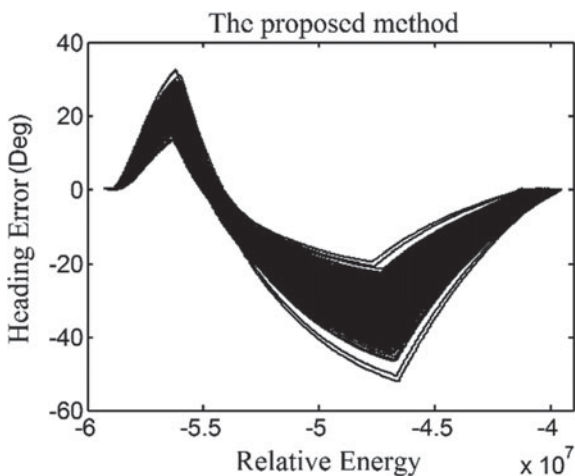


Fig. 16.31 Heading error histories

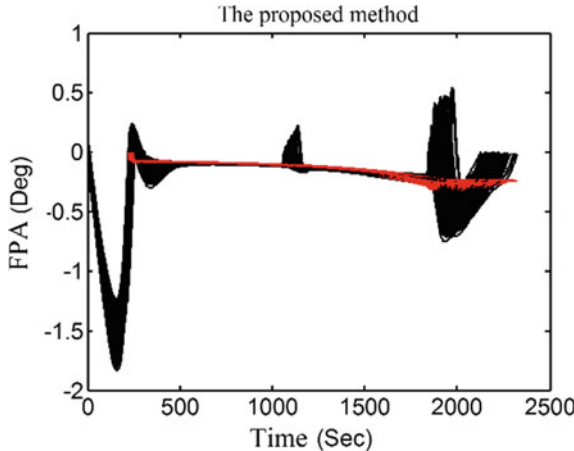


Fig. 16.32 FPA histories

perfectly follow the special FPA curves presented in the red-lines except the initial moment and when the bank reversal is happened. Moreover, all final FPAs converge to zeros at the TDEM interface.

The statistical distribution of the final errors including altitude, bank angle, heading error, velocity, and FPA are shown in Figs. 16.33, 16.34 and 16.35. For the proposed method, all final bank angle errors are within 1 Deg, all final altitude errors are within 3 m, all heading errors are within 8E-3 Deg, and the final velocity errors are mainly concentrated within 0.1 Mach. Obviously, the existing method not only is unable to ensure the zero final bank angle, but also does not satisfy the final requirements on altitude and heading error properly. By comparison, the existing method will result in much larger final errors on bank angle, altitude, heading error, and FPA. For the final velocity, the existing method performs slightly better than

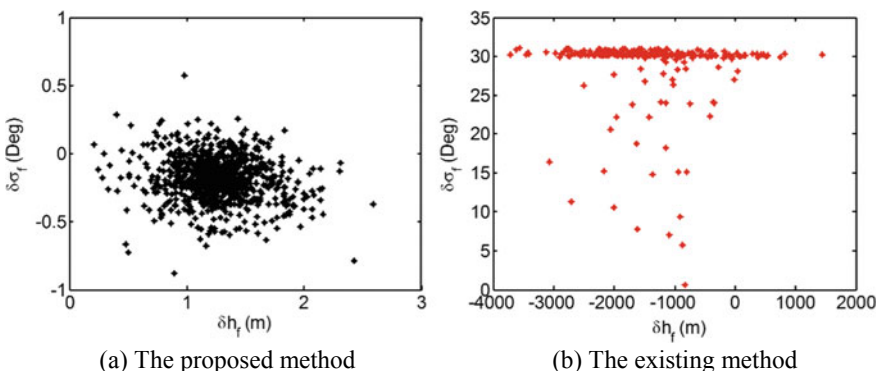
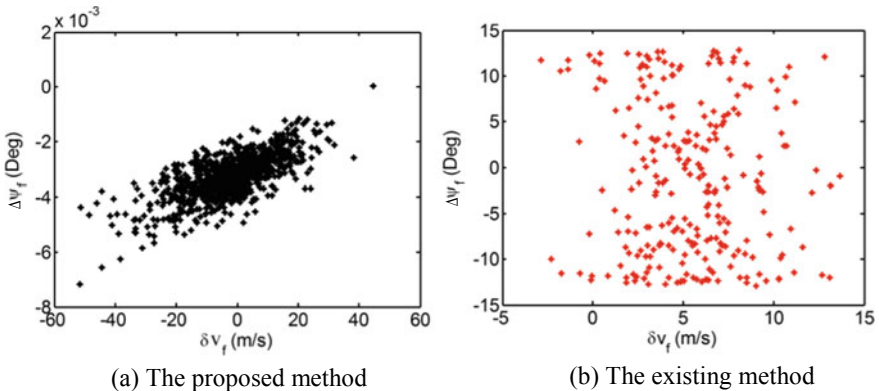
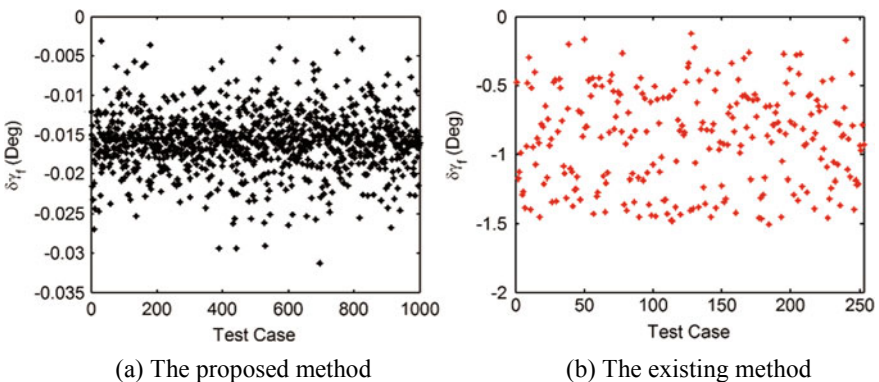


Fig. 16.33 Final altitude and bank angle

**Fig. 16.34** Final heading error and velocity**Fig. 16.35** Final FPA

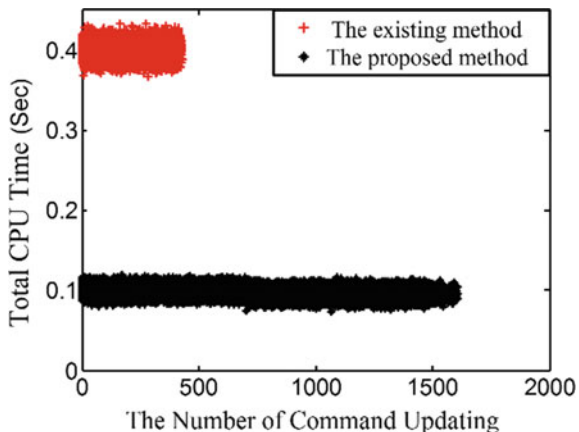
the proposed method. But they are under the same order of magnitude. And that the mean terminal velocity for the proposed method is only 9.520 2 m/s completely satisfies the mission requirement. Note that, because the virtual target is located at the place which is 50 m behind the TAEM interface along the sight-line direction, the distribution of the terminal deviations on altitude, bank angle and FPA are not zero-mean. The statistics on terminal constraints is presented in Table 16.6. Note that 50% denotes the measured value below which fifty percent of statistical deviations are. Overall, it reveals that the proposed method has superior performance in guidance accuracy even considering multiple terminal constraints.

Another point should be noted is computational efficiency. Thus, we compare the time taken of all Monte Carlo runs between both methods in Fig. 16.36. The calculation times for the existing method are around 0.4 s, but the equivalent ones for the proposed method are only around 0.1 s. it should be pointed out that the number of command update in each guidance period is only one for the existing

Table 16.6 Statistics on the terminal constraints

	Mean	Mean variance	50%
δh_f (m)	1.2663	0.2975	1.2584
δv_f (m/s)	-9.5902	8.7614	7.0148
$\delta \gamma_f$ (Deg)	-0.0158	0.0037	0.0158
$\delta \psi_f$ (Deg)	0.0033	7.5231E-4	0.0032
$\delta \sigma_f$ (Deg)	0.2013	0.1258	0.1864

Fig. 16.36 Comparison of total CPU time



method, but 2 or 3 for the proposed method. Note that because the guidance period is set to be 10 times of the CPU time, the number of command updating for the exiting method is much less than that for the proposed method. Conclusively, the proposed method not only has much higher computational efficiency and guidance accuracy than the exiting method, but also is capable of providing precise bank reversal point so as to fully exploit the lateral trajectory shaping capability.

16.5 Conclusion

A robust entry guidance algorithm using multi-segment linear pseudospectral model predictive control is proposed. This algorithm is capable of guiding high lift-to-drag ratio entry vehicle to its destination while satisfying path constraints and terminal requirements, which are altitude, velocity, FPA, bank angle, and heading error. The precise longitudinal L/D and bank reversal commands are calculated through a series of analytical formulas derived via model predictive control, multi-segment linear pseudospectral method and calculus of variations. Proportional navigation guidance and polynomial guidance are used to accurately meet multiple terminal constraints after the last bank reversal. Nominal simulations with various destination and Monte

Carlo with random dispersions and model uncertainties are carried out to evaluate and verify the features of the algorithm. Additionally, a comparison with other typical method is also provided. The results show that this algorithm not only is applicable for various destinations, but also has fast convergence rate, high computational efficiency and guidance accuracy. It only takes about 0.1 s to complete the command update in each guidance cycle, thereby meeting the requirement of close-loop entry guidance application. Importantly, it substantially enhances the lateral trajectory shaping capability via providing precise bank reversal point. Furthermore, even in highly dispersed case, this algorithm consistently performs well.

References

1. Yang, L., Chen, W.C., Lin, X.M., Zhou, H.: Robust entry guidance using multi-segment linear pseudospectral model predictive control. *J. Syst. Eng. Electron.* **28**(1), 103–125
2. Harpold, J.C., Graves, C.A.: Shuttle entry guidance. *J. Astronaut. Sci.* **37**(3), 239–268 (1979)
3. Mease, K.D., Kremer, J.P.: Shuttle entry guidance revisited using nonlinear geometric methods. *J. Guidance, Control Dyn.* **17**(6), 1350–1356 (1994)
4. Bharadwaj, S., Rao, A.V., Mease, K.D.: Entry trajectory tracking law via feedback linearization. *J. Guidance, Control Dyn.* **21**(5), 726–732 (1998)
5. Mease, K.D., Chen, D.T., Teufel, P., et al.: Reduced-order entry trajectory planning for acceleration guidance. *J. Guidance, Control Dyn.* **25**(2), 257–266 (2002)
6. Dukeman, G.A.: Profile-following entry guidance using linear quadratic regulator theory. AIAA paper 2002-4457, Aug (2002)
7. Xie, Y., Liu, L., Tang, G., et al.: Highly constrained entry trajectory generation. *Acta Astronaut.* **88**, 44–60 (2013)
8. Tian, B., Zong, Q.: Optimal guidance for reentry vehicles based on indirect legendre pseudospectral method. *Acta Astronaut.* **68**, 1176–1184 (2011)
9. Morio, V., Cazaurang, F., Vernis, P.: Flatness-based hypersonic reentry guidance of a lifting-body vehicle. *Control Eng. Pract.* **17**, 588–596 (2009)
10. Zimmerman, C., Dukeman, G., Hanson, J.: Automated method to compute orbital reentry trajectories with heating constraints. *J. Guidance, Control Dyn.* **26**(4), 523–529 (2003)
11. Shen, Z., Lu, P.: On-board generation of three-dimensional constrained entry trajectories. *J. Guidance, Control Dyn.* **26**(1), 111–121 (2003)
12. Shen, Z., Lu, P.: Dynamic lateral guidance logic. *J. Guidance, Control Dyn.* **27**(6), 949–959 (2004)
13. Lu, P.: Entry guidance: a unified method. *J. Guidance, Control Dyn.* **37**(3), 713–728 (2014)
14. Yu, W.B., Chen, W.C.: Guidance scheme for glide range maximization of a hypersonic vehicle. AIAA Paper 2011-6714, Aug (2011)
15. Yu, W.B., Chen, W.C.: Entry guidance with real-time planning of reference based on analytical solutions. *Adv. Space Res.* **55**, 2325–2345 (2015)
16. Dwivedi, P.N., Bhattacharya, A., Padhi, R.: Suboptimal midcourse guidance of interceptors for high-speed targets with alignment angle constraint. *J. Guidance, Control Dyn.* **34**(3), 860–877 (2011)
17. Yang, L., Zhou, H., Chen, W.C.: Application of linear gauss pseudospectral method in model predictive control. *Acta Astronaut.* **96**, 175–187 (2014)
18. Rahman, T., Zhou, H., Yang, L., et al.: Pseudospectral model predictive control for exo-atmospheric guidance. *Int. J. Aeronaut. Space Sci.* **16**(1), 112–121 (2015)
19. Vinh, N.X., Busemann, A., Culp, R.D.: Hypersonic and Planetary Entry Flight Mechanics. Ann Arbor, MI: Univ. of Michigan Press, 1980, Chap. 7

20. Phillips, T.H.A.: Common aero vehicle (CAV) model, description, and employment guide. Schafer Corp. for Air Force Research Laboratory and Air Force Command (2003)
21. Benson, D.A.: A gauss pseudospectral transcription for optimal control. Ph.D Thesis, Department of Aeronautics and Astronautics, MIT (2004)
22. Benson, D.A., Huntington, G.T., Thorvaldsen, T.P., et al.: Direct trajectory optimization and costate estimation via an orthogonal collocation method. *J. Guidance, Control Dyn.* **29**(1), 1435–1440 (2006)
23. Garg, D., Patterson, M.A., Hager, W.W., et al.: A unified framework for the numerical solution of optimal control problem using pseudospectral methods. *Automatica* **46**(11), 1843–1851 (2010)
24. Elnagar, G., Kazemi, M., Razzaghi, M.: The pseudospectral legendre method for discretizing optimal control problem. *IEEE Trans. Autom. Control* **40**(10), 1793–1796 (1995)
25. Fahroo, F., Ross, I.M.: Costate estimation by a legendre pseudospectral method. *J. Guidance, Control Dyn.* **24**(2), 270–277 (2001)
26. Ross, I.M., Kapenko, M.: A review of pseudospectral optimal control: from theory to flight. *Ann. Rev. Control* **36**, 182–197 (2012)
27. Xue, S.B., Lu, P.: Constrained predictor-corrector entry guidance. *J. Guidance, Control, Dyn.* **33**(4), 1273–1281 (2010)
28. Zarchan, P.: *Tactical and Strategic Missile Guidance*, fifth ed. Reston, VA: AIAA Progress in Aeronautics and Astronautics, chap.2.
29. Lee, C.H., Kim, T.H., Tahk, M.J.: Polynomial guidance laws considering terminal impact angle and acceleration constraints. *IEEE Trans. Aerosp. Electron. Syst.* **49**(1), 74–92 (2013)
30. Kim, T.H., Lee, C.H., Tahk, M.J.: Time-to-go polynomial guidance with trajectory modulation for observability enhancement. *IEEE Trans. Aerosp. Electron. Syst.* **49**(1), 55–73 (2013)
31. Kim, T.H., Lee, C.H., Jeon, I.S.: Augmented polynomial guidance with impact time and angle constraints. *IEEE Trans. Aerosp. Electron. Syst.* **49**(4), 2806–2817 (2013)

Chapter 17

Trajectory-shaping Guidance with Final Speed and Load Factor Constraints



17.1 Introduction

The terminal guidance problem of a hypersonic gliding vehicle [1] is studied in this paper. In this problem, in order to let the seeker have a good field of view, the guidance law needs to steer the vehicle to destination from a near-vertical orientation. Meanwhile, it is required that the guidance law can adjust the final speed, because if the final speed is too large, the constraints on heating rate and dynamic pressure would be violated, and if the final speed is too small, it is not conducive to breaking through the hostile defense system. Moreover, if the payload of the vehicle is an earth penetrator, it is desired that the vehicle hits the target with a small Angle Of Attack (AOA). If the final AOA is too large, a huge asymmetric force relative to the vehicle's axis of symmetry would act on the vehicle, which causes that the penetration path become curvilinear and the effective penetration depth is markedly reduced [2–4]. In fact, it is not easy to design a guidance law which can adjust the final AOA while keeping a small miss distance. However, we can design a guidance law whose acceleration command goes to zero finally, and thus achieve the goal of obtaining a small final AOA indirectly.

In 1964, Cherry [5] first put forward a trajectory shaping guidance, named Explicit Guidance (E Guidance), by assuming that the acceleration command was a polynomial function of time. E Guidance was used to control the Apollo spacecraft to land on the moon with a desired final velocity vector. Now E Guidance is the typical representative of the trajectory-shaping guidance laws. Bryson [6] derived E Guidance by solving the energy- optimizing problem. Lin [7] applied E Guidance to the flight vehicle whose control force was perpendicular to its velocity, and then optimized E Guidance coefficients with considering the aerodynamic and propulsion parameters. Zarchan [8] evaluated E Guidance in depth. In the later research, Ohlmeyer and

Reprinted from ISA Transactions, Vol 56, Yu Wenbin, Chen Wanchun, Trajectory- Shaping Guidance with final speed and load factor constraints, Pages 42, Copyright (2015), with permission from Elsevier.

Phillips [9] expanded the set of E Guidance coefficients using a new cost function that involves the integral of control energy divided by time-to-go to the n th power. Ben-Asher and Yaesh [10] augmented the E Guidance with an extra term to account for target maneuver. For powered vehicles, such as the Apollo spacecraft, E Guidance is able to control both the final speed and orientation, but for unpowered vehicles, E Guidance can only control the final orientation because the commanded acceleration along the velocity vector cannot be achieved. In [11–15], other types of trajectory shaping guidance laws are presented. In [16], a novel guidance law is proposed for guiding vehicle against a maneuvering target while satisfying a circular no fly zone constraint. The key mechanism of this guidance law is to distort the real space such that the boundary of the no fly zone becomes a straight line.

At present, only reference-tracking guidance laws [17–20] can be used practically to handle the guidance problem studied in this paper. In such guidance laws, before the hypersonic vehicle is launched, a reference trajectory satisfying all constraints is planned using trajectory optimization methods [6, 17, 20–22], and stored in the guidance system. In the terminal guidance phase, the reference trajectory is followed by a tracking algorithm based on Linear-Quadratic Regulator (LQR) [17–19, 23]. Reference-tracking guidance laws are effective and reliable if the state errors and external disturbances are small. To cope with the cases with large state errors and external disturbances, Oza [24] proposes an approach that updates the reference trajectory periodically in flight and then directly uses the results as the commands. However, in this approach, two new problems arise: (1) because the guidance problem is a strongly nonlinear problem with multiple constraints, the optimization calculation usually takes too much time, and thus it is possible that the computation time exceeds the time limit, and (2) sometimes, the planning process may be divergent. Both of these two problems may lead to mission failure.

In this paper, a new guidance law is proposed for steering a hypersonic gliding vehicle to destination from a near-vertical orientation with a desired final speed and a near-zero final load factor. The guidance law consists of Trajectory-Shaping Guidance (TSG) and Final-Speed-Control Scheme (FSCS). TSG can steer the vehicle to the target from the specified orientation, and FSCS can adjust the final speed by controlling the vehicle to perform lateral maneuver. Since the acceleration command of FSCS goes to zero as the vehicle gets close to the target, FSCS does not hinder TSG from steering the vehicle to the target. Further, in order that the proposed guidance law achieve a near zero final load factor, we study the TSG analytically. We get a linear time-varying system by linearization, and then obtain the closed form solutions of TSG. Different from the traditional closed form solutions [8], the speed of the vehicle in the new solutions can be an arbitrary positive function of time. So we name the new solutions the generalized closed form solutions. In the derivation of these solutions, we propose an innovative approach based on spectral decomposition [25] for solving a special type of linear time-varying system, in which the system matrix can be expressed as the product of a time-varying scalar function and a constant matrix. By analyzing the generalized solutions, the stability domain of TSG coefficients is obtained such that the acceleration command goes to zero finally. Because the proposed guidance law does not need a reference trajectory, it

can deal well with the cases with large external disturbances and dispersions in initial states, and also allows the mission to be changed in flight. Therefore, the proposed guidance law is superior to the reference-tracking guidance laws.

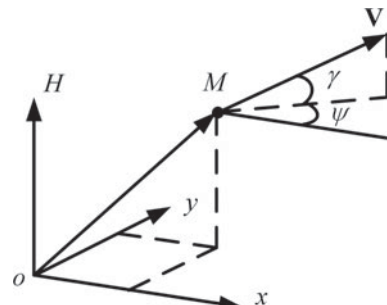
In Sect. 17.7, to observe the influence of the response lag of the Flight Control System (FCS), wind and atmospheric density dispersion on the proposed guidance law, the simulations of 6 Degrees of Freedom (DOF) motion are conducted where the vehicle is treated as a rigid body. In these simulations, the autopilots are used to control the attitude of the vehicle. The most commonly used autopilot in the flight vehicle control field is the so-called three loop autopilot [8] which can response quickly and track the command closely in the presence of disturbances and uncertainties. By the way, some other robust controllers and techniques [26–29] have the potential of being applied to the flight control system. In [26], a recursive technique was proposed for finding roots of equations in the presence of noisy measurements. In [27], the PI and PID parametric conditions guaranteeing the robust stability of the closed-loop systems were derived. In [28], a hybrid reference control with adaptive neuro-fuzzy inference system was proposed for improving transient response performance of the PID controller. In [29], a controller based on radial-basis-function neural network was proposed. This controller can easily adapt to different operation modes.

This chapter is organized as follows: Sect. 17.2 shows the equations of motion; Sect. 17.3 gives the guidance law overview; Sect. 17.4 shows TSG, derives the generalized closed form solutions, and obtains the stability domain of the guidance coefficients; Sect. 17.5 shows FSCS in details; Sect. 17.6 illustrates the model of CAV; Sect. 17.7 shows the performance of the proposed guidance law; Sect. 17.8 draws the conclusions, the references are listed finally.

17.2 Equations of Motion

Figure 17.1 illustrates the inertial frame of reference $o\text{-}xyH$ and the state variables defined in this frame. $o\text{-}xyH$ is fixed on the Earth. The vehicle is regarded as a particle and denoted by M . x is the downrange in meter. y is the crossrange in meter. H is the altitude in meter. V is the speed in m/s. γ is the flight-path angle in radian which is

Fig. 17.1 Inertial reference frame $o\text{-}xyH$ and the corresponding state variables



the angle between the velocity vector and the horizontal plane. γ is treated as positive when the altitude increases. ψ is the heading angle in radian which is the angle of the horizontal projection of the velocity vector measured counterclockwise from the x -axis.

The equations of motion over the non-rotating flat Earth can be found in [30] as

$$\frac{dx}{dt} = V \cos(\gamma) \cos(\psi) \quad (17.1)$$

$$\frac{dy}{dt} = V \cos(\gamma) \sin(\psi) \quad (17.2)$$

$$\frac{dH}{dt} = V \sin(\gamma) \quad (17.3)$$

$$\frac{dV}{dt} = -\frac{D}{m} - g \sin(\gamma) \quad (17.4)$$

$$\frac{d\gamma}{dt} = \frac{L \cos(\sigma)}{mV} - \frac{g \cos(\gamma)}{V} \quad (17.5)$$

$$\frac{d\psi}{dt} = -\frac{L \sin(\sigma)}{mV \cos(\gamma)} \quad (17.6)$$

where m is the mass in kg, σ is the bank angle in radian which is the angle between the lift vector and the vertical plane containing the current velocity vector, g is the gravitational acceleration, and L and D are lift and drag in Newton respectively. Equation (17.7)–(17.9) show the formulas of L , D , and g . The load factor is calculated by $n = L/(mg_0)$ where g_0 is the gravitational acceleration at sea level.

$$L = C_L q S_{\text{ref}} \quad (17.7)$$

$$D = C_D q S_{\text{ref}} \quad (17.8)$$

$$g = \frac{\mu}{(R_e + H)^2} \quad (17.9)$$

where C_L and C_D are the lift and drag coefficients respectively, $q = 0.5\rho V^2$ is the dynamic pressure in Pa, ρ is the atmospheric density in kg/m³ and will be almost reduced by half if H increases by 4.6 km, S_{ref} is the reference area in m², μ is a constant of about 3.96272×10^{14} , and R_e is the average radius of Earth with a value of 6 356.766 km.

17.3 Guidance Law Overview

As shown in Eq. (17.10), the acceleration command of the proposed guidance law consists of two terms: the first is TSG used for steering the vehicle to destination from a near vertical orientation, the second is FSCS used for adjusting the final speed by controlling the vehicle to perform lateral maneuver. \mathbf{a}_{cmd} is perpendicular to the velocity vector.

$$\mathbf{a}_{\text{cmd}} = \mathbf{a}_{\text{TSG}} + \mathbf{a}_{\text{speed}} \quad (17.10)$$

17.4 Trajectory Shaping Guidance

17.4.1 Guidance Form

TSG presented in [9] is used here to guide the vehicle against the target from a near-vertical orientation. As shown in Eq. (17.11), \mathbf{a}_{TSG} consists of three terms: the first is used to steer the vehicle to the target, the second is used to control the direction of the final velocity vector, and the third is used to balance the component of the gravity perpendicular to the velocity vector. \mathbf{a}_{TSG} is normal to the velocity vector.

$$\mathbf{a}_{\text{TSG}} = \frac{V^2}{R} \{ C_1 [\hat{\mathbf{r}} - (\hat{\mathbf{r}} \cdot \hat{\mathbf{v}}) \hat{\mathbf{v}}] + C_2 [\hat{\mathbf{v}}_f - (\hat{\mathbf{v}}_f \cdot \hat{\mathbf{v}}) \hat{\mathbf{v}}] \} - \mathbf{g}_n \quad (17.11)$$

where the range to go R is defined as the length of the Line Of Sight (LOS), C_1 and C_2 are the guidance coefficients, $\hat{\mathbf{r}}$ is the unit vector from the vehicle to the target, $\hat{\mathbf{v}}$ is the unit vector of velocity, $\hat{\mathbf{v}}_f$ is the unit vector of the desired final velocity and obtained by Eq. (17.12), and \mathbf{g}_n is the component of the gravitational acceleration perpendicular to the velocity vector.

$$\hat{\mathbf{v}}_f = \begin{bmatrix} \cos(\gamma_f) \cos(\psi_{\text{LOS}}) \\ \cos(\gamma_f) \sin(\psi_{\text{LOS}}) \\ \sin(\gamma_f) \end{bmatrix} \quad (17.12)$$

where γ_f is the desired final flight path angle, and ψ_{LOS} is the azimuth angle of LOS and can be calculated by

$$\psi_{\text{LOS}} = \arctan \left(\frac{\hat{\mathbf{r}}|_y}{\hat{\mathbf{r}}|_x} \right) \quad (17.13)$$

where $\hat{\mathbf{r}}|_x$ and $\hat{\mathbf{r}}|_y$ are the x -axis and y -axis components of $\hat{\mathbf{r}}$ respectively.

17.4.2 Generalized Closed Form Solutions for TSG

In order to determine the stability domain of the guidance coefficients (i.e. C_1 and C_2) such that the final load factor is zero, we need to get the generalized closed form solutions for TSG, where the speed can arbitrarily change with time, but should always be positive throughout the flight to ensure the success of hitting the target. Since the final velocity vector is almost normal to the horizontal plane, the magnitude of \mathbf{g}_n is quite small when the vehicle is close enough to the target, and thereby can be neglected in the following analysis process. As shown in Fig. 17.2, the motion is only considered in vertical plane.

Thus, the command of TSG can be rewritten as

$$V \frac{d\gamma}{dt} = \frac{V^2}{R} [-C_1 \sin(\gamma - \gamma_{\text{LOS}}) - C_2 \sin(\gamma - \gamma_f)] \quad (17.14)$$

where γ_{LOS} is the angle of the LOS measured counterclockwise from the horizontal reference and its change rate can be obtained by

$$\frac{d\gamma_{\text{LOS}}}{dt} = -\frac{V \sin(\gamma - \gamma_{\text{LOS}})}{R} \quad (17.15)$$

We assume that $(\gamma - \gamma_{\text{LOS}})$ and $(\gamma - \gamma_f)$ are small enough to obtain the following linear time-varying system

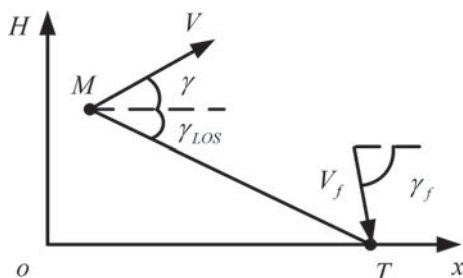
$$\begin{bmatrix} \dot{\gamma} \\ \dot{\gamma}_{\text{LOS}} \end{bmatrix} = f_1(t) \mathbf{A}_1 \begin{bmatrix} \gamma \\ \gamma_{\text{LOS}} \end{bmatrix} + f_1(t) \mathbf{B}_1 \gamma_f \quad (17.16)$$

where

$$f_1(t) = \frac{V(t)}{R(t)} \quad (17.17)$$

$$\mathbf{A}_1 = \begin{bmatrix} -(C_1 + C_2) & C_1 \\ -1 & 1 \end{bmatrix} \quad (17.18)$$

Fig. 17.2 Engagement geometry in vertical plane



$$\mathbf{B}_1 = [C_2 \ 0]^T \quad (17.19)$$

where γ and γ_{LOS} are the state variables, and γ_f is the control variable. The superscript “T” outside the brackets represents the transpose of a matrix. It can be easily obtained that the equilibrium point of the system satisfies that $\gamma = \gamma_{\text{LOS}} = \gamma_f$. Since Eq. (17.16) is a linear time-varying system, it cannot be solved by traditional methods such as Laplace transform, which is widely used to solve linear time-invariant systems. To solve Eq. (17.16), we proposed an innovative approach based on spectral decomposition [25] here. We define $\mathbf{Q}(t, t_0)$ as

$$\mathbf{Q}(t, t_0) = \exp\left(-\int_{t_0}^t \mathbf{A}_1 f_1(\tau) d\tau\right) = \exp(-\mathbf{A}_1 f_2(t, t_0)) \quad (17.20)$$

where t_0 is the initial time, and

$$f_2(t, t_0) = \int_{t_0}^t f_1(\tau) d\tau = \int_{t_0}^t \frac{V(\tau)}{R(\tau)} d\tau \quad (17.21)$$

Note that $dR = -V d\tau$ because we assume that $(\gamma - \gamma_{\text{LOS}}) \approx 0$. Then we have

$$f_2(t, t_0) = - \int_{R(t_0)}^{R(t)} \frac{1}{R} dR = \ln\left(\frac{R(t_0)}{R(t)}\right) \quad (17.22)$$

Left multiplying both sides of Eq. (17.16) by $\mathbf{Q}(t, t_0)$ yields

$$\begin{aligned} & \exp(-\mathbf{A}_1 f_2(t, t_0)) \begin{bmatrix} \dot{\gamma} \\ \dot{\gamma}_{\text{LOS}} \end{bmatrix} - \exp(-\mathbf{A}_1 f_2(t, t_0)) \\ & f_1(t) \mathbf{A}_1 \begin{bmatrix} \gamma \\ \gamma_{\text{LOS}} \end{bmatrix} = \exp(-\mathbf{A}_1 f_2(t, t_0)) f_1(t) \mathbf{B}_1 \gamma_f \end{aligned} \quad (17.23)$$

The above equation can be rewritten as

$$\begin{aligned} & \exp(-\mathbf{A}_1 f_2(t, t_0)) \frac{d}{dt} \begin{bmatrix} \gamma \\ \gamma_{\text{LOS}} \end{bmatrix} + \frac{d}{dt} [\exp(-\mathbf{A}_1 f_2(t, t_0))] \\ & \begin{bmatrix} \gamma \\ \gamma_{\text{LOS}} \end{bmatrix} = \exp(-\mathbf{A}_1 f_2(t, t_0)) f_1(t) \mathbf{B}_1 \gamma_f \end{aligned} \quad (17.24)$$

By inversely using the product rule for finding the derivative, we have

$$\frac{d}{dt} \left\{ \exp(-\mathbf{A}_1 f_2(t, t_0)) \begin{bmatrix} \gamma \\ \gamma_{LOS} \end{bmatrix} \right\} = \exp(-\mathbf{A}_1 f_2(t, t_0)) f_1(t) \mathbf{B}_1 \gamma_f \quad (17.25)$$

Integrating both sides of Eq. (17.25) yields

$$\begin{aligned} & \exp(-\mathbf{A}_1 f_2(t, t_0)) \begin{bmatrix} \gamma \\ \gamma_{LOS} \end{bmatrix} - \exp(-\mathbf{A}_1 f_2(t_0, t_0)) \\ & \begin{bmatrix} \gamma_0 \\ \gamma_{LOS0} \end{bmatrix} = \int_{t_0}^t \exp(-\mathbf{A}_1 f_2(\tau, t_0)) f_1(\tau) \mathbf{B}_1 \gamma_f d\tau \end{aligned} \quad (17.26)$$

where γ_0 is the initial flight path angle. γ_{LOS0} is the initial angle of the LOS. Note that $\exp(-\mathbf{A}_1 f_2(t_0, t_0)) = \exp(\mathbf{0}_{2 \times 2}) = \mathbf{I}_{2 \times 2}$ where $\mathbf{0}_{2 \times 2}$ is the 2×2 zero matrix and $\mathbf{I}_{2 \times 2}$ is the 2×2 unit matrix. The inverse of $\mathbf{Q}(t, t_0)$ is

$$\Phi(t, t_0) = [\mathbf{Q}(t, t_0)]^{-1} = \exp(\mathbf{A}_1 f_2(t, t_0)) \quad (17.27)$$

where $\Phi(t, t_0)$ is the so-called state-transition matrix. Left multiplying Eq. (17.26) by Eq. (17.27) yields

$$\begin{bmatrix} \gamma(t) \\ \gamma_{LOS}(t) \end{bmatrix} = \Phi(t, t_0) \begin{bmatrix} \gamma_0 \\ \gamma_{LOS0} \end{bmatrix} + \int_{t_0}^t \gamma_f f_1(\tau) \Phi(t, \tau) \mathbf{B}_1 d\tau \quad (17.28)$$

The characteristic polynomial for \mathbf{A}_1 is

$$|\lambda \mathbf{I} - \mathbf{A}_1| = \lambda^2 + (C_1 + C_2 - 1)\lambda - C_2 \quad (17.29)$$

Then we can get the eigenvalues for \mathbf{A}_1 as

$$\begin{cases} \lambda_1 = \frac{-(C_1 + C_2 - 1) + \sqrt{\Delta}}{2} \\ \lambda_2 = \frac{-(C_1 + C_2 - 1) - \sqrt{\Delta}}{2} \end{cases} \quad (17.30)$$

where

$$\Delta = C_1^2 + C_2^2 + 1 + 2C_1C_2 - 2C_1 + 2C_2 \quad (17.31)$$

Conversely, we have

$$\begin{cases} C_1 = 1 - \lambda_1 - \lambda_2 + \lambda_1 \lambda_2 \\ C_2 = -\lambda_1 \lambda_2 \end{cases} \quad (17.32)$$

Define $f_3(x, t, t_0)$ as

$$f_3(x, t, t_0) = \exp(x f_2(t, t_0)) = \left(\frac{R(t_0)}{R(t)} \right)^x \quad (17.33)$$

Since C_1 and C_2 are real, λ_1 and λ_2 may be different real numbers, the same real number, or complex conjugates. We can calculate the matrix exponential $\Phi(t, t_0)$ in two aspects: one is that $\lambda_1 \neq \lambda_2$, the other is that $\lambda_1 = \lambda_2$.

(1) If $\lambda_1 \neq \lambda_2$, then.

By innovatively using the spectral decomposition of A_1 [25], obtain

$$\Phi(t, t_0) = f_3(\lambda_1, t, t_0)\mathbf{G}_1 + f_3(\lambda_2, t, t_0)\mathbf{G}_2 = \left(\frac{R(t_0)}{R(t)} \right)^{\lambda_1} \mathbf{G}_1 + \left(\frac{R(t_0)}{R(t)} \right)^{\lambda_2} \mathbf{G}_2 \quad (17.34)$$

where \mathbf{G}_1 and \mathbf{G}_2 are the spectral projectors of A_1 and can be calculated by

$$\mathbf{G}_1 = \frac{\mathbf{A}_1 - \lambda_2 \mathbf{I}}{\lambda_1 - \lambda_2}, \mathbf{G}_2 = \frac{\mathbf{A}_1 - \lambda_1 \mathbf{I}}{\lambda_2 - \lambda_1} \quad (17.35)$$

Then obtain

$$\begin{cases} \mathbf{G}_1 = \frac{1}{\sqrt{\Delta}} \begin{bmatrix} -\frac{C_1+C_2+1-\sqrt{\Delta}}{2} & C_1 \\ -1 & \frac{C_1+C_2+1+\sqrt{\Delta}}{2} \end{bmatrix} \\ \mathbf{G}_2 = \frac{1}{\sqrt{\Delta}} \begin{bmatrix} \frac{C_1+C_2+1+\sqrt{\Delta}}{2} & -C_1 \\ 1 & -\frac{C_1+C_2+1-\sqrt{\Delta}}{2} \end{bmatrix} \end{cases} \quad (17.36)$$

Substituting Eq. (17.34) into the integral term of Eq. (17.28) yields

$$\begin{aligned} \int_{t_0}^t \gamma_f f_1(\tau) \Phi(t, \tau) \mathbf{B}_1 d\tau &= \int_{t_0}^t \gamma_f \left[\left(\frac{R(\tau)}{R(t)} \right)^{\lambda_1} \mathbf{G}_1 + \left(\frac{R(\tau)}{R(t)} \right)^{\lambda_2} \mathbf{G}_2 \right] \\ &\quad \frac{1}{R(\tau)} \begin{bmatrix} C_2 \\ 0 \end{bmatrix} [V(\tau) d\tau] \\ &= \int_{R(t_0)}^{R(t)} \gamma_f \left[\frac{R^{\lambda_1-1}(\tau)}{R^{\lambda_1}(t)} \mathbf{G}_1 + \frac{R^{\lambda_2-1}(\tau)}{R^{\lambda_2}(t)} \mathbf{G}_2 \right] \begin{bmatrix} C_2 \\ 0 \end{bmatrix} [-dR(\tau)] \\ &= \left[\frac{\gamma_f}{\lambda_1} \left(\frac{R^{\lambda_1}(t_0)}{R^{\lambda_1}(t)} - 1 \right) \mathbf{G}_1 + \frac{\gamma_f}{\lambda_2} \left(\frac{R^{\lambda_2}(t_0)}{R^{\lambda_2}(t)} - 1 \right) \mathbf{G}_2 \right] \begin{bmatrix} C_2 \\ 0 \end{bmatrix} \end{aligned} \quad (17.37)$$

Therefore we get the solution of $\gamma(t)$ for $\lambda_1 \neq \lambda_2$, and then we can get the generalized solution of the acceleration command by $a_L(t) = V\dot{\gamma}(t)$ as

$$a_L(t) = \frac{\lambda_1 V^2(t)}{\sqrt{\Delta}} \frac{R^{-\lambda_1-1}(t)}{R^{-\lambda_1}(t_0)} \left[C_1 \gamma_{LOS0} - \frac{C_1 + C_2 + 1 - \sqrt{\Delta}}{2} \left(\gamma_0 + \frac{C_2 \gamma_f}{\lambda_1} \right) \right] \\ + \frac{\lambda_2 V^2(t)}{\sqrt{\Delta}} \frac{R^{-\lambda_2-1}(t)}{R^{-\lambda_2}(t_0)} \left[-C_1 \gamma_{LOS0} + \frac{C_1 + C_2 + 1 + \sqrt{\Delta}}{2} \left(\gamma_0 + \frac{C_2 \gamma_f}{\lambda_2} \right) \right] \quad (17.38)$$

Now there are two cases about the above closed form solutions.

- (a) If λ_1 and λ_2 are different real numbers.

At the final time t_f , the vehicle hits the target, i.e. $R(t_f) = 0$. Then from Eq. (17.38), we can get two conclusions: (1) if $\lambda_1 \leq -1, \lambda_2 \leq -1$ and $\lambda_1 \neq \lambda_2$, then a_L does not go to infinite as the time goes to t_f , and (2) if $\lambda_1 < -1, \lambda_2 < -1$ and $\lambda_1 \neq \lambda_2$, then $\lim_{t \rightarrow t_f} a_L(t) = 0$.

Now an example is given to show that the generalized closed form solution is a reasonable approximation to the result of the engagement simulation. The gravity is neglected here. The considered case is that the vehicle slows down throughout the flight where $V(t) = 1000 - 5t$ (m/s). The initial conditions are $x_0 = 0$ km, $H_0 = 10$ km, and $\gamma_0 = 0$ deg. The target position is $x_T = 50$ km and $H_T = 0$ km. The desired final flight path angle γ_f is 0 deg. By assuming that $\gamma - \gamma_{LOS} \approx 0$, we have $\dot{R} = -V$, and thus obtain $R(t) = \sqrt{26} \times 10^4 - 1000t + 2.5t^2$. Then the final time t_f can be estimated by solving $R(t_f) = 0$. λ_1 and λ_2 are set to -2 and -2.5 respectively, and then from Eq. (17.32), we get $C_1 = 10.5$ and $C_2 = -5$. Then we can get the generalized solution of a_L as

$$a_L(t) = \frac{V^2(t)R(t)}{R^2(0)} [12\gamma_0 - 42\gamma_{LOS0} + 30\gamma_f] \\ + \frac{V^2(t)R^{1.5}(t)}{R^{2.5}(0)} [-17.5\gamma_0 + 52.5\gamma_{LOS0} - 35\gamma_f] \quad (17.39)$$

Zarchan [8] shows the traditional closed form solutions for TSG with $C_1 = 6$ and $C_2 = -2$. In the derivation of the traditional solutions, the speed in the x direction is limited to constant, and the equations of motion in the H direction are linearized, which yields a Cauchy–Euler equation as

$$\ddot{H} + \frac{(C_1 + C_2)\dot{H}}{t_{f2} - t} + \frac{C_1 H}{(t_{f2} - t)^2} = \frac{C_2 \dot{H}_f}{t_{f2} - t} \quad (17.40)$$

where t_{f2} is the estimated final time under the assumption that the speed in the x direction is constant, and can be calculated by $R(t_0) \cos(\gamma_{LOS0}) / [V(t_0) \cos(\gamma_0)]$.

\dot{H}_f is the desired final speed in the H direction. The traditional solution of a_L for $C_1 = 10.5$ and $C_2 = -5$ can be obtained from the above equation as

$$a_L(t) = \frac{t_{f2} - t}{(t_{f2} - t_0)^2} \left[\frac{42H_0}{(t_{f2} - t_0)} + 12\dot{H}_0 + 30\dot{H}_f \right] - \frac{(t_{f2} - t)^{1.5}}{(t_{f2} - t_0)^{2.5}} \left[\frac{52.5H_0}{(t_{f2} - t_0)} + 17.5\dot{H}_0 + 35\dot{H}_f \right] \quad (17.41)$$

where H_0 is the initial altitude and \dot{H}_0 is the initial speed in the H direction. By comparing Eq. (17.39) with Eq. (17.41), we can find that $H_0 = -R(t_0)\gamma_{\text{LOS}0}$, $\dot{H}_0 = V(t_0)\gamma_0$, and $\dot{H}_f = V(t_0)\gamma_f$, and can also find that if the change rate of speed in the generalized solution is neglected, the generalized solution becomes the traditional solution.

In Figs. 17.3 and 17.4, the thin solid curves show the trajectory and acceleration command history obtained by the nonlinear engagement simulation. In Fig. 17.4, the acceleration commands for the generalized and traditional solutions are shown by the thick dashed and dotted curves, respectively. The results show that the generalized solution is an excellent approximation to the result of the nonlinear engagement model. The results also verify that the acceleration command goes to zero as the vehicle gets close to the target. In addition, since the change rate of speed is not considered in the traditional solution, the traditional solution has obvious estimation errors in the final time and acceleration command.

Fig. 17.3 Trajectory obtained by the nonlinear engagement simulation when $\lambda_1 = -2$ and $\lambda_2 = -2.5$

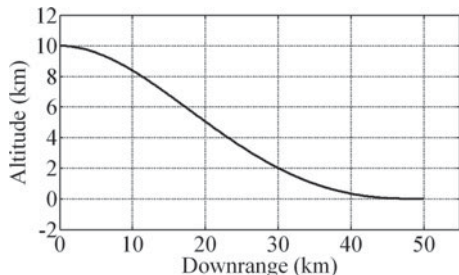
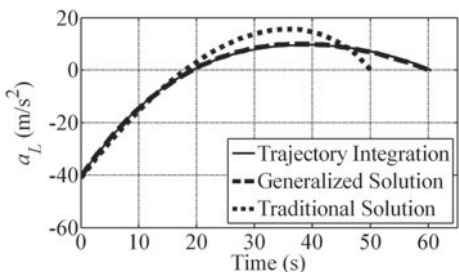


Fig. 17.4 Acceleration command goes to zero finally when $\lambda_1 = -2$ and $\lambda_2 = -2.5$



(b) If λ_1 and λ_2 are complex conjugates.

Let λ_1 and λ_2 be

$$\begin{cases} \lambda_1 = p + iq \\ \lambda_2 = p - iq \end{cases} \quad (17.42)$$

where p and q are real numbers, and $i = \sqrt{-1}$. Substituting Eq. (17.42) into Eq. (17.32) yields

$$\begin{cases} C_1 = 1 - 2p + p^2 + q^2 \\ C_2 = -p^2 - q^2 \end{cases} \quad (17.43)$$

Substituting Eqs. (17.42) (17.43) into Eq. (17.38) yields

$$\begin{aligned} a_L(t) &= \frac{V^2(t)R^{-p-1}(t)}{R^{-p}(t_0)} \sin \left[q \ln \left(\frac{R(t)}{R(t_0)} \right) \right] \\ &\quad \underbrace{[-pC_1\gamma_{\text{LOS}0} + (p - p^2 + q^2)\gamma_0 + (1 - p)C_2\gamma_f]}_q \\ &\quad + \frac{V^2(t)R^{-p-1}(t)}{R^{-p}(t_0)} \cos \left[q \ln \left(\frac{R(t)}{R(t_0)} \right) \right] [C_1\gamma_{\text{LOS}0} - (1 - 2p)\gamma_0 + C_2\gamma_f] \end{aligned} \quad (17.44)$$

From Eq. (17.44), we can conclude that the acceleration has an oscillation where the frequency goes to infinity as t goes to t_f because $R(t_f) = 0$. If $p < -1$, then

$$\lim_{t \rightarrow t_f} \left| R^{-p-1}(t) \sin \left[q \ln \left(\frac{R(t)}{R(t_0)} \right) \right] \right| \leq \lim_{t \rightarrow t_f} |R^{-p-1}(t)| = 0 \quad (17.45)$$

$$\lim_{t \rightarrow t_f} \left| R^{-p-1}(t) \cos \left[q \ln \left(\frac{R(t)}{R(t_0)} \right) \right] \right| \leq \lim_{t \rightarrow t_f} |R^{-p-1}(t)| = 0 \quad (17.46)$$

Therefore it is proved that if $p < -1$, then $\lim_{t \rightarrow t_f} a_L(t) = 0$.

An example is given here. The assumptions and boundary conditions are the same as that in the previous example except that λ_1 and λ_2 are set to $-2 + 2i$ and $-2 - 2i$ respectively. Thus, we have that $C_1 = 13$ and $C_2 = -8$. We can get the generalized closed form solution of a_L as

$$\begin{aligned} a_L(t) &= \frac{V^2(t)R(t)}{R^2(t_0)} \sin \left[2 \ln \left(\frac{R(t)}{R(t_0)} \right) \right] (13\gamma_{\text{LOS}0} - \gamma_0 - 12\gamma_f) \\ &\quad + \frac{V^2(t)R(t)}{R^2(t_0)} \cos \left[2 \ln \left(\frac{R(t)}{R(t_0)} \right) \right] (13\gamma_{\text{LOS}0} - 5\gamma_0 - 8\gamma_f) \end{aligned} \quad (17.47)$$

Fig. 17.5 Trajectory obtained by the engagement simulation when $\lambda_1 = -2 + 2i$ and $\lambda_2 = -2 - 2i$

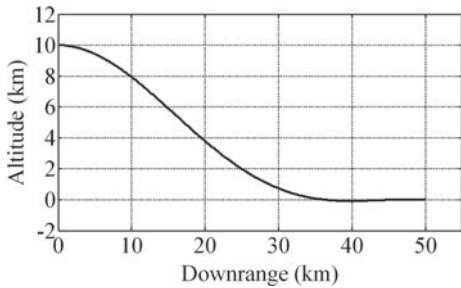
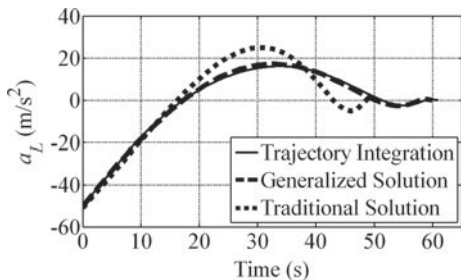


Fig. 17.6 Acceleration command goes to zero finally when $\lambda_1 = -2 + 2i$ and $\lambda_2 = -2 - 2i$



The traditional solution of a_L can be obtained from Eq. (17.40).

$$a_L(t) = -\frac{t_{f2} - t}{(t_{f2} - t_0)^2} \sin \left[2 \ln \left(\frac{t_{f2} - t}{t_{f2} - t_0} \right) \right] \left(\frac{13H_0}{(t_{f2} - t_0)} + \dot{H}_0 + 12\dot{H}_f \right) \\ - \frac{t_{f2} - t}{(t_{f2} - t_0)^2} \cos \left[2 \ln \left(\frac{t_{f2} - t}{t_{f2} - t_0} \right) \right] \left(\frac{13H_0}{(t_{f2} - t_0)} + 5\dot{H}_0 + 8\dot{H}_f \right) \quad (17.48)$$

Figure 17.5 shows the trajectory of the nonlinear engagement simulation. In Fig. 17.6, the thin solid curve is the acceleration command for the engagement simulation, the thick dashed curve is the acceleration command for the generalized solution, and the thick dotted curve is the acceleration command for the traditional solution. The results also show that the generalized solution is an excellent approximation to the acceleration command of the nonlinear engagement model, and verify that the acceleration command has an oscillation and goes to zero as the vehicle gets close to the target. The traditional solution is inaccurate because it does not consider the change rate of the speed.

(2) If $\lambda_1 = \lambda_2$, i.e. $\Delta = 0$, then.

It is easy to verify that

$$\begin{cases} \mathbf{A}_1 - \lambda_1 \mathbf{I} \neq \mathbf{0} \\ (\mathbf{A}_1 - \lambda_1 \mathbf{I})^2 = \mathbf{0} \end{cases} \quad (17.49)$$

Then we can conclude that the minimal polynomial $m(x)$ of \mathbf{A}_1 is

$$m(x) = (x - \lambda_1)^2 \quad (17.50)$$

Then the spectral resolution of $\Phi(t, t_0)$ [25] is

$$\begin{aligned} \Phi(t, t_0) &= f_3(\lambda_1, t, t_0)\mathbf{I} + \frac{\partial f_3(x, t, t_0)}{\partial x} \Big|_{x=\lambda_1} (\mathbf{A}_1 - \lambda_1\mathbf{I}) \\ &= \left(\frac{R(t_0)}{R(t)} \right)^{\lambda_1} \mathbf{I} + \left(\frac{R(t_0)}{R(t)} \right)^{\lambda_1} \ln\left(\frac{R(t_0)}{R(t)} \right) \mathbf{A}_2 \end{aligned} \quad (17.51)$$

where

$$\mathbf{A}_2 = (\mathbf{A}_1 - \lambda_1\mathbf{I}) = \begin{bmatrix} -\frac{C_1+C_2+1}{2} & C_1 \\ -1 & \frac{C_1+C_2+1}{2} \end{bmatrix} \quad (17.52)$$

Substituting Eq. (17.51) into the integral term of Eq. (17.28) yields

$$\begin{aligned} &\int_{t_0}^t \gamma_f f_1(\tau) \Phi(t, \tau) \mathbf{B}_1 d\tau \\ &= \int_{t_0}^t \gamma_f \left[\left(\frac{R(\tau)}{R(t)} \right)^{\lambda_1} \mathbf{I} + \left(\frac{R(\tau)}{R(t)} \right)^{\lambda_1} \ln\left(\frac{R(\tau)}{R(t)} \right) \mathbf{A}_2 \right] \frac{1}{R(\tau)} \begin{bmatrix} C_2 \\ 0 \end{bmatrix} [V(\tau) d\tau] \\ &= \int_{R(t_0)}^{R(t)} \gamma_f \left[\frac{R^{\lambda_1-1}(\tau)}{R^{\lambda_1}(t)} \mathbf{I} + \frac{R^{\lambda_1-1}(\tau)}{R^{\lambda_1}(t)} \ln\left(\frac{R(\tau)}{R(t)} \right) \mathbf{A}_2 \right] \begin{bmatrix} C_2 \\ 0 \end{bmatrix} [-dR(\tau)] \\ &= \frac{\gamma_f}{\lambda_1^2} \left[1 - \left(\frac{R(t_0)}{R(t)} \right)^{\lambda_1} \right] \mathbf{A}_3 \begin{bmatrix} C_2 \\ 0 \end{bmatrix} + \frac{\gamma_f}{\lambda_1} \left(\frac{R(t_0)}{R(t)} \right)^{\lambda_1} \ln\left(\frac{R(t_0)}{R(t)} \right) \mathbf{A}_2 \begin{bmatrix} C_2 \\ 0 \end{bmatrix} \end{aligned} \quad (17.53)$$

where

$$\mathbf{A}_3 = \mathbf{A}_2 - \lambda_1\mathbf{I} = \begin{bmatrix} -1 & C_1 \\ -1 & C_1 + C_2 \end{bmatrix} \quad (17.54)$$

The generalized closed form solution of $\gamma(t)$ for $\lambda_1 = \lambda_2$ can be obtained from Eqs. (17.28), (17.51), and (17.53), and then we can get the generalized closed form solution of the acceleration command by $a_L(t) = V\dot{\gamma}(t)$ as

$$a_L(t) = V^2(t) \frac{R^{-\lambda_1-1}(t)}{R^{-\lambda_1}(t_0)} [-(C_1 + C_2)\gamma_0 + C_2\gamma_f + C_1\gamma_{\text{LOS}0}]$$

$$\begin{aligned}
& -V^2(t) \frac{R^{-\lambda_1-1}(t)}{R^{-\lambda_1}(t_0)} \frac{C_1 + C_2 - 1}{2} \ln\left(\frac{R(t_0)}{R(t)}\right) (C_1 \gamma_{\text{LOS0}} \\
& - \frac{C_1 + C_2 + 1}{2} \gamma_0 + \frac{C_1 + C_2 + 1}{C_1 + C_2 - 1} C_2 \gamma_f)
\end{aligned} \quad (17.55)$$

Now it is needed to prove that if $\lambda_1 = \lambda_2 < -1$, then $\lim_{t \rightarrow t_f} a_L(t) = 0$. Obviously, the problem is equivalent to the following problem:

$$\text{If } \lambda_1 < -1 \text{ then } \begin{cases} \lim_{t \rightarrow t_f} R^{-\lambda_1-1}(t) = 0 \\ \lim_{t \rightarrow t_f} \left(R^{-\lambda_1-1}(t) \ln\left(\frac{R(t_0)}{R(t)}\right) \right) = 0 \end{cases}$$

Proof Because $R(t_f) = 0$, we have that

$$\lambda_1 < -1 \Rightarrow (-\lambda_1 - 1) > 0 \Rightarrow \lim_{t \rightarrow t_f} R^{-\lambda_1-1}(t) = 0$$

The second limit is a $0 \cdot \infty$ -type limit. It can be converted into the ∞/∞ -type limit and then solved by L' Hospital's rule [31].

$$\begin{aligned}
\lim_{t \rightarrow t_f} \left(R^{-\lambda_1-1}(t) \ln\left(\frac{R(t_0)}{R(t)}\right) \right) &= \lim_{t \rightarrow t_f} \frac{\ln\left(\frac{R(t_0)}{R(t)}\right)}{\frac{1}{R^{-\lambda_1-1}(t)}} \\
&= \lim_{t \rightarrow t_f} \frac{\left[\ln\left(\frac{R(t_0)}{R(t)}\right) \right]'}{\left[\frac{1}{R^{-\lambda_1-1}(t)} \right]'} = -\lim_{t \rightarrow t_f} \frac{R^{-\lambda_1-1}(t)}{(\lambda_1 + 1)} = 0
\end{aligned}$$

where the symbol prime ('') represents the derivative of a function with respect to time. Thereby it has been proved that if $\lambda_1 = \lambda_2 < -1$, then $\lim_{t \rightarrow t_f} a_L(t) = 0$.

An example with the same assumptions and boundary conditions as that in the first example is given here. Both λ_1 and λ_2 are set to -2 , and then we have that $C_1 = 9$ and $C_2 = -4$. We can get the generalized solution of a_L as

$$\begin{aligned}
a_L(t) &= V^2(t) \frac{R(t)}{R^2(t_0)} [-5\gamma_0 + 9\gamma_{\text{LOS0}} - 4\gamma_f] \\
&\quad - 2V^2(t) \frac{R(t)}{R^2(t_0)} \ln\left(\frac{R(t_0)}{R(t)}\right) [-3\gamma_0 + 9\gamma_{\text{LOS0}} - 6\gamma_f]
\end{aligned} \quad (17.56)$$

The traditional solution of a_L can be obtained from Eq. (17.40) as

$$a_L(t) = -\frac{(t_{f2} - t)}{(t_{f2} - t_0)^2} \left[\frac{9H_0}{(t_{f2} - t_0)} + 5\dot{H}_0 + 4\dot{H}_f \right]$$

Fig. 17.7 Trajectory obtained by the nonlinear engagement simulation when $\lambda_1 = \lambda_2 = -2$

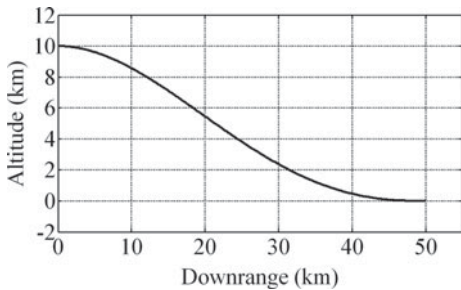
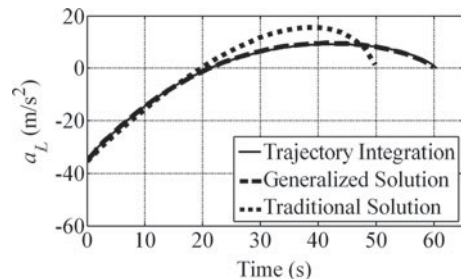


Fig. 17.8 Acceleration command also goes to zero finally when $\lambda_1 = \lambda_2 = -2$



$$+ 2 \frac{(t_{f2} - t)}{(t_{f2} - t_0)^2} \ln\left(\frac{t_{f2} - t_0}{t_{f2} - t}\right) \left[\frac{9H_0}{(t_{f2} - t_0)} + 3\dot{H}_0 + 6\dot{H}_f \right] \quad (17.57)$$

Figure 17.7 shows the trajectory of the engagement simulation. In Fig. 17.8, the thin solid curve is the acceleration command for the nonlinear engagement simulation, the thick dashed curve is the acceleration command for the generalized solution, and the thick dotted curve is the acceleration command for the traditional solution. The results also verify that the acceleration goes to zero finally.

17.4.3 Stability Domain of Guidance Coefficients

Define $\text{Re}(x)$ as a function that returns the real part of a number. For instance, if $x = p + iq$, then $\text{Re}(x) = p$. From the analysis shown in Sect. 4.2, we can get two conclusions:

Conclusion 1: If $\text{Re}(\lambda_1) \leq -1$, $\text{Re}(\lambda_2) \leq -1$, and $\text{Re}(\lambda_1)$ and $\text{Re}(\lambda_2)$ are not simultaneously -1 , then the TSG system is stable and the acceleration command of TSG does not go to infinity as the vehicle gets close to the target.

Conclusion 2: If $\text{Re}(\lambda_1) < -1$ and $\text{Re}(\lambda_2) < -1$, then the TSG system is also stable and the acceleration command of TSG goes to zero as the vehicle gets close to the target.

Note that the above conclusions still hold even if the vehicle accelerates or decelerates. Therefore, we can obtain C_1 and C_2 by setting λ_1 and λ_2 to appropriate values. Now we determine the domain of C_1 and C_2 .

(1) If λ_1 and λ_2 are real

According to the second sub-equation of Eq. (17.32), we have that $C_2 < -1$ and $\lambda_1 \geq (-\lambda_2)\lambda_1 = C_2$ since $\lambda_1 < -1$, $\lambda_2 < -1$, and λ_1 and λ_2 are not simultaneously -1 . Reshaping the second sub-equation of Eq. (17.32) yields

$$\begin{cases} \lambda_2 = -C_2/\lambda_1 \\ C_2 \leq \lambda_1 \leq -1 \\ C_2 < -1 \end{cases} \quad (17.58)$$

Substituting Eq. (17.58) into the first sub-equation of Eq. (17.32) yields

$$\begin{cases} C_1 = 1 - \lambda_1 + C_2/\lambda_1 - C_2 \\ C_2 \leq \lambda_1 \leq -1 \\ C_2 < -1 \end{cases} \quad (17.59)$$

In order to facilitate the writing, we denote the derivative of a function $f(x)$ with respect to x by $(f)_x$. If C_2 is fixed, the derivative of C_1 with respect to λ_1 is

$$\frac{dC_1}{d\lambda_1} = -\left(1 + \frac{C_2}{\lambda_1^2}\right) \quad (17.60)$$

When $-\sqrt{-C_2} < \lambda_1 \leq -1$, $(C_1)_{\lambda_1} > 0$, so C_1 increases with increasing λ_1 .

When $C_2 \leq \lambda_1 \leq -\sqrt{-C_2}$, $(C_1)_{\lambda_1} > 0$, so C_1 decreases with increasing λ_1 .

Note that for $C_2 < -1$, $C_2 < -\sqrt{-C_2} < -1$ holds. So we have that.

At $\lambda_1 = -\sqrt{-C_2}$, C_1 takes the minimum value, i.e.

$$C_1 \geq 1 + 2\sqrt{-C_2} - C_2 \quad (17.61)$$

At $\lambda_1 = -1$ or $\lambda_1 = C_2$, C_1 takes the maximum value, i.e.

$$C_1 \leq 2 - 2C_2 \quad (17.62)$$

Now we conversely consider the above analysis process. Let $1 + 2\sqrt{-C_2} - C_2 \leq C_1 \leq 2 - 2C_2$ and $C_2 < -1$. Then, after some algebra, we have $0 < 2\sqrt{-C_2} \leq C_1 + C_2 - 1 \leq 1 - C_2$. The first sub-equation of Eq. (17.30) can be rewritten as

$$\lambda_1 = \frac{-(C_1 + C_2 - 1) + \sqrt{\Delta}}{2} \cdot \frac{(C_1 + C_2 - 1) + \sqrt{\Delta}}{(C_1 + C_2 - 1) + \sqrt{\Delta}} \quad (17.63)$$

Since $\Delta = (C_1 + C_2 - 1)^2 + 4C_2$, the above equation can be simplified as

$$\lambda_1 = \frac{2C_2}{(C_1 + C_2 - 1) + \sqrt{(C_1 + C_2 - 1)^2 + 4C_2}} \quad (17.64)$$

Since $0 < 2\sqrt{-C_2} \leq C_1 + C_2 - 1$, we have $(C_1 + C_2 - 1)^2 + 4C_2 \geq 0$, so Eq. (17.64) is a real function. If the term $(C_1 + C_2 - 1)$ increases, the denominator increases, and then λ_1 also increases because $C_2 < -1$. Therefore, by substituting $2\sqrt{-C_2} \leq C_1 + C_2 - 1 \leq 1 - C_2$ into Eq. (17.64), we can obtain

$$-\sqrt{-C_2} \leq \lambda_1 \leq -1 \quad (17.65)$$

λ_2 is obtained by the second sub-equation of Eq. (17.30) and rewritten again as

$$\lambda_2 = \frac{-(C_1 + C_2 - 1) - \sqrt{(C_1 + C_2 - 1)^2 + 4C_2}}{2} \quad (17.66)$$

If the term $(C_1 + C_2 - 1)$ increases, then λ_2 decreases. Substituting $2\sqrt{-C_2} \leq C_1 + C_2 - 1 \leq 1 - C_2$ into Eq. (17.66) yields

$$C_2 \leq \lambda_2 \leq -\sqrt{-C_2} \quad (17.67)$$

Therefore, we can draw three conclusions as:

Conclusion 3: If $C_1 = 2 - 2C_2$ and $C_2 < -1$, then $\lambda_1 = -1$ and $\lambda_2 = C_2$.

Conclusion 4: If $1 + 2\sqrt{-C_2} - C_2 < C_1 < 2 - 2C_2$ and $C_2 < -1$, then $-\sqrt{-C_2} < \lambda_1 < -1$ and $C_2 < \lambda_2 < -\sqrt{-C_2}$.

Conclusion 5: If $C_1 = 1 + 2\sqrt{-C_2} - C_2$ and $C_2 < -1$, then $\lambda_1 = \lambda_2 = -\sqrt{-C_2}$.

(2) If λ_1 and λ_2 are complex conjugates

From Conclusion 1, we have that $\operatorname{Re}(\lambda_1) = \operatorname{Re}(\lambda_2) < -1$. Then from Eq. (17.30), we get

$$\begin{cases} C_1 + C_2 - 1 > 2 \\ \Delta = C_1^2 + C_2^2 + 1 + 2C_1C_2 - 2C_1 + 2C_2 < 0 \end{cases} \quad (17.68)$$

After some algebra, obtain

$$\begin{cases} C_1 > 3 - C_2 \\ (C_1 + C_2 - 1)^2 < -4C_2 \end{cases} \quad (17.69)$$

Then we have

$$\begin{cases} C_1 > 3 - C_2 \\ 1 - 2\sqrt{-C_2} - C_2 < C_1 < 1 + 2\sqrt{-C_2} - C_2 \end{cases} \quad (17.70)$$

Since $-\sqrt{-C_2} < 0$, we have $1 - 2\sqrt{-C_2} - C_2 < 3 - C_2$, and further have

$$3 - C_2 < C_1 < 1 + 2\sqrt{-C_2} - C_2 \quad (17.71)$$

In order to ensure that the inequality $3 - C_2 < C_1 < 1 + 2\sqrt{-C_2} - C_2$ holds, we can obtain that $C_2 < -1$.

Now we conversely consider the above analysis process. Let $3 - C_2 < C_1 < 1 + 2\sqrt{-C_2} - C_2$ and $C_2 < -1$. After some algebra, we have $2 < C_1 + C_2 - 1 < 2\sqrt{-C_2}$. Thus, $\Delta = (C_1 + C_2 - 1)^2 + 4C_2 < -4C_2 + 4C_2 = 0$. So from Eq. (17.30), we can see that λ_1 and λ_2 are complex conjugates. Also from Eq. (17.30), the real parts of λ_1 and λ_2 are

$$\operatorname{Re}(\lambda_1) = \operatorname{Re}(\lambda_2) = \frac{-(C_1 + C_2 - 1)}{2} \quad (17.72)$$

Since $2 < C_1 + C_2 - 1 < 2\sqrt{-C_2}$, we have $-\sqrt{-C_2} < \operatorname{Re}(\lambda_1) = \operatorname{Re}(\lambda_2) < -1$. So we can get Conclusion 6 as:

Conclusion 6: If $3 - C_2 < C_1 < 1 + 2\sqrt{-C_2} - C_2$ and $C_2 < -1$, then λ_1 and λ_2 are complex conjugates, and their real parts are smaller than -1 .

Combining Conclusions 1–6 together, we can draw the following two conclusions:

Conclusion 7: If $C_1 = 2 - 2C_2$ and $C_2 < -1$, then the TSG system is stable and the acceleration command of TSG does not go to infinity as the vehicle gets close to the target.

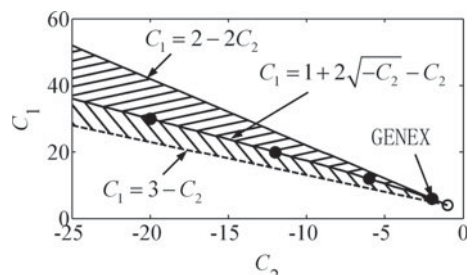
Conclusion 8: If $3 - C_2 < C_1 < 2 - 2C_2$ and $C_2 < -1$, the TSG system is also stable and the acceleration command of TSG goes to zero as the vehicle gets close to the target.

In [5, 6] and [8], the guidance coefficients are $C_1 = 6$ and $C_2 = -2$. In [9], the Generalized Vector Explicit Guidance (GENEX) is derived using a time-to-go weighted cost function. The form of GENEX is the same as that of E Guidance, but the set of the guidance coefficients is expanded as

$$\begin{cases} C_1 = (k+2)(k+3) \\ C_2 = -(k+1)(k+2) \\ k = 0, 1, 2, \dots \end{cases} \quad (17.73)$$

In Fig. 17.9, the shaded area excluding the point $(-1, 4)$ marked by the hollow circle ‘o’ is the stability domain of the guidance coefficients described by Conclusions

Fig. 17.9 The stability domain of the trajectory-shaping guidance coefficients



7–8, and as a comparison, the solid points show the guidance coefficients of GENEX. It should be mentioned that, because the above conclusions are independent of the change rate of the speed, the stability domain is not affected by the change rate of the speed, i.e. the domain remains unchanged even if the vehicle accelerates or decelerates.

17.5 Final Speed Control Scheme

As shown in Eq. (17.74), FSCS generates the command $\mathbf{a}_{\text{speed}}$ which is in the horizontal plane and perpendicular to the velocity vector.

$$\mathbf{a}_{\text{speed}} = \text{sgn}(\psi_0 - \psi_{\text{LOSO}}) k_{Vf} g_0 \left(\frac{R}{R_0} \right)^2 \begin{bmatrix} -\sin(\psi) \\ \cos(\psi) \\ 0 \end{bmatrix} \quad (17.74)$$

where k_{Vf} is a positive parameter, g_0 is the gravitational acceleration at sea level, R_0 is the initial range to go, ψ_0 is the initial heading angle, ψ_{LOSO} is the initial azimuth angle of the line of sight, and $\text{sgn}(x)$ is a sign function as shown in Eq. (17.75). In Eq. (17.74), the expression $\text{sgn}(\psi_0 - \psi_{\text{LOSO}})$ determines the direction of $\mathbf{a}_{\text{speed}}$ such that $\mathbf{a}_{\text{speed}}$ steers the vehicle away from the target. k_{Vf} determines the magnitude of $\mathbf{a}_{\text{speed}}$. Increasing k_{Vf} has two effects: one is to extend the length of the trajectory; the other is to increase the drag force since $\mathbf{a}_{\text{speed}}$ generates an additional AOA. Thus the final speed decreases with increasing k_{Vf} . The expression $(R/R_0)^2$ in Eq. (17.74) makes the magnitude of $\mathbf{a}_{\text{speed}}$ go to zero finally in order that $\mathbf{a}_{\text{speed}}$ does not hinder \mathbf{a}_{TSG} from steering the vehicle to the target. The vector expression in Eq. (17.74) makes $\mathbf{a}_{\text{speed}}$ be in the horizontal plane and perpendicular to the velocity vector.

$$\text{sgn}(x) = \begin{cases} 1 & x \geq 0 \\ -1 & x < 0 \end{cases} \quad (17.75)$$

The value of k_{Vf} is obtained by iteration: the onboard computer predicts the final speed $V_f(j)$ by trajectory simulation, and then corrects the value of k_{Vf} by the secant method, as shown in Eq. (17.76).

$$k_{Vf}(j+1) = k_{Vf}(j) - \frac{(V_f(j) - V_f)(k_{Vf}(j) - k_{Vf}(j-1))}{(V_f(j) - V_f(j-1))} \quad (17.76)$$

where j represents the ordinal number of simulations. The above process is repeated until $|V_f(j) - V_f| < 1 \text{ m/s}$.

17.6 Model of CAV-H

The model of CAV-H is provided in [1]. The vehicle has a mass of 907.2 kg and a reference area of 0.483 87m². The allowable AOA is between -25 deg and 25 deg. The aerodynamic coefficients can be obtained by the following fitting formulas

$$C_L = C_{L0} + C_L^\alpha \alpha \quad (17.77)$$

$$C_D = C_{D0} + K C_L^2 \quad (17.78)$$

where C_L and C_D are the lift and drag coefficients respectively, α is the AOA in radians, C_{L0} is the zero angle-of-attack lift coefficient, C_L^α is the lift-curve slope, C_{D0} is the zero-lift drag coefficient, and K is the induced drag parameter. As shown in the following figures, C_{L0} , C_L^α , C_{D0} , and K are functions of Mach number (Ma), the ratio of the vehicle's speed and the local speed of sound (Figs. 17.10 and 17.11).

CAV-H employs the Bank to Turn (BTT) control where the AOA and bank angle are used to as the control variables. They are determined by \mathbf{a}_{cmd} as

$$\alpha = (m||\mathbf{a}_{cmd}|| - C_{L0}q S_{ref}) / (C_L^\alpha q S_{ref}) \quad (17.79)$$

$$\sigma = \arctan\left(\frac{\mathbf{a}_{cmd} \cdot \mathbf{x}_1}{\mathbf{a}_{cmd} \cdot \mathbf{x}_2}\right) \quad (17.80)$$

Fig. 17.10 C_{L0} and C_L^α as functions of Ma

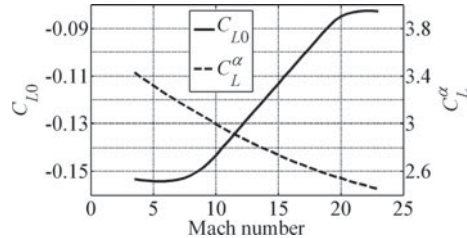
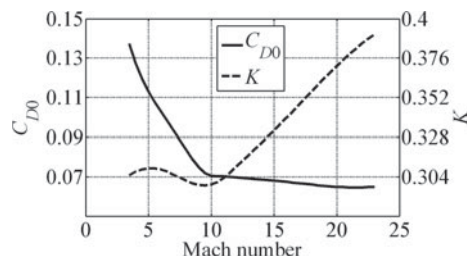


Fig. 17.11 C_{D0} and K as functions of Ma



where \mathbf{x}_1 is the unit vector perpendicular to the vertical plane S containing the current velocity vector, and \mathbf{x}_2 is the unit vector perpendicular to the current velocity vector in the plane S . They can be calculated by

$$\mathbf{x}_1 = [\sin(\psi), -\cos(\psi), 0]^T \quad (17.81)$$

$$\mathbf{x}_2 = [-\sin(\gamma) \cos(\psi), -\sin(\gamma) \sin(\psi), \cos(\gamma)]^T \quad (17.82)$$

17.7 Results and Discussion

According to Conclusion 2, in order that the acceleration command of the proposed guidance law goes to zero finally, we set both λ_1 and λ_2 to -2 , and then obtain that the guidance coefficients are $C_1 = 9$ and $C_2 = -4$ by Eq. (17.32). In the following example, the initial conditions are $x_0 = y_0 = 0$ km, $H_0 = 20$ km, $V_0 = 2500$ m/s, $\gamma_0 = 0$ deg, and $\psi_0 = 0$ deg, and the desired final conditions are $x_f = 50$ km, $y_f = 5$ km, $H_f = 0$ km, and $\gamma_f = -80$ deg. There are two cases about the desired final speed considered: one is $V_f = 1300$ m/s, the other is $V_f = 1100$ m/s. In addition, it is desired that the final load factor is near zero so as to indirectly achieve the purpose of impacting the target with a small AOA. After conducting a large number of simulations, we obtain the profile of V_f with respect to k_{Vf} as shown in Fig. 17.12. Since the greater k_{Vf} tends to extend the length of the tortuous path, V_f is a decreasing function of k_{Vf} . As shown in Fig. 17.13, since V_f changes monotonically with k_{Vf} , only 4 trajectory simulations are needed by the iteration shown in Sect. 17.5 to get sufficient precision solution of k_{Vf} . The iteration program is written in C programming language and runs on a desktop computer, and the initial two values of k_{Vf} for the two cases are set arbitrarily. The iteration results are $k_{Vf} = 36.789$ 3 for $V_f = 1300$ m/s and $k_{Vf} = 61.976$ 4 for $V_f = 1100$ m/s.

The results of the proposed guidance law are shown in Figs. 17.14, 17.15, 17.16, 17.17, 17.18 and 17.19. As a comparison, the results of the traditional trajectory shaping guidance presented in [8] are also given here. In these figures, the solid curves represent the results of the proposed guidance for $V_f = 1300$ m/s, the dashed curves

Fig. 17.12 The final speed V_f is a decreasing function of k_{Vf}

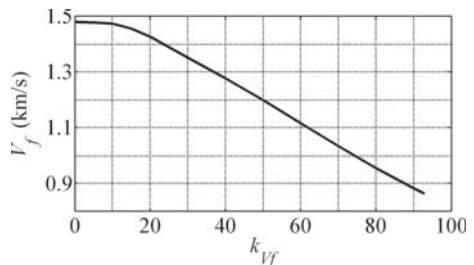


Fig. 17.13 The iteration algorithm converges quickly

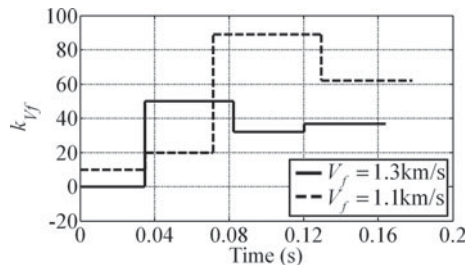


Fig. 17.14 Trajectories and ground tracks

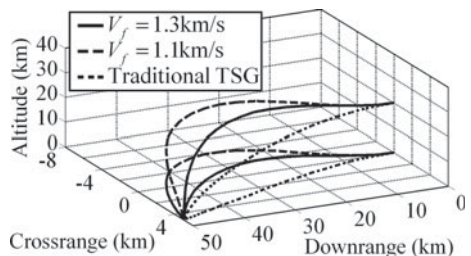


Fig. 17.15 Speed histories

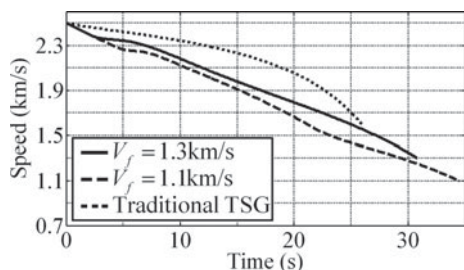
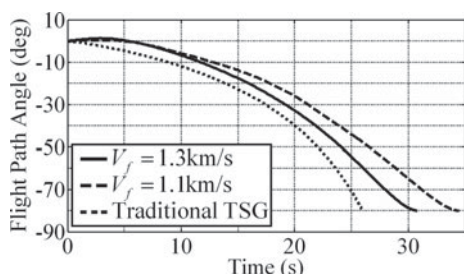


Fig. 17.16 Flight-path angle histories



represent the results of the proposed guidance for $V_f = 1100$ m/s, and the dotted curves represent the results of the traditional guidance. Note that, in Fig. 17.14, the ground tracks, the projections of the trajectories onto the surface of Earth, are also provided. As can be seen from these figures, under the control of the proposed

Fig. 17.17 Load factor histories

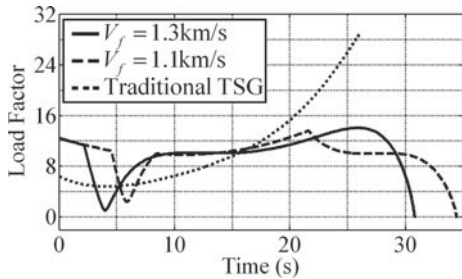


Fig. 17.18 Bank angle histories

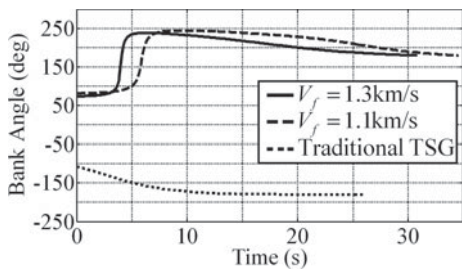
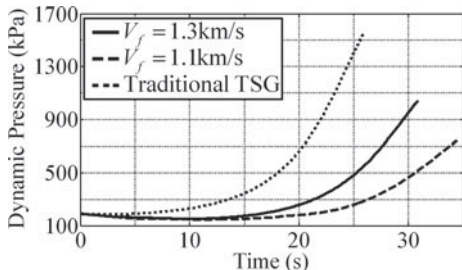


Fig. 17.19 Dynamic pressure histories



guidance law, the vehicles hit the target while meeting the requirements on final speed, flight path angle, and load factor. As obviously can be seen from Fig. 17.14, the vehicles perform lateral maneuvers to adjust the final speed. Figure 17.19 shows that adjusting V_f is an effective way to limit the maximum dynamic pressure. In addition, from Fig. 17.15, we can see that the traditional guidance cannot control the final speed, because the vehicle is unpowered, thus only the component of the acceleration command perpendicular to the velocity vector can be tracked by adjusting the AOA and bank angle, while the component of the acceleration command along the velocity vector has to be discarded. From Fig. 17.17, we can see that the load factor of the traditional guidance does not go to zero finally, because the eigenvalues of \mathbf{A}_1 corresponding to $C_1 = 6$ and $C_2 = -2$ are $\lambda_1 = -1$ and $\lambda_2 = -2$, and then, from Eq. (17.38), we can see that if $\lambda_1 \geq -1$, then a_L will not go to zero finally.

Now we observe the influence of the response lag of the Flight Control System (FCS), wind and atmospheric density dispersion on the proposed guidance law. The

simulations of 6-DOF motion are conducted where the vehicle is treated as a rigid body and thus its rotational motion is taken into account. In these simulations, the autopilots in the pitch, yaw and roll channels are needed to control the attitude of the vehicle. The following briefly illustrates the autopilots used in the 6-DOF simulations. In both pitch and yaw channels, the three-loop autopilots [8] are employed. This kind of autopilot is widely used in the flight vehicle control field due to its good performance. Because the vehicle uses the bank-to-turn steering, the autopilot in the pitch channel makes the lift acceleration closely follow the commanded acceleration by adjusting the AOA, while the autopilot in the yaw channel maintains a zero sideslip angle. Since the autopilots in these two channels are similar, only the autopilot in the pitch channel is displayed here as

$$\delta_z = K_R \omega_z + K_R \omega_I \int_0^t \omega_z d\tau + K_A K_R \omega_I \int_0^t a_L d\tau - K_{DC} K_A K_R \omega_I \int_0^t a_{L\text{cmd}} d\tau \quad (17.83)$$

where δ_z is the pitch fin deflection, ω_z is the component of the vehicle's angular velocity along the lateral axis normal to the vehicle's plane of symmetry, a_L is the achieved lift acceleration, and $a_{L\text{cmd}}$ is the commanded lift acceleration. The autopilot gains K_{DC} , K_A , K_R and ω_I are determined by properly specifying the desired time constant, damping, and open-loop crossover frequency of the FCS [8]. In fact, the three-loop autopilot is a special type of PID controller that adequately considers the characteristics of the rotational motion of the airframe and the measurement capability of the Inertial Navigation System (INS), by which ω_z and a_L can be directly measured. In the roll channel, a PID controller is used to track the commanded bank angle σ_{cmd} . The roll fin deflection δ_x determined by the PID controller is as

$$\delta_x = \frac{J_x}{C_{mx}^{\delta_x} q S_{\text{ref}} L_{\text{ref}}} \left[-k_1 \omega_x - k_2 (\sigma - \sigma_{\text{cmd}}) - k_3 \int_0^t (\sigma - \sigma_{\text{cmd}}) d\tau \right] \quad (17.84)$$

where $C_{mx}^{\delta_x}$ is the partial derivative of the rolling moment coefficient with respect to δ_x , L_{ref} is the reference diameter, J_x is the moment of inertia about the longitudinal axis of the vehicle, ω_x is the component of the vehicle's angular velocity along the longitudinal axis, and σ is the achieved bank angle. The controller parameters k_1 , k_2 and k_3 are determined by the pole placement method [32].

In this example, the boundary conditions are the same as that in the previous 3-DOF case with $V_f = 1300 \text{ m/s}$ except that $y_0 = 100 \text{ m}$. Assume that there is a constant wind of 30 m/s along the positive direction of x -axis, and assume that the actual atmospheric density is 5% greater than the standard atmospheric density. The wind will have a significant impact on the AOA when the vehicle drops vertically. In our proposed guidance law, the 3-DOF simulations, in which the vehicle is treated as a particle, are still used by the iterative algorithm of determining k_{Vf} because the 3-DOF

Table 17.1 Comparison of the simulation results

	Proposed guidance law	Reference-tracking guidance
Miss distance (m)	0.0891	-2.0525
Error in γ_f (deg)	0.0480	-0.0420
Error in V_f (m/s)	-30.66	-87.00
Final load factor	1.0076	0.5238

simulations can be accomplished in a short period of time while achieving a sufficient accuracy. As a comparison, the results of the reference-tracking guidance law based on LQR [18, 19] are also provided here. This guidance law uses the results obtained in the previous 3-DOF case with $V_f = 1300$ m/s as the reference profiles, and thus treats $y_0 = 100$ m as the initial state deviation. Table 17.1 shows the comparison of the simulation results of the proposed guidance law and reference-tracking guidance. From this table, we can see that the miss distance and error in V_f of the former are much smaller than that of the latter, whereas the final load factor of the former is larger than that of the latter. Overall, both of the two guidance laws can meet the practical requirements, but the former performs better than the latter. Figure 17.20 shows the trajectory and ground track for the proposed guidance law. Figure 17.21 shows the reference and real trajectories and the corresponding ground tracks for the reference-tracking guidance. Figure 17.22 shows the load factor histories for the proposed guidance, where the thin solid curve represents the achieved load factor and the thick dashed curve represents the commanded load factor. From this figure, we can see that the achieved load factor lags behind the commanded load factor

Fig. 17.20 Trajectory for the proposed guidance

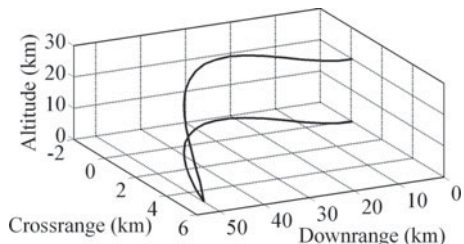


Fig. 17.21 Trajectory for the reference-tracking guidance

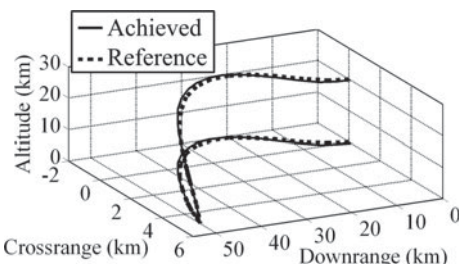


Fig. 17.22 Load factor histories for the proposed guidance

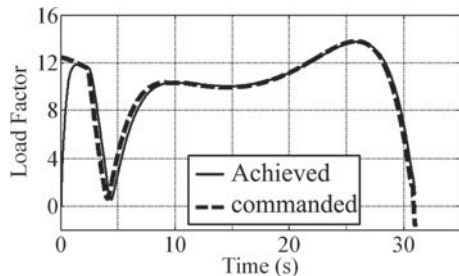
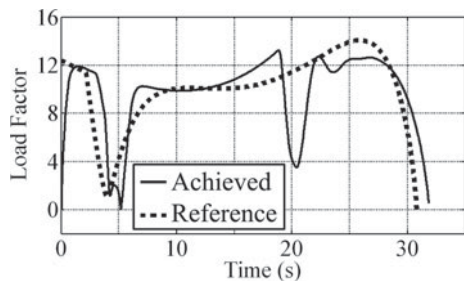


Fig. 17.23 Load factor histories for the reference-tracking guidance



due to the response lag of the FCS. Figure 17.23 shows the load factor histories for the reference-tracking guidance, where the thin solid curve represents the achieved load factor and the thick dotted curve represents the reference load factor. Mainly because of the wind disturbance, there is a relatively large deviation between the achieved and reference load factors. Figure 17.24 shows the bank angle histories for the proposed guidance, where the thin solid curve represents the achieved bank angle and the thick dashed curve represents the commanded bank angle. Figure 17.25 shows the bank angle histories for the reference-tracking guidance, where the thin solid curve represents the achieved bank angle and the thick dotted curve represents the reference bank angle (Table 17.1).

Fig. 17.24 Bank angle histories for the proposed guidance

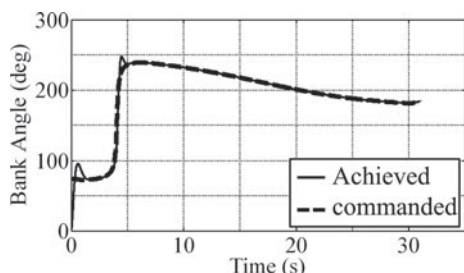
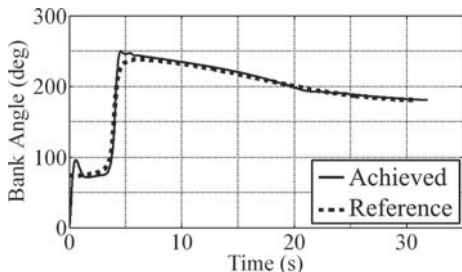


Fig. 17.25 Bank angle histories for the reference tracking guidance



17.8 Conclusions

In this paper, a new guidance law is proposed for steering a hypersonic vehicle to a ground target from a near- vertical direction while meeting the requirements on final speed and load factor. The guidance law consists of TSG and FSCS. TSG can steer the vehicle to the target from the specified direction. FSCS is used to adjust the final speed by controlling the vehicle to perform lateral maneuver. By analyzing the generalized closed form solutions of TSG, we obtain the stability domain of the guidance coefficients such that the acceleration command goes to zero finally. So we can properly select the guidance coefficients in the stability domain such that the proposed guidance law can achieve a near-zero final load factor. Different from the traditional solutions, the generalized solutions take into account the case where the speed changes with time. In the derivation of the generalized solutions, we proposed an innovative approach based on spectral decomposition for solving a special type of linear time-varying system, where the system matrix can be expressed as the product of a time-varying scalar function and a constant matrix. From the 6-DOF simulations where the wind and atmospheric density dispersion are considered, we can see that both of the proposed guidance law and reference-tracking guidance can meet the practical requirements, but the former performs better than the latter.

References

1. Phillips, T.H.: A Common Aero Vehicle (CAV) Model, Description, and Employment Guide. Schafer Corporation for AFRL and AFSPC, Arlington (2003)
2. Jonas, G.H., Zukas, J.A.: Mechanics of penetration: Analysis and experiment. *Int. J. Eng. Sci.* **16**(11), 879–903 (1978)
3. Liu, R.C., He, M.C., Ren, H.Q., et al.: Effect of attack angle on a projectile's penetration. *Trans. Beijing Inst. Technol.* **23**(1), 26–29 (2003)
4. Ma, A.E., Huang, F.L., Chu, Z., et al.: Numerical simulation on yawed penetration into concrete. *Explosion Shock Waves* **28**, 34–37 (2008)
5. Cherry, G.W.: A General, Explicit Optimal Guidance Law for Rocket-Propelled Spacecraft. *Astrodynamics Guidance and Control Conference*. Los Angeles (1964)
6. Bryson, A.E., Ho, Y.C.: *Applied Optimal Control: Optimization, Estimation and Control*. Blaisdell Publishing Company, Waltham (1969)

7. Lin, C.F., Tsai, L.: Analytical solution of optimal trajectory-shaping guidance. *J. Guidance Control Dyn.* **10**(1), 60–66 (1987)
8. Zarchan, P.: *Tactical and Strategic Missile Guidance*. AIAA Progress in Aeronautics and Astronautics, Reston (2007)
9. Ohlmeyer, E.J., Phillips, C.A.: Generalized vector explicit guidance. *J. Guidance Control Dyn.* **29**(2), 261–268 (2006)
10. Ben-Asher, J.Z., Yaesh, I.: *Advances in Missile Guidance Theory*. AIAA Progress in Aeronautics and Astronautics, Virginia (1998)
11. Kim, M., Grider, K.V.: Terminal guidance for impact attitude angle constrained flight trajectories. *IEEE Trans. Aerosp. Electron. Syst. AES* **9**(6):852–859 (1973)
12. Ryoo, C.K., Cho, H., Tahk, M.J.: Time-to-go weighted optimal guidance with impact angle constraints. *IEEE Trans. Control Syst. Technol.* **14**(3), 483–492 (2006)
13. Xiong, S., Wang, W., Liu, X., et al.: Guidance law against maneuvering targets with intercept angle constraint. *ISA Trans.* **53**, 1332–1342 (2014)
14. Yang, L., Zhou, H., Chen, W.: Application of linear gauss pseudospectral method in model predictive control. *Acta Astronaut.* **96**, 175–187 (2014)
15. Lin, C.L., Lin, Y.P., Chen, K.M.: On the design of fuzzified trajectory shaping guidance law. *ISA Trans.* **48**(2), 148–155 (2009)
16. Yu, W., Chen, W.: Guidance law with circular no-fly zone constraint. *Nonlinear Dyn.* **78**(3), 1953–1971 (2014)
17. Tawfiqur, R., Zhou, H., Sheng, Y.Z., et al.: Trajectory optimization of hypersonic vehicle using gauss pseudospectral method. *Appl. Mech. Mat.* **110–116**, 5232–5239 (2011)
18. Dukeman, G.A.: Profile-following entry guidance using linear quadratic regulator theory. In: *AIAA Guidance, Navigation, and Control Conference and Exhibit*. Monterey (2002)
19. Jian, T.G., Yuan, Z.H.: A study of the optimal feedback-gain-coefficients of reentry guidance for spacecraft. *J. National Univ. Defense Technol.* **22**, 53–56 (2000)
20. Rahimi, A., Dev Kumar, K., Alighanbari, H.: Particle swarm optimization applied to spacecraft reentry trajectory. *J. Guidance Control Dyn.* **36**(1), 307–310 (2013)
21. Stryk, O.V., Bulirsch, R.: Direct and indirect methods for trajectory optimization. *Ann. Oper. Res.* **37**(1), 357–373 (1992)
22. Yokoyama, N., Suzuki, S.: Modified genetic algorithm for constrained trajectory optimization. *J. Guidance Control Dyn.* **28**(1), 139–144 (2005)
23. Kwakernaak, H., Sivan, R.: *Linear Optimal Control Systems*. John Wiley and Sons Inc., New York (1972)
24. Oza, H.B., Padhi, R.: Impact-angle-constrained suboptimal model predictive static programming guidance of air-to-ground missiles. *J. Guidance, Control, Dyn.* **35**(1), 153–164 (2012)
25. Meyer, C.D.: *Matrix Analysis and Applied Linear Algebra*. Society for Industrial and Applied Mathematics, Philadelphia (2000)
26. Spall, J.C.: Multivariate stochastic approximation using a simultaneous perturbation gradient approximation. *IEEE Trans. Autom. Control* **37**(3), 332–341 (1992)
27. Precup, R.E., Preitl, S.: PI and PID controllers tuning for integral-type servo systems to ensure robust stability and controller robustness. *Electr. Eng.* **88**(2), 149–156 (2006)
28. Joelianto, E., Anura, D.C., Priyanto, M.P.: ANFIS—Hybrid reference control for improving transient response of controlled systems using PID controller. *Int. J. Artif. Intell.* **10**(13), 88–111 (2013)
29. Jafarnejadsani, H., Pieper, J., Ehlers, J.: Adaptive control of a variable-speed variable-pitch wind turbine using radial-basis function neural network. *IEEE Trans. Control Syst. Technol.* **21**(6), 2264–2272 (2013)
30. Hull, D.G.: *Fundamentals of Airplane Flight Mechanics*. Springer, Berlin (2007)
31. Rudin, W.: *Principles of Mathematical Analysis*. McGraw-Hill Inc., New York (1976)
32. Sontag, E.: *Mathematical Control Theory: Deterministic Finite Dimensional Systems*. Springer, New York (1998)